

Qing Li
Yiu-Wing Mai *Editors*

Biomaterials for Implants and Scaffolds

Springer Series in Biomaterials Science and Engineering

Volume 8

Series editor

Prof. Min Wang

Department of Mechanical Engineering

The University of Hong Kong

Pokfulam Road, Hong Kong

e-mail: memwang@hku.hk

Aims and scope

The Springer Series in Biomaterials Science and Engineering addresses the manufacture, structure and properties, and applications of materials that are in contact with biological systems, temporarily or permanently. It deals with many aspects of modern biomaterials, from basic science to clinical applications, as well as host responses. It covers the whole spectrum of biomaterials – polymers, metals, glasses and ceramics, and composites/hybrids – and includes both biological materials (collagen, polysaccharides, biological apatites, etc.) and synthetic materials. The materials can be in different forms: single crystals, polycrystalline materials, particles, fibers/wires, coatings, non-porous materials, porous scaffolds, etc. New and developing areas of biomaterials, such as nano-biomaterials and diagnostic and therapeutic nanodevices, are also focuses in this series. Advanced analytical techniques that are applicable in R & D and theoretical methods and analyses for biomaterials are also important topics. Frontiers in nanomedicine, regenerative medicine and other rapidly advancing areas calling for great explorations are highly relevant.

The Springer Series in Biomaterials Science and Engineering aims to provide critical reviews of important subjects in the field, publish new discoveries and significant progresses that have been made in both biomaterials development and the advancement of principles, theories and designs, and report cutting-edge research and relevant technologies. The individual volumes in the series are thematic. The goal of each volume is to give readers a comprehensive overview of an area where new knowledge has been gained and insights made. Significant topics in the area are dealt with in good depth and future directions are predicted on the basis of current developments. As a collection, the series provides authoritative works to a wide audience in academia, the research community, and industry.

More information about this series at <http://www.springer.com/series/10955>

Qing Li • Yiu-Wing Mai
Editors

Biomaterials for Implants and Scaffolds

 Springer

Editors

Qing Li
School of Aerospace, Mechanical
& Mechatronic Engineering
The University of Sydney
Sydney, NSW
Australia

Yiu-Wing Mai
School of Aerospace, Mechanical
& Mechatronic Engineering
The University of Sydney
Sydney, NSW
Australia

ISSN 2195-0644

ISSN 2195-0652 (electronic)

Springer Series in Biomaterials Science and Engineering

ISBN 978-3-662-53572-1

ISBN 978-3-662-53574-5 (eBook)

DOI 10.1007/978-3-662-53574-5

Library of Congress Control Number: 2016960306

© Springer-Verlag GmbH Germany 2017

This work is subject to copyright. All rights are reserved by the Publisher, whether the whole or part of the material is concerned, specifically the rights of translation, reprinting, reuse of illustrations, recitation, broadcasting, reproduction on microfilms or in any other physical way, and transmission or information storage and retrieval, electronic adaptation, computer software, or by similar or dissimilar methodology now known or hereafter developed.

The use of general descriptive names, registered names, trademarks, service marks, etc. in this publication does not imply, even in the absence of a specific statement, that such names are exempt from the relevant protective laws and regulations and therefore free for general use.

The publisher, the authors and the editors are safe to assume that the advice and information in this book are believed to be true and accurate at the date of publication. Neither the publisher nor the authors or the editors give a warranty, express or implied, with respect to the material contained herein or for any errors or omissions that may have been made.

Printed on acid-free paper

This Springer imprint is published by Springer Nature

The registered company is Springer-Verlag GmbH Germany

The registered company address is: Heidelberger Platz 3, 14197 Berlin, Germany

Preface

Contemporary biomaterials signify a class of synthesised materials to replace or support lost/damaged living tissues for restoring proper functionality. Over the past few decades, biomaterials have made enormous impacts on improvement of quality of life for millions of patients. Many leading causes of death, such as cardiovascular diseases, cancer, musculoskeletal trauma and injury, etc., have been alleviated by using substitutive biomaterials devices. Strong motivation to further advance healthcare and lower socioeconomic burden has continuously fuelled new breakthrough and innovation of biomaterials, making it one of the most exciting fields of research recently. The latest generation of biomaterials encompasses interdisciplinary sciences and cutting-edge technologies in materials, medicine, cellular and molecular biology, biochemistry, nanotechnology, multiscale modelling, advanced design and biomanufacturing, largely expanding materials knowledge and broadening biomedical applications.

Biomaterials have seen fast growth in two major areas on implantable prostheses and scaffold tissue engineering. Traditional implants aim to replace or support damaged and/or lost tissues, and as substituted, implanted devices stay with the living system temporarily or permanently. Rapid increase of implant recipients and life expectancy has been stimulating continuous inventions of new implant materials and novel treatment protocol. Modern implantable biomaterials, such as alloys, polymers and composites, possess enhanced mechanical, chemical and biological properties, enriched functionality and augmented biomedical performance, allowing them to be tailored in a particular application and for a specific patient. As a class of bio-products, implants have now evolved into a mature industry that employs more than 300,000 people and counts for over US\$200 billion revenue globally.

By contrast, tissue engineering provides a relatively new therapeutical strategy to generate functional tissues or organs for the human body. As a fast emerging interdisciplinary area, tissue engineering offers great promise in solving the issue of significant shortage of organs or tissues facing healthcare nowadays. A landmark of tissue engineering has been the development of scaffolds, which use structured

biomaterials to guide cells to generate neotissue under proper conditions. The current status of tissue engineering bears an overwhelming resemblance to that of implants in the 1970–1980s. The concept of repair or replacing with regenerated tissues/organs is being widely accepted in medical fields, and the demand has been becoming surprisingly high. It is for this reason that the biomedical industry is spawning a new revolution at present, where tissue engineering is rendering the next generation of implants that offers enormous potential to healthcare.

While being used for different therapeutical strategies, implants and tissue scaffolds share considerable commonality from a biomaterials perspective. First, biomaterials remain a central vehicle in both treatments by enabling materialised devices to interact with biological systems properly. Second, they both necessitate certain mechanical, chemical and physical properties of materials for support of and integration with surrounding tissues. Third, the boundary between them is becoming less distinguishable as witnessed by the developments of implants that are porous and degradable as well as scaffolds that are non-degradable for various treatment applications. In this book, we introduce the critical issues and challenges of biomaterials for both implants and tissue scaffolds.

This volume comprises 14 chapters with the balanced foci on both implantable and scaffolding biomaterials, each part consisting of 7 chapters. Just as the nature of biomaterials per se, the expertise of the authors in this book spans from a wide range of disciplines, including materials science, biochemistry, nanotechnology, biomedical engineering and clinical sciences. For understanding the sophistication of biomaterials development, the methodologies outlined in this volume range from computational modelling and design analysis (in silico), fabrication and laboratory tests (in vitro) to animal and human trials (in vivo). Each chapter offers a succinct but comprehensive discussion of fundamental concepts, research approaches and scientific data relevant to a particular area of applications, such as orthopaedics, prosthetic dentistry, interventional cardiology, vascular system and hard and soft tissue regeneration, while it is more a material-orientated, rather than application-orientated, volume.

For better understanding on the interaction of implants or scaffolds with hosting tissue, Chap. 1 introduces multiscale modelling of musculoskeletal tissues through micro-CT images, which provides an effective approach to analysing osseointegration of implants and bone ingrowth in scaffold. The comprehensions of structural details of tissues would potentially help optimise implant morphology and scaffold microstructures for creating a desired microenvironment. To surgically place an implant or scaffold to its host site in vivo, drilling or sectioning of bone or other tissues is often required. Chapter 2 introduces a computational procedure for modelling the insertion process of dental implant, allowing the assessment of the initial outcome of implantation by quantifying the biomechanical responses of bone, aiming to improve implantation surgery for short- and long-term outcomes.

Metals and alloys, as the most common constitutive materials for implants, have been long used and extensively studied. The latest progress seen in this area includes surface modification for promoting osseointegration. Chapter 3 proposes a novel mechanobiological framework for multiscale analysis and topographical

design of implant *in silico*. Following this, Chap. 4 discusses different treatment techniques for desired surface properties and further describes cellular and molecular responses to surface topography and surface chemistry through the *in vitro* and *in vivo* studies.

Bioglass and ceramic materials have been widely used in prostheses, implants and scaffolds for their desired biocompatibility and mechanical properties. Chapter 5 provides a comprehensive overview in the advances in bioglass and glass ceramics from a materials perspective, which portrays the effects of different constituents, synthesis approaches as well as biochemical and biomechanical properties with an outline of broad clinical applications. Chapter 6 describes a specific application of glass ceramics in prosthetic dentistry, where *in situ* preparation and clinical resurfacing of glass ceramic prosthesis are studied through multiscale analyses *in vitro* and *in silico*, aiming to provide an in-depth understanding of their mechanical behaviours when delivering such materials to clinical use. Chapter 13, on the other hand, introduces bioglass to tissue engineering by developing novel bioactive scaffolds with multifunctional properties and desired nano-/microstructural features. It also explores the additive manufacturing approach for fabricating bioglass-based scaffolds. The *in vitro* and *in vivo* studies exemplify the capacity and advantages of such materials in tissue regeneration.

Polymer signifies another class of important biomaterials which have been extensively used in both implants and scaffolds. Polymer has been seen as a trend to replace metals and ceramics in many biomedical applications attributable to its versatility and flexibility in physical and chemical properties. Chapter 7 depicts two key applications of polymeric composites in arterial stents and tissue scaffolds. Arterial stents have been traditionally metal dominated, and the introduction of polymeric materials in this field has shown considerable potential for rendering the next generation of stents. Polymeric scaffolds featured in this chapter cover several important aspects of materials, microstructures, fabrication and *in vitro* and *in vivo* studies. Chapters 8 and 9 introduce the electrospinning technologies, further demonstrating the versatility of polymer materials in tissue engineering. Chapter 8 concentrates on biomechanical and biochemical properties of electrospun polymer scaffolds with a broad range of applications, such as bone. Chapter 9 focuses on tailoring materials properties specifically for soft tissue regeneration, such as wound healing. Chapter 10 explores differently structured polymeric scaffolds for periosteum tissue engineering, further demonstrating the flexibility for compositional and structural design. Chapter 14 also outlines the applications in cartilage tissue engineering. Following these *in vitro* and *in vivo* studies, Chap. 12 provides a series of computational design approaches for optimising scaffold structures made of polymers or other biomaterials, in which tissue ingrowth is modelled to predict the outcome *in silico*.

Hydrogel has seen extensive applications in tissue engineering in recent years for its compelling chemical and biological properties. Chapter 11 outlines the characterisation procedures of hydrogel scaffolds and provides some important biomechanical data through monotonic and fatigue tests. The damage assessment methods outlined in this chapter enable further understanding of scaffolding

behaviours of the materials. Chapter 10 discusses the role of co-deposited hydrogel in polymeric scaffolds for periosteum tissue regeneration. Chapter 14 provides an overview in a range of naturally derived and synthesised injectable hydrogels for scaffold cartilage tissue engineering with substantial *in vitro* and *in vivo* data.

The book is expected to be of interest to the readers who are willing to become familiar with biomaterials knowledge and research methodologies for broad implant and/or scaffold applications. The style and language used in this book are intended to appeal to senior students, practising engineers and materials and biomedical scientists from a diverse background in materials synthesis and cellular and molecular studies to computational biomechanics. Substantial overviews are also provided for better appreciation to the background and progress in the field.

The book would not be possible without the tremendous contributions from all the authors, who are recognised experts and active researchers in the related fields. To them we sincerely apologise for the lengthy delay in seeing their manuscripts in print after rigorous reviews and final revisions. We would like to particularly thank Professor Min Wang, the series editor of Springer, of the University of Hong Kong for giving us this excellent opportunity and technical guidance to edit this volume. We would also like to extend our gratitude to the Springer Beijing Office, especially Ms June Tang and Mr Heather Feng, for their patience and professional work during the entire process of publication.

Sydney, Australia
March 2016

Qing Li
Yiu-Wing Mai

Contents

1	Multiscale Modelling and Simulation of Musculoskeletal Tissues for Orthopaedics	1
	Clayton J. Adam	
2	Performance Evaluation of Bone–Implant System During Implantation Process: Dynamic Modelling and Analysis	45
	Rudi C. van Staden, Hong Guan, Newell W. Johnson, and Yew-Chaye Loo	
3	Multiscale Remodelling and Topographical Optimisation for Porous Implant Surface Morphology Design	71
	Wei Li, Junning Chen, Chaiky Rungsiyakull, Michael V. Swain, and Qing Li	
4	Implant Surface Modifications and Osseointegration	107
	Nishant Chakravorty, Anjali Jaiprakash, Saso Ivanovski, and Yin Xiao	
5	Advances in Bioglass and Glass Ceramics for Biomedical Applications	133
	Besim Ben-Nissan, Andy H. Choi, and Innocent Macha	
6	Clinical Resurfacing of Feldspar and Leucite Glass Ceramics Using Dental Handpieces and Burs	163
	Ling Yin, Xiao-Fei Song, and Richard Stoll	
7	Polymer Blends and Composites for Biomedical Applications	195
	S.T. Lin, L. Kimble, and D. Bhattacharyya	
8	Electrospun Polymer Scaffolds: Their Biomedical and Mechanical Properties	237
	Gui-Ying Liao, Xing-Ping Zhou, Xiao-Lin Xie, and Yiu-Wing Mai	

9	Electrospun Nanofibrous Scaffolds for Soft Tissue Regeneration	271
	Dave Wei-Chih Chen and Shih-Jung Liu	
10	Biomimic Design of Periosteum: Construction Strategies, Scaffold Design and Cell Sources	303
	Yin Xiao, Wei Fan, Ross Crawford, and Dietmar W. Hutmacher	
11	Characterisation of Hydrogel Scaffolds Under Compression	319
	J. Tong, Y.-H. Hsu, K. Madi, A. Cossey, and A. Au	
12	Computational Design for Scaffold Tissue Engineering	349
	Che-Cheng Chang, Yuhang Chen, Shiwei Zhou, Yiu-Wing Mai, and Qing Li	
13	Bioactive Scaffolds with Multifunctional Properties for Hard Tissue Regenerations	371
	Chengtie Wu, Jiang Chang, and Yin Xiao	
14	Challenges for Cartilage Regeneration	389
	Fariba Dehghani and Ali Fathi	

Contributors

Clayton J. Adam School of Chemistry, Physics and Mechanical Engineering, Faculty of Science and Engineering, Queensland University of Technology, Brisbane, Australia

A. Au Smith & Nephew, Andover, MA, USA

Besim Ben-Nissan University of Technology, Broadway, NSW, Australia

D. Bhattacharyya Centre for Advanced Composite Materials, The University of Auckland, Auckland, New Zealand

Nishant Chakravorty Institute of Health & Biomedical Innovation, Queensland University of Technology, Brisbane, QLD, Australia

Che-Cheng Chang School of Aerospace, Mechanical & Mechatronic Engineering, The University of Sydney, Sydney, NSW, Australia

Jiang Chang State Key Laboratory of High Performance Ceramics and Superfine Microstructure, Shanghai Institute of Ceramics, Chinese Academy of Sciences, Shanghai, People's Republic of China

Dave Wei-Chih Chen Chang Gung Memorial Hospital, Taoyuan City, Taiwan

Junning Chen School of Aerospace, Mechanical & Mechatronic Engineering, The University of Sydney, Sydney, NSW, Australia

Yuhang Chen School of Engineering & Physical Sciences, Mechanical, Process & Energy Engineering, Heriot-Watt University, Edinburgh, UK

Andy H. Choi University of Technology, Broadway, NSW, Australia

A. Cossey Spire Portsmouth Hospital, Portsmouth, UK

Ross Crawford Institute of Health and Biomedical Innovation, Queensland University of Technology, Kelvin Grove, QLD, Australia

Fariba Dehghani School of Chemical and Biomolecular Engineering, The University of Sydney, Sydney, Australia

Wei Fan Institute of Health and Biomedical Innovation, Queensland University of Technology, Kelvin Grove, QLD, Australia

Ali Fathi School of Chemical and Biomolecular Engineering, The University of Sydney, Sydney, Australia

Hong Guan Griffith School of Engineering, Griffith University, Nathan, QLD, Australia

Y-H Hsu School of Engineering, University of Portsmouth, Portsmouth, UK

Dietmar W. Hutmacher Institute of Health and Biomedical Innovation, Queensland University of Technology, Kelvin Grove, QLD, Australia

Saso Ivanovski School of Dentistry and Oral Health, Griffith Health Institute, Griffith University, Gold Coast, QLD, Australia

Anjali Jaiprakash Institute of Health & Biomedical Innovation, Queensland University of Technology, Brisbane, QLD, Australia

Newell W. Johnson Menzies Health Institute Queensland, Griffith University, Nathan, QLD, Australia

L. Kimble Centre for Advanced Composite Materials, The University of Auckland, Auckland, New Zealand

Qing Li School of Aerospace, Mechanical & Mechatronic Engineering, The University of Sydney, Sydney, NSW, Australia

Wei Li School of Aerospace, Mechanical & Mechatronic Engineering, The University of Sydney, Sydney, NSW, Australia

Gui-Ying Liao China University of Geosciences, Wuhan, China

S.T. Lin Centre for Advanced Composite Materials, The University of Auckland, Auckland, New Zealand

Shih-Jung Liu Chang Gung University, Tao-Yuan, Taiwan

Yew-Chaye Loo Griffith School of Engineering, Griffith University, Nathan, QLD, Australia

Innocent Macha University of Technology, Broadway, NSW, Australia

K. Madi School of Engineering, University of Portsmouth, Portsmouth, UK

Yiu-Wing Mai School of Aerospace, Mechanical & Mechatronic Engineering, The University of Sydney, Sydney, NSW, Australia

Chaïy Rungsiyakull School of Aerospace, Mechanical & Mechatronic Engineering, The University of Sydney, Sydney, NSW, Australia

Xiao-Fei Song School of Mechanical Engineering, Tianjin University, Tianjin, China

Richard Stoll College of Medicine and Dentistry, James Cook University, Cairns, QLD, Australia

Michael V. Swain School of Aerospace, Mechanical & Mechatronic Engineering, The University of Sydney, Sydney, NSW, Australia

J. Tong School of Engineering, University of Portsmouth, Portsmouth, UK

Rudi C. van Staden College of Engineering and Science, Structural Mechanics and Sustainable Materials Research Group, Victoria University, Melbourne, VIC, Australia

Chengtie Wu State Key Laboratory of High Performance Ceramics and Superfine Microstructure, Shanghai Institute of Ceramics, Chinese Academy of Sciences, Shanghai, People's Republic of China

Yin Xiao Institute of Health & Biomedical Innovation, Queensland University of Technology, Brisbane, QLD, Australia

Xiao-Lin Xie School of Chemistry and Chemical Engineering, Huazhong University of Science and Technology, Wuhan, China

Ling Yin College of Science and Engineering, James Cook University, Townsville, QLD, Australia

Shiwei Zhou Centre for Innovative Structures and Materials (CISM), RMIT University, Melbourne, Australia

Xing-Ping Zhou School of Chemistry and Chemical Engineering, Huazhong University of Science and Technology, Wuhan, China

Chapter 1

Multiscale Modelling and Simulation of Musculoskeletal Tissues for Orthopaedics

Clayton J. Adam

Abstract Successful development of implants for orthopaedic surgical procedures depends on a comprehensive understanding of the interaction between implant biomaterials and the host tissues of the musculoskeletal system. Mechanical factors are a key part of this interaction. This chapter investigates the potential of computational modelling and simulation approaches at multiple length scales to elucidate the response of musculoskeletal tissues to orthopaedic implants, leading to improved treatment outcomes. To a large extent, musculoskeletal tissues derive their load-bearing function from their hierarchically arranged structure; therefore we pay particular attention to modelling of the musculoskeletal tissues themselves from the nano- and micro-scales to the macro-scale. The most well-characterised musculoskeletal tissue are bone, and this chapter covers recent work on micro- and nanoscale modelling of bone and collagen and on defining the elasto-plastic constitutive response of the bone extracellular matrix using finite element models of bone nanoindentation combined with atomic force microscopy to map the inelastic deformation of the tissues. The use of serial milling and block face imaging techniques to determine soft tissue anatomy at multiple length scales for definition of model geometry is also covered. The potential for further development of multiscale computational biomechanics through modelling cell and tissue mechanobiology is discussed, including more detailed mechanical characterisation of the tissue–implant interface, modelling the strain fields experienced by cells within the extracellular matrix and within scaffolds and coupled modelling of other physical and biological phenomena within tissues and biomaterials.

Keywords Biomechanics • Computational mechanics • Elasto-plastic constitutive model • Extracellular matrix • Finite element method • Mechanobiology • Multiscale modelling • Nanoindentation • Orthopaedic implant

C.J. Adam (✉)

School of Chemistry, Physics and Mechanical Engineering, Faculty of Science and Engineering, Queensland University of Technology, GPO Box 2434, 2 George St, Brisbane Q4000, Australia

e-mail: c.adam@qut.edu.au

1.1 Introduction

In the same way that computational mechanics has revolutionised the design and analysis of manufactured objects in many industries, the rapidly growing subfield of computational biomechanics (CB) offers much promise in using modelling and simulation to better understand degenerative processes in the musculoskeletal system and to improve orthopaedic treatments for musculoskeletal disorders. Since the function of the musculoskeletal system is predominantly a load-bearing one, it follows that the mechanics of interaction between an implant and its surrounding host tissues are of key importance in the design of orthopaedic implants and surgical procedures. This holds true both at the scale of whole bones, joints and implants (here designated the macro-scale) and at the micro- and nanosized scales of the implant surface and its mechanical interaction with hierarchically structured host tissues. From a biological perspective, the microenvironment within tissues and at the interface between tissues and implants is extremely important because this is the scale at which cells sense and respond to mechanical signals to control gene expression for tissue growth, repair and remodelling.

A key advantage of mechanics-based modelling in orthopaedic biomechanics is the ability to model many different design variants of an implant, with the aim of finding optimal design characteristics of that implant. This would be impossible in human trials and would be prohibitively time consuming and expensive in either *in vitro* or *in vivo* animal studies. Models also allow the same implant design to be simulated following virtual placement into a wide variety of different patients. A third possibility in computational biomechanics, and the focus of this chapter, is the ability to model biomechanical processes over a range of length and timescales, providing insights into the coupling between macro-scale loading and the micro- and nano-mechanical processes occurring within the tissues themselves. These micro- and nanoscale physical processes are the drivers of the biological response to mechanical loading and therefore affect the responses of the musculoskeletal system to orthopaedic implants. To date, cell-mediated processes such as tissue modelling and remodelling have been treated phenomenologically in macro-scale simulations of tissue response to implants; however, modelling at finer scales has the potential to provide a deeper physics-based mechanistic understanding of tissue response to loading.

With these considerations in mind, this chapter highlights the use of biomechanical modelling and simulation approaches to investigate the loading response of musculoskeletal tissues and orthopaedic implants at multiple scales. It is important to note that although the biomaterials used in an orthopaedic implant may themselves be intricate in geometry and surface topography, the much greater challenge is modelling host tissue responses to loading, because natural tissues are much more sophisticated than their synthetic replacements [1]. Therefore the focus of this chapter is on modelling of tissues as ‘natural biomaterials’ rather than modelling the metals, polymers and ceramics used for implants or scaffolds. Furthermore, the focus here is on the passive osseoligamentous tissues, bone, cartilage, ligament and

tendon, i.e. excluding the muscle. While many of the considerations that follow are also relevant to muscle, its active contractile force-generating ability introduces additional complexities in modelling which are beyond the scope of this discussion.

It is also important to note that due to the complexities of modelling living tissues [2,3] and the resulting nascent (although rapidly developing) state of multi-scale modelling in the musculoskeletal system, the use of the term ‘multiscale’ here does not carry the same emphasis on bridging between scales and on algorithms and strategies for the concurrent solution of multiscale problems as in some other literature on the topic. The focus here can be expressed in terms of firstly a recognition that scales other than the macro-scale (which has been the scale mostly modelled in orthopaedic biomechanics) are important, especially when attempting to model the biological response, and secondly a consideration of how to define models at these other scales of interest, including what information is required at each scale and how this information might be obtained using existing imaging and measurement technologies. Scale bridging is clearly an important consideration in tissue modelling [4], but must necessarily come after efforts to define and model the scales of relevance for cellular and extracellular matrix loading response.

1.1.1 Orthopaedic Implants and Treatment Outcomes

The aim of orthopaedic surgery is to correct problems which arise in the human musculoskeletal system. Disorders of the musculoskeletal system are a major contributor to the global burden of disease, and there is intense interest in developing new treatments for musculoskeletal disease. In childhood, bone deformities during growth can require major corrective surgery. In adults, disorders such as osteoarthritis and intervertebral disc degeneration cause immobility, pain and lost productivity. In the elderly, osteoporosis causes increased fracture risk with subsequent loss of mobility and high mortality rates after a fracture. At all ages, cancer, trauma and infectious disease can lead to bone, joint and soft tissue destruction.

The dominant paradigm in orthopaedic practice today is the use of non-biodegradable implants which may have various surface treatments or coatings applied to enhance osseointegration with host bone (Fig. 1.1), although we note that there is also intensive research underway in the field of tissue engineering, in which the implanted load-bearing structure is in fact a temporary scaffold which is designed to resorb in the body and eventually be replaced by host tissue.

The course of degeneration of musculoskeletal tissues is itself a topic of intense research, because prevention of bone and joint diseases with conservative treatments is a preferable goal to surgical procedures. However, at present there are no effective conservative treatments for musculoskeletal disorders such as osteoarthritis, degenerative disc disease and progressive spinal deformity, so that arthrodesis (joint immobilisation) and arthroplasty (joint replacement) using implants are the only treatment options in progressive cases. Orthopaedic procedures are expensive and invasive; therefore once the decision has been made to operate, it is crucial that

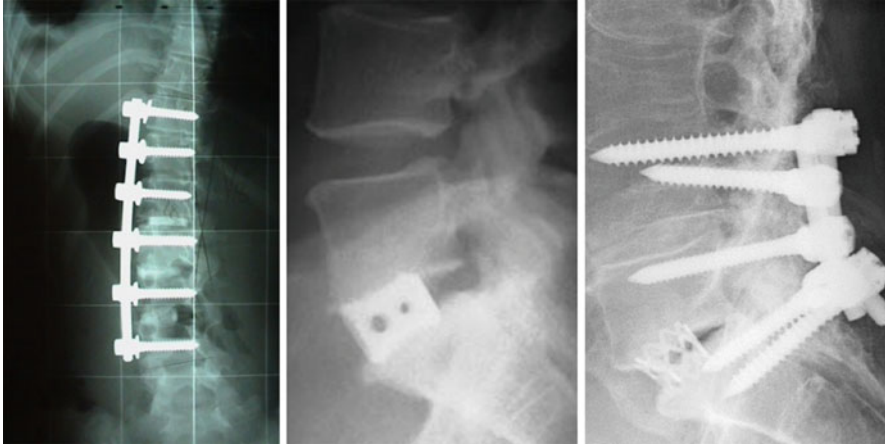


Fig. 1.1 Orthopaedic implants used in spinal surgery. In each case, significant rates of implant loosening are reported in the literature; (*left*) single anterior rod for scoliosis correction, (*centre*) anterior lumbar interbody fusion implant, (*right*) pedicle screw and posterior rod fusion construct with anterior interbody spacer in the L5-S1 disc space

the design of the surgical intervention (including the implant) is optimal to achieve the desired corrective outcome. From a structural point of view, orthopaedic surgery represents an interesting challenge, because the aim is to instantaneously correct a biological structure which has been degenerating over years or even decades and which will continue to adapt to the newly placed surgical implant for several years after the operation. The challenge is to ensure successful integration of the implant with host tissues after surgery so that joint stability and/or function is restored.

While some orthopaedic surgical procedures have a high success rate (most notably hip and knee replacement), there are other disorders for which procedures involving implant placement are risky and the postoperative response of the implant constructed within the host tissue environment is poorly understood. For example, previous studies have shown that bone resorption around implants is a potential cause of loosening following surgery [5] and that when loosening occurs, failed bone fusion is more likely to be the result [6]. In the field of orthopaedic spine surgery, a meta-analysis covering 82 studies and 5780 procedures for scoliosis treatment by Hawes and O'Brien [7] revealed an overall complication rate of 20 %, with nine of the studies in the meta-analysis reporting complication rates of 40 % or higher.¹

¹We note that it is not possible to deduce from this meta-analysis which of the complications were directly implant related or which were due to other causes.

1.1.2 Load-Bearing Tissues of the Musculoskeletal System

Derived from the embryonic mesoderm, the human musculoskeletal system is a complex assembly of 206 bones, 360 joints and 640 muscles. The role of the musculoskeletal system is mechanical, exerting and bearing the forces associated with movement and body weight. Each of the tissues in the musculoskeletal system is exquisitely adapted to its particular mechanical role. The bone achieves lightweight stiffness and strength through a hierarchical assembly of mineralised collagen fibres, built from the nanoscale up [8]. In addition to its mechanical role, the bone also acts as a calcium reservoir and a host for bone marrow. The ligaments which connect one bone to another are tough, collagenous tension-bearing structures with nonlinear force versus stretch characteristics, and variable elastic energy storage capacity according to their biomechanical role is conferred by the presence of elastic fibres together with the collagen [9]. Smooth articulating movement under high contact pressures between adjacent bones occurs between the lubricated sliding surfaces of articular cartilage, which is comprised of a network of graduated zones of self-assembled type II collagen fibres pre-stained by physicochemical swelling of hydrophilic proteoglycan molecules within the network [10]. The intervertebral discs of the spine are the largest avascular structures in the body, resisting forces of up to nine times the body weight, and are comprised of a series of annular rings of collagenous fibres criss-crossed in alternating orientations, surrounding a gel-like inner nucleus pulposus which is pressurised to about 70kPa due to pre-stretch in the ligamentum flavum within the annular outer layers [11]. The skeletal muscle is comprised of a repeated hierarchical assembly of actin and myosin fibres again held in place by a collagen network (the endomysium) [12]. The muscles are attached to the bone via flexible tendons. The tendon is a tough and resilient collagenous tissue with a highly aligned longitudinal fibrous structure which allows transmission of high forces from the muscles to their bony attachment points [13].

At the microstructural level, the defining characteristic of musculoskeletal tissues is their dense, tough extracellular matrix (ECM) comprised of hierarchically assembled fibrous proteins. The ECM is built and maintained by a network of living cells both within the tissue and on its surface. Cellular activity is in turn controlled by soluble signaling molecules, as well as by biophysical and biochemical signals from the ECM itself, so that the ECM acts as both a substrate for cell attachment and a signaling source to control cell activity [14]. Within this general framework, musculoskeletal tissues exhibit a diverse range of morphologies and mechanical properties specifically adapted for their structural role, and tissue adaptation to changing loading conditions occurs throughout the lifespan.

The general form of this adaptation response in skeletally mature adults is an increase in ECM density and size (hypertrophy) in response to increased mechanical load and loss of ECM (atrophy) in regions of decreased loading. For example, it is well known that rapid bone loss occurs during extended bed rest and space flight or on a local scale adjacent to a stiff, metallic load-bearing implant after

surgical implantation [15–18]. The change in ECM composition in response to increased loading is achieved through cell-mediated ‘remodelling’, in which damaged ECM is resorbed [19] and new ECM is deposited by cells. Because highly loaded tissues, such as the ligament, tendon and the intervertebral disc, are avascular (presumably for reasons of structural integrity and limitations on blood flow in the presence of high hydrostatic ECM stresses), cellular repair and remodelling activity must rely on nutrient and oxygen diffusion through dense ECM, so that healing responses can be slow.

The hierarchical structure of musculoskeletal tissues has been defined according to various schemas [20–22]. For simplicity here we adopt a three-level nomenclature as follows: the term ‘nanoscale’ is used when referring to either anatomical structures or computational models of these structures with characteristic dimensions of less than 1 μm ; ‘micro-scale’ covers the range 1–100 μm ; and ‘macro-scale’ refers to structural features and characteristic element dimensions above 100 μm . We note that other authors have defined ‘meso-scales’ as intermediate levels between other scales; however, due to the variability in the usage of the term, we avoid it here.

1.2 Macro-scale Modelling in Orthopaedic Biomechanics

In any mathematical model, the aim is to capture the salient features of the system being modelled using as simple a representation of the system as possible. Overly complicated models incur computational expense and the required input data may not be available, while overly simplistic models miss important features of system response. In structural mechanics, spatiotemporal representations of the structure are usually defined and solved using the finite element (FE) method, and so in what follows we are referring to FE modelling unless otherwise stated. In orthopaedic biomechanics, the starting point is often a ‘top-level’ whole bone/joint/implant FE model where the surgical procedure is simulated under quasi-static loading using relatively simple material constitutive properties. The geometry of bones and joints is not known a priori; therefore, the ability to prescribe model geometry is dependent on state-of-the-art scanning and imaging technologies.

1.2.1 3D Imaging and Medical Image-Based Modelling

Since the geometries of musculoskeletal tissues are not known in advance, three-dimensional biomechanical models rely on digital data from scanners. At present, clinical whole-body computed tomography (CT) and magnetic resonance imaging (MRI) scanners are limited to maximum resolutions of approximately 250 μm . These resolutions are usually sufficient to define macrostructure, although we note that they may be only marginally acceptable when defining the thickness of certain

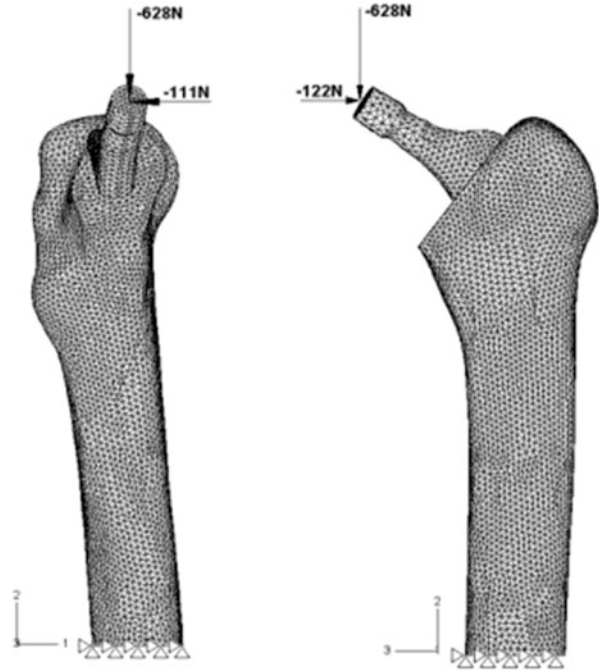
anatomical structures such as the cartilage in articulating joints or the cortical wall in the spinal vertebrae. Also, scans for clinical purposes are usually performed at lower resolution than this and do not usually involve 3D acquisition protocols, necessitating special ‘research scans’ to obtain submillimetre voxel dimensions in 3D. In the case of CT scans of the bone, voxel sizes of several hundred microns are one or two orders of magnitude coarser than the resolution needed to represent tissue microstructure. Therefore, the top-level models of bones and joints derived from medical image datasets are limited to macro-scale.

There are several possible approaches to geometric generation of macro-scale models and FE meshing from 3D medical image datasets; image voxels can be directly converted into hexahedral finite elements; or the surface of an implant or organ can be calculated using image processing techniques, which then forms the boundary of a solid that is meshed using volumetric meshing techniques (e.g. [23]). Mesh matching between implants and surrounding host tissues is an important part of model generation; and various approaches have been proposed to ensure mesh compatibility across tissue–implant interfaces [24] (Fig. 1.2). Even at the macro-scale, models based on medical scan image data can be too complex to solve using current computational power. For example, a voxel-based FE model of a whole femur with 0.25-mm voxel size would contain in the order of 15 million hexahedral elements.

1.2.2 Continuum Representation of Tissues and Constitutive Relations

In such macro-scale models, the structure being modelled is the bone, joint or implant in question, and the tissues are treated as continua. This top-down, ‘organ equals structure, tissue equals continuum material’ approach has been widely used in orthopaedic biomechanics [25]. Using this approach, mechanical property characterisation for each ‘material’ (the cortical bone, trabecular bone, cartilage, ligament, tendon) can be performed using either direct experimental measurements (e.g. a four-point bending test of a sample of cortical bone) or inverse characterisation where, for example, an FE model of a complex bone anatomy is built and then the material properties in the model are iteratively adjusted to obtain agreement with the experiment. In this approach, the effects of the hierarchical structure and inhomogeneity of the tissues at scales below that of the geometry being modelled are ‘built into’ the material properties in a statistical sense. Furthermore, a degree of material inhomogeneity can be introduced (at least for the bone) by taking advantage of the effect of bone density on X-ray beam attenuation, so that radiographically derived bone models can be assigned specimen-specific inhomogeneous material properties based on the greyscale values of each voxel in the CT scan used to build the model.

Fig. 1.2 Macro-scale FE model of a hip replacement implant showing applied loads and boundary conditions. The outer cortical bone of the femur, inner cancellous bone, poly (methyl methacrylate) bone cement and implant are each modelled using different sets of homogeneous material properties (From [24], used with permission)



Although it is well known that musculoskeletal tissues exhibit nonlinear stress–strain phenomena such as creep, rate dependence and hyperelasticity, many models use linear elastic (isotropic or orthotropic) material properties for bone and cartilage, and tendons and ligaments are sometimes modelled as linear or nonlinear springs with properties defined from *in vitro* tensile tests [26]. Assumptions of linearity enable much faster computational solutions (since the stiffness matrix need only be assembled and inverted once); however, they are also valid over a limited range of tissue responses. To provide just one example, it is well known that relaxation of surrounding tissues after orthopaedic implant insertion can cause large decreases in the loading experienced by the implant after surgery [27]. Such time-dependent, nonlinear behaviour is missed by linear quasi-static material constitutive models. Of course it is a matter of engineering judgement as to the importance of including such behaviours in macro-scale models of tissue–implant interaction. Having said this, a large body of work has also been performed on the development of nonlinear, macro-scale continuum constitutive relations for musculoskeletal tissues. Detailed coverage of all the constitutive relations which have been developed and employed is beyond the scope of this chapter; however, in light of the focus on trabecular bone in Sect. 1.3, we note that Carretta et al. [28] provide a useful overview of apparent-level constitutive models developed for trabecular bone.

Having defined macro-scale geometry and material properties, prescription of loads and boundary conditions must be applied. Due to the difficulties of direct load

measurement in living humans, rigid body dynamics approaches have been used in conjunction with clinical or laboratory data to estimate loads during various postoperative activities. Here the musculoskeletal system is represented mathematically as an assembly of structural elements (beams, struts, springs and joints) in which forces generated by the muscles acting against gravity and body mass generate motion. Solving the inverse problem, in which motion is known (using motion tracking systems), allows calculation of internal forces² which can in turn be used as inputs to the macro-scale continuum FE models. In more trivial cases than gait, simple statics calculations may provide a reasonable estimate of the loads on the musculoskeletal system for input to macro-scale FE models. In a few cases, *in vivo* loads have been directly measured using strain gauges or pressure needles during daily activities, thus providing useful reference data for biomechanical models [29–31].

1.2.3 Phenomenological Treatment of Biological Processes

So far, nothing has been said regarding the main distinguishing feature of musculoskeletal tissues, that they are *living* structural entities. Tissues grow, remodel and self-heal over the course of an organism's lifespan. These behaviours are characteristic of a complex living biological system. The primary function of a musculoskeletal tissue may indeed be load bearing, but the means by which these tissues are built and adapted to the changing environment of an organism over a lifetime involves cell-mediated physiological processes of great complexity.

In recent years the role of mechanical loading in governing tissue growth and remodelling has been increasingly studied. This research field at the interface of mechanics and biology has been coined 'mechanobiology' and is an active field with particular interest in understanding how cells transduce mechanical signals. The use of spatiotemporal modelling in mechanobiology spans both phenomenological macro-scale continuum descriptions of tissue remodelling and differentiation and micro-scale simulations (discussed further in Sect. 1.3.1) designed to provide greater insight into the cellular processes behind tissue growth and remodelling. An example of a macro-scale mechanobiological model is the incorporation of 'Frost's mechanostat' [32] into a trilinear model to simulate bone response to altered loading around an orthopaedic implant after insertion. Such models are solved iteratively by defining bone density as a state variable and iteratively increasing density in regions of high strain energy and decreasing it in regions of low strain energy (e.g. [33]). Elastic properties are in turn defined as a

²Even in this supposedly simple case of modelling the body as a multi-jointed mechanism, modelling uncertainties abound: muscle lines of action are complex and involve wrapping and contact with other muscles; joints are polycentric, the axis of rotation changing with the degree of rotation. Intra-abdominal pressure affects trunk stiffness, and muscle activation strategies vary during repeated performance of the same task.

function of bone density. The resulting models can reproduce aspects of the radiographically observed remodelling response around the implant following insertion [34].

Another example of phenomenological modelling of a mechanically mediated biological process is the differentiation of newly formed tissue in a haematoma (e.g. in a fracture site or adjacent to a newly placed implant) into various mature tissue types according to the stress or strain state in the callus tissue. Several groups have developed empirically based mechanobiological FE models to describe the differentiation of newly formed tissue into different types depending on the stress–strain state in the tissue [35–38].

Thus biological processes of growth and remodelling have been incorporated to some extent in top-down continuum models of bones and joints, but the phenomenological relations on which they are based afford little insight into the finer scale biological processes which drive them, and they are therefore of unknown value outside the range of experimental conditions for which they were calibrated.

1.2.4 Rationale for Multiscale Modelling

This issue of phenomenological versus physics-based, mechanistic modelling is at the heart of the question regarding the need for multiscale approaches in modelling tissues and tissue–implant interaction. If a macroscopic model with appropriately defined continuum material properties (in other words a phenomenological relationship which is an adequate statistical representation of the relationship between stress and strain in the tissue without considering the finer scale processes which result in this relationship) can satisfactorily predict the outcomes of a particular implant being inserted, is it necessary to make additional effort to model processes mechanistically at finer spatial or temporal resolution?

The response to this question is that there are a host of processes occurring at the micro- and nanoscales in musculoskeletal tissues which are relevant to tissue–implant interaction and for which a mechanistic³ rather than a purely phenomenological understanding could potentially improve implant design. Biological structures are built and maintained from the bottom-up, not from the top-down [40], and phenomenological rules, such as Frost’s mechanostat, although conceptually useful, represent a simplification of actual growth and remodelling processes. Furthermore, even if a phenomenological model could provide equivalent predictive ability to a mechanistic model across the current problem space, the understanding provided by mechanistic modelling at finer scales may provide new insights into the

³The physics-based, mechanistic models we refer to here are spatio-temporal models, i.e. they represent tissues and implants as structures in three-dimensional space. Pivonka and Komarova [39] provide an overview of other types of (temporal only) mathematical models used in bone biology.

problem which may in turn allow new design paradigms outside of current design space. Finally, phenomenological models calibrated to represent the response of healthy tissues provide no insight into the micro- and nanoscale aspects of disease processes, and similarly empirical tissue responses based on measurements in patients with a particular pathology provide no clues as how to best prevent or treat that pathology from a biological perspective. They tell us ‘what’ without any insight into the ‘how’ or ‘why’ of musculoskeletal mechanobiology.

Having established that micro- and nanoscale processes are crucial in understanding musculoskeletal tissue loading response to implants, we go further and state that computational modelling and simulation have a valuable role to play in elucidating these. Observation and hypothesis testing through laboratory-based experiments and clinical studies are essential, but are also expensive and inherently limited in the range of tissue states and implant designs which can be investigated. Cost and ethical considerations combine to severely limit the scope of *in vivo* (large animal or human) studies on living musculoskeletal tissues relevant to orthopaedics. Small animal (mouse and rat) studies of orthopaedic implant designs are possible and are performed; however, these raise questions regarding the transferability of outcomes across species varying by three orders of magnitude in mass. Therefore modelling and simulation can play a key role in studying micro- and nanostructure aspects of tissue loading response and tissue–implant interaction at various levels of the structural hierarchy.

One way to classify the processes of interest for micro- and nanoscale modelling in orthopaedics is by dividing them into processes related to the extracellular matrix (ECM) and cells, respectively. ECM processes are those micro- and nanoscale activities which govern the response of the implant extracellular matrix construct to loading, including noncellular processes which alter the structure and composition of the ECM in certain ways (e.g. ECM damage or non-enzymatic glycation). The cellular processes are those by which cells mediate the addition or removal of extracellular matrix to change ECM structure during growth and remodelling. Note that in the passive musculoskeletal tissues, the ECM is the key structural element. The cells themselves do not play a significant load-bearing role, rather they act as autonomous agents which sense the conditions within the ECM and modify extracellular matrix structure accordingly. Therefore the mechanics of cell deformation are still of interest, but from the perspective of mechanotransduction of ECM loading and the resulting response. Using this ECM/cell division, some key processes are listed below.

Extracellular matrix physicochemical processes (structural response to load and noncellularly mediated structural modifications)

- Micro- and nanostructural basis of ECM force–displacement response (elasticity and plasticity as well as time-dependent behaviours; creep, viscoelasticity)
- Micro- and nanoscale fracture in the ECM
- Coupled fluid flow and diffusion within the micro- and nanoporosity of ECM

- Physicochemical swelling in proteoglycan-rich tissues as a function of ion concentration
- Piezoelectricity and streaming potentials induced during ECM deformation
- Biomineralisation of bone
- Non-enzymatic glycation

Cellular processes (ECM modifying physicochemical processes)

- ECM synthesis by cells during growth and tissue remodelling
- Mesenchymal cell differentiation according to stress and fluid flow conditions
- ECM self-assembly outside the cell
- ECM resorption via enzymatic digestion
- Membrane strain experienced by cells attached to the ECM
- Fluid flow-induced mechanotransduction by cells within the ECM
- Cell metabolism (nutrient, oxygen and waste product transport to and from cells)
- Intercellular signaling within the ECM

In addition, it is possible to add several more micro- and nanoscale processes specifically related to tissue interaction with an implant.

Implant-related physicochemical processes

- Microscopic damage and wear particle formation from implant surfaces
- Protein adsorption on implant surfaces
- Surface chemistry of implant biomaterials in body fluids

It should be clear from the lists above that the complexity of the micro- and nanoscale processes occurring within tissues is daunting from a modelling perspective. Even if the problem is reduced to solely considering physical structure–function relationships of the ECM (without any cell-mediated matrix modification and without any ECM chemical modification processes such as mineralisation or glycation), then the problem of modelling load–deformation behaviour in a hierarchically arranged, nanostructured, hydrated matrix of biological macromolecules and its interaction with a metallic, polymeric or ceramic implant is highly challenging. Note also that although the extracellular matrix is the key structural element in musculoskeletal tissue response to loading, it is clear from the last four points in the list of cell-mediated processes above that understanding how cells transduce physical signals from the matrix is a vital step in revealing how cells modify the matrix in response to these signals.

In summary, a full understanding of how the body responds to an orthopaedic implant involves multiple lengths and timescales: the macro-scale (that of the whole bone or joint) and its physiological loads, the micro-scale (the level of cells, tissue microarchitecture and implant surface roughness) and the nanoscale (the level of proteins and individual molecules of the implant material). Associated timescales range from years (for tissue growth and remodelling, i.e. the clinical timescale), to hours (for fluid diffusion in musculoskeletal tissues), to seconds (for gait). It is these complexities that necessitate multiscale approaches to the study of

orthopaedic implants, both from experimental and modelling perspectives. Macroscopic studies of orthopaedic implants, whether *in vitro*, *in vivo* or more recently *in silico*, have led to many advances in the development of orthopaedic implants to date, but without coupling a proposed implant design to the micro- and nanoscale processes which occur within the host tissue and at the implant–tissue interface, the macro-scale descriptions of tissue response remain phenomenological, so that proposed new designs (which may depart substantially from the existing designs upon which heuristic ‘rules’ have been developed) cannot be adequately assessed and refined. Similarly, a micro- or nanoscale biological or materials-based approach to implant characterisation can be successful only insofar as it is also cognisant of the macro-scale mechanics of the problem, since it is at this level that the overall forces and motions to which the construct is subjected are determined.

1.3 Micro- and Nanoscale Modelling in Orthopaedic Biomechanics

Having summarised the dominant top-down continuum mechanics paradigm which has been used in much orthopaedic biomechanics modelling to date and pointed out the rationale for multiscale biomechanical modelling in the musculoskeletal system, this section now provides a more detailed overview of existing models of passive musculoskeletal tissues at the micro- and nanoscales. The focus in Sects. 1.3.1–1.3.3 is on trabecular bone, which is chosen for three reasons: (i) because its highly porous and heterogeneous microstructure provides challenges to macro-scale continuum representations, (ii) because it has been intensively imaged and modelled at the micro-scale and (iii) because trabecular bone is a metabolically active tissue and high rates of cell-mediated remodelling at certain anatomical sites provide a good example of the challenges faced when incorporating biological activity into multiscale FE models. Multiscale models of collagenous tissues more generally are discussed in Sect. 1.3.4, including the models at the atomistic scale because they provide important insights into the macromolecular nano-mechanics underpinning musculoskeletal tissue load response.

1.3.1 Micro-scale Modelling of Trabecular Bone

Trabecular bone is the spongy, porous tissue which lies within whole bones, providing lightweight structural support, participating in calcium homeostasis and acting as a reservoir for bone marrow. Trabecular bone is metabolically active [41] and is the tissue at most risk of loss in postmenopausal osteoporosis. The role of trabecular bone loss in reducing overall bone stiffness and strength in osteoporosis has been extensively studied [42]. Although trabecular bone has been mechanically

characterised in terms of its ‘apparent-level’ macroscopic constitutive behaviour (i.e. neglecting the porous microstructure, see Sect. 1.2.2), apparent level continuum representations of trabecular bone which are not informed by finer-scale models only provide limited insight into the deformation processes of interest because the underlying porous microstructure plays a key role in defining the deformation and damage mechanics of the tissue. Therefore modelling at the micro-scale is a necessity for understanding trabecular bone function. Once such models have been developed, they can, if desired, be used to upscale to macro-scale continuum representations. Harrigan et al. [43] suggested that the use of apparent-level continuum models for trabecular bone is suspect when close to an interface or in regions where stress gradients of more than 20–30 % occur across a distance of 3–5 trabeculae.

The importance of microstructure in trabecular bone mechanics is further reinforced by the limited correlation found clinically between radiographic measures of bone quantity and fracture risk in osteoporosis [44]. That is to say, it is not just the quantity of bone lost in osteoporosis that determines bone strength, but its microstructure, the level and type of pre-existing in vivo microdamage and the properties of the mineralised tissue itself. These factors have been collectively referred to as ‘bone quality’ (in contrast to bone quantity) [45]. In osteoporosis, the initially plate-like structure of healthy trabecular bone gradually changes to a rod-like structure during bone loss. In rod-like trabecular bone, longitudinally oriented ‘trabeculae’ or struts (oriented parallel to the principal physiological loading direction) act as columns in compression and are susceptible to buckling, and transverse struts act as tensile stabilisers and are susceptible to microfracture.

Given the importance of the porous microstructure, micro-scale FE modelling has been extensively used to explore the structural response of trabecular bone to load.⁴ High-resolution imaging techniques, in particular micro-computed tomography, have played a key role in the development of micro-FE models of trabecular bone, because they allow image-based models of actual bone specimens to be generated, such as those shown in Fig. 1.3. With regard to material constitutive relations, note that because the microstructure is represented explicitly in micro-scale FE models, the material constitutive response is moved down a level relative to macro-scale models as described in Sect. 1.2.2, so that the constitutive relation now represents the ‘tissue level’, i.e. the mineralised bone matrix rather than the ‘apparent level’.

Early image-based linear elastic micro-FE analyses of small regions of trabecular bone were performed with element sizes of several hundred microns in the mid-1990s [47,48]. By adjusting the tissue elastic modulus in the model so that the predicted specimen stiffness agreed with the experimentally measured specimen stiffness, tissue level elastic properties for trabecular bone could be inversely determined [49], and the resulting models correctly predicted the anisotropic elastic

⁴Micro-scale FE models of bone are sometimes described in the literature as ‘high-resolution finite element models’ (see, e.g. [46]).

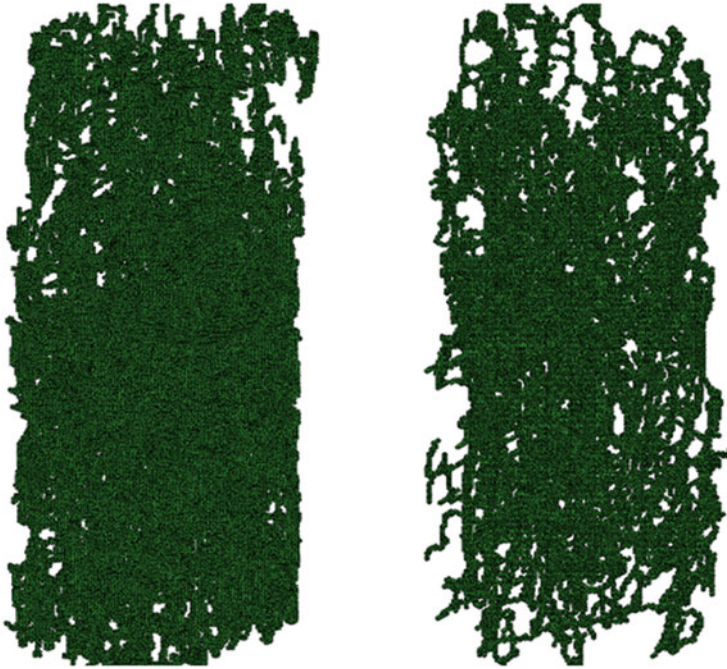


Fig. 1.3 Voxel-based FE meshes of cylindrical vertebral trabecular bone cores generated from micro-CT scans of (*left*) a 91-year-old male and (*right*) a 97-year-old female. Hexahedral element sizes are $100 \times 100 \times 100 \mu\text{m}$. The 91-year-old model has approximately 135,000 elements, and the age 97 model has approximately 45,000 elements (From [128], used with permission)

behaviour of trabecular bone at the apparent level [50,51]. In order to predict strength as well as stiffness, isotropic (von Mises) yield criteria were then added to the micro-FE models [52,53]. In order to improve the prediction of apparent strength (which was limited by the assumption of isotropic yield), Niebur et al. [46] performed a 3D voxel-based FE study in which the material constitutive relation incorporated tensile-compressive yield strength asymmetry (0.61% tensile and 1.01% compressive yield strains, respectively). This tensile-compressive yield asymmetry allowed the microstructural FE models to capture apparent trabecular bone strength to ‘an outstanding level of accuracy’.

Having established that apparent trabecular bone stiffness and strength could be accurately predicted using micro-FE models with relatively simple homogenous tissue properties, several groups then attempted to model the post-yield response of trabecular bone by incorporating material nonlinearity [54,55]. Stolken and Kinney [56] pointed out the need to include geometric nonlinearity in such solutions. Verhulst et al. [57] used voxel-based micro-FE models of 5.35-mm-diameter cylinders of bovine proximal tibia trabecular bone to simulate the post-yield compressive response and compared the simulation results with actual experiments up to 5% apparent compressive strain. These simulations incorporated both material and

geometric nonlinearity. The authors found that although element size effects were minimal, element type (linear vs. quadratic) and the material model used (bilinear elastic, elasto-plastic with isotropic Hill yield function, elasto-plastic with von Mises yield surface) both had significant effects. However, none of the three material models investigated provided satisfactory prediction of the experimentally observed post-yield strain softening. As an indication of the solution time required to perform these nonlinear simulations, a full analysis with 156,000 elements took 1.7 GB of memory and 14 h on a single processor. The authors estimated that running the same model with quadratic elements would require approximately 8 GB of memory and take 130–140 h on a single processor.

Numerous subsequent studies have utilised voxel-based micro-FE models to investigate different aspects of trabecular bone loading response, including models based on *in vivo* images of trabecular bone obtained using peripheral quantitative computed tomography (pQCT) [58]. A recent study by Vilayphiou et al. [59] demonstrated the use of pQCT-based micro-FE analysis in large groups of patients. Micro-FE-derived stiffness, stress and failure load of distal radius and tibia were assessed in 185 men with prevalent fragility fractures and compared to 185 age-, height- and weight-matched controls. The micro-FE-derived stiffness and failure load were found to be 8–9 % lower in the fracture group ($P < 0.01$), suggesting that microarchitecturally derived mechanical properties at anatomical sites which can be accessed using pQCT are relatively representative of bone properties at less accessible fracture sites. A recent multiscale study used homogenisation to determine apparent macro-scale (orthotropic) trabecular bone properties based on micro-structure and isotropic elasticity at the micro-scale and then applied progressive meshing and a porosity-based modification of material properties to allow rapid model generation at intermediate scales [60]. Another recent multiscale study [61] used homogenisation together with stochastic incorporation of uncertainties in apatite crystal orientation and image-based modelling to derive distributions of trabecular bone stiffness at the apparent level from the underlying microstructure.

These studies suggest that by using two scales (micro and macro), both of which have scanning technologies available to derive the 3D geometry, the apparent level, quasi-static stiffness and strength of trabecular bone can be satisfactorily modelled. However, as mentioned above, current micro-FE models still do not adequately capture the post-yield softening response. Post-yield behaviour in trabecular bone is important not only because of its role in reducing apparent-level compressive load-bearing ability but also because cell-mediated bone remodelling is triggered in response to the formation of microcracks within the tissue. Therefore there is both a structural imperative and a biological imperative for studying the post-yield mechanics of trabecular bone.

It is now widely accepted that the primary role of bone remodelling is to repair microscopic cracks formed during physical loading before they can grow to a dangerous size [62]; therefore post-yield and continuum-to-discrete fracture mechanics in trabecular bone tissue are important in elucidating the remodelling response.

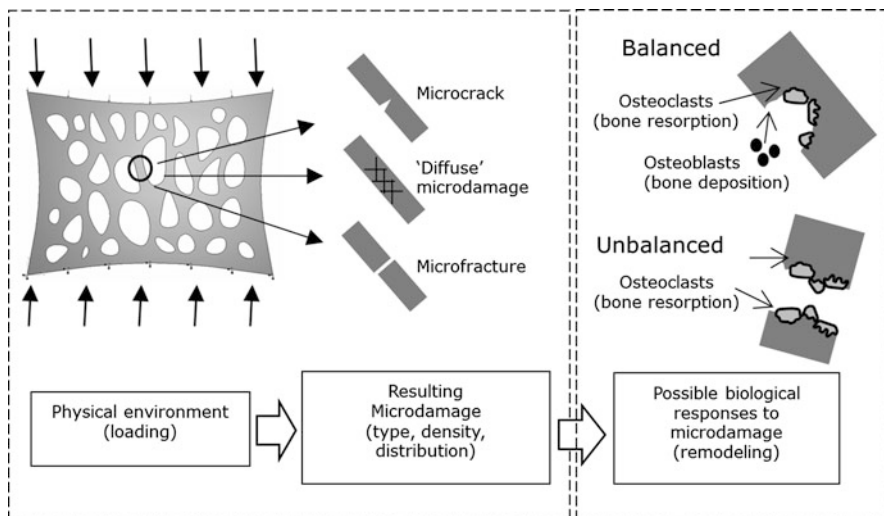


Fig. 1.4 The role of mechanically induced microdamage in the bone remodelling process. The remodelling response is dependent on the type of microdamage. Balanced remodelling maintains bone mass, while imbalance leads to bone loss. The *left dotted box* represents the mechanics of damage formation, while the *right dotted box* represents the biological response

Three⁵ types of microcracks have been observed in trabecular bone: (i) discrete microcracks up to about 100 microns in length; (ii) ultra microcracks smaller than 1 micron, usually described as diffuse microdamage [63]; and (iii) trabecular microfractures, in which an entire trabecular strut is broken. Microcracks formed by physical loading activate the cellular remodelling response [64]. Microfractures can lead to aggressive resorption of the broken strut by osteoclasts because of the loss of strain signal within the disconnected trabecular strut [65,66]. This in turn reduces the integrity of the trabecular bone network [67,68]. Figure 1.4 shows the three types of microdamage schematically in vertebral trabecular bone and the possibility for either balanced (no net bone loss) or unbalanced (bone loss) cellular responses depending on the nature of the microdamage.

In order to model the onset of microdamage within trabecular bone under compression, Yeh and Keaveny [68] developed a 3D lattice beam FE model, again using asymmetrical tensile (0.67%) and compressive (1.1%) yield strains to explore microdamage formation under simulated compressive loading. Eighty percent of trabecular struts developed microdamage at 2% apparent compressive strain. Nagaraja [69] used micro-CT and image-based FE of bovine tibial trabecular cores loaded in compression to register experimentally observed regions of microdamage with estimated microstructural stresses, strains and strain energy. Significant positive relationships between microdamage and estimated tissue stress and strain were found. Jungmann et al. [70] developed idealised (cylindrical) linear

⁵We note that several studies refer to four types of microcracks rather than three.

elastic FE models of a single trabecular strut undergoing three-point bending in order to correlate experimentally observed stress whitening (indicative of microscopic damage accumulation) with predicted local tissue strains. Predicted maximum tensile strain at the lower surface of the three-point bending sample ($\epsilon_x^{\max} = 0.03$ for 66 μm mid-span displacement of a 2.5-mm long, 480- μm diameter strut with 2-mm support span) was around three times less than the value measured experimentally using digital image correlation ($\epsilon_x^{\max} = 0.09$), a discrepancy which the authors attributed to sample heterogeneity. Attempts to explicitly model crack formation in bone using cohesive zone FE methods have been made by Ural and Vashishth [71] for cortical bone and by Tomar [72] for trabecular bone, although we note that both of these models were limited to 2D with homogenous tissue properties. Rather than modelling cracks explicitly, other studies have incorporated damage mechanics (modulus reduction) approaches in 2D micro-FE models of trabecular bone [73,74]. Although the focus here is on trabecular bone, studies by Budyn [75] (using the extended finite element method, XFEM) and by Yang et al. [76] pointing out the need for nonlinear fracture models when modelling cracks in cortical bone are also noteworthy.

When considering the formation and growth of cracks in trabecular bone tissue from a mechanical modelling perspective, it is clear that the use of homogenous tissue properties in micro-FE models, although suitable for predicting apparent stiffness and strength, can only provide a simplified view of the plastic and crack formation processes occurring in the tissue. In actual bone tissue the variations in mineralisation, inter-lamellar cement lines and osteocyte lacunae which can all be clearly seen under the microscope will influence the mechanics of the tissue at the scale at which damage occurs. Several studies [77,78] have explored the bio-mechanical effects of mineral heterogeneity by comparing the predictions of homogenous and heterogeneous FE models of trabecular bone. In these studies, the models which included the observed gradient of mineralisation from centre to edges of a trabecular strut (by incorporating graded material properties) predicted substantially different stress distributions throughout the trabecular thickness compared to those assuming homogenous properties.

In addition to the formation of damage within trabecular tissue, FE models have also been used to study the cellular remodelling which occurs in bone's response to damage. A key question in bone remodelling is how bone cells sense extracellular matrix strain, and micro-FE modelling studies in this area necessarily bridge the micro- and nanoscales because osteocyte lacunae are in the order of 10 μm in size, whereas the fluid-filled canaliculi processes which connect osteocyte lacunae are only a few hundred nanometres in diameter [79]. Several models have been developed to calculate the strain magnification which occurs between tissue level apparent strain and local matrix strains adjacent to an osteocyte lacuna which acts as a 'stress raiser' [80]. Deligianni and Apostolopoulos [81] used a four-scale FE analysis to conclude that strain amplification of matrix could account for local strains of 10,000 $\mu\epsilon$ adjacent to osteocyte lacunae during apparent level tissue level strains of only 2,000 $\mu\epsilon$.

Other models have been developed to explore the extent to which interstitial fluid flow driven by extracellular matrix deformation may be responsible for

osteocyte mechanotransduction. The review articles by Knothe-Tate [79] and Jacobs et al. [82] provide the lists of models. It is important to keep in mind that until recently, there were few experimental studies quantifying flow within the lacuno-canalicular system (see [83] for a thorough overview), so that bone fluid flow models generally use idealised geometry, and have not usually been validated by comparison with experiments to date. We also note that the existing fluid flow models focus on osteonal bone with Haversian canals [84,85]; therefore fluid flow in the lacuno-canalicular system of trabecular bone (with its absence of Haversian canals) remains unexplored. Rémond et al. [86] modelled fluid flow within an idealised osteon and demonstrated that spatially varying permeability and elastic properties had a significant effect on model results. Cowin et al. [87] developed governing equations for fluid flow in the bone with hierarchical permeability using an analytical approach with idealised cylindrical geometries for the whole bone and for the osteon. This theoretical formulation provides a promising basis for multi-scale numerical modelling with more realistic anatomy, which highlights the importance of accounting for the vascular porosity in bone fluid flow models. Nguyen et al. [88] modelled the bone as a periodic osteonal structure with anisotropic elastic properties using frequency domain poroelastic finite element analysis. Lemaire et al. [89,90] developed a multiscale model of coupled electro-osmotic and osmotic diffusion in addition to Darcy flow occurring within the canalicular and collagen-apatite matrix porosity of the osteon. Upscaling was performed using periodic homogenisation. Given the uncertainties in many of the parameters required to generate such models, the same group [91] recently published a sensitivity study to identify key parameters for further analytical and experimental investigations. Verbruggen et al. [92] recently used fluid-structure interaction modelling with model geometry based on confocal imaging of actual osteocytes to investigate fluid velocities and shear stresses experienced by the cells during physiological loading. The model indicated that the greatest stimulation occurred in the region of the osteocytic cell processes and that these flows were in the range known to generate osteogenic responses by osteoblastic cells *in vitro*. Although the focus in this section is on micro-scale models, for completeness we note that poroelastic models of the bone have also been developed at the macro-scale, effectively smearing the effects of the lacuno-canalicular porosity into a continuum tissue permeability, in which the vascular permeability may either be modelled explicitly [93] or omitted due to the perceived primary importance of the lacuno-canalicular porosity [94].

With respect to the effect of microcracks on fluid flow in bone, Galley et al. [85] developed a 2D (non-coupled) fluid flow model and found that the presence of a fatigue microcrack in Haversian bone affected fluid velocities up to a distance of 150 μm from the crack. Nguyen et al. [95] used poroelastic models to determine that the presence of an interstitial crack could dramatically reduce fluid flow/pressure in neighbouring osteons.

Once cellular activity has been initiated, bone remodelling involves removal of damaged bone by osteoclasts, followed by deposition of new osteoid tissue by osteoblasts. The newly formed osteoid then mineralises over time. This subtractive

and additive process changes the bone microstructure over time, and as already illustrated in Fig. 1.4, unbalanced remodelling can lead to net bone loss. Computational mechanics approaches have again been used to simulate both the end result of the remodelling process in trabecular bone and the process itself. In an early 2D model with idealised trabecular microstructure, Silva and Gibson [96] showed that when net bone loss occurs in osteoporosis, loss of a few struts had a much more important effect than thinning of many struts in terms of reducing the apparent stiffness and strength of trabecular bone. Langton et al. [97] incorporated stochastic bone remodelling in a 2D micro-FE of trabecular bone remodelling, observing simulated trabecular perforation. The same authors used a similar approach to simulate anabolic treatment following various degrees of bone resorption [98]. Another example of stochastic remodelling simulation was done by Huiskes et al. [99,100], in which 2D models of small regions of trabecular bone were simulated and elements in the model were assigned a relative bone density between 0.01 (no bone) and 1.0 (fully mineralised). Strain energy density (SED) rate was used as the mechanical stimulus driving remodelling, such that mineralisation was reduced in the elements with low SED rate and increased in regions with high SED rate. The resulting simulations of metabolic activity demonstrated qualitatively plausible adaptation of trabecular orientation to altered loading direction and increases or decreases in bone mass which were approximately proportional to the amount of increased or decreased loading, respectively. The approach was later extended to 3D simulations [101]. In subsequent studies by the same group [102,103], the 2D modelling approach was extended to incorporate damage accumulation, as well as modelling the action of individual osteoclasts and the ability of osteoclasts to both deposit new bone and act as bone lining cells. These more recent simulations suggested that cell-mediated remodelling is beneficial under moderate fatigue, but has a detrimental effect under intense fatigue because resorption cavities create more damage than they remove. Again using the concept of trabecular bone as an optimised structure, Chen et al. [104] adopted the evolutionary structural optimisation algorithm to predict bone remodelling around an implant.

Several authors have based their remodelling simulations on micro-CT data of actual trabecular bone samples. Van der linden et al. [105] performed 3D simulation of age-related trabecular remodelling based on the micro-CT scans of human vertebral trabecular bone specimens. Remodelling parameters were based on biological data, including partial refilling of resorption cavities to simulate age-related imbalances in bone metabolism. The predicted bone loss rates varied between 0.3 and 1.1 % per year. Hernandez et al. [106] studied the effect of resorption cavities on bone strength by adding idealised resorption cavities to image-based micro-FE models of trabecular bone. Cavities added in the regions of high strain (targeted remodelling) caused significantly greater decreases in bone stiffness and strength than when resorption cavities were randomly located (nontargeted remodelling).

Smit and Burger [107] investigated the strain distributions in the immediate vicinity of remodelling cavities using micro-FE models. A secondary osteon in cortical bone was idealised as a 700- μm diameter cylinder with a 200- μm diameter tunnel, while a Howship lacuna in trabecular bone was modelled as a 200- μm

diameter pit in a single cylindrical trabecula of diameter 200 μm . The FE results showed that reduced strains occur in front of the osteonal tunnel tip (where osteoclasts are active), and elevated strains occur at the flanks of the tunnel behind the tip (where osteoblasts are active). For the trabecular model, high strains were found at the base and transverse border of the lacunar cavity (which would inhibit further osteoclast activity), whereas lower strains were found on the surface of the trabeculae. The authors concluded that strain fields within the tissue could be related to osteoclast and osteoblast remodelling activity.

McNamara et al. [108,109] used a 2D poroelastic FE model of an axially loaded trabecular strut containing a resorption cavity to simulate remodelling in response to both strain and damage stimuli. The simulation results showed that there was a critical resorption pit depth beyond which remodelling was incapable of refilling the cavity; therefore trabecular perforation occurred. The authors concluded that a system which can respond to either strain or microdamage, but which prioritises removal of damaged bone after a damage threshold is reached, was the only process which provided plausible remodelling predictions. A subsequent study [110] suggested that a rule governing osteoblast attachment was required to produce realistic remodelling cycles.

Ryser et al. [111] developed a 2D spatiotemporal simulation of microfracture remodelling in the bone, incorporating mathematical descriptions of biochemical regulation of cellular activity through OPG and RANKL signaling. This model shows a different approach to remodelling simulation, since it is entirely biochemical and cell based, with no consideration of the mechanics of the bone matrix being modelled. The study also demonstrates the difficulties in parameter estimation for even relatively idealised models, since 21 separate model parameters had to be estimated.

Adachi et al. [112] developed a 2D plane strain poroelastic FE model of a single trabecula which incorporated fluid flow-induced shear stresses acting on the osteocyte mechanosensory system as a remodelling stimulus. They suggested that the simulated trabecular orientation coincided with *in vivo* observations of trabecular remodelling. Gerhard et al. [113] provided a useful and relatively more recent overview of bone remodelling simulations. Hambli et al. [114–116] used a novel approach combining FE simulation with neural network computation to link the macro- and micro-scale mechanics of damage accumulation and repair in trabecular bone. Neural networks were trained based on the result of voxel-based micro-FE simulations, and macro-scale continuum mechanical properties were updated based on the neural network computations.

The above-mentioned work on microcracks in bone and the subsequent remodelling response provided valuable insight into normal bone physiology in its own right. However, it is also clearly relevant to orthopaedics because implant insertion causes a sudden change in the biomechanical environment of the bone in the vicinity of the implant, and an intensive remodelling response then follows. Some regions of the bone are overloaded by the implant, and other regions are ‘stress shielded’ due to the presence of a stiff structure. In a recent micro-FE study of trabecular bone response to an orthopaedic implant, Mann and Miller [117]

modelled an idealised trabecula interdigitated with a mass of bone cement and performed fluid–structure analysis of the flow conditions at the bone–cement interface under load. The analysis suggested that supra-physiologic fluid velocities and shear stresses could occur in thin spaces between bone and implant and that these unnatural flow conditions could be responsible for osteolysis (bone resorption at the interface with implants). Although beyond the remit of this discussion, we note that a relevant body of micro-scale modelling work, including detailed bone remodelling simulation, has also been performed in the field of dental biomechanics to study implant osseointegration.

In summary, micro-FE models have been used to explore how the apparent stiffness and strength of trabecular bone are related to its porous microstructure, attempting to simulate damage and post-yield deformation of trabecular bone, to explore crack formation and mechanisms of mechanotransduction in bone and to simulate bone remodelling. There is recognition that tissue heterogeneity is important in post-yield damage processes, but there has been very limited incorporation of heterogeneity in micro-FE models to date. The need for better understanding of damage processes therefore provides an incentive to develop models with element sizes in the order of a few microns to better capture tissue level heterogeneity. We note that although these would still be micro-scale FE models, such models would be 1–2 orders of magnitude finer than the $\sim 100\text{-}\mu\text{m}$ voxel-based element sizes which are now routinely derived from micro-CT scans. The use of nanoindentation to provide local tissue properties for such models is discussed in Sect. 1.3.3. With regard to the link between the micro and macro-scales, there has been limited upscaling between micro- and macro-scale FE models of trabecular bone to date [60,118]. Because of the wide variations in trabecular bone porosity and microstructure which occur even within the same anatomical site, there is limited benefit in building a micro-FE model of a single small region of bone and then upscaling the resulting properties for use in macro-scale continuum models. However, because micro-CT scanners now allow high-resolution imaging of large ($\sim 100\text{ mm}$) regions of bone, it should be possible to perform nonlinear micro-FE analyses in small regions of bone and then upscale these to accurately define heterogeneous apparent tissue properties at the macro-scale, so that whole implant–tissue interactions can be studied. Such studies, although computationally challenging, would provide valuable insight into the response of trabecular bone to orthopaedic implants taking both micro- and macro-scale deformation response of the implant and surrounding bone into account.

1.3.2 Microbeam Models of Trabecular Bone Applied to Vertebroplasty Simulation

Although micro-CT and peripheral quantitative CT scanners now allow routine non-destructive imaging of large regions of bone at the micro-scale, voxel-based FE

modelling from these scans is still severely constrained with regard to computational power, especially when nonlinear material and geometric or contact effects are to be included in the analysis. One way to model large regions of trabecular bone at the micro-scale is to represent the struts and plates of the tissue using beam and shell elements rather than continuum solid elements [119]. This maintains a level of (idealised) microstructural representation while greatly reducing the number of degrees of freedom of the problem compared to continuum analysis. Here we describe the application of one such approach to investigate the compressive loading response of osteoporotic vertebrae to a poly(methyl methacrylate) (bone cement) augmentation process known as vertebroplasty. The work described here is based on a doctoral thesis performed within the author's group and extends the approach reported in [120] to the case of modelling a vertebroplasty intervention. Briefly, a perturbed hexagonal lattice of microbeam elements is used to represent the trabecular bone microstructure. A perturbation factor is used to randomly displace lattice junctions from their regular positions, and several previous studies have suggested that a perturbation factor of 0.3 is appropriate for representing rod-like trabecular bone [121,122].

By using average trabecular microstructural indices obtained from micro-CT scan post-processing (bone volume-to-total volume ratio, strut thickness, strut spacing, degree of anisotropy, structure modal index and others [123,124]) to define microbeam diameter, length and spacing, the microstructural parameters of the microbeam model can be prescribed to represent a particular specimen, even though the locations and dimensions of individual struts are not being reproduced exactly. For example, Fig 1.5 shows microbeam meshes based on microstructural parameters for three age groups of patients based on microstructural indices reported in Mosekilde [125].

The use of microbeam models under simulated compressive loading immediately highlights the importance of strut bending and buckling mechanisms in osteoporotic trabecular bone [126]. For dense, healthy bone, the predominant compressive failure mode is plastic collapse [127], whereas for osteoporotic bone with more slender struts, elastic buckling plays a more significant role. Since the slenderness ratio and degree of end support of the struts in trabecular bone can vary widely, it is

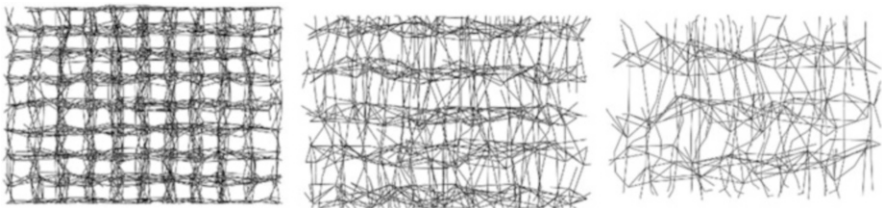


Fig. 1.5 Microbeam models of trabecular bone (age < 50, age 50–75 and age > 75) based on the microstructural indices from Mosekilde et al. [125]. The perturbation factor is 0.3 in all the cases, but the age < 75 model appears more perturbed because of its increased strut spacing (From [128], used with permission)

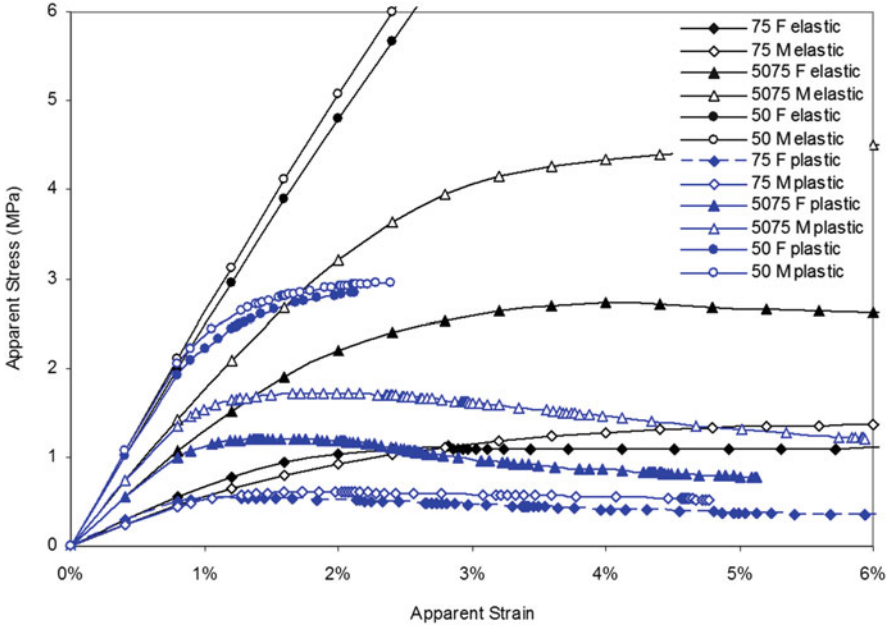


Fig. 1.6 Microbeam FE models of cylindrical cores of trabecular bone under uniaxial compression for differing age and gender (F/M) groups based on microstructure from Mosekilde et al. [125]; age less than 50 years, age 50–75 years and age greater than 75 years. For each core, both elastic only ($E = 8\text{GPa}$, $\nu = 0.3$) and elastic–perfectly plastic analyses were performed ($E = 8\text{GPa}$, $\nu = 0.3$, $\sigma_y = 0.8\%$). Note that even for the elastic analyses, strong nonlinearity is introduced at the apparent level due to strut buckling (From [128], used with permission)

important that microbeam models are able to capture both elastic and plastic buckling modes accurately. Mesh- and element-type sensitivity analysis showed that the use of two quadratic elements per strut was sufficient to capture experimentally observed elastic–plastic and/or analytical (Euler) buckling behaviour with a mean error of 8% [128]. The graph in Fig. 1.6 shows apparent compressive stress vs. strain results for microbeam simulations of a 7-mm-diameter cylindrical core of trabecular bone, in which either isotropic linear elastic ($E = 8\text{GPa}$, $\nu = 0.3$) or elastic perfectly plastic material behaviour was modelled ($E = 8\text{GPa}$, $\nu = 0.3$, $\epsilon_y = 0.8\%$) using the age < 50, age 50–75 and age > 75 microstructures illustrated above. In addition to the loss of load-bearing capacity in vertebral trabecular bone with age, the key point with regard to Fig. 1.6 is that even for purely elastic material constitutive behaviour, elastic buckling of microbeams introduces a strong geometric nonlinearity in the compressive loading response at the apparent (macro) level.

Having established a suitable meshing and solution strategy for capturing elastic and plastic buckling mechanisms in trabecular bone, the microbeam representation was then used to mesh large regions of trabecular bone and integrated with shell element representations of the cortical shell of the anterior vertebral body. Figure 1.7 shows a mesh of an L3 osteoporotic vertebral body with dimensions based

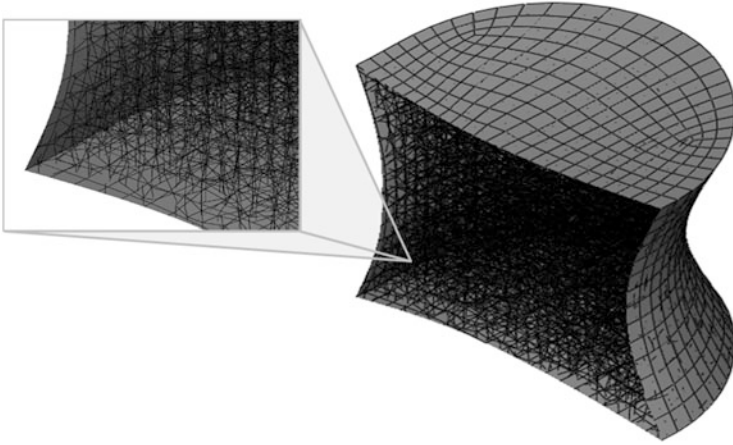


Fig. 1.7 Sectioned view of an idealised L3 lumbar vertebra with trabecular microstructure from Mosekilde et al. [125] with an age > 75 female. Overall vertebral body dimensions from Mizrahi et al. [129] with cortical shell thickness of 200 μm (From [128], used with permission)

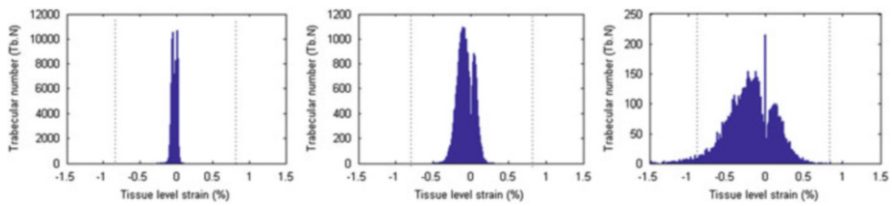


Fig. 1.8 Result histograms showing the distribution of predicted principal strain (-ve compressive, +ve tensile) in all struts of L3 vertebra microbeam FE models for (*left*) healthy, (*centre*) mildly osteoporotic and (*right*) severely osteoporotic L3 vertebral bodies (From [128], used with permission)

on [129], where the vertebral cortical shell has been meshed using four-node shell elements and the inner trabecular core is meshed using the microbeam approach. The cortical shell and trabecular core are connected using tied constraints in the FE model.

Because of the large number of beam elements in the model, it is convenient to report the stress and strain state within the trabecular centrum (under compressive loading) statistically using histograms such as those shown in Fig 1.8. In Fig 1.8, the trabecular microstructure has been altered to represent increasingly severe osteoporosis. The progression of osteoporosis shifts the strain distribution from a relatively optimised structure where all struts are similarly loaded to a more uneven distribution. Struts with zero principal strain are generally those attached to and shielded by the vertebral cortical shell.

The microbeam vertebral body FE model was then used to investigate the biomechanics of a surgical procedure known as vertebroplasty, in which polymethyl

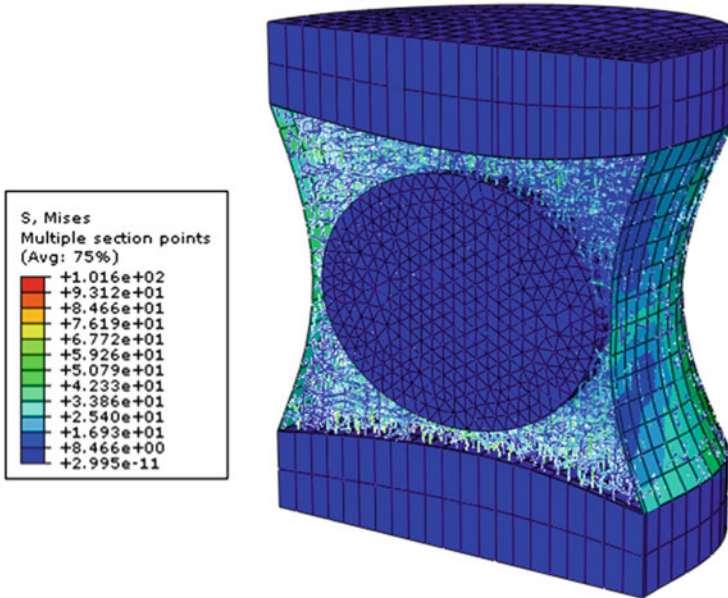


Fig. 1.9 Contour plot of predicted von Mises stress (MPa) in an age 78 T11 vertebroplasty model with microbeam trabecular bone architecture, shell elements representing the cortical shell and spherical cement inclusion (From [128], used with permission)

methacrylate bone cement is injected into the vertebral body in an attempt to stabilise and/or restore the height to an osteoporotic vertebra. Figure 1.9 shows a contour plot of predicted von Mises stresses within the trabecular microbeam network of an osteoporotic vertebra with an embedded sphere of bone cement.

By performing simulations with different volumes of vertebroplasty cement, it was possible to demonstrate that the percentage of trabecular struts that exceeded tissue level yield strain of 0.8% during a physiological compressive load on the vertebra increased as the volume of bone cement increased. For example, the model predicted that yield occurred in 3.6% of the struts under physiological compressive load with a 2-ml volume of cement, where for a 6-ml volume of cement the percentage of struts yielding increased to 8.5%. Therefore, for the same compressive loading, more microdamage and more subsequent bone remodelling activity would be expected with greater volumes of cement. The microbeam models of vertebrae described above are ‘multiscale’ in the sense that they represent two levels of the bone structural hierarchy (microstructure and macrostructure) in one model, which differentiates them from the purely ‘microstructural’ FE models described in Sect. 1.3.1 where a small region of trabecular bone of simplified geometry (usually a cylinder or cube) was modelled. However, they are not multiscale in the sense of requiring separately solved models at different scales and information passing between the scales.

1.3.3 Nano-mechanical Modelling of Trabecular Bone Post-yield Mechanics

Micromechanical models of trabecular bone such as those discussed in Sects. 1.3.1 and 1.3.2 still use continuum mechanics representations of the ‘tissue’, except that the definition of ‘tissue’ from the perspective of material constitutive relations has now been pushed down a scale compared to the macro-scale models. In micro-FE models the voxel-based element dimensions may be only a few tens of microns, but the tissue is still assumed to be a homogenous continuum for the prescription of constitutive relations. One troublesome issue with the voxel-based micro-FE models discussed in Sect. 1.3.1 is that the elastic modulus required in the models to match experimentally measured overall compressive stiffness tends to be much lower than direct experimental measurements of bone tissue elastic modulus. For example, Chevalier et al. [130] found that elastic moduli derived from voxel-based FE models exhibited ‘surprisingly low values when compared to nanoindentation results’. This discrepancy, together with the difficulty in accurately modelling trabecular bone post-yield response mentioned earlier, hints at the fact that characterising micro-scale and nanoscale heterogeneity in bone tissue properties is important for understanding all aspects of the loading response.

Nanoindentation has emerged as an important experimental tool to probe the deformation response of bone at the nanoscale and, when combined with FE modelling, can provide insights into the tissue-level response at submicron scales. Here we discuss the use of FE models of bone nanoindentation to inform the development of elasto-plastic constitutive relations for bone tissue at scales small enough to study heterogeneity due to lamellar structure and varying mineralisation levels. The principle of nanoindentation is simple; an indenter tip with dimensions in the order of several hundred nanometres is pushed into the material to be measured with a known force. The force versus tip displacement profile is measured during both the loading and unloading phases of the indentation. By using the load–displacement curve and knowing in advance the geometry of the indenter tip, material properties such as elastic modulus (E) and hardness (H) can be obtained.

Nanoindentation has been used to measure bone modulus and hardness in a large number of experimental studies. However, nanoindentation has the potential to provide further valuable information on the post-yield mechanics of bone tissue at the nanoscale [131]. Firstly, by modelling the nanoindentation process using nanoscale continuum FE models and using an atomic force microscope (AFM) to measure the shape of the residual indent left after indenter removal, model predictions can be assessed directly against AFM measurements with regard to the amount of elastic recovery of the tissue after indenter removal and with respect to the presence or absence of phenomena such as ‘pile up’ or ‘sink in’ adjacent to the indenter flank (Fig. 1.10). Secondly, by modelling time-dependent effects during indentation (creep under constant load and relaxation under constant displacement), material properties governing viscous and poroelastic [132] behaviour at the nanoscale can again be inversely estimated by comparison of model predictions with

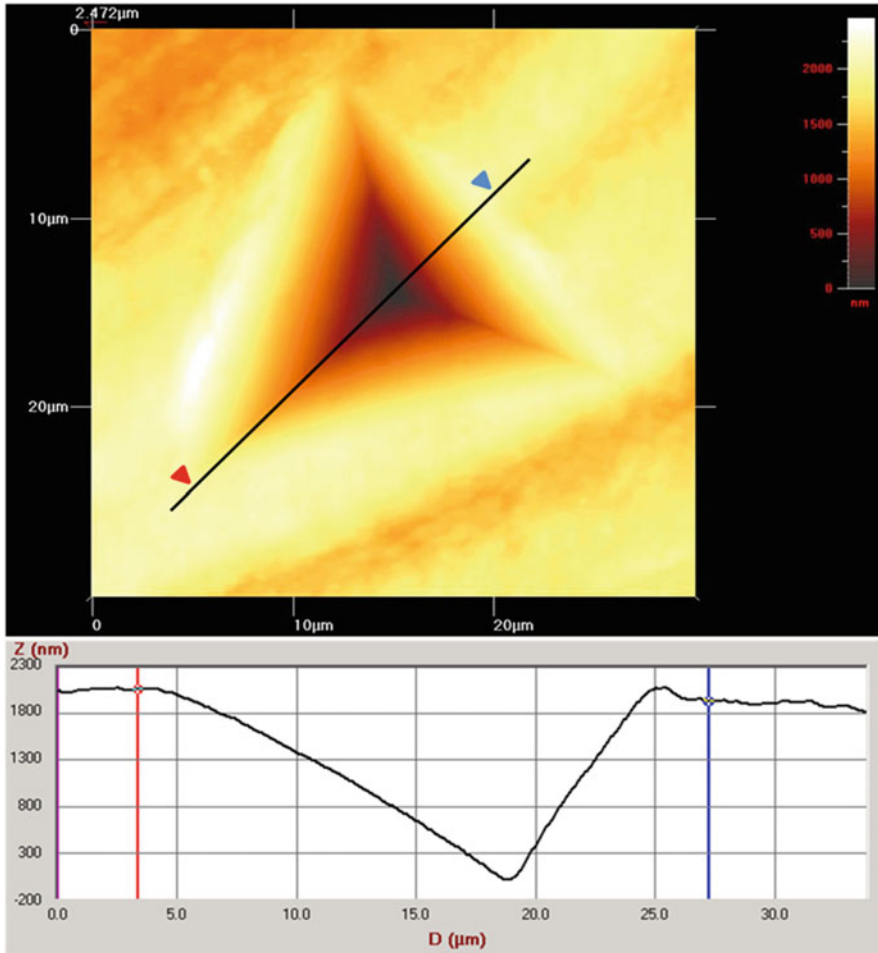


Fig. 1.10 Atomic force microscope image of the impression left by a Berkovich indenter on a sample of trabecular bone. The line profile beneath the image shows a cross section through the indent (z-axis in nm, y-axis in μm), showing a small degree of pile up to the right of the indent in this case (From [131], used with permission)

experimental results. Thirdly, because nanoindentation is highly localised, the material composition at the indent site (e.g. the degree of mineralisation of bone tissue as measured by quantitative back-scattered electron imaging, qBEI) can be imaged and correlated with the mechanical properties measured using indentation [133].

A number of authors have developed FE models of bone nanoindentation [134–146] and explored the effect of various elasto-plastic constitutive relations on the

predicted force and deformation response. Wang et al. [136] identified material parameters for a Mohr–Coulomb material model of canine vertebral trabecular bone following bisphosphonate therapy. Mullins et al. [137] reported an extended Drucker–Prager model which can more accurately predict deformation and load–displacement response than a von Mises yield surface. A recent model by the author [147] pointed out that including friction between the bone and indenter could strongly affect predictions of pile up adjacent to the indenter. Carnelli et al. [141,144] used constitutive models with anisotropic elasticity and anisotropic plasticity (tensile-compressive yield asymmetry) to simulate nanoindentation of cortical bone. Schwiedrzik et al. [148] developed and applied a general anisotropic quadric yield criterion to model nanoindentation of lamellar bone.

Figure 1.11 shows the contours of maximum (most tensile) and minimum (most compressive) logarithmic principal strains in the FE model of nanoindentation developed by the author [147]. The model used in this case was a 2D axisymmetric representation of a spheroconical indenter with tip radius 600 nm and tip angle 90°. The material constitutive model in this case was based on the values used by Mullins et al. [137] (isotropic linear elasticity $E = 13.56\text{GPa}$, $\nu = 0.3$ with a Drucker–Prager yield surface, cohesion 122 MPa and friction angle 46°). At the instant shown in the figure, the indenter penetration into the material is 0.63 μm , and it can be seen from the contour plots that the maximum (tensile) principal strains are slightly below 20%, while the minimum (compressive) principal strains reach nearly 80%. This figure demonstrates that the nanoindentation experiments together with tightly integrated modelling are able to probe bone tissue mechanical response well into the post-yield region. Although the strain states in the tissue cannot be directly extracted from the experimental data, the tissue stress and strain state can be inferred by modelling the indentation process. We envisage that future combined modelling–experimental studies using a range of different tip types (including cube corner tips designed to induce cracks in the tissue) will further elucidate the elasto-plastic constitutive response of bone tissue at the

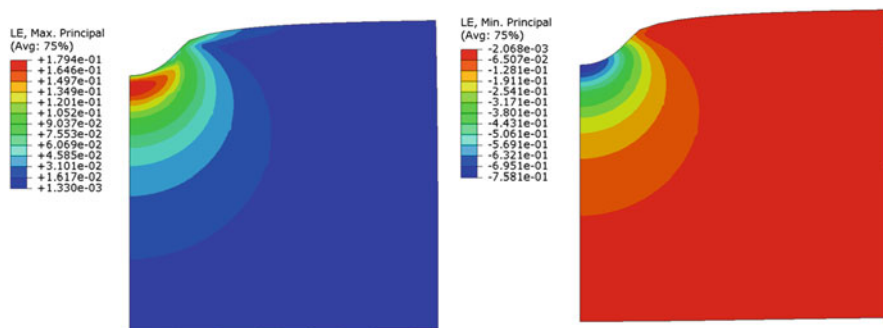


Fig. 1.11 Contours of (left) the maximum and (right) minimum (logarithmic) principal strains in the axisymmetric FE models of bone nanoindentation for an indenter vertical displacement of 0.63 μm . Note that only a subsection of the total mesh is shown for visualisation purposes so that the lower boundaries appear tilted

nanoscale [148]. Furthermore, imaging of the mineral and organic matrix composition at the indent site will allow nanoindentation-based constitutive properties to be correlated with tissue composition, providing a basis for models which incorporate heterogeneity of both elastic and inelastic constitutive responses at the micro-scale.

Bone modelling at the nanoscale also covers bone response to loading at the level of interactions between the organic matrix and plate-like apatite crystals with dimensions in the order of 2–100 nm [149]. Various collagen–apatite models have been developed to explore the mechanics of this interaction and how it confers higher level stiffness and strength. To date, given the paucity of experimental data, such models have tended to assume simple stiffness properties and idealised geometry for the mineral and organic phases [150–153]. Only one atomistic simulation of mineralised collagen in the bone has been published to date [154], which suggested that mineral crystals bear up to four times more stress than the collagen fibrils. With respect to the dynamics of bone–implant interactions at the nanoscale, Ganazzoli and Raffaini [155,156] and De Nardo et al. [157] describe atomistic and coarse-grained molecular dynamics simulations of protein absorption onto the surfaces of implant biomaterials.

1.3.4 Multiscale Models of Non-mineralised Tissues

Orthopaedic implants are usually anchored to bone; however, joint function and stability also depend on the mechanical response of ligaments and cartilage. Compared to the amount of modelling work on bone, there have been relatively fewer micro-scale modelling studies on non-mineralised musculoskeletal tissues to date. One limiting factor is the ability to perform the 3D high-resolution imaging across large regions of non-mineralised tissue which is necessary for image-based micro-FE modelling (to be discussed further in Sect. 1.4.1). Shim et al. [158] used a micro-FE model of the bone–cartilage interface to explore the initiation of osteoarthritis, in which a macro-model was used to derive input strains to a micro-model, which in turn drove a set of ordinary differential equations governing cellular remodelling activity, which in turn altered matrix structure. The model was run iteratively in this fashion to simulate three months of loading and remodelling. Further, a cartilage damage prediction model linked peak cartilage strains to pro-inflammatory response. Lavagnino et al. [159] developed a multiscale FE tendon model to explore the role of fluid flow-induced shear stresses and ECM-induced cell deformation in governing the cellular remodelling response. Hadi and Barocas [160] developed a multiscale FE model consisting of stochastically generated networks of type I collagen fibres to study damage and failure in collagen gel tissue analogues. Reese et al. [161] developed a micromechanical FE model to study force transfer across scales in a collagen gel containing extruded collagen fibres under tension. The results showed strong heterogeneity at the micro-scale due to size and boundary effects, and the authors concluded that traditional

continuum assumptions were not valid for describing the macro-scale load–deformation response. We note that 1D (mathematical rather than finite element) multiscale models of the tendon have also recently been developed, with a two-step homogenisation technique being used to bridge between the scales [162,163]. Gronau et al. [164] reviewed multiscale approaches to the design of biopolymers (elastin, silk and collagen), finding that although there are difficulties in relating the disparate length and timescales of relevance, bottom-up multiscale approaches integrating both experiment and computational modelling offer much promise in biomaterial design.

In order to better understand the molecular basis of the load–deformation response in collagenous tissues, atomistic simulations of triple-helical tropocollagen molecules have also been performed [165–168]. Models at the molecular scale have been successful in elucidating the mechanisms which confer extensibility, strain hardening and toughness at the fibril scale through twisting, stretching and uncoiling of individual molecules. Having said this, it is challenging to contemplate bridging between nano- and micro-scales because of the limitations on nano (molecular)-scale imaging in 3D across microns of tissue.

1.4 Future Directions for Multiscale Modelling in Orthopaedics

1.4.1 *Serial Milling and Block Face Imaging Techniques*

Micro-scale models of musculoskeletal tissues require 3D imaging modalities which can accurately characterise structure at these scales. As already mentioned, micro-CT scanners now allow resolutions of a few microns to be achieved with large (~100 mm) bone specimens. However, micro-CT relies on X-ray attenuation by the mineral phase of bone to provide contrast and therefore is not capable of imaging non-mineralised tissues in their native state. One possible solution for micro-CT imaging of non-mineralised musculoskeletal tissues is the use of osmium tetroxide (OsO_4) as a radiographic contrast agent [169]; however, OsO_4 is highly poisonous. Another possibility for soft tissue imaging at the micro-scale is micro-MRI, which can achieve resolutions of 30 microns, i.e. sufficient to image the upper end of tissue microstructure. However, scan times at this resolution are in the order of 30 h, and the cost of such scanners is prohibitive [169]. Higher resolutions (~200 nm) are possible with 3D light microscopy techniques such as laser scanning confocal microscopy and multiphoton microscopy. However, these techniques can only image small volumes of tissue sample in a single field of view. More importantly, the penetration depth of these modalities into tissues is limited to ~100 μm for the confocal microscope and ~1 mm for two-photon microscopy. Optical coherence tomography (OCT) allows 3D imaging with resolutions less than 10 μm , but again the penetration depth is limited to a few millimetres. Therefore imaging intact

microstructure deep within a musculoskeletal soft tissue is not readily achievable at present.

The field of view of an imaging modality relative to its resolution is an important issue in musculoskeletal imaging for model generation, because the tissues are not generally self-similar, and therefore it is not sufficient to image a small region of the structure at high resolution and assume that this is representative of the entire structure. Therefore imaging modalities are required which can image large (several centimetre) regions of tissue at high resolution.

One such technique, which is not limited to solely imaging mineralised tissues, is serial sectioning and block face imaging. The technique is conceptually simple; the structure to be imaged is embedded in a rigid block, and one surface of the block is either sliced or milled away layer by layer, using a microscope with a motorised stage to perform multi-pass imaging of each successive block face. The grid of microscope images taken on a particular block face slice can be stitched together using image post-processing software to form one large image of each block face, and the series of block face images with known separation forms a 3D z-stack. The advantage of the technique is that it allows high-resolution imaging for large regions of tissue, effectively decoupling resolution from specimen size [170]. Also, both soft and mineralised tissues can be imaged together, including tissues with implants when using appropriate milling cutters. The technique is also flexible in regard to which various stains and microscopy modalities (white light, polarised light, fluorescence, even spectroscopy) can be used to obtain the desired specimen contrast. The resolution of the technique is limited by the microscope used to perform the block face imaging and by the mechanical resolution of the sectioning/milling tool used to cut the block face together with the cutting properties of the embedding medium. The limitations of the technique are that it is destructive and that the imaging is performed on the block face so that reflected incident (rather than transmitted) light microscopy must be performed. Also, opacifier must be added to the embedding medium to prevent light reflection or fluorescence from subsurface structures from reducing image contrast. We note that previous authors have developed similar systems to examine both bone and non-mineralised tissues, particularly in the field of embryology and developmental biology (e.g. [171–175]). As pointed out by Viceconti [176], serial sectioning techniques fell into relative disuse for bone imaging following the development of desktop micro-CT scanners, but for the reasons given above, they have continuing potential for imaging musculoskeletal soft tissues and joints, where both cells and matrix can be imaged and used as a basis for micro-FE modelling.

Here we briefly describe a custom-designed serial milling and block face imaging system developed by the author in order to allow high-resolution 3D imaging of the intervertebral disc for use in multiscale biomechanical models of healthy and degenerative intervertebral discs. The focus here is on the capability of the imaging technique to enable high-resolution mapping of the entire anatomical structures rather than on the subsequent modelling, which is a work in progress.

The system comprised a Proxxon MF70 micro-miller (Proxxon, Germany) which was converted to computer numerical control (CNC) through the addition

of stepper motors on all three axes. A digital microscope with inbuilt reflected white light illumination and adjustable polarisation was mounted to the head of the mill. Custom code was written to control the mill and microscope camera, in order to perform a milling and imaging sequence in which each milling pass was followed by multiple microscope images of the resulting block face, which were later stitched together to produce a single high-resolution image of the entire milled surface. Milling was performed using 3-mm-diameter, two-flute tungsten carbide end mills (Kyocera Corporation, Kyoto, Japan) at a feed per tooth of approximately 1–2 μm . By using a new end mill for each specimen, a surface finish in the order of 5 μm can be achieved, which is less than the depth of field of the microscope. Vacuum and compressed air were used during milling to safely collect dust and particles of embedding resin and organic matter and to clear milling debris from the block face prior to imaging.

The resolution of the image dataset in the z-direction is controlled by the depth of each milling pass and was typically 10–20 μm . The resolution in the x–y plane was controlled by the microscope camera which had a maximum 5MP resolution (2592 \times 1944 pixels) at 240 \times magnification, corresponding to 0.66- μm minimum pixel size. Since the technique produces very large datasets, images were often taken at a lower in-plane resolution. When imaging a block face, each microscope image was taken with approximately 100- μm overlap with the boundaries of the neighbouring images, in order to facilitate more accurate stitching of the reconstructed image during post-analysis (ImageJ software, version 1.47b, National Institutes of Health, USA). Background correction was also performed using ImageJ in order to correct for nonuniformities in illumination by the microscope light source. Other than the image stitching and background correction, no post-alteration or digital enhancement of the raw microscope images was performed.

Figure 1.12 shows a resulting single block face image of a bovine tail intervertebral disc in the sagittal plane. The stitched image is comprised of 15 \times 17 = 255 reflected polarised light microscope images, covering a total disc cross section of 25.6 \times 16.6 mm with 1.5- μm resolution. The full image size is 15823 \times 10727 pixels. In this specimen a small (<0.1 %) amount of Sudan black opacifier was added to the epoxy embedding media. Other than that, the tissue is unstained.

The ability to image microstructure in 3D through an entire disc using a technique such as this forms a basis for multiscale model generation. Clearly it is not possible in this situation to simply convert voxels to finite elements due to computing power constraints; however, using combined imaging modalities, it should be possible to obtain the necessary contrast between tissue types to segment the collagen and elastic fibre networks in the annulus fibrous of the disc, the bony and cartilaginous endplates and the proteoglycan-rich nucleus pulposus and thereby to generate microstructural models of the disc based on actual (rather than idealised) specimen anatomy. As an example of the ability to differentiate between tissue types using multimodal block face imaging, the strongly reflecting fibrous network in the annulus fibrous (outer region) of the disc shown in Fig. 1.12 is the elastic fibre network, since the amorphous molecular structure of elastic tissue is a strong

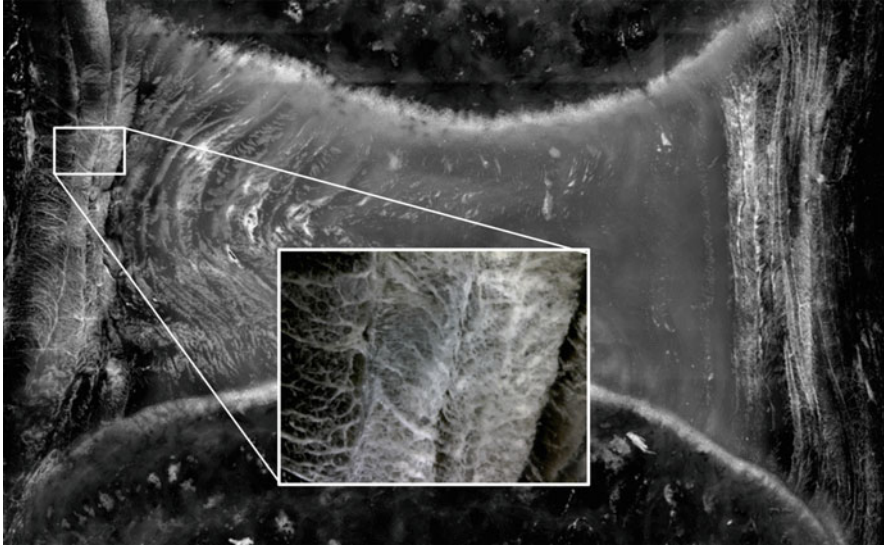


Fig. 1.12 High-resolution block face reflected polarised light image of bovine tail intervertebral disc

diffuse reflector. However, by performing complementary fluorescent block face imaging on the same block face (not shown here), it is possible to see more detail of the collagen fibre bundles in the annulus, since collagen and elastin fluoresce at similar intensities under the 365-nm excitation used for the fluorescence imaging used in our pilot work to date.

In principle therefore, the 3D morphologies of the collagen and elastic fibre networks could be defined and biomechanically modelled, either by physically embedding networks of beam elements within a ‘macro-scale’ representation of the proteoglycan-rich disc ground substance or by homogenisation of subregions of the image dataset. Clearly there are challenges with attempts to develop image-based microstructural models such as these: fibres smaller than the imaging resolution will not be visible; it will not be possible to know whether touching fibres are physically joined or just touching, and tissue processing during embedding may alter the microstructure from its native state. Notwithstanding, the potential of such approaches to improve our biomechanical understanding of non-mineralised fibrous tissues by coupling the micro- and macro-scales is significant.

1.4.2 Modelling Cells Within the Cellular Microenvironment

As mentioned above, the response of cells within musculoskeletal tissues is crucial to understanding disease states and the effect of orthopaedic treatments. Although the cells themselves in musculoskeletal tissues do not contribute appreciably to the

short-term load–deformation response of the extracellular matrix, their importance lies in their ability to modify the ECM in response to physicochemical cues throughout the lifespan. The common theme underlying the studies discussed in Sect. 1.3.1 was that they came from the perspective of matrix mechanics, i.e. they were concerned with modelling strains, cracks, fluid pressures and velocities within the ECM from a biomechanics perspective. The models that attempted to include bone remodelling also used a matrix-centred approach, incorporating phenomenological descriptions of matrix alteration according to various candidate stimuli in the ECM such as strain energy density or fluid flow. However, several recent attempts to explicitly model cell behaviour within the ECM microenvironment have been made. Fernandez et al. [177] coupled synchrotron-based micro-FE and smoothed particle hydrodynamics models (2- μm voxel size) with cell models from the CellML repository. The cells were not modelled mechanically in the spatio-temporal framework of the ECM model, but outputs from the ECM mechanical model drive biochemical ODE-based models of cell response via the RANK–RANKL–OPG pathway, which in turn drives remodelling of the matrix. Thus cell and matrix behaviour were coupled in both directions. The previously mentioned study by Verbruggen et al. [92] explicitly modelled osteocytes and their cellular processes subject to pericellular fluid flow within the lacuno-canalicular system. This study is significant which mechanistically couples cell and matrix mechanics via fluid–structure interaction simulation. From a mechanobiological perspective, such coupling is ‘one way’ at present, but there is much potential for further multiphysics-based modelling of intercellular signaling and subsequent matrix remodelling.

We note that multiscale, multiphysics approaches, in which cells and matrix are both explicitly modelled, are also being adopted in the field of tissue engineering to better understand matrix formation on artificial cartilage constructs grown in dynamically perfused bioreactors (e.g. [178,179]). FE models of cell attachment to tissue engineering scaffolds were developed by Stops et al. [180], in which both scaffold and cells were modelled structurally. This model predicted that for uniaxial strains of 10% in a collagen–GAG scaffold, cell strains as high as 49% were generated, though the majority of cells experienced less than 5% strain. Again, the next stage with such models is to link cell membrane stress or strain to cellular signaling and subsequent ECM modification from a spatiotemporal, coupled structural–biochemical perspective.

1.5 Conclusions

The main challenge in modelling orthopaedic procedures lies in modelling the musculoskeletal tissues within which the implant is placed. While implants themselves and the biomaterials used in their construction can be complex in topography and microstructure, the response of the cells and extracellular matrix of the host tissue is far more challenging to simulate. Due to the recognition that cellular and

matrix deformation, flow and damage processes on the micro- and nanoscale drive the tissue remodelling response, modelling efforts in recent years have shifted from the traditional top-down macro-scale approach to a bottom-up approach. While top-down approaches use phenomenological descriptions of tissue behaviour, bottom-up approaches attempt to gain a more fundamental understanding of the system by incorporating mechanistic descriptions of tissue behaviour as much as possible. The potential rewards of such bottom-up multiscale modelling are high, though the models must be informed by imaging and experimental data at the scales of interest.

Multiscale modelling and experimentation are thus intricately related. In fact, for multiscale models to have true explanatory power, they should ideally be derived from 3D imaging datasets of individual tissue specimens and then be validated against experimental (flow, deformation, remodelling, etc.) measurements on these same specimens wherever possible. This is a challenging requirement, but is becoming increasingly possible due to rapid development and wide availability of micro-scale imaging technologies which can be used both *in vitro* and *in vivo*. As micro-scale models become more advanced in their ability to represent tissue-level heterogeneity and spatially varying mechanical properties across large regions of tissue, micro/macro-scale bridging methodologies will become increasingly important. Even with massively parallel computing, it will not be possible to model clinically relevant regions of tissue using voxel-based meshing. Also, as mechanistically driven descriptions of cell behaviour are incorporated in such models, the issue of short- and long-term temporal timescales will become increasingly important, coupling deformation, fluid flow and diffusion events in the order of milliseconds with tissue healing and adaptation over months and years.

The design of treatments for musculoskeletal disease and degeneration is a multidisciplinary field, and spatiotemporal, mechanics-based computer modelling is just one approach among the armoury of expertise which can be brought to bear on the problem. The problems which multiscale modelling attempts to address should be informed by clinicians, biologists, biochemists and materials scientists, especially with regard to the behaviour of the cell within the ECM in response to the physical signals captured by computational simulations. Clearly, the issues of biocompatibility, wear, degeneration and degradation of the implants themselves are also important. In the emerging field of tissue engineering, the physico-chemistry of controlled scaffold degradation is a highly complex problem which again will benefit from computational modelling approaches.

While nanoscale mechanics of musculoskeletal tissues at the molecular level are clearly important, it is the author's opinion that the most pressing current issue in this field is the development of micro-macro frameworks which can incorporate micro-scale mechanistic models of ECM deformation and cellular response with macro-scale continuum models of whole implant-tissue constructs. Such models will need to take account of micro-scale heterogeneity to better describe nonlinear deformation and fracture behaviour, will need to be coupled with mathematical models of cell signaling and will need to be verified and validated against an integrated program of experimental measurements. All of these are challenging;

however, the potential to drive genuine improvements in the outcomes of orthopaedic procedures is worth the effort.

Acknowledgements The author wishes to acknowledge Dr Victoria Toal, Dr Katrina McDonald and Dr Cameron Bell for providing images.

References

1. Whitesides G, Wong A (2006) The intersection of biology and materials science. *MRS Bulletin* 31:19–27
2. Hunter PJ, Borg TK (2003) Integration from proteins to organs: the Physiome Project. *Nat Rev Mol Cell Biol* 4:237–43
3. Horstemeyer MF (2010) Multiscale modelling: a review. In: Leszczynski J, Shukla MK (eds) *Practical aspects of computational chemistry*. Springer, New York, pp 87–135
4. Fish J (ed) (2010) *Multiscale Methods: Bridging the scales in science and engineering*. Oxford University Press, Oxford
5. Tsubota K, Adachi T, Tomita Y (2003) Effects of a fixation screw on trabecular structural changes in a vertebral body predicted by remodelling simulation. *Ann Biomed Eng* 31: 733–40
6. Ebraheim NA, Rupp RE, Savolaine ER et al (1994) Use of titanium implants in pedicular screw fixation. *J. Spinal Disord* 7:478–86
7. Hawes MC, O'Brien JP (2008) A century of spine surgery: what can patients expect? *Disabil Rehabil* 30:808–17
8. Paris O, Zizak I, Lichtenegger H et al (2000) Analysis of the hierarchical structure of biological tissues by scanning X-ray scattering using a micro-beam. *Cell Mol Biol* 46: 993–1004
9. Mandel U, Dalgaard P, Viidik A (1986) A biomechanical study of the human periodontal ligament. *J Biomech* 19:637–45
10. Maroudas A (1976) Balance between swelling pressure and collagen tension in normal and degenerate cartilage. *Nature* 260:808–809
11. Evans JH, Nachemson AL (1969) Biomechanical study of human lumbar ligamentum flavum. *J Anat* 105:188–9
12. Borg TK, Caulfield JB (1980) Morphology of connective tissue in skeletal muscle. *Tissue Cell* 12:197–207
13. Rigozzi S, Müller R, Snedeker JG (2010) Collagen fibril morphology and mechanical properties of the Achilles tendon in two inbred mouse strains. *J Anat* 216:724–31
14. Kim SH, Turnbull J, Guimond S (2011) Extracellular matrix and cell signalling: the dynamic cooperation of integrin, proteoglycan and growth factor receptor. *J Endocrinol* 209:139–51
15. Chen JH, Liu C, You L et al (2010) Boning up on Wolff's Law: mechanical regulation of the cells that make and maintain bone. *J Biomech* 43:108–18
16. Sievänen H (2010) Immobilization and bone structure in humans. *Arch Biochem Biophys* 503:146–52
17. LeBlanc A, Schneider V, Shackelford L et al (2000) Bone mineral and lean tissue loss after long duration space flight. *J Musculoskelet Neuronal Interact* 1:157–60
18. Merle C, Streit MR, Volz C et al (2011) Bone remodelling around stable uncemented titanium stems during the second decade after total hip arthroplasty: a DXA study at 12 and 17 years. *Osteoporos Int* 22:2879–86
19. Burr DB (1993) Remodelling and the repair of fatigue damage. *Calcif Tissue Int* 53:S75–80
20. Weiner S, Wagner HD (1998) The material bone: structure mechanical function relations. *Annu Rev Mater Sci* 28:271–298

21. Rho JY, Kuhn-Spearing L, Zioupos P (1998) Mechanical properties and the hierarchical structure of bone. *Med Eng Phys* 20:92–102
22. Buehler MJ (2007) Nano- and micromechanical properties of hierarchical biological materials and tissues. *Mater Sci* 42(21):8765–8770
23. de d’Otreppe BV (2012) From medical imaging to finite element simulations : a contribution to mesh generation and locking-free formulations for tetrahedra. Universite de Liège, PhD Dissertation
24. Bell CG (2005) A finite element and experimental investigation of the femoral component distraction rods in a total hip arthroplasty. Queensland University of Technology, PhD Dissertation
25. An YH, Draughn RA (eds) (2000) Mechanical testing of bone and the bone-implant interface. CRC Press, Boca Raton
26. Little JP, de Visser H, Pearcy MJ et al (2008) Are coupled rotations in the lumbar spine largely due to the osseo-ligamentous anatomy?--a modelling study. *Comp Meth Biomech Biomed Eng* 11:95–103
27. Nachemson A, Elfström G (1971) Intravital wireless telemetry of axial forces in Harrington distraction rods in patients with idiopathic scoliosis. *J Bone Joint Surg Am* 53:445–65
28. Carretta R, Lorenzetti S, Müller R (2013) Towards patient-specific material modelling of trabecular bone post-yield behavior. *Int j numer method biomed eng* 29:250–72
29. Hoshaw SJ, Fyhrie DP, Takano Y et al (1997) A method suitable for in vivo measurement of bone strain in humans. *J Biomech* 30:521–4
30. Nachemson AL (1981) Disc pressure measurements. *Spine* 6:93–7
31. Wilke HJ, Neef P, Caimi M et al (1999) New in vivo measurements of pressures in the intervertebral disc in daily life. *Spine* 24:755–62
32. Frost HM (2003) Bone’s mechanostat: a 2003 update. *Anat Rec A Discov Mol Cell Evol Biol* 275:1081–101
33. Dabirrahmani D, Hogg M, Kohan L et al (2010) Primary and long-term stability of a short-stem hip implant. *Proc Inst Mech Eng H* 224:1109–19
34. Dickinson A, Taylor A, Browne M (2012) Implant-bone interface healing and adaptation in resurfacing hip replacement. *Comp Meth Biomech Biomed Eng* 15:935–47
35. Geris L, Van Oosterwyck H, Vander Sloten J et al (2003) Assessment of mechanobiological models for the numerical simulation of tissue differentiation around immediately loaded implants. *Comp Meth Biomech Biomed Eng* 6:277–88
36. Prendergast PJ, Huiskes R, Søballe K (1997) Biophysical stimuli on cells during tissue differentiation at implant interfaces. *J Biomech* 30:539–548
37. Huiskes R, Van Driel WD, Prendergast PJ et al (1997) A biomechanical regulatory model for periprosthetic fibrous-tissue differentiation. *J Matl Sci: Materials in Medicine* 8:785–788
38. Claes LE, Heigele CA (1999) Magnitudes of local stress and strain along bony surfaces predict the course and type of fracture healing. *J Biomech* 32:255–266
39. Pivonka P, Komarova SV (2010) Mathematical modelling in bone biology: from intracellular signaling to tissue mechanics. *Bone* 47:181–9
40. Meyers MA, Chen PY, Lopez MI et al (2010) Biological materials: a materials science approach. *J Mech Behav Biomed Mat* 4:626–57
41. Parfitt AM (2002) Misconceptions (2): turnover is always higher in cancellous than in cortical bone. *Bone* 30:807–9
42. Eswaran SK, Gupta A, Adams MF, Keaveny TM (2006) Cortical and trabecular load sharing in the human vertebral body. *J Bone Miner Res* 21:307–14
43. Harrigan TP, Jasty M, Mann RW et al (1988) Limitations of the continuum assumption in cancellous bone. *J Biomech* 21:269–75
44. McDonnell P, McHugh PE, O’Mahoney D (2007) Vertebral osteoporosis and trabecular bone quality. *Ann Biomed Eng* 35:170–189
45. Seeman E, Delmas PD (2006) Bone quality--the material and structural basis of bone strength and fragility. *N Engl J Med* 354:2250–61

46. Niebur GL, Feldstein MJ, Yuen JC (2000) High-resolution finite element models with tissue strength asymmetry accurately predict failure of trabecular bone. *J Biomech* 33:1575–83
47. Müller R, Rüegsegger P (1995) Three-dimensional finite element modelling of non-invasively assessed trabecular bone structures. *Med Eng Phys* 17:126–33
48. van Rietbergen B, Weinans H, Huiskes R et al (1995) A new method to determine trabecular bone elastic properties and loading using micromechanical finite-element models. *J Biomech* 28:69–81
49. Jacobs CR, Davis BR, Rieger CJ et al (1999) The impact of boundary conditions and mesh size on the accuracy of cancellous bone tissue modulus determination using large-scale finite-element modelling. *J Biomech* 32:1159–64
50. van Rietbergen B, Kabel J, Odgaard A et al (1997) Determination of trabecular bone tissue elastic properties by comparison of experimental and finite element results. In: Sol H, Oomens CWJ (eds) *Material identification using mixed numerical experimental methods*. Kluwer Academic Publisher, Norwell (MA)
51. Kabel J, van Rietbergen B, Dalstra M et al (1999) The role of an effective isotropic modulus in the elastic properties of cancellous bone. *J Biomech* 32:673–680
52. Fyhrie DP, Hou FJ (1995) Prediction of human vertebral cancellous bone strength using non-linear, anatomically accurate, large-scale finite element analysis. *Proc Bioeng Conf ASME* 29:301–2
53. Van Rietbergen B, Ulrich D, Pistoia W et al (1998) Prediction of trabecular bone failure parameters using a tissue failure criterion. *Trans Orthop Res Soc* 23:550
54. Niebur GL, Yuen JC, Burghardt AJ et al (2001) Sensitivity of damage predictions to tissue level yield properties and apparent loading conditions. *J Biomech* 34:699–706
55. Pistoia W, van Rietbergen B, Lochmuller EM et al (2002) Estimation of distal radius failure load with micro-finite element analysis models based on three-dimensional peripheral quantitative computed tomography images. *Bone* 30:842–8
56. Stölken JS, Kinney JH (2003) On the importance of geometric nonlinearity in finite-element simulations of trabecular bone failure. *Bone* 33:494–504
57. Verhulp E, Van Rietbergen B, Muller R et al (2008) Micro-finite element simulation of trabecular-bone post-yield behaviour-effects of material model, element size and type. *Comp Meth Biomech Biomed Eng* 11:389–95
58. Pistoia W, van Rietbergen B, Laib A et al (2001) High-resolution three-dimensional-pQCT images can be an adequate basis for in-vivo microFE analysis of bone. *J Biomech Eng* 123:176–83
59. Vilayphiou N, Boutroy S, Szulc P et al (2011) Finite element analysis performed on radius and tibia HR-pQCT images and fragility fractures at all sites in men. *J Bone Miner Res* 26:965–73
60. Podshivalov L, Fischer A, Bar-Yoseph PZ (2011) Multiscale FE method for analysis of bone micro-structures. *J Mech Behav Biomed Mater* 4:888–99
61. Basaruddin KS, Takano N, Nakano T (2013) Stochastic multiscale prediction on the apparent elastic moduli of trabecular bone considering uncertainties of biological apatite (BAp) crystallite orientation and image-based modelling., *Comp Meth Biomech Biomed Eng*, (epub ahead of print)
62. Taylor D, Hazenber JG, Lee TC (2007) Living with cracks: Damage and repair in human bone. *Nature Materials* 6:263–8
63. Fazzalari NL, Forwood MR, Manthey BA et al (1998) Three-dimensional confocal images of microdamage in cancellous bone. *Bone* 23:373–8
64. Mori S, Burr DB (1993) Increased intracortical remodelling following fatigue damage. *Bone* 14:103–9
65. Mulvihill BM, McNamara LM, Prendergast PJ (2008) Loss of trabeculae by mechano-biological means may explain rapid bone loss in osteoporosis. *J R Soc Interface* 5:1243–53

66. Mosekilde L (1990) Consequences of the remodelling process for vertebral trabecular bone structure: a scanning electron microscopy study (uncoupling of unloaded structures). *Bone and Mineral* 10:13–35
67. Burr DB, Forwood MR, Fyhrrie DP et al (1997) Bone microdamage and skeletal fragility in osteoporotic and stress fractures. *J Bone Miner Res* 12:6–15
68. Yeh OC, Keaveny TM (2001) Relative roles of microdamage and microfracture in the mechanical behavior of trabecular bone. *J Orthop Res* 19:1001–7
69. Nagaraja S, Couse TL, Guldberg RE (2005) Trabecular bone microdamage and microstructural stresses under uniaxial compression. *J Biomech* 38:707–16
70. Jungmann R, Szabo ME, Schitter G et al (2011) Local strain and damage mapping in single trabeculae during three-point bending tests. *J Mech Behav Biomed Mater* 4:523–34
71. Ural A, Vashishth D (2006) Cohesive finite element modelling of age-related toughness loss in human cortical bone. *J Biomech* 39:2974–82
72. Tomar V (2008) Modelling of dynamic fracture and damage in two-dimensional trabecular bone microstructures using the cohesive finite element method. *J Biomech Eng* 130:021021
73. Kosmopoulos V, Keller TS (2003) Finite element modelling of trabecular bone damage. *Comp Meth Biomech Biomed Eng* 6:209–16
74. Kosmopoulos V, Keller TS (2008) Predicting trabecular bone microdamage initiation and accumulation using a non-linear perfect damage model. *Med Eng Phys* 30:725–32
75. Budyn E, Hoca T (2006) Multiscale Modelling of Human Cortical Bone: Aging and Failure Studies. *Mat Res Soc Fall Meeting* 975:27–32
76. Yang QD, Cox BN, Nalla RK et al (2006) Fracture length scales in human cortical bone: the necessity of nonlinear fracture models. *Biomaterials* 27:2095–113
77. Renders GA, Mulder L, Langenbach GE et al (2008) Biomechanical effect of mineral heterogeneity in trabecular bone. *J Biomech* 41:2793–8
78. Renders GA, Mulder L, van Ruijven LJ et al (2011) Mineral heterogeneity affects predictions of intratrabecular stress and strain. *J Biomech* 44:402–7
79. Knothe Tate ML (2003) "Whither flows the fluid in bone?" An osteocyte's perspective. *J Biomech* 36:1409–24
80. McNamara LM, Van der Linden JC, Weinans H et al (2006) Stress-concentrating effect of resorption lacunae in trabecular bone. *J Biomech* 39(4):734–41
81. Deligianni DD, Apostolopoulos CA (2008) Multilevel finite element modelling for the prediction of local cellular deformation in bone. *Biomech Model Mechanobiol* 7:151–9
82. Jacobs CR, Temiyasathit S, Castillo AB (2010) Osteocyte mechanobiology and pericellular mechanics. *Annu Rev Biomed Eng* 12:369–400
83. Cardoso L, Fritton SP, Gailani G et al (2013) Advances in assessment of bone porosity, permeability and interstitial fluid flow. *J Biomech* 46:253–65
84. Swan CC, Lakes RS, Brand RA et al (2003) Micromechanically based poroelastic modelling of fluid flow in Haversian bone. *J Biomech Eng* 125:25–37
85. Galley SA, Michalek DJ, Donahue SW (2006) A fatigue microcrack alters fluid velocities in a computational model of interstitial fluid flow in cortical bone. *J Biomech* 39:2026–33
86. Rémond A, Naïli S, Lemaire T (2008) Interstitial fluid flow in the osteon with spatial gradients of mechanical properties: a finite element study. *Biomech Model Mechanobiol* 7:487–95
87. Cowin SC, Gailani G, Benalla M (2009) Hierarchical poroelasticity: movement of interstitial fluid between porosity levels in bones. *Philos Trans A Math Phys Eng Sci* 367:3401–44
88. Nguyen VH, Lemaire T, Naïli S (2010) Poroelastic behaviour of cortical bone under harmonic axial loading: a finite element study at the osteonal scale. *Med Eng Phys* 32:384–90
89. Lemaire T, Naïli S, Rémond A (2006) Multiscale analysis of the coupled effects governing the movement of interstitial fluid in cortical bone. *Biomech Model Mechanobiol* 5:39–52
90. Lemaire T, Capiez-Lernout E, Kaiser J (2011) What is the importance of multiphysical phenomena in bone remodelling signals expression? A multiscale perspective. *J Mech Behav Biomed Mater* 4:909–20

91. Sansalone V, Kaiser J, Naili S et al (2012) Interstitial fluid flow within bone canaliculi and electro-chemo-mechanical features of the canalicular milieu : A multi-parametric sensitivity analysis., *Biomech Model Mechanobiol.* (epub ahead of print)
92. Verbruggen SW, Vaughan TJ, McNamara LM (2013) Fluid flow in the osteocyte mechanical environment: a fluid-structure interaction approach., *Biomech Model Mechanobiol.* (epub ahead of print)
93. Goulet GC, Hamilton N, Cooper D (2008) Influence of vascular porosity on fluid flow and nutrient transport in loaded cortical bone. *J Biomech* 41:2169–75
94. Steck R, Niederer P, Knothe Tate ML (2003) A finite element analysis for the prediction of load-induced fluid flow and mechanochemical transduction in bone. *J Theor Biol* 220:249–59
95. Nguyen VH, Lemaire T, Naili S (2011) Influence of interstitial bone microcracks on strain-induced fluid flow. *Biomech Model Mechanobiol* 10:963–72
96. Silva MJ, Gibson LJ (1997) Modelling the mechanical behavior of vertebral trabecular bone: Effects of age-related changes in microstructure. *Bone* 21:191–199
97. Langton CM, Haire TJ, Ganney PS et al (1998) Dynamic stochastic simulation of cancellous bone resorption. *Bone* 22:375–80
98. Langton CM, Haire TJ, Ganney PS et al (2000) Stochastically simulated assessment of anabolic treatment following varying degrees of cancellous bone resorption. *Bone* 27:111–8
99. Huiskes R, Ruimerman R, van Lenthe GH, Janssen JD (2000) Effects of mechanical forces on maintenance and adaptation of form in trabecular bone. *Nature* 405:704–6
100. Ruimerman R, Van Rietbergen B, Hilbers P et al (2003) A 3-dimensional computer model to simulate trabecular bone metabolism. *Biorheology* 40:315–20
101. Ruimerman R, Van Rietbergen B, Hilbers P (2005) The effects of trabecular-bone loading variables on the surface signaling potential for bone remodelling and adaptation. *Ann Biomed Eng* 33:71–8
102. van Oers RF, Ruimerman R, Tanck E et al (2008) A unified theory for osteonal and hemi-osteonal remodelling. *Bone* 42:250–9
103. van Oers RF, van Rietbergen B, Ito K et al (2011) Simulations of trabecular remodelling and fatigue: is remodelling helpful or harmful? *Bone* 48:1210–5
104. Chen G, Pettet GJ, Pearcy M et al (2007) Modelling external bone adaptation using evolutionary structural optimisation. *Biomech Model Mechanobiol* 6:275–85
105. Van Der Linden JC, Verhaar JA, Weinans H (2001) A three-dimensional simulation of age-related remodelling in trabecular bone. *J Bone Miner Res* 16:688–96
106. Hernandez CJ, Gupta A, Keaveny TM (2006) A biomechanical analysis of the effects of resorption cavities on cancellous bone strength. *J Bone Miner Res* 21:1248–55
107. Smit TH, Burger EH (2000) Is BMU-coupling a strain-regulated phenomenon? A finite element analysis. *J Bone Miner Res* 15:301–7
108. McNamara LM, Prendergast PJ (2005) Perforation of cancellous bone trabeculae by damage-stimulated remodelling at resorption pits: a computational analysis. *Eur J Morphol* 42:99–109
109. McNamara LM, Prendergast PJ (2007) Bone remodelling algorithms incorporating both strain and microdamage stimuli. *J Biomech* 40:1381–91
110. Mulvihill BM, McNamara LM, Prendergast PJ (2008) Loss of trabeculae by mechano-biological means may explain rapid bone loss in osteoporosis. *J R Soc Interface* 5:1243–53
111. Ryser MD, Nigam N, Komarova SV (2009) Mathematical modelling of spatio-temporal dynamics of a single bone multicellular unit. *J Bone Miner Res* 24:860–70
112. Adachi T, Kameo Y, Hojo M (2010) Trabecular bone remodelling simulation considering osteocytic response to fluid-induced shear stress. *Philos Trans A Math Phys Eng Sci* 368: 2669–82
113. Gerhard FA, Webster DJ, van Lenthe GH et al (2009) In silico biology of bone modelling and remodelling: adaptation. *Philos Trans A Math Phys Eng Sci* 367:2011–30
114. Hambli R (2010) Application of neural networks and finite element computation for multi-scale simulation of bone remodelling. *J Biomech Eng* 132:114502

115. Hambli R, Katerchi H, Benhamou CL (2011) Multiscale methodology for bone remodelling simulation using coupled finite element and neural network computation. *Biomech Model Mechanobiol* 10:133–45
116. Hambli R (2011) Apparent damage accumulation in cancellous bone using neural networks. *J Mech Behav Biomed Mater* 4:868–78
117. Mann KA, Miller MA (2013) Fluid-structure interactions in micro-interlocked regions of the cement-bone interface., *Comput Methods Biomech Biomed Engin*, (epub ahead of print)
118. Hollister SJ, Fyhrie DP, Jepsen KJ et al (1991) Application of homogenization theory to the study of trabecular bone mechanics. *J Biomech* 24:825–39
119. van Lenthe GH, Stauber M, Müller R (2006) Specimen-specific beam models for fast and accurate prediction of human trabecular bone mechanical properties. *Bone* 39:1182–9
120. McDonald K, Little J, Pearcy M et al (2010) Development of a multi-scale finite element model of the osteoporotic lumbar vertebral body for the investigation of apparent level vertebra mechanics and micro-level trabecular mechanics. *Med Eng Phys* 32:653–61
121. Yeh OC, Keaveny TM (1999) Biomechanical effects of intraspecimen variations in trabecular architecture: A three-dimensional finite element study. *Bone* 25:223–228
122. Jensen KS, Mosekilde L, Mosekilde L (1990) A model of vertebral trabecular bone architecture and its mechanical properties. *Bone* 11:417–423
123. Hildebrand T, Rüeggsegger P (1997) Quantification of Bone Microarchitecture with the Structure Model Index. *Comput Methods Biomech Biomed Engin* 1:15–23
124. Odgaard A (1997) Three-dimensional methods for quantification of cancellous bone architecture. *Bone* 20:315–328
125. Mosekilde L (1989) Sex differences in age-related loss of vertebral trabecular bone mass and structure-biomechanical consequences. *Bone* 10:425–432
126. Pugh JW, Rose RM, Radin EL (1973) A structural model for the mechanical behavior of trabecular bone. *Journal of Biomechanics* 6:657–670
127. Gibson LJ, Ashby MF, Schajer GS, et al. (1982) The mechanics of three-dimensional cellular materials. In: *Proceedings of the Royal Society of London. Series A, Mathematical and physical sciences* A 382
128. McDonald K (2009) An experimental and finite element investigation of the biomechanics of vertebral compression fractures. Queensland University of Technology, PhD Dissertation
129. Mizrahi J, Silva MJ, Keaveny TM et al (1993) Finite-element stress analysis of the normal and osteoporotic lumbar vertebral body. *Spine* 18:2088–2096
130. Chevalier Y, Pahr D, Allmer H et al (2007) Validation of a voxel-based FE method for prediction of the uniaxial apparent modulus of human trabecular bone using macroscopic mechanical tests and nanoindentation. *J Biomech* 40:3333–40
131. Toal V (2013) The mechanics of microdamage and microfracture in trabecular bone. Queensland University of Technology, PhD Dissertation
132. Galli M, Oyen ML (2009) Fast identification of poroelastic parameters from indentation tests. *Comp Model Eng Sci* 48:241–268
133. Fratzl-Zelman N, Roschger P, Gourrier A et al (2009) Combination of nanoindentation and quantitative backscattered electron imaging revealed altered bone material properties associated with femoral neck fragility. *Calcif Tissue Int* 85:335–43
134. Tai K, Qi HJ, Ortiz C (2005) Effect of mineral content on the nanoindentation properties and nanoscale deformation mechanisms of bovine tibial cortical bone. *J Mater Sci Mater Med* 16: 947–959
135. Tai K, Ulm FJ, Ortiz C (2006) Nanogranular origins of the strength of bone. *Nano Letters* 6: 2520–2525
136. Wang X, Allen MR, Burr DB et al (2008) Identification of material parameters based on Mohr-Coulomb failure criterion for bisphosphonate treated canine vertebral cancellous bone. *Bone* 43:775–780
137. Mullins LP, Bruzzi MS, McHugh PE (2009) Calibration of a constitutive model for the post-yield behaviour of cortical bone. *J Mech Behav Biomed Mater* 2:460–70

138. Oyen ML, Ko CC (2007) Examination of local variations in viscous, elastic, and plastic indentation responses in healing bone. *J Mater Sci Mater Med* 18:623–8
139. Brockaert H, Mazerain PE, Rachik M, Ho Ba Tho MC (2009) Nanoindentation on isotropic and anisotropic materials confrontation with FEM simulations. *Comp Meth Biomech Biomed Eng* 12:63–64
140. Paietta R, Campbell SE, Ferguson VL (2011) Influences of spherical tip radius, contact depth and contact area on nanoindentation properties of bone. *J Biomech* 44:285–90
141. Carnelli D, Gastaldi D, Sassi V et al (2010) A finite element model for direction-dependent mechanical response to nanoindentation for cortical bone allowing for anisotropic post-yield behavior of the tissue. *J Biomech Eng* 132:081008
142. Wolfram U, Wilke HJ, Zysset PK (2010) Valid micro finite element models of vertebral trabecular bone can be obtained using tissue properties measured with nanoindentation under wet conditions. *J Biomech* 43:1731–7
143. Reisinger AG, Pahr DH, Zysset PK (2011) Elastic anisotropy of bone lamellae as a function of fibril orientation pattern. *Biomech Model Mechanobiol* 10:67–77
144. Carnelli D, Lucchini R, Ponzoni M et al (2011) Nanoindentation testing and finite element simulations of cortical bone allowing for anisotropic elastic and inelastic mechanical response. *J Biomech* 44:1852–8
145. Lucchini R, Carnelli D, Ponzoni M et al (2011) Role of damage mechanics in nano-indentation of lamellar bone at multiple sizes: experiments and numerical modelling. *J Mech Behav Biomed Mater* 4:1852–63
146. Vaughan TJ, McCarthy CT, McNamara LM (2012) A three-scale finite element investigation into the effects of tissue mineralisation and lamellar organisation in human cortical and trabecular bone. *J Mech Behav Biomed Mater* 12:50–62
147. Adam CJ, Swain MV (2011) The effect of friction on indenter force and pile-up in numerical simulations of bone nanoindentation. *J Mech Behav Biomed Mater* 4:1554–8
148. Schwiedrzik JJ, Wolfram U, Zysset PK (2013) A generalized anisotropic quadric yield criterion and its application to bone tissue at multiple length scales., *Biomech Model Mechanobiol*, (epub ahead of print)
149. Currey JD (2002) *Bones: Structure and mechanics*. Princeton University Press, Oxfordshire
150. Jäger I, Fratzl P (2000) Mineralized collagen fibrils: a mechanical model with a staggered arrangement of mineral particles. *Biophys J* 79:1737–46
151. Nikolov S, Raabe D (2008) Hierarchical modelling of the elastic properties of bone at submicron scales: the role of extrafibrillar mineralization. *Biophys J* 94:4220–32
152. Siegmund T, Allen MR, Burr DB (2008) Failure of mineralized collagen fibrils: modelling the role of collagen cross-linking. *J Biomech* 41:1427–35
153. Hambli R, Barkaoui A (2012) Physically based 3D finite element model of a single mineralized collagen microfibril. *J Theor Biol* 301:28–41
154. Nair AK, Gautieri A, Chang SW et al (2013) Molecular mechanics of mineralized collagen fibrils in bone. *Nat Commun* 16:1724
155. Ganazzoli F, Raffaini G (2005) Computer simulation of polypeptide adsorption on model biomaterials. *Phys Chem Chem Phys* 7:3651–63
156. Raffaini G, Ganazzoli F (2007) Understanding the performance of biomaterials through molecular modelling: crossing the bridge between their intrinsic properties and the surface adsorption of proteins. *Macromol Biosci* 7:552–66
157. De Nardo L, Raffaini G, Ebramzadeh E et al (2012) Titanium oxide modelling and design for innovative biomedical surfaces: a concise review. *Int J Artif Organs* 35:629–41
158. Shim VB, Hunter PJ, Pivonka P et al (2011) A multiscale framework based on the physiome markup languages for exploring the initiation of osteoarthritis at the bone-cartilage interface. *IEEE Trans Biomed Eng* 58:3532–6
159. Lavagnino M, Arnoczky SP, Kepich E et al (2008) A finite element model predicts the mechanotransduction response of tendon cells to cyclic tensile loading. *Biomech Model Mechanobiol* 7:405–16

160. Hadi MF, Barocas VH (2013) Microscale fiber network alignment affects macroscale failure behavior in simulated collagen tissue analogs. *J Biomech Eng* 135:021026
161. Reese SP, Ellis BJ, Weiss JA (2013) Micromechanical model of a surrogate for collagenous soft tissues: development, validation and analysis of mesoscale size effects., *Biomech Model Mechanobiol*, (epub ahead of print)
162. Maceri F, Marino M, Vairo G (2010) A unified multiscale mechanical model for soft collagenous tissues with regular fiber arrangement. *J Biomech* 43:355–63
163. Maceri F, Marino M, Vairo G (2012) An insight on multiscale tendon modelling in muscle-tendon integrated behavior. *Biomech Model Mechanobiol* 11:505–17
164. Gronau G, Krishnaji ST, Kinahan ME et al (2012) A review of combined experimental and computational procedures for assessing biopolymer structure-process-property relationships. *Biomaterials* 33:8240–55
165. Israelowitz M, Rizvi SW, Kramer J et al (2005) Computational modelling of type I collagen fibers to determine the extracellular matrix structure of connective tissues. *Protein Eng Des Sel* 18:329–35
166. Buehler MJ (2006) Nature designs tough collagen: explaining the nanostructure of collagen fibrils. *Proc Natl Acad Sci* 103:12285–90
167. Buehler MJ (2008) Nanomechanics of collagen fibrils under varying cross-link densities: atomistic and continuum studies. *J Mech Behav Biomed Mater* 1:59–67
168. Gautieri A, Vesentini S, Redaelli A et al (2011) Hierarchical structure and nanomechanics of collagen microfibrils from the atomistic scale up. *Nano Lett* 11:757–66
169. Kim JS, Min J, Recknagel AK et al (2011) Quantitative three-dimensional analysis of embryonic chick morphogenesis via microcomputed tomography. *Anat Rec* 294:1–10
170. Kazakia GJ, Lee JJ, Singh M et al (2007) Automated high-resolution three-dimensional fluorescence imaging of large biological specimens. *J Microsc* 225:109–17
171. Bigley RF, Singh N, Hernandez CJ et al (2008) Validity of serial milling-based imaging system for microdamage quantification. *Bone* 42:212–15
172. Odgaard A, Andersen K, Melsen F et al (1990) A direct method for fast three-dimensional serial reconstruction. *J Microsc* 159:335–42
173. Ewald AJ, McBride H, Reddington M et al (2002) Surface imaging microscopy, an automated method for visualizing whole embryo samples in three dimensions at high resolution. *Dev Dyn* 225:369–75
174. Boyde A, Lovicar L, Zamecnik J (2005) Combining confocal and BSE SEM imaging for bone block surfaces. *Eur Cell Mater* 26:33–8
175. Slyfield CR Jr, Niemeyer KE, Tkachenko EV et al (2009) Three-dimensional surface texture visualization of bone tissue through epifluorescence-based serial block face imaging. *J Microsc* 236:52–9
176. Viceconti M (2012) *Multiscale modelling of the skeletal system*. Cambridge University Press, Cambridge
177. Fernandez JW, Shim VB, Hunter PJ (2012) Integrating degenerative mechanisms in bone and cartilage: a multiscale approach. In: *Proceedings of IEEE Engineering in Medical and Biology Society* 6616–6619.
178. Causin P, Sacco R, Verri M (2012) A multiscale approach in the computational modelling of the biophysical environment in artificial cartilage tissue regeneration., *Biomech Model Mechanobiol*, (epub ahead of print)
179. Sacco R, Causin P, Zunino P et al (2011) A multiphysics/multiscale 2D numerical simulation of scaffold-based cartilage regeneration under interstitial perfusion in a bioreactor. *Biomech Model Mechanobiol* 10:577–89
180. Stops AJ, McMahan LA, O'Mahoney D et al (2008) A finite element prediction of strain on cells in a highly porous collagen-glycosaminoglycan scaffold. *J Biomech Eng* 130:061001–1

Chapter 2

Performance Evaluation of Bone–Implant System During Implantation Process: Dynamic Modelling and Analysis

Rudi C. van Staden, Hong Guan, Newell W. Johnson, and Yew-Chaye Loo

Abstract Inappropriate choice of dental implant type in relation to the detailed structure of bone at the site, and inadequate surgical technique has led to 5 % failure of dental implants worldwide. By using the finite element method, three typical implant insertion scenarios are modelled and evaluated in this chapter. The scenarios are implant thread forming, cutting and the combination of forming and cutting. The bone–implant system is modelled using three-dimensional finite element technique which incorporates realistic material properties in simulating the cancellous and cortical bone. The bone–implant contact is defined using ‘surface-to-surface’ discretisation and the arbitrary Lagrangian–Eulerian adaptive meshing scheme. In current practice many implant companies recommend thread cutting for normal bone and forming for compact bone so that implant stability can be ensured. Based on the findings of the present study, the combination of forming and cutting may also be recommended for clinical practice because it best matches the specified ideal stress level resulting in positive bone stimulation with minimum resorption. Stress information obtained in these three implant insertion scenarios will advance the understanding of bone response at an early stage of the osseointegration process and primary stability.

Keywords Dental implant • Implant insertion • Bone–implant system • Finite element modelling technique • Stress analysis

R.C. van Staden
College of Engineering and Science, Structural Mechanics and Sustainable Materials Research Group, Victoria University, Melbourne, VIC, Australia

H. Guan (✉) • Y.-C. Loo
Griffith School of Engineering, Griffith University, Gold Coast, QLD, Australia
e-mail: h.guan@griffith.edu.au

N.W. Johnson
Menzies Health Institute Queensland, Griffith University, Gold Coast, QLD, Australia

2.1 Introduction

2.1.1 Background

Development of an ideal substitute for missing teeth has been a major aim of dentistry for millennia [1]. Mouths which have missing teeth are frequently restored by ‘conventional’ prostheses (partial or total), fabricated from plastic and/or metal alloys supported by the remaining teeth and/or the soft tissues. In many cases, however, removable prostheses will not be satisfactory, e.g. because of the lack of retention and/or psychological inability to accept such an appliance. In these cases, dental prostheses retained by an implant are an attractive alternative. A dental implant is a biocompatible ‘fixture’, usually screw-like and commonly made from titanium which is surgically placed into a jawbone to support a crown which forms an artificial tooth. Implants made of commercially available pure titanium have established a benchmark in osseointegration, against which no other materials can compare in a number of ways. Osseointegration is defined as the formation of bony interface which links bone to the implant surface [2].

The long-term benefits of dental implants include restored oral functions, improved appearance, comfort, speech clarity and self-esteem. With the implant, the patient can eat more conveniently, and the associated inconvenience of removable partial or full dentures does not exist. In addition, an implant is able to protect the remaining natural teeth, stop bone loss and restore facial skeletal structure. As far as the cost is concerned, implants have been shown to be comparable or even less expensive overall than conventional prostheses such as crown and bridge restorations [3]. Although the cost of an implant is generally higher than that of a crown or a bridge, the life time of an implant can be longer [4].

Worldwide implant statistics show a high success rate: in excess of 95% retention over a 5-year period if the devices are correctly designed, manufactured and inserted [5–12]. Implants are expected to function for life, and this may well be possible in many cases, given that the retention rate at 15 years has been reported to be as high as 90% if proper and professional care was taken by the practitioner and patient [13]. Despite all these advantages, only 10% of Australian patients have received single or multiple dental implants [14]. This is mainly due to the initial high costs. However, it has been suggested [14] that another reason of low implant usage in Australia could be the lack of clinical skills [15] and knowledge of comparatively more complicated and less well-known implantation techniques. This is because the failure mechanisms consequential to the stress distribution characteristics in the jawbone during the implantation process itself, as well as the healing and maintenance phases, are poorly understood. Inaccurate implant manufacturer guidelines and inadequate surgical techniques also contribute to the 5% failure of implants.

2.1.2 Implantation Procedure and Scenarios

Prior to commencement of implant placement, careful and detailed planning is required to identify the shape and dimensions of the bone to correctly orientate the implant. Periapical, panoramic and tomographic radiographs or computer tomography (CT) scans are often taken to assist in identifying these anatomical details and also to locate the nerve. The implantation process is initiated by making a small incision into the gingival tissue at the proposed implantation site. After the bone is made visible, a pilot hole is drilled into the cortical bone using a round bur. Drills of diameters 2.2, 3.0, 3.6 and 3.9 mm may be used successively, to create the implantation site in the cortical and cancellous bone, when inserting a single implant of diameter 4.5 mm [12]. Other operations, such as countersinking or screw tapping, may be a further stage before the implant is placed into the jawbone. The entire operation is performed under local anaesthesia, and a constant supply of physiological saline during the procedure reduces heat and flushes away blood and bone fragments.

The implant is finally inserted manually, using a ratchet or using a surgical micromotor mechanically. Manual insertion of the implant generally requires an increased torque with insertion depth as a result of the relatively low insertion velocity. On the other hand, mechanical insertion is performed at increased velocity, and thus the torque remains constant regardless of the insertion depth. Generally, 1 week after surgery, the implantation site is checked by the clinician for complete soft tissue healing around the healing abutment (one-stage implants) or over the implants (two-stage healing) [12]. The healing period for osseointegration varies and is dependent on criteria such as primary stability of implant at time of placement, bone quality, the use of any grafted bone or otherwise, overall patient health and the expected masticatory forces.

The bone strength and cortical thickness are generally the determining factors for the insertion drill sizes and finally the implant diameter. As such, three typical implant insertion scenarios are often adopted clinically. They are implant thread forming (scenario one, S1), thread cutting (scenario two, S2) or forming and cutting (scenario three, S3). If the bone cavity is 0.25 mm smaller in diameter than the implant, S1 takes place. Sennerby and Meredith [16] have shown that stability is reduced at sites of S1, thereby increasing the possibility of implant failure. For a bone cavity that is 0.6 mm smaller in diameter than the implant, S2 occurs. S2 is ideal in which the implant cuts a new thread pattern into the bone around a cavity of smaller diameter. In this case, optimum implant stability can be achieved through the entire length of the implant. In practice, S2 is often recommended by implant companies [12, 17, 18]. Note that if an implant is placed into a cavity created by a newly extracted tooth, the diameter of the cavity will vary. Generally, this cavity will be of a larger diameter at the top than the bottom. Therefore S3 takes place during insertion [12]. The amount of forming or cutting would ultimately contribute to the biological response of the bone and subsequently the outcome of the implantation procedure.

2.1.3 *Finite Element Technique*

While inserting the implant, elevated compressive stress can obstruct blood supply and damage the cells particularly for dense bone which in turn would affect osseointegration. On the other hand, inadequate stress cannot stimulate bone remodelling properly, thereby compromising implant stability. An optimal stress level and distribution must therefore be sought during and after implantation for the jawbone to remain strong and healthy.

There have been limited publications available on the response of bone cells to mechanical forces [19]. Limited data from animal studies suggest a large range of stress–strain values for the mandible [20]. Furthermore, bone densities and the local cell and tissue responses are also dependent on the general health and systematic responses of the patient. As such, the stress condition in the jawbone will change accordingly. The effects of such a phenomenon on bone resorption or healing has not been researched adequately, and the long-term effects of such stresses are still unclear.

The finite element method (FEM) is showing overwhelming capability and versatility in its application to dentistry [21–26]. The FEM has proven to be a reliable tool in analysing stress levels and distributions in biological bone tissues and in tissue-implant interacting structures. The primary difficulties in simulating the mechanical behaviour of dental implants are the complex finite element meshing process and the modelling of living human bone tissue and its response to applied mechanical forces. In an attempt to reduce the potential risks of clinical failure, research has been mainly directed towards finding the most biocompatible materials with which the dental implants are manufactured.

Despite the considerable research efforts on finite element analysis (FEA) of implant-mandible structure under a condition of full osseointegration, research into the modelling of the entire implantation process is non-existent. The purpose of this study is to model the insertion process in a dynamic manner, including further advancement on the bone–implant contact modelling. The major implantation scenarios to be considered are S1, S2 and S3. The aim of this study is to advance the work of van Staden et al. [27] on stepwise simulation of the implantation process. This will help provide an improved understanding of how various thread forming or cutting processes affect the outcome of implantation.

2.2 Dynamic Modelling

Summarised herein are the bone–implant geometry and material properties, modelling details and contact simulation for simulating the implantation process. The dynamic modelling of the implantation process requires the definition of complex bone–implant contact behaviour and material properties.

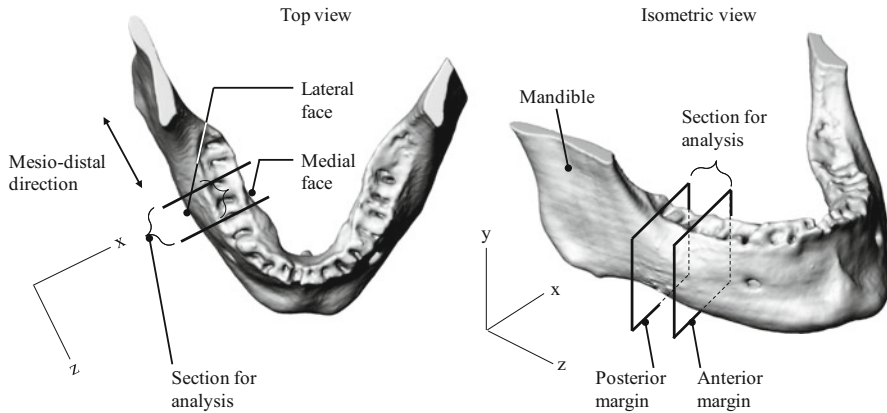


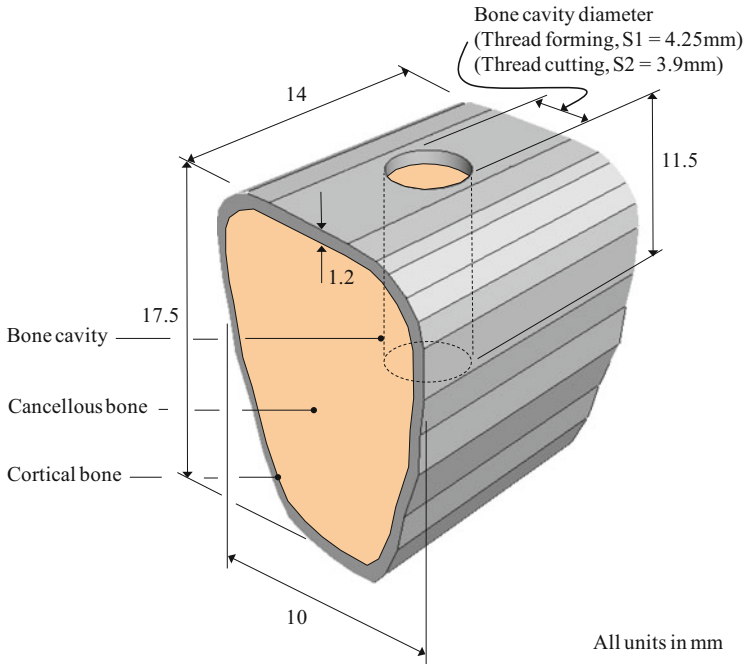
Fig. 2.1 Location of three-dimensional slice in a mandible

2.2.1 Bone–Implant System Geometry and Material Properties

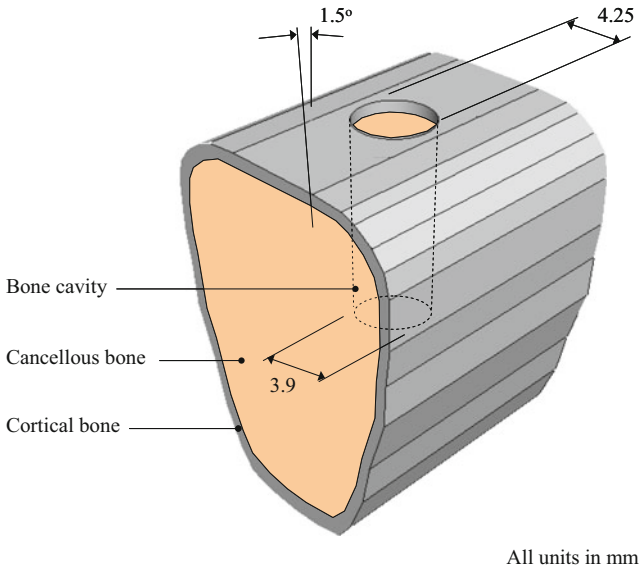
All the modelling and analyses are carried out using ABAQUS in this study [28]. Data acquisition for bone dimensions are based on computed tomography (CT) scanned images. From these images, a section from the human mandible is taken as illustrated in Fig. 2.1. The bone is categorised as ‘soft quality’ or type IV bone.

The geometry of the sectioned bone structure for analysis, as identified in Fig. 2.1, has been smoothed out with geometrical discontinuities removed. This model is illustrated in Fig. 2.2 with different dimensions of bone cavities. S1, S2 and S3 take place, respectively, for bone cavity diameters of 4.25, 3.9 mm and the combination of these two. Note that for S3 the bone cavity has a 1.5° taperage due to the difference in the top (4.25 mm) and bottom (3.9 mm) diameters of the cavity, as shown in Fig. 2.2 (b). A conical implant is considered herein with 2° of taper angle, a helical thread and three primary cutting faces. A typical implant of 4.5 mm in diameter and 11 mm in length is presented in Fig. 2.3.

Realistic material behaviour of the cancellous bone requires the definition of elastic and plastic properties. Plastic behaviour is defined because it is expected that the bone would exceed its maximum yield stress during implantation. Note that the stress–strain relationship for the bone is defined up to the point of fracture (see Fig. 2.4), as obtained by Burstein et al. [29] from human femur and tibia specimens. The detailed material properties of the bone adopted in this study are listed in Table 2.1. The friction coefficient between the surfaces of bone and commercially available pure titanium was obtained from Choubey et al.’s [30] fretting wear tests performed in a salt solution. Young’s modulus, Poisson’s ratio and density of the implant are, respectively, 102GPa, 0.3 and $4.54 \times 10^{-6} \text{ kg/mm}^3$.



a) Thread forming, S1 or cutting, S2



b) Thread forming and cutting, S3

Fig. 2.2 Details of mandibular bone and cavity

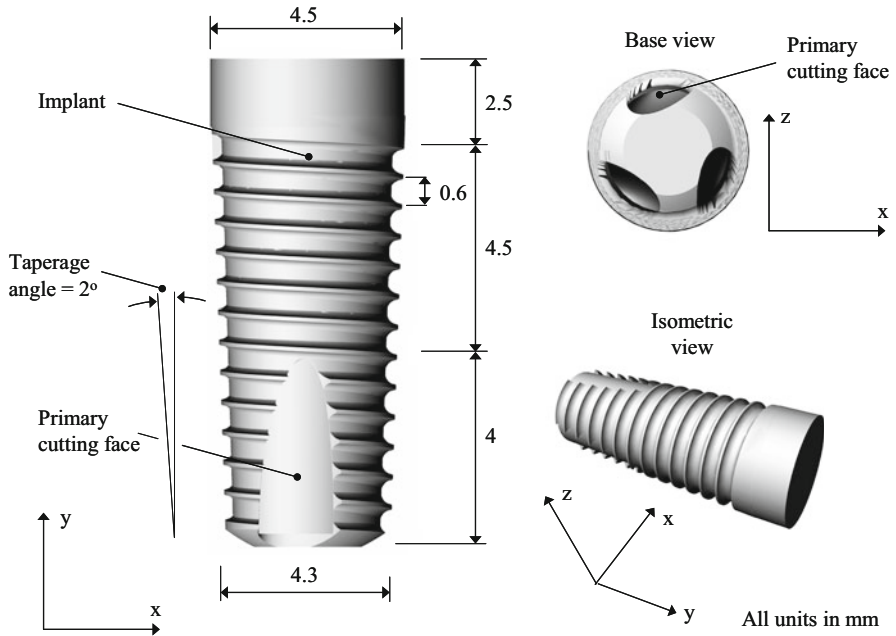


Fig. 2.3 Details of a typical implant design

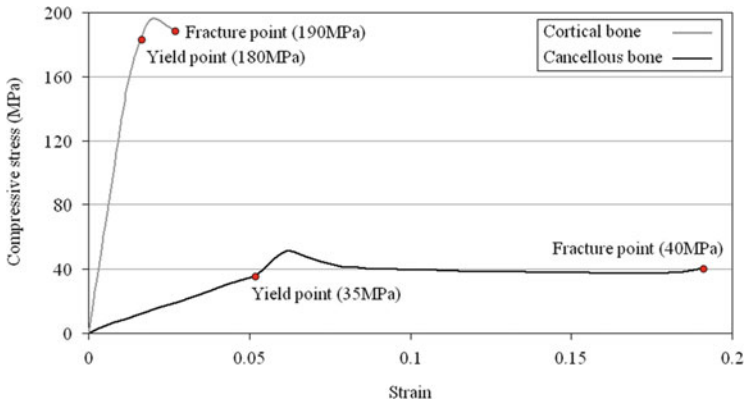


Fig. 2.4 Stress–strain behaviour [29]

2.2.2 Modelling Details

During implantation, the implant can be inserted manually or mechanically. A manual insertion process was modelled previously [27] in a stepwise manner with a torque applied to the implant that increases with time. The present study

Table 2.1 Material properties of cancellous and cortical bone

		Cancellous bone	Cortical bone	Sources	Specimen details
Elastic	Young's modulus, E ($\times 10^3$ N/mm ²)	0.7	9	[29]	Human femur and tibia (type IV)
	Poisson's ratio, ν	0.35	0.3		
	Density, ρ ($\times 10^{-7}$ kg/mm ³)	5.3	18		
Plastic	Yield stress (N/mm ²)	35	180	(Fig. 2.4)	
	Plastic strain	0.135	0.015		
Contact	Friction coefficient	0.61		[30]	Human femur

deals with mechanical insertion whereby the process of implantation is continuous with a constant torque.

Figure 2.5 illustrates a constant torque of 450 Nmm with an insertion velocity of 0.31 mm/s applied to the top of the implant. The velocity is based on an insertion depth of 11 mm over a total period of 36 s. Note that the bone cavity is 11.5 mm in depth, thereby leaving 0.5 mm between the bottom of the implant and bone to store blood and bone fragments. Shown in Fig. 2.5 are the fixed constraints on the bone surfaces (anterior and posterior) along the mesiodistal direction of such a hypothetical human mandible.

The finite element models of the bone and implant are meshed automatically within the program by using tetrahedral elements. As an example, for the bone and implant models of S2, the total numbers of elements and nodes are 85,234 and 67,567, respectively. The elements on the entire cavity surface are refined to 40 % of the average mesh size on the anterior and posterior faces. This would enable to obtain more accurate results during implant insertion. Mesh convergence was undertaken on the similar models in our previous work [31].

2.2.3 Contact Simulation

Interaction between the bone and implant during dynamic simulation of the implantation process is complex and requires proper definition of contact conditions. In the present study, the contact is defined in ABAQUS [28] using 'surface-to-surface' discretisation because it provides more accurate stress and pressure results than node-to-surface discretisation. Surface-to-surface contact is incorporated in the modelling by using the constraint enforcement methods where the surfaces do not require matching meshes (i.e. node-to-node contact). This is because ABAQUS [28] enforces conditional constraints on each surface to simulate contact conditions. In addition, the contact interaction properties are also required to be defined for the contact pair.

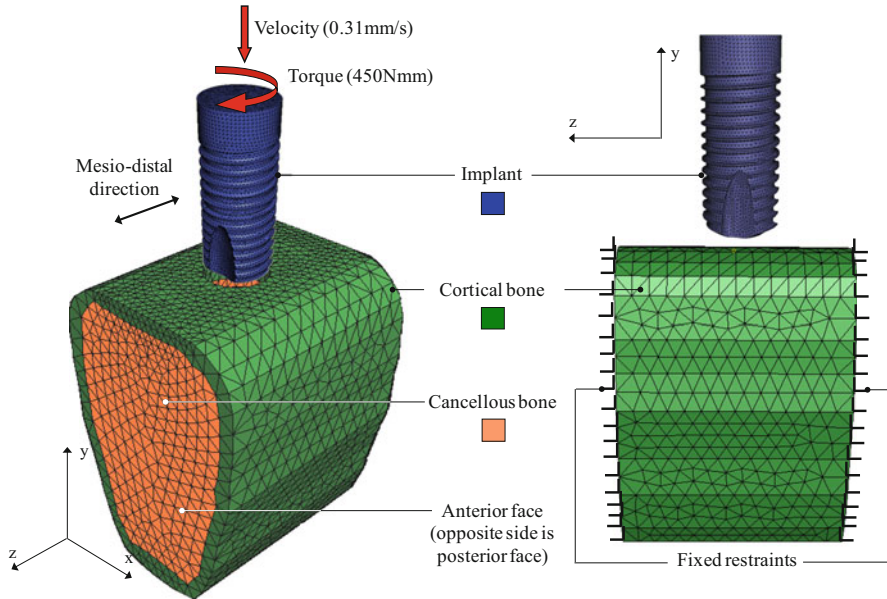


Fig. 2.5 Loading and restraint conditions applied to the bone and implant

As illustrated in Fig. 2.6, the definition of the two contact surfaces is achieved by setting the side and bottom surfaces of the implant as the master surface. The slave surface includes the entire inner surface of the bone cavity and the top ring area of 0.5 mm width on the cortical surface. This top ring area defines the contact between the implant and the top of cortical bone because the implant diameter is larger than the cavity. In accordance with the surface-to-surface definition, contact constraints are enforced in an average sense over the slave surface, rather than at discrete points, such as at slave nodes in the case of node-to-surface discretisation. Therefore, penetration of individual master nodes into the slave surface is allowed; however, the reverse is not permitted.

Defining the contact is yet to be completed because under large deformation, ABAQUS [28] defaults the slave surface to be penetrated by the master nodes, as illustrated in Fig. 2.7 (a). As such, the material properties of the slave surface cannot be properly defined after deformation. Therefore, adaptive meshing technique must be employed so that the material moves with the slave surface mesh at all times during the insertion simulation.

The adaptive meshing scheme specified in ABAQUS [28] is termed ‘arbitrary Lagrangian–Eulerian’ (ALE) because it combines the Lagrangian and Eulerian methods. The Lagrangian method is used to track the path of the element so that no nodal penetrations occur. However, this method alone still allows material to move independently of the mesh. The Eulerian method, on the other hand, takes into account conservation of mass so that the material is conserved within the elements. The ALE combines these two methods so that if nodal penetrations occur,

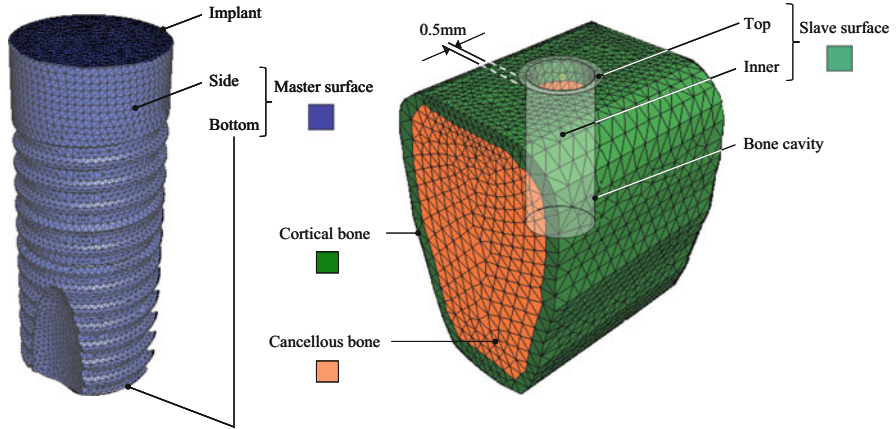


Fig. 2.6 Master and slave surfaces

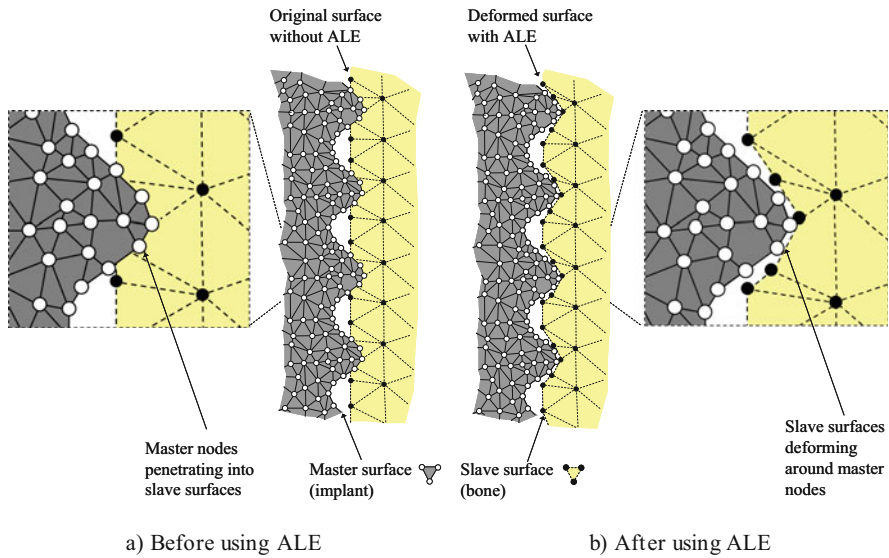


Fig. 2.7 Adaptive meshing

forces that are a function of the penetration distance are applied to the master nodes to counteract the penetration, with equal and opposite forces acting on the slave surface at the penetration points. Detailed in Fig. 2.7 (b) is an example of the slave surface deforming around the master nodes after ALE is applied.

The next step in defining a surface-based contact is to model the contact interaction properties. In this study, the tangential properties of the surface are defined using friction coefficient (see Table 2.1) and the normal properties defined as hard contact. Hard contact is implemented to ensure that the master nodes are in

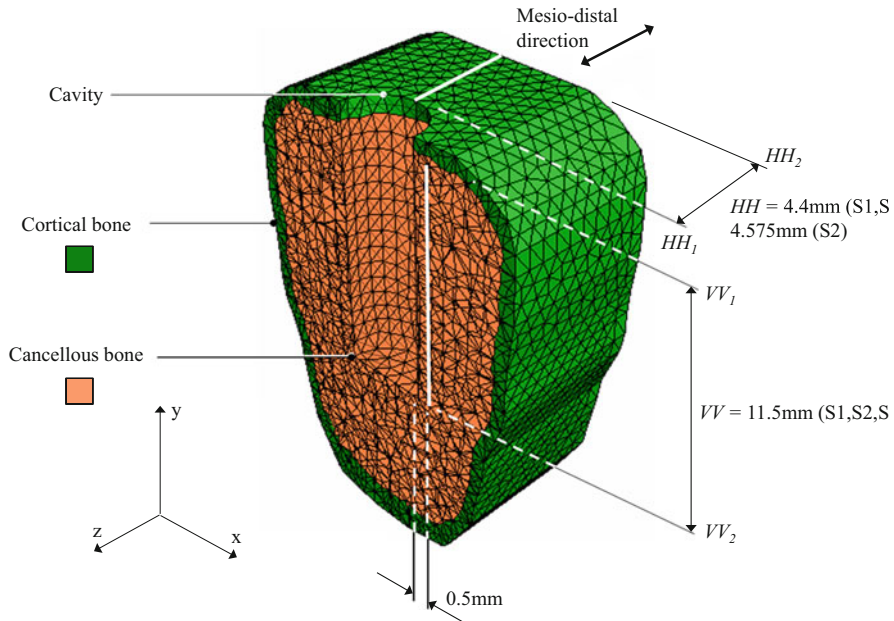


Fig. 2.8 Stress measurement within cancellous and cortical bone

complete contact with the slave surface therefore not allowing transfer of any tensile stresses across the interface.

2.2.4 Criteria for Stress Measurements

The stress within the bone are considered to be the determining factor for understanding both bone fracturing during insertion and subsequent bone resorption. The von Mises stresses are measured along the lines VV in the cancellous bone and HH in the cortical bone, as shown in Fig. 2.8. Line VV is 11.5 mm in length for all bone cavity diameters; however, the length of HH is dependent on the bone cavity dimensions. The length of line HH is 4.4 mm for S1 and S3 and 4.6 mm for S2. Due to the irregularity of the mesh, a straight line of nodes at which the stress is measured is only approximated for both VV and HH . The distance of VV away from the bone cavity surface is fixed at 0.5 mm. The stress measurement line, HH , is positioned to capture the most severe stress levels. The beginning and end points of VV (i.e. V_1 and V_2) and HH (i.e. H_1 and H_2) are also identified in Fig. 2.8 for ease of discussion.

2.3 Results and Discussion

The following subsections detail the von Mises stresses in both cancellous and cortical bone, each with discussions for the three insertion scenarios (S1, S2 and S3). The stresses are measured along the lines VV and HH during the entire insertion process. Sections 2.3.1 and 2.3.2 present the stress characteristics within the cancellous and cortical bone, respectively, for S1, S2 and S3. The stress profile within the cancellous and cortical bone for the selected stages of insertion is presented followed by stress contour plots in subsequent figures illustrating the stress characteristics. It is assumed that the implant tip is pushed slightly into the top surface of cortical bone prior to the application of the torque. This corresponds to 1.8 s or 0.5 mm insertion depth where the stresses are measured from the stress profiles shown in Figs. 2.9, 2.10, 2.12, 2.13, 2.14 and 2.15 (a). For ease of discussion, stress profiles produced for 3.6–36 s at 10.8 s time steps (Figs. 2.9, 2.10, 2.12, 2.13, 2.14 and 2.15 (b), (c), (d), (e) and (f)) are detailed in Sections 2.3.1 and 2.3.2.

2.3.1 Cancellous Bone

2.3.1.1 Thread Forming, S1

For most of the time steps, it is evident that when the insertion depth increases, the stress level also increases. This is because the surface area of contact between the bone and implant increases, and therefore a larger amount of the applied torque is transferred to the bone.

As seen in Fig. 2.9 (a) and (b), when the implant is inserted 0.5 mm into the cortical bone, the stress level within the cancellous bone is relatively low (0.07 MPa) because the implant and cancellous bone are not yet in direct contact. At this stage, the only stresses experienced in the cancellous bone are those transferred from the cortical bone. Figure 2.9 (c) also indicates that for an insertion depth of 1.1 mm, the global stress peak occurs at VV_1 . This peak is caused by the primary cutting faces together with the stresses transferred from the cortical bone.

At a depth of 4.4 mm, the cancellous bone experiences an increase in the stress further away from VV_1 because the implant is inserted deeper into the bone (Fig. 2.9 (d)). At 7.7 mm depth, the stress increases slightly compared to the previous stages (i.e. average from 0.93 to 1.24 MPa). The stress contour distributes more evenly throughout the bone adjacent to the implant as the insertion depth increases, as illustrated in Fig. 2.9 (e).

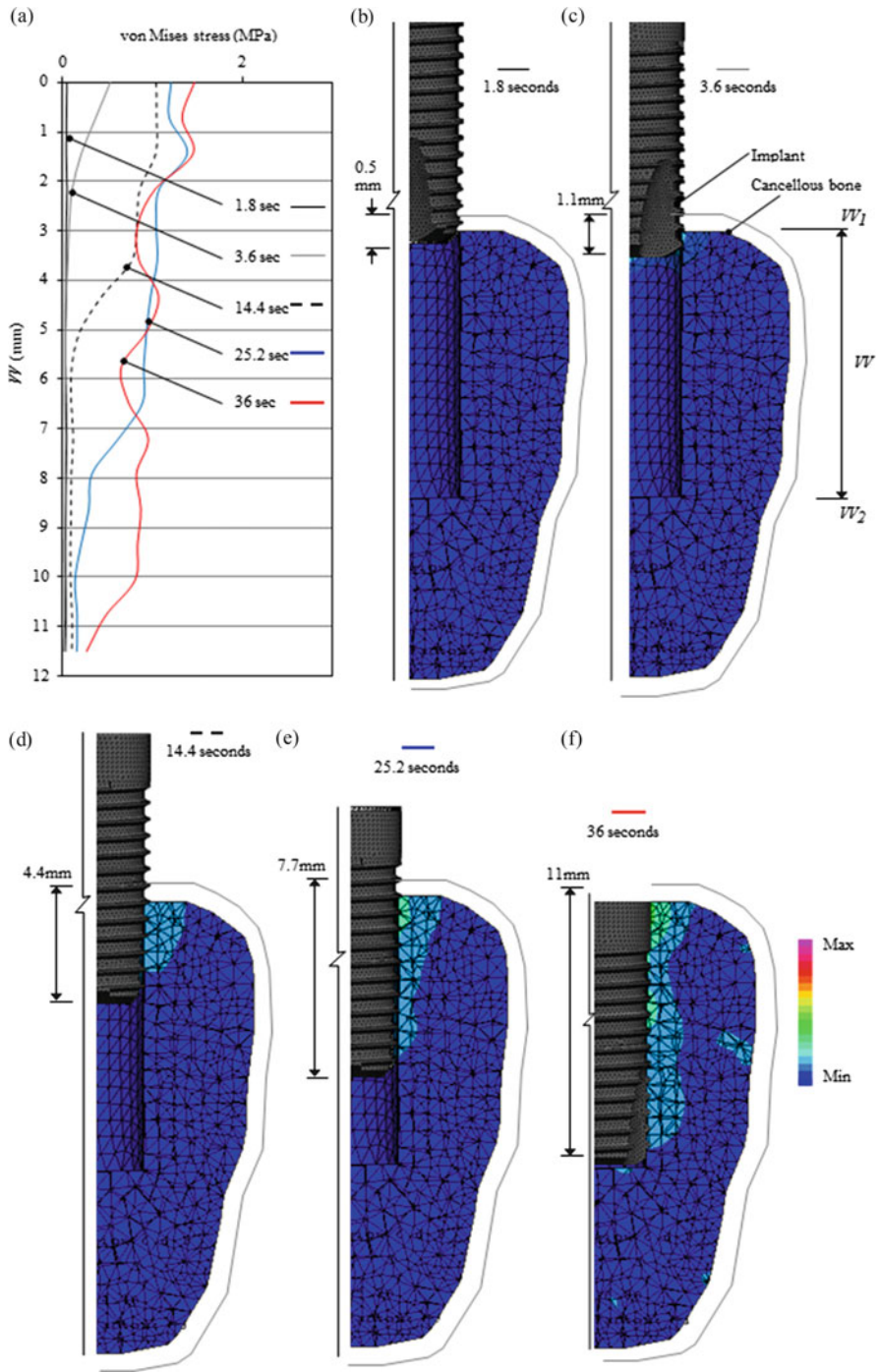


Fig. 2.9 Stress characteristics in cancellous bone at five insertion stages during thread forming

At the final stages of insertion (Fig. 2.9 (f)), the stress at 11 mm insertion depths increase (1.48 MPa) compared to all the previous stages. The global stress peak for this insertion step is a result of the abrupt change in implant geometry where the implant neck establishes contact with the cancellous bone.

2.3.1.2 Thread Cutting, S2

Similar to S1, S2 also causes increased stresses when the insertion depth increases. From the time periods 1.8 and 3.6 s, the stresses (0.3 and 1.2 MPa) are significantly higher than those found during S1 (0.07 and 0.51 MPa, correspondingly), as illustrated in Fig. 2.10. This is because the diameter of the bone cavity is reduced in S2. This also results in a larger stressed region towards the outer edge of the cortical bone, as evident in the stress contour plots (Fig. 2.10 (b), (c), (d), (e) and (f)). It is also found that stress peaks occur at the same locations as found for S1.

At 14.4 s, as detailed in Fig. 2.10 (d), the increased stresses move further down and away from VV_1 due to the increased insertion depth. The stress contours show to be more unevenly distributed when compared to the previous stages. The stress peak at VV_1 is much higher (4.0 MPa) than that found in S1.

At the final insertion stages, the stress profile and contour are shown to be more evenly distributed as compared to the corresponding ones in S1. The stress peak occurs at 4.7 mm (5.34 MPa) from VV_1 for the insertion depth of 11 mm. Similar to S1, this stress peak is again a result of the implant neck commencing contact with the cancellous bone.

Figure 2.11 illustrates, as an example, the progressive stress contours within the cancellous bone during the entire implantation process for the thread cutting scenario (S2). The corresponding time, insertion depth and implant revolutions are also indicated in the figure. Note that only the exterior surface of the implant is shown for ease of viewing the stress contours within the bone.

2.3.1.3 Thread Forming and Cutting, S3

Similar to S1 and S2, when the insertion depth increases, the stresses within the cancellous bone also increase for S3. From 1.8 to 3.6 s, as presented in Fig. 2.12 (a), the stress levels (0.09 and 0.4 MPa) are similar to those of S1 (0.07 and 0.5 MPa) but smaller than those for S2 (0.3 and 1.2 MPa). This is due to the geometrical changes of the bone cavity. The stress contours are also more comparable to those of S1, as detailed in Fig. 2.12 (b) and (c).

At 14.4 s, as illustrated in Fig. 2.12 (d), the stress level (1.3 MPa) is slightly higher than that of S1 (1.0 MPa) but significantly lower than S2 (4.0 MPa). A global stress peak at 14.4 s occurs along the line VV because of the geometry of the primary cutting faces and the reduced diameter of the bone cavity which induce a slight change in the stress contour when compared to S1.

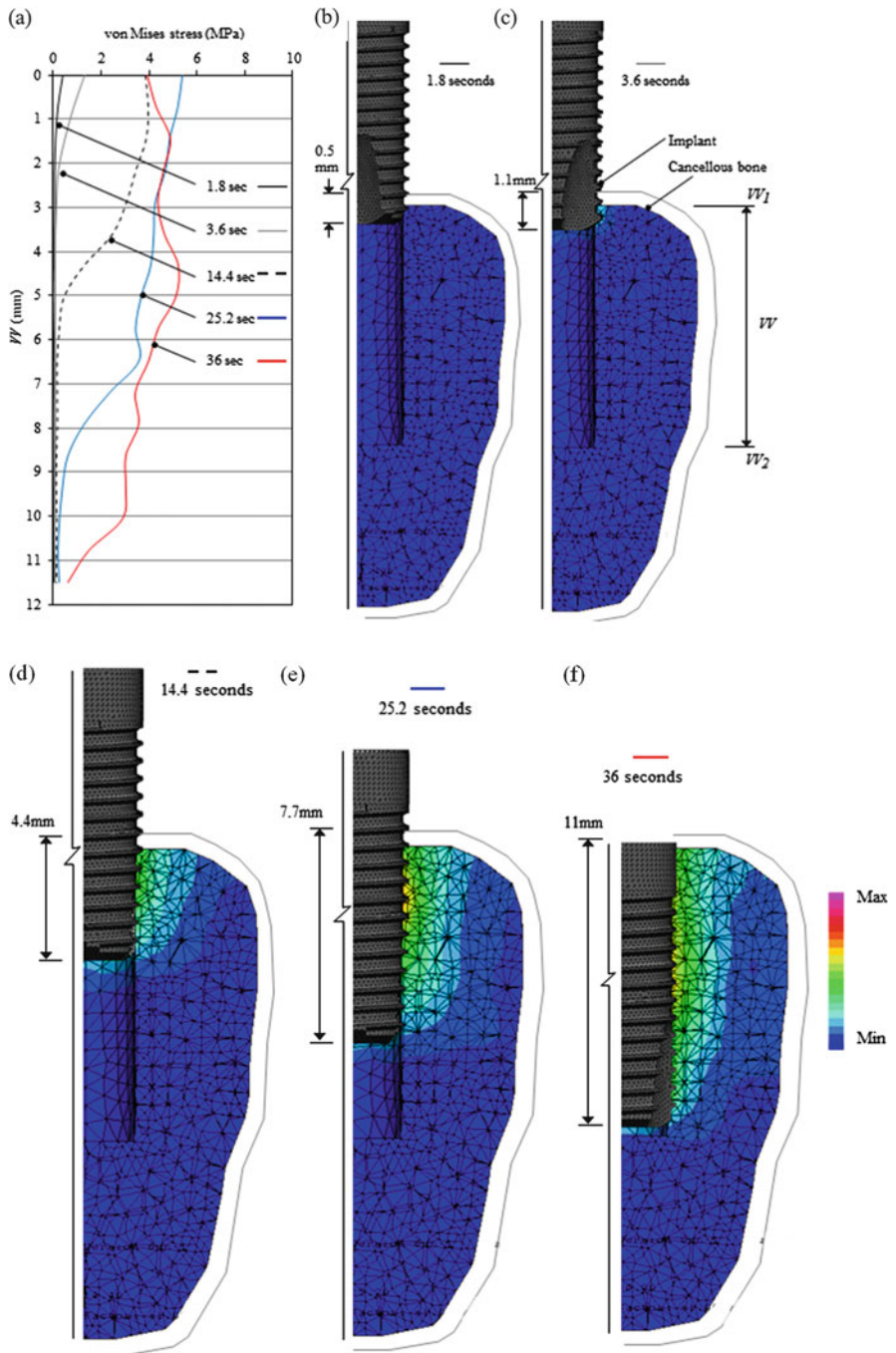


Fig. 2.10 Stress characteristics in cancellous bone at five insertion stages during thread cutting

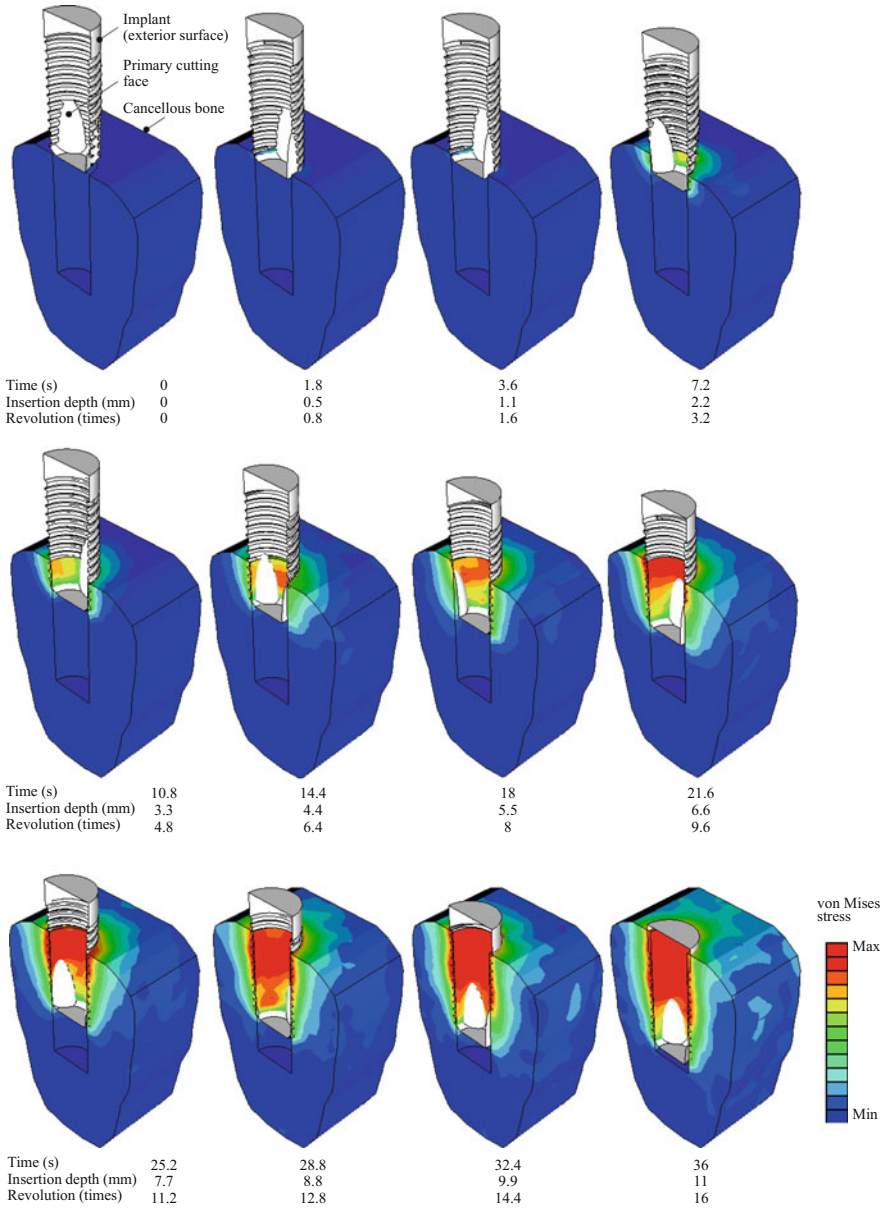


Fig. 2.11 Progressive stress contours in cancellous bone during the entire implantation process (thread cutting, S2)

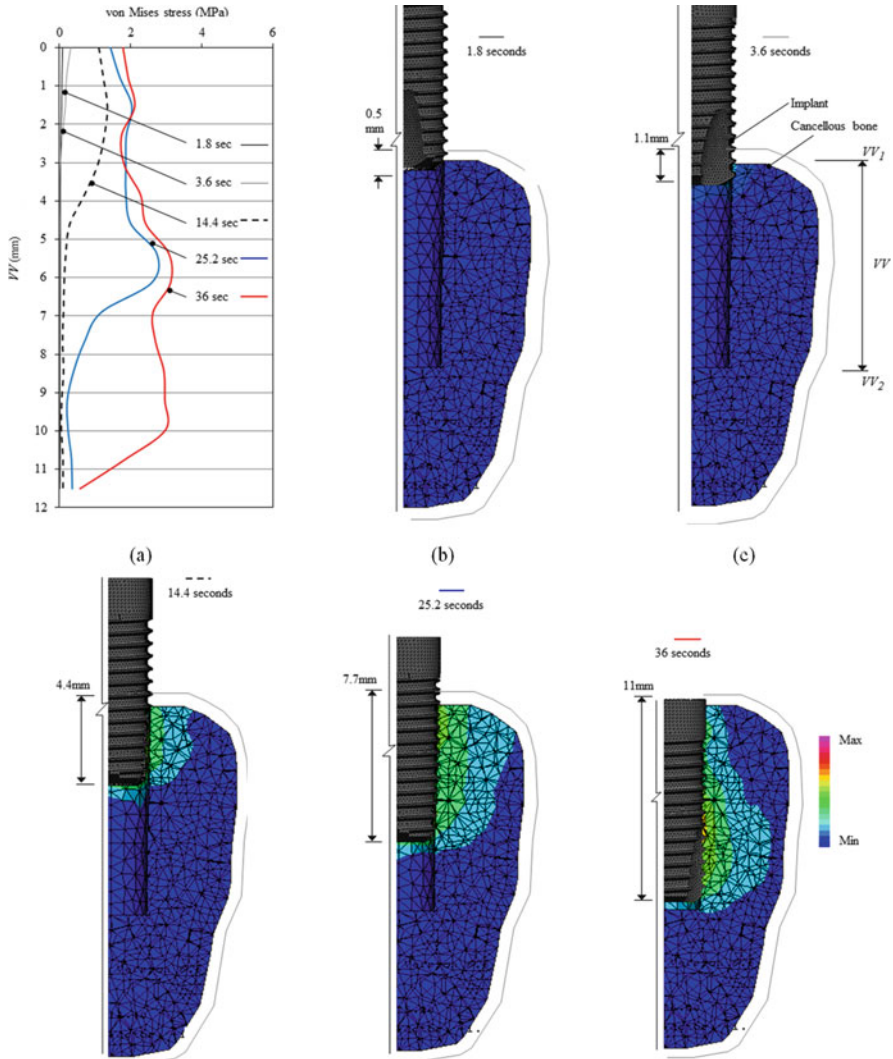


Fig. 2.12 Stress characteristics in cancellous bone at five insertion stages during thread forming and cutting

The stress characteristics at 25.2 s show an increase in magnitude (2.7 MPa) when compared to that of S1 (1.4 MPa) and a decrease as compared to S2 (5.2 MPa). The stress profile shown in Fig. 2.12 (a) indicates that a stress peak occurs at a region close to the primary cutting faces. A reduction in bone cavity diameter gives a stress contour that is more comparable to that of S1 than S2.

At 11 mm insertion depth, the stress shows a significant increase; however, the stress at VV_1 remains comparable to that found for S1. The increase in stress is a result of the reduced cavity diameter. Note also that the stress contour is more comparable to S2.

2.3.2 Cortical Bone

2.3.2.1 Thread Forming, S1

In general, the stress within the cortical bone decreases from HH_1 towards HH_2 for all insertion steps. The stress profiles presented in Fig. 2.13 (a), shows a significant stress increase at point HH_1 from 1.6 MPa (1.8 s, before the primary cutting faces are in contact) to 9.2 MPa (3.6 s, when contact is established). Such a large variation in stress is particularly evident in the contour plots (Figs. 2.13 (b) and (c)).

For 14.4 s, the stress next to the implant increases to 14.4 MPa. Such an increase is due to the increased cortical bone to implant contact as a result of the narrowing gaps between the cutting faces as the insertion step increases.

At 25.2 s, the stress contour only exhibits a marginal increase in stress (i.e. 16.4 MPa) because the cutting faces are no longer in contact with the cortical bone at HH_1 . For the 36 s, an increase in stress (i.e. 20.4 MPa) is found when compared to 25.2 s because the implant neck is in contact with the cortical bone at this stage.

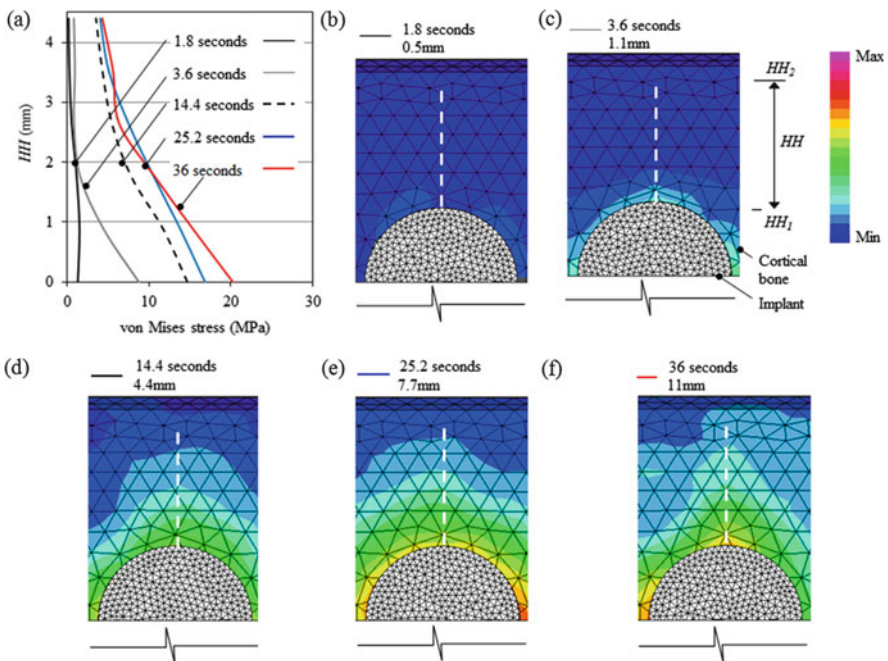


Fig. 2.13 Stress characteristics in cortical bone at five insertion stages during thread forming

2.3.2.2 Thread Cutting, S2

Similar stress characteristics are found for S2 as with S1. However, S2 induces significantly higher stresses within the cortical bone, with a maximum of 11.4 MPa compared to 9.2 MPa at 3.6 s, as illustrated in Fig. 2.14 (a). At an insertion depth of 4.4 mm, a maximum stress of 20.1 MPa occurs at the implant neck, which is significantly higher than that found at the same insertion step during S1 (14.4 MPa). The stress contours shown in Figs. 2.14 (b) to (f) also confirm such an increase in stresses.

2.3.2.3 Thread Forming and Cutting, S3

The stress characteristics are again comparable to those found for S1 or S2, as detailed in Fig. 2.15. In general, the stress characteristics are between those of S1 and S2, but closer to the S1 scenario. This is because the stresses are only measured at the top of the bone cavity where its diameter is identical to that of forming (i.e. S1).

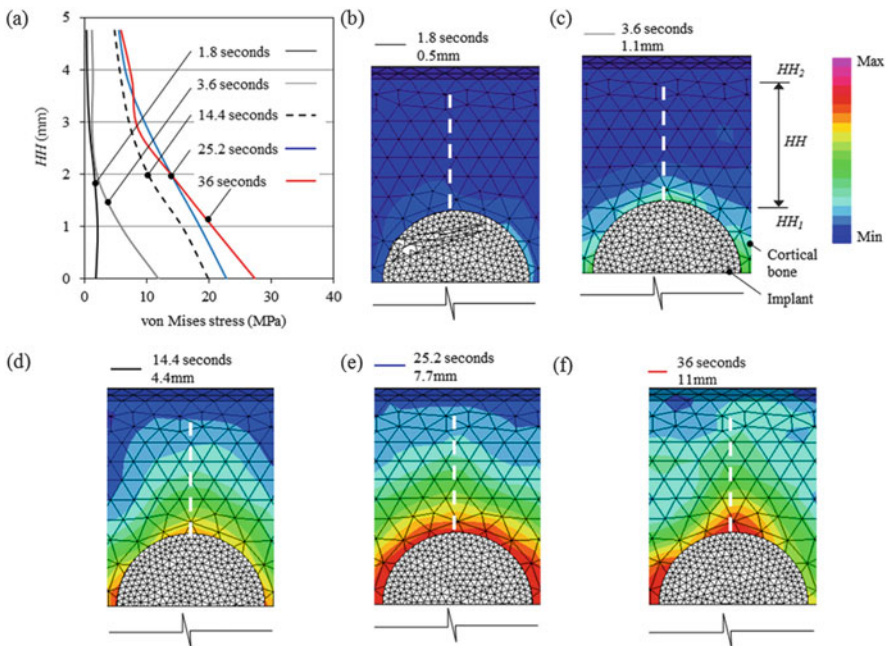


Fig. 2.14 Stress characteristics in cortical bone for five insertion stages during thread cutting

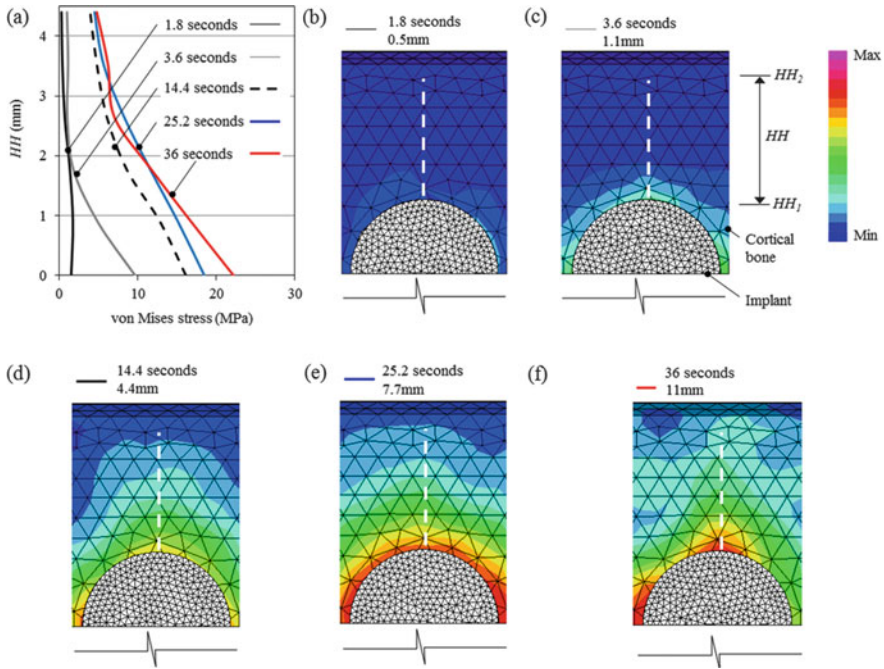


Fig. 2.15 Stress characteristics in cortical bone for five insertion stages during thread forming and cutting

2.3.3 Maximum Stresses in Different Implantation Scenarios

This subsection summarises the maximum von Mises stresses for 11 selected insertion depths of the S1, S2 and S3 scenarios. Based on the data shown in Figs. 2.9, 2.10, 2.11, 2.12, 2.13, 2.14 and 2.15, the maximum stresses along lines *VV* and *HH* are summarised in Table 2.2. As the insertion depth increases, the maximum stress along the line *VV* takes place at varied distances, d_v away from VV_1 . However for cortical bone, the maximum stresses always occur at HH_1 .

Table 2.2 reveals that for the cancellous bone, the maximum stresses for S3 are closer in magnitude to those of S1 at initial insertion depths. This is because the upper bone cavity diameters are similar to each other for these two case scenarios. As the insertion depth increases, the maximum stress of the combined scenario (S3) approaches a magnitude which is approximately halfway between the S1 and S2 scenarios. This is due to the reduction in bone cavity diameter in the lower region which is approaching to that of the S2 scenario. In the initial insertion depths in general, the maximum stresses along the line *VV* occur on or close to VV_1 . However, for the insertion depths 8.8–11 mm, the maximum stresses occur further away from VV_1 due to the decrease in the bone cavity diameter. For the cortical bone, the maximum stresses at HH_1 for S3 are in between those of S1 and S2 from 0.5 to 2.2 mm insertion depths. For the insertion depths from 3.3 to 11 mm, the

Table 2.2 Maximum von Mises stresses (MPa) along line VV and at point HH_1

Insertion depth (mm)	Forming, S1			Cutting, S2			Forming and cutting, S3		
	VV	dv	HH_1	VV	dv	HH_1	VV	dv	HH_1
0.5	0.07	0.0	1.6	0.3	0.0	2.1	0.09	0.0	2.06
1.1	0.51	0.0	9.2	1.2	0.0	11.44	0.44	0.0	9.8
2.2	0.96	0.7	9.9	3.92	0.71	12.1	0.99	0.82	10.9
3.3	0.8	0.0	14.37	2.5	0.0	20.3	1.09	1.48	16.1
4.4	1.08	0	14.4	4.02	0.79	20.1	1.34	1.66	16.14
5.5	0.9	1.47	23.4	4.8	0	32	1.11	0.87	26.3
6.6	1.09	0	22.1	4.57	0.97	30.2	1.48	1.59	24.7
7.7	1.46	1.41	16.4	5.2	0	22.6	2.76	5.6	18.4
8.8	1.18	1.65	20.7	5.24	2.75	28.5	2.21	3.91	22.9
9.9	1.94	3.62	17.2	5.1	4.07	22.8	2.32	7.52	19
11	1.48	1.47	20.4	5.34	4.61	28.1	3.02	9.77	22.2

dv in mm

stress levels of S3 are closer in magnitude to S1 than S2, because the cavity diameters at the top of the cortical bone are the same for S2 and S3.

2.3.4 Clinical Significance

The optimal or desirable stress levels to be experienced by local bone during implantation have not yet been firmly established. However, according to Rieger et al. [32] and O'Mahony et al. [33], the desirable stress level lies between 1.72 and 2.76 MPa. The material structure of the cancellous bone makes it more sensitive to fracture than the cortical bone. The minimum and maximum stress profiles along the line VV produced by S1, S2 and S3 are plotted in Fig. 2.16 together with an ideal stress range (presented by the lower and upper limits) for cancellous bone growth and repair. Note that the minimum stress profiles are obtained at 1.8 s and the maximum at 36 s. On the basis of present knowledge, if the stress falls below 1.72 MPa, bone may not be stimulated adequately for effective healing and osseointegration. On the other hand, if the stress exceeds 2.76 MPa, bone resorption may occur, which contributes to loosening and potential failure of the implant. The ideal bone response will be achieved when the stress remains between these limits.

For all three insertion scenarios, the minimum stress profiles at 1.8 s are considerably below the lower limit of the stimulation stress (i.e. 1.72 MPa). For S1 (forming), the maximum stress profile (at 36 s) still does not reach the lower stress limit of 1.72 MPa. The low stress level produced by S1 may adversely affect initial retention of the implant which confirms the findings of Sennerby and Meredith [16] in that thread forming reduces implant stability. For S2 (cutting), the maximum stress profile at 36 s shows that bone resorption may occur around the implant because the upper stress limit of 2.76 MPa is exceeded for most of the

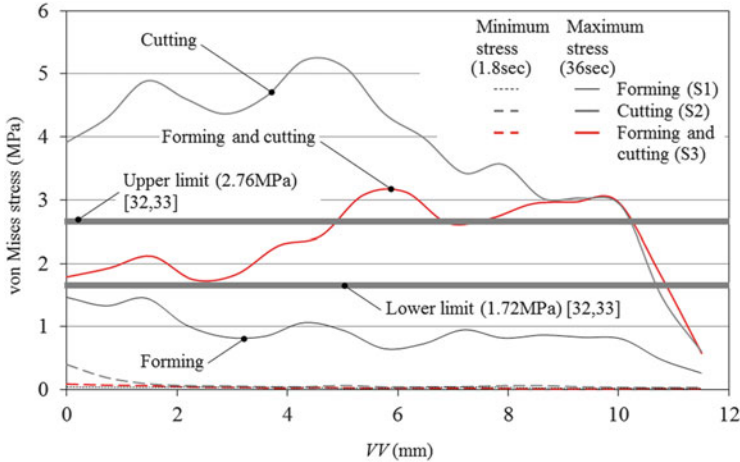


Fig. 2.16 Maximum and minimum stress profiles during implantation

locations along line VV. Overall, S3 (forming and cutting) best satisfies the ideal level of stress suggested in the literature. In current practice, many implant companies [12, 17, 18] generally recommend S2 for normal bone (i.e. type III or IV [34]) and S1 for compact bone (i.e. type I or IV) so that implant stability can be compromised. Based on the findings of this study, S3 may also be recommended for clinical practice.

It is important to note, however, that these findings have not modelled the fracture of bone through element deletion nor the effects of blood flow which influences contact friction. Incorporating such aspects into the finite element analysis merits further investigation.

2.4 Conclusion

2.4.1 Research Outcomes

The von Mises stress characteristics within the cancellous and cortical bone are evaluated for thread forming (scenario one, S1), cutting (scenario two, S2) and combined forming and cutting (scenario three, S3). With the adaptive meshing and contact interaction properties available in ABAQUS [28], realistic stress characteristics are modelled. The continuous dynamic simulation and implant cutting faces prove to be the major factors that distinguish the present results from those achieved in the stepwise simulation [14].

For S1, the stress levels within the cancellous and cortical bone are less than those in S2 and S3 because of the reduced bone to implant surface contact area. However, the stresses within the cancellous bone are only slightly reduced for S3

during the initial insertion steps. Then at later insertion steps, the stress within the cancellous bone (at any location along the line *VV*) increases to be at a level approximately halfway between those of *S1* and *S2*. For cortical bone, the magnitude increases less significantly as the implant insertion depth progresses. The minor variation is due to the geometrical differences of the bone cavity. In both cancellous and cortical bone, the primary cutting faces induce stress peaks during the initial insertion stages (0.55–2.2 mm). This is because of the abrupt changes in geometry of the cutting faces. For the final insertion stages (9.9 and 11 mm) the change in implant section (i.e. implant neck establishes a contact with the cancellous bone) results in stress peaks within the cancellous bone.

The innovation of this research lies in the increased understanding of the stress characteristics in bone during the implantation process. This is likely to advance biomechanics of implantation surgery appreciably. Mechanical loosening after implantation is a significant challenge for most endoprosthetic procedures, and this research presents useful insights.

2.4.2 Recommendations for Further Developments

Optimisation techniques such as the application programming interface and/or design of experiment and response surface function of commercial software may be used to determine the highs and lows and the sensitivities of the stresses to a range of bone and implant parameters during implantation. Parameters that can be considered include element deactivation, contact friction, optimum combination of insertion torque/speed, implant diameter, length, tapers, thread design and primary cutting face and secondary cutting flute dimensions for each bone type.

References

1. Irish JD (2004) A 5,500 year old artificial human tooth from Egypt: a historical note. *Int J Oral Maxillofac Implants* 19(5):645–647
2. Brånemark PI (1983) Osseointegration and its experimental background. *J Prosthet Dent* 50(3):399–410
3. Bragger U, Krenander P, Lang NP (2005) Economic aspects of single-tooth replacement. *Clin Oral Implants Res* 16(3):335–341
4. van der Wijk P, Bouma J, van Oort RP, van Waas MA, van't Hof MA, Rutten FF (1996) Cost-effectiveness analysis of dental implants. *Ned Tijdschr Tandheelkd* 103(10):382–385
5. Albrektsson T, Dahl E, Enbom L, Engevall S, Engquist B, Eriksson AR, Feldmann G, Freiberg N, Glantz PO, Kjellman O (1988) Osseointegrated oral implants. A Swedish multi-center study of 8139 consecutively inserted Nobelpharma implants. *J Periodontol* 59(5): 287–296
6. Arvidson K, Bystedt H, Frykholm A, von Konow L, Lothigius E (1992) A 3-year clinical study of Astra dental implants in the treatment of edentulous mandibles. *Int J Oral Maxillofac Implants* 7:321–329

7. Spiekermann H, Jansen VK, Richter EJ (1995) A 10-year follow-up study of IMZ and TPS implants in the edentulous mandible using bar-retained overdentures. *Int J Oral Maxillofac Implants* 10:231–243
8. Mericski-Stern R, Schaffner TS, Marti P, Geering AH (1994) Peri-implant mucosal aspects of ITI implants supporting overdentures: a five-year longitudinal study. *Clin Oral Implants Res* 5:9–18
9. Fritz ME (1996) Implant therapy. II. *Ann Periodontol* 1:796–815
10. Jemt T, Johansson J (2006) Implant treatment in the edentulous maxillae: a 15-year follow-up study on 76 consecutive patients provided with fixed prostheses. *Clin Implant Dent Relat Res* 8(2):61–69
11. Nobel Biocare (2012) <http://www.nobelbiocare.com/>. Accessed 12 July 2012
12. Neoss, Pty Ltd (2009) Neoss implant system surgical guidelines. Neoss, Pty Ltd, Harrogate
13. O'Brien WJ (1989) Dent mats: properties and selection. Quintessence Publishing, Chicago/London
14. McClarence E (2004) Close to the cutting edge. Brånemark and the development of Osseointegration. Quintessence Publishing, London
15. Porter JA, von Fraunhofer JA (2005) Success or failure of dental implants? A literature review with treatment considerations. *Gen Dent* 53(6):423–432
16. Sennerby L, Meredith N (2008) Implant stability measurements using resonance frequency analysis: biological and biomechanical aspects and clinical implications. *Periodontol* 47(1): 51–66. doi:10.1111/j.1600-0757.2008.00267.x
17. 3i (2013) 3i implant innovations Inc. <http://biomet3i.com/>. Accessed 13 Apr 2013
18. Lambert FE, Weber HP, Susarla SM, Belser UC, Gallucci GO (2009) Descriptive analysis of implant and prosthodontic survival rates with fixed implant-supported rehabilitations in the edentulous maxilla. *J Periodontol* 80(8):1220–1230. doi:10.1902/jop.2009.090109
19. Mullender M, El Haj AJ, Yang Y, van Duin MA, Burger EH, Klein-Nulend J (2004) Mechanotransduction of bone cells in vitro: mechanobiology of bone tissue. *Med Biol Eng Comput* 42:14–21
20. Miyata T, Kobayashi Y, Araki H, Ohto T, Shin K (2002) The influence of controlled occlusal overload on peri-implant tissue. Part 4: a histologic study in monkeys. *Int J Oral Maxillofac Implants* 17(3):384–390
21. Tada S, Stegaroiu R, Kitamura E, Miyakawa O, Kusakari H (2003) Influence of implant design and bone quality on stress/strain distribution in bone around implants: a 3-dimensional finite element analysis. *Int J Oral Maxillofac Implants* 18(3):357–368
22. Petrie CS, Williams JL (2005) Comparative evaluation of implant designs: influence of diameter, length, and taper on strains in the alveolar crest. A three-dimensional finite-element analysis. *Clin Oral Implants Res* 16(4):486–494
23. Kitagawa T, Tanimoto Y, Nemoto K, Aida M (2005) Influence of cortical bone quality on stress distribution in bone around dental implant. *Dent Mater J* 24(2):219–224
24. Satoh T, Maeda Y, Komiyama Y (2005) Biomechanical rationale for intentionally inclined implants in the posterior mandible using 3D finite element analysis. *Int J Oral Maxillofac Implants* 20(4):533–539
25. Perez del Palomar A, Arruga A, Cegonino J, Doblare M (2005) A finite element comparison between the mechanical behaviour of rigid and resilient oral implants with respect to immediate loading. *Comput Meth Biomech Biomed Eng* 8(1):45–57
26. Sevimay M, Turhan F, Kiliçarslan MA, Eskitascioglu G (2005) Three-dimensional finite element analysis of the effect of different bone quality on stress distribution in an implant-supported crown. *J Prosthet Dent* 93(3):227–234
27. van Staden R, Guan H, Johnson NW, Loo YC, Meredith N (2008) Step-wise analysis of dental implant insertion process using finite element technique. *Clin Oral Implants Res* 19(3): 303–313
28. ABAQUS (2013) <http://www.simulia.com>. Accessed 5 Feb 2013

29. Burstein AH, Reilly DT, Martens M (1976) Aging of bone tissue: mechanical properties. *J Bone Joint Surg Am* 58(1):82–86
30. Choubey A, Basu B, Balasubramaniam R (2004) Tribological behaviour of Ti-based alloys in simulated body fluid solution at fretting contacts. *Mater Sci Eng A* 379(1–2):234–239. doi: <http://dx.doi.org/10.1016/j.msea.2004.02.027>
31. van Staden R (2008) Finite element analysis of dental implant-bone system during and after implantation, PhD thesis. Griffith University, Australia
32. Rieger MR, Mayberry M, Brose MO (1990) Finite element analysis of six endosseous implants. *J Prosthet Dent* 63(6):671–676
33. O’Mahony A, Bowles Q, Woolsey G, Robinson SJ, Spencer P (2000) Stress distribution in the single-unit osseointegrated dental implant: finite element analyses of axial and off-axial loading. *Implant Dent* 9(3):207–218
34. Rho JY, Ashman RB, Turner CH (1993) Young’s modulus of trabecular and cortical bone material: ultrasonic and microtensile measurements. *J Biomech* 26(2):111–119

Chapter 3

Multiscale Remodelling and Topographical Optimisation for Porous Implant Surface Morphology Design

Wei Li, Junning Chen, Chaïy Rungsiyakull, Michael V. Swain, and Qing Li

Abstract Solid titanium and its alloys have been the most prevalent materials for dental and orthopaedic implants attributable to their advantageous mechanical and biocompatible properties. Nevertheless, there still is a range of biomechanics and biomaterials issues with titanium implants, such as delayed/insufficient osseointegration and limited shear-load bearing capacity in clinic. In order to tackle these problems, various physical and chemical treatment technologies have been developed to modify surface morphology of such implantable dental prostheses. Fully porous coating (FPC) is one of such techniques, where beads or particles are sintered to bond onto a solid core of implants under specific conditions. This process forms a layer of porous structure on the surface of the implant, whose morphology relies on the bead size, volume fraction and pattern of distribution. Given the critical roles that porous surface could play to enhance osseointegration, a major interest consists in how to optimise morphological parameters. This chapter aims to address this issue through a new multiscale modelling and design framework for optimising the surface morphology to enhance bone–implant interface stability and osseointegration in a biomechanics context. Four different measurements in the microscopic model are used as the design criteria to assess osseointegration outcomes: (1) peri-implant bone density, (2) uniformity of peri-implant bone density, (3) bone–implant contact (BIC) ratio, and (4) Tresca stress (maximum shear). To achieve these osseointegrative criteria, multiobjective optimisation is formulated with respect to the design variables of particle size, volume fraction and gradient. The optimised surface morphology allows creating a better microenvironment for cell attachment, differentiation and proliferation. While cells are seeded in a passive way during implantation in vivo, the tailored surface topography enables to better engage cellular activities in both biomechanical and biochemical aspects, thereby generating better short- and long-term clinical outcomes.

W. Li (✉) • J. Chen • C. Rungsiyakull • M.V. Swain • Q. Li
School of Aerospace, Mechanical & Mechatronics Engineering, The University of Sydney,
Sydney, NSW 2006, Australia
e-mail: wei.li@sydney.edu.au

Keywords Multiscale remodelling • Surface topography • Osseointegration • Implant • Functionally graded coating • Computational biomechanics

3.1 Introduction

Titanium and its alloys have been one class of the most prevalent implantable materials achieving considerable success in orthopaedic, prosthodontic and cardiological applications, for their advantageous mechanical and biocompatible properties [1–6]. This broad range of applications signified a main concern on the strength of implant anchorage onto host tissues, and a series of biomechanics and biomaterials challenges remain with titanium implants, including poor or delayed osseointegration and limited shear-load bearing capacity [1, 5–9].

In order to enhance osseointegration, various physical and chemical surface treatment technologies have been developed to modify the external surfaces of an implant, to achieve desirable morphologies [6, 7, 9–12]. A rough or porous implant surface has been reported to provide more space and favourable biomechanical microenvironment to facilitate cell attachment and tissue ingrowth, thereby promoting a higher level of bone–implant interaction with improved cell migration and osteoblast adhesion to the implant surfaces [5–7, 12–18]. Fully porous coating (FPC) is one of such approaches, in which beads or particles are sintered onto a solid substrate core of implants to form desirable surface morphology [19, 20]. A layer of porous structure forms on the surface of the implant through such a process, and the topographical characteristics largely depend on the bead/particle sizes, volume fraction and internal bindings [21, 22]. Accordingly, the shear stress can be more evenly transferred across the interface, leading to better stimulation to the surrounding tissues for the establishment of osseointegration and biomechanical binding [9, 23, 24].

Several *in vivo* studies have been conducted to investigate the effects of these morphological factors on osseointegration and to examine the advantages in using the porous-coated endosseous implants [5, 6, 9, 12–14, 25–32]. Among these reports, the implants with the greater porosities were found to stabilise the healing more quickly than those with less porous ones, based upon radiographic analysis on the bone remodelling on dogs [31]. Further analysis confirmed these observed advantages of porously coated implants over a bare threaded design by using a histological comparison of harvested dental implants from the dogs [33]. In general, increasing porosity to a certain extent can provide a greater space to enable more efficient nutrient delivery and metabolite removal for cellular activities, thereby better promoting bone mineralisation and stabilisation over a shorter period [5, 9, 28–30].

The topographical characteristics of a porous surface are believed to be the critical determinants to the implant performance. Certain pore sizes were reported to facilitate the adhesion of fibrin blood clots and to promote osteoid formation, as

well as the subsequent mineralisation, thereby helping develop a stable connection of implant with the surrounding bony tissues [34, 35]. One study [29] suggested that the pore sizes between 50 and 120 μm would allow bone ingrowth, while another orthopaedic study [34] suggested a minimum pore size of 100–150 μm for bone ingrowth into a porous ceramic scaffold. Marginal differences of the stabilisation rates were shown between pore sizes up to 100 μm and in excess of 100 μm , on porously coated cobalt-base alloy implants [36].

Given the important role of a porous surface in enhancing osseointegration, an optimal morphology remains a major interest in implant research. Despite indicative relations between morphological parameters and osseointegration rates that were revealed in these above-mentioned *in vivo* studies, the empirical approaches are often quite invasive and can be very difficult (if not impossible) to precisely define important details in the biomechanical interaction for the development of proper porous implants. As an alternative, computer modelling (namely, *in silico*) provides a non-destructive means to understanding the effect of pores and capturing time-dependent process of osseointegration for predicting the possible outcomes of bone remodelling, which has proven to be efficient and low risk to complement *in vivo* studies [37]. For example, Shen and Brinson developed computational models to determine the effects of porosity and particle sizes of porous titanium [3], and their further study modelled the bone's responses to surface morphology [38]. Few *in silico* studies have, however, addressed the computational design of implant topography for optimising treatment outcomes [6].

Most of these *in silico* studies have considered nearly uniform morphology across the porous thickness except for microscopic randomness. A major concern associated with such uniformly coated implants is the ability of gradually transferring load from implant core to the surrounding bony tissue. A potential upgrade to such uniform coatings is a specially designed graded surface morphology [6, 39–43]. For this purpose, some attempts have been made to develop functionally graded implants for a lower mismatch of mechanical properties and to further improve osseointegration between the implant and bone with different morphological gradients [7, 41, 44]. A few experimental studies have actually been carried out to evaluate the advantages of graded surfaces in promoting osseointegration [7, 42, 43, 45]. Computationally, Lin et al. [39] developed the finite element (FE) models at a macroscopic level for the axially graded hydroxyapatite–titanium implants; and some indicative results were obtained to seek an optimal material gradient for bone remodelling [39, 41, 46]. Nevertheless, most of these graded implant studies focused on either a macroscopic length scale or an axial gradient. However, a macroscopic FEA may not be adequate to capture the biomechanical details within the microstructural features; few reports have been available to model a graded porous surface morphology in radial direction of an implant through examining microscopic responses and none has genuinely searched for an optimal radial gradient to date.

This chapter aims to introduce a multiscale finite element framework of simulating bone remodelling activities and quantifying the effects of different surface morphological parameters. In order to evaluate the osseointegration and interface

stability, four critical indicators to implant success have been considered here, including the average apparent bone density, uniformity of density distribution, bone–implant contact (BIC) ratio and averaged peak Tresca shear stress (PTS) through the porous layer and peri-implant regions. Based upon the remodelling results obtained, the response surface method (RSM) will be employed to formulate the relation between these above-mentioned remodelling indicators and the morphological parameters, thereby deriving an optimal configuration of surface coating through a multiobjective optimisation approach.

3.2 Materials and Methods

3.2.1 *Finite Element Modelling*

With state-of-the-art fabrication technologies, a range of desired nano- and/or microstructured materials can be generated. In this context, traditional mono-scale finite element analysis (FEA) is facing significant challenge as it is inadequate to capture detailed interaction between biomaterials and host tissues at different scales in an effective way. In order to tackle this problem, multiscale analysis techniques have been developed by bridging macro-scale (global) homogenised materials to micro-scale (local) heterogeneous structures with more insightful information [39, 41, 46]. Typical examples in this area include simulating bone internal structures and implant compositions [47, 48], trabecular bone remodelling for correlation to empirical data [49] and implant morphological effects on bone biomechanics and remodelling [50].

In this chapter, the threaded and non-threaded implant configurations are considered as two typical examples in dental implants. In both cases, the implant core is coated with beads at different sizes by sintering [9]. The macroscopic (global) model herein is based upon a 3D solid model created from a set of computerised tomography (CT) data at a human mandibular canine section. The image in DICOM format is firstly segmented in ScanIP (Simpleware Ltd, Exeter, UK) and then processed in Rhinoceros 3D (Robert McNeel & Associates, Seattle, USA). To avoid the structural complexity of the 3D multiscale model and associative high computational costs for remodelling analyses [6, 21, 51], a 2D demonstrative model is adopted in this study, capable of capturing the major biomechanical features under the occlusal loading scenario of mandible section [52]. In essence, a 2D model facilitates capturing many randomly located particles/beads and pores in a reasonably dense mesh, requiring relatively lower computational cost for iterative remodelling simulations compared to the 3D version of multiscale models. Other computational pros and cons between 2D and 3D models can be consulted from literature [6, 51, 53–56]. Therefore, the complete 3D solid model is then converted into a 2D macro-scale model by sectioning in a bucco-lingual plane as shown in Fig. 3.1. A typical implantation is adopted, which consists of a metallic abutment, a

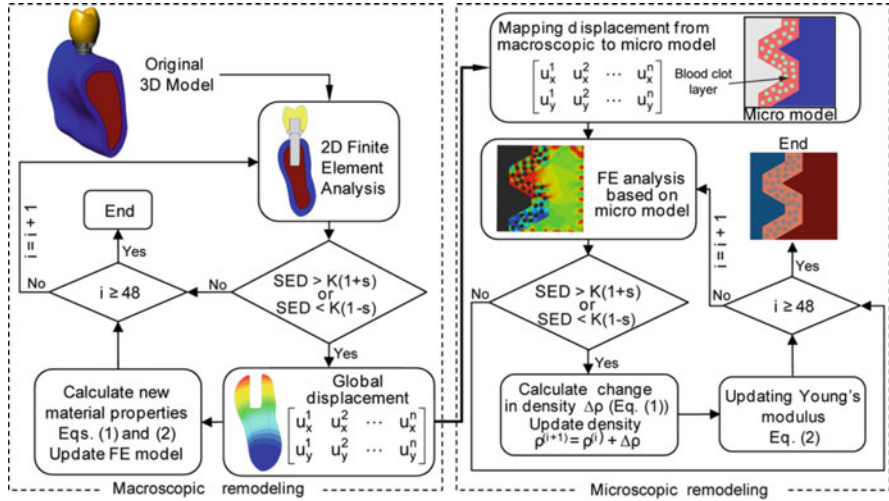


Fig. 3.1 Multiscale remodelling algorithm on a threaded implant with a homogenous porous surface morphology by randomness (Reprinted from Ref. [6], Copyright 2010, with permission from Elsevier)

ceramic crown and a metallic screw body (threaded or non-threaded types). A 202.23 N load is applied vertically to the crown cusp with a 2-mm horizontal offset from the centre to the buccal side [6, 39, 51]. It must be noted that such a macroscopic model is not capable of presenting the microscopic details of either bone or implant surface morphology, just like other mono-scale FE studies.

To capture microscopic morphological features, micro-scale models are created by selecting a region of interest (ROI) with a size of 1 mm × 1 mm (Fig. 3.1). The microscopic model consists of bone, implant substrate (core) and a layer of 200-µm transitional region between them. This transitional layer presents a mixture of pores formed by the implant surface morphology and blood clot that will gradually turn into connective tissues and form host bone [14, 57]. In this chapter, two types of surface morphological patterns, namely homogeneous and gradient, are considered to explore the effect of the coating topography on osseointegration.

For the homogeneous pattern (Case 1), a threaded implant is considered, with sintered (fully bonded) Ti6Al4V alloy particles in spherical shapes, in a randomised manner. Forty microscopic models are created to represent different coating scenarios for the localised cortical and cancellous ROIs (20 models each, Fig. 3.1). Two key topological parameters, the particle diameters and volume fractions, are considered to create different morphological configurations. The former varies at 30, 50, 75 and 100 µm, and the latter adopts 15, 20, 25, 30 and 35% [6, 19, 21, 22], resulting in 20 microscopic models for both the cortical and cancellous ROIs.

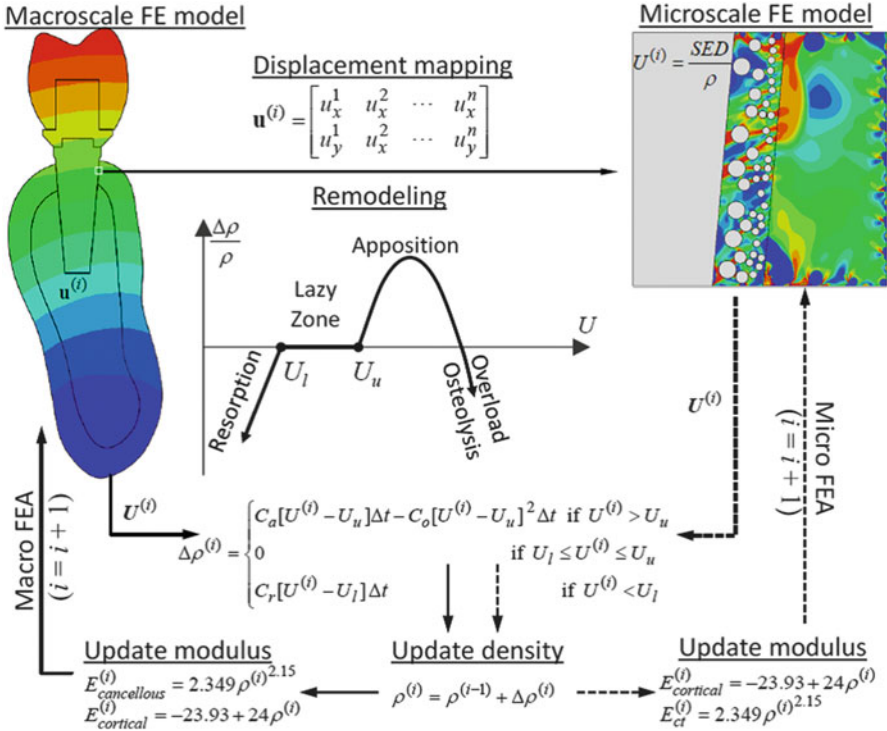


Fig. 3.2 Multiscale remodelling procedure considering overload resorption on a non-threaded implant with a gradient porous surface morphology (Reprinted from Ref. [52], Copyright 2013, with permission from Elsevier)

For the gradient pattern (Case 2), a non-threaded implant surface is considered for another common implant body type (Fig. 3.2). The surface morphological gradient is created by dividing the transitional zone into three sub-layers with different combinations of particle sizes of 30, 50 and 70 μm in diameter [6, 14, 19, 57]. The volume fractions of particles are kept constant at 30 %, equivalent to a porosity of 70 %; so our attention can be focused on the net effects from the particle sizes and morphological gradients. For Case 2, 27 microscopic models are created for the cortical ROI, to represent all possible gradients determined from the given design parameters.

Both macro-scale and micro-scale models are meshed in ABAQUS Ver. 6.9.2 (Dassault Systemes, USA) with three-node linear triangular plain strain elements (CPE3). Verified by a convergence test [6, 51, 53, 58–66], the global adaptive mesh size is set at 1.0×10^{-6} with a curvature deviation factor of 0.01, resulting in an average mesh density of 1.7 elements per μm^2 to ensure a sufficient numerical accuracy. All the finite element analyses are performed using ABAQUS.

3.2.2 Material Properties

The mechanical properties for different materials in this chapter are adopted from literature data; and they are assumed to be linear elastic and isotropic for the sake of simplification in the remodelling analysis [51, 53, 61–63, 67, 68]. In the macroscopic models, the screw body and the abutment are made of titanium alloy [9, 69], and the crown is made of zirconia [53, 69]. The initial properties of the cortical and cancellous bones are obtained from the experimental results reported in the literature [9, 69, 70]; and the remodelling activities will be simulated based on these initial statuses. Poisson's ratios of the same types of tissues are assumed to remain constant during remodelling. The microscopic models adopted the same material properties for the implant region, and the bone region adopts as those in the macroscopic models. The transitional region is assumed to be fully filled by blood clot after 30 min of implantation [71] as its initial status, which will gradually turn into connective tissues, immature bone and mature bone with the corresponding material property changes [70, 72, 73]. Through the remodelling activities, both the existing bone and the transitional area will turn into a heterogeneous status with different bone mineral densities over the cross-sectional plane. All the material properties used in this simulation are summarised in Table 3.1. Following the literature, the densities of cancellous and cortical bones are assumed to be limited by an upper limit of 1.2 and 2.0 g/cm³, respectively [6, 51, 53, 54].

Table 3.1 Initial properties of multiscale models for remodelling simulation

<i>Macro-scale model</i>						
	Implant core and abutment	Crown	Cortical bone	Cancellous bone		
Young's modulus (MPa)	110,000	201,000	1,970	14.8		
Poisson's ratio	0.35	0.28	0.33	0.33		
<i>Micro-scale model</i>						
	Native bone	Implant core and particles	Host tissue (blood clots)	Mature bone	Immature bone	Soft tissues
Young's modulus (MPa)	1,970 (cortical)	110,000	0.001	6,000	1,000	1
	14.8 (cancellous)					
Poisson's ratio	0.33	0.3	0.33	0.33	0.33	0.167

Adapted from Ref. [52], Copyright 2013, with permission from Elsevier

3.2.3 Multiscale Remodelling Algorithm

The remodelling activities are occurring in both these two length scales. The macroscopic model determined the bone response in terms of the apparent mineral density change in the global scale; and the microscopic model stimulated the detailed tissue ingrowth in the ROIs specified from the macroscopic models. The widely accepted Wolff's rule is used to model the turnover of cortical and cancellous bones and connective tissues for both scales [6, 51, 54, 63, 74–76]. In the remodelling simulation, the apparent density ($\Delta\rho$) is set to change over a time increment (Δt) and is proportional to the mechanobiological stimulus. The time increment is chosen at a month here, and the stimulus is defined as the difference between an instant strain energy density (SED) per unit mass (i.e. $U = 0.5\sigma : \epsilon$) and either upper or lower reference [53, 54, 74, 77–80]. This governing remodelling equation can be mathematically formulated in Eq. (3.1) as below.

$$\Delta\rho = \begin{cases} C_a \left[\frac{U}{\rho} - K(1+s) \right] \Delta t, & \text{if } \frac{U}{\rho} > K(1+s) \\ 0 & \text{if } K(1-s) \leq \frac{U}{\rho} \leq K(1+s) \\ C_r \left[\frac{U}{\rho} - K(1-s) \right] \Delta t, & \text{if } \frac{U}{\rho} < K(1-s) \end{cases} \quad (3.1)$$

In this equation, ρ is the local apparent density, and C_a and C_r are the remodelling rate constants [6, 51, 63]. K is the median of the stimulus over the lazy zone, determined at 0.036 mJ/g/cm^3 from the in vivo data [53]. $2s$ is the width of the lazy zone where we adopt $s = 10\%$ as suggested in the literature [76]. Bone resorption can also be induced by mechanical overload once the stimulus level exceeds the physiological limit [12, 81–83]. To represent this factor, a quadratic term can be added to the remodelling equation for an adjusted Wolff's rule [51, 54, 84].

The change in apparent density will lead to the changes in consequential mechanical property, and the empirical relationships between Young's modulus of elasticity (E in GPa) and apparent density (ρ in g/cm^3) are used here [85, 86] as in Eq. (3.2):

$$E = \begin{cases} -23.93 + 24\rho, & \text{for cortical bone} \\ 2.349\rho^{2.15}, & \text{for cancellous bone} \end{cases} \quad (3.2)$$

The bone remodelling simulation is initially conducted on the macroscopic model. The displacement fields are extracted around the ROI boundaries at each time step of this global remodelling simulation. These time-dependent displacement fields are then mapped onto the microscopic models as the loading conditions at each time step. The strain energy density (SED) determined in the microscopic model interpolates the microscopic remodelling responses for further design analysis and optimisation.

Both macroscopic and microscopic remodelling simulations are implemented in ABAQUS system by using FORTRAN user-defined subroutines. This multiscale bone remodelling algorithm is summarised in a flowchart for a threaded implant in Fig. 3.1 and for a non-threaded implant in Fig. 3.2.

3.2.4 Evaluation of Osseointegration

To evaluate the degree of osseointegration, there are several different indicative measures. A primary indicator for the extent of tissue ingrowth is the apparent density in the peri-implant region, which is often calculated by using an area (or volume for 3D) average in a finite element context [3, 87], as formulated in Eq. (3.3). In this equation, A_e is the area of element e , NE is the total number of elements in this region, ρ_e is the apparent density in element e , and \mathbf{x} denotes design variables, such as particle size and volume fraction, namely, $\mathbf{x} = (\alpha, \nu)^T$. A higher bone density typically represents better osseointegration.

$$F_1(\mathbf{x}) = \tilde{\rho} = \frac{1}{A} \int_A \rho dA \approx \frac{1}{\sum_{e=1}^{NE} A_e} \sum_{e=1}^{NE} \rho_e A_e \quad (3.3)$$

There is an alternative indicator for the amount of tissue ingrowth considering bone–implant contact (BIC) ratio, which has been widely used in literature to measure how the bone anchors into and becomes mature in the pore space of the transitional porous region [72, 88]. The BIC ratio can be determined by the proportion of elemental areas with Young's modulus higher than the threshold of mature bone (MB) to the total element area (AE) of connecting tissues, as in Eq. (3.4).

$$\begin{aligned} F'_1(\mathbf{x}) = f_{BIC} = \%BIC &= \frac{\text{Mature Bone Area}}{\text{All Elemental Areas}} \times 100\% \\ &= \frac{\sum_{i=1}^{MB} A_i}{\sum_{i=1}^{AE} A_i} \times 100\% \end{aligned} \quad (3.4)$$

In conjunction with the primary indicators, the homogeneity of the final bone density can be a secondary indicator for quantifying a successful osseointegration and stability. It can be represented by the standard deviation of apparent density in the distribution of established bone density in the region. The less the standard deviation, the more uniform the apparent density. The standard deviation ($\tilde{\epsilon}$) concerned is defined as in Eq. (3.5).

$$F_2(\mathbf{x}) = \tilde{\varepsilon} = \sqrt{\frac{1}{NE} \sum_{e=1}^{NE} (\rho_e - \bar{\rho})^2} \quad (3.5)$$

Similar to the primary indicator, the secondary indicator can also be interpreted in an alternative way, as the capability of the consequential implant–bone interface structure to withstand mechanical loading without debonding. In practice, a pull-out test is a common method to test the degree of shear resistance [19, 89–91]. The Tresca stress is adopted to assess how well the shear stress concentration can be avoided. Nevertheless, the peak Tresca stress may occur in a single element, leading to the misinterpretation of the shear failure for entire transitional region; therefore, the elemental Tresca stress is averaged out over 10 % of the total volume with the highest stress level to provide more statistical meaning. The overall risk of shear failure is thus measured in Eq. (3.6), where n is the number of elements counting for 10 % the total volume that withstands the peak Tresca stresses (PTS).

$$F'_2(\mathbf{x}) = f_{PTS} = \frac{\sum_{e=1}^n \sigma_{10\% \text{ Peak Tre}}^e \times V_{10\% \text{ Peak Tre}}^e}{\sum_{e=1}^n V_{10\% \text{ Peak Tre}}^e} \quad (3.6)$$

3.2.5 Response Surface Method (RSM)

It is often very difficult to establish analytical functions for these above-mentioned multiple biological indicators, especially in complex nonlinear mechanobiological processes, such as osseointegration. The surrogate modelling techniques such as RSM are considered an effective and sometimes unique, alternative approach to modelling these responses [6, 46, 51, 92]. Through RSM, an approximated function $f(\mathbf{x})$ is formulated in terms of a series of simple basis functions [92, 93]. Eq. (3.7) denotes a typical example, where $\tilde{f}(\mathbf{x})$ stands for the surrogate model that is used to approximate the true function $f(\mathbf{x})$, and N denotes the number of the basis functions $\varphi_j(\mathbf{x})$.

$$\tilde{f}(\mathbf{x}) = \sum_{j=1}^N a_j \varphi_j(\mathbf{x}) \quad (3.7)$$

To determine the unknown parameters $\mathbf{a} = (a_1, a_2, \dots, a_N)^T$ in Eq. (3.7), M ($M > N$) sampling points $\mathbf{x}^{(i)}$ ($i = 1, 2, \dots, M$) are needed, which is often not linearly proportional to N . If the remodelling results for each sample point are obtained to form a response vector $f = (f^{(1)}, f^{(2)}, \dots, f^{(M)})^T$, the typical least-square method can be applied to determine the unknown parameter vector \mathbf{a} by minimising

$$E(\mathbf{a}) = \sum_{i=1}^M \left[\mathbf{f}^{(i)} - \mathbf{a}^T \boldsymbol{\varphi}_i(\mathbf{x}^{(i)}) \right]^2 \quad (3.8)$$

thereby determining the unknown vector, $\mathbf{a} = (a_1, a_2, \dots, a_N)^T$ from

$$\mathbf{a} = (\boldsymbol{\Phi}^T \boldsymbol{\Phi})^{-1} (\boldsymbol{\Phi}^T \mathbf{f}), \quad (3.9)$$

where the matrix $\boldsymbol{\Phi}$ denotes the values of the basis functions evaluated at these M sampling points, as

$$\boldsymbol{\Phi} = \begin{bmatrix} \varphi_1(\mathbf{x}^{(1)}) & \cdots & \varphi_N(\mathbf{x}^{(1)}) \\ \vdots & \ddots & \vdots \\ \varphi_1(\mathbf{x}^{(M)}) & \cdots & \varphi_N(\mathbf{x}^{(M)}) \end{bmatrix}_{M \times N} \quad (3.10)$$

By substituting Eq. (3.9) into Eq. (3.7), the expression of $\tilde{f}(\mathbf{x})$ can be fully defined, which mathematically relates the objective functions to the design variables.

To ensure an adequate accuracy of the response surface model, the degree of approximation to the FEA results can be evaluated by the relative error (RE) as,

$$RE = \frac{\tilde{f}(\mathbf{x}) - f(\mathbf{x})}{f(\mathbf{x})} \quad (3.11)$$

3.2.6 Design Optimisation

With multiple indicators for osseointegration, we introduce multiobjective optimisation techniques to address the above-mentioned design issue. Three types of optimisation algorithms are considered in this chapter, namely, linear weighted average (LWA), geometrical average (GA) and multiple objective particle swarm optimisation (MOPSO) methods [92, 94–96].

In Case 1, the particle size (diameter) α and associated volume (or the area in the 2D model) fraction ν are the key design variables, i.e. $\mathbf{x} = (\alpha, \nu)^T$, to the homogeneous porous morphology on the threaded implant surface. For this typical case, we employ the primary and the secondary indicators (F_1 and F_2) to measure the overall osseointegration. From a clinical perspective, successful osseointegration expects the maximised (or the minimised reciprocal of) bone mineral density gain in the peri-implant region as the first indicator. Meanwhile, it is also expected to minimise the variance of bone mineral density distribution as the second indicator as per the standard deviation in the apparent density. In order to achieve both these two objects simultaneously, the multiobjective optimisation problem can be formulated

using the linear weighted average method [94], as in Eq. (3.12), where f_{avg}° and f_{std}° are the normalising values. By varying the weights w_1 and w_2 systematically, a Pareto set can be generated to include a range of the optimal design solutions for different design requirements. The Pareto set provides the entire optimal solution space for the multiobjective optimisation problem. The weights (w_1, w_2) play an important role in emphasising on these two different design objectives, differently.

$$\left\{ \begin{array}{l} \min J_{u,LWA} = F_1^{-1}(\alpha, v) + F_2(\alpha, v) = w_1 \frac{f_{avg}^\circ}{f_{avg}} + w_2 \frac{f_{std}^\circ}{f_{std}} \\ \text{s.t. : } \quad w_1 + w_2 = 1, w \in [0, 1], \\ \quad \quad 30\mu\text{m} \leq \alpha \leq 100\mu\text{m}, \\ \quad \quad 15\% \leq v \leq 35\% \end{array} \right. \quad (3.12)$$

The geometric average (GA) method is similar to the LWA method. In this method, the cost function is formulated from the relative performance index of each objective (Eq. (3.13)). In other words, the multiobjective problem is constructed in terms of a geometric average of the relative distance of each objective to its corresponding ideal value, as in Eqs. (3.14) and (3.15), where $f_{avg}^L, f_{avg}^U, f_{std}^L$ and f_{std}^U denote the minimum and maximum objective values of the density and standard deviation, respectively:

$$\left\{ \begin{array}{l} \max J_{u,GA}(\alpha, v) = \sqrt{F_1^* F_2^*} = \sqrt{f_{avg}^*(\alpha, v) f_{std}^*(\alpha, v)} \\ \text{s.t. : } \quad 30\mu\text{m} \leq \alpha \leq 100\mu\text{m} \\ \quad \quad 15\% \leq v \leq 35\%, \end{array} \right. \quad (3.13)$$

$$f_{avg}^* = \frac{f_{avg}(\alpha, v) - f_{avg}^L}{f_{avg}^U - f_{avg}^L} \leq 100\% \quad (3.14)$$

$$f_{std}^* = 1 - \frac{f_{std}(\alpha, v) - f_{std}^L}{f_{std}^U - f_{std}^L} \leq 100\% \quad (3.15)$$

Compared with the LWA and GA methods, the MOPSO method provides a more efficient solution to seeking for optimal solutions. MOPSO is an extended version of the particle swarm optimisation (PSO) procedure that has been successfully used in a broad range of the single-objective design problems. Coello and Lechuga [95] introduced the MOPSO algorithm by incorporating the ability to handle the multiple objectives without sacrificing typical fast convergence of PSO. This method incorporates the mechanism of crowding distance, which is specifically benefited on global best selection of dominated solutions from an external archive. More details of this algorithm can be found in the literature [95, 96]. In this case, the design problem is formulated mathematically as in Eq. (3.16).

$$\begin{cases} \min J_{u,PSO}(\alpha, v) = [F_1^{-1}(\alpha, v), F_2(\alpha, v)]^T = [f_{avg}^{-1}, f_{std}]^T \\ s.t. : \quad 30\mu m \leq \alpha \leq 100\mu m \\ \quad \quad 15\% \leq v \leq 35\%, \end{cases} \quad (3.16)$$

In Case 2, the particle sizes, α_1 , α_2 and α_3 , in these three different sub-layers, are considered as the design variables $\mathbf{x} = (\alpha_1, \alpha_2, \alpha_3)^T$ for the graded porous surface morphology on a non-threaded implant. For this case, alternative indicators (F'_1 and F'_2) are adopted to evaluate the overall osseointegration and load-bearing capacity. Similar to Case 1, it is expected to maximise (or minimise the reciprocal of) the first indicator of BIC and minimise the second one in terms of averaged top 10 % Tresca stress. For this typical case, we adopted LWA and MOPSO methods for this multiobjective optimisation. The LWA method formulates the optimisation scenario in Eq. (3.17) [6, 46, 51, 92], where the normalisation by means of the minimum f_{BIC}° and maximum f_{Tre}° is used to eliminate the dimensional difference for better combining these two different objective functions.

$$\begin{cases} \min J_{g,LWA} = F_1'^{-1}(\alpha_1, \alpha_2, \alpha_3) + F_2'(\alpha_1, \alpha_2, \alpha_3) = w_1 \frac{f_{BIC}^\circ}{f_{BIC}} + w_2 \frac{f_{PTS}}{f_{PTS}^\circ} \\ s.t. : \quad w_1 + w_2 = 1, \quad (w_1 \geq 1, w_2 \geq 1) \\ \quad \quad 30\mu m \leq \alpha_1, \alpha_2, \alpha_3 \leq 70\mu m \end{cases} \quad (3.17)$$

The MOPSO method, on the other hand, is also expressed directly as Eq. (3.18), similar to the homogenous case.

$$\begin{cases} \min J_{g,PSO} = [F_1'^{-1}(\alpha_1, \alpha_2, \alpha_3), F_2'(\alpha_1, \alpha_2, \alpha_3)]^T = [f_{BIC}^{-1}, f_{PTS}]^T \\ s.t. \quad 30\mu m \leq \alpha_1, \alpha_2, \alpha_3 \leq 70\mu m \end{cases} \quad (3.18)$$

3.3 Results

In this chapter, both cases are simulated for bone remodelling responses with different surface morphological gradients over the 48 months, in which the host bone can grow into the void space and the corresponding osseointegration performance is measured by the different indicators. The first few months (as the first few increments) in the simulation are critical for the establishment of the secondary stability of an implant; after a certain period, bone could gradually achieve a dynamic equilibrium with both apposition and resorption occurring to a similar extent. Both the short-term and long-term implant performance assessments are considered here.

3.3.1 Homogeneous Coating Configuration with Threaded Implant (Case 1)

3.3.1.1 Bone Remodelling Responses

In Case 1, the effects of design variables, i.e. particle size and volume fraction of the coated material to void space, are first explored at month 48. The apparent densities for the cortical and cancellous bones are assumed to approach their upper limits of 2.00 and 1.2 g/cm³, respectively, during this period as suggested in the literature [97]. As reported being a critical period for the osseointegration and stabilisation of implant, month 12 is also considered to be the initial time point to assess the remodelling outcomes in the short term, for comparing the mechanobiological responses induced by various designs in this case.

Table 3.2 summarises all the 40 ROIs in the homogenous surface morphology case, in terms of their area average density (ρ) and corresponding standard deviation (STD) after 12-month remodelling with regard to each design variable in the cortical and cancellous regions, respectively. During the first year, an increase in the volume fraction from 15 % to 35 % results in an average of 8.40 % and 8.12 % increase in density for the cortical and cancellous regions, respectively. Increasing the particle size from 30 μm to 100 μm , however, induces insignificant and fluctuating changes in the density, mainly because the location randomness of the particles may have resulted in a non-negligible effect on the biomechanical stimulation and thus leads to an inconsistent density variation.

Such finding is in good agreement with the study by Shen et al. [3], who concluded that the pore size has an insignificant effect on the stress–strain response, while the arrangement of the particles has a determinant influence on the stiffness.

Table 3.2 Area average density and standard deviation in the cortical and cancellous regions (12 months)

v	30 μm		50 μm		75 μm		100 μm	
	ρ	STD	ρ	STD	ρ	STD	ρ	STD
Cortical region								
15 %	1.4315	0.3100	1.5172	0.3302	1.4988	0.3348	1.5074	0.3189
20 %	1.5247	0.3407	1.5687	0.3361	1.6645	0.3389	1.5739	0.3281
25 %	1.5344	0.3472	1.6638	0.3645	1.5045	0.3472	1.5424	0.3326
30 %	1.5680	0.3486	1.5879	0.3461	1.5367	0.3418	1.5896	0.3444
35 %	1.5962	0.3499	1.5948	0.3501	1.6029	0.3487	1.6590	0.3279
Cancellous region								
15 %	0.8369	0.1970	0.8716	0.2183	0.8643	0.2191	0.8680	0.2227
20 %	0.8942	0.2208	0.8959	0.2392	0.9167	0.2523	0.8758	0.2244
25 %	0.8851	0.2315	0.9236	0.2398	0.8486	0.2416	0.8763	0.2351
30 %	0.9098	0.2354	0.9084	0.2389	0.8956	0.2382	0.9122	0.2340
35 %	1.5962	0.3499	1.5948	0.3501	1.6029	0.3487	1.6590	0.3279

Reprinted from Ref. [6], Copyright 2010, with permission from Elsevier

According to Bobyn et al. [19], the spherical particles with size ranging from 45 to 150 μm were estimated to provide the morphology with a pore size ranging from 50 to 200 μm . This range of pore size, in the adult canine (beagle) femurs, generated the maximum strength from the pull-out test at 8 weeks postoperatively. This could be another reason why there was small difference in remodelling responses when the particle size increased from 30 to 100 μm .

Table 3.2 also suggests that the surface morphologies with a greater volume fraction of spherical particles could potentially provide a better initial stability than those with a less volume fraction. This is simply due to the fact that the design containing more particles within the same volume provides a greater contact area with bone, thereby enabling it to achieve a higher interfacial or bonding force [19].

From the bone engagement perspective, the 100 μm particles are found to deliver the best bone density outcome under various volume fractions. The cortical and cancellous remodelling progressions are plotted for the design with a particle size of 100 μm in Fig. 3.3a and b, respectively, which show that the average bone density increases throughout the entire 48-month remodelling period in all different surface morphologies. Particularly in the first 12 months, the rate of density gain is very high and then gradually slows down until the end of the remodelling period considered (48 months). From the clinical perspective, it is important that bone formation is initiated at the earliest possible stage to establish sufficient stability for implant functions. In these two particular ROIs, the bone remodelling over the 48 months does not yet reach the full dynamic equilibrium status, signifying the existence of a remaining stimulus concentration in the peri-implant region, possibly resulting in further bone apposition and/or resorption.

The density contours in the transitional layer are displayed as the inserts in Fig. 3.3. In the cortical region (Fig. 3.3a), the dense bone is distributed in a way perpendicular to the inclined surface of implant threads, whereas the dense cancellous bone (Fig. 3.3b) distributes in a pattern preferentially along the horizontal direction and propagates into the implant fixture side of the bony tissues through the coated particles. This agrees with the macroscopic analysis where the occlusal loading is mainly borne by the cortical bone, while the cancellous bone stabilises the implant by accommodating the bending moments.

3.3.1.2 Response Surface Model

Based on the above remodelling results, the uniform morphological configuration can be further optimised by controlling the two topological factors, namely, the particle size (α) and the volume fraction (ν), as the design variables. To do so, a full factorial design of experiments (DoE) is first considered with these two design variables, i.e. the particle sizes at 30, 50, 75 and 100 μm and the volume fractions at 15, 20, 25, 30 and 35%. Consequently, 20 design samples of the surface morphologies have been generated for the cortical and cancellous ROIs, respectively, evenly distributing the entire design domain. With these sampled points, several polynomial basis functions at different orders ranging from 1 to 4 are tested to

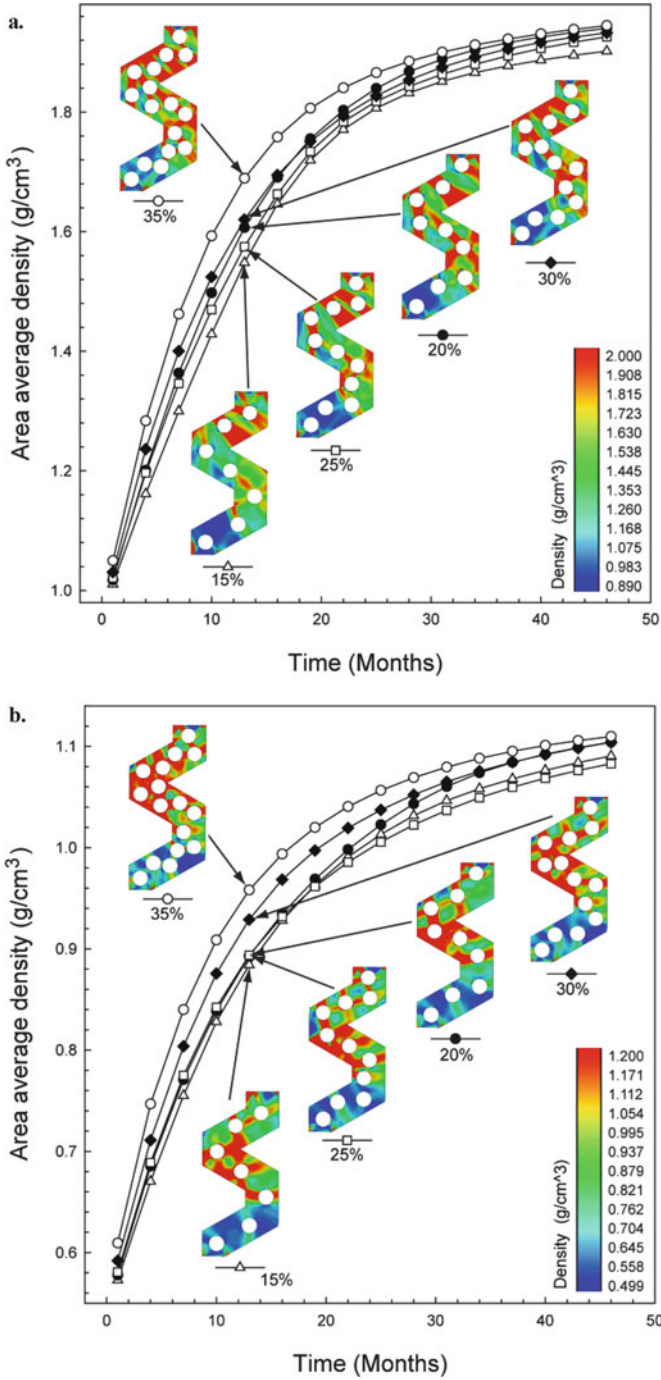


Fig. 3.3 Micro-scale remodelling progressions of area average of bone density with different volume fractions (at particle size 100 μm) at (a) cortical and (b) cancellous regions (Reprinted from Ref. [6], Copyright 2010, with permission from Elsevier)

Table 3.3 Response surface modelling accuracies for different polynomials (Reprinted from ref. [6], Copyright 2010, with permission from Elsevier)

	RS model (polynomial order)	Max RE (Cortical) (%)	Max RE (Cancellous) (%)
Density	Linear	6.38	5.47
	Quadratic	5.66	5.51
	Cubic*	4.86*	4.24*
	Quartic	558	2868
Standard deviation	Linear	7.66	11.02
	Quadratic	3.72	6.34
	Cubic*	3.37*	3.87*
	Quartic	2763	394

*The most accurate polynomial function

validate the response surface (RS) models. As evaluated by their modelling accuracies using Eq. (3.11), the outcomes are summarised in Table 3.3. Note that the smaller the relative error (RE), the better the regression for the RS model. Obviously, the cubic polynomial function provided the best overall approximation for both the cortical and cancellous regions considered.

The resulting response surfaces shown in Figs. 3.4 and 3.5 graphically illustrate the effects of particle sizes and volume fractions on the apparent density and the standard deviation in the cortical and cancellous regions, respectively. It is clear that the response surfaces of the average densities in both ROIs largely resemble each other. The least average densities in both the regions occur when the particle size and the volume fraction are at their lowest values. In contrast, the average density reaches the maximum at the largest particle size and volume fraction (i.e. 100 μm and 35 %, respectively).

3.3.1.3 Surface Morphology Design Optimisation

As mentioned in Sect. 3.2.6, two different design criteria are adopted to measure the subsequent osseointegration and bone remodelling. In the linear weighted averaged (LWA) method, the weighting factors w_1 and w_2 can be systematically varied to generate different optimal solutions from Eq. (3.12), which forms a Pareto solution set as plotted in Fig. 3.6 (blue circle). These two objective functions (F_1 and F_2), for the average bone density and its standard deviation in this case, vary from their upper to lower bounds as the results of different weights. As shown in Fig. 3.6a, three isolated optimal solution clusters (overlapping each other around 30 μm , 15 %; 100 μm , 30 %; and 100 μm , 35 %) can be determined for the cortical region. It must be noted that within the Pareto frontier, any further improvement in one objective must sacrifice the other, e.g. to increase the bone density further, and its uniformity must be compromised and vice versa. Similarly, the optimal designs for the cancellous bone are shown in Fig. 3.6b. Although the number of optimal

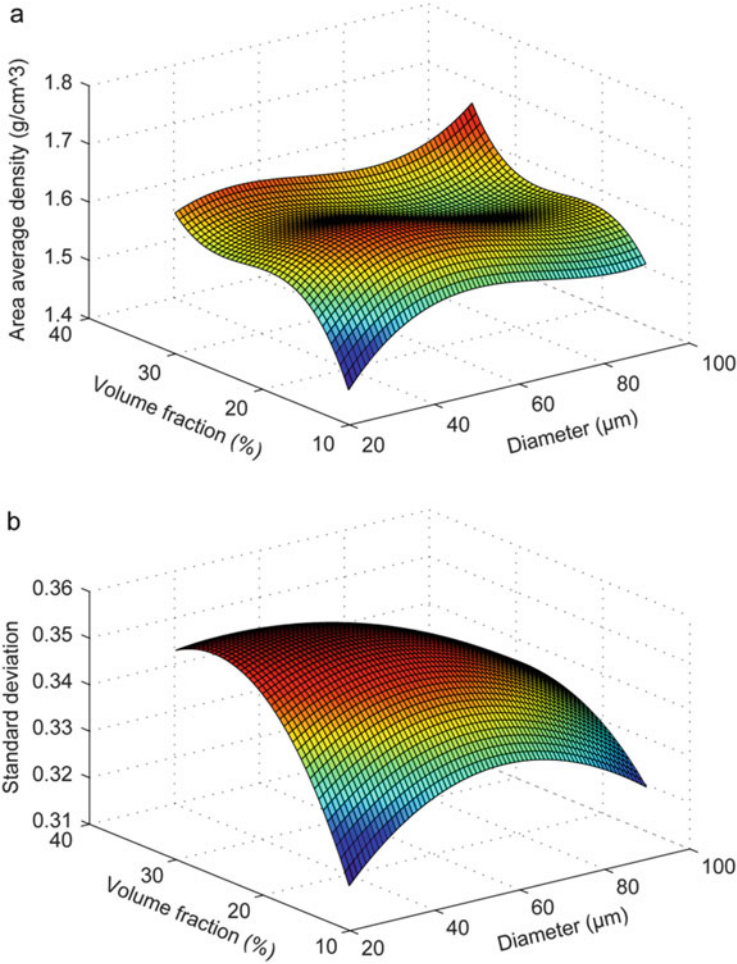


Fig. 3.4 Response surface plots showing the effects of particle size and volume fraction on the average density (a) and standard deviation (b) in the cortical regions (Reprinted from Ref. [6], Copyright 2010, with permission from Elsevier)

solutions appears more than that in the cortical bone, it would be preferable to generate more uniformly distributed optimal points in the Pareto space.

The other approach, namely multiobjective particle swarm optimisation (MOPSO) method, generates the Pareto solutions through gradually moving particles for Pareto dominance. Note that as any Pareto point denotes an optimum, which enables us to obtain the entire solution domain for the multiobjective optimisation problem. Its outcomes are plotted in the same figure as the LWA method with red dots. For the cortical ROI (Fig. 3.6a), the three isolated solution clusters are well positioned in the Pareto curves produced from the MOPSO method, showing the coincident trends as expected. Obviously, the MOPSO

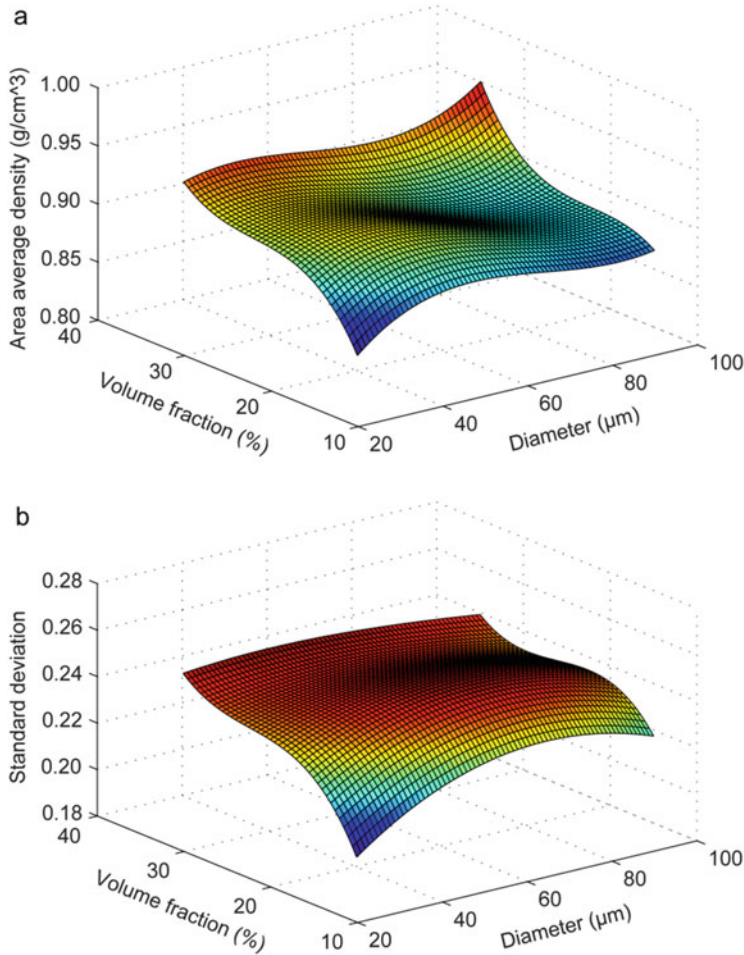


Fig. 3.5 Response surface plots showing the effects of particle size and volume fraction on the average density (a) and standard deviation (b) in the cancellous regions (Reprinted from Ref. [6], Copyright 2010, with permission from Elsevier)

method has provided much more uniform distribution of solution points, showing a significantly improved efficiency in pursuing optimal solutions, compared to the overlapped clusters of solutions from LWA. Importantly, the MOPSO method well demonstrates the competition between the two objective functions. When reaching the Pareto fronts, any further improvement in one must sacrifice the other.

Figure 3.6b plots the Pareto front for the implant design in the cancellous region, where the LWA method leads to slightly broader distribution than that in the cortical region. Again, all the optimal designs from the LWA method are well located on the Pareto frontiers resulted from the MOPSO method, indicating the

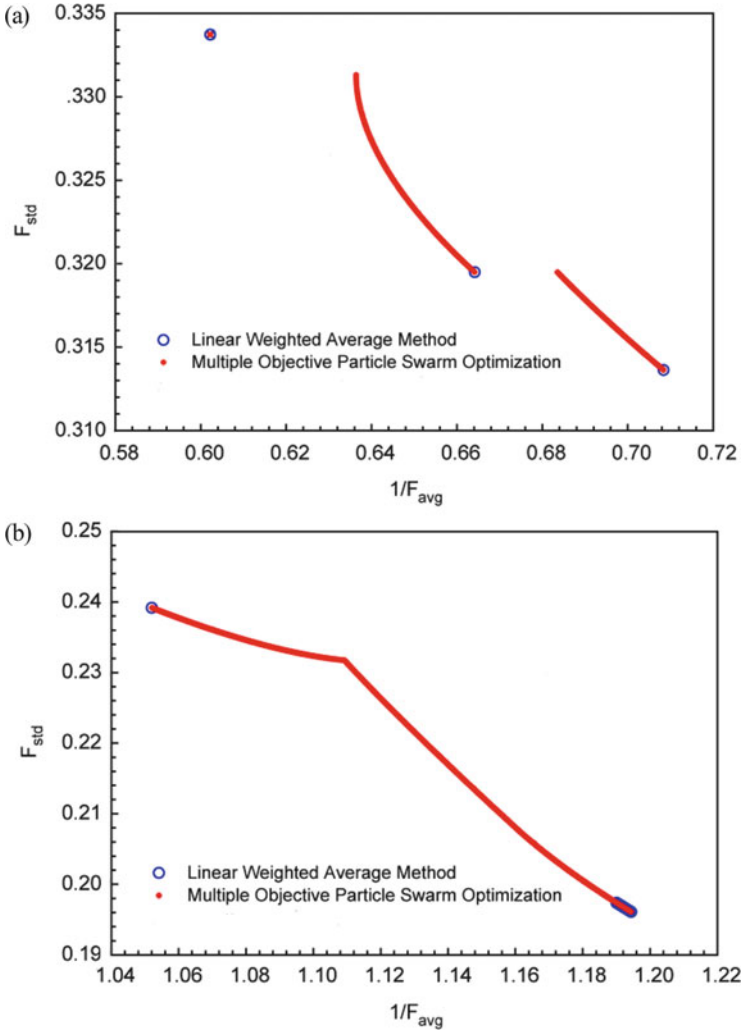


Fig. 3.6 Pareto frontiers resulted from the LWA and MOPSO multiobjective optimisation algorithms: (a) cortical region and (b) cancellous region (Reprinted from Ref. [6], Copyright 2010, with permission from Elsevier)

effectiveness of these two methods when searching for the optima in the design domain. This design further confirms that the MOPSO method is more effective by presenting much more uniform distribution of the Pareto solution points than the LWA method in the scenarios where the sophisticated nonlinear mechanobiological processes are involved.

The last optimisation method applied to this case is the geometrical average (GA) method. Different to the LWA and MOPSO methods, the GA method aims to chase a single optimal solution by minimising the relative distances of the two

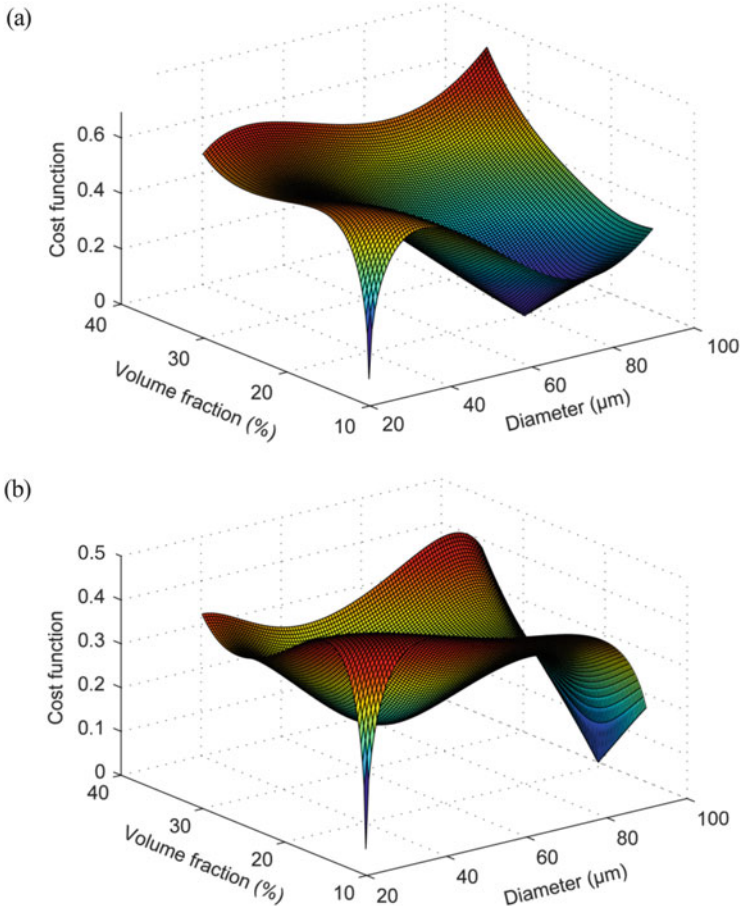


Fig. 3.7 Surface of efficiency coefficient function versus design variables of cortical region (a), where the optimum appears at the boundary of the design domain, and the cancellous region (b), where the optimum occurs around the lower bounds (Reprinted from Ref. [6], Copyright 2010, with permission from Elsevier)

objective functions from a geometric average point of view. Considering the both design criteria, the cost functions $F_g(\alpha, v)$ against the design variables are plotted in Fig. 3.7a and b for the cortical and cancellous ROIs, respectively, in which non-monotonic relationships can be seen for the both regions except at a lower volume fraction ($v < 20\%$) and a greater particle size ($\alpha > 60\ \mu\text{m}$).

Table 3.4 summarises the GA optimisation outcomes, in which the performance index (f_{avg}^*, f_{std}^*) and overall cost functions $F_g(\alpha, v)$ indicate how close these functions approach to the maximum degree of optimisation. From this perspective, the greater the values of f_{avg}^*, f_{std}^* and $F_g(\alpha, v)$, the better the design. It is interesting to note that the optimal designs are somewhat different for the cortical and

Table 3.4 Optimisation results from the geometrical average method

Region	Optimal design variables ($\alpha; \mu\text{m}$), ($v; \%$)	Cost function $F_s(\alpha, v)$	Performance index f_{avg}^*	Performance index f_{std}^*	Density (g/cm^3)	Standard deviation
Cortical	$\alpha = 100, v = 35$	0.7069	1.0000	0.5003	1.6605	0.3538
Cancellous	$\alpha = 37.7, v = 17.4$	0.6498	1.0000	0.8555	0.8827	0.2203

Reprinted from Ref. [6], Copyright 2010, with permission from Elsevier

cancellous regions. The optimisations occur at the upper bound of the design domain (i.e. $100\ \mu\text{m} - 35\%$) for the cortical bone, but at the middle of design domain (i.e. $38\ \mu\text{m} - 17.5\%$) for the cancellous bone. This difference implies that, to achieve a maximum osseointegration, a functionally graded morphology of the surface coating may be needed for the different locations along the implant–bone interface.

3.3.2 Graded Coating Configuration with Non-threaded Implant (Case 2)

3.3.2.1 Bone Remodelling Responses

In the case of the graded porous surface morphologies, we adopt the alternative indicators (F'_1 and F'_2) for the bone remodelling response over the 48 months of healing, in terms of the bone–implant contact (BIC) ratio and the 10 % average peak Tresca stress (PTS), as the load-bearing capacity is more crucial for such a the non-threaded implant considered. The porosity of each sub-layer in the graded surface is kept constant at 70 % (i.e. 30 % volume fraction of particles) in this case, which provides all the models in different sub-layers with the same void space for tissue ingrowth. All the gradient configurations are presented in a form of $(\alpha_1\text{-}\alpha_2\text{-}\alpha_3)$, in which α_1 is for the sub-layer closest to the implant core, whereas α_3 is next to the host bone.

Figure 3.8 (a) compares the highest and the lowest BIC ratios in the graded surface morphologies with the three homogenous ones comprising 30, 50 and 70 μm particles. It clearly shows the evident effect of morphological gradients on osseointegration rates. All the five morphologies plotted here may have similar rates of mature bone apposition during the first 3 months of acute healing; however,

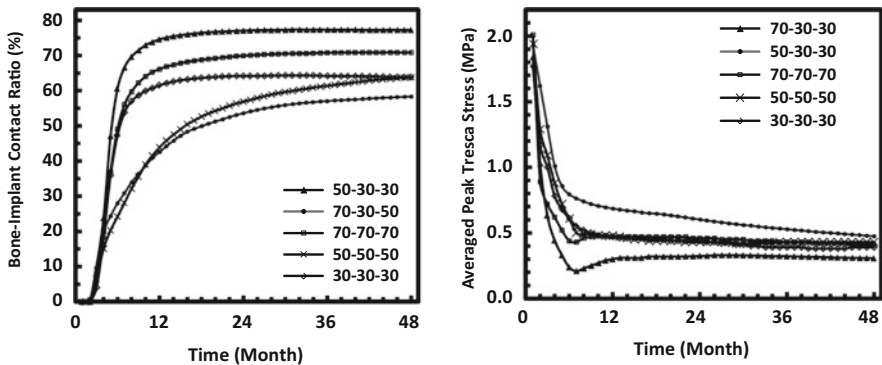


Fig. 3.8 (a) Highest/lowest bone–implant contact (BIC) ratios and (b) average peak Tresca stresses comparing to the three uniform morphologies (with porosity of 70 %) (Reprinted from Ref. [52], Copyright 2013, with permission from Elsevier)

there is a significant difference in the BIC ratio after month 6. Gradient 50-30-30 maintained a steep growth rate till the end of the first year, showing superior stimulation for bone mass growth over the entire simulation period than the others, and finally it has 6.41 % more bone mass than the best homogenous configuration of 70-70-70 by month 48. It is noted that not all graded surface morphologies increase the extent of osseointegration. Gradient 70-30-50, on the other hand, has an earlier take-off but a slower growth thereafter. It shows a reverse effect on osseous tissue ingrowth, even worse than the uniform morphologies, despite its rapid density gain in the first few months. At the end of 48 months, the best and worst gradients ended up with around 20 % difference in the BIC ratios.

Figure 3.8 (b) compares the evolutions of the highest and lowest averaged peak Tresca stress (10 %) with those three uniform morphologies. Note that the quick drops in the first 6 months indicate the rapid growth of osseous tissues, with the reductions of 86.9 % for gradient 70-30-30 and 58.5 % for gradient 50-30-30, respectively. A similar pattern is observed in all the uniform surface morphologies which fall in between the highest (worst) and lowest (best) gradient ones. It is interesting to see that in addition to its highest BIC ratio, gradient 50-30-30 delivers the highest stress concentration over the 48 month. On the other hand, gradient 70-30-30, rather than 70-30-50, has the highest averaged peak Tresca stress, indicating the highest risk of shear failure. Nevertheless, the final difference between the lowest (gradient 70-30-30) and highest (gradient 50-30-30) values at month 48 is fairly marginal (0.17 MPa, approximately 10 % of the initial stress concentration).

Different to the BIC outcomes, all the gradients show a slower and more gradual convergence for PTS. Figure 3.9 compares the trends between the best and worst performers under these two different indicators of osseointegration. The PTS

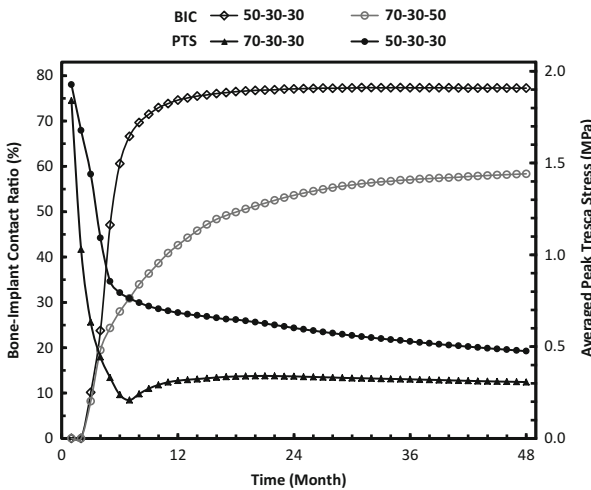


Fig. 3.9 Best and worst gradient implant performance under different design criteria

bumps back after the quick drop and then levels off to an equilibrium over time, instead of approaching to a steady state straightway as in BIC. Based on the monthly data obtained, however, it seems unclear to draw a direct relationship between BIC and PTS.

3.3.2.2 Response Surface Model

Similar to the homogeneous cases, these two alternative indicators (BIC and PTS) are also difficult to formulated with respect to the design variables. Again, RSM models are considered effective for approximating the indicators. As already observed in the bone remodelling responses, month 6 and month 48 are the two critical stages to evaluate the short-term and long-term performances of remodelling outcomes.

The sample data provides the essential information to extrapolate design analysis and optimisation. Based upon the above remodelling results, the assessment criteria, BIC and PTS, are related to the design variables of coating parameters in each layer as $(\alpha_1, \alpha_2, \alpha_3)$. Combined with the experience in the homogeneous case, three different orders (linear, quadratic and cubic) of polynomials are attempted by the least-square method, to evaluate the fitness of response surface (RS) models. The R^2 and root-mean-square error (RMSE) between simulation and RS functions (Max and Min) are used to assess which polynomial is most accurate. As summarised in Table 3.5, the cubic polynomial functions provide the best fits to both BIC and PTS in these two selected time points for the short- and long-term osseointegration (months 6 and 48, respectively).

Table 3.5 Response surface models (polynomial) for months 6 and 48

	Time (month)	RSM	R ²	Max	RSM* Max	Min	RSM* Min	RMSE**
BIC (%)	6	1st	0.8828	60.59	45.79	21.51	27.33	8.69
		2nd	0.9035		50.54		23.02	6.21
		3rd	0.9536		59.15		21.83	4.30
	48	1st	0.9950	77.25	71.92	58.36	63.23	4.88
		2nd	0.9968		73.69		57.90	3.88
		3rd	0.9983		76.95		56.66	2.88
PTS (10 ⁵ Pa)	6	1st	0.9417	9.14	6.50	2.38	4.09	1.35
		2nd	0.9572		8.05		3.15	1.16
		3rd	0.9647		8.89		2.84	1.06
	48	1st	0.9810	4.96	4.03	2.85	3.64	0.54
		2nd	0.9888		4.55		3.21	0.42
		3rd	0.9942		4.83		3.04	0.31

Reprinted from Ref. [52], Copyright 2013, with permission from Elsevier

RSM* response surface method result

RMSE** root-mean-square error

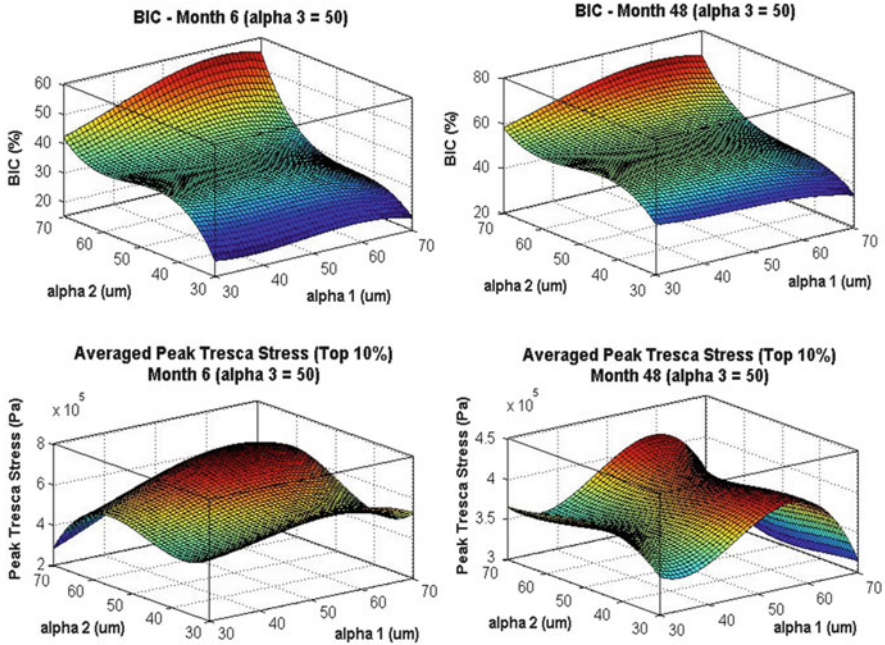


Fig. 3.10 Response surfaces showing the effects of gradient input α_1 and α_2 when α_3 is set to 50 μm on BIC (a, b) and averaged peak Tresca stress (c, d) at months 6 and 48 (Adapted from Ref. [52], Copyright 2013, with permission from Elsevier)

With the three design variables, the ‘response surface’ is literally a three-dimensional isometric response cube. To clearly demonstrate the responses on the surface models, α_3 is set to be 50 μm representing an intermediate size of particles as an example for RSM. Figure 3.10 plots the BIC and PTS for months 6 and 48, respectively. From the BIC perspective, the combinations of medium particles in the inner layer (α_1) with large sizes in the mid-layer (α_2) show their advantages over the other configuration in both short term (month 6 as in Fig. 3.10a) and long term (month 48 as in Fig. 3.10b). The trend is also affected by α_2 (mid-layer) more significantly than α_1 (inner layer), and it drops dramatically along the reverse direction of α_2 axis, with a short level-off at the medium size range. The benefit of using a medium–large combination is being amplified in BIC as healing time progresses. Figure 3.10 (a) and (b) also reflects that gradient 70-30-50 (right bottom corner in the plots) is the worst performer in the design range over the simulation time.

On the other hand, PTS shows more distinct patterns than BIC. From Fig. 3.10 (c), α_2 plays a more important role in the short-term stability than α_1 ; however, this is reversed in the long term as in Fig. 3.10 (d). The minimum PTS appears in the case when small particles in the inner layer are combined with the large ones in the mid-layer in month 6, while it occurs at the medium–large combinations at month 48. Similarly to BIC, the lowest PTS occurs around gradient 70-30-50 which is close to gradient 70-30-30, likely having the least failure chance.

Based on the RS functions obtained, we can determine the gradients for either maximum BIC or minimum PTS outcomes in both months 6 and 48, respectively. It is noted that gradient 61.8-70.0-49.9 has the highest BIC ratio as 61.35 % in month 6, but at the same time has a high PTS of 0.54 MPa. In contrast, gradient 70.0-30.1-70.0 has the lowest PTS of 0.29 MPa accompanied by a lower gain of bone mass, leading to a BIC ratio of 29.81 % only. In month 48, gradient 30.0-30.0-32.1 leads to the maximum BIC ratio of 76.92 % (0.34 MPa PTS), while gradient 70-45.4-40.8 provides with the lowest PTS of 0.28 MPa (40.71 % BIC). Falling into a similar situation to the homogenous case, these two design criteria cannot be achieved concurrently.

3.3.2.3 Surface Morphology Design Optimisation

As determined from the response surfaces in Fig. 3.10, the optimal BIC and PTS are very hard to attain simultaneously. To address both design criteria, we again employ the multiobjective optimisation to maximise BIC and minimise PTS by using the linear weighted average (LWA) and the multiobjective particle swarm optimisation (MOPSO) methods to seek an optimal solution domain for various balances of these two design criteria.

To enhance the uniformity of Pareto distribution, we attempt to vary the weighting factors in a very small increment of 0.0005 in the LWA method. As plotted in Fig. 3.11 (a) and (b) for months 6 and 48, respectively, it is interesting to see that there are multiple optimal solution clusters for month 6 and three separate but highly overlapping clusters for month 48. To tackle the non-uniform distribution problem that occurred in the LWA solutions, the multiobjective particle swarm optimisation (MOPSO) method is again providing a much better distributed Pareto solution set, as already demonstrated in the homogenous case. 2000 Pareto points are generated through 1000 iterations, and 80 of them with uniform intervals are plotted in the same graph as that from the LWA method. Obviously, MOPSO is

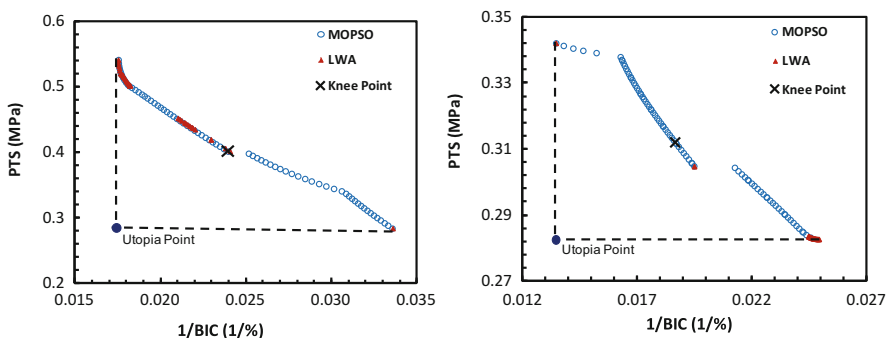


Fig. 3.11 Pareto fronts of optimal surface gradients from the two LWA and MOPSO optimisation algorithms at month 6 (a) and month 48 (b) (Reprinted from Ref. [52], Copyright 2013, with permission from Elsevier)

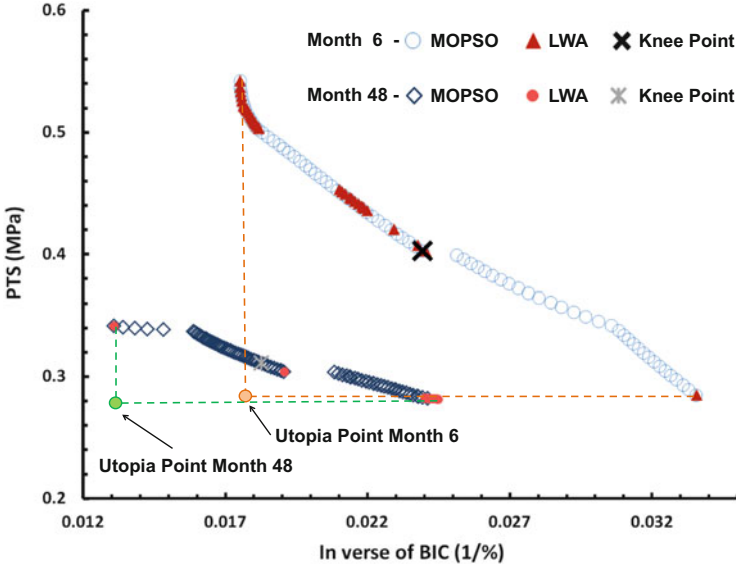


Fig. 3.12 Knee point determined based on the distances to the Utopia point for month 6 and month 48

more effective than LWA in terms of the smoothness of Pareto frontier and extent of uniformity in this design problem. As expected, MOPSO is much more widely distributed and all the LWA results are well located in the MOPSO Pareto frontier. When reflecting the effectiveness of these two approaches, their outcomes are different in the integrity. From the Pareto frontiers at these two different time points (months 6 and 48), it is also noted that further improving either BIC or PTS must sacrifice the corresponding counterpart along the Pareto frontiers.

Hypothetically, any point in the Pareto front can be a solution corresponding to a specific morphological design. Although the Pareto set provides us with multiple choices for different needs, it will be implicating if an overall optimum could be determined. The Utopia point signifies the most ideal solution that has the maximum BIC ratio and the minimum PTS at the same time (as outlined in Fig. 3.12). However, this point cannot be attained in most of design cases. As a compromise, a most ‘satisfactory’ solution, known as a knee point, can be chosen in the Pareto frontier. Here, we adopt the minimum distance selection method (MDSM), a similar approach as the geometric average (GA) optimisation, defined mathematically as

$$\min D = \sqrt{\left(\frac{f_{BIC} - f_{BIC}^L}{f_{BIC}^U - f_{BIC}^L}\right)^2 + \left(\frac{f_{PTS} - f_{PTS}^L}{f_{PTS}^U - f_{PTS}^L}\right)^2} \quad (3.19)$$

where f_{BIC} and f_{PTS} are the objective functions, while f^L and f^U are their corresponding lower and upper bounds in the design space concerned. A most 'satisfactory' solution can be determined by minimising its distance to the Utopia point.

In this case, it is found that the coating with a moderate gradient near the largest particle size (70.0-70.0-61.6) provides a most satisfactory solution in the initial healing up to month 6, giving a BIC outcome of 41.53 % and PTS of 0.40 MPa, whereas for the long-term healing (48 months), a graded coating of 37.1-70.0-67.7 is preferred, leading to a BIC ratio of 54.35 % and PTS of 0.31 MPa. Note that with other selection criteria, for instance, 'the maximum BIC ratio within a tolerated PTS range', it could lead to a different conclusion on the optimal choice.

3.4 Discussion

Despite an increasing importance, there has been a fundamental lack of predicting long-term outcome of a dental implantation in a quantitative way. The multiscale finite element analysis (FEA) framework developed in this study facilitates bone remodelling simulation in macroscopic and microscopic levels. It provides new understanding of the vital roles that biomechanics plays in characterising the time-dependent performance of dental implant that allows clinicians to formulate a more biomechanically sound treatment plan.

Osseointegration process can be affected by both implant surface morphology and physiological conditions. For the latter, age, sex, race, genetics and other medical factors all contribute on bone responses to the implantation, leading to different osseointegration outcomes. This chapter considers a particular set of remodelling parameters derived from literature to demonstrate how the surface topographical gradient of implant can be optimised for the same given mechanical and biological conditions. With sufficient patient data (e.g. from interval time history CT/MRI scans), this approach can be used to individual subject with their own remodelling parameters, aiming for a patient-specific design. For each patient, the predicted Pareto optima consists of a series of solutions at different uniform and balancing points, e.g. in between BIC ratio and PTS, and a clinic decision can be made based upon individual needs of a patient and clinical expectation.

Although this chapter takes dental implant as an example, the graded topographical configuration and corresponding design procedure can be extended to other applications of prosthetic fixation, such as orthopaedic osseointegration. A recent study [98] has examined the macroscopic remodelling outcomes in terms of bone mass density and failure possibility of different prosthetic designs in hip replacements. By applying the design procedure for graded topography proposed in this study, the microscopic surface morphology can be optimised for the hip prosthesis to meet individual patient needs.

Topology optimisation has proven an effective tool for microstructural design aiming to regulate effective material properties for bone remodelling applications

[99–102]. Another recent study [103] demonstrated how to optimise microstructural gradient of hip replacement implant for achieving minimum bone resorption and failure probability. Nevertheless, this technique is restricted to periodic microstructures and may be of limited implication to random morphology as shown in this chapter.

3.5 Conclusion

A novel application of multiscale modelling and remodelling analyses has been presented in this chapter with an aim to optimise the coated porous surface morphology. The remodelling simulation is conducted in the macroscopic level first; then the resultant displacement fields at different time steps are mapped to the microscopic representative volume element (RVE) model as loading for microscopic remodelling simulation. A layer of transitional region between host bone and implant substrate core is considered as the design domain. The osseointegration is measured in terms of four different indicators: (1) area averaged apparent density in the transitional layer, (2) standard deviation of density, (3) bone–implant contact (BIC) ratio and (4) averaged (10 %) peak Tresca stress (PTS). The response surface method (RSM) is employed to formulate these indicators with respect to the design variables. To simultaneously address several different design criteria, the multiobjective optimisation was adopted here using different approaches, including linear weighted average (LWA) and multiobjective particle swarm optimisation (MOPSO) method to provide a range of optimal solutions in a Pareto sense. In pursuing a single balanced optimal solution, the surface topographical parameters can be determined by either a geometric average (GA) method or adopting the minimum distance selection method (TMDSM).

Acknowledgement This work was supported by the fellowship grants from the Australian Research Council (ARC).

References

1. Kutty MG, Bhaduri S, Bhaduri SB (2004) Gradient surface porosity in titanium dental implants: relation between processing parameters and microstructure. *J Mater Sci Mater Med* 15(2):145–150
2. Brånemark PI, Adell R, Albrektsson T et al (1983) Osseointegrated titanium fixtures in the treatment of edentulousness. *Biomaterials* 4(1):25–28
3. Shen H, Li H, Brinson LC (2008) Effect of microstructural configurations on the mechanical responses of porous titanium: a numerical design of experiment analysis for orthopedic applications. *Mech Mater* 40(9):708–720
4. Dewidar MM, Lim JK (2008) Properties of solid core and porous surface Ti-6Al-4V implants manufactured by powder metallurgy. *J Alloys Compd* 454(1–2):442–446

5. Morra M, Cassinelli C, Cascardo G et al (2003) Surface engineering of titanium by collagen immobilization. Surface characterization and in vitro and in vivo studies. *Biomaterials* 24 (25):4639–4654
6. Rungsiyakull C, Li Q, Sun G et al (2010) Surface morphology optimization for osseointegration of coated implants. *Biomaterials* 31(27):7196–7204
7. Kunzler TP, Drobek T, Schuler M et al (2007) Systematic study of osteoblast and fibroblast response to roughness by means of surface-morphology gradients. *Biomaterials* 28 (13):2175–2182
8. Rosa AL, Crippa GE, de Oliveira PT et al (2009) Human alveolar bone cell proliferation, expression of osteoblastic phenotype, and matrix mineralization on porous titanium produced by powder metallurgy. *Clin Oral Implants Res* 20(5):472–481
9. Vaillancourt H, Pilliar RM, McCammond D (1995) Finite-element analysis of crestal bone loss around porous-coated dental implants. *J Appl Biomater* 6(4):267–282
10. Thelen S, Barthelat F, Brinson LC (2004) Mechanics considerations for microporous titanium as an orthopedic implant material. *J Biomed Mater Res A* 69A(4):601–610
11. Wen CE, Yamada Y, Shimojima K et al (2002) Processing and mechanical properties of autogenous titanium implant materials. *J Mater Sci Mater Med* 13(4):397–401
12. Esposito M, Hirsch JM, Lekholm U et al (1998) Biological factors contributing to failures of osseointegrated oral implants (I). Success criteria and epidemiology. *Eur J Oral Sci* 106 (1):527–551
13. Okazaki K, Lee WH, Kim DK et al (1991) Physical characteristics of Ti-6Al-4V implants fabricated by electrodischarge compaction. *J Biomed Mater Res* 25(12):1417–1429
14. Xue W, Krishna BV, Bandyopadhyay A et al (2007) Processing and biocompatibility evaluation of laser processed porous titanium. *Acta Biomater* 3(6):1007–1018
15. Li HL, Oppenheimer SM, Stupp SI et al (2004) Effects of pore morphology and bone ingrowth on mechanical properties of microporous titanium as an orthopaedic implant material. *Mater Trans* 45(4):1124–1131
16. Shen H, Oppenheimer SM, Dunand DC et al (2006) Numerical modeling of pore size and distribution in foamed titanium. *Mech Mater* 38(8–10):933–944
17. Mendonca G, Mendonca DBS, Aragao FJL et al (2008) Advancing dental implant surface technology – from micron- to nanotopography. *Biomaterials* 29(28):3822–3835
18. Park JY, Gemmill CH, Davies JE (2001) Platelet interactions with titanium: modulation of platelet activity by surface topography. *Biomaterials* 22(19):2671–2682
19. Bobynd JD, Pilliar RM, Cameron HU et al (1980) The optimum pore size for the fixation of porous-surfaced metal implants by the ingrowth of bone. *Clin Orthop Relat Res* 150:263–270
20. Pilliar RM (1987) Porous-surfaced metallic implants for orthopedic applications. *J Biomed Mater Res A* 21(A1):1–33
21. Chen J, Chen L, Li W et al (2013) Porous titanium implant and micro-CT based characterization of sub-surface morphology. In: *PRICM 2013*. Wiley, Hoboken, pp 1579–1586
22. Chen LJ, Li T, Li YM et al (2009) Porous titanium implants fabricated by metal injection molding. *Trans Nonferrous Metal Soc* 19(5):1174–1179
23. Xiropaidis AV, Qahash M, Lim WH et al (2005) Bone-implant contact at calcium phosphate-coated and porous titanium oxide (TiUnite (TM))-modified oral implants. *Clin Oral Implants Res* 16(5):532–539
24. Geng JP, Tan KBC, Liu GR (2001) Application of finite element analysis in implant dentistry: a review of the literature. *J Prosthet Dent* 85(6):585–598
25. Schenk RK, Buser D (1998) Osseointegration: a reality. *Periodontol* 17:22–35
26. Cochran DL (1999) A comparison of endosseous dental implant surfaces. *J Periodontol* 70 (12):1523–1539
27. Knabe C, Howlett CR, Klar F et al (2004) The effect of different titanium and hydroxyapatite-coated dental implant surfaces on phenotypic expression of human bone-derived cells. *J Biomed Mater Res A* 71A(1):98–107

28. Suzuki K, Aoki K, Ohya K (1997) Effects of surface roughness of titanium implants on bone remodeling activity of femur in rabbits. *Bone* 21(6):507–514
29. Itala AI, Ylanen HO, Ekholm C et al (2001) Pore diameter of more than 100 μm is not requisite for bone ingrowth in rabbits. *J Biomed Mater Res* 58(6):679–683
30. Bradley N (2007) The response surface methodology, in *Department of Mathematical Sciences*. Indiana University, South Bend, pp 36–38
31. Alsayyed A, Deporter DA, Pilliar RM et al (1994) Predictable crestal bone remodeling around 2 porous-coated titanium-alloy dental implant designs – a radiographic study in dogs. *Clin Oral Implants Res* 5(3):131–141
32. Anil S, Anand PS, Alghamdi H et al (2011) Chapter 4: Dental implant surface enhancement and osseointegration. In: *Turkyilmaz I (ed) Implant dentistry – a rapidly evolving practice*. InTech, Rijeka, pp 86–90
33. Deporter DA, Watson PA, Pilliar RM et al (1990) A histological comparison in the dog of porous-coated vs threaded dental implants. *J Dent Res* 69(5):1138–1145
34. Klawitter JJ, Hulbert SF (1971) Application of porous ceramics for the attachment of load bearing internal orthopedic applications. *J Biomed Mater Res* 5(6):161–229
35. Meyer U, Joos U, Mythili J et al (2004) Ultrastructural characterization of the implant/bone interface of immediately loaded dental implants. *Biomaterials* 25(10):1959–1967
36. Camron HU, Pilliar RM, Macnab I (1976) The rate of bone ingrowth into porous metal. *J Biomed Mater Res* 10(2):295–302
37. Magne P (2007) Efficient 3D finite element analysis of dental restorative procedures using micro-CT data. *Dent Mater* 23(5):539–548
38. Shen H, Brinson LC (2011) A numerical investigation of porous titanium as orthopedic implant material. *Mech Mater* 43(8):420–430
39. Lin D, Li Q, Li W et al (2010) Bone remodeling induced by dental implants of functionally graded materials. *J Biomed Mater Res B* 92B(2):430–438
40. Kim SJ, Kim MR, Rim JS et al (2010) Comparison of implant stability after different implant surface treatments in dog bone. *J Appl Oral Sci* 18(4):415–420
41. Yang J, Xiang H-J (2007) A three-dimensional finite element study on the biomechanical behavior of an FGDM dental implant in surrounding bone. *J Biomech* 40(11):2377–2385
42. Yang YZ, Tian JM, Deng L et al (2002) Morphological behavior of osteoblast-like cells on surface-modified titanium in vitro. *Biomaterials* 23(5):1383–1389
43. Yang YZ, Tian JM, Tian JT et al (2000) Preparation of graded porous titanium coatings on titanium implant materials by plasma spraying. *J Biomed Mater Res* 52(2):333–337
44. Hedia HS, Fouda N (2013) A new design of dental implant coating using functionally graded material. *Mater Testing* 55(10):765–771
45. Chen CC, Huang TH, Kao CT et al (2006) Characterization of functionally graded hydroxyapatite/titanium composite coatings plasma-sprayed on Ti alloys. *J Biomed Mater Res B* 78B(1):146–152
46. Lin D, Li Q, Li W et al (2009) Design optimization of functionally graded dental implant for bone remodeling. *Compos Part B* 40(7):668–675
47. Podshivalov L, Fischer A, Bar-Yoseph PZ (2011) 3D hierarchical geometric modeling and multiscale FE analysis as a base for individualized medical diagnosis of bone structure. *Bone* 48(4):693–703
48. Podshivalov L, Fischer A, Bar-Yoseph PZ (2011) Multiscale FE method for analysis of bone micro-structures. *J Mech Behav Biomed* 4(6):888–899
49. Fritsch A, Hellmich C, Dormieux L (2009) Ductile sliding between mineral crystals followed by rupture of collagen crosslinks: experimentally supported micromechanical explanation of bone strength. *J Theor Biol* 260(2):230–252
50. Buti F, Cacciagrano D, Corradini F et al (2010) Bone remodelling in BioShape. *Electron Notes Theor Comput Sci* 268:17–29
51. Chen J, Rungsiyakull C, Li W et al (2013) Multiscale design of surface morphological gradient for osseointegration. *J Mech Behav Biomed* 20:387–397

52. Romeed SA, Fok SL, Wilson NHF (2006) A comparison of 2D and 3D finite element analysis of a restored tooth. *J Oral Rehabil* 33(3):209–215
53. Lin D, Li Q, Li W et al (2010) Mandibular bone remodeling induced by dental implant. *J Biomech* 43(2):287–293
54. Lin D, Li Q, Li W et al (2009) Dental implant induced bone remodeling and associated algorithms. *J Mech Behav Biomed* 2(5):410–432
55. Field C, Li Q, Li W et al (2010) Prediction of mandibular bone remodelling induced by fixed partial dentures. *J Biomech* 43(9):1771–1779
56. Field C, Li Q, Li W et al (2012) A comparative mechanical and bone remodelling study of all-ceramic posterior inlay and onlay fixed partial dentures. *J Dent* 40(1):48–56
57. Traini T, Mangano C, Sammons RL et al (2008) Direct laser metal sintering as a new approach to fabrication of an isoelastic functionally graded material for manufacture of porous titanium dental implants. *Dent Mater* 24(11):1525–1533
58. Li W, Swain MV, Li Q et al (2005) Towards automated 3D finite element modeling of direct fiber reinforced composite dental bridge. *J Biomed Mater Res B* 74B(1):520–528
59. Li W, Swain MV, Li Q et al (2004) Fibre reinforced composite dental bridge. Part II: numerical investigation. *Biomaterials* 25(20):4995–5001
60. Chen J, Li W, Swain MV et al (2014) A periodontal ligament driven remodeling algorithm for orthodontic tooth movement. *J Biomech* 47(7):1689–1695
61. Li W, Lin D, Chen J et al (2014) Role of mechanical stimuli in oral implantation. *J Biosci Med* 2:63–68
62. Li W, Rungsiyakull C, Field C et al (2010) Computational biomechanics of bone's responses to dental prostheses – osseointegration, remodeling and resorption. In: Khalili N et al (eds) 9th world congress on computational mechanics and 4th Asian Pacific congress on computational mechanics. IOP Publishing, Sydney. doi:[10.1088/1757-899X/10/1/012122](https://doi.org/10.1088/1757-899X/10/1/012122)
63. Rungsiyakull C, Chen J, Rungsiyakull P et al (2014) Bone's responses to different designs of implant-supported fixed partial dentures. *Biomech Model Mechanobiol* 14(2):403–411
64. Ahmad R, Chen J, Abu-Hassan MI et al (2015) Investigation of mucosa-induced residual ridge resorption under implant-retained overdentures and complete dentures in the mandible. *Int J Oral Maxillofac Implants* 30(3):657–666
65. Chen J, Ahmad R, Suenaga H et al (2015) A comparative study on complete and implant retained denture treatments – a biomechanics perspective. *J Biomech* 48(3):512–519
66. Suenaga H, Chen J, Yamaguchi K et al (2015) Mechanobiological bone reaction quantified by positron emission tomography. *J Dent Res* 94(5):738–744
67. Li J, Li H, Shi L et al (2007) A mathematical model for simulating the bone remodeling process under mechanical stimulus. *Dent Mater* 23(9):1073–1078
68. Rungsiyakull C, Li Q, Li W et al (2008) Effect of particle size of Fully Porous-Coated (FPC) implants on osseointegration. *Adv Mat Res* 47–50:916–919
69. O'Brien WJ (2008) Dental materials and their selection. Quintessence Pub. Co., Hanover Park
70. Carr ME, Carr SL (1995) Fibrin structure and concentration alter clot elastic-modulus but do not alter platelet-mediated force development. *Blood Coagul Fibrinolysis* 6(1):79–86
71. Riha P, Wang X, Liao R et al (1999) Elasticity and fracture strain of whole blood clots. *Clin Hemorheol Microcirc* 21(1):45–49
72. Liu XY, Niebur GL (2008) Bone ingrowth into a porous coated implant predicted by a mechano-regulatory tissue differentiation algorithm. *Biomech Model Mechanobiol* 7(4):335–344
73. Isaksson H, van Donkelaar CC, Ito K (2009) Sensitivity of tissue differentiation and bone healing predictions to tissue properties. *J Biomech* 42(5):555–564
74. Keaveny TM (2001) Strength of trabecular bone. In: Cowin SC (ed) *Bone mechanics handbook*. CRC Press LLC, Danvers, p 7
75. Frost HM (2003) Bone's mechanostat: a 2003 update. *Anat Rec A: Discov Mol Cell Evol Biol* 275A(2):1081–1101

76. Weinans H, Huiskes R, Grootenboer HJ (1992) The behavior of adaptive bone-remodeling simulation models. *J Biomech* 25(12):1425–1441
77. Frost HM (1964) *The laws of bone structure*. C.C. Thomas, Springfield
78. Carter DR (1984) Mechanical loading histories and cortical bone remodeling. *Calcif Tissue Int* 36:S19–S24
79. Huiskes R, Weinans H, Grootenboer HJ et al (1987) Adaptive bone-remodeling theory applied to prosthetic-design analysis. *J Biomech* 20(11–12):1135–1150
80. Weinans H, Huiskes R, Grootenboer HJ (1992) Effects of material properties of femoral hip components on bone remodeling. *J Orthop Res* 10(6):845–853
81. Noble BS, Reeve J (2000) Osteocyte function, osteocyte death and bone fracture resistance. *Mol Cell Endocrinol* 159(1–2):7–13
82. Wernig F, Xu Q (2000) Mechanical stress-induced apoptosis in the cardiovascular system. *Prog Biophys Mol Biol* 78(2–3):105–137
83. Xie M, Yang SH, Win HL et al (2010) Rabbit annulus fibrosus cell apoptosis induced by mechanical overload via a mitochondrial apoptotic pathway. *J Huazhong Uni Sci Tech Med* 30(3):379–384
84. Tanaka E, Yamamoto S, Nishida T et al (1999) A mathematical model of bone remodelling under overload and its application to evaluation of bone resorption around dental implants. *Acta Bioeng Biomech* 1(1):117–121
85. Rho JY, Hobatho MC, Ashman RB (1995) Relations of mechanical-properties to density and Ct numbers in human bone. *Med Eng Phys* 17(5):347–355
86. O’Mahony AM, Williams JL, Katz JO et al (2000) Anisotropic elastic properties of cancellous bone from a human edentulous mandible. *Clin Oral Implants Res* 11(5):415–421
87. Shen H, Brinson LC (2007) Finite element modeling of porous titanium. *Int J Solids Struct* 44(1):320–335
88. Sollazzo V, Pezzetti F, Scarano A et al (2008) Zirconium oxide coating improves implant osseointegration in vivo. *Dent Mater* 24(3):357–361
89. Abron A, Hopfensperger M, Thompson J et al (2001) Evaluation of a predictive model for implant surface topography effects on early osseointegration in the rat tibia model. *J Prosthet Dent* 85(1):40–46
90. Anderson RC, Cook SD, Weinstein AM et al (1984) An evaluation of skeletal attachment to LTI pyrolytic carbon, porous titanium, and carbon-coated porous titanium implants. *Clin Orthop Relat Res* 182:242–257
91. Feighan JE, Goldberg VM, Davy D et al (1995) The influence of surface-blasting on the incorporation of titanium-alloy implants in a rabbit intramedullary model. *J Bone Joint Surg Am* 77(9):1380–1395
92. Hou SJ, Li Q, Long SY et al (2008) Multiobjective optimization of multi-cell sections for the crashworthiness design. *Int J Impact Eng* 35(11):1355–1367
93. Hou S, Li Q, Long S et al (2007) Design optimization of regular hexagonal thin-walled columns with crashworthiness criteria. *Finite Elem Anal Des* 43(6–7):555–565
94. Athan TW, Papalambros PY (1996) A note on weighted criteria methods for compromise solutions in multi-objective optimization. *Eng Optimiz* 27(2):155–176
95. Coello CA, Lechuga MS (2002) MOPSO: a proposal for multiple objective particle swarm optimization. In: *Proceedings of evolutionary computation 2002*. Honolulu, p 1051–1056.
96. Raquel CR, Naval PCJ (2005) An effective use of crowding distance in multiobjective particle swarm optimization. In: *Proceedings of the 2005 conference on genetic and evolutionary computation 2005*. ACM, Washington, DC, pp 257–264
97. O’Mahony AM, Williams JL, Spencer P (2001) Anisotropic elasticity of cortical and cancellous bone in the posterior mandible increases peri-implant stress and strain under oblique loading. *Clin Oral Implants Res* 12(6):648–657
98. Tomaszewski PK, van Diest M, Bulstra SK et al (2012) Numerical analysis of an osseointegrated prosthesis fixation with reduced bone failure risk and periprosthetic bone loss. *J Biomech* 45(11):1875–1880

99. Sturm S, Zhou S, Mai Y-W et al (2010) On stiffness of scaffolds for bone tissue engineering-a numerical study. *J Biomech* 43(9):1738–1744
100. Chen Y, Zhou S, Li Q (2009) Computational design for multifunctional microstructural composites. *Int J Mod Phys B* 23(6–7):1345–1351
101. Adachi T, Osako Y, Tanaka M et al (2006) Framework for optimal design of porous scaffold microstructure by computational simulation of bone regeneration. *Biomaterials* 27 (21):3964–3972
102. Chen Y, Zhou S, Li Q (2011) Microstructure design of biodegradable scaffold and its effect on tissue regeneration. *Biomaterials* 32(22):5003–5014
103. Arabnejad Khanoki S, Pasini D (2012) Multiscale design and multiobjective optimization of orthopedic hip implants with functionally graded cellular material. *J Biomech Eng* 134 (3):031004

Chapter 4

Implant Surface Modifications and Osseointegration

Nishant Chakravorty, Anjali Jaiprakash, Saso Ivanovski, and Yin Xiao

Abstract Osseointegration and osteogenic differentiation are important determinants of clinical outcomes involving implants in orthopaedics and dentistry. Implant surface microstructure and hydrophilicity are known to influence these properties. Recent research has focused on several modifications of surface topography and chemistry aimed at improving bone formation to achieve faster and better healing. Topographically modified titanium implant surfaces, like the sandblasted, large-grit, acid-etched (SLA) surface and chemically modified hydrophilic SLA (modSLA) surface, have shown promising results when compared with smooth/polished titanium surfaces. Although most studies consider an average roughness (Ra) of 1–1.5 μm to be favourable for bone formation, there is no consensus regarding the appropriate roughness and chemical modifications necessary to achieve optimal osseointegration. Studies on microstructurally modified surfaces have revealed intricate details pertaining to the molecular interactions of osteogenic cells with implant surfaces. The *in vivo* and *in vitro* findings from these studies highlight the ability of modified titanium surfaces to support the establishment of a native osteogenic niche for promoting bone formation on the implant surfaces. Improved osteogenic properties of modified surfaces are evidenced *in vitro* by the differential regulation of the molecular transcriptome on such surfaces. Recent studies indicate that post-transcriptional modulators like microRNAs also play an important role in osteogenic regulation on implant surfaces. In this chapter, we discuss the current concepts and considerations in orthopaedic and dental implant research and the new knowledge in the field, which will assist in the development of novel approaches and designs of future implant devices.

Keywords Implants • Osseointegration • Surface modification • Surface topography • Cell signaling • Osteogenic differentiation • Molecular regulation

N. Chakravorty • A. Jaiprakash • Y. Xiao (✉)
Institute of Health & Biomedical Innovation, Queensland University of Technology, 60 Musk Avenue, Kelvin Grove, Brisbane, QLD 4059, Australia
e-mail: yin.xiao@qut.edu.au

S. Ivanovski
School of Dentistry and Oral Health, Griffith Health Institute, Griffith University, Gold Coast, QLD, Australia

4.1 Introduction

Orthopaedic and dental implants have become important treatment options for replacement and restoration of missing/damaged parts of bones and teeth. The science of orthopaedic and dental implants has come a long way since its beginning which possibly dates back to around 600 AD when the Mayan civilisation started using seashells and stones as endo-osseous implants. Implant structures and surfaces have subsequently undergone a multitude of modifications. The quest for superior clinical outcomes has led researchers to a continually evolving search for the ideal implantation material. The choice of materials to be used as implants depends on several properties, such as mechanical stability, elasticity, biocompatibility, hydrophilicity, corrosivity, etc. Several materials have been used as implants for the human body. The ready availability and established processing methods initially made stainless steel a popular material for orthopaedic implants. The progressive search for improved implants led to the use of alloys made out of iron and other metals like nickel, cobalt and molybdenum. Titanium with its significant potential to support bone regeneration with little evidence of rejection has been the material of choice clinically for a long time now.

The primary aim of implant research is to create materials with functional designs that serve the purpose of achieving structural and functional restoration of a body part, and in the context of bone integration, we need to understand the phenomenon known as osseointegration. The term ‘osseointegration’ was coined by the Swedish orthopaedic surgeon Per-Ingvar Brånemark in the 1950s, when he observed difficulty in the removal of titanium chambers implanted in animals for vital microscopic studies [1]. Osseointegration may be defined as the structural and functional amalgamation of the load-bearing surface of an implant with the surrounding bone tissue. Osseointegration is a biological process guided by a highly regulated cascade of molecular steps that lead to osteogenic differentiation and new bone formation on the implant surfaces. Several research studies have emphasised the importance of surface topography on the bone-to-implant contact [2–6]. The present chapter discusses the current knowledge and concepts pertaining to the surface topography of implants, with a focus on modified titanium implant surfaces as a model to understand the mechanisms of osteogenic differentiation and osseointegration.

4.2 Discovery of Osseointegration

A chapter on osseointegration without a tribute to Professor Per-Ingvar Brånemark and his pioneering work with the implant material titanium would be an injustice to the topic itself. Titanium was first identified as an element in 1791 by Revd. William Gregor when he was examining samples of black sands sent to him from the valley of Manaccan located in the Lizard peninsula, Cornwall, in England

[7]. Based on his experiments, Gregor was able to identify an unknown metallic substance in the samples; however, he was unable to reduce it to its metallic form. He had originally named it as ‘manaccanite’ after the region from where he had identified the element. Later in 1795, Martin Heinrich Klaproth from Germany isolated a metal from an abundant ore called ‘rutile’ and named this metal as ‘titanium’. Klaproth also analysed the new element Gregor had identified and found it to be the same as titanium and recognised Gregor as the scientist who discovered the new metal. Subsequently, scientists realised the properties and significance of this material, and it is now widely utilised in various areas like aircrafts, naval ships, spacecrafts, missiles, jewellery, etc.

After one-and-a-half century of the discovery of titanium, its importance as an implant material was discovered by Professor Per-Ingvar Brånemark. During the 1950s and 1960s, Brånemark was studying the formation of blood vessels in the bone marrow using *in vivo* models. Micro-optical devices enveloped in titanium cases were incorporated into tissues to observe the human microcirculation. He subsequently observed extreme difficulty in removal of these devices. These were the initial observations that led to the discovery of the phenomenon of osseointegration. A modified experimental setup for the rabbit ear chamber was subsequently conducted, whereby a titanium implant with a central canal and a transverse opening was placed into the bone to enable the bone and blood vessels to grow into the chamber [1]. These observations led to the findings that the integration of titanium with live tissue could enable a prolonged fixation of dental prostheses and eventually unfolded the path to the unanimous clinical success of titanium for dental implants and reconstructive surgeries.

On 9 April 2002 the International Society of Osseointegration and the Associated Brånemark Osseointegration Centers (ABOC) visited Manaccan and unveiled a plaque made of titanium commemorating the discovery of titanium and recognising the scientific achievements of the two great scientists – Revd. William Gregor and Professor Per-Ingvar Brånemark.

4.3 Titanium and Its Modifications

Titanium is the 22nd element in the periodic table and has an atomic mass of 47.867 and its symbol is Ti (Fig. 4.1). It is classified in group 4 (transition elements) of the periodic table along with zirconium, hafnium and rutherfordium. The element is strong and lustrous with a metallic silver shade. It is usually found in the form of its ores: rutile (TiO_2), anatase (TiO_2) and ilmenite (Fe, TiO_3). Ilmenite is the most abundant form of titanium. Four grades of commercially pure titanium and two alloys of titanium are recognised by the American Society for Testing and Materials (ASTM) Committee F04 on Materials for Surgical Implants. Commercially pure titanium is graded as between I and IV; and the ASTM recognised that titanium alloys are Ti-6Al-4 V and Ti-6Al-4 V extra low interstitial (ELI) [8]. Essential

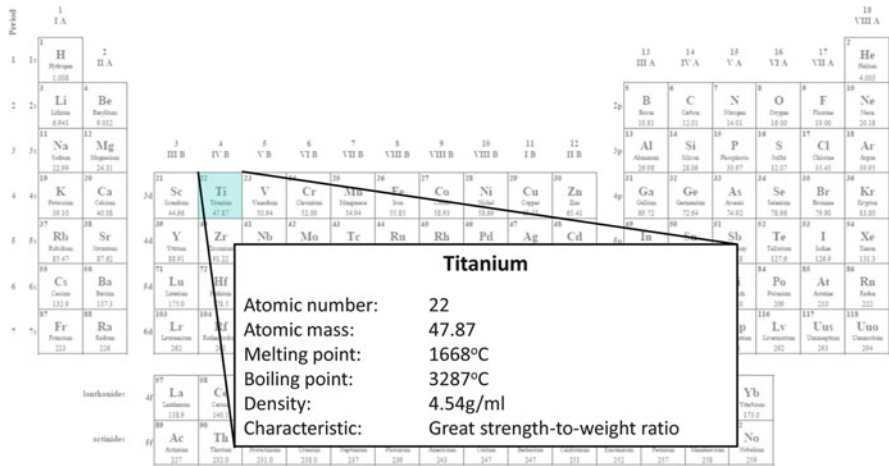


Fig. 4.1 Titanium – the element of choice for orthopaedic and dental implants

qualities that make titanium a highly compatible material in the field of implantology include:

1. High strength-to-weight ratio – titanium is 60 % the density of steel but has tensile strengths reaching as high as 63,000 psi (434.4 MPa).
2. High melting point (1668 °C) – commercial titanium alloys have the capability of safely withstanding temperatures of up to 600 °C.
3. Resistance to corrosion – usually due to the formation of a titanium dioxide layer on the surface.
4. Ability to be passivated and therefore be resistant to corrosion with acids.
5. Inert to body fluids.
6. Relatively low modulus of elasticity akin to human bone.
7. Ability to osseointegrate.

Titanium has certain shortcomings like low resistance to wear and notch sensitivity. However, its advantages outweigh the disadvantages, and therefore it is considered one of the most suitable elements for implants.

4.3.1 Surface Modifications

Implant research has focused on technologies to improve osteoinduction (ability to induce differentiation of undifferentiated cells towards osteogenic lineage), osteoconduction (allowing growth of bone on the surface of the implant) and osseointegration [9]. Surface modification techniques have been an integral part of implant research. Implant surface quality has been considered one of the most important factors implicated in successful osseointegration [3]. The most common

parameters used in describing surface roughness are R_a , R_q , R_z and R_t (in - two-dimensional) and their three-dimensional counterparts: S_a , S_q , S_z and S_t .

R_a/S_a Arithmetic mean deviation (average roughness) of the roughness profile (R_a) or of a surface (S_a in 3D)

R_q/S_q Root mean square deviation of profile (R_q) or of a surface (S_q in 3D)

R_z/S_z Arithmetic mean deviation of the sum total of 10 (5 of the lowest peaks and 5 of the highest peaks) of the profile (R_z) or the surface (S_z)

Several different methods are employed to alter surface topographies. Some of the most common techniques include polishing, surface blasting, plasma spraying, anodic oxidation, etching and chemical coatings. A brief description of some of the most commonly employed techniques for modifying surfaces is outlined below.

4.3.1.1 Topographical Modifications

Polishing Polishing is a technique used to smoothen implant surfaces. The most common method of polishing is machining. Electropolishing is another technique often utilised to prepare polished surfaces, whereby metal is electrochemically removed by oxidation and subsequent dissolution into the electrolyte. Polished surfaces usually have an average roughness measuring $<0.5 \mu\text{m}$. Turning and milling are other techniques employed to modify surfaces, which would result in regular grooves on the implant surfaces and are known as ‘minimally rough’ surfaces.

Blasting Blasting is an abrasive technique usually employed to roughen a smooth or polished surface. The most common method of blasting surfaces is known as ‘sandblasting’ which is usually a dry process of thrusting a jet of abrasive media like alumina, corundum, crushed glass, silica and steel grit on to the surface at accelerated velocity. Blasting surfaces with alumina particles of 25–75 μm have been shown to create isotropic surface modifications with R_a/S_a around 1.1–1.5 μm in contrast to blasting with 250- μm particles that creates anisotropic surfaces with deviation around 2 μm [10]. Blasted surfaces have been observed to have improved cellular adhesion and osteoblastic differentiation [11]. Proper cleaning of blasted surfaces after the process is essential as retained particles of blasting materials like alumina can impair bone formation [12].

Etching	Etching is a subtractive process using strong acids or alkalis capable of eroding the surface of implants to create roughened surfaces. Hydrochloric acid, hydrofluoric acid and sulphuric acid are the most commonly used acids for etching implant surfaces. A mixture of acids is also used often to erode surfaces to make them more conducive for bone formation. Alkaline etching is commonly performed using sodium hydroxide solutions. Varying the concentration of the acid/alkali in use, time of exposure and temperature are important considerations during the process of etching.
Oxidation	Oxidation is the technique of chemically converting the titanium surface into an oxide layer, thereby increasing the surface titanium dioxide coating. This has been observed to impart improved biocompatibility to the implant surface. An oxide layer is allowed to deposit on the titanium surface placed at the anode, and this leads to a thicker layer of titanium oxide on the surface.
Bioactive coating	Several bioactive coating methods have been attempted on titanium surfaces to improve the efficacy of implants. The key property that makes bioactive coating technique an attractive modification option is their ability to exert a particular response in the biological system. The most common coatings on titanium surfaces include hydroxyapatite, calcium phosphate, bone morphogenetic proteins and collagen. Hydroxyapatite coating is a very commonly used method owing to its excellent biocompatibility and ability to bond with the surrounding bone.
Titanium plasma spraying	Plasma spraying technology is a ‘non-bioactive’ coating technique used to create porous titanium surfaces that can favour ingrowth of bone. A jet of molten titanium is sprayed on to the implant surface during the process of titanium plasma spraying (TPS). TPS is an additive procedure that imparts a roughened surface architecture. TPS implants have been observed to have variable R_a , and some studies have reported improved osseointegration of TPS compared to smooth surfaces [13]. Plasma spraying technique is also used to create hydroxyapatite coatings. Although plasma spraying is an established method, controlling the variables involved in the process is quite complicated, and small variations may lead to completely different properties than expected. There are several other techniques of coating implant surfaces like sputter coating, pulsed laser deposition, dip coating, electrophoretic deposition and thermal spraying. Deposition

techniques have an inherent drawback that they take a long time.

Laser ablation Laser ablation is a subtractive technique commonly used to create microstructures with improved physical properties like toughness, rigidity and corrosion resistance. This technique has the ability to generate nanostructures on the titanium surfaces [14].

4.3.1.2 Physicochemical Modifications

Physicochemical modifications involve changing the surface free energy, surface charge and hydrophilicity. Studies have revealed improved osseointegration and bone formation on hydrophilic surfaces [15–18]. Certain topographical modifications of surfaces also impart changes in surface charge. Sandblasting techniques have been shown to create a negative surface charge. A negative surface charge is known to improve cellular attachment [19]. Modifications of surface energy have been showing to increase the hydrophilicity and thereby help adsorption of proteins necessary for cellular growth and development [20]. Titanium is highly reactive to fluoride ions. Fluoride-treated titanium surfaces have been found to enhance osteoblastic differentiation [21].

Several combinations of these techniques have been used in the field of implantology to achieve better clinical outcomes and success. Sandblasting and acid-etching techniques have been commonly used to modify dental implants with improved clinical success. Recent research has further focused on combining the topographical methods with the physicochemical modifications leading to the development of topographically and chemically modified titanium implant surfaces like the modSLA surface.

4.3.2 Micro-roughened Surfaces

Wennerberg et al. [22–24] classified implant surfaces based on their surface topography into the following subtypes:

1. Smooth ($<0.5 \mu\text{m}$)
2. Minimally rough ($0.5\text{--}1 \mu\text{m}$)
3. Intermediately rough ($1\text{--}2 \mu\text{m}$)
4. Rough ($2\text{--}3 \mu\text{m}$)

There has been a consensus among majority of the scientific reports that suggest improved bone-to-implant contacts with higher surface roughness (micro-roughness). Wennerberg and Albrektsson's suggested guidelines for evaluation of implant surfaces based on topography [25] advocated that the positive correlation of surface roughness with bone formation works in a particular range: R_a/S_a value from 1 to $1.5 \mu\text{m}$. However, Shalabi et al.'s systematic review on surface roughness

and healing of the bone in 2006 [26] did not substantiate this. Their assessment of the literature on implant fixation/bone formation and surface roughness revealed a positive correlation between bone formation and surface roughness of implants from R_a/S_a 0.5 μm to 8.5 μm . Machined and polished titanium implant surfaces are usually used as control surfaces to test the efficacy of modified surfaces in terms of osseointegration and other improved functionalities.

Recent reports have also demonstrated the importance of nanoscale roughness to improve bone-forming properties. Newer modifications have also focused on modulating the surface free energy to enhance the wettability and hydrophilicity. Improving surface hydrophilicity has been demonstrated to increase osteogenic differentiation in vitro and osseointegration in vivo [18, 20, 27, 28]. Newer advances in implant surface technology have enabled researchers to incorporate nanostructural modifications to implant surfaces. ‘Nano’ modifications are conventionally defined as alterations in the range of 1–100 nm. Topographical manipulations in the nanoscale have been found to have a positive influence on the phenomenon of osseointegration and osteogenic differentiation [29].

The implication of topographical and chemical modification of titanium implants on clinical outcomes is documented by the success of micro-roughened dental implants like sandblasted, large-grit and acid-etched (SLA) surface and its successor the chemically modified hydrophilic modSLA surfaces. Both SLA and modSLA surfaces are micro-roughened surface, and the SLA surface has largely been considered the gold standard in implant dentistry. Recent studies have demonstrated the presence of nanoparticles on the modSLA surfaces [30–32]. Studies on the various implant surface modifications have enabled us to begin to unravel the molecular mechanisms of osseointegration.

4.3.3 Properties of Topographically Modified Implant Surfaces

Osseointegration is a biological phenomenon that involves the interaction of osteoblastic cells with their microenvironment. The biological response that takes place at the interface between implant surfaces and osteogenic cells is the key to the phenomenon of osseointegration. It is important to understand the physiology of the cellular response to implant surfaces, especially in light of the properties conferred on to the newer implant surfaces by virtue of their modifications. The native niche of osteoblastic cells is interspersed with proteins and structural elements at the micro- and nanoscale. Therefore modifying implant surfaces topographically (at the micro- and nanoscale) results in structural features that influence cells to directly interact with such surfaces. Micro- and nanoscale roughness allows surfaces to have an increased surface area, which allows such surfaces to adhere greater amounts of proteins and mediators necessary for growth and differentiation. Hydrophilic surfaces have the capability to attract and retain proteins necessary for growth and

differentiation of cells. Cells differentiating towards an osteoblastic lineage have been observed to show higher expression of integrins and focal adhesion proteins on micro-roughened titanium surfaces, when compared to smooth surfaces [33].

4.3.4 The SLA and modSLA Titanium Surfaces

The sandblasted, large-grit and acid-etched (SLA) titanium and its successor, the chemically modified hydrophilic modSLA surfaces, designed by Institut Straumann AG (Waldenburg, Switzerland) are micro-roughened titanium implant surfaces known to have improved osseointegrative and osteoconductive properties compared to their smooth-surfaced counterparts. These surfaces have proven to be remarkable features for investigating and elucidating the mechanisms of osteogenic differentiation *in vitro* and osseointegration *in vivo*. A brief discussion about the method of preparation of these surfaces and their physical and chemical characteristics is worth detailing in this section of the chapter.

4.3.4.1 Method of Fabrication

The acronym 'SLA' was first used by Buser et al. in their 1991 publication [2] where they demonstrated higher bone-to-implant contact on titanium implant surfaces prepared by sandblasting using large-grit particles and etching using hydrochloric and sulphuric acid. The modSLA surface (commercially known as SLActive surface, Fig. 4.2a) was described for the first time by Buser et al. in 2004 [34], where they demonstrated increased bone apposition to modSLA surfaces compared to the SLA surfaces. The modSLA surface is essentially a physicochemically modified version of the SLA surface (Fig. 4.2b) that allows maintenance of the initial hydrophilicity of microstructured titanium surfaces after their fabrication. Both the SLA and modSLA surfaces are commercially produced by Institut Straumann (Basel, Switzerland) and have achieved the status of industry standards, with many other companies in the field of implant dentistry adopting the methods to fabricate surfaces similar to SLA and modSLA.

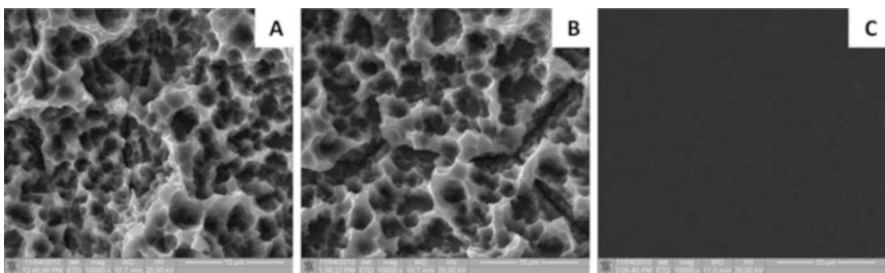


Fig. 4.2 Scanning electron microscope (SEM) images of (a) modSLA, (b) SLA and (c) smooth (SMO) titanium surfaces (10,000 \times magnification)

The SLA surface is achieved by sandblasting grade II commercially pure titanium surfaces using 250–500- μm large-grit corundum (crystalline form of Al_2O_3) and subsequently acid etching using a hot solution of hydrochloric and sulphuric acids, thereby combining the principles of blasting and acid etching. This technique gives rise to a micro-roughened topography of the titanium surface. Titanium, on exposure to air, gets converted to titanium dioxide (TiO_2) which in turn may get hydroxylated upon exposure to water. Variations in net charges may lead to ionic interactions on the surface, and exposure to air may also lead to contamination of the TiO_2 , which may collectively lead to decrease in the initial hydrophilicity developed after the topographical modification [20].

The modSLA surface was introduced as a successor to the SLA surface, wherein a chemical modification was introduced to the SLA surface immediately post-production, so that the hydrophilicity generated can be maintained. Baier and Meyer's publication in 1988 on the future directions of implant surface preparations discussed the importance of surface cleaning methods on the retention of high surface energy [35]. A similar concept was employed in the creation of the modSLA titanium implant surfaces. The surfaces are produced in the same way as the SLA surface using sandblasting and acid-etching technique. Immediately after generation of the surface, they are rinsed in a nitrogen-protected environment and then stored in an isotonic sodium chloride solution in a nitrogen environment [20]. This has been observed to retain the hydrophilic properties of the surface.

4.3.4.2 Characteristic Features of modSLA and SLA Surfaces

As a result of their proven superior osseointegration properties, the modSLA and SLA surfaces have been the subject of extensive investigation. They provide us with a suitable model to study the molecular mechanisms of osteogenic differentiation and osseointegration in an *in vitro* setting. The essential attribute that makes these surfaces suitable for studying molecular interactions lies in the fact that they do not provoke any chemical interactions with cells and therefore provide us with physiologically relevant models to study the intricate mechanisms of osteoblastic differentiation.

Topographical features of the modSLA and SLA surfaces appear similar, when observed using conventional scanning electron microscope (SEM) and atomic force microscopy (AFM). Both the surfaces are observed to have micro-roughness with S_a values varying between $1.15 \pm 0.05 \mu\text{m}$ for SLA and $1.16 \pm 0.04 \mu\text{m}$ for modSLA [20]. The roughness values observed in different studies seem to vary slightly, e.g. Vlacic et al. have described an S_a value of $1.8 \mu\text{m}$ [36], whereas Olivares-Navarrete et al.'s study demonstrated R_a to be around $3.22 \mu\text{m}$ [37]. Using AFM, we observed RMS roughness values in the range of 1.6 – $2.1 \mu\text{m}$ for the modSLA and SLA surfaces, in contrast to mirror-finished polished titanium surfaces that showed RMS values in the range 0.006 – $0.009 \mu\text{m}$ [38].

The roughness features of modSLA and SLA surfaces are not seen to be distributed evenly throughout the surfaces and therefore seem to indicate that

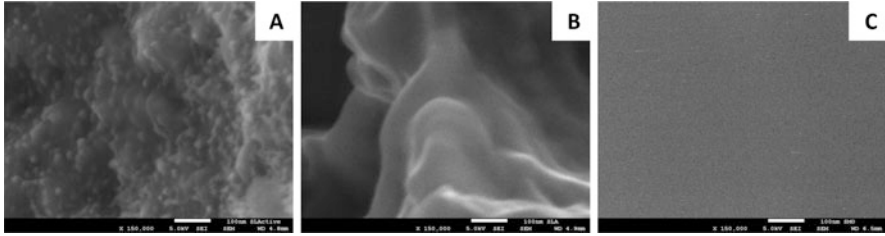


Fig. 4.3 High-resolution SEM images of (a) modSLA, (b) SLA and (c) smooth (SMO) titanium surfaces depicting the presence of nanostructures only on the modSLA surface (150,000× magnification)

uniformity in the topographical pattern is not a prerequisite for improved osseointegration and osteodifferentiation on implant surfaces. Recent studies using high-resolution SEM imaging techniques have observed the presence of nanostructures interspersed on the micro-roughened modSLA surface [30, 31, 39]. We also have observed similar nanostructures on the modSLA surfaces using high-resolution SEM imaging (Fig. 4.3) which corroborates with others. Chemical analysis using X-ray photoelectron spectroscopy (XPS) has confirmed that these nanostructures are not the result of crystallisation of sodium chloride present in the isotonic solution used to store the modSLA surfaces [31]. Wennerberg et al. further observed the formation of similar nanostructures when freshly prepared sandblasted and acid-etched titanium surfaces were stored in water (instead of isotonic saline solution) [31]. The impact of these nanostructures on the superior clinical outcomes of modSLA surfaces has not been established as yet.

Chemical analyses of the modSLA and SLA surfaces have demonstrated titanium, oxygen, nitrogen and carbon as the key elements present [40]. Traces of sodium and chlorine have also been observed in modSLA surfaces in some studies [28, 41] which could be a result of storing them in saline solution. The modSLA surface has a contact angle close to 0° , which exemplifies its extraordinary hydrophilic nature.

4.4 Biology of Healing on Implant Surfaces

Bone formation and healing on implant surfaces are multifaceted processes involving several factors and considerations. Several factors contribute towards successful osseointegration and bone formation on implant surfaces. Some of the key factors that play an important role in this process are summarised in Table 4.1

Insertion of any implant into the human body is akin to any other wound healing process. Bone healing starts immediately after an implant is inserted into the human body. The first tissue to come in contact with the implant surface is blood and its components. The large accessible surface area provided by micro-roughened implant surfaces allows for greater adsorption of proteins. Hydrophilic implant

Table 4.1 Key factors important for the process of osseointegration

Factors influencing osseointegration
Material biocompatibility
Implant shape and design
Surface characteristics – roughness, hydrophilicity, surface energy
Age of the patient
Pre-existing conditions – systemic diseases like diabetes, cancer, immunosuppressive conditions, hypersensitive conditions, infections, bone diseases like osteoporosis, osteomalacia, Paget's disease, etc.
Condition of the implant bed – poor bone quality, presence of debris, local infection, etc.
Surgical technique – minimal tissue damage is favourable for osseointegration
Relative mobility of implant – higher degree of movement of implant in the initial stages of healing inhibits osseointegration
Timing of loading

surfaces further improve the process of protein adsorption. The contact of blood with implants gives rise to a cascade of reactions involving coagulation, inflammation, release of chemoattractants and eventually recruitment, proliferation and differentiation of mesenchymal stem cell and pre-osteoblasts.

Coagulation of blood on the implant surface leads to the conversion of fibrinogen to fibrin. Fibrin forms a mesh-like scaffold on the implant surface that can retain other proteins and mediators to allow for appropriate progression of the healing process. Platelet activation and release of proteins like adenosine diphosphate (ADP), platelet-derived growth factor (PDGF), histamines, platelet factor 4 and transforming growth factor- β (TGF- β) and serotonin are important steps in the process of implant healing and osseointegration. The aggregation of platelets is instrumental in clot formation and eventually in the formation of the fibrin mesh network. Activated platelets have von Willebrand factor (VWF) and glycoprotein IIb/IIIa (GP IIb/IIIa) receptors on their surface. Fibrinogen binds to the GP IIb/IIIa receptors, leading to platelet aggregation. The process of activation of thrombin from prothrombin is catalysed by activated platelets. Thrombin in turn helps in the stabilisation of the fibrin network and therefore the platelet plug [42] (Fig. 4.4).

Leucocytes are next in line in the inflammatory response that happens upon the insertion of any implant. Neutrophils are the first white blood cells (WBCs) that are recruited to the site within 24–48 h. After this duration, monocytes and macrophages become the dominant cells at the implant site. Activation of leucocytes leads to release of inflammatory mediators that include cytokines like interleukin (IL)-1, IL-6, IL-8 and tumour necrosis factor (TNF)- α .

The extent and duration of the inflammatory response to any biomaterial define the biocompatibility of the material [43]. Inflammation is essentially a biological response to any injury to the body, and it may progress through the phases of acute inflammation, chronic inflammation and granulation tissue formation.

In cases of biocompatible materials, the acute inflammatory process eventually evolves into the bone formation phase of the wound healing and thereby integration of the implant material. Persistence of any inflammatory stimulus may lead to a

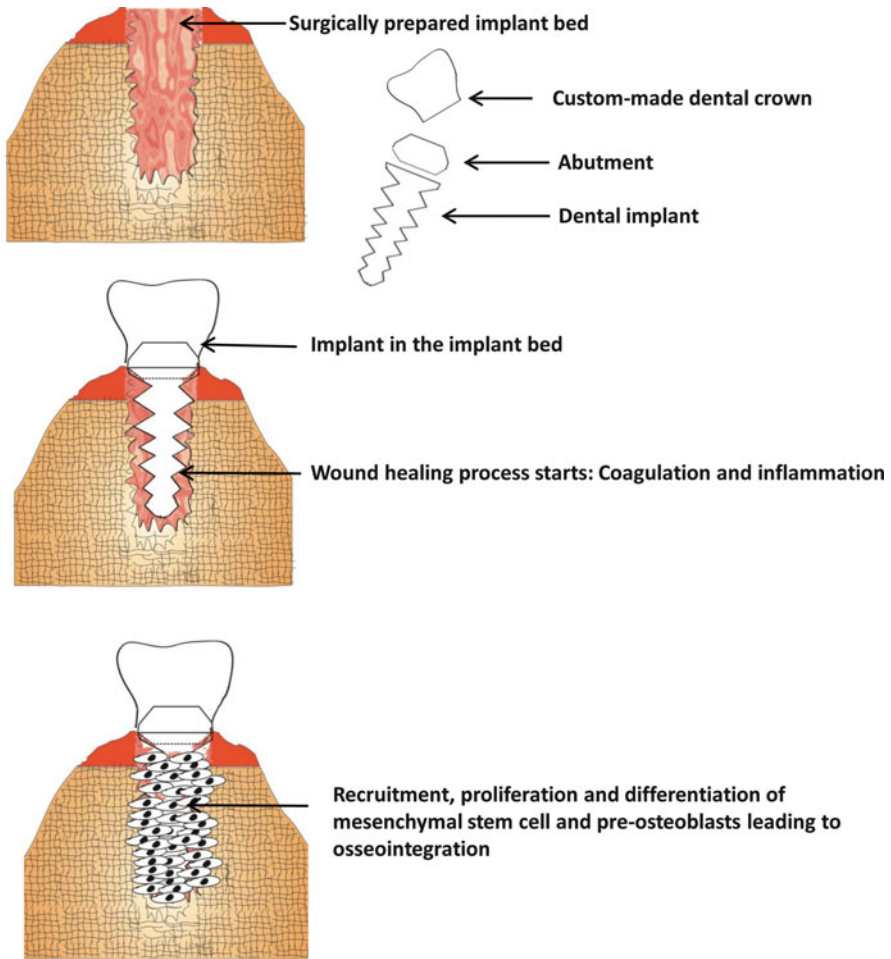


Fig. 4.4 The biology of implant healing process and osseointegration

chronic inflammatory response. The post-implantation inflammatory response may keep progressing depending on the properties of the material and may lead to a chronic inflammatory condition. The fundamental cells determining the nature of the inflammatory response are macrophages, lymphocytes and fibroblasts. Chronic inflammation may eventually lead to healing by fibrosis and scar tissue formation – an outcome not very conducive to bone formation. Higher levels of cytokines and inflammatory mediators have been observed to be deterrents to osteogenic differentiation *in vitro* [44] and bone formation *in vivo* [45].

The initial inflammatory response and haematoma formation are essential for the recruitment and differentiation of mesenchymal and osteoprogenitor cells which eventually leads to a successful osseointegration of the implant. This stage of

healing leads to osteogenesis, deposition and integration of mineralised matrix on the surface of the implant. From this stage onwards, bone remodelling takes over giving rise to well-defined lamellar bone on the implant surface, thereby finally leading to bone bonding or, in other words, osseointegration.

4.5 Molecular Regulation of Osteogenic Differentiation and Osseointegration on Implant Surfaces

Multipotent mesenchymal stem cells (MSCs) have the capability to differentiate into osteogenic, chondrogenic or adipogenic cell types and other cell types such as myocytes, marrow stroma and tendons [46]. The precise cellular signaling mechanisms involved in osteogenic differentiation of progenitor cells remain indeterminate. However, before delving deeper into the phenomena of osteogenic differentiation and osseointegration on implant surfaces, it would be useful to briefly discuss normal bone architecture and physiology.

4.5.1 Bone Cells

The essential living components of bone tissue include three different types of cells – osteoblasts, osteocytes and osteoclasts. Some of the terminally differentiated osteoblast cells eventually get trapped in the lacunae of the matrix and form osteocytes.

4.5.1.1 Osteoblasts

Osteoblasts are the key bone cells that form the building blocks of the bone and are responsible for the deposition of mineralised matrix. These are mononucleate cells which have the potential to form osteoid (organised un-mineralised portion of a typical bone, characteristically composed of type I collagen). Subsequently they are also responsible for the mineralisation of the osteoid.

Osteoblasts arise from osteoprogenitor cells present in the human body (usually located in the deeper layers of the periosteum and bone marrow). Studies have demonstrated the presence of several niches of osteoprogenitor cells in the human body [47–50]. Multiple reports support the presence of mesenchymal progenitor cells with potential to differentiate into various cell types including osteoblasts. These cells under specific culturing or growing conditions give rise to osteoblasts.

Osteoprogenitor cells are known to express the RUNX2/Cbfa1 transcription factor. These osteoprogenitor cells differentiate to osteoblasts and start expressing gene markers that include Osterix, Col1, BSP, M-CSF, ALP, osteocalcin,

osteopontin and osteonectin. Mature osteoblasts are cuboidal in shape. Osteoblasts have cytoplasmic projections that allow them to form communications with adjacent osteoblasts and osteocytes. Osteoblasts become flattened and elongated upon maturation. These cells usually form a single layer of cells on the surface of the bone. However, in cases where there is active bone formation, they may be present in the form of layers.

The principal function of osteoblasts is bone formation. As mentioned earlier, osteoblasts are the cells that facilitate the deposition of mineralised matrix in bones. They are also responsible for the synthesis of various bone-related proteins and polysaccharides. These cells also play an important role in bone remodelling by maintaining a balance between bone formation and resorption during new bone formation. Rarely, osteoblasts are also known to initiate the bone resorption process. Mature osteoblasts synthesise several phenotypic markers, including type I collagen, alkaline phosphatase (ALP) and osteocalcin (Fig. 4.5).

4.5.1.2 Osteocytes

Osteocytes are the most abundant type of bone cells (90–95 %) and cannot proliferate further to form new cells. They are known to function as mechanosensors of bone [51].

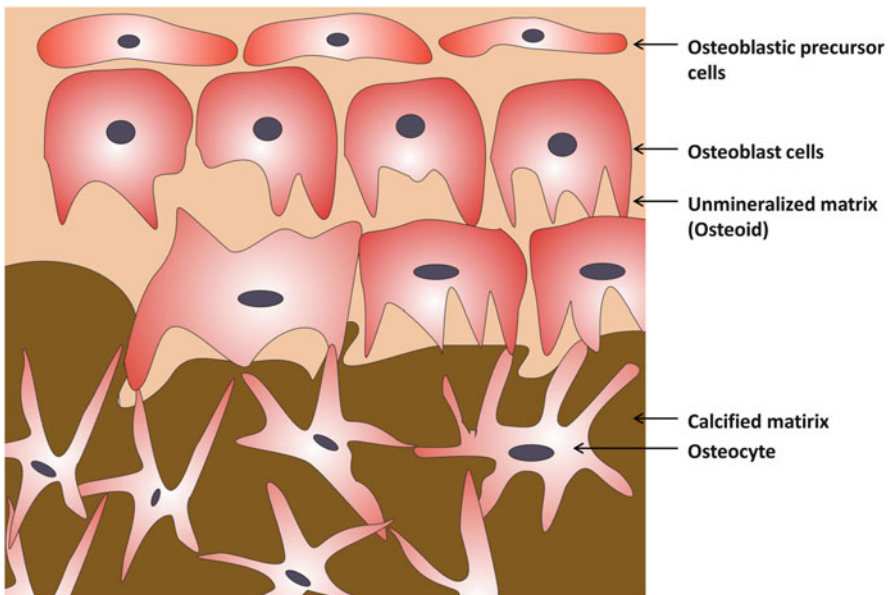


Fig. 4.5 Origin of osteoblasts in humans. The osteoblast precursors proliferate and give rise to osteoblasts which in turn lay the bone matrix and also give rise to the osteocytes

4.5.1.3 Osteoclasts

Osteoclasts are the cells responsible for bone resorption and thereby help in bone remodelling. These cells are formed by the fusion of mononuclear cells of the monocyte/macrophage lineage. The interplay between the osteoblasts and osteoclasts is responsible for maintaining normal bone homeostasis in the human body.

4.5.2 *Osseointegration and New Bone Formation*

The phenomenon of osseointegration is initiated simultaneously with the healing phase. Schenk and Buser have divided the process of osseointegration into three different stages [52]. Firstly, the implant surface is internalised by the formation of woven bone. They stated that the woven bone tends to form in two different patterns – ‘distance osteogenesis’, which occurs when the woven bone forms from the surrounding bone moving towards the implant surface, and ‘contact osteogenesis’, where osteogenesis occurs via direct deposition of new bone on the implant surface itself.

The second stage of osseointegration conditions the implant for its load-bearing function, wherein the woven bone laid on the implant surface slowly changes to a well-defined lamellar pattern. Lamellar bone consists of concentrically (in compact bones) or parallelly (in spongy bones) organised lamellae of collagen fibres and needs a firm base to be laid onto. The newly formed woven bone, existing bone and the implant surface supposedly provide the solid structure on which lamellar bone can be formed.

Schenk and Buser further described that bone remodelling takes place in the last stage of osseointegration which involves a balance and coordination between the osteoclastic resorptive activity and osteoblastic formative activity. The osseointegrative activities on dental implants, according to Schenk and Buser, vary with the different regions of the implant depending on the type of bone the region is in contact with. The coronal part of the implant integrates with cortical bone, whereas the remainder of the implant is in contact with cancellous bone and bone marrow. The compact structure of the cortical bone provides much of the initial stability, whereas the spongy cancellous bone ensures greater exposure to the vascular network and osteogenic cells.

Osteogenic differentiation and osteoinduction have been recognised as important processes leading to the formation of new bone during fracture healing and implant osseointegration. It has been argued that pre-existing osteoblasts play a minor role in bone formation in the regions of fracture healing or implant placement [53, 54]. The surrounding niche created in the region of the implant placement is rich in biochemical mediators that assist in recruitment and subsequent differentiation of cells towards osteogenesis, similar to fracture healing. Therefore, the process of osteogenic differentiation on implant surfaces provides important cues

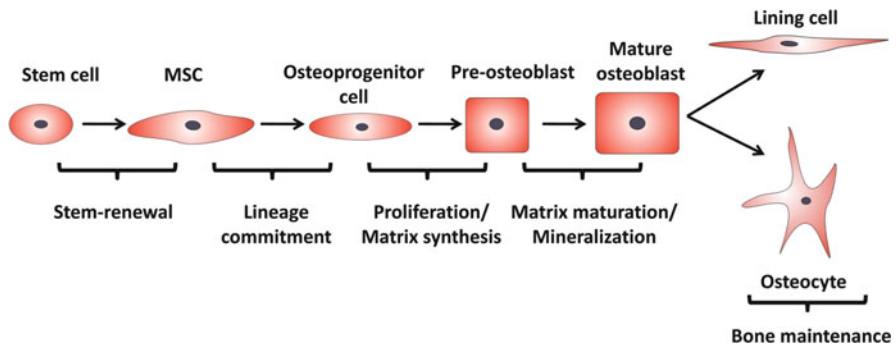


Fig. 4.6 Stages of osteoblastic differentiation (MSC mesenchymal stem cell)

in regard to the biocompatibility features of the material and the surface. Indeed, the implant surfaces with proven superior osseointegrative properties like the modSLA and SLA titanium surfaces have enabled us to learn some of the intricate details regarding the process of osteogenesis.

The process of osteogenic differentiation progresses through the stages of lineage commitment, pre-osteoblast cells, mature osteoblasts and ultimately forming the terminal bone cell – the osteocyte. Committed pre-osteoblasts are the first to express alkaline phosphatase (ALP-early marker of osteoblast differentiation). Mature osteoblasts express high levels of ALP and are involved in the production of extracellular matrix (ECM). Several genes and factors are involved in the process of commitment of mesenchymal stem cells to osteoblastic differentiation. The TGF- β /BMP molecules appear to play an important role in the process of commitment of MSCs to osteoprogenitor cells [55, 56] (Fig. 4.6).

4.5.3 Modulation of Molecular Pathways on Topographically Modified Implant Surface

Several studies have been conducted to observe the differences in osteogenic properties of different titanium surfaces. Most studies suggest that there is a similar initial cell attachment to all of the surfaces [40, 57]. Brett et al.'s study (2004) on the pattern of gene expression in osteoblasts cultured on different titanium surfaces (SLA, SMO and titanium plasma sprayed) revealed that surface roughness of Ti had profound effect on the pattern of gene expression by bone cells. Topographically modified titanium surfaces like the modSLA and SLA surfaces have been observed to stimulate cell signaling pathways. The BMP-2 gene is seen to be highly upregulated (greater than fivefold change) in osteoprogenitor cells as early as 24 h of culture on SLA surfaces, when compared with SMO surfaces. The osteogenic response of modSLA is considered to be better than the hydrophobic SLA surface, possibly because of the activation of WNT5A molecule [57].

4.5.3.1 Cell Signaling Pathways and Osteogenesis

Regulation of cellular interactions, differentiation and maturation are mediated by several factors, conditions and activation of different cell signaling pathways. The integrin signaling pathway is responsible for communication and adhesive interactions of cells with the implant surface, and activation of integrins leads to activation of different biological processes. Osteogenesis and osseointegration are among the various processes that become activated subsequent to stimulation of the integrin signaling pathway. Mesenchymal stem cells (MSC) undergo proliferation, and under specific conditions they become committed towards osteogenesis and thereby form mature osteoblast cells. Osteoprogenitor cells undergo a process of differentiation giving rise to osteoblasts and ultimately to osteocytes. Several cell signaling pathways are known to be instrumental in the process of osteogenic differentiation. The most important cell signaling pathways considered to be imperative to the process of osteodifferentiation are the TGF- β /BMP, Wnt, hedgehog and fibroblast growth factor (FGF) and Notch signaling.

TGF- β /BMP Pathway

The TGF- β /BMP pathway is identified as one of the most important molecular pathways that are influential in guiding the differentiation process. The bone morphogenetic proteins (BMPs) are a part of the transforming growth factor (TGF- β) superfamily of ligands, and they work through the SMAD receptors. BMP-2 and BMP-4 knockout mice do not even survive the gastrulation phase of the embryo due to failure of mesenchymal tissue induction [58]. The BMP molecules interact with the BMP receptors (BMPRs), leading to the activation of SMADs which ultimately enter the nucleus and activate several downstream transcription factors such as Dlx5, Cbfa1, Osx, etc. Several pathways have been shown to interact with the TGF- β /BMP pathway [59].

Wnt Signaling Pathway

The Wnt family of growth factors is an important pathway known to regulate growth and differentiation of tissues and organs. The canonical Wnt/ β -catenin pathway has been found to be of vital significance for regulation of bone mass [60]. In fact, mutations in LRP5, a protein co-receptor in Wnt signaling, have been seen to produce osteoporosis–pseudoglioma features [61]. Moreover, the production of antagonists for the Wnt pathway, like DKK-1, is correlated with the osteolytic features seen in multiple myeloma [62].

The canonical Wnt/ β -catenin pathway is probably the best understood pathway. β -catenin is a transcription factor that is central to the functioning of the pathway. The interaction of the TCF (T-cell factor) with SMAD4 potentially connects the

Wnt and the BMP signaling pathways. The canonical Wnt/ β -catenin pathway has been found to be significant for regulation of bone mass [60]. The conservation of the β -catenin molecule is the prime factor responsible for the activation of downstream genes which in turn leads to the activation of SMAD4 and thereby raises the possibility of the BMP and the Wnt pathway to be closely related in the process of osteogenic differentiation.

The non-canonical Wnt pathways include the planar cell polarity (PCP) and Wnt/ Ca^{2+} pathways. The distinguishing feature of the non-canonical pathways is that they are independent of β -catenin, LRP5/6 co-receptor and Dsh-DEP domain. Non-canonical Wnt pathways haven't been studied in extensive details, especially in relation to osteogenic differentiation. However, the studies on investigating interaction of osteoprogenitor cells with implant surfaces have revealed the upregulation of non-canonical Wnt pathway during osteogenic differentiation [32, 36, 63, 64].

Hedgehog Signaling Pathway

The hedgehog gene family consists of three members among which the Sonic (Shh) and Indian (Ihh) hedgehogs have been shown to be involved in skeletal development and repair. The hedgehog–BMP interaction is quite conserved in the process of differentiation [58]. Shh is seen to regulate BMP-2 expression in chicken limb buds [65]. The hedgehogs via their interaction with the BMP molecules might be important in the regulation of osteogenesis.

Fibroblast Growth Factor (FGF) Signaling Pathway

The FGF signaling pathway works through the tyrosine kinase receptors (FGFR1, FGFR2, FGFR3 and FGFR4) and leads to the activation of different cellular processes. FGFR1 signaling is known to activate osteogenic differentiation in osteoprogenitor cells. FGF ligands act on the FGF receptors and lead to downstream molecular processes. One of the key transcription factors RUNX2 is known to be phosphorylated under the influence of FGF2 ligand via the mitogen-activated protein kinase (MAPK) pathway [66].

Notch Signaling Pathway

The Notch pathway is a pathway for cellular communication that helps communication between neighbouring cells. The Notch pathway is known to work through its four receptors, NOTCH1, NOTCH2, NOTCH3 and NOTCH4. Notch signaling is believed to regulate osteogenic differentiation through its interaction with the BMP-2-mediated cell signaling pathway [67] and has been shown to induce the expression of Osterix.

4.5.3.2 Insights into the Molecular Regulation on modSLA and SLA Surfaces

Topographically modified surfaces are well recognised in the field of implant dentistry for their improved osteogenic properties. Several research groups across the world have been trying to explore the possible molecular mechanisms involved in accruing these osteogenic features. These surfaces have also been used as models to study the process of osteogenesis *in vitro* as they are considered to provide a substrate to osteoprogenitor cells that is akin to the native niche seen *in vivo*.

The SLA and modSLA surfaces have been seen to activate the integrin signaling pathway in cells capable of differentiating towards osteogenic lineage like mesenchymal stem cells and osteoprogenitor cells. Higher expression of integrins $\alpha 2$ and $\beta 1$ has been observed on these surfaces [68, 69]. Integrin molecules are presumed to be important for anchorage of cells to surfaces, and this is possibly the first step before the process of cellular differentiations begins. We have observed higher expression of genes encoding integrins $\alpha 2$ (ITGA2) and $\beta 1$ (ITGB1) within 24 h of culturing osteoprogenitor cells on modSLA and SLA surfaces compared to SMO surfaces [38]. Cell signaling pathways are stimulated subsequent to the activation of integrins and anchorage of cells to these surfaces. Studies on these surfaces have revealed stimulation of the key osteogenic pathways, TGF- β /BMP and Wnt [32, 36, 37, 64, 70].

The Wnt signaling pathway is subdivided into the canonical Wnt/ β -catenin and the non-canonical Wnt pathways. The non-canonical Wnt is further subclassified into different pathways among which the planar cell polarity (PCP) and Wnt/ Ca^{2+} pathways have been best known. The role of the Wnt/ β -catenin pathway in osteogenesis and new bone formation is well established. However, the results from studies on the modSLA and SLA surfaces revealed upregulation of the Wnt/ Ca^{2+} pathway during osteogenic differentiation [32, 63, 64]. Ivanovski et al.'s work assessing the transcriptional profile during osseointegration in human subjects also showed activation of the TGF- β /BMP and Wnt pathways [18]. In addition to these cell signaling pathways, their study also observed the upregulation of the Notch pathway [18]. The Notch pathway has also been shown to be important for osteogenic differentiation in other studies [67], yet it generally has received scant attention in the context of osteogenesis. Our studies exploring the differential regulation of cell signaling pathways when osteoprogenitor cells are cultured on modSLA and SLA surfaces have also shown an early stimulation of the Notch pathway along with the TGF- β /BMP and Wnt (especially the non-canonical Wnt/ Ca^{2+} pathway) [32].

The modSLA and SLA surfaces have also been shown to increase the expression of osteogenic markers like alkaline phosphatase (ALP), osteocalcin (OCN), osteopontin (SPP1) and RUNX2 [57, 71–73]. These *in vitro* observations confirmed their *in vivo* osteogenic properties. The sequential stimulation of different cell signaling pathways eventually leads to the activation of osteogenic transcription factors and ultimately leads to osteogenic differentiation. We also explored the

regulation of microRNAs, which are small RNA molecules that have the potential to modulate the expression of messenger RNA (mRNA) molecules, on the modSLA and SLA surfaces. Several microRNAs that are known to mediate cell development and differentiation were seen to be downregulated on both the modSLA and SLA surfaces in comparison to the SMO surfaces [38]. Bioinformatic target predictions for the downregulated miRNAs using an online tool, TargetScan, have revealed several genes of the TGF- β /BMP and Wnt/Ca²⁺ pathway as potential targets. Inhibitors of osteogenesis were found to be potential targets for miRNAs that were found to be upregulated.

4.6 Conclusion

Osseointegration is a phenomenon that is integral to the successful incorporation of orthopaedic and dental implants into the human body. In this chapter we have presented the current concepts in the field of implant surface modification and osseointegration. The modSLA and SLA micro-roughened titanium dental implant surfaces are known for their improved osteogenic and osseointegration properties, thereby highlighting the importance of topographically modified surfaces. These surfaces have been studied in-depth by researchers across the globe. Findings from such studies have enabled us to learn a great deal about the molecular mechanisms involved in osteogenic differentiation and osseointegration on micro-roughened implant surfaces. Such implant surfaces have also helped us in exploring the various signaling pathways involved in osteogenesis and therefore have provided us with a model to study the molecular mechanisms involved in osteogenic differentiation in vitro without using chemical mediators to induce differentiation.

The positive impact of micro-roughened titanium implants on osseointegration is proven. However, with the advent of nanotechnological modifications and the recent evidence from nano-topographically modified implant surfaces that show better osseointegration and bone formation, it is apparent that we haven't been able to identify all the factors and underlying mechanisms responsible for successful osseointegration and osteogenic differentiation. This in turn means that we need to explore these processes and their molecular regulation in greater depths. It is also clear that research focused on further exploring modifications of implant surfaces is ongoing, and this will likely lead to the development of different kinds of surfaces that will enable us to learn more about the process of osseointegration.

Acknowledgements The modSLA, SLA and SMO discs were supplied by Institut Straumann (Basel, Switzerland). We thank Dr. Sanjleena Singh and Dr. Mohammed Alfarsi for assisting us with the scanning electron microscope images.

References

1. Branemark R, Branemark PI, Rydevik B, Myers RR (2001) Osseointegration in skeletal reconstruction and rehabilitation: a review. *J Rehabil Res Dev* 38(2):175–181
2. Buser D, Schenk RK, Steinemann S, Fiorellini JP, Fox CH, Stich H (1991) Influence of surface characteristics on bone integration of titanium implants. A histomorphometric study in miniature pigs. *J Biomed Mater Res* 25(7):889–902
3. Albrektsson T, Branemark PI, Hansson HA, Lindstrom J (1981) Osseointegrated titanium implants. Requirements for ensuring a long-lasting, direct bone-to-implant anchorage in man. *Acta Orthop Scand* 52(2):155–170
4. Gotfredsen K, Wennerberg A, Johansson C, Skovgaard LT, Hjorting-Hansen E (1995) Anchorage of TiO₂-blasted, HA-coated, and machined implants: an experimental study with rabbits. *J Biomed Mater Res* 29(10):1223–1231
5. Wennerberg A, Albrektsson T, Johansson C, Andersson B (1996) Experimental study of turned and grit-blasted screw-shaped implants with special emphasis on effects of blasting material and surface topography. *Biomaterials* 17(1):15–22
6. Gotfredsen K, Nimb L, Hjorting-Hansen E, Jensen JS, Holmen A (1992) Histomorphometric and removal torque analysis for TiO₂-blasted titanium implants. An experimental study on dogs. *Clin Oral Implants Res* 3(2):77–84
7. Bristow CM, Cleavelly RJ (2005) Scientific enquiry in late 18th century Cornwall and the discovery of titanium. In: Brånemark P-I (ed) *The osseointegration book: from calvarium to calcaneus*. Quintessenz Verlags-GmbH, Berlin, pp 1–11
8. McCracken M (1999) Dental implant materials: commercially pure titanium and titanium alloys. *J Prosthodont* 8(1):40–43
9. Albrektsson T, Johansson C (2001) Osteoinduction, osteoconduction and osseointegration. *Eur Spine J* 10(Suppl 2):S96–S101
10. Hemlata Garg GB, Garg A (2012) Implant surface modifications: a review. *J Clin Diagn Res* 6(2):319–324
11. Zhu X, Chen J, Scheideler L, Reichl R, Geis-Gerstorfer J (2004) Effects of topography and composition of titanium surface oxides on osteoblast responses. *Biomaterials* 25(18):4087–4103
12. Cochran DL, Nummikoski PV, Higginbottom FL, Hermann JS, Makins SR, Buser D (1996) Evaluation of an endosseous titanium implant with a sandblasted and acid-etched surface in the canine mandible: radiographic results. *Clin Oral Implants Res* 7(3):240–252
13. Wennerberg A, Albrektsson T (2009) Effects of titanium surface topography on bone integration: a systematic review. *Clin Oral Implants Res* 20:172–184
14. Zeng H, Du X-W, Singh SC, Kulinich SA, Yang S, He J, Cai W (2012) Nanomaterials via laser ablation/irradiation in liquid: a review. *Adv Funct Mater* 22(7):1333–1353
15. Donos N, Hamlet S, Lang NP, Salvi GE, Huynh-Ba G, Bosshardt DD, Ivanovski S (2011) Gene expression profile of osseointegration of a hydrophilic compared with a hydrophobic microrough implant surface. *Clin Oral Implants Res* 22(4):365–372
16. Mardas N, Schwarz F, Petrie A, Hakimi AR, Donos N (2011) The effect of SLActive surface in guided bone formation in osteoporotic-like conditions. *Clin Oral Implants Res* 22(4):406–415
17. Linares A, Mardas N, Dard M, Donos N (2011) Effect of immediate or delayed loading following immediate placement of implants with a modified surface. *Clin Oral Implants Res* 22(1):38–46
18. Ivanovski S, Hamlet S, Salvi GE, Huynh-Ba G, Bosshardt DD, Lang NP, Donos N (2011) Transcriptional profiling of osseointegration in humans. *Clin Oral Implants Res* 22(4):373–381
19. Guo CY, Matinlinna JP, Tang AT (2012) Effects of surface charges on dental implants: past, present, and future. *Int J Biomater* 2012:381535
20. Rupp F, Scheideler L, Olshanska N, de Wild M, Wieland M, Geis-Gerstorfer J (2006) Enhancing surface free energy and hydrophilicity through chemical modification of microstructured titanium implant surfaces. *J Biomed Mater Res A* 76(2):323–334

21. Ellingsen JE (1995) Pre-treatment of titanium implants with fluoride improves their retention in bone. *J Mater Sci Mater Med* 6(12):749–753
22. Wennerberg A, Albrektsson T, Andersson B, Krol JJ (1995) A histomorphometric and removal torque study of screw-shaped titanium implants with three different surface topographies. *Clin Oral Implants Res* 6(1):24–30
23. Wennerberg A, Hallgren C, Johansson C, Danelli S (1998) A histomorphometric evaluation of screw-shaped implants each prepared with two surface roughnesses. *Clin Oral Implants Res* 9(1):11–19
24. Sykaras N, Iacopino AM, Marker VA, Triplett RG, Woody RD (2000) Implant materials, designs, and surface topographies: their effect on osseointegration. A literature review. *Int J Oral Maxillofac Implants* 15(5):675–690
25. Wennerberg A, Albrektsson T (2000) Suggested guidelines for the topographic evaluation of implant surfaces. *Int J Oral Maxillofac Implants* 15(3):331–344
26. Shalabi MM, Gortemaker A, Van't Hof MA, Jansen JA, Creugers NH (2006) Implant surface roughness and bone healing: a systematic review. *J Dent Res* 85(6):496–500
27. Lang NP, Salvi GE, Huynh-Ba G, Ivanovski S, Donos N, Bosshardt DD (2011) Early osseointegration to hydrophilic and hydrophobic implant surfaces in humans. *Clin Oral Implants Res* 22(4):349–356
28. Hamlet S, Alfarsi M, George R, Ivanovski S (2012) The effect of hydrophilic titanium surface modification on macrophage inflammatory cytokine gene expression. *Clin Oral Implants Res* 23(5):584–590
29. de Oliveira PT, Nanci A (2004) Nanotexturing of titanium-based surfaces upregulates expression of bone sialoprotein and osteopontin by cultured osteogenic cells. *Biomaterials* 25(3):403–413
30. Wennerberg A, Galli S, Albrektsson T (2011) Current knowledge about the hydrophilic and nanostructured SLActive surface. *Clin Cosmet Investig Dent* 3(1):59–67
31. Wennerberg A, Svanborg LM, Berner S, Andersson M (2012) Spontaneously formed nanostructures on titanium surfaces. *Clin Oral Implants Res* 24(2):203–209
32. Chakravorty N, Hamlet S, Jaiprakash A, Crawford R, Oloyede A, Alfarsi M, Xiao Y, Ivanovski S (2013) Pro-osteogenic topographical cues promote early activation of osteoprogenitor differentiation via enhanced TGFbeta, Wnt, and Notch signaling. *Clin Oral Implants Res* 2013:1–12
33. Mathieu PS, Lobo EG (2012) Cytoskeletal and focal adhesion influences on mesenchymal stem cell shape, mechanical properties, and differentiation down osteogenic, adipogenic, and chondrogenic pathways. *Tissue Eng B Rev* 18(6):436–444
34. Buser D, Broggin N, Wieland M, Schenk RK, Denzer AJ, Cochran DL, Hoffmann B, Lussi A, Steinemann SG (2004) Enhanced bone apposition to a chemically modified SLA titanium surface. *J Dent Res* 83(7):529–533
35. Baier RE, Meyer AE (1988) Future directions in surface preparation of dental implants. *J Dent Educ* 52(12):788–791
36. Vlacic-Zischke J, Hamlet SM, Friis T, Tonetti MS, Ivanovski S (2011) The influence of surface microroughness and hydrophilicity of titanium on the up-regulation of TGFbeta/BMP signalling in osteoblasts. *Biomaterials* 32(3):665–671
37. Olivares-Navarrete R, Hyzy SL, Hutton DL, Erdman CP, Wieland M, Boyan BD, Schwartz Z (2010) Direct and indirect effects of microstructured titanium substrates on the induction of mesenchymal stem cell differentiation towards the osteoblast lineage. *Biomaterials* 31(10):2728–2735
38. Chakravorty N, Ivanovski S, Prasadam I, Crawford R, Oloyede A, Xiao Y (2012) The microRNA expression signature on modified titanium implant surfaces influences genetic mechanisms leading to osteogenic differentiation. *Acta Biomater* 8(9):3516–3523
39. Gittens RA, McLachlan T, Olivares-Navarrete R, Cai Y, Berner S, Tannenbaum R, Schwartz Z, Sandhage KH, Boyan BD (2011) The effects of combined micron-/submicron-

- scale surface roughness and nanoscale features on cell proliferation and differentiation. *Biomaterials* 32(13):3395–3403
40. Brett PM, Harle J, Salih V, Mihoc R, Olsen I, Jones FH, Tonetti M (2004) Roughness response genes in osteoblasts. *Bone* 35(1):124–133
 41. Zinelis S, Silikas N, Thomas A, Syres K, Eliades G (2012) Surface characterization of SLActive dental implants. *Eur J Esthet Dent* 7(1):72–92
 42. Kuzyk PR, Schemitsch EH (2011) The basic science of peri-implant bone healing. *Indian J Orthop* 45(2):108–115
 43. Spector M, Cease C, Xia TL (1989) The local tissue-response to biomaterials. *Crit Rev Biocompat* 5(3):269–295
 44. Gilbert L, He X, Farmer P, Boden S, Kozlowski M, Rubin J, Nanes MS (2000) Inhibition of osteoblast differentiation by tumor necrosis factor-alpha. *Endocrinology* 141(11):3956–3964
 45. Dimitriou R, Babis GC (2007) Biomaterial osseointegration enhancement with biophysical stimulation. *J Musculoskelet Neuronal Interact* 7(3):253–265
 46. Muraglia A, Cancedda R, Quarto R (2000) Clonal mesenchymal progenitors from human bone marrow differentiate in vitro according to a hierarchical model. *J Cell Sci* 113(7):1161–1166
 47. Erlebacher A, Filvaroff EH, Gitelman SE, Derynck R (1995) Toward a molecular understanding of skeletal development. *Cell* 80(3):371–378
 48. Friedenstein AJ, Chailakhyan RK, Lalykina KS (1970) The development of fibroblast colonies in monolayer cultures of guinea pig bone marrow and spleen cells. *Cell Prolif* 3(4):393–403
 49. Friedenstein AJ (1976) Precursor cells of mechanocytes. In: G.H. Bourne JFD, Jeon KW (eds) *Int Rev Cytol*, vol. 47. Academic Press, pp 327–359
 50. Friedenstein AJ, Chailakhyan RK, Gerasimov UV (1987) Bone marrow osteogenic stem cells: in vitro cultivation and transplantation in diffusion chambers. *Cell Tissue Kinet* 20(3):263–272
 51. Ehrlich PJ, Lanyon LE (2002) Mechanical strain and bone cell function: a review. *Osteoporos Int* 13(9):688–700
 52. Schenk RK, Buser D (1998) Osseointegration: a reality. *Periodontol* 2000 17:22–35
 53. Frost HM (1989) The biology of fracture healing. An overview for clinicians. Part II. *Clin Orthop Relat Res* 248:294–309
 54. Frost HM (1989) The biology of fracture healing. An overview for clinicians. Part I. *Clin Orthop Relat Res* 248:283–293
 55. Aubin JE, Liu F, Malaval L, Gupta AK (1995) Osteoblast and chondroblast differentiation. *Bone* 17(2 Suppl):77S–83S
 56. Malaval L, Liu F, Roche P, Aubin JE (1999) Kinetics of osteoprogenitor proliferation and osteoblast differentiation in vitro. *J Cell Biochem* 74(4):616–627
 57. Wall I, Donos N, Carlqvist K, Jones F, Brett P (2009) Modified titanium surfaces promote accelerated osteogenic differentiation of mesenchymal stromal cells in vitro. *Bone* 45(1):17–26
 58. Yamaguchi A, Komori T, Suda T (2000) Regulation of osteoblast differentiation mediated by bone morphogenetic proteins, hedgehogs, and Cbfa1. *Endocr Rev* 21(4):393–411
 59. von Bubnoff A, Cho K W Y (2001) Intracellular BMP signaling regulation in vertebrates: pathway or network? *Dev Biol* 239(1):1–14
 60. Krishnan V, Bryant HU, MacDougald OA (2006) Regulation of bone mass by Wnt signaling. *J Clin Invest* 116(5):1202–1209
 61. Gong Y, Slee RB, Fukai N, Rawadi G, Roman-Roman S, Reginato AM, Wang H, Cundy T, Glorieux FH, Lev D, Zacharin M, Oexle K, Marcelino J, Suwairi W, Heeger S, Sabatakos G, Apte S, Adkins WN, Allgrove J, Arslan-Kirchner M, Batch JA, Beighton P, Black GCM, Boles RG, Boon LM, Borrone C, Brunner HG, Carle GF, Dallapiccola B, De Paeppe A, Floege B, Halfhide ML, Hall B, Hennekam RC, Hirose T, Jans A, Juppner H, Kim CA, Keppeler-Noreuil K, Kohlschuetter A, LaCombe D, Lambert M, Lemyre E, Letteboer T, Peltonen L, Ramesar RS, Romanengo M, Somer H, Steichen-Gersdorf E, Steinmann B, Sullivan B, Superti-Furga A, Swoboda W, van den Boogaard M-J, Van Hul W, Vikkula M, Votruba M,

- Zabel B, Garcia T, Baron R, Olsen BR, Warman ML (2001) LDL Receptor-Related Protein 5 (LRP5) affects bone accrual and eye development. *Cell* 107(4):513–523
62. Tian E, Zhan F, Walker R, Rasmussen E, Ma Y, Barlogie B, Shaughnessy JD (2003) The role of the Wnt-signaling antagonist DKK1 in the development of osteolytic lesions in multiple myeloma. *N Engl J Med* 349(26):2483–2494
63. Olivares-Navarrete R, Hyzy SL, Hutton DL, Dunn GR, Appert C, Boyan BD, Schwartz Z (2011) Role of non-canonical Wnt signaling in osteoblast maturation on microstructured titanium surfaces. *Acta Biomater* 7(6):2740–2750
64. Olivares-Navarrete R, Hyzy SL, Park JH, Dunn GR, Haithcock DA, Wasilewski CE, Boyan BD, Schwartz Z (2011) Mediation of osteogenic differentiation of human mesenchymal stem cells on titanium surfaces by a Wnt-integrin feedback loop. *Biomaterials* 32(27):6399–6411
65. Laufer E, Nelson CE, Johnson RL, Morgan BA, Tabin C (1994) Sonic hedgehog and Fgf-4 act through a signaling cascade and feedback loop to integrate growth and patterning of the developing limb bud. *Cell* 79(6):993–1003
66. Xiao G, Jiang D, Gopalakrishnan R, Franceschi RT (2002) Fibroblast growth factor 2 induction of the osteocalcin gene requires MAPK activity and phosphorylation of the osteoblast transcription factor, Cbfa1/Runx2. *J Biol Chem* 277(39):36181–36187
67. Nobta M, Tsukazaki T, Shibata Y, Xin C, Moriishi T, Sakano S, Shindo H, Yamaguchi A (2005) Critical regulation of bone morphogenetic protein-induced osteoblastic differentiation by Delta1/Jagged1-activated Notch1 signaling. *J Biol Chem* 280(16):15842–15848
68. Raz P, Lohmann CH, Turner J, Wang L, Poythress N, Blanchard C, Boyan BD, Schwartz Z (2004) 1 alpha,25(OH)(2)D-3 regulation of integrin expression is substrate dependent. *J Biomed Mater Res A* 71A(2):217–225
69. Olivares-Navarrete R, Raz P, Zhao G, Chen J, Wieland M, Cochran DL, Chaudhri RA, Ormoy A, Boyan BD, Schwartz Z (2008) Integrin alpha2beta1 plays a critical role in osteoblast response to micron-scale surface structure and surface energy of titanium substrates. *Proc Natl Acad Sci U S A* 105(41):15767–15772
70. Olivares-Navarrete R, Hyzy S, Wieland M, Boyan BD, Schwartz Z (2010) The roles of Wnt signaling modulators Dickkopf-1 (Dkk1) and Dickkopf-2 (Dkk2) and cell maturation state in osteogenesis on microstructured titanium surfaces. *Biomaterials* 31(8):2015–2024
71. Zhao G, Schwartz Z, Wieland M, Rupp F, Geis-Gerstorf J, Cochran DL, Boyan BD (2005) High surface energy enhances cell response to titanium substrate microstructure. *J Biomed Mater Res A* 74A(1):49–58
72. Klein MO, Bijelic A, Toyoshima T, Gotz H, von Koppenfels RL, Al-Nawas B, Duschner H (2010) Long-term response of osteogenic cells on micron and submicron-scale-structured hydrophilic titanium surfaces: sequence of cell proliferation and cell differentiation. *Clin Oral Implants Res* 21(6):642–649
73. Klein MO, Bijelic A, Ziebart T, Koch F, Kammerer PW, Wieland M, Konerding MA, Al-Nawas B (2013) Submicron scale-structured hydrophilic titanium surfaces promote early osteogenic gene response for cell adhesion and cell differentiation. *Clin Implant Dent Relat Res* 15(2):166–175

Chapter 5

Advances in Bioglass and Glass Ceramics for Biomedical Applications

Besim Ben-Nissan, Andy H. Choi, and Innocent Macha

Abstract Tissue engineering and advanced biomedical technologies have proved to be potential to improve the quality of human life. During the last four decades, the capability to engineer or repair new functional tissues has been a very effective approach to improve the quality of life of patients. Since its discovery by Hench and co-workers in the 1960s, bioglasses and glass ceramics have attracted considerable attention of many researchers because of their unique properties which can easily be tailored by manipulating its compositions and morphology. Over the years, many questions concerning its interactions with both hard and soft tissues have been answered with a multidisciplinary team of surgeons, scientists and engineers. Many clinical Bioglass® and other similar structures and compositions are being used for bone augmentation and restoration, in orthopaedic, dental and maxillofacial surgery and in general in the field of tissue engineering. They have proved to be efficient and effective, some with outperformance over other bioceramic and metal prostheses. It is our aim in this chapter to present the development of these important biomaterials focusing on the history, synthesis, properties, modern characterisation methods and the current development of nano- and biocomposite materials for clinical applications.

Keywords Bioglass • Glass ceramics • A-W glass • Osteosimulation • Sol–gel

5.1 Introduction

When a person suffers from a pain, the main concern for that individual is relieving the pain and returning to a healthy and functional lifestyle. Degeneration and diseases often result in the replacement of skeletal parts, such as the knees, hips, finger joints, elbows, vertebrae and teeth, and repair of the mandible surgically.

It is anticipated that the growth in these areas will continue due to a number of factors, for instance, the need due to the ageing population, improvements in

Dedicated to Prof Larry Hench who has given us the 'Bioglass' and beyond.

B. Ben-Nissan (✉) • A.H. Choi • I. Macha
Faculty of Science, University of Technology, Broadway, NSW 2007, Australia
e-mail: b.ben-nissan@uts.edu.au

technology and lifestyle, a better understanding of body functionality, an increasing preference by younger to middle-aged candidates for undergoing surgery, improved aesthetics and the need for better functions [1].

By definition, a biomaterial is a nondrug substance which is ideal to be placed in a system that can replace or enhance the roles of bodily organs or tissues. These materials are able to be in contact with bodily fluids and tissues while showing little or if any adverse reactions for prolonged periods of time.

The major key factors that are pertinent for the success of an implant are its biocompatibility and biofunctionality. Engineers and surgeons have identified, even at the initial stages of this field, the problems related to the design and materials selection that resulted in premature loss of implant function through mechanical failure, corrosion or inadequate biocompatibility of the component. Depending on the applications, bioactive glass and glass ceramics in addition to ceramic materials are ideal candidates with respect to the above functions, except for their brittle behaviour under functional loading.

In this chapter, our aim is to examine the general definitions of glass as well as the preparation methods, properties and applications of glass, glass ceramics and bioactive glasses currently available and in use. We will also introduce the development and progress of the commercially available and currently investigated bioglasses and glass ceramics. Furthermore, their chemistry, bioactivity and mechanisms of their bonding and interactions within a physiological environment, their preparation methods and their applications in the biomedical field will also be covered.

5.2 Glass and Glass Ceramics

Glass is an amorphous, hard and brittle material created from the molten product of oxides. The molten material is normally cooled rapidly in order to prevent crystallisation or devitrification.

For over thousands of years, glass has been known to mankind. A natural glass produced from silicate magna called obsidian was known to prehistoric people long before how to make glass was discovered. The Phoenicians are thought by many to have been the first people to make glass [1].

It is now possible from the means of how glass is manufactured to predict and control the properties. Much of this control derives from the purity and use of appropriate raw materials. The choice of raw materials is generally based on their glass-making properties, which will be discussed in the following sections.

5.2.1 *Raw Materials*

5.2.1.1 Glass Formers

In general, glass formers are oxides which can be turned into a glass without the need to use any other oxides. However, they require very high temperatures in order to melt initially. Silica (SiO_2) normally obtained from sand is the most common type of glass former. Other examples of glass formers include B_2O_3 and P_2O_5 .

5.2.1.2 Modifiers

Modifiers, as their name suggests, are materials that may alter the properties of the glass-forming oxides. They are also the major groups of compounds typically added to silica. In addition, they may also be employed to avoid defects in the final glass products. Generally, two types of modifiers are added to glass-forming oxides: fluxes and stabilisers.

Fluxes

In chemical terms, fluxes are the components that change the underlying properties of the oxides when added to glass formers. For instance, the melting point of glass-forming oxides can be lowered by the addition of fluxes.

Some of the most common fluxes include oxides of sodium (NaO_2) and potassium (K_2O). In particular, the viscosity of the glass can be lowered through the addition of boric oxide (B_2O_3), which in turn increases the fluidity and thus permitting the compounds to move with a greater degree of freedom.

Stabilisers

Stabilisers can be used to improve the chemical durability of glass as well as prevent the crystallisation of oxides. In certain applications, crystallisation may be undesirable due to its effect on light scattering, hence a reduction in transparency. Stabilisers, similar to fluxes, may also affect the working temperature of glass formers. Examples of stabilisers include oxides of aluminium (Al_2O_3), calcium (CaO) and magnesium (MgO).

Refining and Melting Agents

During the conventional melt-based manufacturing of glass, small bubbles are detrimental as the properties of the glass are significantly affected by their presence.

To decrease the number of bubbles, compounds such as sodium nitrate, sodium sulphate, sodium chloride, calcium fluoride and carbon are added to the glass, and the glass is said to be refined. On the other hand, the purity and close control of additives are critically important during the synthesis of glasses for biomedical applications due to the issues of toxicity and biocompatibility.

5.3 Types of Glasses

The specific properties of glass can be obtained through its chemical composition. An indication of some types of glasses produced in this manner, together with the desired properties for a number of engineering applications, is given in Table 5.1.

5.3.1 Aluminosilicate Glasses

Aluminosilicate glasses are hard, usually have a good chemical resistance and do not devitrify readily. They also have high heat shock resistance and can withstand heat even better than borosilicate glasses. One specific type of aluminosilicate glass is used in the production of E-glass fibres (also contains CaO).

5.3.2 Borosilicate Glasses

Boron oxide (B_2O_3) serves as both a glass former and a modifier. Boron oxide also produces a glass with a low coefficient of thermal expansion, which results in a glass that is better equipped to deal with thermal shock. A common trade name for

Table 5.1 Types of glasses showing their chemical composition in weight percentage

Component	Soda–lime glass	Lead glass	Borosilicate glass	Aluminosilicate glass	High-silica glass Vycor®	45S5 Bioglass®
SiO ₂	70–75	53–68	73–82	57	96	45
Na ₂ O	12–18	5–10	3–10	1.0	–	24.5
K ₂ O	0–1	1–10	0.4–1	–	–	–
CaO	5–14	0–6	0–1	5.5	–	24.5
PbO	–	15–40	0–10	–	–	–
B ₂ O ₃	–	–	5–20	4.0	3	–
Al ₂ O ₃	0.5–2.5	0–2	2–3	20.5	–	–
MgO	0–4	–	–	12.0	–	–
P ₂ O ₅	–	–	–	–	–	6

borosilicate glasses is Pyrex, and they are often used in the areas where temperature differences are an issue. Crystallisation is prevented by the presence of alumina (Al_2O_3) in large quantities. They also improve the chemical durability and the hardness of the glass.

5.3.3 *Lead Glasses*

Lead glass is often referred to as crystal glass as a result of an improvement in machinability, thus permitting the glass to be more easily engraved. It also gives the glass a heaviness and blue appearance.

One of the most important properties of lead glass is its high refractive index, which gives brilliance when properly cut or graved. The melting point and hot working (shaping) temperature of the glass are lowered as the lead oxide (PbO) acts as a flux and a modifier to acceptable levels. Radiation shielding is another useful application for the lead glasses.

Flint and crown glasses are some of the older terms associated with glass. Flint glass was a term originally used to describe lead glass since flint was used as a source of good-quality silica free from colour. It is now more loosely used to describe glasses with good colour. Crown glasses are alkali–lime–silica based, such as soda–lime glass.

5.3.4 *Soda–Lime Glasses*

The presence of soda (Na_2O) in glass lowers the melting point of the glass, and the lime (CaO) keeps the glass from crystallising.

5.3.5 *Glass Ceramics*

By definition, a glass ceramic is essentially a glass in which the formation of nuclei is enhanced by using specific compositions, which are self-nucleating, or by adding an additional nucleating agent [2]. Very small crystals are contained inside the resultant material. A number of factors influence the glass ceramics' final properties: crystal orientation; intergranular bonding; percentage of crystallinity, of crystalline phase distribution and of any remaining glassy phase; and grain size. In the past, by controlling the base composition, the choice of nucleant (nucleating agent) and an appropriate heat treatment schedule, above-mentioned factors have been successfully controlled [2]. In the early days, work on glass ceramics was focused on the lithia–silica (Li_2O – Si_2O) system. Later on, alumina was presented to destabilise the basic composition (Li_2O – Si_2O – Al_2O_3). β -Spodumene, a polymorph

of LiAlSiO_4 , is precipitated to inhabit most of the volume of the glass ceramic, such as in a Pyroceram system. In this system, Si^{4+} is replaced by Al^{3+} in the network structure, and Li^+ is held in close proximity to maintain the charge balance. The preceding system was an $\text{MgO-Al}_2\text{O}_3\text{-SiO}_2$ system, in which the lithia is replaced completely by MgO . Nucleation is accomplished by TiO_2 , ZrO_2 and SnO_2 . In another composition, Na_2O is used to replace the lithia.

Extensive investigation has been carried out on glasses and glass ceramics and fabricated as bioactive or surface-active biomaterials with additions of CaO and P_2O_5 to their base compositions. A key advantage of phosphate-based materials is their chemical relationship with carbonated apatite which is one of the main constituents of bone and teeth. The structures of phosphate glasses and glass ceramics are based on the networks of corner-sharing phosphate tetrahedra. In addition, apatite-mullite glass ceramics based on $\text{SiO}_2\text{-Al}_2\text{O}_3\text{-P}_2\text{O}_5\text{-CaO-CaF}_2$ compositions have also been developed and observed to form fluorapatite and mullite with a specific heat treatment procedure.

5.3.6 *Machinable Glass Ceramics*

In order to improve the machinability of glass ceramics, the base composition ($\text{MgO-Al}_2\text{O}_3\text{-SiO}_2$) can be modified by replacing Li_2O with a mixture of MgF_2 and K_2O . By reheating these specific glasses in the temperature range of $650\text{-}1150\text{ }^\circ\text{C}$, machinable glass ceramics are produced with an emphasis of inducing a randomly oriented dispersion of tetra-silicic mica crystals. These crystals have the chemical formula of $\text{KMg}_{2.5}\text{Si}_4\text{O}_{10}\text{F}_2$ and a structure similar to the tri-silicic mica fluorophlogopite, $\text{KMg}_3\text{AlSi}_3\text{O}_{10}\text{F}_2$. Hence, the structure is analogous to the natural mica mineral phlogopite. It is relatively easy for rotation or cleavage to occur in the K^+ planes, and since the crystals in the glass ceramic are in random orientations, the propagating cracks are continuously deflected in different directions within the material which leads to a rapid absorption of the propagation energy. The fracture paths follow the mica-glass interfaces or mica cleavage planes, removing very small fragments during the process, so that a good machined finish is easily obtained [2].

5.3.7 *Bioglasses and Glass Ceramics*

Since the discovery by Hench and Wilson [3] of the bioglasses which bond to living tissue (Bioglass®), various types of bioactive glasses and glass ceramics with different functions such as high machinability, mechanical strength and fast setting ability have been developed.

Glasses that are primarily based on silica (SiO_2) which may also contain small amounts of other crystalline phases have been examined for implantation purposes.

The most successful and prominent application is Bioglass®, which is described in detail in various comprehensive reviews [4–6].

The first-generation bioactive glass compositions lie in the $\text{Na}_2\text{O}-\text{CaO}-\text{P}_2\text{O}_5-\text{SiO}_2$ system. In 1971, the first development of such a bioglass began when 45S5 Bioglass® with a composition of 45 % SiO_2 , 24.5 % CaO , 24.5 % Na_2O and 6 % P_2O_5 by weight was proposed [7].

It was suggested by Hench [4] and Vrouwenvelder et al. [8] that when compared to hydroxyapatite (HAp), 45S5 Bioglass® has greater osteoblastic activity which is accredited to a rapid exchange of alkali ions with hydronium ions at the surface. This in turn led to the formation of a silica-rich layer over a period of time. The migration of Ca^{2+} and PO_4^{3-} is permitted on this layer to the silica-rich surface where they combine with soluble calcium and phosphate ions from the solution and the formation of an amorphous $\text{CaO}-\text{P}_2\text{O}_5$ layer takes place. Upon the interaction with OH , CO_3^{2-} and F from solution, this layer will then undergo crystallisation. Andersson and Kangasniemi [9] have also observed a similar phenomenon in bioglass with slightly modified compositions.

Glass ceramics from a similar composition with various degrees of crystallinity was prepared by Li et al. [10]. They discovered that the formation of an apatite layer was directly influenced by the amount of glassy phase that still remains, with total inhibition when the glassy phase constitutes less than about 5 weight percent (wt%). These specific glasses (for instance, Bioglass®) have been accepted as bioactive materials as a result of their surface activity; and they have been utilised for non-load-bearing applications. Bioglasses® have been used successfully in clinical applications as artificial middle ear bone implants and alveolar ridge maintenance implants [3] and recently as toothpaste additives.

A bioactive glass with precipitated crystalline apatite and reduced alkaline oxide content can be produced by using a specific heat treatment method. The resultant glass ceramic is referred to as Ceravitals, and it has been shown to have a higher mechanical strength but lower bioactivity compared to Bioglass®.

Kokubo et al. [11] produced a glass ceramic named A-W glass ceramic (Cerabone A-W) that contains oxyfluorapatite ($\text{Ca}_{10}(\text{PO}_4)_6(\text{OH},\text{F}_2)$) and wollastonite ($\text{CaO}.\text{SiO}_2$) in an $\text{MgO}-\text{CaO}-\text{SiO}_2$ glassy matrix. It was reported in the early 1990s that the A-W glass ceramic spontaneously bonded to living bone without the formation of fibrous tissue around the glass. They have also developed a bioactive and machinable glass ceramic containing apatite and phlogopite ($(\text{Na},\text{K})\text{Mg}_3(\text{Al}-\text{Si}_3\text{O}_{10})(\text{F})_2$) called Bioverits that were utilised in the past in such clinical applications as the artificial vertebra [11]. Currently the production and application of A-W glass are only restricted to research, whereas its commercial production has been discontinued.

5.4 Synthesis of Bioactive Glass

Bioactive glasses have been manufactured using conventional glass technology. The glass components of oxides or carbonates in the form of grains are mixed, melted and then homogenised at a temperature between 1250 and 1400 °C [12]. Bulk implants are produced when the molten glass is cast into steel or graphite moulds. It is often necessary for a final grind and polish to achieve the required tolerances. Even though this process has been changed in many ways in order to avoid grinding and polishing by producing different particle sizes directly, still the processes have many advantages.

Nanoparticles and nanofibres of bioactive glass have been made available several years ago, and they have been used either alone or combined with polymers in the form of a nanocomposite in the biomedical field. In the following section, various processing methods used to fabricate nanoscale bioactive glasses are presented.

5.4.1 *Microemulsion Techniques*

Microemulsions are thermodynamically stable dispersions of oil and water stabilised by a surfactant and, in many cases, a cosurfactant. The microemulsions can be of the droplet type, either with spherical oil droplets dispersed in a continuous medium of water or vice versa with spherical water droplets dispersed in a continuous medium of oil. Researchers have discovered that the key in controlling polydispersity and nanoparticle size is provided by adjusting the microemulsion and/or operation variables [13, 14]. It has been well known that this method is an ideal technique which is also capable of obtaining nanometre-sized inorganic particles with minimum agglomeration [15, 16].

On the other hand, the main disadvantages of the microemulsion techniques are the usage of a large quantity of oil and surfactant phases and the low yield in production [17]. Only a limited number of papers are currently available on the production of nanosized bioactive particles using this approach even though microemulsion technique provides an alternative means for synthesising several types of organic and inorganic nanometre-sized particles compared to other production methods [18, 19].

5.4.2 *Laser Spinning Techniques*

Extensive experimental work has been carried out over the past few years in the development of laser spinning techniques with definite control of the results to fabricate tailored products [20–22]. Recently, researchers have for the first time

developed a novel technique for producing bioglass nanofibres, by using ‘laser spinning’ [23]. In this technique, a small quantity of precursor material is melted using a high-energy laser, to produce a superfine filament that is then lengthened and cooled by a powerful gas current.

The advantages of laser spinning technique include that the process is relatively fast and the nanofibres are produced within several microseconds. It is also able to produce glass nanofibres of compositions that would be difficult to obtain using other methods. The diameters of the fibres produced from laser spinning technique range from hundreds down to tenths of microns; in addition the types of products vary from disordered mats to continuous filaments [21]. On the other hand, the major drawback of laser spinning is that high energy is required during the production process, which consequently increases the production cost.

Laser spinning technique has been demonstrated to be an efficient approach for the production of nanofibres of bioactive glasses and new nanostructures with potential for tissue engineering scaffolds, as fillers in bone defects and as reinforcing agents in nanocomposites. The capability of the laser spinning technique to produce nanofibres with a wide range of compositions makes evident its potential to create nanofibres with different rates of bioresorption to control the release of active ions that have the potential to stimulate the gene expression and cellular response necessary for tissue regeneration [22, 23].

5.4.3 Gas Phase (Flame Spray) Synthesis

Flame spray technology has been used by ancient Chinese in Chinese ink artwork and with painting on cave walls [24]. Currently metal–organic precursor compounds are used by flame spray technology to generate nanoparticles at temperatures above 1000 °C. The formation of molecular nuclei is the basic principle of all gas phase synthesis methods. This is followed by condensation and coalescence that induce the subsequent growth of nanoparticles in high-temperature regions during the process [17, 25].

Numerous studies have been conducted in relations to the understanding of the dynamics and key variables of flame spray process as well as how they can be controlled in order to obtain nanoparticles of given size range and chemical compositions [26, 27]. Athanassiou et al. [27] discovered that the metal–carboxylate system is a very convenient precursor as it permits the synthesis of oxide nanoparticles of almost any composition. Furthermore, metal–organic salts are highly stable in air and tolerate humidity, and above all they are fully miscible among each other. Accordingly, the production of any type of nanoparticulate mixed oxides with high chemical homogeneity is allowed using this process.

Using the flame spray technique, bioactive glass nanoparticles in the 20–50-nm range were successfully produced by Vollenweider et al. [28], and they reported within the dentin samples a pronounced increase in mineral content which suggested rapid remineralisation. Mohn et al. [29] also demonstrated the ability

of the flame spray technique to synthesise radio-opaque bioactive glass nanoparticles for potential root canal application.

Compared to other gas phase techniques, the advantage is the precursors do not require an additional energy despite the fact that the flame spray technique is an energy-intensive approach.

5.4.4 Sol–Gel Bioglass

The sol–gel processing of ceramics and glass materials began more than 150 years ago on silica gel [30, 31]. Preliminary studies on sol–gel indicated that under acidic conditions, the hydrolysis of $\text{Si}(\text{OC}_2\text{H}_5)_4$, tetraethyl orthosilicate (TEOS), resulted in SiO_2 in the form of a glass-like material [30] that could be drawn into fibres. In the early days, the silica gels were dried for more than a year in order to avoid the gel fracturing into a fine powder, and because of this, the whole process lost technological interest.

A considerable amount of attention has been attracted as the result of the formation of Liesegang rings [32] which led to numerous investigations carried out by researchers on the problem of the periodic precipitation phenomena which result in the formation of Liesegang rings and the growth of crystals from gels.

Using the sol–gel method, various types of coatings and films have also been developed. In particular are the antireflection coatings of indium tin oxide (ITO) and related compositions applied to glass window panes [33]. Compared with traditional glass melting or ceramic powder methods, the motivation for the sol–gel processing is first and foremost the potentially higher homogeneity and purity and the lower processing temperatures associated with the approach [33].

For the past two decades, the production of bioglass using the sol–gel process has become an interesting research field [33–38]. Sol–gel process involves the synthesis of an inorganic network by mixing the metal alkoxides in solution, followed by hydrolysis, gelation and low-temperature firing to produce a dense and stable glass powder. The network structure of the gel can be modified by controlling hydrolysis and polycondensation reactions during productions. Hence, structural variation can be produced without compositional changes (c.f. Fig. 5.1).

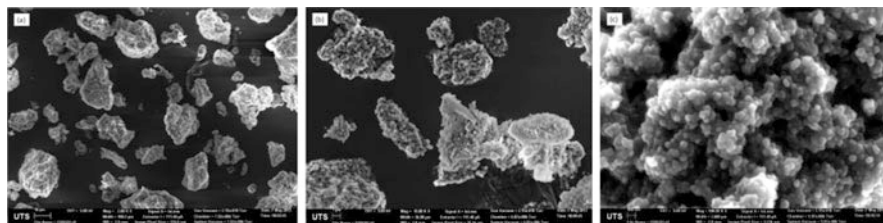


Fig. 5.1 SEM images of sol–gel-derived agglomerated 45S5 Bioglass® nanoparticles at (a) magnification $\times 2$, (b) magnification $\times 10$ and (c) magnification $\times 100$

Using gels, bioactive glasses can be prepared by sintering at temperatures between 600 and 700 °C, which reduces most of the disadvantages of high temperature processing with much better control over purity. Furthermore, by either modifying the microstructure or composition through processing parameters, a broader range as well as better control of bioactivity can be achieved [39].

Li et al. [12] reported that $\text{SiO}_2\text{-CaO-P}_2\text{O}_5$ powders produced by sol-gel are more bioactive than the melt-derived glasses of the same composition. In addition, Sepulveda et al. [40] examined the rates of dissolution and formations of surface layer on sol-gel and melt-derived bioglass, and they noticed the melt-derived 45S5 Bioglass® exhibited a lower rate than the 58S sol-gel bioglass powder. The high bioactivity of the sol-gel-derived materials is related to the microstructural features of the gels, i.e. grain and pore size associated with the large surface area, higher rate of dissolution and negative surface charge [41]. Furthermore, the sol-gel-derived bioactive glass has been proposed as alternative to glasses produced by melt and quenching methods, as they exhibit excellent degradation/resorption properties, more rapid bone bonding, improved homogeneity and purity and higher rate of apatite layer formation [12].

5.5 Biological and Adhesion Properties of Bioactive Glass

A certain compositional range of bioactive glasses containing SiO_2 , Na_2O , CaO and P_2O_5 in specific proportions has demonstrated proper bonding of glass to bone. As mentioned earlier, there are three compositional changes separating them from soda-lime-silica glasses: high Na_2O and CaO content, less than 60 % SiO_2 and a high $\text{CaO/P}_2\text{O}_5$ ratio. Highly reactive surfaces are created from these compositional features when exposed to an aqueous medium. On the other hand, the amount of SiO_2 in bioactive glasses ranging between 45 and 60 % and as a result of repeated hot working can easily lead to problems in the formation of phase separation and crystallisation of the glassy material [7, 42]. Crystallisation of the material can cause a reduction in the rate of bioactivity of the glass [43], and a glassy phase of incontrollable composition is the result of partial crystallisation. Crystallisation of a bioactive glass can be controlled by its chemical composition [44, 45].

It has been reported that a new generation of bioactive glasses in the $\text{Na}_2\text{O-K}_2\text{O-MgO-CaO-B}_2\text{O}_3\text{-P}_2\text{O}_5\text{-SiO}_2$ system can be repeatedly heated without the risk of devitrification [46]. Hence, microspheres can be produced and sintered into porous implants of different shapes and sizes [47]. The porosity of a bioactive glass body does not only noticeably increase the total reacting surface of the glass but also allows a three-dimensional formation of the healing bony tissue. The mechanical strength and porosity of the bioactive glass implants can be controlled with different sintering times and temperatures [48]. To achieve the best mechanical strength of the sintered implant, the glass must retain its amorphous structure during the heat treatment.

5.5.1 *Bioactivity of the Glass*

As mentioned earlier the rates of osteostimulation of various types of bioactive particulates have been quantified by Oonishi et al. that provided the fundamental in vivo comparisons of Class A with Class B bioactive materials [49].

Bioactive glasses in Class A rapidly release soluble silicic acid and subsequently Ca^{2+} , leading to fast precipitation of calcium phosphate on the depleted Si-rich glass surface. On the other hand, bioactive glasses in Class B possess a low network dissolution rate [50, 51]. Glasses with a high rate of dissolution contain less than 55 wt% SiO_2 [51]. It has been shown that the higher the concentration of SiO_2 in the glass, the lower the rate of network dissolution and formation of a Si-rich layer. The rate of Si-rich gel formation on the glass surface is so low when the concentration of SiO_2 exceeds about 60 wt% that it has no practical significance on the bioactivity.

Strnad [52] and, later on, Karlsson and Ylänen [53] provided the reasonable explanations and revealed that the bioactivity of glass is based on the mean number of non-bridging oxygen ions in the silica tetrahedron. The charge of the oxygen ion in the corner is balanced by a network modifier anion which is Na^+ , K^+ or Ca^{2+} instead of sharing a corner with another tetrahedron. Due to a rapid exchange of these anions for H^+ or H_3O^+ from the solution which occurs when exposed to body fluid, a hydration of the gel structure ($=\text{Si}(\text{OH})$) instead of ($=\text{Si}-\text{O Na}^+$, K^+) occurs.

Each silicon in silicate glasses is bonded to four oxygen atoms; hence the number of non-bridging oxygen ions in the tetrahedron can take any value between 0 and 4. When the number is 0, it represents a fully polymerised, three-dimensional network of silica tetrahedral. However, when the number is 4, it signifies a dissolved SiO_4 ion. The number must be greater than 2.6 in order to get bioactivity for a glass with the SiO_2 content of less than 60 wt% (c.f. Fig. 5.2).

Two to three non-bridging oxygen ions will result when the concentration of SiO_2 reaches between 50 and 55 wt% on the surfaces of glasses. This causes hydration of two or three oxygen ions with each silica tetrahedron, namely, forming $\frac{1}{4} \text{Si}(\text{OH})_2$ or $-\text{Si}(\text{OH})_3$. Serra et al. [54, 55] examined the influence of non-bridging oxygen ions on the bioactivity of the glass. The number of non-bridging oxygen ions as a function of SiO_2 and Na_2O content in a glass is presented in Table 5.2.

The silica network is partially broken during the dissolution of the glass; and the SiOH and $\text{Si}(\text{OH})_4$ groups are found on the uppermost layer of the glass. The higher the number of non-bridging oxygen ions in the gel, the higher the bioactivity of the glass. Finally, a totally dissolved monomeric SiO_4 ion is formed if none of the four oxygen ions is bridged. Yet, in this case the concentration of SiO_2 needs to be very low, i.e. less than 40 wt%, and it is questionable whether obtaining a glass phase of this composition is possible [56]. In summary, the crucial factor controlling the bioactivity of a glass is said to be the formation of the hydrated Si-rich gel on the glass surface for which the SiO_2 content should be 50–60 wt%.

Fig. 5.2 Computational atomistic model of 45S5 Bioglass® compiled from a number of solid-state ^{17}O and ^{23}Na MQMAS, ^{29}Si , ^{31}P and ^{23}Na static and MAS NMR spectra simulation studies

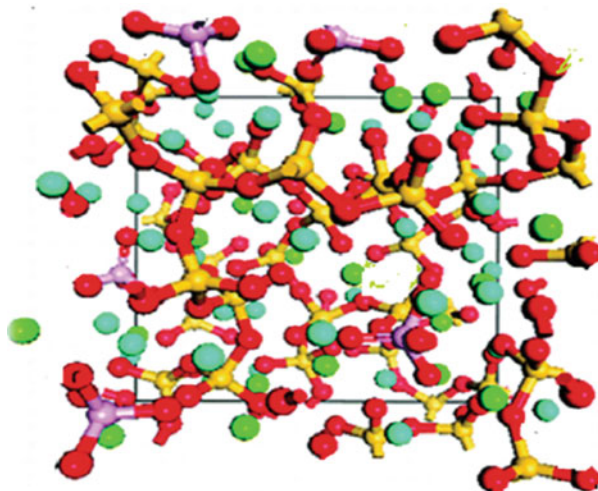


Table 5.2 Number of non-bridging oxygen ions as a function of SiO_2 and Na_2O content in a glass (wt%)

Q^n	SiO_2	Na_2O	Non-bridging oxygen ions
4	100	0	0
3	66.6	33.3	1
2	50	50	2
1	40	60	3
0	33.3	66.6	4

5.5.2 Interfacial Bond Strength of Bioactive Glass and Bone

A number of investigations have reached a conclusion that the interfacial chemical reactions on the surface of bioactive glass result in a unique and firm bonding of bone to the glass implant. Mechanical testing has been used to emphasise the strength of the bonding in which the interfacial strengths of different biomaterials are compared with each other by determination of the push-out to failure forces.

Anderson et al. [57] revealed that true bioactive glasses bond to host bone through a firm layer of calcium phosphate. Nonetheless, glasses with SiO_2 amounts of approximately 60 wt% but containing 42.5 wt% of Al^{3+} showed only a low interfacial strength. Titanium cones were also used as reference, and they discovered the bonding strength of titanium implants was only about one-tenth of that of the bioactive glass implants. They also discovered the glass containing both SiO_2 and Al^{3+} greater than 60 wt% and 2.5 wt%, respectively, showed no bone contact at all.

Niki et al. [58] using the same method demonstrated the similar difference in bonding strength between titanium and bioactive glass implants. The bonding of bioactive glass to bone is based on the formation of a calcium phosphate layer connecting the bioglass implant to the host bone and an even dissolution of

material. It can also be seen by comparing the bonding strength of HAp implants with those of bioactive glass, which depends on the difference in the type of the interfacial bonding between HAp and bone [58–60].

The interfacial bonding strength of bioactive glass to bone has been superior compared with that of HAp in most studies. The principle of categorising the bioactive materials in two distinct classes based on their bioactivity is supported by these findings. The silica-rich gel, in theory, is the weakest point of the interface between bioactive glass and bone. However, according to mechanical testing in most of the cases, the push-out failure by the maximum force occurs by fracture of the bone close to the glass implant [57, 61].

The valuable property of bioactive glasses being able to bond firmly to bone through chemical reactions and to ultimately be replaced by bone allows them to be used for medical applications. The constituents in bioactive glass are more importantly physiological chemicals or minerals found in the body: calcium, phosphorus, oxygen, silicon, sodium, potassium and magnesium. It has been reported that the concentration of the specific elements never increases to a level that could disturb the adjacent tissues during the bonding and formation of bone [60, 62]. On the other hand, the use of bioactive glass as an implant material or in manufacturing medical devices is limited by the mechanical properties of glass.

Consequently, the brittleness of glass implies that they cannot be used in the applications where load-bearing properties are required. Glass can be cast to plates, rods, etc., or it can be formed by sawing or grinding cast rods to rigid medical devices. Alternatively, glass can be used as a filler material in the form of particulate. The use of bioactive glass as a bioactive coating on mechanically stronger implant materials is also an option that has been widely studied.

5.6 Bioactive Glasses from Various Research Groups

In 1969, the concept of a strong bonding by chemical reactions between bone and glass-based synthetic materials occurring on a glass surface was first proposed by Hench et al. [63, 64]. The innovation concerned the chemical reactivity of the surface of a silica-based material, which had the amorphous structure of silicate glass. In the early 1970s, Hench appropriately named this Bioglass® [7]. In fact, bioactive glasses can be thought of as the precursors to all bioactive ceramics. The amorphous structure is a major characteristic of glasses. As stated earlier the structure of silicate glass in general is based on the SiO_4 tetrahedron. The tetrahedra are only linked to the oxygen ions at the corners. In crystalline silica, the tetrahedra are regularly arranged, which is characteristic of all crystalline materials. The tetrahedra in the structure of silica glass are present, but they are no longer regularly arranged; however, as in crystalline quartz, each of the oxygen ions still connects two tetrahedra.

Bioactive glasses bear a resemblance to ordinary soda–lime silica glass. Compared with ordinary glass, there is one main difference with the composition of

bioactive glass. The amount of the network former SiO_2 in ordinary glass is 45 %, and the network modifier component consists mainly of approximately 14 % Na_2O and 10 % CaO , while bioactive glass consists of a significantly lower amount of network former that is replaced primarily by metal oxides or network modifiers. Usually in the bioglass compositions, the Na_2O (or K_2O) content and the ratio of Ca/P are relatively high [65].

Clinically bioactive glasses have been used successfully as bone-filling materials in orthopaedic and dental surgery [66–68]. This stimulates researchers to combine excellent mechanical properties of metals or polymers with a bioactive phase of either particles or fibres to produce a bioactive composite with optimised properties. For most of the bioactive glass compositions, the tensile bending strength is between 40 and 60 MPa with a low modulus of elasticity between 30 and 35 GPa.

5.6.1 *Bioglass®: Hench and Co-workers*

During the last five decades, bioglasses have attracted extensive attention of many researchers because of their unique properties which can easily be tailored by manipulating its compositions. The pioneering work of Hench [68] led to the first development of a bioactive silicate glass called 45S5 Bioglass® with a composition of 45 wt% SiO_2 , 24.5 wt% Na_2O , 24.5 wt% CaO and 6 wt% P_2O_5 . This is also commercially available as Bioglass® which provides an alternative interfacial bonding of an implant with host tissues.

This group of glasses has become known as bioactive glasses based on upon the following definition: a bioactive material is one that elicits a specific biological response at the interface of the material that results in the formation of bond between the host tissues and the material [69]. Many questions regarding its interactions with both soft and hard tissues have been answered over the years by a multidisciplinary team of materials scientists, orthopaedic surgeons, dental researchers, biomechanics experts and biologists. Many clinical Bioglass® devices, such as MEP®, ERMI®, HAPEX®, NovaBone®, NovaMin® and NovaThera®, are being utilised as substitute for bone augmentation and restoration, in orthopaedic, dental and maxillofacial surgery as well as in the field of tissue engineering [34]. They have proven to be efficient and some even outperformed other bioceramic and metal prostheses [66, 68].

Bioactive glasses are a class of biomaterials that bond to both soft and hard living tissues through the formation of a hydroxycarbonate apatite (HCA) layer on their surfaces [3, 7, 70]. Yet, it has been shown that controlled rates of release of ionic dissolution products from bioglass surface are the key phenomenon for bioactivity or bond formation, particularly critical concentrations of soluble silica and calcia ions [71, 72]. Reactions occurring on the surface of the glass lead to the formation of a silica gel layer and subsequent crystallisation of HCA. It was as assumption for many years that formation of biologically active HCA surface reaction layer was the critical requirement for bioactive behaviour [73–

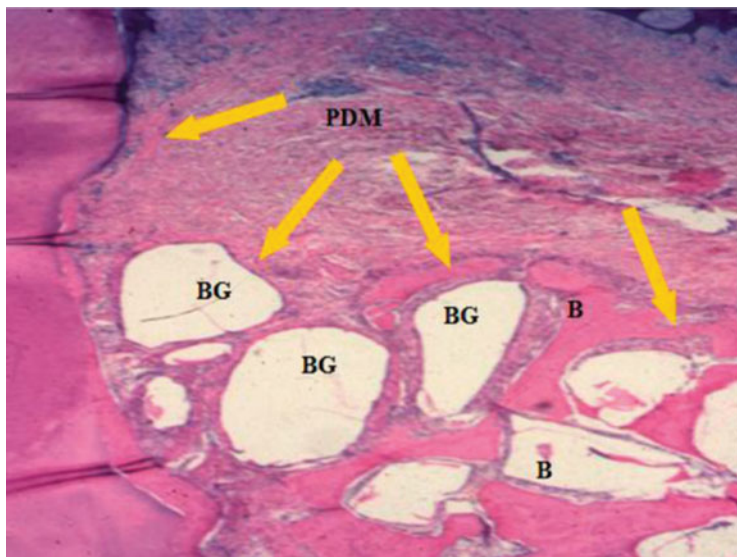


Fig. 5.3 Bioactive glass (BG) particulate used to enhance bone [B] formation around the tooth [T] and thereby restoring its function following treatment of periodontal, gum, disease in a Patas monkey periodontal defect model. The mineralised collagen is shown to surround the bioactive glass particles forming a regenerated bone structure. The periodontal ligament-labelled PDM that is stable above the regenerated bone. (Magnification 20×) (Photo courtesy of Dr. June Wilson [124])

75]. Numerous investigations have shown the formation of a surface HCA layer to be useful but not critical stage of reaction for bone regeneration [71, 76, 77]. As stated above, the key phenomenon is the controlled rates of release of ionic dissolution products, especially critical concentrations of soluble silica and calcium ions. Osteostimulation occurs only when the ions are at a particular ratio of ions and at a particular concentration range of 15–30 ppm Si and 60–90 ppm Ca.

The rate of bone bonding is dependent on the composition of the material. Compared with other glass compositions, a faster rate of bone bonding as well as bonding to soft tissues can be achieved when the SiO_2 content is less than 52% by weight [60]. Rapid regeneration of trabecular bone with an amount, architecture and biomechanical quality of bone that matches that originally present in the site can be produced from compositions such as 45S5 Bioglass® with high rates of bioactivity [49, 51, 60, 65, 78]. The rapid regeneration of bone is the result of a combination of processes referred to as osteostimulation and osteoconduction (Fig. 5.3).

5.6.2 Åbo Akademi: Bioactive Glass from Finland

The research at the Åbo Akademi University initiated in the early 1980s when Yli-Urpo, Ylänen and Andersson et al. [9, 42] examined the glass transition temperature and biological behaviour of glasses in or near the bioactive compositional region in the system $\text{SiO}_2\text{-Na}_2\text{O-CaO-P}_2\text{O}_5\text{-Al}_2\text{O}_3\text{-B}_2\text{O}_3$. Later, an alumina-free bioactive glass was developed with a given composition of 53 % SiO_2 , 23 % Na_2O , 20 % CaO and 4 % P_2O_5 , and it is available as S53P4 [79].

Contributions of the group at the early stages were on the chemistry and viscosity relationship of a range of bioglasses. An extensive study was conducted by Brink [44, 80, 81] on the viscosity temperature dependence and biological activity of several different glass compositions in the $\text{SiO}_2\text{-Na}_2\text{O-CaO-P}_2\text{O}_5\text{-Al}_2\text{O}_3\text{-B}_2\text{O}_3$ system. She discovered that certain glass compositions possess a wider working range compared to conventional bioactive glasses. When the SiO_2 composition is too low, bioactivity can be obtained but the glass will crystallise, and this restricts their use only in the forms of crushed particles. On the other hand, when the SiO_2 content increases to 53–56 wt%, the working range is widened, and crystallisation of devitrification can be avoided [80]. The working range of the glasses examined was also influenced by the amounts of alkali and alkali earth oxides present. The larger working range allows the expanded medical use of the bioactive glasses due to the possibility, for instance, of fibre spinning and flame spraying into microspheres [44, 80].

The development of third generation of bioactive glasses denoted 13–93 has enabled spinning of high-quality thin bioactive glass fibres. From these fibres, a variety of bioactive glass fabrics can be manufactured. Furthermore, an impulse laser beam can be used to melt a fine powder made from the new bioactive glass. As a result, a glass coating on a titanium implant can be produced relatively easily. This coating consists of very small glass droplets firmly attached to the titanium. The glass shows excellent bioactivity in spite of the repeated high temperature procedures involved in the process [82, 83].

5.6.3 A-W Bioactive Glass from Japan

Various research groups in the 1980s and 1990s such as Gross et al., Bromer et al., Kitsugi et al., Nakamura and Yamamuro and Kokubo et al. [50, 84–93] introduced a range of phosphate-based glass and glass ceramics. Kokubo and Nakamura and their colleagues steadily heated glass powder in the $\text{MgO-CaO-P}_2\text{O}_5\text{-CaF}_2\text{-SiO}_2$ system up to 1050 °C. Consequently, a material consisting of crystalline wollastonite (CaO.SiO_2) and oxyfluorapatite ($\text{Ca}_{10}(\text{PO}_4)_6(\text{O},\text{F}_2)$) within a homogenous glassy phase was produced [84, 85]. As mentioned earlier, this bioactive glass ceramic was referred to as A-W, derived from the names of the crystalline phases.

The bioactive A-W glass ceramic (A-W-GC) is a two-phase structure and reported to resemble the composite structure of bone, which can be machined into various shapes with diamond tools. The bending strength of the A-W-GC is almost double that of dense HAp and even higher than that of human cortical bone [86]. Other groups of researchers introduced different glass ceramics (Ceravitals, Bioverit I-III, Implants, BAS-O) during the 1970s and 1980s [87–90]. All these glass ceramics consist of apatite crystals or apatite/wollastonite/phlogopite crystals within a homogenous glassy matrix. It was reported that A-W-GC elicits the highest mechanical strength and bioactivity (Class A) of all the glass ceramics [11, 50].

The dissolution of calcium from wollastonite or the glassy phase is believed to be the reason for the bioactivity of glass ceramic. The bonding between glass ceramic and bone is formed by the precipitation of the dissolved calcium from the material and phosphate originating from the body fluid [91, 92]. It was believed that the nucleation sites for the formation of calcium phosphate are provided by the silicate ions [85, 91]. Different calcium contents in the materials have an effect on the bioactivities of the glass ceramics. Rigid non-degradable bioactive glass ceramics can be produced with various methods for different applications [92]. Their applications include orthopaedics, odontology and in head and neck surgery as prostheses, spacers or granulated defect fillers.

Questions were raised regarding their appropriateness as a coating material with the development of next-generation bioactive glass ceramics. Using various techniques, the bioactive glass ceramics was fixed on load-bearing implants in early experiments [93, 94]. Takatsuka et al. [95] modified A-W-GC in 1993 and was successfully sintered on Ti-alloy due to their similar coefficients of thermal expansion. The bioactive coating showed the bonding strengths comparable with A-W-GC implants, which were used as the control. It has also been demonstrated that A-W-GC coatings have encouraging results in various other investigations [96–98]. It is believed that the glassy part of the material is mainly responsible for the ion dissolution from the material as stated earlier and, subsequently, the chemical reactions occurring on the material surface. Thus, one part of the coating substance is resorbed, and changes in the material's mechanical properties occur.

Investigation conducted by Kitsugi et al. [98] suggested that the use of A-W-GC-coated metal implants should be limited to short-term implantation only, due to the risk of fracture of the coating layer. Although successfully commercialised and clinically applied, currently no commercial production of A-W glass is available.

5.6.4 Silicate Bioactive Glass

One of the important trace elements in the human body is silicon (Si), and they are found at a level of 100 ppm in the bone and 200–550 ppm bound to extracellular matrix compounds [99]. The location of Si was reported to be at active calcification sites in the bones and directly involves in the mineralisation process of bone growth [100].

In the past decade, stimulated by the Si function in human body and the bioactive compositions of silicate-based bioglass, a new family of bioactive silicate ceramics has been developed with a wide range composition. It was discovered that bioactive silicate ceramics with specific compositions could significantly stimulate in vitro osteogenic differentiation for several stem cells and in vivo osteogenesis and angiogenesis. Bioactive silicate ceramics also possess distinct osteostimulation properties.

5.6.5 Bioactive Glass Composites

The purpose of bioactive glass composites is to combine and optimise the bioactive phase of either glass particles or fibres with the excellent mechanical properties of metals or polymers to improve properties such as flexibility and capacity to stand to deformation under loads. Numerous bioglass composites have been developed and tested for such biomedical applications as bone regeneration matrix and scaffolds [101–105], dental implant [106] and drug delivery systems [107–109].

An improvement in the bioactivity, degradation kinetics, mechanical properties and osteoblast responses has been reported by the presence of bioactive glasses in the composites compared to the pure bioglass or polymer [101, 110, 111]. For mechanical properties, such factors as the bioglass content and the dispersion of bioglass particles in the polymeric matrix are solely responsible for its improvement. As the amount of bioactive glass particles increases, the mechanical properties of the composites increase until the amount reaches 30 % where the mechanical properties begin to drop. Nonetheless, the optimal bioglass content in the composites is dependent on the applications of the composite materials [112].

5.7 Applications of Bioactive Glasses and Glass Ceramics

5.7.1 Ear, Nose, Throat and Maxillofacial Applications

Table 5.3 shows the compositions of the first bioactive glass, Bioglass®, and S53P4, both of which have been widely used for clinical applications. The glass can be cast into shaped implants for use as small medical devices in places subject to only minor mechanical loading. The glass is also relatively soft which makes it ideal for microsurgical drilling techniques [113].

Bioglass® has been used as cone-shaped implants to fill defects in the mandible and maxilla as well as to replace small bones in the middle ear. It also elicits a property of bonding to soft tissue, which has opened new possibilities for wider applications, such as, in ear, nose and throat surgery. Various electronic components are used within appropriate devices in the treatment of profound deafness.

Table 5.3 Compositions of Bioglass® and S53P4 (wt%)

Component	Bioglass®	S53P4
SiO ₂	45	53
Na ₂ O	24.5	23
CaO	24.5	20
P ₂ O ₅	6	4

Electrodes attached to the electronic devices outside and inside the middle ear are coated with Bioglass® [113]. The device is inserted so that a part is in contact with the bone, resulting in a firm anchoring. The other part of the bioactive glass-coated anchor passes through the eardrum and bonds to the soft tissue, thus providing a seal between the inner and outer ear.

The concept of filling a hole in the mandible after tooth extraction in an attempt to prevent resorption was introduced by Stanley et al. [114]. For this procedure, injection moulding was used to produce conical implants. A mating drill bit is used to prepare the bone for the implant to achieve the best possible fit of the conical implant.

Solid-shaped bioactive glass of a different composition (S53P4) has also been used in the treatment of facial injuries to replace the bone that supports the eye [115, 116]. The clinical results of Aitasalo et al. [116] suggested that thin, slowly resorbable bioactive glass provides a promising option for the reconstruction of orbital floor defects.

In odontology, bioactive glass particles are widely used to fill defects associated with periodontal disease, for instance, the loss of the bone surrounding teeth [75]. Some recent studies show promising results from using crushed bioactive glass or paste as obliteration material in frontal sinusitis and in special types of rhinitis [116–121].

The findings from Stoor et al. [120–122] suggested that the encouraging results of using bioactive glass crush in ear, nose and throat surgery are partially because of the antibacterial effects of bioactive glass paste on oral microorganisms and bacterial infections [122]. Sintering of bioactive glass microspheres enables the manufacture of rigid porous bioactive glass bodies. The rate of bone ingrowth into the three-dimensional porosity of the bioactive glass material is significantly higher compared with the similar porosity of porous titanium [123].

5.7.2 Treatment for Dentin Hypersensitivity

During the past decade, a number of consumer and professional products containing bioactive glass (45S5 Bioglass®) have been introduced into the market. The first product developed by NovaMin® Technologies was Oravive®, a daily use, fluoride-free dentifrice that contains 5% of the bioactive glass ingredient NovaMin®. This product was cleared for use by FDA through a 510(k) product as a medical device for the rapid and continual reduction of tooth sensitivity

through physical tubule occlusion. Today, CSPS has been formulated into over 15 products and is sold in over 20 countries, including the USA, Canada, India, China and a number of countries in Europe. These products have proven to be highly effective and the CSPS material has an unparalleled safety profile. Sensodyne Repair and Protect, manufactured by GlaxoSmithKline (GSK), is an over-the-counter dentifrice that provides NovaMin® technology to the consumer in many parts of the world [124].

5.7.3 Bone Graft Applications

Solid-shaped bioactive glass implants have been investigated using animal models for the reconstruction of deep osteochondral defects (joint surface defects, which penetrate the bone under the joint cartilage) [125–127]. Based on these studies, the bioactive glass implants bonded to the bone, but minimal, or at best moderate, rate of hyaline-like cartilage formation was observed. The use of porous bioactive glass implants resulted in more promising results [47].

Critical size defect can be defined as the smallest size defect that cannot heal spontaneously during the lifetime of a clinical subject. A number of clinical trials showed that an 8-mm diameter defect created in the calvaria of Sprague Dawley rats did not heal after a 12-week period. In contrast, many long bones contain a primary nutrient artery, whereas no primary nutrient artery exists in human calvaria.

The results of Lee et al. [128] have indicated that calcium phosphate glass (bioglass) can affect the differentiation and calcification of the pre-osteoblastic (MC3T3-E1) cells in vitro and promote new bone formation in the calvarial defects. Lim et al. [129] examined the osteoconductive effect of newly developed calcium phosphate glass cement (CPGC) in rabbit calvarial defects. They noticed bone formation rate of CPGC is initially slow, but increases at a specific time, showing the possibility of greater bone formation with time. The resorption rate of CPGC was greater than biphasic calcium phosphate.

It has been reported that by using bioactive glass as granules, bonding can be improved due to the factors such as the chemistry associated with the bioactivity, the reactivity caused by an increase in surface area and the method of application [51, 130–132]. They have also been documented to provide a promising option that can be utilised alone as a filler material to fill the gap around the implants or in bone defects [133–135]. However, according to Virolainen et al. [136], the bone-forming capacity of bioactive glass particulate seems to be lower compared with an autogenous bone graft.

Oonishi et al. used a critical-size defect model in a rabbit femoral condyle to quantify the histological sequence of osteostimulation by 45S5 Bioglass® particulate [49]. In comparison with synthetic HAp particles or bioactive A-W glass-ceramic particles, the studies on bioglass showed that there are both more rapid bone formation in the presence of the osteostimulation particles and regeneration of

a more highly mineralised quality of bone in the defect. The rate of bone regeneration in the Oonishi model is related to the rate of release of the soluble Si and Ca ions from the particulates tested. A rapid rate of release is necessary for rapid bone regeneration and optimal fill of the defect by regenerated trabecular bone.

5.7.4 *Bioglasses in In Situ Radiotherapy and Hyperthermia*

In the treatment of cancer, one of the most common approaches is the removal of the diseased parts. However, recovery or return of full function is unfortunately seldom achieved. The mid-1980s saw the introduction of non-invasive treatment techniques in which only the cancer cells are destroyed.

In 1987, microspheres of $17Y_2O_3-19Al_2O_3-64SiO_2$ (mol%) glass with a diameter of 20–30 μm were shown to be effective for in situ radiotherapy of liver cancer [137, 138]. Using neutron bombardment, the nonradioactive ^{89}Y in this glass can be activated to ^{90}Y , which is a β -emitter with a half-life of 64.1 h. The microspheres are usually injected into diseased liver through the hepatic artery and entrapped in small blood vessels, which block the blood supply to the cancer and directly irradiate the cancer with β -rays. As the β -ray transmits living tissue only 2.5 mm in diameter and the glass microspheres have high chemical durability, the surrounding normal tissue is hardly damaged by the β -rays.

These glass microspheres are commercially available and already used clinically in Australia, Canada and the USA. However, since they are produced by conventional glass melting techniques, the content of Y_2O_3 in the microsphere is limited to only 17 mole%. Pure Y_2O_3 polycrystalline microspheres with a diameter of 20–30 μm was successfully prepared by Kawashita et al. [138, 139] using a high-frequency induction thermal plasma melting technique. It was reported that they observed higher chemical durability than the Y_2O_3 -containing glass microspheres. It was further reported that these ceramic microspheres are more effective for in situ radiotherapy of cancer.

Oxygen is known to be poorly supplied to cancerous cells to produce lactic acid and hence can be destroyed around 431 °C, whereas the normal living cells can be kept alive even around 481 °C. If ferri- or ferromagnetic materials are implanted around cancers and placed under an alternating magnetic field, it is expected that locally heated cancer cells can be destroyed by magnetic hysteresis loss of the ferri- or ferromagnetic materials.

Ferrimagnetic glass-ceramic compositions containing 36 wt% of magnetite (Fe_3O_4) nanoparticles (200 nm) within a $CaO-SiO_2$ matrix was prepared by Kawashita et al. [140, 141]. It was reported that cancerous cells in the medullary canal of a rabbit tibia were completely destroyed when this glass ceramic was inserted into the tibia and placed under an alternating magnetic field of 300 Oe with 100 kHz [140, 141]. Due to the size of the cancer cells, this kind of invasion treatment cannot be used on humans. In the case of humans, ferri- or ferromagnetic microspheres of 20–30 μm in diameter must be injected into the cancer through

blood vessels similar to the radioactive microspheres. For this purpose, the heat-generating efficiency of the ferrimagnetic material must be further increased.

It has been reported that microspheres of 20–30 μm in diameter, in which the number of layers of magnetite particles is of 50 nm, were deposited on silica microspheres. The technique involved deposition of $\text{FeO}(\text{OH})$ from a solution and its subsequent transformation into Fe_3O_4 by a specific heat treatment at 600 $^\circ\text{C}$ under $\text{CO}_2\text{--H}_2$ gas atmosphere [140, 141]. The heat-generating efficiency of this material was reported to be about four times that of the glass ceramic described above.

5.8 Concluding Remarks

As discussed in this chapter, bioactive glasses and glass ceramics are strongly influenced by the synthesis methods employed, the chemistry and the compounds used and any other thermal processes used. All of these factors contribute to their final structure and hence to their long-term performance as bioactive materials. In the early 1970s, bioceramics were employed to perform biologically inert roles, such as providing parts for bone replacement. The realisation that cells and tissues in the body perform many other vital regulatory and metabolic roles has highlighted the limitations of inert synthetic materials as tissue substitutes. The demands placed on bioceramics have changed from maintaining an essentially physical function without eliciting a host response to providing a more integrated interaction with the host, which has been accompanied by increasing the demands on medical devices to improve the quality of life, as well as to extend its longevity.

Bioglasses can be employed as body-interactive materials, helping the body to heal or promoting regeneration of tissues, thus restoring physiological functions. This approach could be further explored in the development of next-generation bioglasses incorporating biogenic materials and specific drugs with a widened range of applications. Recently, the tissue engineering field has been directed to take advantage of the combined use of living cells and three-dimensional (3D) ceramic or bioglass structures to engineer neotissue to a patient's damaged site. Currently feasible and productive strategies have been aimed at combining a relatively traditional approach such as bioglass implants with the acquired knowledge applied to the field of cell growth and differentiation of osteogenic cells.

Bonding of glass ceramic to bone has been observed to occur between 2 weeks and 2 months after implantation. Clinical studies are promising and their use in the orthopaedic field is increasing. Glass ceramics are known to have high bending and compressive strength, and it has been reported that they could be used in the reconstruction of acetabular defects. Nevertheless, the challenge of providing safe and efficacious glass and glass ceramics with an acceptable biocompatibility level and the required properties remains. As the field of biomaterials finds increasing applications in cellular and tissue engineering, it will continue to be used in new ways as part of the most innovative therapeutic strategies.

References

1. Ben-Nissan B, Ylänen HO (2006) Bioactive glasses and glass ceramics, Wiley encyclopedia of biomedical engineering. Wiley, Hoboken
2. McMillan PW (1964) Glass ceramics. Academic, London
3. Hench LL, Wilson J (1984) Surface active materials. *Science* 226:630–636
4. Hench LL (1988) Bioactive ceramics. In: Ducheyne P, Lemons JE (eds) *Bioceramics: materials characteristics vs. in vivo behavior*. New York Academy of Science, New York
5. Kokubo T (1991) Recent progress in glass-based materials for biomedical applications. *J Ceram Soc Japan* 99:965–973
6. Kokubo T (1990) Novel biomaterials derived from glasses. In: Soga W, Kato A (eds) *Ceramics: towards the 21st century*. *J Ceram Soc Japan*, pp. 500–518.
7. Hench LL, Splinter RJ, Allen WC et al (1972) Bonding mechanisms at the interface of ceramic prosthetic materials. *J Biomed Mater Res Symp* 2:117–141
8. Vrouwenvelder WCA, Groot CG, de Groot K (1993) Histological and biochemical evaluation of osteoblasts cultured on bioactive glass, hydroxylapatite, titanium alloy, and stainless steel. *J Biomed Mater Res* 27:465–475
9. Andersson OH, Kangasniemi I (1991) Calcium phosphate formation at the surface of bioactive glass in vitro. *J Biomed Mater Res* 25:1019–1030
10. Li P, Yang Q, Zhang F et al (1992) The effect of residual glassy phase in a bioactive glass-ceramic on the formation of its surface apatite layer in vitro. *J Mater Sci: Mater Med* 3:452–456
11. Kokubo T, Shigematsu M, Nagashima Y et al (1982) Apatite-wollastonite containing glass-ceramic for prosthetic application. *Bull Inst Chem Res* 60:260–268
12. Li R, Clark AE, Hench LL (1991) An investigation of bioactive glass powders by sol-gel processing. *J Appl Biomater* 2:231–239
13. Arriagada FJ, Osseo-Asare K (1999) Synthesis of nanosize silica in a nonionic water-in-oil microemulsion: effects of the water/surfactant molar ratio and ammonia concentration. *J Colloid Interf Sci* 211:210–220
14. Singh S, Bhardwaj P, Singh V et al (2008) Synthesis of nanocrystalline calcium phosphate in microemulsion-effect of nature of surfactants. *J Colloid Interf Sci* 319:322–329
15. Karagiozov C, Momchilova D (2005) Synthesis of nano-sized particles from metal carbonates by the method of reversed mycelles. *Chem Eng Process* 44:115–119
16. Sun Y, Guo G, Tao D et al (2007) Reverse microemulsion-directed synthesis of hydroxyapatite nanoparticles under hydrothermal conditions. *J Phys Chem Solids* 68:373–377
17. Boccaccini AR, Erol M, Stark WJ et al (2010) Polymer/bioactive glass nanocomposites for biomedical applications: A review. *Compos Sci Technol* 70:1764–1776
18. Lim GK, Wang J, Ng SC et al (1996) Processing of fine hydroxyapatite powders via an inverse microemulsion route. *Mater Lett* 28:431–436
19. Lim GK, Wang J, Ng SC et al (1999) Formation of nanocrystalline hydroxyapatite in nonionic surfactant emulsions. *Langmuir* 15:7472–7477
20. Quintero F, Mann AB, Pou J et al (2007) Rapid production of ultralong amorphous ceramic nanofibers by laser spinning. *Appl Phys Lett* 90:153109–3
21. Quintero F, Pou J, Lusquiños F et al (2007) Experimental analysis of the production of micro- and nanofibres by Laser Spinning. *Appl Surf Sci* 254:1042–1047
22. Quintero F, Dieste O, Pou J et al (2009) On the conditions to produce micro- and nanofibres by laser spinning. *J Phys D: Appl Phys* 42:1–10
23. Quintero F, Pou J, Comesaña R et al (2009) Laser spinning of bioactive glass nanofibers. *Adv Funct Mater* 19:3084–3090
24. Pratsinis SE (1998) Flame aerosol synthesis of ceramic powders. *Prog Energ Combust Sci* 24:197–219
25. Stark WJ, Madler L, Maciejewski M et al (2003) Flame synthesis of nanocrystalline ceria-zirconia: effect of carrier liquid. *Chem Comm* 5:588–589

26. Madler L, Stark WJ, Pratsinis SE (2002) Flame-made ceria nanoparticles. *J Mater Res* 17:1356–1362
27. Athanassiou EK, Grass RN, Stark WJ (2010) Chemical aerosol engineering as a novel tool for material science: from oxides to salt and metal nanoparticles. *Aerosol Sci Tech* 44:161–172
28. Vollenweider M, Brunner TJ, Knecht S et al (2007) Remineralization of human dentin using ultrafine bioactive glass particles. *Acta Biomater* 3:936–943
29. Mohn D, Zehnder M, Imfeld T et al (2010) Radio-opaque nanosized bioactive glass for potential root canal application: evaluation of radiopacity, bioactivity and alkaline capacity. *Int Endod J* 43:210–217
30. Ebelmen M (1846) On the synthesis of silica gels from alkoxides. *Annales de chimie et de physique* 16:129
31. Graham T (1864) On the properties of silicic acid and other analogous colloidal substances. *J Chem Soc* 17:318–327
32. Liesegang RE (1896) Ueber einige Eigenschaften von Gallerten. *Naturwissenschaftliche Wochenschrift* 11:353–362
33. Hench LL, West JK (1990) The sol-gel process. *Chem Rev* 90:33–72
34. Cacciotti I, Lombardi M, Bianco A et al (2012) Sol-gel derived 45S5 bioglass: synthesis, microstructural evolution and thermal behaviour. *J Mater Sci Mater Med* 23:1849–1866
35. Chen QZ, Thouas GA (2011) Fabrication and characterization of sol-gel derived 45S5 Bioglass (R)-ceramic scaffolds. *Acta Biomater* 7:3616–3626
36. Saboori A, Rabiee M, Mutarzadeh F et al (2009) Synthesis, characterization and in vitro bioactivity of sol-gel-derived $\text{SiO}_2\text{-CaO-P}_2\text{O}_5\text{-MgO}$ bioglass. *Mat Sci Eng C-Bio S* 29:335–340
37. Jie Q, Lin KL, Zhong JP et al (2004) Preparation of macroporous sol-gel bioglass using PVA particles as pore former. *J Sol-Gel Sci Technol* 30:49–61
38. Greenspan DC, Zhong JP, Chen XF et al (1997) The evaluation of degradability of melt and sol-gel derived Bioglass (R) in-vitro. *Bioceramics* 10:391–394
39. Sakka S (1985) Glasses and glass-ceramics from gels. *J Non-Cryst Solids* 73:651
40. Sepulveda P, Jones JR, Hench LL (2001) Characterization of melt-derived 45S5 and sol-gel-derived 58S bioactive glasses. *J Biomed Mater Res* 58:734–740
41. Pereira MM, Hench LL (1996) Mechanisms of hydroxyapatite formation on porous gel-silica substrates. *J Sol-Gel Sci Technol* 7:59–68
42. Andersson ÖH (1992) Glass transition temperature of glasses in the $\text{SiO}_2\text{-Na}_2\text{O-CaO-P}_2\text{O}_5\text{-Al}_2\text{O}_3\text{-B}_2\text{O}_3$ system. *J Mat Sci Mat Med* 3:326–328
43. Peitl Filho O, LaTorre GP, Hench LL (1996) Effect of crystallization on apatite-layer formation of bioactive glass 45S5. *J Biomed Mater Res* 30:509–514
44. Brink M (1997) Bioactive glasses with a large working range. Dissertation, Åbo Akademi University
45. Hayakawa S, Tsuru K, Ohtsuki C (1999) Mechanism of apatite formation on a sodium silicate glass in a simulated body fluid. *J Am Ceram Soc* 82:2155–2160
46. Arstila HE, Vedel L, Hupa L et al (2004) Measuring the devitrification of bioactive glasses. *Key Eng Mater* 254–256:67–70
47. Ylänen HO, Helminen T, Helminen A et al (1999) Porous bioactive glass matrix in reconstruction of articular osteochondral defects. *Ann Chir Gyn* 83:237–245
48. Fröberg L, Hupa L, Hupa M (2004) Porous bioactive glasses with controlled mechanical strength. *Key Eng Mater* 254–256:973–976
49. Oonishi H, Hench LL, Wilson J et al (2000) Quantitative comparison of bone growth behaviour in granules in bioglass®, A-W glass-ceramic, and hydroxyapatite. *J Biomed Mater Res* 51:37–46
50. Hench LL (1997) Glass and genes: a forecast to future. *Glastech Ber Glass Sci Technol* 70:439–452
51. Hench LL (1998) *Bioceramics*. *J Am Ceram Soc* 81:1705–1727
52. Strnad Z (1992) Role of the glass phase in bioactive glass-ceramic. *Biomaterials* 13:317–321

53. Karlsson KH, Ylänen HO (1998) Porous bone implants. In: Vincenzini P (ed) *Materials in clinical applications, advances in science and technology* 28. 9th Cimtec-World Forum on New Materials, Florence
54. Serra J, González P, Liste S et al (2002) Influence of the non-bridging oxygen groups on the bioactivity of silicate glasses. *J Mater Sci Mater Med* 13:1221–1225
55. Serra J, González P, Liste S et al (2003) FTIR and XPS studies of bioactive silica based glasses. *J Noncryst Solids* 332:20–27
56. Ducheyne P, Brown S, Blumenthal N et al (1988) Bioactive glasses, aluminum oxide, and titanium. Ion transport phenomena and surface analysis. *Ann NY Acad Sci* 523:257–261
57. Andersson ÖH, Karlsson KH, Kangasniemi K (1990) Calcium-phosphate formation at the surface of bioactive glass in vivo. *J. Non-Cryst Solids* 119:290–296
58. Niki M, Ito G, Matsuda T et al (1991) Comparative push-out data of bioactive and non-bioactive materials of similar rugosity. In: Davies JE (ed) *Bone-material interface*. University of Toronto Press, Toronto
59. Fujii T, Ogino M (1984) Difference of bone bonding behavior among surface active glasses and sintered apatite. *J Biomed Mater Res* 18:845–859
60. Wilson J, Pigott GH, Schoen FJ et al (1981) Toxicology and biocompatibility of bioglasses. *J Biomed Mater Res* 15:805–817
61. LeGeros RZ, LeGeros JP (1993) Dense hydroxyapatite. In: Hench LL, Wilson J (eds) *An introduction to bioceramics*, vol 1. World Scientific, Singapore
62. Lai W, Ducheyne P, Garino J (1998) Removal pathway of silicon released from bioactive glass granules in vivo. In: LeGeros RZ, LeGeros JP (eds) *Bioceramics*, vol 11. World Scientific, New York
63. Hench LL, West JK (1996) Biological applications of bioactive glasses. *Life Chem Rep* 13:187–241
64. Hench LL, Paschall HA (1973) Direct chemical bond of bioactive glass-ceramic materials to bone and muscle. *J Biomed Mater Res* 7:25–42
65. Hench LL (1991) Bioceramics: from concept to clinic. *J Am Ceram Soc* 74:1487–1510
66. Merwin GE (1990) Review of bioactive materials for otologic and maxillofacial applications. In: Yamamuro T, Hench LL, Wilson J (eds) *Handbook of bioactive ceramics*, vol 1. CRC Press, Florida
67. Cai YR, Zhou L (2005) Effect of thermal treatment on the microstructure and mechanical properties of gel-derived bioglasses. *Mater Chem Phys* 94:283–287
68. Hench LL (2006) The story of bioglass. *J Mater Sci Mater Med* 14:967–978
69. Hench LL, Andersson ÖH (1993) Bioactive glasses. In: Hench LL, Wilson J (eds) *An introduction to bioceramics*, vol 1. World Scientific, Singapore
70. Gross U, Kinne R, Schmitz HJ et al (1988) The response of bone to surface active glass/glass-ceramics. *CRC Crit Rev Biocomput* 4:2–15
71. Hench LL, Polak JM, Xynos ID et al (2000) Bioactive materials to control cell cycle. *Mater Res Innov* 3:313–323
72. Ylänen HO, Karlsson KH, Itälä A et al (2000) Effect of immersion in SBF on porous bioactive bodies made by sintering bioactive glass microspheres. *J Noncryst Solids* 275:107–115
73. Cao WP, Hench LL (1996) Bioactive materials. *Ceram Int* 22:493–507
74. Hench LL (1998) Bioactive materials: the potential for tissue regeneration. *J Biomed Mater Res* 41:511–518
75. Hench LL (1998) Bioceramics, a clinical success. *Am Ceram Soc Bull* 77:67–74
76. Loty C, Sautier J, Loty S et al (1998) Bioglass(R) promoted differentiation of cultured rat osteoblasts and created a template for bone formation. In: LeGeros RZ, LeGeros JP (eds) *Bioceramics*, vol 11. World Scientific, New York
77. Xynos ID, Hukkanen MVJ, Batten JJ et al (2000) Bioglass (R) 45S5 stimulates osteoblast turnover and enhances bone formation in vitro: Implications and applications for bone tissue engineering. *Calcified Tissue Int* 67:321–329

78. Hench LL, Hench JW, Greenspan DC (2004) Bioglass: a short history and bibliography. *J Aust Ceram Soc* 40:1–42
79. Andersson Ö (1990) The bioactivity of silicate glass. Dissertation. Åbo Akademi University
80. Niemelä T (2010) Self-reinforced bioceramic and polylactide based composites. Dissertation. Tampere University of Technology
81. Brink M (1997) The influence of alkali and alkaline earths on the working range for bioactive glasses. *J Biomed Mater Res* 36:109–117
82. Moritz N, Vedel E, Ylänen H et al (2003) Creation of bioactive glass coating on titanium by local laser irradiation, Part I: Optimisation of the processing parameters. *Key Eng Mater* 240–242:221–224
83. Vedel E, Moritz N, Ylänen H et al (2003) Creation of bioactive glass coating on titanium by local laser irradiation, Part II: Effect of the irradiation on the bioactivity of the glass. *Key Eng Mater* 240–242:225–228
84. Kokubo T, Ito S, Sakka S et al (1986) Formation of high-strength bioactive glass-ceramic in the system MgO-CaO-SiO₂-P₂O₅. *J Mater Sci* 21:536–540
85. Nakamura T, Yamamuro T (1993) Development of a bioactive ceramic, A/W glass-ceramic. In: Ducheyne P, Christiansen D (eds) *Bioceramics*, vol 6. Butterworth-Heinemann, Oxford
86. Kokubo T (1992) Bioactivity of glasses and glass-ceramics. In: Ducheyne P, Kokubo T, Van Blitterswijk CA (eds) *Bone-bonding*. Reed Healthcare Communications, Leiderdorp
87. Blencké BA, Brömer H, Deutscher KK (1978) Compatibility and long-term stability of glass-ceramic implants. *J Biomed Mater Res* 12:307–316
88. Vogel W, Höland W (1990) Development, structure, properties and application of glass-ceramics for medicine. *J Non-Cryst Solids* 123:349–353
89. Berger G, Sauer R, Steinborn G et al (1989) Clinical application of surface reactive apatite/wollastonite containing glass-ceramics. In: Mazurin OV (ed) *Proceedings of XV international congress on glass*. Leningrad, Nauka.
90. Pavek V, Novak Z, Strnad Z et al (1994) Clinical application of bioactive glass-ceramic BAS-O for filling cyst cavities in stomatology. *Biomaterials* 15:353–358
91. Kokubo T (1990) Surface chemistry of bioactive glass-ceramics. *J Non-Cryst Solids* 120:138–151
92. Kokubo T (1991) Bioactive glass-ceramics: properties and applications. *Biomaterials* 12:155–163
93. Strunz V, Bunte M, Gross UM et al (1978) Coating of metal implants with the bioactive glass-ceramics. *Ceravital Dtsch Zahnarztl Z* 33:862–865
94. Fuchs GA, Deutscher K (1981) Glass-ceramic coated implants. A simple model for a loaded hip prosthesis with a bioactive interface. *Arch Orthop Trauma Surg* 98:121–126
95. Takatsuka K, Yamamuro T, Kitsugi T et al (1993) A new bioactive glass-ceramic as a coating material on titanium alloy. *J Appl Biomater* 4:317–329
96. Ido K, Matsuda Y, Yamamuro T et al (1993) Cementless total hip replacement. Bioactive glass ceramic coating studied in dogs. *Acta Orthop Scand* 64:607–612
97. Li ZL, Kitsugi T, Yamamuro T et al (1995) Bone-bonding behavior under load-bearing conditions of an alumina ceramic implant incorporating beads coated with glass-ceramic containing apatite and wollastonite. *J Biomed Mater Res* 29:1081–1088
98. Kitsugi T, Nakamura T, Oka M et al (1996) Bone-bonding behavior of plasma-sprayed coatings of Bioglass[®], AW-glass ceramic, and tricalcium phosphate on titanium alloy. *J Biomed Mater Res* 30:261–269
99. Schwarz K (1973) A bound form of silicon in glycosaminoglycans and polyuronides. *Proc Natl Acad Sci USA* 70:1608–1612
100. Carlisle EM (1970) Silicon: a possible factor in bone calcification. *Science* 167:279–280
101. Chen QZ, Boccaccini AR (2006) Poly(D, L-lactic acid) coated 45S5 Bioglass-based scaffolds: processing and characterization. *J Biomed Mater Res A* 77:445–457
102. Kim HW, Song JH, Kim HE (2006) Bioactive glass nanofiber-collagen nanocomposite as a novel bone regeneration matrix. *J Biomed Mater Res A* 79:698–705

103. Hong Z, Reis RL, Mano JF (2009) Preparation and in vitro characterization of novel bioactive glass ceramic nanoparticles. *J Biomed Mater Res A* 88:304–313
104. Hajiali H, Karbasi S, Hosseinalipour M et al (2010) Preparation of a novel biodegradable nanocomposite scaffold based on poly (3-hydroxybutyrate)/bioglass nanoparticles for bone tissue engineering. *J Mater Sci Mater Med* 21:2125–2132
105. Valenzuela F, Covarrubias C, Martinez C et al (2012) Preparation and bioactive properties of novel bone-repair bionanocomposites based on hydroxyapatite and bioactive glass nanoparticles. *J Biomed Mater Res B Appl Biomater* 100:1672–1682
106. Mehdikhani-Nahrkhalaji M, Fathi MH, Mortazavi V et al (2012) Novel nanocomposite coating for dental implant applications in vitro and in vivo evaluation. *J Mater Sci Mater Med* 23:485–495
107. Arcos D, Ragel CV, Vallet-Regi M (2001) Bioactivity in glass/PMMA composites used as drug delivery system. *Biomaterials* 22:701–708
108. Soundrapandian C, Datta S, Kundu B et al (2010) Porous bioactive glass scaffolds for local drug delivery in osteomyelitis: development and in vitro characterization. *Aaps Pharmscitech* 11:1675–1683
109. Zhu M, Wang H, Liu J et al (2011) A mesoporous silica nanoparticulate/beta-TCP/BG composite drug delivery system for osteoarticular tuberculosis therapy. *Biomaterials* 32:1986–1995
110. Kim HW, Lee HH, Chun GS (2008) Bioactivity and osteoblast responses of novel biomedical nanocomposites of bioactive glass nanofiber filled poly(lactic acid). *J Biomed Mater Res A* 85:651–663
111. Lee HH, Yu HS, Jang JH et al (2008) Bioactivity improvement of poly(epsilon-caprolactone) membrane with the addition of nanofibrous bioactive glass. *Acta Biomater* 4:622–629
112. Niemelä T, Niiranen H, Kellomäki M et al (2005) Self-reinforced composites of bioabsorbable polymer and bioactive glass with different bioactive glass contents. Part I: Initial mechanical properties and bioactivity. *Acta Biomater* 1:235–242
113. Wilson J, Yli-Urpo A, Happonen RP (1993) Bioactive glasses: clinical applications. In: Hench LL, Wilson J (eds) *An introduction to bioceramics*, vol 1. World Scientific, Singapore
114. Stanley HR, Hall MB, Clark AE et al (1997) Using 45S5 bioglass cones as endosseous ridge maintenance implants to prevent alveolar ridge resorption: a 5-year evaluation. *Int J Oral Maxillofac Implants* 12:95–105
115. Suominen E, Kinnunen J (1996) Bioactive glass granules and plates in the reconstruction of defects of the facial bones. *Scand J Plast Reconstr Surg Hand Surg* 30:281–289
116. Aitasalo K, Suonpää J, Kinnunen I et al (1999) Reconstruction of orbital floor fractures with bioactive glass (S53P4). In: Ohgushi H, Hastings GW, Yoshikawa T (eds) *Bioceramics*, vol 12. World Scientific, Singapore
117. Suonpää J, Sipilä J, Aitasalo K et al (1997) Operative treatment of frontal sinusitis. *Acta Otolaryngol Suppl (Stockh)* 529:181–183
118. Peltola M, Suonpää J, Aitasalo K et al (1998) Obliteration of the frontal sinus cavity with bioactive glass. *Head Neck* 20:315–318
119. Peltola M, Aitasalo K, Suonpää J et al (2006) Bioactive glass S53P4 in frontal sinus obliteration: A long-term clinical experience. *Head Neck-J Sci Spec* 28:834–841
120. Stoor P, Söderling E, Salonen JI (1998) Antibacterial effects of a bioactive glass paste on oral microorganisms. *Acta Odontol Scand* 56:161–165
121. Stoor P, Söderling E, Grenman R (1999) Interactions between the bioactive glass S53P4 and the atrophic rhinitis-associated microorganism *Klebsiella ozaenae*. *J Biomed Mater Res* 48:869–874
122. Stoor P, Pulkkinen J, Grenman R (2010) Bioactive glass s53p4 in the filling of cavities in the mastoid cell area in surgery for chronic otitis media. *Ann Oto Rhinol Laryn* 119:377–382
123. Ylänen HO (2000) Bone ingrowth into porous bodies made by sintering bioactive glass microspheres. Dissertation, Åbo Akademi University

124. Hench LL, Greenspan D (2013) Interactions between bioactive glass and collagen: a review and new perspectives. *J Aust Ceram Soc* 49:1–40
125. Heikkilä JT, Aho AJ, Yli-Urpo A et al (1993) Bioactive glass versus hydroxyapatite in reconstruction of osteochondral defects in the rabbit. *Acta Orthop Scand* 64:678–682
126. Suominen E, Aho AJ, Vedel E et al (1996) Subchondral bone and cartilage repair with bioactive glasses, hydroxyapatite, and hydroxyapatite-glass composite. *J Biomed Mater Res* 32:543–551
127. Aho AJ, Tirri T, Kukkonen J et al (2004) Injectable bioactive glass/biodegradable polymer composite for bone and cartilage reconstruction: Concept and experimental outcome with thermoplastic composites of poly(epsilon-caprolactone-CO-D, L-lactide) and bioactive glass S53P4. *J Mater Sci Mater Med* 15:1165–1173
128. Lee YK, Song J, Moon HJ et al (2004) In Vitro and in vivo evaluation of non-crystalline calcium phosphate glass as a bone substitute. *Key Engineer Mater* 254–256:185–188
129. Lim HC, Sohn JY, Park JC et al (2010) Osteoconductive effects of calcium phosphate glass cement grafts in rabbit calvarial defects. *J Biomed Mater Res B* 95B:47–52
130. Schepers E, De Clercq M, Ducheyne P et al (1991) Bioactive glass granulate material as a filler for bone lesions. *J Oral Rehabil* 18:439–452
131. Gatti AM, Zaffe D (1991) Long-term behavior of active glasses in sheep mandibular bone. *Biomaterials* 12:345–350
132. Garcia AJ, Ducheyne P (1994) Numerical analysis of extra- cellular fluid flow and chemical species transport around and within porous bioactive glass. *J Biomed Mater Res* 28:947–960
133. Gatti AM, Valdre G, Tombesi A (1996) Importance of micro-analysis in understanding mechanism of transformation in active glassy biomaterials. *J Biomed Mater Res* 31:475–480
134. Heikkilä JT, Aho HJ, Yli-Urpo A et al (1995) Bone formation in rabbit cancellous bone defects filled with bioactive glass granules. *Acta Orthop Scand* 66:463–467
135. Oonishi H, Hench LL, Wilson J et al (1999) Comparative bone growth behavior in granules of bioceramic materials of various sizes. *J Biomed Mater Res* 44:31–43
136. Virolainen P, Heikkilä J, Yli-Urpo A et al (1997) Histomorphometric and molecular biologic comparison of bioactive glass granules and autogenous bone grafts in augmentation of bone defect healing. *J Biomed Mater Res* 35:9–17
137. Kawashita M, Shineha R, Kim HM et al (2003) Preparation of ceramic microspheres for in situ radiotherapy of deep-seated cancer. *Biomaterials* 24:2955–2963
138. Kawashita M (2002) Ceramic microspheres for in situ radiotherapy of cancer. *Mat Sci Eng C-Bio S* 22:3–8
139. Kawashita M, Kokubo T, Inoue Y (1999) Preparation of Y_2O_3 microspheres for In Situ radiotherapy of cancer. In: Ohgushi H, Hastings GW, Yoshikawa T (eds) *Bioceramics*, vol 12. World Scientific, Singapore
140. Kawashita M, Tanaka M, Kokubo T et al (2002) Preparation of magnetite microspheres for hyperthermia of cancer. In: Brown S, Clarke I, Williams P (eds) *Bioceramics*, vol 14. Trans Tech Pub, Switzerland
141. Kawashita M, Tanaka M, Kokubo T et al (2005) Preparation of ferrimagnetic magnetite microspheres for in situ hyperthermic treatment of cancer. *Biomaterials* 26:2231–2238

Chapter 6

Clinical Resurfacing of Feldspar and Leucite Glass Ceramics Using Dental Handpieces and Burs

Ling Yin, Xiao-Fei Song, and Richard Stoll

Abstract This chapter summarises the resurfacing characteristics and material removal mechanisms of feldspar and leucite glass ceramics in simulated clinical resurfacing procedure by using air-turbine dental handpieces. It begins with description of feldspar and leucite glass ceramics as restorative and prosthetic materials in dentistry. A description of condition monitoring of simulated clinical resurfacing processes is provided, including in-process measurement of resurfacing forces, force ratios, torques and specific energy using force sensors and a high-speed data acquisition system. Information on surface roughness and surface morphology is also detailed. In particular, this chapter presents the studies on surface and subsurface damage mechanism using both finite element analysis (FEA) and experimental measurement. At the end of the chapter, potential future developments of dental ceramic resurfacing are given.

Keywords Dental ceramics • Resurfacing • Forces • Surface roughness • Brittle fracture • Ductile removal

6.1 Introduction

Ceramics are widely used as crown materials to replace missing teeth attributable to their excellent resemblance of tooth colours, chemical durability, wear resistance, biocompatibility and environmental friendliness [1–5]. Recent fast chair-side computer-aided design and computer-aided manufacturing (CAD/CAM) techniques performed in dental clinic have made them an even more attractive option

L. Yin (✉)

College of Science and Engineering, James Cook University, Townsville, QLD 4811, Australia
e-mail: ling.yin@jcu.edu.au

X.-F. Song

School of Mechanical Engineering, Tianjin University, Tianjin 300072, China

R. Stoll

College of Medicine and Dentistry, James Cook University, Cairns, QLD 4870, Australia

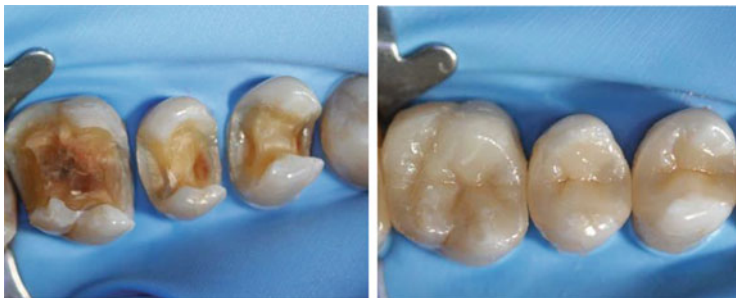


Fig. 6.1 Preparation for ceramic inlays 24–26 (*left*) and ceramic inlays made from leucite glass ceramic, IPS Empress (Ivoclar Vivadent), directly after cementation (*right*) (Clinical case: Prof. Dr. Richard Stoll, College of Medicine and Dentistry, James Cook University, Cairns, Australia)

[3, 6–8]. Ceramic crowns cost \$2 billion annually worldwide [9]. Among many available dental ceramics, feldspar and leucite glass ceramics play an essential role in porcelain-fused metal (PFM) structures and all-ceramic restorations as veneers, inlays, onlays and single crowns [1, 10]. Conventionally, feldspar and leucite glass ceramic restorations are sintered and shaped using ceramic powder sintering and moulding techniques. Both materials in sintered states are machinable and can be directly fabricated to different shapes using chair-side dental CAD/CAM systems in dental offices [3, 8, 11]. Figure 6.1 shows a clinical case study conducted by the third author of this chapter, in which leucite glass ceramics were used as inlays for three crowns. In this case, the damaged enamel and dentin were removed. The teeth were prepared and three inlays created in one dental appointment using the chair-side dental CAD/CAM system. These inlays were then cemented directly to the prepared teeth. After occlusal and marginal adaptations, leucite glass ceramic inlays were polished to achieve aesthetic quality.

During the installation of ceramic restorations in the oral environment, they must be resurfaced and/or adjusted for occlusal and marginal adaptations (Fig. 6.2) using dental handpieces and diamond burs manipulated by dentists (Fig. 6.3). Such a resurfacing or adjusting process induces surface and subsurface damage in the ceramic prostheses, resulting in poor reliability of ceramic prostheses [3, 9–15]. This chapter presents our overview on resurfacing characteristics and material removal mechanisms of feldspar and leucite glass ceramics in simulated clinical conditions using air-turbine dental handpieces. It covers basic microstructures and properties of feldspar and leucite glass ceramics; in-process monitoring of speed, force, torque and energy involved in simulated clinical resurfacing; and surface quality such as roughness, surface morphology and phase transformation. In addition, recently findings related to surface and subsurface damage using both finite element analysis (FEA) and scanning electron microscopy (SEM) measurement are presented below.

Fig. 6.2 Ceramic only after occlusal corrections.

Resurfacing with diamond burs is necessary to adjust the occlusal contacts. Note that green spots represent undisturbed bites and free functional movements (Clinical case: Prof. Dr. Richard Stoll, College of Medicine and Dentistry, James Cook University, Cairns, Australia)



Fig. 6.3 Use of a dental handpiece for resurfacing of crowns on a manikin model. The handpiece is held with three fingers in a writing position (Clinical teaching case: Prof. Dr. Richard Stoll, College of Medicine and Dentistry, James Cook University, Cairns, Australia)



6.2 Feldspar and Leucite Glass Ceramics

6.2.1 Feldspar Porcelains

Porcelains have been used in dentistry to replace enamel and dentin since the eighteenth century. The first porcelains based on triaxial Chinese porcelain formulations have shown limited aesthetic results due to their white appearance and high opacity. Around 1830, Widman introduced feldspar porcelains, which rapidly became the preferred materials for dental restorations [16]. These porcelains were made of 78 % feldspar, kaolin, potash silicate and dehydrated borax [16]. Later, feldspar porcelains were made from potash feldspar ($K_2O \cdot Al_2O_3 \cdot 6SiO_2$) and

quartz (SiO_2), which decompose to leucite crystals ($\text{K}_2\text{O} \cdot \text{Al}_2\text{O}_3 \cdot 4\text{SiO}_2$) and an amorphous glass phase at high temperatures [17]. The glass phase enhances translucency but is susceptible for crack propagation. The crystalline phases can function as a scaffold and increase mechanical strength by dispersion hardening. These components were then mixed with alkali metal carbonates as fluxes and metallic oxides for colouration in melting states at high temperatures. The melt porcelains were then rapidly quenched in cold water and finally ground to ceramic frits with average particle sizes of 20–30 μm [18].

In 1889, Land created the first dental crowns and patented them as “jacket crowns” using feldspar and aluminous ceramics baked on a thin platinum foil [19]. Unfortunately, due to the low mechanical strength and the lack of ideal cementation techniques, these jacket crowns were only used for low-load-bearing anterior teeth. In addition, fracture-induced high failure rates often occurred in these jacket crowns.

In 1925, Adriaansen invented a new layering and sintering process of porcelain in a special kiln [16]. This process enabled porcelain masses to be layered with different colours and translucencies for mimicking layered natural tooth substances by using slightly different sintering temperatures. Classic feldspathic porcelains are commonly used for veneering metal frameworks. Unfortunately, the thermal expansion behaviours of these porcelains were not ideal to match the thermal expansions of cast metal frameworks. Further, these porcelains lack desired strength, which are approximately 70–80 MPa [4], and are prone to brittle fracture under mechanical loading.

Porcelain-fused metal techniques were developed by Weinstein in the late 1950s as a solution to the high failure rate of feldspathic jacket crowns [19]. Cast frameworks are achieved with high accuracy for improved marginal fit. Adding nonprecious metal to the alloy formulation makes it possible to create an intentional oxide layer on the metal surface by controlled firing in a normal atmosphere with oxygen. This oxide layer forms the interface for the connection to the fired porcelain.

In 1965, higher-strength ceramics were developed by adding alumina crystals into the feldspathic glass matrix. Unfortunately, the aesthetic properties of these materials became inferior because the strengthened alumina scaffolds made the material opaque. To improve aesthetics, Mclean and Hughes developed the all-ceramic core–veneer structure using high-strength aluminous porcelain as a core framework veneered with a feldspathic porcelain with high translucency [19].

Modern feldspar porcelains are modified, containing sanidine, nepheline and anorthoclase crystals reinforced with glass matrix, as an example shown in X-ray diffraction spectra (Fig. 6.4) [20] for Cerec Vitablocs Mark II (VITA Zahnfabrik, Germany). These porcelain blocks contain fine-particle feldspar crystals with matching abrasion characteristics of natural tooth enamel. They have been used clinically with considerable success since 1991 [1] and are now widely used as inlays, onlays, veneers and anterior crowns for VITA Cerec Dental CAD/CAM systems [21–23]. The mechanical properties are reported with Vickers

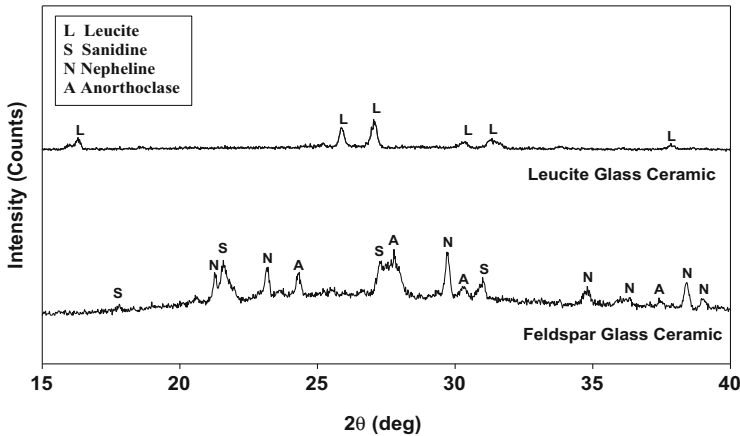


Fig. 6.4 X-ray diffraction pattern of the feldspar and leucite glass ceramics (Reprinted with permission from Ref. [20]. Copyright 2013 by Elsevier)

hardness = 6.2 GPa, Young's modulus = 68 GPa, fracture toughness = $0.9 \text{ MPa}\cdot\text{m}^{1/2}$ and strength = 100 MPa [24, 25].

6.2.2 Leucite Glass Ceramics

Leucite glass ceramics are specially designed to fit the thermal expansion coefficients of different metal frameworks (gold alloys, cobalt chromium alloys, titanium alloys) and later the frameworks made of high-strength ceramics. Adding finely dispersed leucite grains ($\text{K}(\text{AlSi}_2\text{O}_6)$) results in increased flexural strength and improved wear patterns [26].

Typical ceramic masses for porcelain-fused metal techniques contain 15–25 % leucite crystals, which have a high thermal expansion coefficient ($25 \times 10^{-6}/^\circ\text{C}$) compared with the glass matrix ($8 \times 10^{-6}/^\circ\text{C}$) [4]. The difference in thermal expansion creates strong compressive stress around leucite crystals after cooling to reinforce the structure and improve the crack resistance. Special materials for all-ceramic crowns contain up to 45 % leucite crystals, which enhance the fracture strength to approximately 104 MPa in comparison to 70 MPa strength of classic feldspathic porcelains [4]. Porcelain-fused metal crowns and bridges have been used now for more than four decades and are still fairly popular, even if good aesthetics are difficult to achieve due to the necessity of an opaque layer. By 2005 more than 50 % of all dental restorations were based on porcelain-fused metal techniques [27].

Fine-structured leucite glass ceramics, ProCAD blocks (Ivoclar Vivadent), are widely used in dental CAD/CAM systems. The X-ray diffraction spectrum of this material is shown in Fig. 6.4 [20], indicating that it contains mainly leucite crystals

in a glass matrix. The sizes of leucite crystals were measured to be approximately 5–10 μm [28] in a glass matrix. The mechanical properties of the material are Vickers hardness $H = 5.6$ GPa, Young's modulus $E = 70$ GPa, fracture toughness $K_c = 1.3$ $\text{MPa}\cdot\text{m}^{1/2}$ and flexural strength $\sigma = 127$ MPa [29].

6.3 Simulated Clinical Resurfacing Using Dental Handpieces

6.3.1 Clinical Resurfacing Process

When installing dental restorations in the human mouth, clinical resurfacing of restorations is necessary to adjust the occlusal contacts and marginal fits [30, 31]. Figure 6.2 demonstrates a clinical case of a ceramic inlay after occlusal corrections. This process starts with the necessary reshaping followed by a finishing and polishing process using dental handpieces and abrasive tools in the oral environment as shown in Fig. 6.3. In order to reduce the surface roughness, abrasive tools with decreasing grit sizes are used for finishing. These tools include diamond burs, flexible discs and strips to adjust to the tooth morphology and the intraoral conditions. Polishing process is carried out with rubber polishing tips or polishing paste and brushes [32–34].

Usually a dental ceramic surface is covered with a layer of glaze. Dental glazes are made mainly of a glassy material and applied as the last firing step during the production of ceramic restorations. After clinical adjustments or reshaping, it is usually recommended to reglaze the surfaces in the laboratory. Because this would take another appointment, many dentists prefer to polish the surfaces intraorally through four to five finishing/polishing steps to reduce the surface roughness of the resurfaced areas. Intraoral resurfacing is controlled by manual operations of individual dentists and resurfacing quality determines the life and function of restorations. Therefore, it requires a fundamental understanding of material responses for avoiding adverse effects when carried out inadequately. In this regard, surface and subsurface damages have been particularly identified in resurfacing brittle materials like dental ceramics [35–38].

6.3.2 Dental Handpieces and Burs

Like human enamel, ceramic restorations are usually ground intraorally by dental diamond burs, which are single-layered diamond grinding wheels of 1-mm diameters manufactured by electroplating. The cutting portion of these burs consists of a single layer of synthetic or natural diamond held in place on the form or hub by an

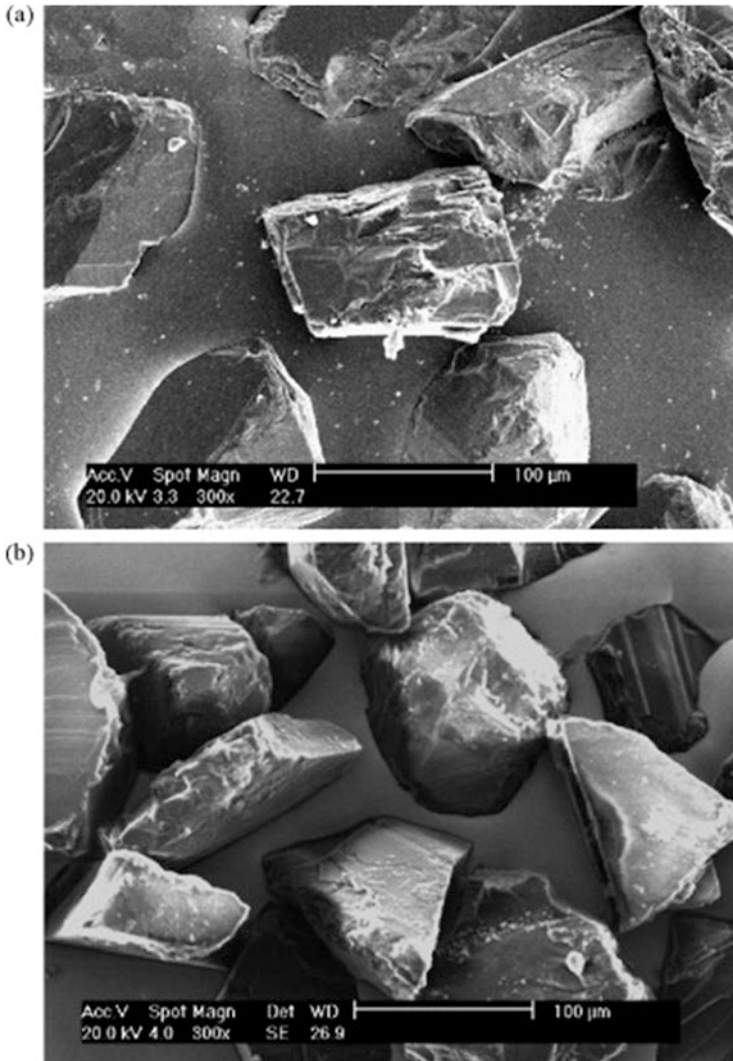


Fig. 6.5 Scanning electron micrographs of a new coarse grit diamond bur (a) before cutting and (b) after cutting (Reprinted with permission from Ref. [41]. Copyright 2009 by Elsevier)

electroplated nickel or chromium binder [39, 40]. Figure 6.5 shows the surface of an electroplated diamond bur with abrasive grains tips protruded above the electroplated nickel [41]. Typically the nickel or chromium layer is equal to about 30% the grain dimensions, although its thickness may be varied. Since these diamond burs contain only a single layer of superabrasive, they are generally less expensive than bonded types and widely used as disposable or single-patient-use burs to minimise the risk of cross-contamination of blood-borne pathogens

[42]. Diamond burs have ultrafine, fine, medium, coarse and supercoarse grit sizes ranging from 10 to 150 μm . Fine-particle diamonds are used for finishing (grit size 15–30 μm); coarse diameters (125–150 μm) are used for quick removal.

Diamond burs are usually rotating at high speed, which depending on their diameter and grit size ranges between 40,000 and 450,000 rpm driven by dental handpieces (usually angulated) either for lab work or for intraoral preparation and surface reduction. Traditionally, high speeds were achieved using the air turbine, invented by Borden in 1957 [43]. A handpiece with an air turbine is called a high-speed handpiece containing ball bearings and a tiny turbine wheel driven by a mixture of water and pressurised air. Wear of ball bearings can cause the diamond bur to oscillate, resulting in additional surface damage to the workpiece. High-speed handpieces have limited optimal torque–speed characteristics. Thus, it is very difficult to adjust the cutting speed to the needs through these diamond instruments. The cutting speed is reduced by reducing the handpiece air pressure, resulting in reduced torque applied in the cutting process. Typically, most dentists use high-speed handpieces at high speeds and do not adjust the rotational speed to the optimal work characteristics of the bur. As an alternative they use electric dental handpieces to have constant torques at a large range of rotational speeds of 100–40,000 rpm electronically driven by electrical motors. These motors can be operated at nearly constant torques under different loads and rotational speeds. The range of rotational speed can be extended by using speed-increasing handpieces which use cogwheel to raise the maximum speed of 40,000–200,000 rpm using a factor of 1:5. It has been demonstrated that electric handpieces are more efficient than air-turbine handpieces in cutting various materials used in dentistry, especially machinable glass ceramics [43].

Generally diamond instruments grind the surface by scratching dents into the surface, resulting in roughness. These rough surfaces have to be finished to create a smooth surface. For high gloss, a polishing process is necessary additionally. In finishing process, fine abrasives embedded in a metallic carrier or a rubber polishing instrument are used.

6.3.3 Testing Apparatus and Methodology for Simulation of Clinical Resurfacing

Although high-speed air turbines provide poor torque characteristics, they are commonly used in dental clinical cutting and finishing for proper occlusal contacts and removal of the damaged crowns/inlays/onlays and cementing media [44] due to their high-speed capabilities. In intraoral clinical adjusting, the performance of the dental handpieces and burs is essential to control adjusting quality which determines the function and life of a restoration. The quality measures in adjusting a restoration include material removal rate, surface roughness and degree of surface damage [39, 45–47]. However, reliable standardised testing of high-speed dental

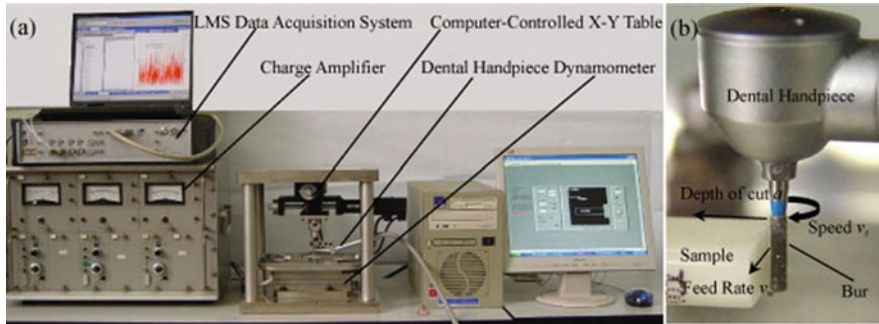


Fig. 6.6 Computer-assisted experimental setup for in-process assessment and monitoring of dental cutting (Reprinted with permission from Ref. [41]. Copyright 2009 by Elsevier)

handpieces is a challenge [48] because rotational speed, force, torque and finishing energy are very difficult to quantify precisely. Therefore, accurate measurement systems enabling quantitative assessment of these parameters for studies of intraoral adjusting process using dental handpieces are highly desirable [49, 50].

Early handpiece testing systems were mechanically controlled, enabling only force control [51, 52]. These apparatus were used in studying the effects of handpiece loads [51, 53], bur grit sizes [54], handpiece spray patterns [55], coolant flow rates [56], irrigation solutions and pressures [57] and chemomechanical influences [58, 59] on cutting efficiency of enamel and mica glass ceramics. Modified apparatus were developed adding air pressure regulators, displacement transducers, revolution counters and torque transducers for force, rotational and torque measurements [50, 52]. However, all these mechanically controlled apparatus cannot be used to simulate the handpiece movement in clinical adjusting with variable depths of cut and feed rates, which can cause the changes in cutting speeds.

Computer-assisted dental cutting systems were later developed [45, 48]. One apparatus consisted of a piezoelectric force dynamometer, a charge amplifier and a computer data acquisition system [45] for providing constant loads to the handpiece during cutting. With this apparatus, dental ceramics with a wide range of mechanical properties were studied with respect to material response to dental cutting, including mica-containing glass ceramics [45, 46], glass-infiltrated alumina [47], feldspathic porcelain and yttria-stabilised tetragonal zirconia [39]. Another apparatus comprised two platforms on precision microslides, a transducer for monitoring the dental handpiece rotations and a strain gauge for force measurement [48], with which the cutting performances of clinical and industrial handpieces against glass were evaluated. These computer-assisted cutting devices can only be used to cut grooves at the fixed loads due to the lack of two-degree-of-freedom (2-DOF) moving functionality. Meanwhile, the measurement of cutting speeds depended on a strobe-type tachometer [45], or a photodiode [52], or a fibre optic tachometer [60–62], resulting in instantaneous or discontinuing speed assessment. How the rotation speed varies with the depth of cut and feed rate remained immeasurable, which are constantly variable and virtually indefinable during the clinical dental finishing.

The recently developed computer-assisted 2-DOF apparatus shown in Fig. 4.6 enabled the simulation of the common clinical adjusting practice in which both feed

rate and depth of cut can be controlled and measured and in-process assessment of in vitro handpiece adjusting process [63]. This device is a mini-CNC machine, consisting of a two-dimensional numerical controlled coordinate worktable serving as the carrier of a clinical dental handpiece and a three-component piezoelectric force dynamometer, an electric charge amplifier, and a high-speed LMS data acquisition system for in-process measurement. Details of this device can be found in Ref. [63]. With this device, both the tangential and normal cutting forces can be monitored and measured in both time and frequency domains. The handpiece rotational speeds can be subsequently obtained via fast Fourier transform (FFT) in the frequency domain. Further, cutting torque T and specific cutting energy U can be determined using the following equations:

$$T = F_t d_s / 2 \quad (6.1)$$

$$U = F_t v_s / a v_w b \quad (6.2)$$

where F_t is the tangential force, d_s is the diameter of the diamond bur, v_s is the grinding speed, a is the depth of the cut, v_w is the feed rate and b is the thickness of the work sample.

6.4 Resurfacing Speeds, Forces, Torques and Energy

As coarse burs are often used to remove a large amount of materials, resulting in the poorest surface roughness and most surface and subsurface damage, it is important to understand the cutting characteristics of coarse diamond burs using high-speed dental handpieces. The average diameter of the diamond grits was estimated to be 106–125 μm from a series of micrographs obtained by scanning electron microscopy [64]. In this section, utilising some published data [65], the investigation attempted to compare the material responses of feldspar and leucite glass ceramics to resurfacing process.

6.4.1 Resurfacing Speeds

Resurfacing speeds for feldspar and leucite glass ceramics as the functions of depth of cut at the feed rates of 15 mm/min and 60 mm/min are shown in Fig. 6.7a. The results show that the resurfacing speeds for these two materials (feldspar and leucite) decreased with the depth of cut. Resurfacing speeds for feldspar and leucite glass ceramics as the functions of feed rate at the depths of cut of 10 μm and 50 μm are shown in Fig. 6.7b, showing that the resurfacing speeds for both materials decreased with the feed rate. In particular, cutting leucite at the high feed rate of 60 mm/min and the deep depth of cut of 50 μm caused the speed reduction by

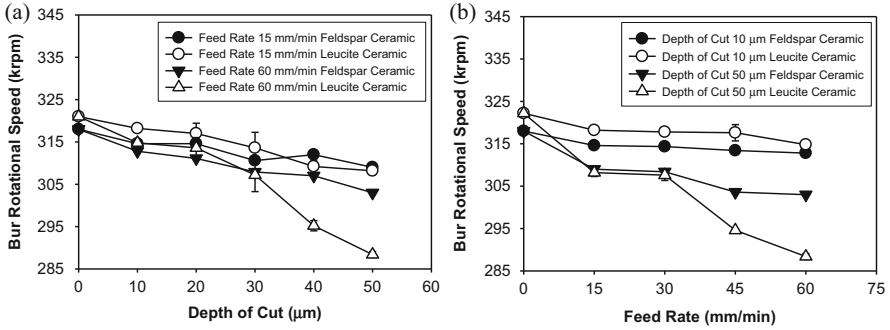


Fig. 6.7 Bur rotational speed versus (a) depth of cut and (b) feed rate

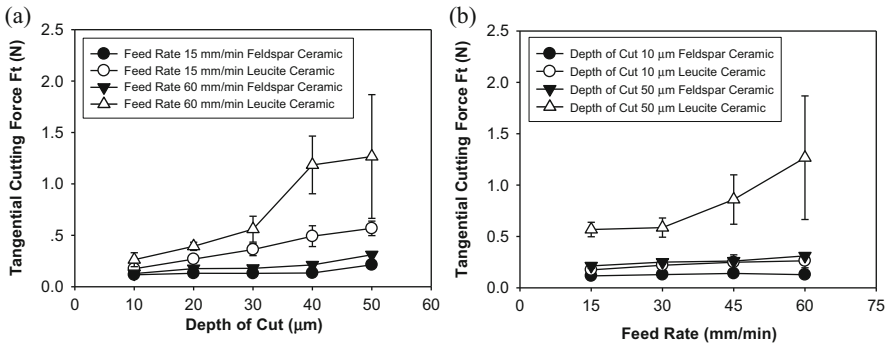


Fig. 6.8 Tangential cutting force F_t versus (a) depth of cut and (b) feed rate

approximately 10% to 288 krpm from the average unloaded rotational speeds of approximately 320 krpm.

6.4.2 Resurfacing Forces

Tangential cutting forces for feldspar and leucite glass ceramics as the functions of depth of cut at the feed rates of 15 mm/min and 60 mm/min are shown in Fig. 6.8a. The tangential forces for both materials increased with the depth of cut at any feed rate. However, the tangential forces for leucite glass ceramic at both feed rates of 15 mm/min and 60 mm/min are significantly higher than those of the feldspar glass ceramic (ANOVA, $p < 0.05$). Tangential cutting forces for the two materials as the functions of feed rate at the depths of cut of 10 μm and 50 μm are shown in Fig. 6.8b. For the feldspar ceramic, the increased depth of cut only resulted in a slight increase in the tangential force. In comparison, the tangential forces for the leucite glass ceramic at the small depth of cut of 10 μm were similar to the force values for feldspar ceramic. However, at the deep depth of cut at 50 μm , the

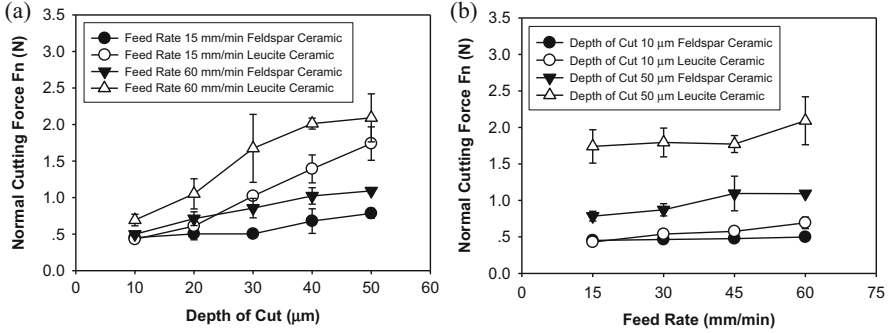


Fig. 6.9 Normal cutting force F_n versus (a) depth of cut and (b) feed rate

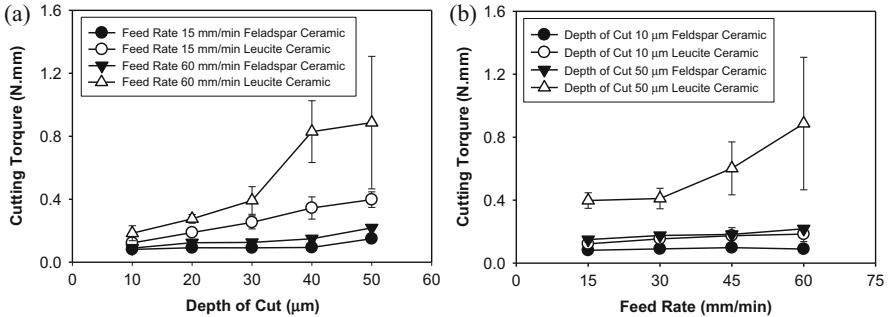


Fig. 6.10 Cutting torque versus (a) depth of cut and (b) feed rate

tangential forces for the leucite glass ceramic are 2–4 times higher than those for the feldspar glass ceramic.

Normal cutting forces for feldspar and leucite glass ceramics as the functions of depth of cut at the feed rates of 15 mm/min and 60 mm/min are shown in Fig. 6.9a. The normal forces for both materials also significantly increased with the depth of cut at any feed rate (ANOVA, $p < 0.05$). Also, the forces for the leucite glass ceramic are higher than those for the feldspar glass ceramic. In particular, at a higher feed rate and depth of cut, the normal forces for the leucite glass ceramic nearly doubled. Normal cutting forces for the two materials as the functions of feed rate at the depths of cut of 10 μm and 50 μm are shown in Fig. 6.9b. At the depth of cut of 10 μm , the normal forces for these two materials were very close, slightly increasing with the feed rate. At the depth of cut of 50 μm , the normal forces for the leucite glass ceramic were twice of the forces for the feldspar ceramic.

6.4.3 Resurfacing Torques

Cutting torques for the feldspar and leucite glass ceramics as the functions of depth of cut at the feed rates of 15 mm/min and 60 mm/min are shown in Fig. 6.10a. It

shows the torques for leucite glass ceramic are higher than those for the feldspar ceramic. The torques for the feldspar ceramic did not change much with the feed rate and depth of cut, while cutting leucite glass ceramic, the torques increased significantly with the depth of cut (ANOVA, $p < 0.05$). Cutting torques for the feldspar and leucite glass ceramics as the functions of feed rate at the depths of cut of 10 μm and 50 μm are plotted in Fig. 6.10b. It shows that the torques for cutting the leucite glass ceramic at the depth of cut of 50 μm are at least 2–5 times higher than those for the two materials cut at the other conditions.

6.4.4 Resurfacing Energy

The specific cutting energy for feldspar and leucite glass ceramics as functions of the depth of cut at the feed rates of 15 mm/min and 60 mm/min is shown in Fig. 6.11a. Overall, the specific cutting energy for these two materials significantly decreased with the increase in depth of cut (ANOVA, $p < 0.05$). The specific cutting energy values for leucite glass ceramic were always higher than those of the feldspar glass ceramic. For instance, at the feed rate of 60 mm/min, the specific cutting energy for leucite ranged from 84 to 128 J/mm^3 in comparison with the specific energy at the level of 24–59 J/mm^3 for the feldspar ceramic. At the feed rate of 15 mm/min, the specific cutting energy for leucite ranged from 205 to 325 J/mm^3 in comparison with the specific energy at the level of 61–214 J/mm^3 for the feldspar ceramic. The specific cutting energy for these two materials as the function of feed rate at the depths of cut 10 μm and 50 μm is given in Fig. 6.11b. It demonstrates that the specific cutting energy decreased when increasing the feed rate at any depths of cut. At the depth of cut of 10 μm , the specific cutting energy for both materials was consumed at higher values than that at the larger depths of cut. Also it shows at any cutting conditions, the specific cutting energy for leucite glass ceramic was much higher than that of the feldspar ceramic.

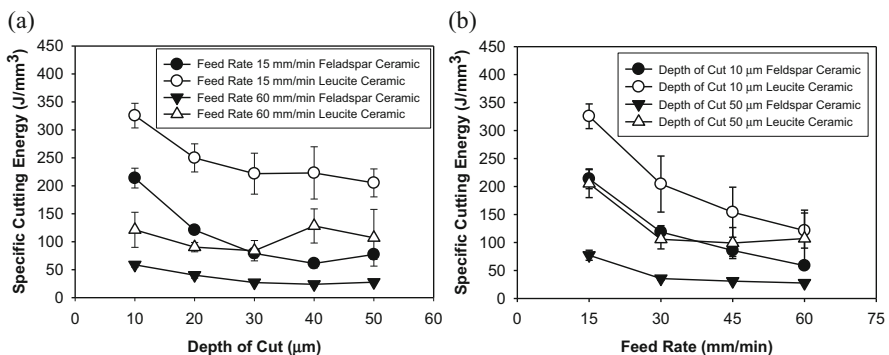


Fig. 6.11 Specific cutting energy versus (a) depth of cut and (b) feed rate

6.5 Surface Quality in Simulated Clinical Resurfacing

The reliability of dental ceramic restorations, especially for high-load-bearing posterior restorations, is often critically dependent upon the quality of the surface produced by dental resurfacing using diamond burs. Surface quality is considered to consist of two aspects: surface integrity and surface topography [66]. Surface integrity is associated with mechanical and microstructural alternations to the surface layer induced by machining. For brittle material machining, the most important aspects of surface integrity are associated with fracture, i.e., surface and subsurface damage, and thermal damage caused by excessive grinding temperatures, i.e., phase transformation. Surface topography refers to the geometry of machined surfaces, which is usually characterised by surface roughness.

The present section is mainly concerned with surface roughness in dental ceramic resurfacing using coarse diamond burs. We begin with measurement of surface roughness using stylus profilometry, followed by the distractive morphological features of machined surfaces for the feldspar and leucite glass ceramics. Quantitative characterisation of subsurface damage for both materials is carried out using non-destructive manner, namely, finite element analysis (FEA), and destructive measurement with SEM. The FEA model is then considered for describing the generation of subsurface stresses at the material–bur interfaces to theoretically predict subsurface damage of dental ceramic during resurfacing. This provides a certain degree of insight into how various cutting conditions might affect the resurfacing quality. Machining heat-induced phase transformation in resurfacing leucite glass ceramic is also described. Finally, material removal mechanisms in resurfacing of dental ceramics are discussed.

6.5.1 Surface Roughness

The arithmetic mean surface roughness R_a values as function of depth of cut at the feed rate of 15 mm/min and 60 mm/min are shown in Fig. 6.12a. The arithmetic mean surface roughness R_a values as a function of feed rate at the depths of cut of 10 μm and 50 μm are shown in Fig. 6.12b. These data show that the roughness values are in the range of 5–7 μm under the applied cutting conditions. The effects of depth of cut and feed rate on surface roughness are not significant (ANOVA, $p > 0.05$).

6.5.2 Surface Morphology

The SEM micrographs obtained from the feldspar ceramic surfaces through the coarse diamond burs at a depth of cut of 10 μm for a complete variation of the feed

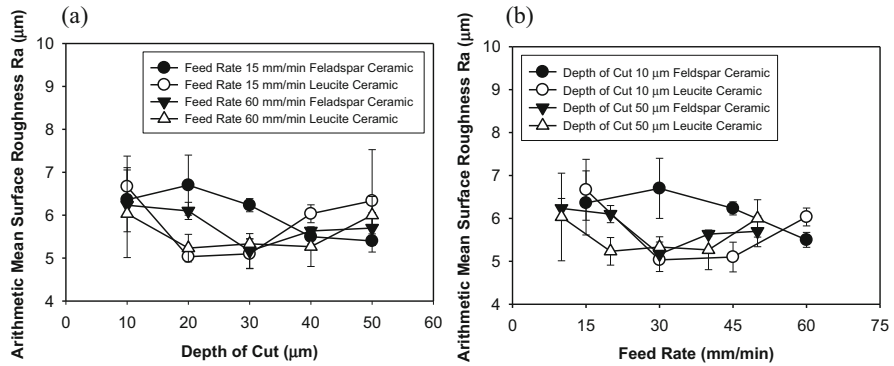


Fig. 6.12 Arithmetic mean surface roughness versus (a) depth of cut and (b) feed rate

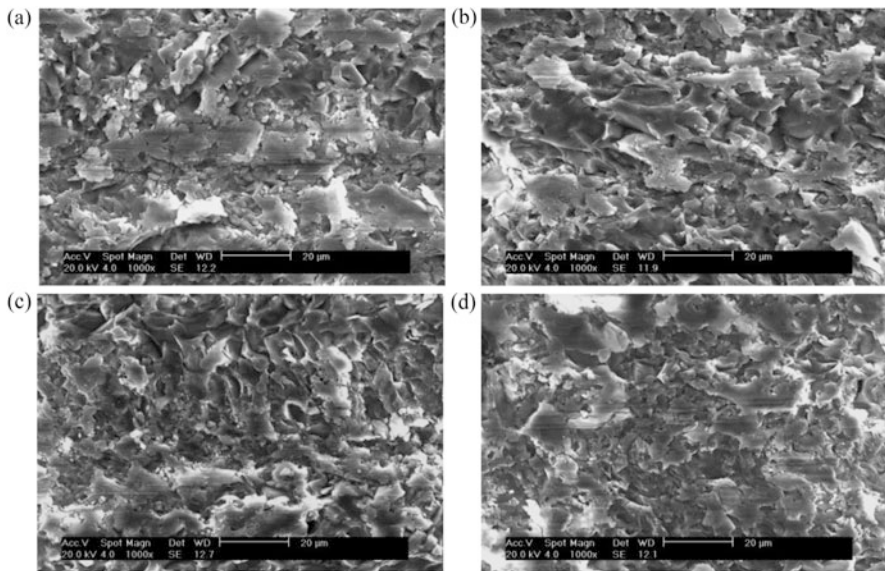


Fig. 6.13 SEM micrographs of the surfaces adjusted for the feldspar ceramic at depth of 10 µm with feed rates (a) 15 mm/min, (b) 30 mm/min, (c) 45 mm/min and (d) 60 mm/min (Reprinted with permission from Ref. [64]. Copyright 2006 by Wiley Periodicals, Inc.)

rates from 15 to 60 mm/min are shown in Fig. 6.13 [64]. No significant differences on the feldspar ceramic surfaces machined at the feed rates from 15 to 60 mm/min can be observed. The machined surfaces obtained at a much large depth of cut of 50 µm are shown in Fig. 6.14 [64]. The structures of the surfaces machined at different depths of cut of 10 and 50 µm looked similar, although it is expected to have larger machining grooves and coarser surfaces at the larger feed or depth of cut. All these feldspar ceramic surfaces featured with plastic deformation, microfracture, smeared areas and micro debris.

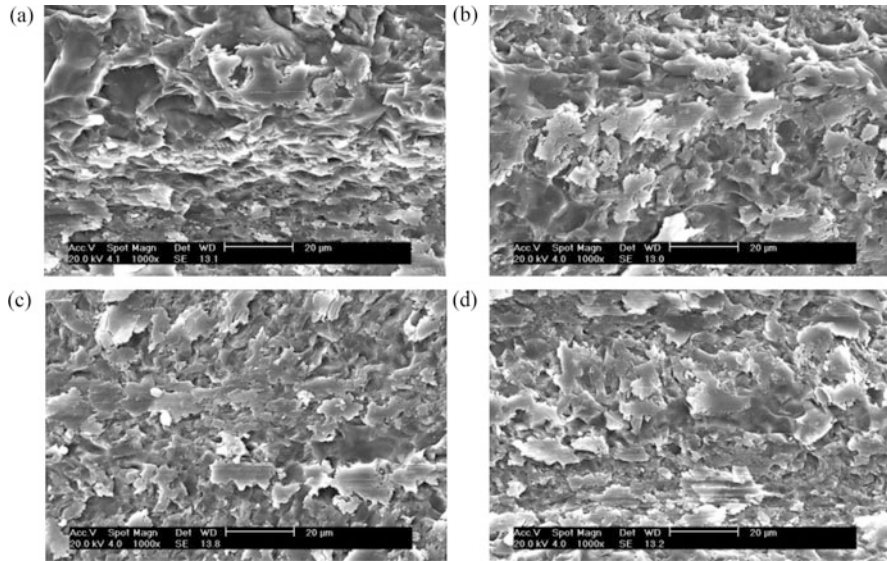


Fig. 6.14 SEM micrographs of the surfaces adjusted for feldspar ceramic at depth of 50 μm with feed rates (a) 15 mm/min, (b) 30 mm/min, (c) 45 mm/min and (d) 60 mm/min (Reprinted with permission from Ref. [64]. Copyright 2006 by Wiley Periodicals, Inc.)

The SEM micrographs obtained from the leucite glass ceramic surfaces from the coarse diamond burs at a depth of cut of 10 μm for a complete variation of the feed rates from 15 to 60 mm/min are shown in Fig. 6.15 [67]. Although these leucite ceramic surfaces featured with plastic deformation, microfracture, smeared areas and micro debris, the surface produced at the low feed rate of 15 mm/min shows more smoothness than the surface generated at the high feed rate of 60 mm/min. The surface morphologies obtained at a much large depth of cut of 50 μm are shown in Fig. 6.16 [67]. These surfaces also demonstrate similar characteristics, i.e., coexistence of plastic deformation and brittle fracture. It is also observed that at the great depth of cut of 50 μm and high feed rate, more microfracture occurred on the machined surface (Fig. 6.15d).

Comparing the feldspar and leucite surfaces in Figs. 6.13 and 6.15 at the depth of cut of 10 μm and in Figs. 6.14 and 6.16 at the depth of cut of 50 μm , both materials revealed the mixed mode of material removal characteristics, i.e., ductile removal and brittle fracture, as the dominant removal mechanisms. However, the leucite glass ceramic showed more plastic than feldspar ceramic with more plastically deformed regions generated in particular at the small depth of cut and feed rate (Fig. 6.15a versus Fig. 6.13a). Although both material surfaces contained cracks, chipping and brittle fracture, intergranular and transgranular fractures of the fine-grained feldspar and leucite crystals in the fractured regions were not easily identified. Irregular fracture without clear reinforced crystal–glass interfaces was the feature due to lateral/median cracks. In the plastically removed regions, the interactions of diamond grits produced similar machining traces of metallic

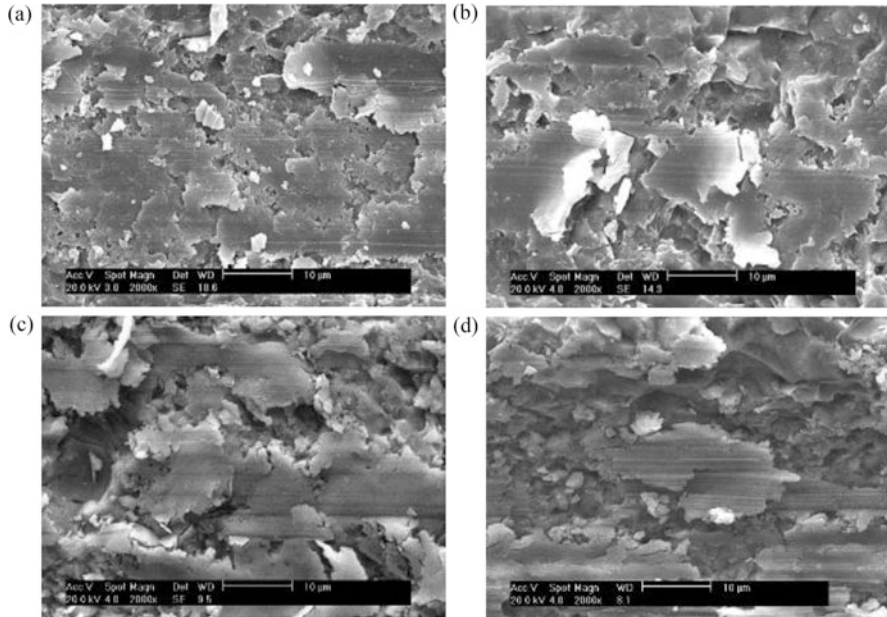


Fig. 6.15 SEM micrographs of the surfaces adjusted for leucite ceramic at depth of 10 μm with feed rates (a) 15 mm/min, (b) 30 mm/min, (c) 45 mm/min and (d) 60 mm/min (Reprinted with permission from Ref. [67]. Copyright 2012 by Elsevier)

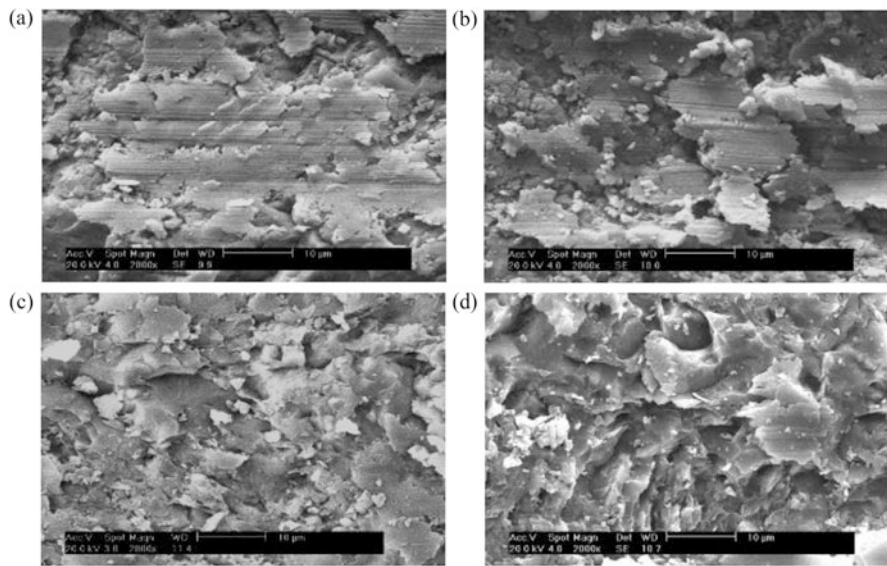


Fig. 6.16 SEM micrographs of the surfaces adjusted for leucite ceramic at depth of 50 μm with feed rates (a) 15 mm/min, (b) 30 mm/min, (c) 45 mm/min and (d) 60 mm/min (Reprinted with permission from Ref. [67]. Copyright 2012 by Elsevier)

materials on the feldspar and leucite glass ceramic surfaces accompanied with microcracks.

6.5.3 Subsurface Damage: FEA Modelling and Experimental Measurement

The FEA simulation was conducted to model the dental resurfacing process based on workpiece–bur contact mechanics described in Fig. 6.6b. A two-dimensional FEA was developed to predict tensile, shear, compressive and equivalent von Mises stresses. Details of the establishment of this model can be found in Ref. [68]. Surface and subsurface damage in the resurfacing process resulted from the severe tensile stresses exceeding the ultimate strength σ of the workpiece material underneath the workpiece–bur contact zone. Thus, the failure criterion was established based on the maximum normal stress σ_t (the first principal stress) criterion. For the given work materials, the ultimate strength σ values for the feldspar and leucite glass ceramics are 100 MPa [24] and 127 MPa [29], respectively. Subsequently, the depths of subsurface damage of the workpiece under the different resurfacing conditions were determined as functions of resurfacing operational parameters. To validate the FEA-predicted values, the destructively revealing subsurface damage measurement was applied to the work materials by manually polishing the cross-sections of the machined materials using progressively smaller alumina abrasives and diamond pastes of sizes down to 0.5 μm [68]. The subsurface damage depths were then measured under SEM [68].

Figure 6.17a demonstrates the contour plot of the maximum principal stress distribution for feldspar ceramic at the workpiece–bur contact zone at the depth of 10 μm and feed rate of 15 mm/min [69]. Figure 6.17b shows the detailed plot of the stress distribution in Fig. 6.17a [69]. The results show that the tensile stresses were distributed under the workpiece–bur contact zone and increased with the decrease in the distance to the resurfaced surface. The maximum tensile stress was estimated to be 875 MPa at the diamond grit exit point. Figure 6.17c demonstrates the contour plot of the maximum principal stress distribution for feldspar ceramic at the workpiece–bur contact zone at the depth of 50 μm and feed rate of 60 mm/min [69]. Figure 6.17d shows the detailed plot of the stress distribution in Fig. 6.17c [69]. The results also show similar stress distribution features, but the maximum tensile stress was estimated to be 1215 MPa at the diamond grit exit point, which is much higher than the maximum stress obtained at the depth of cut 10 μm and the feed rate of 15 mm/min.

Figure 6.18a displays the contour plot of the maximum principal stress distribution for leucite glass ceramic at the workpiece–bur contact zone at the depth of 10 μm and feed rate of 15 mm/min [70]. Figure 6.18b shows the detailed plot of the stress distribution in Fig. 6.18a [70]. The results exhibit the similar distributions for leucite glass ceramic to those for feldspar ceramic comparing Fig. 6.17a with 6.17b.

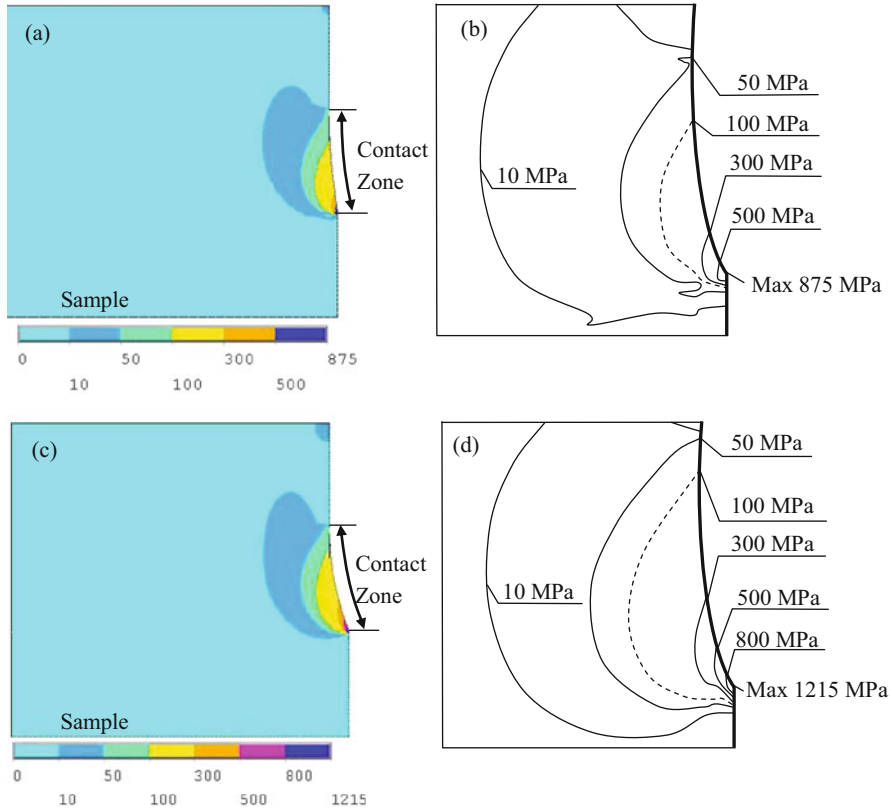


Fig. 6.17 (a) Contour plot of maximum principal stress distribution and (b) detailed plot of the stress distribution at the bur–prosthesis contact zone at the depth of cut of 10 μm and feed rate of 15 mm/min; (c) maximum principal stress distribution and (d) detailed plot of the stress distribution at the depth of cut of 50 μm and feed rate of 60 mm/min for feldspar ceramic (Reprinted with permission from Ref. [69]. Copyright 2009 by Elsevier)

However, the maximum principal stress of 866 MPa for the leucite glass ceramic is lower than the maximum stress of 875 MPa for the feldspar ceramic. Figure 6.18c demonstrates the contour plot of the maximum principal stress distribution for the leucite glass ceramic at the workpiece–bur contact zone at the depth of 50 μm and feed rate of 60 mm/min [70]. Figure 6.18d shows the detail plot of the stress distribution in Fig. 6.18c [70]. The maximum tensile stress was estimated to be 1203 MPa at the diamond grit exit point, which is much higher than the maximum stress obtained at the depth of cut 10 μm and the feed rate of 15 mm/min. This maximum stress for the leucite glass ceramic is lower than that for the feldspar ceramic at the same machining condition.

The SEM micrographs of the cross-sections of feldspar ceramic material machined at the depths of cut 10 μm and 50 μm and the feed rates of 15 mm/min and 60 mm/min are shown in Fig. 6.19 [69]. The maximum subsurface damage

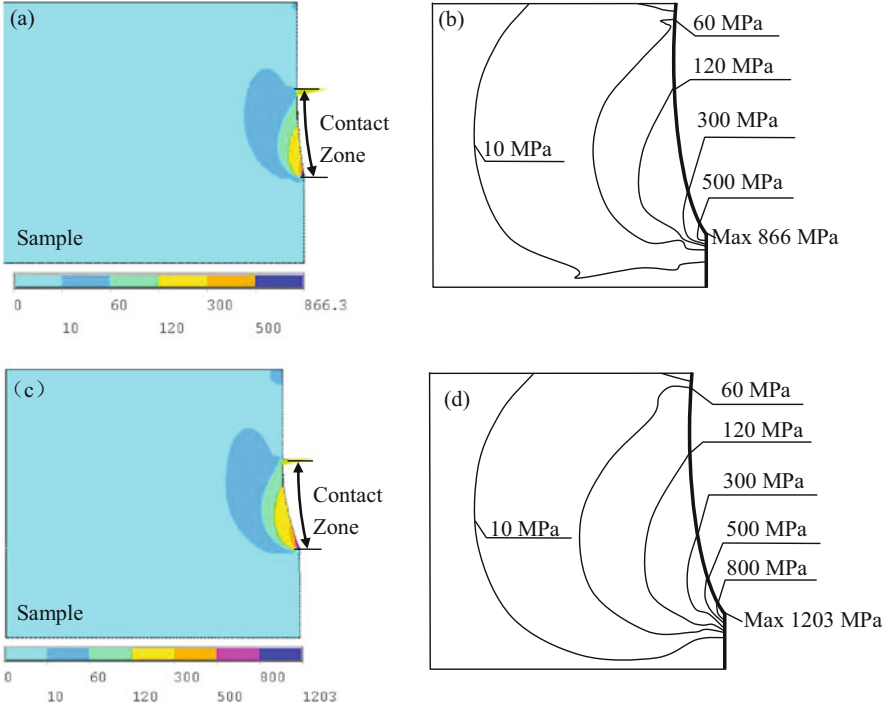


Fig. 6.18 (a) Contour plot of maximum principal stress distribution and (b) detailed plot of the stress distribution at the bur–prosthesis contact zone at the depth of cut of 10 μm and feed rate of 15 mm/min; (c) maximum principal stress distribution and (d) detailed plot of the stress distribution at the depth of cut of 50 μm and feed rate of 60 mm/min for leucite ceramic (Reprinted with permission from Ref. [70] 2010. Blackwell Publishing Ltd)

depth was estimated to be 74 μm (Fig. 6.19d) at the depth of 50 μm and the feed rate of 60 mm/min, which is about 2.6 times the minimum subsurface damage depth of 28 μm at the depth of cut of 10 μm and the feed rate of 15 mm/min (Fig. 6.19a).

The SEM micrographs of the cross-sections of leucite glass ceramic machined at the depths of cut 10 μm and 50 μm and the feed rates of 15 mm/min and 60 mm/min are shown in Fig. 6.20 [70]. The maximum subsurface damage depth was estimated to be 65 μm (Fig. 6.20d) at the depth of 50 μm and the feed rate of 60 mm/min, which is about 3.4 times the minimum subsurface damage depth of 19 μm at the depth of cut of 10 μm and the feed rate of 15 mm/min.

Based on the FEA modelling and SEM measurement, it is found that the resurfacing process parameters, the depth of cut and the feed rate, greatly affected the degree of subsurface damage, which are associated with the diamond grit depth of cut. Figure 6.21 shows the maximum FEA-predicted and the average maximum SEM-measured depths of subsurface damage for the feldspar ceramic versus diamond grit depth of cut [69]. It is seen that the maximum FEA-predicted subsurface damage depths are in agreement with the average maximum

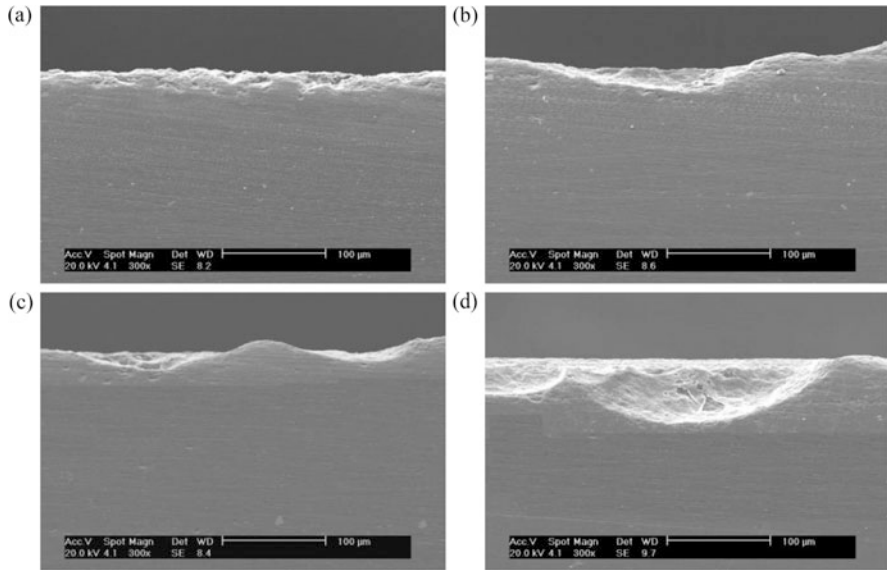


Fig. 6.19 SEM micrographs of the maximum depths of subsurface damage induced in the feldspar ceramics at the depth of cut of 10 μm and the feed rates of (a) 15, (b) 60 mm/min; at the depth of cut of 50 μm and the feed rates of (c) 15, (d) 60 mm/min (Reprinted with permission from Ref. [69]. Copyright 2009 by Elsevier)

SEM-measured values. Both predicted and measured subsurface damage depths approximately linearly increased with the diamond grit depth of cut with coefficients of determination of 0.92 and 0.89, respectively.

Figure 6.22 shows the maximum FEA-predicted and the average maximum SEM-measured depths of subsurface damage for the leucite glass ceramic versus diamond grit depth of cut [70]. A great validation of the maximum FEA-predicted subsurface damage depth in comparison with the average maximum SEM-measured values is also seen. Both predicted and measured subsurface damage depths in leucite glass ceramic also approximately linearly increased with the diamond grit depth of cut with coefficients of determination of 0.92 and 0.89, respectively.

6.5.4 Surface Phase Transformation

The dental resurfacing process requires extremely high-energy expenditure per unit volume of material removed. Virtually all of this energy is converted to heat which is concentrated within the workpiece–bur contact area. The high temperatures produced can cause various types of thermal damage to dental ceramics, in particular, phase transformation, thermal residual stresses, cracks and reduced fatigue

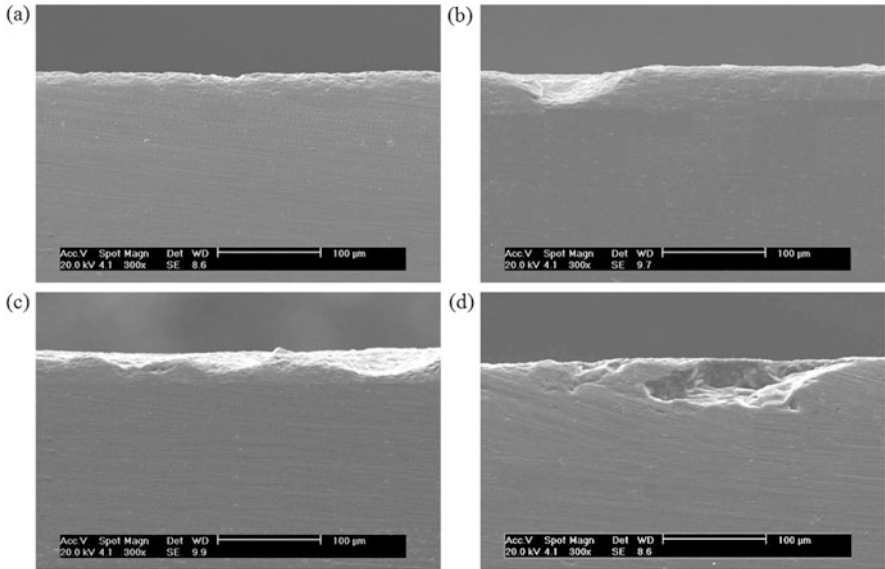


Fig. 6.20 SEM micrographs of the maximum depths of subsurface damage induced in the leucite ceramics at the depth of cut of 10 μm and the feed rates of (a) 15, (b) 60 mm/min; at the depth of cut of 50 μm and the feed rates of (c) 15, (d) 60 mm/min (Reprinted with permission from Ref. [70]. Copyright 2010 Blackwell Publishing Ltd)

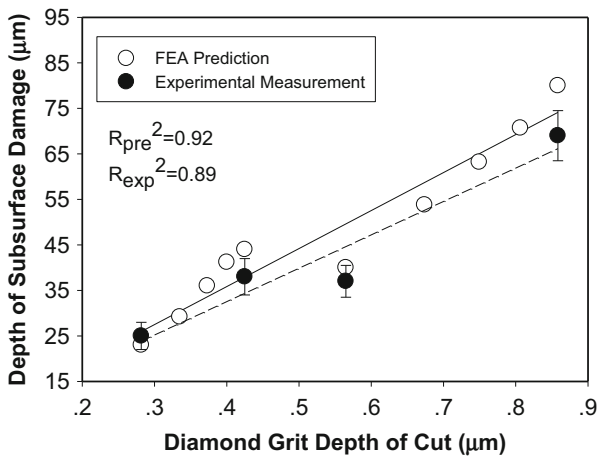
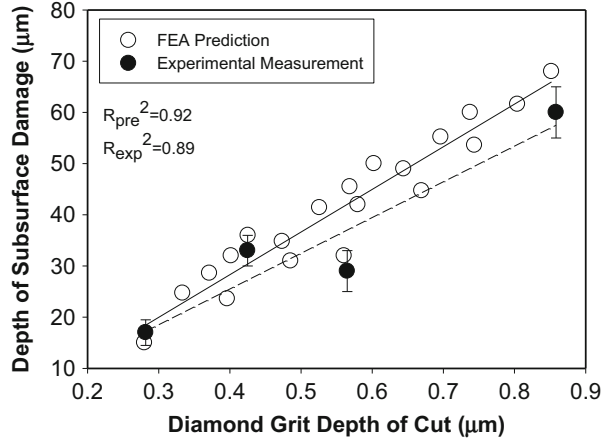


Fig. 6.21 Predicted and measured depths of subsurface damage versus diamond grit depth of cut for feldspar ceramic (Reprinted with permission from Ref. [69]. Copyright 2009 by Elsevier)

strength. Although thermal aspects in engineering grinding have been extensively studied [66], thermal-related issues in dental resurfacing largely remain mysteries.

Abrasive machining occurs by the interaction of discrete diamond abrasive grains on the bur surface with the ceramic workpiece. In dental resurfacing of

Fig. 6.22 Predicted and measured depths of subsurface damage versus diamond grit depth of cut for leucite ceramic (Reprinted with permission from Ref. [70]. Copyright 2010 by Blackwell Publishing)



dental ceramics using high-speed handpieces and diamond abrasives, the workpiece materials undergo both mechanical and thermal impacts due to resurfacing forces and heat. The resurfacing energy can induce crack initiation and propagation, debris generation and plastic deformation. In this process, the maximum temperature rise T_m in the cutting zone can be estimated as a band source of heat, which moves along the surface to the part being cut at the workpiece velocity, and expressed [71] as

$$T_m = \frac{1.13RUV_w^{1/2}a^{3/4}}{(k\rho c)^{1/2}d_s^{1/4}} \tag{6.3}$$

where R = the fraction of the grinding energy heating the workpiece, k = thermal conductivity, ρ = density, c = the specific heat of the workpiece material, V_w = workpiece feed rate, a = depth of cut and d_s = diameter of wheel.

In dental resurfacing of ceramics discussed in this chapter, the resurfacing conditions are as follows: $V_w = 15\text{--}60$ mm/min, $a = 10\text{--}50$ µm and $d_s = 1.4$ mm. For the leucite glass ceramic, the specific cutting energy U spanned $107\text{--}326$ J/mm³ [41]. R was selected to be 25% based on the general observation of approximately 25% of the machining energy transported as heat to the workpiece in ceramic machining [72, 73]. The physical properties of leucite glass ceramic are $\rho = 2.47$ g/cm³, $k = 1$ (W/m-K) [74] and $c = 0.9$ J/g-K [75]. Adding an ambient temperature of 25 °C, the estimated maximum resurfacing temperatures in machined leucite glass ceramic surfaces were estimated to be 651–1727 °C [67]. These high resurfacing temperatures provided the external driving conditions for the phase transformations of leucite crystals in the glass ceramic.

There are several methods which can be used to measure phase transformation in machined surfaces, including X-ray diffraction, transmission electron microscopy and Raman spectroscopy. To provide the evidence of phase transformation in dental ceramic resurfacing, laser micro-Raman spectroscopy was applied to the control

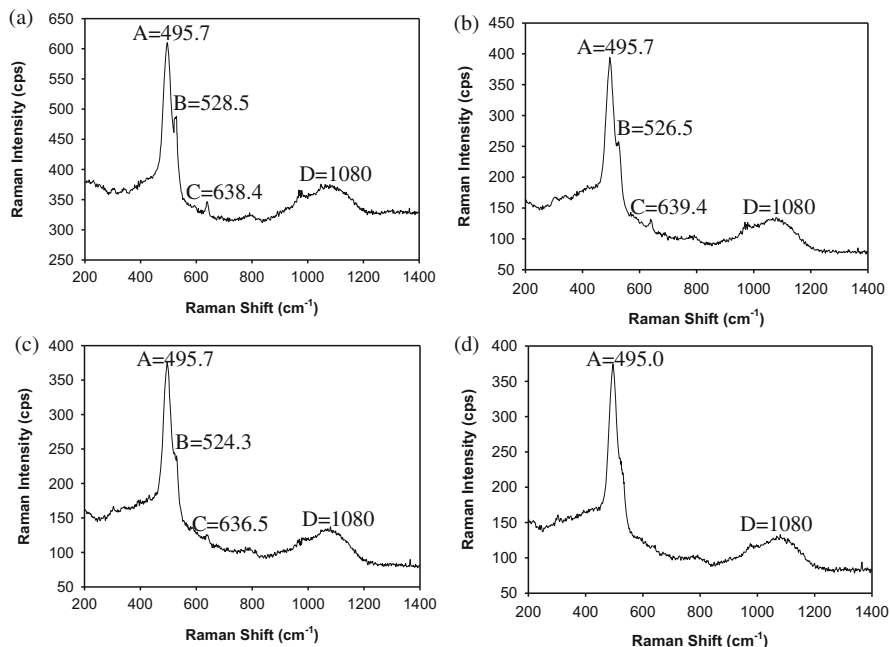


Fig. 6.23 Raman spectra of (a) the unadjusted leucite glass ceramic surface, (b) the leucite glass ceramic surface adjusted at 10 μm depth of cut and 15 mm/min feed rate, (c) the leucite glass ceramic surface adjusted at 30 μm depth of cut and 15 mm/min and (d) 500 μm depth of cut and 60 mm/min feed rate (Reprinted with permission from Ref. [67]. Copyright 2013 by Elsevier)

and machined leucite glass ceramic surfaces. Figure 6.23 shows the Raman spectra of the control and resurfaced leucite glass ceramic surfaces at different resurfacing conditions [67]. Figure 6.23a shows the Raman spectrum for the control surface which was in sintered state. Figure 6.23b–d is the Raman spectra of the adjusted surfaces at 10 μm depth of cut and 15 mm/min feed rate, 30 μm depth of cut and 15 mm/min feed rate and 50 μm -depth of cut and 60 mm/min feed rate, respectively. Compared to the control surface in Fig. 6.23a, intensities for peak A at 495 cm^{-1} Raman line frequency gradually weakened on the machined surfaces shown in Fig. 6.23b–d. Peak B at 529 cm^{-1} wave number was shifted to lower wave numbers of 526 cm^{-1} and 524 cm^{-1} on the machined surfaces and finally merged with peak A at 495 cm^{-1} wave number. Peak C at 638 cm^{-1} wave number in the control surface was also shifted and finally disappeared on the machined surfaces. The intensity of peak D at 1080 cm^{-1} wave number was noticeably stronger in the control surface than those in the machined surfaces. The Raman shifts shown in Fig. 6.23 evidently indicate that phase transformations occurred in the resurfacing process.

In the leucite crystals, the phase transformation from a tetragonal to a cubic polymorph occurs at 625 $^{\circ}\text{C}$ [76, 77]. The high temperatures during resurfacing

leucite glass ceramic provided the phase transformation temperature conditions. In dental resurfacing process, coolant was also applied to the resurfacing area, resulting in a complex cooling and heating condition where more complicated phase transformations of leucite crystals from tetragonal–cubic–tetragonal transformations might have occurred. Phase transformations in machined leucite glass ceramic can cause volume contraction. From cubic to tetragonal structures, leucite crystals have approximately 1.2% volume contraction [78], leading to the microcrack initiation and propagation in and around the crystals [78]. Thus, resurfacing-induced phase transformations promoted crack generation and fracture in resurfaced ceramic surfaces.

6.5.5 Material Removal Mechanisms

The mechanisms of material removal in abrasive machining of ceramics are often explored using indentation and scratching mechanics because the types of damage produced in these two processes are alike. Therefore, indentation mechanics can predict machining performance with reasonably good accuracy [79–81] although the thermal effect in indentation and scratching is generally neglected but it plays an important role in machining.

Resurfacing with a diamond bur containing multiple abrasive grits is a much more complex process than indentation [82–85]. For the feldspar and leucite glass ceramics, material removal mechanisms in resurfacing include fracture and plastic deformation (Figs. 6.13, 6.14, 6.15 and 6.16). Although the measured tangential and normal cutting forces are all less than 3 N (Figs. 6.8 and 6.9), the fundamental removal processes are controlled by the single-diamond abrasives of the two materials and their forces. Thus, the estimation of the cutting forces per grit, particularly, the normal cutting forces per grit, is essential in understanding the material removal mechanisms. The cutting force per grit is defined as a ratio of the measured cutting force against the active diamond abrasive particles involved in cutting. Thus, the average normal force per grit F_n' can be expressed as [79]

$$F_n' = F_n / l_c b N \quad (6.4)$$

where F_n = measured normal cutting force, l_c = contact length between the bur and the workpiece, b = width of contact and N = total number of active grits per unit area.

The density of diamond abrasives can be determined from the SEM imaging of diamond bur surfaces (Fig. 6.8). However, not all the abrasives on the bur surfaces were involved in cutting. It is generally accepted that the fraction of active abrasive grits on fixed abrasive tools, such as single-layered diamond burs, engaging in cutting process, is approximately 1–10% [86].

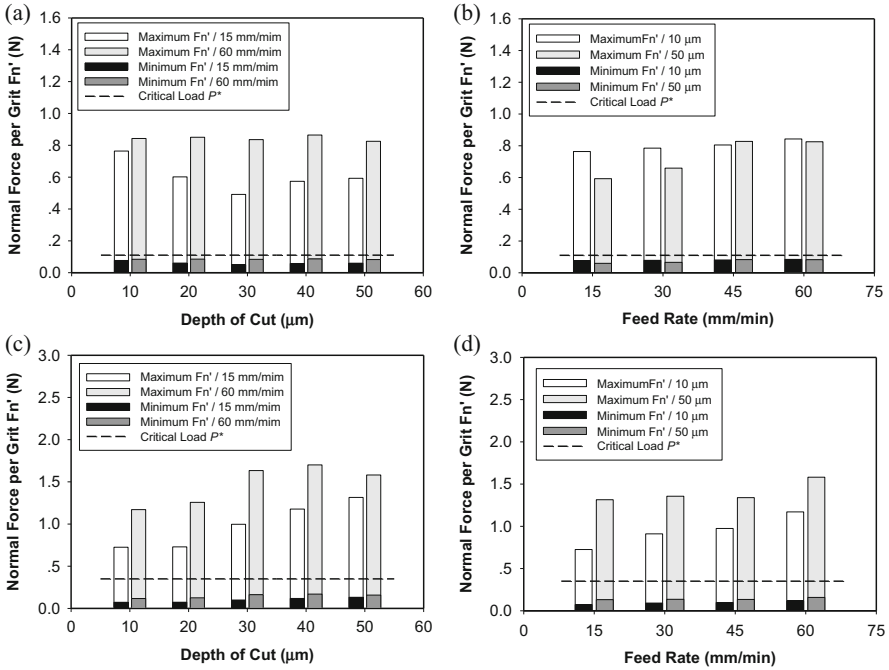


Fig. 6.24 Maximum and minimum normal forces per grit versus (a) depth of cut and (b) feed rate for the feldspar ceramic; maximum and minimum normal forces per grit versus (c) depth of cut and (d) feed rate for the leucite ceramic. Fig. 6.24c, d (Reprinted with permission from Ref. [67]. Copyright 2012 Elsevier)

For the feldspar ceramic, the maximum and minimum normal forces per grit versus depth of cut and feed rate are plotted in Fig. 6.24a, b, respectively. At the 15 mm/min feed rate, the maximum normal forces per grit range from 0.59 to 0.76 N when increasing the depth of cut from 10 to 50 μm. Accordingly, the minimum normal forces per grit are in the range of 0.059–0.076 N. At 60 mm/min, the maximum normal forces per grit are in the range of 0.82–0.86 N for 10–50 μm depth of cut, while the minimum normal forces per grit scale are between 0.082 and 0.086 N. For the leucite glass ceramic, the maximum and minimum normal forces per grit versus feed rate and depth of cut are plotted in Fig. 6.24c, d, respectively [67]. At the 15 mm/min feed rate, the maximum normal forces per grit range from 0.73 to 1.32 N when increasing the depth of cut from 10 to 50 μm. Accordingly, the minimum normal forces per grit are in the range of 0.073–0.13 N. At the 60 mm/min, the maximum normal forces per grit are in the range of 1.17–1.58 N for 10–50 μm depth of cut, while the minimum normal forces per grit scale are between 0.12 and 0.16 N.

Both fracture and plastic deformation were observed in dental surfacing of feldspar and leucite glass ceramics. It is of interest to compare the estimated normal

cutting forces per grit with the force thresholds for brittle–ductile fracture transitions, P^* , which is expressed as [87]

$$P^* = (54.47\alpha/\eta^2\theta^4) (K_c/H)^3 K_c \quad (6.5)$$

where $\alpha = 2/\pi$, $\theta = 0.2$ and $\eta = 1$ for the typical intensity and extent of tensile field, K_c = toughness and H = Vickers hardness. For the feldspar and leucite glass ceramics, the force thresholds P^* are determined to be 0.11 N and 0.35 N.

Under the applied dental resurfacing conditions, the minimum normal forces per grits for feldspar and leucite glass ceramics are lower than their critical thresholds, while the maximum normal forces per grits for the two materials are higher than their critical thresholds. This explains the reason why both fracture and plastic deformation occurred in the resurfacing processes for the two materials. Attributed to the nature of the mixed brittle and ductile mode in dental resurfacing, the changes in depth of cut or feed rate did not significantly influence surface roughness for both materials (Fig. 6.12). However, the increase in diamond grit depth of cut produced the much deeper subsurface damage in both materials (Figs. 6.21 and 6.22). Further, the resurfacing conditions profoundly affected the specific cutting energy and created the thermal impact to dental ceramics, resulting in complex phase transformations (Fig. 6.23). The resurfacing temperature and machining temperature-induced phase transformations also contributed to crack initiation and propagation in the resurfacing process.

Dentists usually use coarse diamond grit burs in highly efficient gross material reduction for both enamel and ceramic restorative materials. In restorative dentistry, feldspar and leucite glass ceramics for veneers, onlays and inlays are required to obtain precise marginal and occluding fits with neighbouring and mating enamel or prosthetic teeth. The final adjustment with diamond burs must achieve good surface integrity with minimum resurfacing-induced damage in ceramic restorations. Clinical failure rates in multilayer ceramic restorations, especially in external ceramic veneers, are found to be high [88–90]. Therefore, for high reliability of ceramic restorations, resurfacing brittle feldspar porcelains and leucite glass ceramics with coarse diamond burs must be carefully conducted.

6.6 Concluding Remarks

Dental resurfacing using handpieces and diamond burs is a manual cutting process in which the resurfacing quality depends on manual skills of individual dentists. Dental care costs associated with ceramic restorations are very expensive, and the use of diamond burs for resurfacing often imparts resurfacing-induced damage with a concomitantly negative impact on reliability of ceramic restorations. A great amount of work has been performed in order to understand the dental resurfacing of feldspar and leucite glass ceramics. Understanding of the fundamental of the

mechanics of material deformation and removal is becoming clearer. This will generate information that can be used by dentists to optimise the resurfacing process in clinical process selection and by engineers to develop new dental handpieces and dental materials for durable ceramic restorations.

The research results presented in this chapter confirmed that the response of dental ceramics to the resurfacing process greatly depends on the microstructure that controls the material removal mechanisms. In resurfacing feldspar and leucite ceramics, both the tangential and normal forces for the two materials were measured to increase with either the depth of cut or the feed rate. An increase in either depth of cut or feed rate did not affect the surface roughness and morphology. The resurfaced surfaces for the two materials consist of microfracture and chipping, ductile removal traces, smeared areas and debris. The mixed microfracture and ductile removal mode was the primary mechanism for resurfacing both materials. Subsurface stresses beneath the two resurfaced materials varied with the resurfacing conditions. Subsurface damage was found to be the linear consequence of the penetration of the diamond grit depth of cut for both feldspar and leucite glass ceramics. Thermal-related phase transformations were discussed towards resurfacing leucite glass ceramic. However, further studies are needed to understand the thermal modelling of fracture and plastic mixed mode in dental ceramic removal. The results presented can be used as a qualitative guidance to clinical dental practice on cutting mechanisms of material removal using dental handpieces with diamond burs.

Acknowledgements This chapter represents an extensive and still ongoing work supported by the National Science Foundation of China via NSFC Project Grant Nos. 50475115 and [51375335](#); the Australian Research Council via ARC LE110100016; the Department of Industry, Innovation, Science, Research and Tertiary Education, Australia, via ACSRF GMB12029; and the James Cook University Collaboration Grants and Incentive Schemes.

References

1. Kelly JR (2004) Dental ceramics: current thinking and trends. *Dent Clin N Am* 48:513–530
2. Thompson JY, Stoner BR, Piascik JR (2007) Ceramics for restorative dentistry: critical aspects for fracture and fatigue resistance. *Mater Sci Eng C* 27:565–569
3. Rekow ED, Silva NRFA, Coelho PG, Zhang Y, Guess P, Thompson VP (2011) Performance of dental ceramics: challenges for improvements. *J Dent Res* 90:937–952
4. Denry I, Holloway JA (2010) Ceramics for dental applications: a review. *Materials* 3:351–368
5. van Noort R (2002) Introduction to dental materials, 2nd edn. Elsevier, Oxford
6. Miyazaki T, Hotta Y, Kunii J, Kuriyama S, Tamaki Y (2009) A review of dental CAD/CAM: current status and future perspectives form 20 years of experience. *Dent Mater J* 28:44–56
7. Mörmann WH (2006) The evolution of the CEREC system. *JADA* 137:75–135
8. Kelly JR (2007) Development of a meaningful systematic review of CAD/CAM reconstructions and fiber-reinforced composites. *Clin Oral Implants Res* 18(Suppl 3):205–217
9. Rekow D, Thompson VP (2007) Engineering long-term clinical success of advanced ceramic prostheses. *J Mater Sci Mater Med* 18:47–56

10. Pjetursson BE, Sailer I, Zwahlen M, Hämmerle CH (2007) A systematic review of the survival and complication rates of all-ceramic and metal-ceramic reconstructions after an observation period of at least 3 years. *Clin Oral Implants Res* 18(suppl 3):73–85
11. Otto T, De Nisco S (2002) Computer-aided direct ceramic restorations: a 10-year prospective clinical study of Cerec CAD/CAM inlays and onlays. *Int J Prosthodont* 15:122–128
12. Rekow D, Thompson VP (2005) Near-surface damage—a persistent problem in crowns obtained by computer-aided design and manufacturing. *Proc Inst Mech Eng H J Eng Med* 219:233–243
13. Chang CW, Waddell JN, Lyons KM, Swain MV (2011) Cracking of porcelain surface arising from abrasive grinding with a dental air turbine. *J Prosthodont* 20:613–620
14. Yin L, Song XF, Song YL, Huang T, Li J (2006) An overview of in vitro abrasive finishing & CAD/CAM of bioceramics in restorative dentistry. *Int J Mech Tools Manufact* 46:1013–1026
15. Guazzato M, Albakry M, Quada L, Swain MV (2004) Influence of grinding, sandblasting, polishing and heat treatment on the flexural strength of a glass-infiltrated alumina-reinforced dental ceramic. *Biomaterials* 25:2153–2160
16. Al-Wahadni A (1999) The roots of dental porcelain: a brief historical perspective. *Dent News* 2:43–44
17. Darvell BW (2009) *Materials sciences for dentistry*, 9th edn. Woodhead Publishing Limited, Cambridge
18. Rasmussen ST, Nagaji-Okumu W, Boenke K, O'Brien WJ (1997) Optimum particle size distribution for reduced sintering shrinkage of a dental porcelain. *Dent Mater* 13:43–50
19. Helvey G (2010) A history of dental ceramics. *Compt Rendus Geosci* 31:309–311
20. Song XF, Yin L, Peng JH, Lin B (2013) Cutting characteristics of dental glass ceramics during in vitro dental abrasive adjusting using a high-speed electric handpiece. *Ceram Int* 39:6237–6249
21. Nakamura T, Dei N, Kojima T, Wakabayashi K (2003) Marginal and internal fit of Cerec 3 CAD/CAM all-ceramic crowns. *Int J Prosthodont* 16:244–248
22. Hansen S (2000) Preparations for Cerec 3: where are the limits. *Int J Comput Dent* 3:197–205
23. Giordano RA (1996) Dental ceramic restorative systems. *Compend Contin Educ Dent* 17:779–794
24. Deng Y, Lawn BR, Lloyd IK (2002) Characterization of damage modes in dental ceramic bilayer structures. *J Biomed Mater Res Part B* 63:137–145
25. Kim HW, Dent Y, Miranda P, Pajares A, Kim HE, Lawn BR (2001) Effect of flaw state on the strength of brittle coatings on soft substrates. *J Am Ceram Soc* 84:2377–2384
26. Ironside JG, Swain MV (1998) Ceramics in dental restorations: a review and critical issues. *J Aust Ceram Soc* 34:78–91
27. Höland W, Schweiger M, Rheinberger VM, Kappert H (2009) Bioceramics and their application for dental restorations. *Adv Appl Ceram* 108:373–380
28. Giordano R (2006) Materials for chairside CAD/CAM-produced restorations. *JADA* 137:14S–21S
29. Bindl A, Mormann WH (2002) An up to 5-year clinical evaluation of posterior in-ceram CAD/CAM core crowns. *Int J Prosthodont* 15:451–456
30. Curtis AR, Wright AJ, Fleming GJP (2006) The influence of surface modification techniques on the performance of a Y-TZP dental ceramic. *J Dent* 34:195–206
31. Stuedevant C, Roberson T, Heymann H, Sturdevant J (1995) *The art and science of operative dentistry*, 3rd edn. Mosby, St. Louis
32. De Jager N, Feilizer AJ, Davidson CL (2000) The influence of surface roughness on porcelain strength. *Dent Mater* 16:381–388
33. Finger WJ, Noack MD (2000) Postadjustment polishing of CAD/CAM ceramic with luminescence diamond gel. *Am J Dent* 13:8–12
34. Wright MD, Masri R, Driscoll CF, Romberg E, Thompson GA, Runyan DA (2004) Comparison of three systems for the polishing of an ultra-low fusing dental porcelain. *J Prosthet Dent* 92:486–490

35. Song XF, Yin L, Han YG, Wang H (2008) In vitro rapid adjustment of porcelain prostheses using a high-speed dental handpiece. *Acta Biomater* 4:414–424
36. Song XF, Yin L, Han YG, Wang H (2008) Micro fine finishing of a feldspar porcelain for dental prostheses. *Med Eng Phys* 30:856–864
37. Song XF, Yin L (2010) Quantitative effect of diamond grit size on subsurface damage induced in dental adjusting of porcelain surfaces. *Proc Inst Mech Eng H J Eng Med* 224:1185–1193
38. Xu HHK, Kelley RJ, Jahanmir S, Thompson V, Rekow ED (1997) Enamel subsurface damage due to tooth preparation with diamonds. *J Dent Res* 76:1698–1706
39. Yin L, Jahanmir S, Ives LK (2003) Abrasive machining of porcelain and zirconia with a dental handpiece. *Wear* 255:975–989
40. Yin L, Han YG, Song XF, Wang H (2007) Effect of diamond burs on process and damage involving in vitro dental resurfacing of a restorative porcelain. *J Phys D Appl Phys* 40:5291–5300
41. Song XF, Yin L, Han YG (2009) In-process assessment of dental cutting of a leucite-reinforced glass-ceramic. *Med Eng Phys* 31:214–220
42. Christensen HJ, Christensen RP (1991) Single patient-use diamond rotary instruments. *CRA Newsl* 15:1–2
43. Choi C, Driscoll CF, Romberg E (2010) Comparison of cutting efficiencies between electrical and air-turbine dental handpieces. *J Prosthet Dent* 103:101–107
44. Dyson JE, Darvell BW (1993) The development of the dental high-speed air turbine handpiece. Part 1. *Aust Dent J* 38:49–58
45. Dong X, Yin L, Jahanmir S, Ives LK, Rekow ED (2000) Abrasive machining of glass-ceramics with a dental handpiece. *Mach Sci Technol* 4:209–233
46. Yin L, Ives LK, Jahanmir S (2004) Effects of fluids on the simulated clinical dental machining of a glass ceramic. *J Am Ceram Soc* 87:173–175
47. Yin L, Ives LK, Jahanmir S, Rekow ED, Romberg E (2001) Abrasive machining of glass-infiltrated alumina with diamond burs. *Mach Sci Technol* 5:43–61
48. Gegauff AG, Rosenstiel SF, Johnston WM, Gangji RK (1998) Handpiece degradation associated with performance testing of diamond rotary cutting instruments. *Aust Dent J* 43:342–348
49. Dyson JE, Darvell BW (1995) Dental air turbine handpiece performance testing. *Aust Dent J* 40:330–338
50. Norling BK, Stanford JW (1976) Evaluation performance of dental rotary cutting instruments. In: *The cutting edge: interfacial dynamics of cutting and grinding*, US Department of Health, Education, and Welfare, DHEW Publication No. (NIH) 76–670, Washington, DC
51. Siegel SC, von Fraunhofer JA (1997) Effect of handpiece load on the cutting efficiency. *Mach Sci Technol* 1:1–13
52. Westland IAN (1980) The energy requirement of the dental cutting process. *J Oral Rehabil* 7:51–63
53. Siegel SC, von Fraunhofer JA (1999) Dental cutting with diamond burs: heavy-handed or light-touch? *J Prosthodont* 8:3–9
54. Siegel SC, von Fraunhofer JA (2000) Cutting efficiency of three diamond bur grit sizes. *JADA* 131:1706–1710
55. Siegel SC, von Fraunhofer JA (2002) The effect of handpiece spray patterns on cutting efficiency. *JADA* 133:184–188
56. von Fraunhofer JA, Siegel SC (2000) Handpiece coolant flow rates and dental cutting. *Oper Dent* 25:544–548
57. Siegel SC, von Fraunhofer JA (1999) Irrigation solution and pressure effects on tooth sectioning with surgical burs. *Oral Surg Oral Med Oral Pathol Oral Radiol Endod* 87:552–556
58. von Fraunhofer JA, Siegel SC (2003) Using chemomechanical assisted diamond bur cutting for improved efficiency. *JADA* 134:53–58
59. von Fraunhofer JA, Siegel SC (2000) Enhanced dental cutting through chemomechanical effects. *JADA* 131:1465–1469

60. Dyson JE, Darvell BW (1997) A laboratory evaluation of two brands of disposable air turbine handpiece. *Br Dent J* 182:15–21
61. Dyson JE, Darvell BW (1999) Torque, power and efficiency characterization of dental air turbine handpieces. *J Dent* 27:573–586
62. Dyson JE, Darvell BW (1999) Flow and free running speed characterization of dental air turbine handpieces. *J Dent* 27:465–477
63. Yin L, Song XF, Qu SF, Huang T, Mei JP, Yang ZY, Li J (2006) Performance evaluation of a dental handpiece in simulation of clinical finishing using a novel 2-DOF in vitro apparatus. *Proc Inst Mech Eng H J Eng Med* 220:929–938
64. Yin L, Song XF, Qu SF, Han YG, Wang H (2006) Surface integrity and removal mechanism in simulated dental finishing of a feldspathic porcelain. *J Biomed Mater Res B Appl Mater* 79B:365–378
65. Yin L, Song XF (2011) Grindability of dental ceramics in the in vitro oral regime. *Int J Abrasive Technol* 4:204–222
66. Malkin S, Guo C (2008) *Grinding Technology: theory & Application of Machining with Abrasives*, 2nd edn. Industrial Press, New York
67. Song XF, Yin L (2012) Surface morphology and fracture in handpiece adjusting of a leucite-reinforced glass ceramics with coarse diamond burs. *Mater Sci Eng A* 534:193–202
68. Song XF, Yin L, Han YG, Li J (2008) Finite element analysis of subsurface damage of ceramic prostheses in simulated intraoral dental resurfacing. *J Biomed Mater Res B Appl Mater* 85B:50–59
69. Song XF, Yin L (2009) Subsurface damage induced in dental resurfacing of a feldspar porcelain with coarse diamond burs. *J Biomechanics* 42:355–360
70. Song XF, Yin L (2010) Stress and damage at the bur-prosthesis interface in dental adjustments of a leucite-reinforced glass ceramic. *J Oral Rehabil* 37:680–691
71. Malkin S, Ritter JE (1989) Grinding mechanisms and strength degradation for ceramics. *ASME J Eng Ind* 111:167–174
72. Zhu B, Guo C, Sundenland JE, Malkin S (1995) Energy partition to the workpiece for grinding of ceramics. *Ann CIRP* 44:1267–1271
73. Brinksmeier E, Aurich JC, Govekar E, Heinzel C, Hoffmeister HW, Klocke F, Peters J, Rentsch R, Stephenson DJ, Uhlmann E, Weinert K, Wittmann M (2006) Advances in modeling and simulation of grinding processes. *Ann CIRP* 55:667–696
74. Ashby MF (2005) *Materials selection in mechanical design*, 3rd edn. Butterworth-Heinemann, Oxford
75. Newton H, Hayward SA, Redfern SAT (2008) Order parameter coupling in leucite: a calorimetric study. *Phys Chem Miner* 35:11–16
76. Heaney PJ, Veblen DR (1990) A high-temperature study of the low-high leucite phase transition using the transmission electron microscope. *Am Mineral* 75:464–476
77. Wyckoff RWC (1963) *Crystal structure*. Wiley, New York
78. Denry IL, Mackert JR Jr, Holloway JA, Rosenstiel SF (1996) Effect of cubic leucite stabilization on the flexural strength of feldspathic dental porcelain. *J Dent Res* 75:1928–1935
79. Jahanmir S, Xu HHK, Ives LK (1999) Mechanism of materials removal in abrasive machining of ceramics. In: Jahanmir S, Ramulu M, Koshy P (eds) *Machining of ceramics and composites*. Marcel Dekker, New York
80. Marinescu I, Rowe B, Yin L, Wobker HG (2000) Abrasive processes. In: Marinescu I, Tonshoff HK, Inasaki I (eds) *Handbook of ceramic grinding and polishing*. Noyes Publications/William Andrew Publishing, New York
81. Xu HHK, Smith DT, Jahanmir S (1996) Influence of microstructure on indentation and machining of dental glass-ceramics. *J Mater Res* 11:2325–2337
82. Song XF, Yin L (2010) Induced damage zone in micro fine dental finishing of a feldspar porcelain. *Med Eng Phys* 32:417–422

83. Song XF, Peng JH, Yin L, Lin B (2013) A machining science approach to dental cutting of glass ceramics using an electric handpiece and diamond burs. *ASME J Manufact Eng* 135:011014-1-6
84. Yin L, Han YG, Song XF, Li J, Wang H (2007) In vitro study on high rotation deep removal of ceramic prostheses in dental surgery. *J Biomed Mater Res B Appl Biomater* 82B:334-345
85. Yin L (2012) Property-process relations in clinical abrasive adjusting of dental ceramics. *J Mech Behav Biomed Mater* 16:55-65
86. Stephenson DJ, Vesalovac D, Manley S, Corbett J (2001) Ultra-precision grinding of hard steels. *Precis Eng* 25:336-345
87. Lawn BR, Evans AG (1977) A model for crack initiation in elastic/plastic indentation fields. *J Mater Sci* 12:2195-2199
88. Lawn BR, Deng Y, Miranda P, Pajares A, Chai H, Kim DK (2002) Overview: damage in brittle layer structures from concentrated loads. *J Mater Res* 17:3019-3036
89. Lawn BR, Deng Y, Lloyd IK, Janal MN, Rekow ED, Thompson VP (2002) Materials design of ceramic-based layer structures for crowns. *J Dent Res* 81:433-438
90. Swain MV (2009) Unstable cracking (chipping) of veneering porcelain on all-ceramic dental crowns and fixed partial dentures. *Acta Biomater* 5:1668-1677

Chapter 7

Polymer Blends and Composites for Biomedical Applications

S.T. Lin, L. Kimble, and D. Bhattacharyya

Abstract The versatility of polymers has enabled to implement many new ideas in the biomedical field and continues to play a significant role in finding new and improved solutions in the exciting multidisciplinary fields of implants and scaffold tissue engineering. Polymers are rapidly replacing other traditional biomaterials such as metals and ceramics attributable to their versatility. Material properties of polymers will be discussed in a context specific to biomedical engineering here, which includes biocompatibility, biodegradation, biochemical and biomechanical behaviours. Biopolymers have been used as implantable materials for a broad range of biomedical applications, such as cardiology, cartilage, vasculature, bone, wound healing, drug delivery and prosthetic dentistry. Also biopolymers have become a primary material used for fabricating scaffolds in tissue engineering, a fast emerging area for tackling a critical issue in tissue and organ shortage. To address these two above-mentioned application areas, this chapter is divided into two sections: The first focuses on tissue scaffolds, including the design requirements, fabrication methods and cellular testing. The second discusses coronary stents and their development, investigating into the potential of biopolymer blends as a candidate for biodegradable coronary stents.

Keywords Polymer blends • Scaffold tissue engineering • Implant • Coronary stent • Composites

7.1 General Introduction

Biomaterial research has proposed a wide variety of applications in the field of tissue engineering and regenerative medicine, ranging from metals and ceramics to polymers, both naturally derived and synthetic materials. Among these, polymers have played a significant role and hold importance mainly due to their flexible and adjustable chemical and physical designs, being able to improve their performance

S.T. Lin • L. Kimble • D. Bhattacharyya (✉)

Centre for Advanced Composite Materials, The University of Auckland, Auckland,
New Zealand

e-mail: s.lin@auckland.ac.nz; d.bhattacharyya@auckland.ac.nz

through easily adaptable production techniques and the possibility of being tailored to suit the requirements of the application.

The versatility of polymers has inspired many new ideas in the biomedical field and continues to play a significant role in finding new and improved solutions in the exciting multidisciplinary field of implants and tissue engineering. Due to the interdisciplinary nature of this field, to develop and enhance further research, the combined knowledge from biological sciences, chemistry and engineering must be utilised to construct indispensable innovations for improving human health.

The term *biomaterials* was defined in the second consensus conference on definitions in biomaterials science, of the European Society for Biomaterials [1], as ‘a material intended to interface with biological systems to evaluate, treat, augment or replace any tissue, organ, or function of the body’. The use of biomaterials dates back to more than 2000 years ago, when gold was extensively used in dentistry [2]. Other applications of biomaterials were used by the old civilisations of Romans, Egyptians, Indians and Chinese people for thousands of years for artificial eyes, ears, teeth and noses for aesthetic purposes or reconstruction of missing or defective parts of the body [3].

Since the middle of the last century, advancements allowed the first biodegradable polymeric sutures to be approved in the 1960s [4]. Another application of biomaterials using poly(2-hydroxyethyl methacrylate) (polyHEMA) was developed by Wichterle, also in the 1960s, for contact lens applications [5].

Advancements over the centuries have improved surgical techniques, sterilisation methods and biomaterials knowledge, which have enabled the development of new methods and devices to improve human health. Biomaterials have been used for implants such as sutures, bone and joint replacements, vascular grafts, heart valves and dental implants and also for medical devices such as pacemakers, biosensors, artificial hearts and tubes [3]. Significant developments in other areas of regenerative medicine has also extensively used biomaterials for repairing damaged tissue such as cartilage, bone, muscle, skin and blood vessels [6].

Polymers are rapidly replacing other traditional material choices such as metals and ceramics in biomedical applications due to their versatility. Applications for biopolymers include neural, cartilage, vascular, bone, wound dressing, drug delivery systems and dental applications. Also biopolymers have been the primary materials used for scaffold fabrication in tissue engineering applications [7]. Polymers can be classified into natural and synthetic polymers. Natural polymers are often considered to be biocompatible due to their natural compositions, and it is no surprise that they were the first used in clinical applications [8]. Natural polymers include collagen, gelatin, elastin, actin, keratin, chitosan, chitin, cellulose, silk and hyaluronic acid. Synthetic polymers include polyethylene, polypropylene, polyvinylchloride, polyurethanes, silicone, rubbers, hydrogels and polytetrafluoroethylene (PTFE).

Armentano et al. [9] has classified biopolymers into two main groups comprising of biodegradable polymers and biosourced polymers. Biodegradable polymers have been used extensively in medical applications and are defined as being capable of breaking down into molecules found in the environment such as carbon dioxide,

carbon and methane, under the enzymatic action of microorganisms, in a defined period of time (European standard EN 13432).

Biodegradable polymers can be further classified into two major groups: (1) naturally derived materials and (2) synthetic materials. Favourable characteristics of naturally derived materials include their biological compatibility which supports cell adhesion and function. However, the drawbacks of poor mechanical properties and their limited supply leading to costly factors encourage alterations or other alternatives to be found. On the other hand, synthetic materials possess hydrophobic surfaces and low cell-recognition signals, whereas their mechanical strength, manufacturing versatility and overall controllable characteristics have encouraged more research to focus on the many new possibilities of synthetic materials to be used [7]. Apart from reconstruction of tissue, polymeric biomaterials are also important in the applications such as bone cement, degradable sutures, bone screws and dental devices.

Biocompatibility is a primary requirement for biomaterials and is a critical characteristic that must be satisfied before it can be used in the body. Cell–material interactions are also crucial when biomaterials are applied clinically. Major factors including surface topography, surface chemistry, mechanical properties and biological cues can all influence cell behaviour and end response to their interactions with biomaterials. Careful design of biomaterials for specific applications can control and modulate the cell adhesion, proliferation, migration and differentiation. By using polymeric biomaterials, it is now possible to adjust the material properties, by modifying chemical composition, varying the fabrication method and altering the physical structure. While many other biomaterials have also been studied intensively and can also be adjusted and designed for different applications, they may not possess as much flexibility as polymeric materials offer.

For a material to be qualified as a biomaterial, it must first satisfy the primary requirement of being biocompatible, which is the ability of a material to perform with an appropriate host response in a specific application, or the quality of not having toxic or injurious effects on biological systems [1]. The host response to a biomaterial implant can depend on a multitude of factors ranging from the chemical, physical, biological, biomechanical and degradation properties to the structure, dimensions and shape of the implant [8].

Another important factor of biomaterials is the biodegradability in numerous applications. Current trends predict that many permanent prostheses and related devices used for temporary biomedical applications will soon be replaced by biodegradable substitutes [8]. Biodegradable materials have become more and more popular with keen interest developing further to solve current challenges such as long-term biocompatibility issues as well as the technical and ethical issues associated with revision surgeries [8]. Both natural and synthetic polymers can be biodegradable. Although degradable natural polymers such as collagen have been used for thousands of years for biomedical applications, synthetic polymers have started to gain popularity over the years since the latter half of the 1960s [10].

Note that while there are advantages of biological materials over synthetic materials such as biodegradability, favourable cell adhesion properties and having

similar mechanical properties to that of natural tissue, there are several major deficiencies of using natural biological materials such as viral infections, antigenicity, unstable material supply and batch inconsistency [10]. These unfavourable deficiencies have led to the decrease in the demand of biological materials and instead have increased the need for synthetic materials with improved properties and flexibility.

Other advantages of synthetic polymers include their uniformity and their predictability, which can be tailored and used to design specific products to fulfil specific applications. The properties of polymers affect the physical structure and thermal and chemical characteristics [11]. The majority of biodegradable polymers available on the market for regenerative medicine and tissue engineering applications are based on collagen or polyester materials. By combining different materials physically or chemically and using appropriate processing methods, many desired characteristics can be created to produce biocompatible products for biomedical applications.

Biodegradation of polymeric biomaterials works by allowing polymer erosion to occur. The mode of degradation can either involve the material degrading hydrolytically or enzymatically [10]. The majority of natural biological polymers rely on enzymatic degradation. However, hydrolytically degradable polymers are preferred for use in implants due to minimal variations compared to enzymatically degradable polymers [12]. Some of the most promising hydrolytically sensitive synthetic polymers developed for biomedical applications include poly(α -esters), polyurethanes, polyanhydrides and poly(ester amide)[8]. The earliest and most extensively studied class of biodegradable polymers is the poly(α -esters) group, and, among this group, the most extensively investigated polymers are the poly(α -hydroxy acid)s, which include poly(glycolic acid) and poly(lactic acid) [8]. Polyglycolide is highly crystalline (45–55 %) and thus possesses a high tensile modulus. It has been processed in a variety of methods including extrusion, injection and compression moulding, particulate leaching and solvent casting, to produce desirable structures for biomedical applications [13]. The first biodegradable synthetic suture called DEXON® was approved by the Food and Drug Administration (FDA) in 1969 and was based on polyglycolide. The degradation product of polyglycolide in the body is glycine, which can be excreted in the urine or converted into carbon dioxide and water via the citric acid cycle [14]. Polylactides exist in two different forms, poly(L-lactic acid) (PLLA) and poly(D-lactic acid) (PDLA), which are formed from L-lactide and D-lactide stereoisomers, respectively. Additionally, copolymers can be produced from L-lactide and D-lactide and are abbreviated PDLLA. PLLA has a crystallinity of approximately 37 %, a glass transition temperature of 60–65 °C and a melting temperature of approximately 175 °C [15]. PLLA is semi-crystalline, while PDLLA copolymers tend to be amorphous [16]. PLLA has a high elastic modulus of 3.2–3.7 GPa and strength of 55–60 MPa, while an equimolar PDLLA copolymer has an elastic modulus of 0.9 GPa and strength of 41 MPa[17]. Orthopaedic products such as BioScrew®, Bio-Anchor® and Phantom Suture Anchor® have been produced based on PLLA. PDLLA is preferred for developing drug delivery systems compared to PLLA, due to its lower strength and subsequent faster degradation rate.

Poly lactides degrade into lactic acid, a normal human metabolic by-product which can be broken down into water and carbon dioxide via the citric acid cycle [14].

A range of poly(lactide-co-glycolide) (PLGA) polymers has also been developed and studied for a wide range of biomedical applications. Different ratios of glycolic acid and L-lactic acid can be used to obtain different characteristics. PLGA has been commercially used as meshes (Vicryl Mesh®), suture reinforcements, skin replacement materials and tissue scaffolding structures. Degradation rates of PLGA depend on such chemical parameters as glycolic acid and L-lactic acid ratios and molecular weight. PLGA has been FDA approved for use in humans, and its versatile processibility enables controllable shapes, structures and degradation rates to be formed.

Poly(caprolactone) (PCL) is a semi-crystalline polyester and is highly processible due to its solubility in a wide range of solvents. PCL has a melting temperature of 55–60 °C and has the ability to form miscible blends with a wide range of polymers. PCL has a relatively low tensile strength of 23 MPa but an extremely high elongation over 700% [13]. The rate of degradation of PCL is much lower than PLA and needs approximately 2–3 years, making it suitable for longer-term drug delivery systems.

Polyurethanes possess excellent mechanical properties with good biocompatibility and structural versatility. This has attracted interest in their usage for biomedical applications which have been used as cardiac pace makers and vascular grafts. Polyanhydrides degrade by surface erosion due to their hydrophobic nature, which makes them suitable for controlled-release applications [13].

Poly(ester amide) has been developed to combine the excellent mechanical properties of polyamides and the biodegradability of polyesters [18]. Poly(ester amide) has been investigated as potential suture materials. CAMEO® is based on a poly(ester amide) blend which has been developed for site-specific delivery of small hydrophobic drug and peptides.

With the few examples given for the types of polymers and their versatility in terms of production method and overall properties, many possibilities can arise by combining the different polymers and other biomaterials available, to create endless innovations for biomedical applications.

The flourishing and rapidly advancing field of tissue engineering aims to replace, regenerate or improve damaged tissues and organs that have lost their functions. The three general strategies that have been adopted by tissue engineering include (1) implantation of isolated cells or cell substitutes; (2) delivery of tissue-inducing substances, such as growth factors, and placing cells onto or within matrices [19]; and (3) the use of tissue scaffolds, where cells are seeded onto the substrate to create implantable tissue constructs.

Tissue scaffolds are porous structures which provide mechanical support for cells, which play an important role in the regeneration of neotissue. Scaffolds mimic the natural extracellular matrix (ECM) and create an environment similar to that of the ECM in our bodies. The ECM is a noncellular component that exists within all tissues and organs. Each type of tissue has its own ECM composition and structure which are generated during tissue development through dynamic and

mutual conversations between the various cellular components. Scaffolds facilitate the regeneration of tissue by acting as a temporary ECM for cell attachment, proliferation, differentiation and subsequent growth until the tissue is completely restored.

Scaffolds have been researched and used in a number of areas such as bone, cartilage, skin, vascular tissues, neural tissues and vehicles for controlled drug delivery. The design and fabrication of tissue scaffolds are of vital importance to the tissue engineering and have become a major focus of biomaterial research recently. The most often used synthetic biopolymers for 3D scaffolds are saturated poly(α -hydroxy esters) which include PLA, PGA, PLGA and PCL. The mechanical properties and cellular adhesion and proliferation are enhanced through incorporation of nanoparticles into the synthetic particles [20].

Another important area of biomaterials is to make the implantable devices for restoring malfunction of the body. A typical example is the use of stents to mechanically support blood vessels inside the human body. Coronary arteries are the vessels commonly treated by stenting strategy due to the prevalence of coronary artery disease (CAD). CAD has become very widespread within developed regions of the world and is the leading cause of death in the US and Europe [21]. CAD is basically the build-up of plaque within the coronary arteries. Excessive plaque build-up leads to constriction of flow through the vessel, in which case the implantable stents need to be deployed to restore normal flow.

To address these two above-mentioned application areas, this chapter is divided into two major sections: The first will focus on tissue scaffolds, including the design requirements, fabrication methods and cellular testing. The second will discuss coronary stents and their development, investigating into the potential of PLLA/PBS blend as a candidate for biodegradable coronary stents.

7.2 Tissue Scaffolds

Tissue engineering and regenerative medicine combines the knowledge and advancements from multiple disciplines with the ultimate goal to create biological substitutes and replacements that can immensely improve the lives of human beings who suffer from loss or damage of body parts due to accidents and diseases. This field has grown to see the many potential applications that the fruits of research can be used for and has recognised the huge international interest that has contributed to this exciting area of improving the quality of lives for mankind.

There are nevertheless many challenges seen in the field of tissue engineering. Nerem [22] pointed out that the challenge of imitating nature to potentially solve tissue engineering issues in terms of donor tissue and organ shortages has three different categories that need to be addressed: *cell technology*, *construct technology* and integration of these into the living system. In summary, Nerem refers to *cell technology* as involving cell sourcing, manipulation of cell function and the effective use of stem cell technology. *Construct technology* includes engineered three-

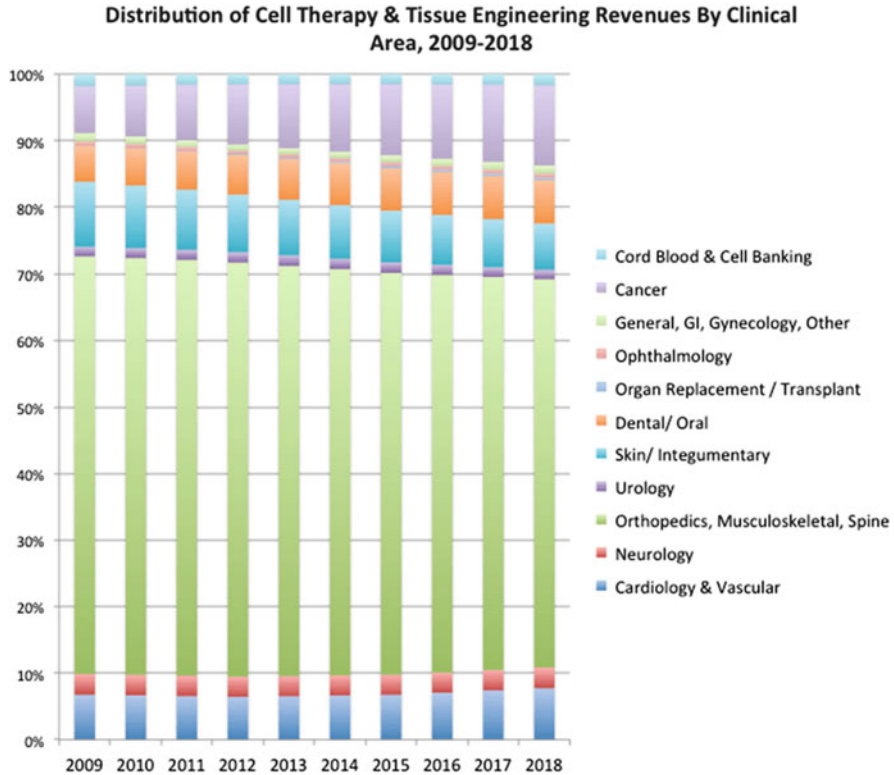


Fig. 7.1 ‘Distribution of cell therapy and tissue engineering revenues by clinical area, 2009–2018’ (Report #S520) (Reprinted from Ref. [23], Copyright 2011, with permission from MedMarket Diligence, LLC)

dimensional architectures which either mimic a specific tissue or provide a delivery vehicle for cells.

Figure 7.1 shows the global market of tissue engineering, cell therapy and transplantation by clinical areas from 2009 to 2018. The orthopaedics, musculo-skeletal and spine sector clearly dominates the market and has been predicted to continue to dominate the market right through to 2018.

Figure 7.2 shows the increase of global solid organ transplantations from 2009 to 2012 based on the Global Observatory on Donation and Transplantation (GODT) data, produced by the WHO-ONT collaboration [24]. Based on the GODT organisation, there was a 9.59% increase in global organ transplantation activity from 2009 to 2012. Although the global activity of organ transplantation increases annually, the statistics for 2012 showed that only less than 10% of global needs were satisfied. Kidneys are the most commonly transplanted organs worldwide, followed closely by the liver, heart, lung, pancreas and then small bowel among

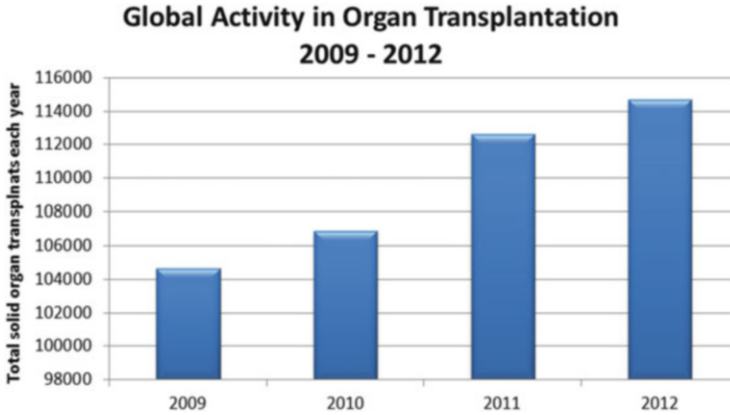


Fig. 7.2 Global activity in solid organ transplantation from 2009–2012. (Plotted based on data from the WHO-ONT Global Observatory on Donation and Transplantation) [24]

Table 7.1 Global activity in solid organ transplantation from 2009–2012

	Kidney	Liver	Heart	Lung	Pancreas	Small bowel	Total
2009	72,100	21,175	5405	3650	2320	–	104,650
2010	73,179	21,602	5582	3927	2362	227	106,879
2011	76,118	23,721	5741	4278	2564	209	112,631
2012	77,818	23,986	5935	4359	2423	169	114,690

Data from the WHO-ONT Global Observatory on Donation and Transplantation [24]

other organs and tissues. The major problem is to access enough donations of tissues and organs for all the patients who need them.

Table 7.1 summarises global activity in solid organ transplantation from 2009 to 2012. Based on the incredible numbers of transplantations annually, even though it is only a small fraction of the amount that is actually required, the field of tissue engineering will continue to motivate researchers worldwide to engage in and be part of the ever increasing health demands of humanity and to constantly improve and develop existing technologies even further.

Another report on the tissue engineering and stem cell technologies by Jaklenec et al. [25] shows that the orthopaedic industry also lead the field in terms of sales for commercial products or services in 2011, taking up 50 % of sales.

As the largest sector of commercial product sales in the tissue engineering and stem cell being taken up by the orthopaedic and wound healing industry, it makes sense to explore more options in construct technology used in this area. An approach to designing tissue-like substitutes pioneered by Langer and Vacanti [19] is the cell-seeded polymeric scaffolds. The challenge here is to design a scaffold that will allow cells to create their own matrix. The structure and morphology of the scaffold is what determines the ‘environment’ that the cells are living in. Hence, it is a great design challenge to create the perfect suitable

environment to stimulate cell matrix deposition and subsequently proliferation, migration and differentiation. Research of suitable scaffolds is one thing; development of cost-effective manufacturing processes to produce these scaffolds is another aspect which many can often overlook. Ultimately, these engineered products will need to be conveniently and readily available to industry and clinicians. Hence, when designing tissue scaffolds, the ease of manufacture and increase of availability of manufactured devices are the important aspects to consider.

What is needed in the development of tissue scaffolds is an understanding of the environment in which specific cells are able to survive, and then recreate the environment using biocompatible and/or biodegradable materials for some specific applications. This has now drawn attention on finding the most suitable material for the specific requirements.

Different materials have different properties that may be better suited for use in specific applications. For example, the skin is a relatively soft tissue and therefore would not require a stiff material to support, whereas bone, on the other hand, needs to withstand much higher compressive stresses and would therefore require a much stiffer scaffold that is able to provide similar mechanical properties to the tissue which we are aiming to regenerate.

Each material would contain more favourable properties suited for specific applications compared to other materials. Since each tissue in the body has its particular role and therefore a specific set of favourable characteristics, it seems illogical to design just one super material that will cater to different purposes in tissue engineering [26]. By recognising that there are multiple aspects that need careful consideration to complete the process of designing a suitable scaffold, one should better understand the things required at each stage of research and development for delivering a product, thereby contributing to the field of tissue engineering. With this in mind, we will now focus on the topic of tissue scaffolds, as it is one of the major components required to regenerate a three-dimensional functional tissue.

7.2.1 Tissue Scaffold Materials

One of the major considerations of tissue scaffolds is the choice of material. The minimum requirement for any material is biocompatibility, both before and after degradation if the material is biodegradable. Biomaterials have recently had an impact on scaffold tissue engineering [27]. For example, by combining scaffolds with cells, the skin can be made and used for patients with burns. Various other applications involving a combination of polymers and cells such as corneas, cartilage, bone and liver have been in clinical trials [27, 28].

Many naturally occurring biological scaffolds that have great biocompatibility are available. However, one of the disadvantages of using these scaffolds is their poor mechanical properties. For this reason, synthetic polymers have emerged to solve this problem. Mechanical properties do play an important role especially for load-bearing applications. Polymers can be chosen based on the mechanical

properties required. They can also be processed in a way that may increase their mechanical properties. In addition to the favourable mechanical properties of polymers, their processing ability is another advantageous aspect, hence drawing popular demands of polymeric research in the biomedical field.

The question is which manufacturing method or process will allow the chosen bulk material to be processed into a structure suitable for the biological application that the scaffold is intended to be used for. Depending on the end application of scaffolds, different mechanical and chemical properties may be required. With so many aspects to consider, designing a scaffold with optimal characteristics such as desired strength, degradation, porosity, structure and surface, shapes and sizes is more manufacturable when using polymers [29].

7.2.2 Scaffold Design

7.2.2.1 General Structural and Morphology Requirements

Scaffolds are typically three-dimensional structures that mimic and promote an *in vivo* environment to support and enhance cell viability for regenerating tissues [30]. Scaffolds need to mimic the architecture of the natural extracellular matrix (ECM) environment to assist the body to heal [31]. When designing scaffolds, the following requirements are often considered:

1. Biomaterials of choice should take into account the physical and chemical properties required for the end application [32].
2. Structure and morphology of biomaterials should mimic the host tissue's structure and biological functions [33].
3. Scaffold must be biocompatible, both before and after degradation [34].
4. Scaffold must possess a porous, interconnected architecture which enables transportation of cells and cell nutrients as well as provides mechanical support during neotissue regeneration [35].
5. Scaffold surface should support cell adhesion, proliferation, migration and differentiation [36].
6. Interconnected pores with appropriate pore size to allow cell infiltration and vascularisation [37, 38].
7. Controlled biodegradability to support growth of new tissue [39, 40].

Cells need a structure to provide mechanical support while regenerating tissue. In the natural human body, the extracellular matrix (ECM) is what provides this support. The goal to imitate nature means that the natural extracellular matrix that is a composite of proteins, glycoproteins and proteoglycans is an important model that researchers are mimicking when designing scaffolds [41]. Collagen is a protein and a major component in the ECM which arranges into a fibrous network with diameters ranging from 50 to 500 nm [42, 43]. With the fibrous property that collagen possesses, ECMs have a porous structure which allows the cells to

proliferate and migrate into the ECM structure thereby differentiating into the required tissue. The architecture of ECM provides the environment that the cells grow in, which strongly influences the behaviour of the cells and the type of tissue it will differentiate into [15, 44, 45]. Generally, scaffolds must have a porous structure with sizes similar to that of the cells to be used for the particular application. By creating an imitation of the ECM using synthetic and artificial materials, limitations such as batch-to-batch variation and disease transmission associated with the materials from mammalian sources when using naturally derived biological materials can be avoided [27].

Porosity

Porosity is one of the most important aspects of a tissue scaffold as mentioned previously and is necessary in bone regeneration as shown by Kuboki et al. where direct osteogenesis occurred on the porous scaffolds [46]. Without these pores, the transport and migration of the cells and nutrients would simply be impossible and would not be assisting the cells to produce their own ECM. It is still a challenge to accurately characterise the porosity of scaffolds as there are many different types of nanostructures created from various manufacturing methods, which lead to very distinctive pore structures.

Different techniques to test and characterise the porosity may be required for different scaffolds fabricated. Some porosity characterisation techniques include mercury porosimetry [47], image analysis [48], gravimetry [49] and liquid displacement [50] methods based upon density and volume. Porosity looks at pore size, pore distribution and interconnectivity of the pores. All of these factors play their part in determining and characterising the porosity of the scaffold. In effect, a change in one could affect the other, so to study the porosity and alter the morphology and dimension, one needs to look at all the aspects that contribute to the porosity of the scaffold as a whole.

Pore Size

Pore size can directly influence the porosity of the scaffold, and in turn, affect the behaviour of the cells. Lower porosity stimulates osteogenesis, as the cell is forced to aggregate due to suppression of cell proliferation, while higher porosity allows the cells to infiltrate into the scaffold, creating more ingrowth [37]. There is, however, a compromise that has to be made for the latter, where mechanical properties maybe sacrificed if a higher porosity needs to be achieved. There is thus a limit to which this balance of porosity and functionality can be achieved, which also depends on the rate of tissue growth and the rate of scaffold degradation. It has also been shown in the previous work [51] that although specific surface area provided by scaffolds with small pores allows better initial cell adhesion, the effect

of larger pores which provide better cell and nutrient infiltration is more important as it better promotes cell proliferation and migration into the centre of the scaffold.

Interconnectivity

Depending on the type of scaffold and how it is produced, the interconnectivity of the material used for producing the porous scaffold can differ vastly. MFC scaffolds are a great example of how the interconnectivity of the structure can vary just by controlling the type of polymer used. In the MFC scaffolds, the fibrils can create an interconnected 3D network or create a fibrillar network by controlling the type of polymers used. Electrospun scaffolds, on the other hand, have a different type of connectivity mechanism, where the individual fibres intertwine and tangle with each other to create the nanofibrillar network. This kind of structure will undoubtedly allow the scaffold to have more elongation as the fibres will be allowed to stretch alongside each other. With this type of structure, the compressive strength may not be as high as that for the MFC scaffolds, where the fibrils are interconnected, forming a more rigid structure. From these examples, it can be seen that although the same type of material is used to create nanofibrous networks, the mechanism for which the nanofibres integrate to form a network is an important factor in determining and characterising the properties of the scaffold.

7.2.2.2 Cell–Scaffold Interactions

The ECM provides a structure which holds cells together to form tissues and organs. It provides anchorage and mechanical support for the cells and is also responsible for controlling and regulation of cell adhesion, spreading, proliferation, migration, differentiation and apoptosis by mechanical and biochemical communications with cells [52]. This bidirectional communication between cell and ECM influences the behaviour of each other and is important in determining how much ECM is synthesised or degraded and subsequently the fate of the cell. The realm of tissue engineering involves the use of biomaterials that can mimic the natural ECM to facilitate in cell proliferation and differentiation for the specific tissue requirements.

Cell adhesion is one of the first interactions that occur between the cell and the ECM followed by cell spreading onto the ECM. Migration of the cells is also an important aspect, especially during development and regeneration of tissues. Cell migration is encouraged by breaking the existing cell from the ECM bonds and formation of new bonds in other areas of the ECM. Cell proliferation and differentiation are also affected by the cell–ECM interaction, even though the precise mechanism for how they cooperate is still unknown. The current understanding of the behaviour of cells, proteins and other key biological factors will no doubt facilitate the amalgamation of cells and constructs to form and recreate new tissues that can be incorporated into the body.

7.2.2.3 Design Requirements for Orthopaedic Applications

Osteoinduction is part of the normal bone healing and formation of bone process, and for it to take place, osteoconduction, the growth of bone on a surface, does not just depend on biological factors but also the response of cells to implants. Successful osseointegration is achieved when there is a stable bone to implant contact where the anchorage will remain over a long period [53], enough to support the formation of new tissue. The four main components required for successful bone regeneration includes osteogenic cells, osteoconductive scaffolds, growth factors and the mechanical environment, which is referred to as the diamond concept [54, 55]. This shows that the development of osteoconductive scaffolds is a significant aspect, in which the synthesis of suitable tissue scaffolds is essential to accomplishing the regeneration of bone tissue.

It is important to be able to control the pore sizes as studies have shown that pore sizes affects cell behaviour and bone formation [37, 56]. The minimum pore size required for bone scaffolds is considered to be 100 μm due to cell size, migration requirements and biotransport [37]. However, pore sizes larger than 300 μm have been recommended to support formation of capillaries and new bone. This is important as vascularised tissue such as bone requires pores that are large enough for cell migration as well as vascular ingrowth [57]. Pore sizes around 1000 μm favour osteoblast phenotype expression, and pores around 500 μm allow more bone formation, so Sicchieri [56] has concluded that the ideal scaffold for bone tissue engineering should present pores in both sizes within the same scaffold.

7.2.3 *Fabrication of Scaffolds and Assessment of Cell Viability*

7.2.3.1 Scaffold Fabrication

Some common techniques as shown in Fig. 7.3 used to fabricate scaffolds include electrospinning, gas foaming [58], rapid prototyping [59], thermally induced phase separation (TIPS) [60], NFC, freeze drying [61], self-assembly [62] and solvent casting/particulate leaching [63].

One of the most important features that a tissue scaffold must possess is porosity. There are many different techniques for synthesising porous structures such as electrospinning, thermally induced phase separation, solvent casting and particulate leaching, porogen leaching, gas foaming and emulsification/freeze drying. Currently, the two main fabrication techniques used in bone tissue engineering are electrospinning and thermally induced phase separation [57]. These will be discussed further later. Recently, there has been research on a novel manufacturing method which uses a basic manufacturing process, extrusion, and further post-processing to fabricate porous scaffolds which have the potential to be completely solvent-free. This technique will also be discussed in more detail later.

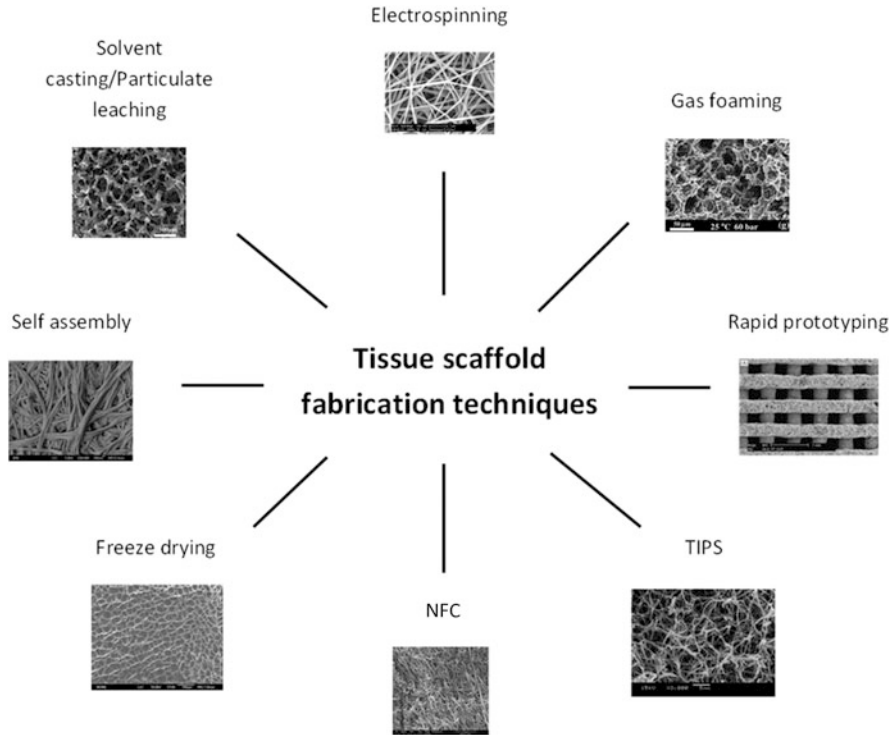
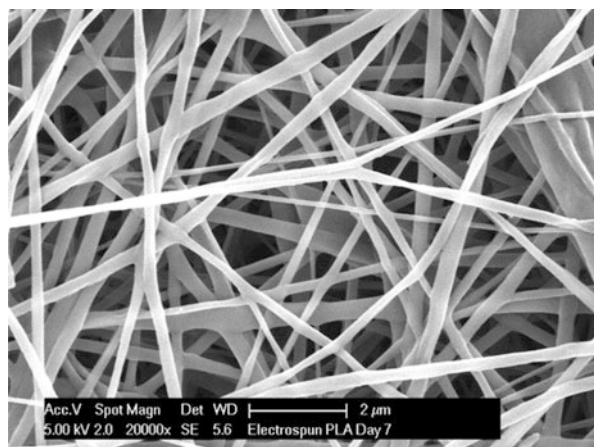


Fig. 7.3 Fabrication techniques for tissue scaffold: electrospinning, gas foaming (Reprinted from Ref. [58], Copyright 2011), rapid prototyping (Reprinted from Ref. [59], Copyright 2005), TIPS (Reprinted from Ref. [60], Copyright 2009), NFC, freeze drying (Reprinted from Ref. [61], Copyright 2009), self-assembly (Reprinted from Ref. [62], Copyright 2011), solvent casting or particulate leaching (Reprinted from Ref. [63], Copyright 2009). All with permission from Elsevier

Electrospinning

Electrospinning has received tremendous interest and been extensively researched in the past decade [64–66]. It has been recognised as a technique to produce nanofibres that have been widely studied for applications in the biomedical field [67–69]. Due to the similarity of the electrospun fibres to natural ECM, electrospinning has gained huge popularity, especially in the field of bone tissue engineering [70, 71]. Figure 7.4 shows a typical electrospun network which is composed of nanofibres overlapping and intertwined to form a fibrillar network with a very porous structure. A major drawback of electrospinning is the use of organic solvents, most of which are toxic to cells. A study by Lederer [72] showed that although the organic solvent content decreases after vacuum treatment of fibrillar scaffolds, there may still be traces that are undetectable, enough to negatively affect cell growth on the scaffolds. For this reason, there is a need for the scaffolds to be produced completely free of organic solvents.

Fig. 7.4 Electrospun PLA scaffold



Thermally Induced Phase Separation (TIPS)

The TIPS technique produces a 3D nanofibrous scaffold by taking advantage of the thermodynamic instability of polymer solutions under certain conditions [33]. As described by Holzwarth [57], the TIPS process involves five steps: polymer dissolution, phase separation and gelatin, solvent extraction, freezing and freeze drying. When phase separation occurs, a polymer-rich phase with a higher concentration of polymer and a polymer lean phase with a lower concentration of polymer are formed. When the solvent is extracted and removed, the polymer-rich phase solidifies; different morphologies will form depending on the conditions of the system [33, 73]. Nanofibrous, synthetic biodegradable scaffolds have been fabricated using this method for use in tissue scaffold applications [74].

Nanofibrillar Composite Technique (NFC)

The nanofibrillar composite (NFC) technique utilises common engineering and commodity polymers to create nanofibrils of high strength and stiffness dispersed in an isotropic matrix. This technique is an emerging concept that employs melt blending of polymers to create an even distribution of insitu reinforcing nanofibrils through simple extrusion, drawing and post-processing [75, 76]. The NFC manufacturing method uses two thermodynamically immiscible polymers to create a fibrillar composite network. The polymers must have sufficient drawability to allow the formation of reinforcing fibrils and must be processed at a single temperature without the degradation of either polymer [75, 76]. One of the main advantages of this technique is that there is the opportunity for creating scaffolds which are completely free of organic solvents, by suitably selecting the isotropic matrix such that only water is required in the matrix removal process. Figure 7.5

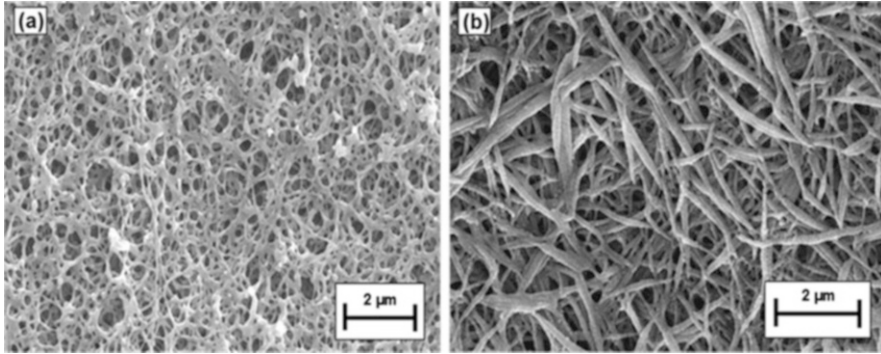


Fig. 7.5 Scaffolds manufactured using the NFC concept produced from (a) PLA and (b) PETG

shows the typical morphology of scaffolds manufactured using the MFC technique from (a) PLA and (b) PETG.

Natural and synthetic polymers have the advantages of processability, decent mechanical properties, immunological stability, manufacturability and the ease of being able to design the shape and architectures for accommodating the host tissues requirements. Where biodegradability is required, the type of polymer used can be chosen to fit the required degradation rate. This can be attributed to the large and diverse polymeric materials that have been available. Not only are they widely available, they are also simple to modify and can also be processed using a large variety of manufacturing techniques that are currently very well known and have been used for many different polymer processing. Some of the most common industrial manufacturing processes include injection moulding, blow moulding and extrusion.

Using extrusion as the main manufacturing process, polymers can be processed to produce nanoscale architectures. With the formation of nanofibres and nanopores, one of the applications which would welcome these nano-features is in the biomedical field. Tissue scaffolds require that the matrix should be highly porous to enable the cells to migrate and infiltrate the structure, transport of cell nutrients and removal of waste products and at the same time to maintain the overall mechanical properties of the synthetic ECM matrix to support cell growth.

The process of extrusion starts off with blending a mixture of polymer pellets which are thermodynamically immiscible so that the polymers will stay separate and preserve their individual properties. The polymers are melted inside a barrel which has either a single or twin screw to further blend the melted polymers. Once the blended polymers leave the die, the blended yarn is drawn by pulling and elongating the extrudate onto a winding drum which continuously rotates and pulls on the blended yarn. The final product produced from this extrusion process is a yarn of thread-like blended polymer composite.

To achieve nanoporous networks using extrusion as the main manufacturing process requires various steps in the post-extrusion section. Once a yarn of blended polymer composite is produced from the extrusion process, this yarn is transferred

to a frame which is in the shape of interest, in this case, a rectangular stainless steel frame. The transfer of the yarn can be done in various ways such as winding manually onto the frame or by using winders or lathes.

To create the porous structure that is required in tissue scaffolds, one of the components of the composite blend will need to be removed. When one component of the composite blend is removed, the remaining structure will be composed of the matrix that was not removed and the porous holes that were once filled up by the polymer that has been removed. There can be a wide variety of polymer blends which can be chosen depending on the type of properties needed. When a polymer which is water soluble is chosen as the polymer that will be removed to form the porosity of the network, then only water is required in the removal process.

7.2.3.2 Assessment of Cell Viability

To assess the cytocompatibility of cells on the scaffold material produced, mouse osteoblasts (bone-forming cells) were used in cell culture techniques to grow the cells on the materials over a period of time. Tenocytes were also used to try different cell types on the same scaffolds. Qualitative analysis was achieved by conducting live/dead staining of cells that have grown on the scaffold up to a total of 20 days and 14 days for osteoblasts and tenocytes, respectively.

One of the most important steps in the cell culture is sterilisation. A common problem with polymers is their sensitivity to heat. The method of sterilisation in most labs is autoclaving which uses pressurised steam to heat the material being sterilised. This is obviously a concern for polymers as the temperature at which lab equipment are sterilised at is typically 121 °C for 15–20 min depending on the size of the load. Polymers are sensitive to heat and typically have low glass transition temperatures. PLLA which is used in the NFC manufacturing process has a glass transition temperature of 55–60 °C. Glass transition temperatures for polyethylene terephthalate and polyvinyl alcohol are 70 °C and 85 °C, respectively. All polymers used in this project have glass transition temperatures below 100 °C.

For the purpose of cell culture, ethanol has been chosen to sterilise the materials which will be used to assess cell growth. Although ethanol technically does not sterilise, it does disinfect by killing microbial cells, but has no effect on spores. Ethanol works by denaturing proteins through a process that requires water; hence, ethanol must be diluted to 60–90 % to work effectively in disinfection of the materials. The manufactured NFC scaffolds were soaked in 70 % ethanol for a minimum of 30 min and left to dry at room temperature under sterile conditions.

UV radiation has damaging effects on cells and also makes a great tool for sterilisation. To further ensure the materials are sterile, they were exposed to UV radiation for 30 min each side. UV radiation was chosen partly due to its convenience and safety of use as it does not have high penetration so is safe to use in small areas such as laminar flow hoods.

In preparation for seeding cells onto the sterilised scaffolds, the materials were soaked overnight in the culture media used for maintenance of the cells. Tenocytes

Fig. 7.6 Tenocytes grown for 7 days on PLA scaffold fabricated using the NFC technique

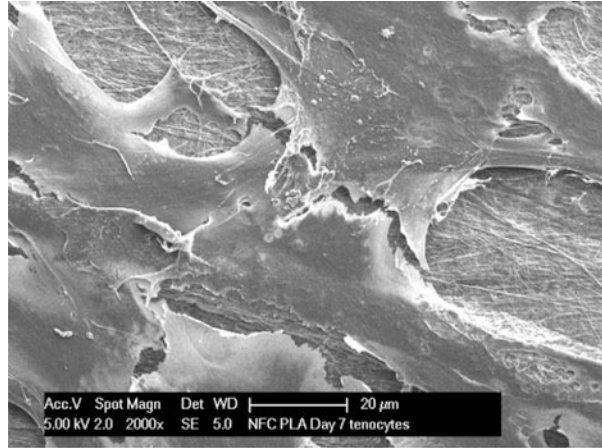
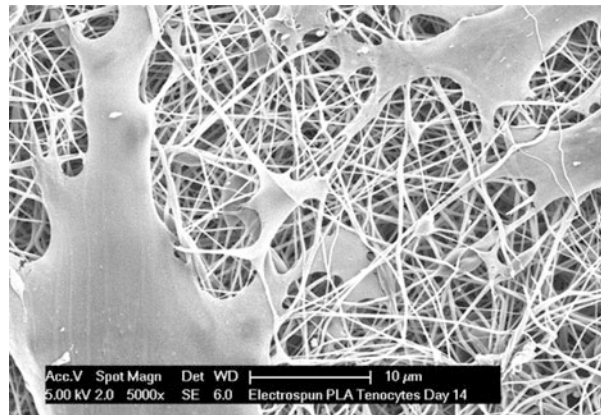


Fig. 7.7 Tenocytes grown on the electrospun scaffold for 14 days



were used to study the cytocompatibility on the scaffolds. Figure 7.6 shows the tenocytes have spread across the surface of the PLA scaffold after 7 days of cell culture. The limited penetration of cells into the scaffold can be improved by increasing the porosity of the scaffold. Cell attachment on the surface of the scaffold demonstrates that the NFC fabrication technique has potential to produce scaffolds which can be completely solvent-free.

Figure 7.7 illustrates how the tenocytes have migrated beneath the top surface of the electrospun network on day 14 of cell culture. This shows the importance of having a porous interconnected structure, creating a three-dimensional space that allows cells to embed themselves within the scaffold. Traditional cell culture practice often uses 2D cell culture plates to study cells. As tissues are 3D structures, the significance of 3D cell culture studies have become paramount in mimicking the natural environment of host cells more closely. Being able to alter the pore size and

porosity of the scaffold through controlling manufacturing process is an important step in mimicking the ECM of the natural host tissue.

7.2.4 Other Porous Scaffolds and Surface Modification Methods

Several porous scaffolds using polymeric materials such as PLGA and PLLA and collagen have been developed and studied by the researchers from the National Institute for Materials Science (NIMS). They have developed funnel-like scaffolds using ice particulates, collagen scaffolds with micro-patterned biological molecules, ECM scaffolds derived from MSCs (chondrocytes and fibroblasts) and hybrid porous scaffolds (synthetic and natural). The surface of scaffolds can be modified to promote cell growth and can be designed to accommodate particular desired characteristics. One example of surface modification of scaffolds can be referred to the work of Lu et al. [77], where funnel-like PLGA–collagen hybrid scaffolds have demonstrated to facilitate cell seeding and homogeneous cell distribution, ECM production and chondrogenesis. These funnel-like collagen sponges were produced by using embossing ice particulates as a template. A diverse range of surface patterns can be formed on the scaffold surfaces by creating and adjusting the pattern of the ice particulates formed.

Cell functions such as angiogenesis have been manipulated by incorporating biological micro-patterned surfaces onto scaffolds. Guided blood vessel formation was achieved by preparing collagen sponges with micro-patterned vascular endothelial growth factor (VEGF). VEGF was micro-patterned in the 3D collagen sponges using micro-patterned collagen/VEGF ice lines, prepared by a dispersing machine [78]. VEGF–micro-patterned collagen sponges have demonstrated blood vessel regeneration after 6 weeks of implantation [78].

Porous ECM scaffolds have also been derived from mesenchymal stem cells (MSCs), chondrocytes and fibroblasts [81, 80]. Cells were initially cultured on poly (lactic-co-glycolic acid) (PLGA) templates until ECM was generated by the cells. The construct was then decellularised and the PLGA mesh was removed, leaving an ECM scaffold (Fig. 7.8). Using this method, three types of ECM scaffolds were produced using MSCs, chondrocytes and fibroblasts. MSCs and fibroblasts were cultured in these cell-derived ECM scaffolds to examine their potential as scaffolds for cartilage and skin tissue engineering. The MSC- and chondrocyte-derived ECM scaffolds supported cell adhesion, promoted cell proliferation and the production of ECM and demonstrated stronger stimulatory effects on the chondrogenesis of MSC. The fibroblast-derived ECM scaffolds were shown to help with fibroblast proliferation and production of ECM.

Hybrid scaffolds have also been developed to create an improved structure that combines the superior qualities of both scaffold materials. He et al. [81] developed a hybrid poly(L-lactic acid) (PLLA)-collagen hybrid sponge in the shape of a cup

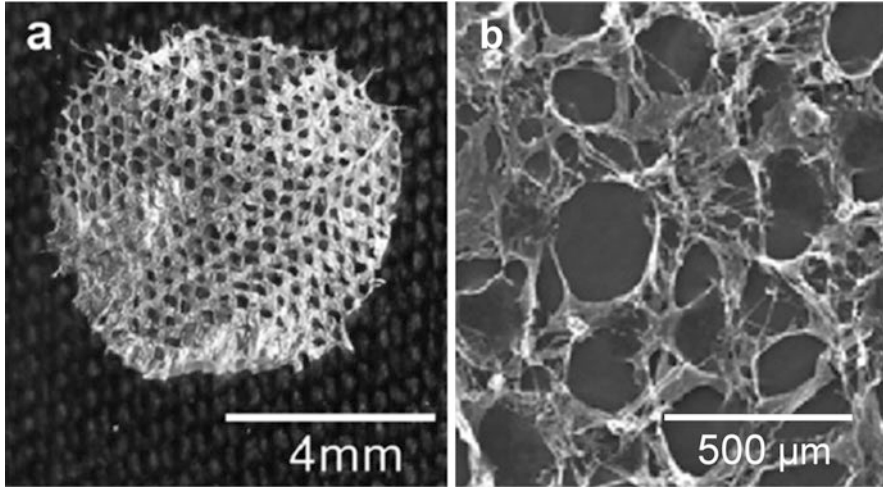


Fig. 7.8 Gross appearance of ECM scaffolds derived from MSCs (a) and SEM image of the scaffold (b). Reprinted from Ref. [80], Copyright 2010, with permission from Elsevier

with the PLLA sponge enclosing a collagen sponge in the centre. The cup-shaped PLLA sponge skeleton provided the hybrid sponge with high mechanical strength, high porosity and high cell retention and protection against cell leakage during cell seeding, while the collagen sponge in the centre contributed to high porosity and facilitated cell adhesion and distribution. Cartilage-like tissue has also been shown to form on the hybrid sponge when cultured with chondrocytes.

Another example of a hybrid scaffold was developed by Dai et al. [82], where the hybrid structure of the 3D scaffold combined the advantages of type I collagen and PLGA-knitted mesh, as shown in Fig. 7.9. The mesh provided the skeleton, while the collagen micro-sponges facilitated cell seeding and tissue formation. Bovine chondrocytes were cultured on these scaffolds and transplanted into mice for up to 8 weeks. The transplants showed homogeneous cell distribution, natural chondrocyte morphology and abundant cartilaginous ECM deposition. The mechanical strength of the engineered cartilage when compared to native articular cartilage reached up to at least 49 % in Young's modulus and 62 % in stiffness.

From these examples, it can be seen that not only is there a wide and varied choice of materials and processing methods available, but also there are many more possibilities by creating different combinations using different materials and processing methods available. There is also the biological aspect that will create even more possibilities, which needs to be taken into account. The inclusion of the biological aspects into the scaffolds, such as bioactive growth factors, will also open up another area to study which includes a large variety of incorporation methods into the scaffolds.

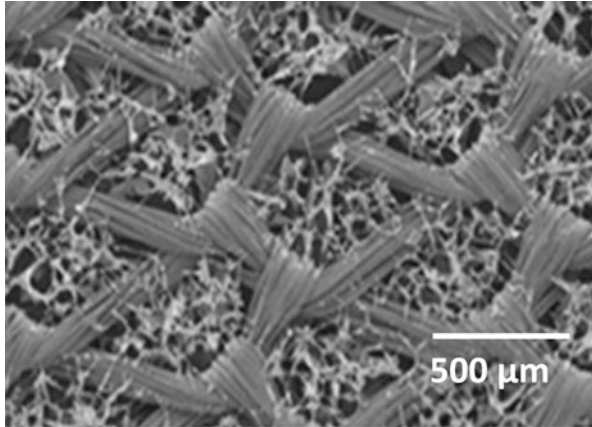


Fig. 7.9 Hybrid PLGA and type I collagen scaffold (Reprinted from Ref. [82], Copyright 2009, with permission from Elsevier)

7.2.5 Commercial and Industry Perspective

The interdisciplinary nature of the tissue engineering is one of the most exciting research areas that have led to rapid advancements as innovations in the related fields have emerged and expanded, while obstacles are being overcome. Tissue scaffold materials and fabrication techniques play a crucial role where significant progress has been achieved to provide structural support for successful tissue regeneration. Nature has provided brilliant examples to mimic, and together with technology, the society is on its way to recreating tissues and organs, with the hope of improving the quality of human lives.

It is no surprise that one of the fastest growing markets for tissue engineering and regenerative medicine products is to improve human health and longevity. To support this, the market has been creating new products based on biomaterial technologies, including both synthetic and naturally derived materials. Other technologies that have developed include genetically engineered materials, stem cell technology and cell culture technology, enabling development of even more innovative devices to enhance this interdisciplinary field of tissue engineering.

The end goal for research and development of tissue scaffolds is to improve the quality of life of humans in need of a tissue or organ replacement. One of the main methods in achieving this which has been discussed in this chapter involves creating scaffolds which mimic the ECM to provide structural support for cells to produce the required tissue naturally. For all the extensive research going on to be fully utilised, there must be a product that is produced for the patient to be able to receive the benefits that the innovations of science and engineering has created. There are numerous companies working to translate and commercialise the research, to create a product or service that can be of use for society. Commercial polymeric scaffolds that are available is summarised in Table 7.2, which has been extracted from [83].

Table 7.2 Commercial polymeric scaffolds extracted from Ref. [83]

Polymer	Biomedical application	Trade name
<i>PGA</i>	First biodegradable synthetic suture in 1969	DEXON
	Bone internal fixation devices	Biofix
<i>PLLA</i>	Orthopaedic fixation devices	Bio-Anchor, Meniscal Stinger
		The Clearfix Meniscal Dart
	High-strength fibres (FDA approved in 1971)	DEXON
	Ligament replacement of augmentation devices	Dacron
	Blood vessel conduits	
	Human immunodeficiency virus or correction of facial fat loss	
<i>PLDLA</i>	Bioresorbable implant material	Resomer
<i>PLGA</i>	Multifilament suture	Vicryl, Vicryl Rapide and CRVL
	Skin graft	Vicryl Mesh
<i>PLGA collagen</i>	Tissue regeneration membrane	Cytoplast Resorb
<i>PLGA</i>	Drug delivery vehicle	Lupron Depot
	First commercially developed monofilament suture (1980)	PDS
<i>PDA</i>	Orthopaedic applications	Pins
<i>PCL</i>	Long-term contraceptive device	Capronor
<i>PDLLA-CL</i>	Monofilament suture	MONOCRYL
<i>PGCL, PLCL, PETG</i>	Drug delivery	SynBioSys
<i>PCLTMC & PGCL</i>	Flexible suture materials	Maxon
	Orthopaedic tacks and screws	Acufex
<i>PHBV</i>	Bone pins, plates, drug delivery	
<i>PEU</i>	Tissue engineering application	DegraPol
<i>LDI-based PU</i>	Orthopaedic applications and bone cement	Polynova
<i>PEAs</i>	Site-specific delivery of small hydrophobic drugs & peptides	CAMEO
<i>POE</i>	Tissue adhesives	Dermabond
	Bilayer skin substitute	INTEGRA Dermal
		Regeneration Template
Wound dressings	Biobrane and AlloDerm	
<i>Collagen</i>	Bioengineered skin equivalents	TransCyte
<i>HA</i>	Wound dressing application	HYAFF
	Synthetic bone graft	Ossigel
<i>HMW viscous HA</i>	Corneal transplantation and glaucoma surgery	Amvisc and Amvisc Plus
<i>Viscous HA</i>	Relieve pain and improve joint mobility for osteoarthritis	Synvisc, Orthovisc

With the promising products that are currently in use on the market as well as many other companies investing in this area of research [25], the growth of the tissue engineering field will continue to flourish in the hopes of creating even more life-saving technologies.

7.2.6 Summary

The interdisciplinary nature of the tissue engineering is one of the most exciting research areas that have led to rapid advancements as innovations in the related fields have emerged and expanded, while obstacles are being overcome. Tissue scaffold materials and fabrication techniques play a crucial role where significant progress has been achieved to provide structural support for successful tissue regeneration. Nature has provided brilliant examples for us to mimic, and together with technology, we are on the way to recreating tissues and organs, with the hope of improving the quality of lives for humans.

7.3 Stents

The human body is an extraordinarily complex system comprised of many parts and systems all working in unison to maintain and sustain health. Being mostly fluid, it is not surprising that there are various tubes within the body with functions ranging from delivery of nutrients to transmission of chemical signals and removal of metabolic waste. Sometimes these vessels may become compromised, thus losing their ability to perform their roles. In such cases, medical intervention can help to restore function by providing the vessels or tubes with support via the use of stents. In general, a stent is *a splint placed temporarily inside a duct, canal or blood vessel to aid healing or relieve an obstruction*, according to the Oxford English Dictionary [84]. The practice of implanting or deploying a stent into a vessel or tube is referred to as ‘stenting’.

Coronary arteries are the vessels commonly treated by stenting because of the prevalence of coronary artery disease (CAD). CAD has become very widespread within developed regions of the world and is the leading cause of death in the US and Europe [21]. From here onwards, ‘stents’ and ‘stenting’ refer to coronary artery stents and the implantation of stents into coronary arteries, respectively. CAD is basically the build-up of plaque within the coronary arteries, as shown in Fig. 7.10. Excessive plaque build-up leads to obstruction of flow through the vessel, in which case the vessel must be treated to restore normal flow.

CAD may be treated in several ways, namely bypass surgery, angioplasty or stenting. Bypass surgery was first introduced in 1968, before angioplasty and stenting were developed [4]. During bypass surgery, a section of healthy artery is extracted from one of the legs of the patient and is used to bypass the blocked

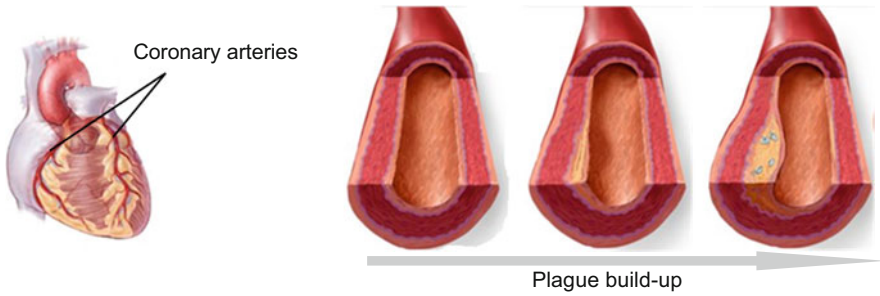


Fig. 7.10 Position of coronary arteries (*left*) and progression of plaque build-up within a coronary artery (*right*). Images adapted from www.medmovies.com

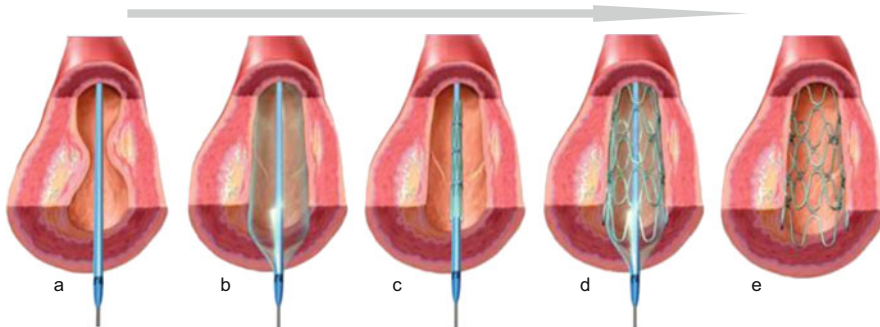


Fig. 7.11 Stenting procedure: (a) catheter insertion, (b) balloon expansion, (c) insertion of catheter with stent mounted on the end after removal of the balloon catheter, (d) stent deployment, (e) stented vessel. Images adapted from www.medmovies.com

section of a coronary artery, hence named bypass surgery (also known as coronary artery bypass grafting, CABG). In 1977, percutaneous transluminal coronary angioplasty (PTCA) was introduced. PTCA is a less invasive technique than CABG and begins with insertion of a catheter into the target vessel. Once the catheter is in position, a balloon on the end of it is expanded to open the blockage caused by the plaque (illustrated by a–b of Fig. 7.11), then the balloon is deflated and the catheter is removed. Unfortunately, the rate of restenosis (re-narrowing of the vessel) after PTCA is high; thus, stenting of coronary arteries after PTCA was introduced. The use of stenting began in 1986, and the procedure begins with PTCA, and then a second catheter, with a stent mounted over the end, is inserted into the vessel. Once the end of the catheter is located at the target region, the stent is deployed by balloon expansion, as shown in c–d of Fig. 7.11. The balloon is then deflated and the catheter is removed, leaving the stent in place to provide support to the vessel (Fig. 7.11e).

7.3.1 Introduction to Coronary Stents

7.3.1.1 Bare Metal Stents

The first stents were relatively simple in nature when compared with stents of today and were primarily made of medical-grade stainless steel [85] (316 L stainless steel) and less commonly of cobalt–chromium or nickel–titanium alloys. Stents of this nature fit into the category of ‘bare metal stents’ (BMSs). Although stainless steel has excellent mechanical properties, it contains small amounts of nickel, molybdenum and manganese to which some people are allergic [86], thus heightening the risk of restenosis (i.e. re-narrowing of the vessel) in some patients [87]. Restenosis occurs via an inflammatory reaction at the stented site of the vessel which causes smooth muscle cells to migrate to the surface of the inner wall of the vessel and proliferate. This proliferation (i.e. multiplication and spreading) of the cells is what causes the vessel to re-narrow [88]. Furthermore, blood platelets (also known as thrombocytes) have a tendency to stick to BMSs which can cause a clot, or thrombus, to form at the stented site, a phenomenon called thrombosis. This is extremely dangerous since a thrombus may break away from the stent and cause a heart attack [89, 90]. Stent thrombosis occurring soon (within 30 days) after implantation is common in the case of BMSs, although the introduction of anti-platelet therapy for patients who received BMS implantations greatly reduced occurrence rates [90].

7.3.1.2 Coated Metal Stents

Due to the common occurrence of restenosis and thrombosis after BMS implantation [91], a need was seen to alter the surface characteristics of BMSs without changing their mechanical properties, since it seemed that restenosis resulted mainly from the body’s chemical interaction with BMSs. Experimentation with coating BMSs began, and a new category of stents was formed called ‘coated metal stents’ (CMSs). Several different coatings have been applied to stents, including platinum, carbon, gold, silicon carbide, phosphorylcholine, polymers and titanium–nitride–oxide [89, 92], in an attempt to lower the restenosis and thrombosis rates. The results of coating stents were mixed, and in some cases, such as in the case of gold-coated stents, restenosis rates were even higher than those of uncoated stents [93].

7.3.1.3 Drug-Eluting Stents

The first stent coatings were passive, and the train of thought was to make stents as benign and stable as possible to prevent undesirable responses within patients’ vessels. Coated stents eventually evolved by way of a new train of thought: what if the coating could play an active role in preventing the body’s responses

responsible for complications after stent implantation? Thus this strategy began the era of drug-eluting stents (DESs), which are metal stents loaded with drugs which are gradually released to provide local treatment to prevent restenosis. DESs are a significant improvement over BMSs and CMSs, but a problem which persists is the presence of a permanent, foreign object in the body. Furthermore, studies on the outcomes of treatment with DESs have revealed that late stent thrombosis rates are sometimes even higher than those of BMSs [94], and the cause may be that endothelialisation of the stent struts is delayed by drug elution [95].

7.3.1.4 Recap and the Next Phase of Stent Evolution: Biodegradable Stents

Taking a step back and considering the challenges faced by stent technology throughout its evolution from BMSs to DESs, it is noted that the initial complications faced after BMS implantation were acute, occurring soon after implantation, and were addressed as stents evolved to DESs. However, complications still persist but tend to occur later after implantation, for example, late stent thrombosis. Naturally, it is expected that the next evolutionary step is able to address this. It is recognised that stented vessels need support for only up to 6 months while they heal [96], so development of stents which degrade and essentially disappear after their jobs are done began; these stents are known as biodegradable or bioabsorbable stents. Biodegradable stents offer the advantage of completely disappearing after their service, making any future intervention less complicated. Furthermore, there is no need for rest-of-life pharmaceutical treatment as is the case for permanent stents in which case aspirin is taken indefinitely after treatment [93, 97].

Figure 7.12 shows a summary of the evolution of CAD treatment and highlights the key issues addressed and remaining with each evolutionary step. Before biodegradable stent development is discussed from a materials perspective, let us lay the foundation for this by looking at stents from an engineering point of view.

7.3.2 Stents: An Engineering Point of View

In order to better understand the challenges of biodegradable stent development, it is useful to first think about what a stent must endure during its lifetime.

7.3.2.1 Stent Deployment: The Need for Ductility

As a starting point to describe what is required of stent materials, imagine that a stent has been navigated to the target site of a vessel needing support. Now, the stent is deployed via balloon expansion in which the stent is mounted is inflated, as shown in Fig. 7.13a, b. Keep in mind that the stent is expanded to a diameter greater than the desired final diameter. Once expansion of the stent is complete, the balloon

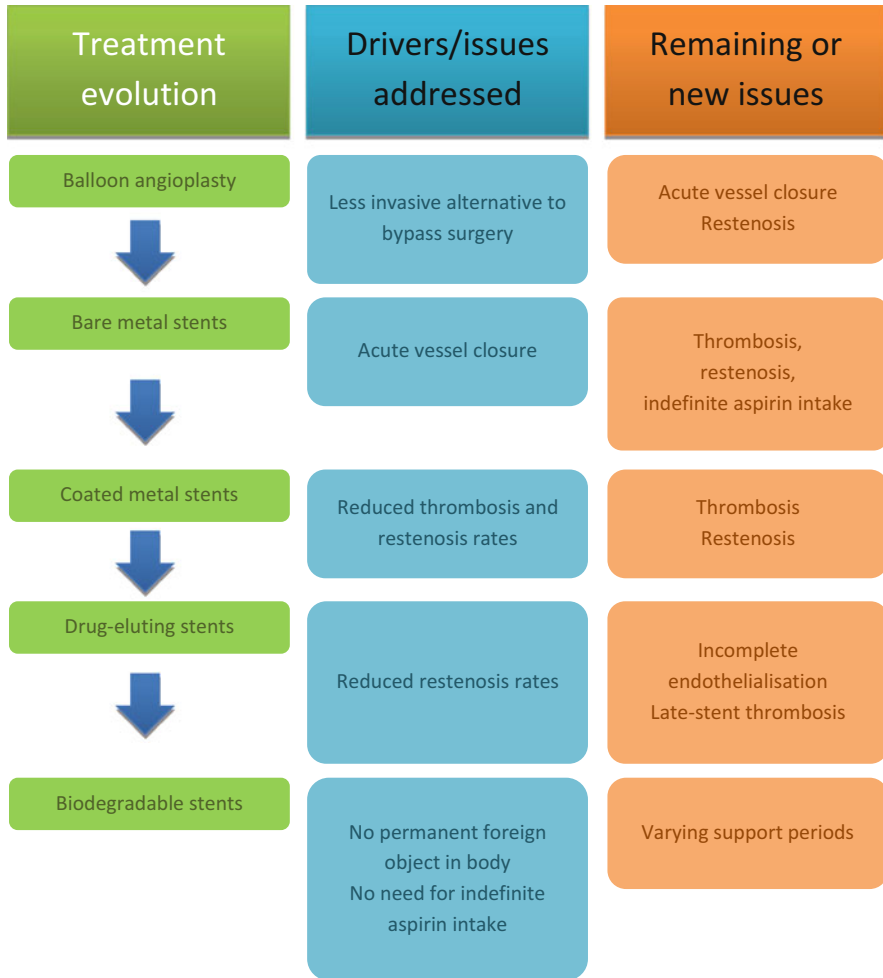


Fig. 7.12 The evolution of stents and the issues addressed with each step in progress as well as issues which remained or new issues which arose

is deflated and withdrawn as shown in Fig. 7.13c. While the balloon is deflated, the stent diameter reduces somewhat because the elastic strains within the stent material are recovered, which is why the stent had to be expanded beyond the desired final diameter. Once the balloon has been deflated and withdrawn, the stent remains in place to support the vessel, Fig. 7.13d.

From a material point of view, the important fact to note is that the stent has to undergo permanent deformation during the deployment process. This permanent deformation leads to the first of many material requirements: ductility. Ductile materials can be subjected to large strains before breaking, while brittle materials fracture instead of deforming and stretching.

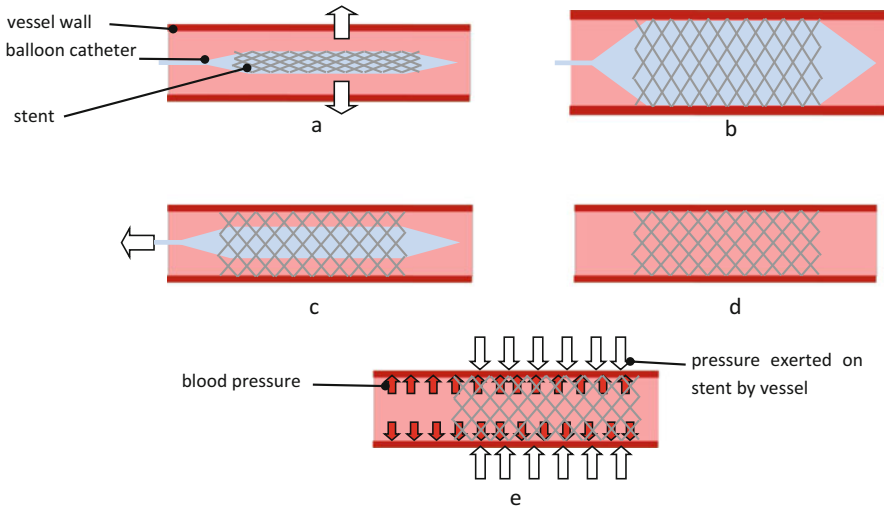


Fig. 7.13 Stent delivery by balloon expansion (a–d) and schematic of stent loading conditions (e). Stent on balloon catheter reaches target site and expansion begins (a), stent expanded beyond final diameter to ensure sufficient permanent deformation of stent material (b), balloon deflated and removed (c), stented vessel (d). The implanted stent experiences a radial crushing load exerted by the vessel which fluctuates since blood pressure in the vessel (which opposes pressure exerted by the vessel) fluctuates during each cardiac cycle

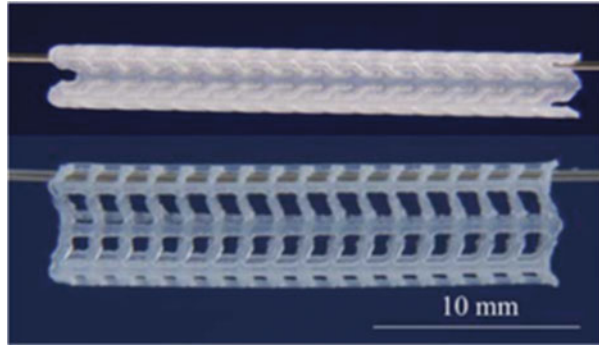
7.3.2.2 Importance of Creep Behaviour After Implantation

Once the stent has been deployed, it provides support to the healing vessel to prevent it from collapsing. This implies that the vessel exerts an inward pressure on the stent which must be supported until the vessel has healed sufficiently, meaning that the stent needs to endure pressure for an extended period of time. With long-term loading comes the possibility of creep, which is the gradual deformation of a material under load even if the stresses caused by this load are well below the maximum load the material can handle. In the case of a stent, creep would cause a gradual collapse, resulting in re-narrowing of the vessel. Creep is an especially important consideration for biodegradable stents for two main reasons, the first being that the majority of biodegradable stents are made of thermoplastic polymers which are prone to creep deformation and the second being the effect of degradation on material performance.

It is fairly challenging to design a stent with creep because of the numerous variables involved. For example, if a stent collapses slightly through creep deformation and the vessel experiences a corresponding narrowing, the pressure exerted on the stent decreases because the vessel is now less ‘stretched’ than it was immediately after stent implantation. Therefore the creep rate would slow down since the lower the stresses in a material, the lower the creep rate.

Furthermore, as a vessel heals, we should expect that the pressure it exerts on a stent decreases as it gradually regains the ability to support itself. This implies that

Fig. 7.14 A stent prototype made of a PLLA/P4HB blend. The stent is shown before (*top*) and after (*bottom*) balloon expansion [98]. The stent diameter remains enlarged because of permanent deformation of the PLLA/P4HB during balloon expansion



resistance to creep deformation is most critical in the early stages after stent implantation, but there seems to be a gap in the knowledge of the healing profile of a stented vessel, from an engineering point of view at least (Fig. 7.14).

7.3.2.3 Material Fatigue Considerations

With every heartbeat, blood pressure in coronary arteries fluctuates [99], and some branches also experience significant curvature changes as they bend and unbend during the cardiac cycle [100]. Blood pressure fluctuations result in subsequent vessel diameter fluctuations which would, in turn, cause the pressure exerted on an implanted stent to fluctuate. Furthermore, a stent implanted in a region where the vessel's curvature changes significantly would be forced to bend and unbend with each heartbeat. Both of these phenomena result in the presence of cyclic stresses in the stent, which raises the concern of fatigue failure. In the case of biodegradable stents, fatigue failure is destined to occur at some point when the stent material integrity has diminished enough, but care must be taken to prevent premature fatigue failures.

7.3.2.4 Material Degradation: A Critical Variable

The material considerations discussed so far apply to both permanent stents and biodegradable stents, but a consideration unique to biodegradable stents is the effect of degradation on the mechanical characteristics of the material. In order to design a biodegradable stent, we first need to understand how the properties of a potential stent material will change with time as it degrades. It is a complex process because there is still much to be learned about the rate at which support required by a healing vessel decreases, whether or not it is linear and how much it varies from patient to patient depending on age, medical conditions, etc. Perhaps when there is more knowledge in this area, biodegradable stents could be tailored to meet the needs of specific patients.

7.3.2.5 Engineering Solutions vs. Clinical Implications

At first glance, some of the challenges of stent design seem trivial to solve in engineering, but these trivial solutions may have negative clinical implications. For example, making stent struts thicker and wider enhances the support provided to the vessel but results in more restriction of blood flow as well as increased risk of small side branches of the vessel being blocked. Furthermore, endothelialisation would be more difficult in the case of thicker struts. To enhance stent performance while minimising negative impacts on clinical outcomes, stent materials must be developed to have desirable mechanical properties. The next section will outline progress of biodegradable stent material development and compare the various materials which have been on, or are currently under, investigation for biodegradable stents.

7.3.3 Materials Under Investigation for Biodegradable Stents

The engineering point of view provides insights into the mechanical requirements of biodegradable stent materials, and some of the medical requirements were discussed under stent evolution. With these in mind, the challenge of developing materials with suitable properties for the application may be getting clearer. Table 7.3 summarises some of the requirements of stents and stent materials.

Because of the array of demands of biodegradable stent materials, it is not surprising that researchers are experimenting with a wide range of materials with a broad spectrum of properties. To illustrate this, a selection of biodegradable stents is shown in Table 7.4. Note that these stents in Table 7.4 have been through clinical trials. The radial support period of these stents varies from days (in the case of a magnesium stent) through to 6 months for a poly(L-lactic acid) (PLLA) stent.

As an example of the pros and cons of different materials, the magnesium and polymer stents can be compared further. The magnesium stent has the distinct

Table 7.3 Stent and stent material requirements

Requirement	References
Biocompatibility of stent material and its degradation products	[101–103]
Low thrombogenicity to prevent stent thrombosis	[85]
The material must retain enough strength for the stent to provide sufficient support for 6 months	[103–105]
Fragments of material must not be released into the bloodstream during degradation	[103]
Radio-opaque for tracking during delivery	[85,103]
Stent must be able to withstand a minimum crush pressure of 100 kPa	[103]
The material must have sufficient flexibility to withstand being bent to get through tortuous vessels during delivery	[85,101]
The material must deform plastically upon balloon expansion to avoid recoil	[103]

Table 7.4 Comparison of biodegradable stents [104]

Stent	Material	Drug eluting?	Drug eluted	Radial support period	Absorption time
Igaki-Tamai	PLLA	No	–	6 months	2 years
BVS	PLLA	Yes	Everolimus	Cohort A – weeks Cohort B – 3 months	2 years
REVA	Tyrosine-derived polycarbonate	No	–	3–6 months	2 years
Magnesium stent	Magnesium alloy	No	–	Days or weeks	4 months
BTI	Salicylate linker	Yes	Sirolimus and salicylic acid	3 months	6 months

disadvantage of a short period of vessel support because it degrades fairly quickly. However, an advantage over the polymeric stents is that magnesium has far superior elastic modulus, so it can be designed to have thinner, narrower struts than polymeric stents while still offering good vessel support. Another advantage of magnesium is the short time for total absorption – just 4 months versus 2 years for a PLLA stent – but, again, this comes at the cost of a short vessel support period.

Magnesium is not the only metal which has been considered. Iron stents have been under investigation too. Iron takes longer to degrade in the body than magnesium, and it has superior mechanical properties to polymers, but it seems that researchers have steered away from it because of toxicity concerns [106].

7.3.3.1 Prominence of PLLA

PLLA is a very prominent material in biodegradable stent material research, both in the case of medical device companies and university research groups. Abbott Vascular (USA), Igaki Medical Planning Company (Japan), Elixir Medical Corporation (USA), ART (France) and possibly others have developed PLLA-based stents, some of which have been through clinical trials. In fact, in the first clinical trial a biodegradable stent in humans was done with Igaki-Tamai stents, which are made of PLLA.

PLLA is attractive because of its relatively high strength and stiffness when compared with other biodegradable polymers. Furthermore, it has a low enough degradation rate that stents made of PLLA can provide support for 6 months. However, PLLA suffers from brittleness which heightens the risk of stent strut fracture during deployment. For this reason, researchers have been investigating ways of modifying PLLA to be more ductile.

7.3.3.2 Modification of PLLA

There are various means of modifying polymers to alter the properties and to enhance ductility, methods such as plasticiser addition, blending with rubbery polymers and copolymerisation.

Attempts at modifying PLLA were made by Grabow et al., who blended PLLA with poly(4-hydroxybutyrate) (P4HB), as well as poly(caprolactone) (PCL), and attempted to produce biodegradable stents from these blends [36, 37]. The ductility of the blends was far greater than that of PLLA, but there were significant reductions in other mechanical properties. In the case of the PLLA/P4HB blend, tensile strength was reduced by 20 %, while stiffness was reduced by 50 %, which is undesirable since sufficient stiffness is a high priority for stenting applications. The PLLA/PCL blend exhibited an increase in strength but also a 50 % decrease in stiffness, as well as a major loss of creep resistance when compared with neat PLLA. Thus the PLLA/PCL blend was found to be unsuitable for application in biodegradable stents because stents made from this blend would possibly collapse prematurely due to low stiffness and insufficient resistance to creep.

Other work done on enhancing the ductility of PLLA involved blending with either poly(butylene succinate) (PBS) or poly(butylene succinate-co-L-lactate) (PBSL). While the work was a general study not aimed at application for biodegradable stents, the results were indicative and promising. In this study, Shibata et al. showed that the tensile elongation at break of PLLA is significantly enhanced by blending it with PBS or PBSL [107]. Furthermore, the losses of strength and stiffness were not as extreme as those exhibited by the PLLA/P4HB and PLLA/PCL blends investigated by Grabow et al. [36, 37]. For this reason, these blends are of considerable interest to the manufacturers of biodegradable stents, but there is still a lot which is unknown about them; for example, how does PBS addition influence the creep resistance of PLLA and how will degradation affect the blends' strength, stiffness and creep resistance?

7.3.3.3 PLLA/PBS: A Potential Candidate for Biodegradable Stents

The ductility of PLLA/PBS blends makes them promising candidates for the manufacture of biodegradable stents. This is the motivation for recent work which has focussed on characterising the changes in material behaviour of PLLA/PBS blends as they degrade.

Specimen Preparation PLLA and PBS were melt-blended in various ratios with up to 25 % PBS using a twin screw extruder. The blends were subsequently used to produce dog bone-type specimens via injection moulding.

Degradation Specimens were submerged in phosphate-buffered saline, with a pH of 7.4, in a temperature-controlled water bath which was used to maintain a

temperature of 37 °C. The degradation period spanned 24 weeks, and specimens were removed at intervals between 0 and 24 weeks for testing.

Tensile and Creep Tests Tensile and constant-load creep tests were performed on non-degraded and degraded specimens. Tensile tests were performed in an Instron universal testing machine at a crosshead extension rate of 50 mm/min, while loads for creep tests were applied by dead weights hanging from the specimen being tested. All tests were performed in an environmental chamber at 37 °C, and degraded specimens were tested immediately after removal from the degradation medium to ensure that they were tested in a saturated state to obtain relevant results.

Results of Tensile Tests Four different PLLA/PBS blends, as well as neat PLLA and neat PBS, were compared to determine the effects of degradation and PBS content on the changes in mechanical characteristics of PLLA/PBS blends. The changes in Young's moduli of the blend specimens as they degrade are of interest. As can be seen in Fig. 7.15, the moduli of the blends decrease gradually from 0 to 24 weeks of degradation, while those of neat PLLA and neat PBS actually increase slightly during the first 8 weeks and then stabilise.

The implications of the gradual decreases in moduli of PLLA/PBS blends during degradation could be positive if we consider that as a stented vessel heals, the amount of support it requires should decrease gradually. Figure 7.16 shows the microstructures of the PLLA/PBS specimens before degrading and after degrading. The latter becomes more porous structurally, lowering its mechanical properties.

Results of Creep Tests Creep tests were done on the specimens of one blend – 75/25 PLLA/PBS and neat PLLA, for comparison. The results of creep tests at different stresses on non-degraded specimens revealed that the initial creep rates of

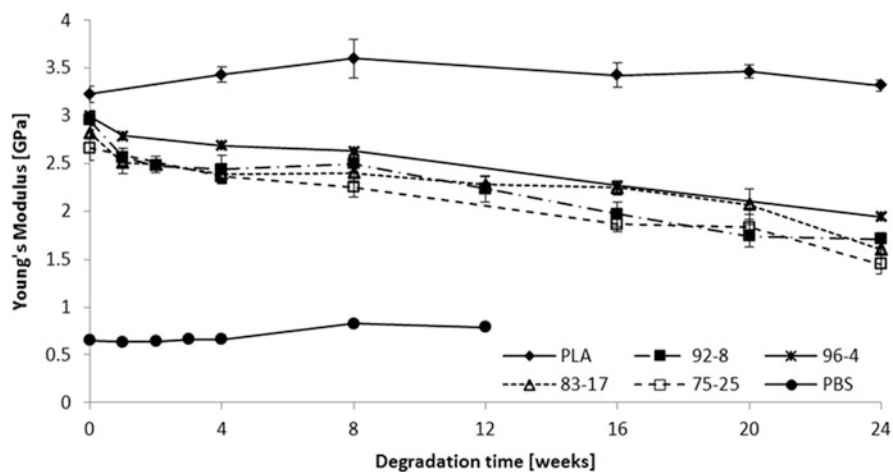


Fig. 7.15 Young's moduli of samples of PLLA/PBS, PLLA and PBS degraded for various periods of time. Error bars represent standard deviations of samples of five specimens each

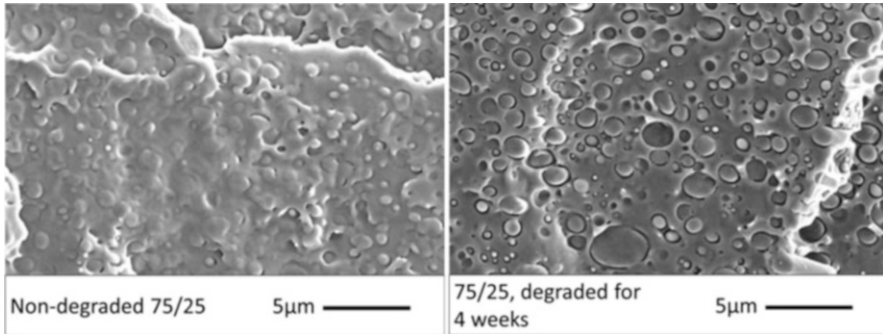


Fig. 7.16 Scanning electron microscope images of cryo-fractured 75/25 PLLA/PBS specimens: non-degraded (*left*) and degraded for 4 weeks (*right*) [108]

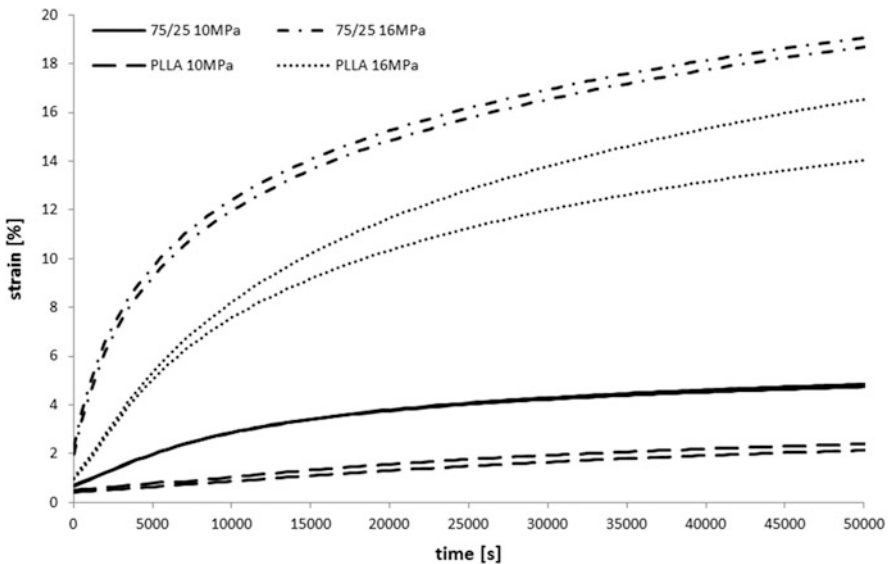


Fig. 7.17 Strain–time plot showing the first 50,000 s of constant-load creep tests performed on PLLA and 75/25 specimens. Results of two specimens from each material type are shown for each load. Stresses indicated are based on initial cross-sectional area (i.e. engineering stresses). All tests were performed at 37 °C

the 75/25 specimens were 3–4 times higher than those of neat PLLA, but physical ageing which occurred during creep tests slowed the creep rates significantly. Once creep rates stabilised after decreasing with physical ageing, the creep rates of the 75/25 blend and neat PLLA were almost the same for a given stress, as shown in Fig. 7.17.

The higher creep rates of the PLLA/PBS blend are not favourable for the application but are an expected result stemming from ductility enhancement.

Annealing was considered as a means of enhancing creep resistance, and the results from creep tests on 75/25 blend specimens annealed for 1 week at 45 °C are compared with the results of as-moulded specimens in Fig. 7.18. It is clear that annealing significantly enhances creep resistance, where the annealed 75/25 specimens exhibit the creep rates well below those of the neat PLLA. However, tensile testing of specimens annealed under the same conditions showed that the ductility enhancement from PBS addition is lost. Shorter annealing time retain some ductility but will result in a less significant boost in creep resistance, so further experiments can be done to find a balance between ductility and creep resistance.

The results of creep tests of non-degraded specimens provide important insights into the behaviour of PLLA/PBS blends, but critical to the application as biodegradable stent materials is understanding of how the creep resistance changes as the material degrades. Thus creep tests were also performed on degraded specimens. Again, a 75/25 PLLA/PBS blend was compared with neat PLLA. All the tests were done at a constant load equivalent to an engineering stress of ~10 MPa. Interestingly, the neat PLLA shows increases in creep resistance up until 8 weeks of degradation and then decreases in creep resistance from 8 to 16 weeks of degradation, as can be seen in Fig. 7.19 (left). The increase in creep resistance during the first 8 weeks of degradation can be attributed to physical ageing.

The 75/25 blend shows a trend of decreasing creep resistance with increasing degradation time. This may, at first, seem like a definite disadvantage, but it must be kept in mind that while a stented vessel heals, it will gradually exert less and less

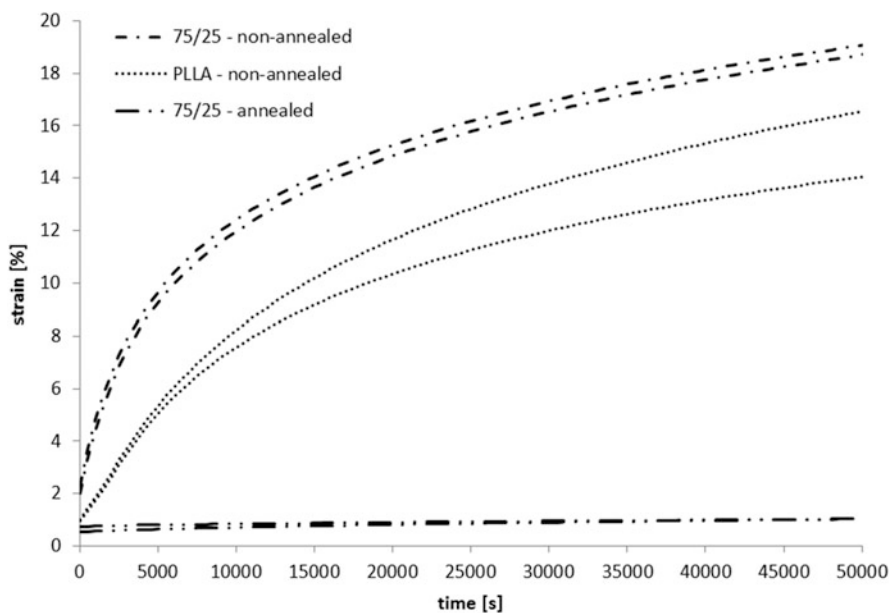


Fig. 7.18 Strain–time plots of 16 MPa creep tests of annealed 75/25 and as-moulded 75/25 and PLLA specimens. Each curve represents the results of an individual specimen

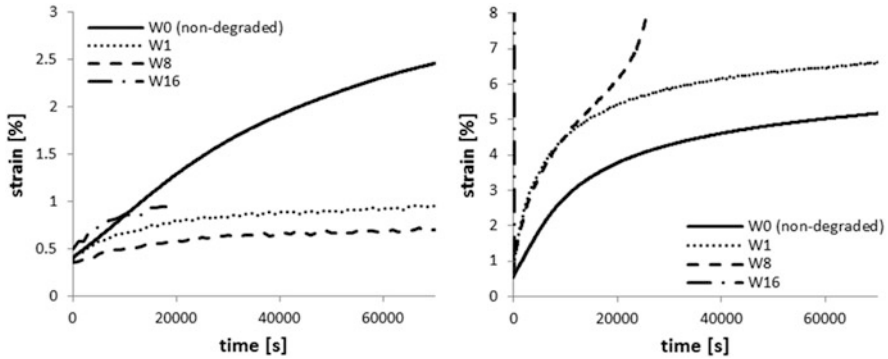


Fig. 7.19 Strain–time plots from constant-load creep tests (engineering stress ~ 10 MPa) of non-degraded and degraded PLLA (*left*) and 75/25 PLLA/PBS (*right*). All tests were performed at 37°C

pressure on the stent, so a gradual decrease in the stent’s ability to support the vessel is not necessarily disadvantageous. The ideal rate of decrease in support provided by a stent is not well understood, as far as the authors are aware.

7.3.4 Summary

Blending PLLA with PBS greatly enhances ductility, which is attractive for application as a biodegradable stent material. This work serves to elucidate the effects of degradation on the mechanical performance of PLLA/PBS blends in order to better understand how biodegradable stents made of these blends would perform. Results show that PLLA/PBS blends exhibit gradual decreases in their moduli as degradation progresses, while neat PLLA showed no loss over the same 24 week period. A 75/25 blend showed a gradual decrease in creep resistance with increasing degradation time, while PLLA exhibited increasing creep resistance during the first 8 weeks of degradation and a decrease from 8 to 16 weeks. The implications of the results are that a stent made of a PLLA/PBS blend would lose its ability to provide support to a healing vessel at a higher rate than a neat PLLA stent, but this may not necessarily be a negative implication since a stented vessel should require a decreasing level of support as it heals.

References

1. The Williams dictionary of biomaterials (1999) Liverpool, Liverpool University Press
2. Ratner BD, Hoffman AS, Schoen FJ, Lemons JE (2004) Biomaterials science: an introduction to materials in medicine. Academic Press, Orlando

3. Ramakrishna S, Mayer J, Wintermantel E, Leong KW (2001) Biomedical applications of polymer-composite materials: a review. *Compos Sci Technol* 61(9):1189–1224
4. Majumdar J, Edmond L (2006) Polymers in biomedical applications. *Australas Biotechnol* 16(2):14–15
5. Wichterle O, Lím D (1960) Hydrophilic gels for biological use. *Nature* 185:117–118
6. Tang X, Thankappan SK, Lee P, Fard SE, Harmon MD, Tran K et al (2014) Chapter 21 – polymeric biomaterials in tissue engineering and regenerative medicine. In: Kumbhar SG, Laurencin CT, Deng M (eds) *Natural and synthetic biomedical polymers*. Elsevier, Oxford, pp 351–371
7. Armentano I, Dottori M, Fortunati E, Mattioli S, Kenny JM (2010) Biodegradable polymer matrix nanocomposites for tissue engineering: a review. *Polym Degrad Stab* 95(11):2126–2146
8. Nair LS, Laurencin CT (2007) Biodegradable polymers as biomaterials. *Prog Polym Sci* 32(8–9):762–798
9. Armentano I, Bitinis N, Fortunati E, Mattioli S, Rescignano N, Verdejo R et al (2013) Multifunctional nanostructured PLA materials for packaging and tissue engineering. *Prog Polym Sci* 38(10–11):1720–1747
10. Barbucci R (2002) *Integrated biomaterials science*. Springer, New York
11. Odian G (2004) *Principles of polymerization*. Wiley, Inc., New Jersey
12. Katti DS, Lakshmi S, Langer R, Laurencin CT (2002) Toxicity, biodegradation and elimination of polyanhydrides. *Adv Drug Deliv Rev* 54(7):933–961
13. Gunatillake P, Mayadunne R, Adhikari R (2006) Recent developments in biodegradable synthetic polymers. In: El-Gewely MR (ed) *Biotechnology Annual Review*, vol 12. Elsevier, New York, pp 301–347
14. Maurus PB, Kaeding CC (2004) Bioabsorbable implant material review. *Oper Tech Sports Med* 12(3):158–160
15. Middleton JC, Tipton AJ (2000) Synthetic biodegradable polymers as orthopedic devices. *Biomaterials* 21(23):2335–2346
16. Letchford K, Sodegraad A, Plackett D, Gilchrist S, Burt H (2011) Lactide and glycolide polymers. Chapter 9. In: Domb A, Kumar N, Azra A (eds) *Biodegradable polymers in clinical use and clinical development*. Chichester/West Sussex, Wiley
17. Harte I, Birkinshaw C, Jones E, Kennedy J, DeBarra E (2013) The effect of citrate ester plasticizers on the thermal and mechanical properties of poly(DL-lactide). *J Appl Polym Sci* 127(3):1997–2003
18. Okada M (2002) Chemical syntheses of biodegradable polymers. *Prog Polym Sci* 27(1):87–133
19. Langer R, Vacanti JP (1993) Tissue engineering. *Science* 260(5110):920–926
20. Okamoto M, John B (2013) Synthetic biopolymer nanocomposites for tissue engineering scaffolds. *Prog Polym Sci* 38(10–11):1487–1503
21. Murray CJ, Lopez AD (1997) Mortality by cause for eight regions of the world: global burden of disease study. *Lancet* 349:1269–1276
22. Nerem RM (2007) Chapter two – the challenge of imitating nature. In: Lanza RP, Langer RS, Joseph V (eds) *Principles of Tissue Engineering*, 3rd edn. Academic Press, Burlington, pp 7–14
23. *Tissue engineering, cell therapy and transplantation: products, technologies & market opportunities, worldwide, 2009–2018*. 2011
24. *Organ Donation and Transplantation Activities 2012: GLOBAL OBSERVATORY ON DONATION AND TRANSPLANTATION; 2012* [cited 2013]. Available from: <http://www.transplant-observatory.org/Pages/Data-Reports.aspx>
25. Ana J, Andrea S, Elizabeth D, Angela S, Robert L (2012) Progress in the tissue engineering and stem cell industry “Are we there yet?”. *Tissue Eng Part B* 18(3):155–166
26. Seal BL, Otero TC, Panitch A (2001) Polymeric biomaterials for tissue and organ regeneration. *Mat Sci Eng R Rep* 34(4–5):147–230

27. Langer R, Tirrell DA (2004) Designing materials for biology and medicine. *Nature* 428 (6982):487–492
28. Vacanti JP, Langer R (1999) Tissue engineering: the design and fabrication of living replacement devices for surgical reconstruction and transplantation. *Lancet* 354 Suppl 1(0): S32–S4.
29. Fuchs JR, Nasser BA, Vacanti JP (2001) Tissue engineering: a 21st century solution to surgical reconstruction. *Ann Thorac Surg* 72(2):577–591
30. Fakirov S, Bhattacharyya D, Huttmacher D (eds) (2009) Applications of microfibrillar polymer-polymer composites for biomedical purposes. In: *Processing and fabrication of advanced materials XVII*, New Delhi, India.
31. Barnes CP, Sell SA, Boland ED, Simpson DG, Bowlin GL (2007) Nanofiber technology: designing the next generation of tissue engineering scaffolds. *Adv Drug Deliv Rev* 59 (14):1413–1433
32. Shoichet MS (2009) Polymer scaffolds for biomaterials applications. *Macromolecules* 43 (2):581–591
33. Ma PX (2008) Biomimetic materials for tissue engineering. *Adv Drug Deliv Rev* 60 (2):184–198
34. Tuzlakoglu K, Bolgen N, Salgado AJ, Gomes ME, Piskin E, Reis RL (2005) Nano- and micro-fiber combined scaffolds: a new architecture for bone tissue engineering. *J Mater Sci Mater Med* 16(12):1099–1104
35. Vacanti JP (2003) Tissue and organ engineering: can we build intestine and vital organs? *J Gastrointest Surg* 7(7):831–835
36. Liu C, Xia Z, Czernuszka JT (2007) Design and development of three-dimensional scaffolds for tissue engineering. *Chem Eng Res Des* 85(7):1051–1064
37. Karageorgiou V, Kaplan D (2005) Porosity of 3D biomaterial scaffolds and osteogenesis. *Biomaterials* 26(27):5474–5491
38. Huttmacher DW (2001) Scaffold design and fabrication technologies for engineering tissues – state of the art and future perspectives. *J Biomater Sci Polym Ed* 12(1):107–124
39. Cima LG, Vacanti JP, Vacanti C, Ingber D, Mooney D, Langer R (1991) Tissue engineering by cell transplantation using degradable polymer substrates. *J Biomech Eng* 113(2):143–151
40. Kweon H, Yoo MK, Park IK, Kim TH, Lee HC, Lee H-S et al (2003) A novel degradable polycaprolactone networks for tissue engineering. *Biomaterials* 24(5):801–808
41. Yurchenco PD, Birk DE, Mecham RP (1994) Collagen fibril assembly, deposition, and organization into tissue-specific matrices. In: Yurchenco PD, Birk DE, Mecham RP (eds) *Extracellular matrix assembly and structure*. Academic Press, San Diego
42. Elsdale T, Bard J (1972) Collagen substrata for studies on cell behavior. *J Cell Biol* 54 (3):626–637
43. Venugopal J, Prabhakaran MP, Zhang Y, Low S, Choon AT, Ramakrishna S (2010) Biomimetic hydroxyapatite-containing composite nanofibrous substrates for bone tissue engineering. *Philos Trans R Soc A Math Phys Eng Sci* 368(1917):2065–2081
44. U.S. Markets for Orthopedic Biomaterials for Viscosupplementation and Cartilage, Ligament/Tendon, and Meniscal Repair and Regeneration. CA, USA: 2013a
45. U.S. Markets for Orthopedic Biomaterials for Bone Repair and Regeneration. CA, USA: 2013b
46. Lin ST, Bhattacharyya D, Fakirov S, Matthews B, Cornish J (2013) A novel microfibrillar composite approach towards manufacturing nanoporous tissue scaffolds. *Mech Adv Mater Struct* 21(3):237–243
47. Giesche H (2006) Mercury porosimetry: a general (practical) overview. *Part Part Syst Charact* 23(1):9–19
48. Ghasemi-Mobarakeh L, Semnani D, Morshed M (2007) A novel method for porosity measurement of various surface layers of nanofibers mat using image analysis for tissue engineering applications. *J Appl Polym Sci* 106(4):2536–2542

49. Intelligent Hydrogel (2012) Handbook of intelligent scaffold for tissue engineering and regenerative medicine. Pan Stanford Publishing, p 97
50. Nazarov R, Jin H-J, Kaplan DL (2004) Porous 3-D scaffolds from regenerated silk fibroin. *Biomacromolecules* 5(3):718–726
51. Murphy CM, Haugh MG, O'Brien FJ (2009) The effect of mean pore size on cell attachment, proliferation and migration in collagen–glycosaminoglycan scaffolds for bone tissue engineering. *Biomaterials* 31(3):461–466
52. Nori A, Yim EKF, Chen S, Leong KW (2008) Cell-substrate interactions, Principles of Regenerative Medicine. Academic Press, San Diego, pp 666–685
53. Albrektsson T, Johansson C (2001) Osteoinduction, osteoconduction and osseointegration. *Eur Spine J* 10:S96–S101
54. Billström GH, Blom AW, Larsson S, Beswick AD (2013) Application of scaffolds for bone regeneration strategies: current trends and future directions. *Injury* 44 Suppl 1(0):S28–S33
55. Giannoudis PV, Einhorn TA, Marsh D (2007) Fracture healing: the diamond concept. *Injury* 38 Suppl 4(0):S3–S6
56. Sicchieri LG, Crippa GE, de Oliveira PT, Beloti MM, Rosa AL (2012) Pore size regulates cell and tissue interactions with PLGA–CaP scaffolds used for bone engineering. *J Tissue Eng Regen Med* 6(2):155–162
57. Holzwarth JM, Ma PX (2011) Biomimetic nanofibrous scaffolds for bone tissue engineering. *Biomaterials* 32(36):9622–9629
58. Ji C, Annabi N, Hosseinkhani M, Sivaloganathan S, Dehghani F (2012) Fabrication of poly-DL-lactide/polyethylene glycol scaffolds using the gas foaming technique. *Acta Biomater* 8(2):570–578
59. Li JP, de Wijn JR, Van Blitterswijk CA, de Groot K (2006) Porous Ti6Al4V scaffold directly fabricating by rapid prototyping: preparation and in vitro experiment. *Biomaterials* 27(8):1223–1235
60. Beachley V, Wen X (2010) Polymer nanofibrous structures: fabrication, biofunctionalization, and cell interactions. *Prog Polym Sci* 35(7):868–892
61. Wu X, Liu Y, Li X, Wen P, Zhang Y, Long Y et al (2010) Preparation of aligned porous gelatin scaffolds by unidirectional freeze-drying method. *Acta Biomater* 6(3):1167–1177
62. Mishra A, Loo Y, Deng R, Chuah YJ, Hee HT, Ying JY et al (2011) Ultrasmall natural peptides self-assemble to strong temperature-resistant helical fibers in scaffolds suitable for tissue engineering. *Nano Today* 6(3):232–239
63. Sin DC, Miao X, Liu G, Wei F, Chadwick G, Yan C et al (2010) Polyurethane (PU) scaffolds prepared by solvent casting/particulate leaching (SCPL) combined with centrifugation. *Mater Sci Eng C* 30(1):78–85
64. Ahn YC, Park SK, Kim GT, Hwang YJ, Lee CG, Shin HS et al (2006) Development of high efficiency nanofilters made of nanofibers. *Curr Appl Phys* 6(6):1030–1035
65. Lannutti J, Reneker D, Ma T, Tomasko D, Farson D (2007) Electrospinning for tissue engineering scaffolds. *Mater Sci Eng C* 27(3):504–509
66. Reneker DH, Yarin AL (2008) Electrospinning jets and polymer nanofibers. *Polymer* 49(10):2387–2425
67. Agarwal S, Wendorff JH, Greiner A (2008) Use of electrospinning technique for biomedical applications. *Polymer* 49(26):5603–5621
68. Bhattarai SR, Bhattarai N, Yi HK, Hwang PH, Cha DI, Kim HY (2004) Novel biodegradable electrospun membrane: scaffold for tissue engineering. *Biomaterials* 25(13):2595–2602
69. Kumbar SG, James R, Nukavarapu SP, Laurencin CT (2008) Electrospun nanofiber scaffolds: engineering soft tissues. *Biomed Mater* 3(3):034002
70. Zhang Y, Reddy V, Wong S, Li X, Su B, Ramakrishna S et al (2010) Enhanced biomineralization in osteoblasts on a novel electrospun biocomposite Nanofibrous substrate of hydroxyapatite/collagen/chitosan. *Tissue Eng A* 16(6):1949–1960
71. Shao S, Zhou S, Li L, Li J, Luo C, Wang J et al (2011) Osteoblast function on electrically conductive electrospun PLA/MWCNTs nanofibers. *Biomaterials* 32(11):2821–2833

72. Lederer A, Harnisch C, Bhattacharyya D, Fakirov S (2010) Organic solvent traces in fibrillar scaffolds for tissue engineering. *J Biomim Biomater Tissue Eng* 7:1–6
73. Martínez-Pérez CA, Olivás-Armendariz I, Castro-Carmona JS, García-Casillas PE (2011) Scaffolds for tissue engineering via thermally induced phase separation, advances in regenerative medicine. In: Wislet-Gendebien S (ed) *InTech*. doi:10.5772/25476. Available from: <http://www.intechopen.com/books/advances-in-regenerative-medicine/scaffolds-for-tissue-engineering-via-thermally-induced-phase-separation>
74. Ma PX, Zhang R (1999) Synthetic nano-scale fibrous extracellular matrix. *J Biomed Mater Res* 46(1):60–72
75. Fuchs C, Bhattacharyya D, Fakirov S (2006) Microfibril reinforced polymer–polymer composites: application of Tsai-Hill equation to PP/PET composites. *Compos Sci Technol* 66 (16):3161–3171
76. Fakirov S, Kamo H, Evstatiev M, Friedrich K (2004) Microfibrillar reinforced composites from PET/LDPE blends: morphology and mechanical properties. *J Macromol Sci Phys* 43 (4):775–789
77. Lu H, Ko Y-G, Kawazoe N, Chen G (2011) Culture of bovine articular chondrocytes in funnel-like collagen-PLGA hybrid sponges. *Biomed Mater* 6(4):045011
78. Oh HH, Lu H, Kawazoe N, Chen G (2012) Spatially guided angiogenesis by three-dimensional collagen scaffolds micropatterned with vascular endothelial growth factor. *J Biomater Sci Polym Ed* 23(17):2185–2195
79. Lu H, Hoshiba T, Kawazoe N, Koda I, Song M, Chen G (2011) Cultured cell-derived extracellular matrix scaffolds for tissue engineering. *Biomaterials* 32(36):9658–9666
80. Lu H, Hoshiba T, Kawazoe N, Chen G (2011) Autologous extracellular matrix scaffolds for tissue engineering. *Biomaterials* 32(10):2489–2499
81. He X, Lu H, Kawazoe N, Tateishi T, Chen G (2010) A novel cylinder-type poly(L-lactic acid)-collagen hybrid sponge for cartilage tissue engineering. *Tissue Eng Part C Methods* 16 (3):329–338
82. Dai W, Kawazoe N, Lin X, Dong J, Chen G (2010) The influence of structural design of PLGA/collagen hybrid scaffolds in cartilage tissue engineering. *Biomaterials* 31 (8):2141–2152
83. Dhandayuthapani B, Yoshida Y, Maekawa T, Sakthi Kumar D (2011) Polymeric scaffolds in tissue engineering application: a review. *Int J Polym Sci* 2011
84. Dictionaries O. “stent”. *Oxford Dictionaries*: Oxford University Press
85. Mani G, Feldman MD, Patel D, Agrawal CM (2007) Coronary stents: a materials perspective. *Biomaterials* 28:1689–1710
86. Hillen U, Haude M, Erbel R, Goos M (2002) Evaluation of metal allergies in patients with coronary stents. *Contact Dermatitis* 47(6):353–356
87. Köster R, Vieluf D, Kiehn M, Sommerauer M, Kahler J, Baldus S et al (2000) Nickel and molybdenum contact allergies in patients with coronary in-stent restenosis. *Lancet* 356 (9245):1895–1897
88. Kraitzer A, Kloog Y, Zilberman M (2008) Approaches for prevention of restenosis. *J Biomed Mat Res Part B Appl Biomater* 85(2):583–603
89. Serruys PW, Kutryk MJB, Ong ATL (2006) Coronary-artery stents. *N Engl J Med* 354 (5):483–495
90. Lemesle G, Delhay C, Bonello L, de Labriolle A, Waksman R, Pichard A (2008) Stent thrombosis in 2008: definition, predictors, prognosis and treatment. *Arch Cardiovasc Dis* 101 (11–12):769–777
91. Van Der Giessen WJ, Serruys PW, Van Woerkens LJ, Beatt KJ, Visser WJ, Jongkind JF et al (1990) Arterial stenting with self-expandable and balloon-expandable endoprostheses. *Int J Card Imaging* 5(2–3):163–171
92. O’Brien B, Carroll W (2009) The evolution of cardiovascular stent materials and surfaces in response to clinical drivers: a review. *Acta Biomater* 5:945–958

93. Kastrati A, Schomig A, Dirschinger J, Mehilli J, von Welser N, Pache J et al (2000) Increased risk of restenosis after placement of gold-coated stents: results of a randomized trial comparing gold-coated with uncoated steel stents in patients with coronary artery disease. *Circulation* 101(21):2478–2483
94. Webster MW, Ormiston JA (2007) Drug-eluting stents and late stent thrombosis. *Lancet* 370 (9591):914–915
95. Finn AV, Joner M, Nakazawa G, Kolodgie F, Newell J, John MC et al (2007) Pathological correlates of late drug-eluting stent thrombosis: strut coverage as a marker of endothelialization. *Circulation* 115(18):2435–2441
96. Ormiston J, Webster M (2007) Absorbable coronary stents. *Lancet* 369(9576):1839–1840
97. Ferrari E, Benhamou M, Cerboni P, Marcel B (2005) Coronary syndromes following aspirin withdrawal: a special risk for late stent thrombosis. *J Am Coll Cardiol* 45(3):456–459
98. Grabow N, Bünger CM, Schultze C, Schmohl K, Martin DP, Williams SF et al (2007) A biodegradable slotted tube stent based on poly(L-lactide) and poly(4-hydroxybutyrate) for rapid balloon-expansion. *Ann Biomed Eng* 35(12):2031–2038
99. Tverdal A (1987) Systolic and diastolic blood pressures as predictors of coronary heart disease in middle aged Norwegian men. *Br Med J* 294(6573):671–673
100. Gross MF, Friedman MH (1998) Dynamics of coronary artery curvature obtained from biplane cineangiograms. *J Biomech* 31(5):479–484
101. Peng T, Gibula P, Yao KD, Goosen MFA (1996) Role of polymers in improving the results of stenting in coronary arteries. *Biomaterials* 17(7):685–694
102. Bertrand OF, Sipehia R, Mongrain R, Rodés J, Tardif JC, Bilodeau L et al (1998) Biocompatibility aspects of new stent technology. *J Am Coll Cardiol* 32(3):562–571
103. Venkatraman S, Boey F, Lao LL (2008) Implanted cardiovascular polymers: natural, synthetic and bio-inspired. *Prog Polym Sci* 33:853–874
104. Ormiston JA, Serruys PWS (2009) Bioabsorbable coronary stents. *Circ Cardiovasc Interv* 2 (3):255–260
105. Colombo A, Karvouni E (2000) Biodegradable stents: “Fulfilling the mission and stepping away”. *Circulation* 102:371
106. Ramcharitar S, Serruys PW (2008) Fully biodegradable coronary stents: progress to date. *Am J Cardiovasc Drugs* 8(5):305–314
107. Shibata M, Inoue Y, Miyoshi M (2006) Mechanical properties, morphology, and crystallization behavior of blends of poly(L-lactide) with poly(butylene succinate-co-L-lactate) and poly(butylene succinate). *Polymer* 47:3557–3564
108. Kimble LD, Bhattacharyya D, Easteal AJ (2011) Degradation characteristics and its effects on mechanical characteristics of a biodegradable polymer composite of PLLA and PBS for use as a stent material. In: *Processing and fabrication of advanced materials*, Auckland 2011

Chapter 8

Electrospun Polymer Scaffolds: Their Biomedical and Mechanical Properties

Gui-Ying Liao, Xing-Ping Zhou, Xiao-Lin Xie, and Yiu-Wing Mai

Abstract In recent years, electrospun polymer scaffolds have shown great promise and potential for biomedical applications. Besides, copolymers and polymer blends, polymer composites with inorganic particles, such as HA and CNT, are widely used. And the alignment of reinforced fibres is beneficial to improve the mechanical properties and biological response of scaffolds. Further, the physical and chemical surface modifications for electrospun fibres are commonly applied to promote the interaction between the scaffold and cells in tissue engineering applications. In this chapter, we reviewed recent advances in electrospun polymer scaffolds with special emphasis on their biomedical and mechanical properties and the effects of the surface modifications.

Keywords Electrospinning • Scaffolds • Modification • Mechanical properties • Biomedical applications

8.1 Introduction

Electrospinning is a simple, relatively efficient technique to fabricate polymer fibrous scaffolds with diameters ranging from several nanometres to several micrometres [1, 2]. The electrospun fibrous scaffolds have extraordinary high surface area-to-volume ratio and high porosity with excellent pore interconnection and have been widely used in a range of hi-tech fields, such as filtration [3], sensors [4, 5], protective clothes and biomaterial applications [6–9].

G.-Y. Liao

Faculty of Material Science and Chemistry, China University of Geosciences, Wuhan 430074, China

X.-P. Zhou • X.-L. Xie (✉)

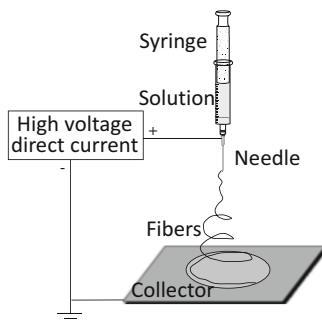
School of Chemistry and Chemical Engineering, Huazhong University of Science and Technology, Wuhan 430074, China

e-mail: xlxie@hust.edu.cn

Y.-W. Mai

School of Aerospace, Mechanical & Mechatronic Engineering, The University of Sydney, Sydney, NSW 2006, Australia

Fig. 8.1 Scheme for electrospinning apparatus



Electrospinning was first introduced by Formhals in 1934 as a patent [10] and later revived by Reneker's groups [11–16]. They studied the electrospinning process for a series of different polymers and demonstrated the mechanism for the formation of electrospun polymer fibres. A basic theory of electrospinning is utilising electrostatic forces of highly charged polymer jets to produce continuous fibres after solvent evaporation in spinning process. A typical electrospinning set-up, as shown in Fig. 8.1, usually consists of three major components: a high-voltage power supply, a nozzle and a grounded collecting plate (usually a metal screen, plate or rotating mandrel). Upon applying an electric field, the polymer solution with a moderate viscosity forms the Taylor cone at the tip of an injecting device. When the electric voltage applied between the injector and the collector exceeds the surface tension force of the Taylor cone, the charged jets are eventually drawn towards the collecting plate. During the travel of the fibrous jets, the solvent in the jet stream gradually evaporates, generating a solidified non-woven fibrous scaffold. The morphological structure and surface properties of electrospun fibres depend on the physical parameters of the polymer solution (e.g. concentration, viscosity, conductivity and surface tension) as well as the spinning process conditions (e.g. applied voltage, distance between capillary tip and collection screen, temperature and humidity of the ambient environment) [14, 17, 18].

In order to meet the demands in biomedical applications, it is essential to control the chemical composition to endow the electrospun fibrous scaffold with desired properties, such as hydrophilicity, mechanical modulus and strength, biocompatibility, biodegradability and cell interactions. Additionally, the fibre diameter, morphology and porosity of the electrospun fibrous scaffolds can be manipulated by the fabrication process, and these structural factors also have important effects on the properties and functionalities of scaffolds. For example, the drugs or biopolymers are incorporated inside the fibre core by two-phase electrospinning process; the electrospun fibrous scaffolds are suitable for the controlled release over a prolonged time [19]. Also, blending modifications with bioactive molecules, such as gelatin, proteins, nucleic acids and carbohydrates, have been employed to enhance the aqueous solubility, biocompatibility and bio-recognition of electrospun fibrous scaffolds [20], which subsequently provides bio-modulating or biomimetic microenvironments for the contacting cells and tissues.

Generally, tissue engineering is a multidisciplinary field that has evolved in parallel with recent advances of materials and biotechnology. The usage of electrospun fibrous scaffolds for tissue engineering has drawn a great deal of attention in the past several years. For examples, the fibrous scaffolds have been demonstrated as suitable substrates for tissue engineering [8, 9, 21, 22], wound dressing [23], artificial blood vessels [24, 25] and vehicles for controlled drug delivery [26]. Furthermore, the electrospun scaffold should physically resemble the nanofibrous features of extracellular matrix (ECM) with suitable mechanical properties, which is beneficial for promoting the adhesion, spreading and proliferation of cells in tissue engineering.

This chapter focused on the recent advances in the use of electrospun polymer scaffolds for biomedical applications, with emphasis on polymer materials, technology, surface modification and biomedical and mechanical properties of the electrospun polymer scaffolds.

8.2 Polymer Materials as Electrospun Scaffolds

There are a wide range of polymer materials that can be electrospun. However, for the applications of fibrous scaffolds, the chosen polymer materials must meet some special requirements, such as biocompatibility and biodegradation.

8.2.1 *Natural, Synthetic Polymers and Copolymers*

Typical natural polymers include collagen, casein, chitosan, chitin, cellulose acetate, gelatin, silk protein, fibrinogen, etc. Scaffolds fabricated from natural polymers promise better clinical functionality. Natural polymers normally exhibit better biocompatibility, low immunogenicity and better inherent capacity for binding cells compared with synthetic polymers. Collagen, the principal structural element of the ECM in tissues, has been fabricated into fibrous scaffolds for cell growth and penetration [21]. Pawlowski et al. [27] reported that collagen is considered as 'ideal' scaffold material in tissue engineering, which provides structural support for the tissue. How et al. [28] for the first time reported that type I collagen fibres were successfully electrospun and characterised with scanning electron microscopy (SEM) and transmission electron microscopy (TEM). Afterwards, many researchers studied the electrospun collagen scaffolds, and these fibrous collagen scaffolds can closely mimic the native collagen network and apply for wound dressings and preliminary vascular tissue engineering [29–34].

Gelatin derived from collagen by controlled hydrolysis is also commonly used for biomedical applications due to its biodegradability and biocompatibility [35–40]. However, gelatin fibres are difficult to be fabricated by the conventional wet/dry spinning because of the polyelectrolytic nature and strong hydrogen

bonding of gelatin [33, 41–43]. So gelatin has been electrospun for tissue engineering scaffolds by blending with other polymers [22, 44].

Attributable to the good biocompatibility, biodegradability, minimal inflammatory reaction and excellent mechanical properties, silk fibroin (SF) protein has been extensively studied for biomedical applications [45–50]. Recently, many research groups found SF protein can be easily electrospun; and the effect of electrospinning parameters on the morphology and the diameter of such fibres were systematically studied [51–55]. Wang et al. [56, 57] electrospun silk fibroin using an aqueous solution from *B. mori* in order to solve the potential concerns of chemical residuals from solvents, and they found that the concentrated silk aqueous solution was needed for increasing the solution spinnability. When the aqueous silk solution was up to 28 % (w/v), silk fibres with circular cross sections and smooth exterior surfaces were formed, and their diameters were 400–800 nm. Zhu et al. [58, 59] investigated the effects of solution pH on morphology and properties of the electrospun silk fibres. They found that reduction of solution pH decreases the concentration of aqueous silk fibroin solutions that could be electrospun. Subsequently, the average diameter and diameter distributions of the electrospun silk fibres became smaller and narrower. Further, the morphology of the electrospun silk fibres changed from ribbon-like to a uniform cylinder with the combined reduction in pH and concentration.

Compared with natural polymers, synthetic polymers have many advantages, such as cheaper cost, predictable uniformity, desired degradation rate and higher mechanical properties. Recently, the synthetic polymers, such as poly(lactic acid) (PLA) [60, 61], poly(glycolic acid) (PGA) [12, 62, 63], polyurethane (PU) [64], PEO [65], poly(vinylalcohol) [66, 67], poly(ϵ -caprolactone) (PCL) and polydioxanone [68] have been electrospun into fibrous scaffolds for biomedical applications thanks to their distinctive degradation and excellent biocompatibility.

It is well known that the morphology, pore size, biodegradability, mechanical and other physical properties of the electrospun scaffolds can be tailored by using copolymers. Generally, the biodegradable hydrophobic polyesters, such as PLA and PCL, lack cell affinity for tissue engineering, but the incorporation of a proper hydrophilic polymer segment efficiently solves the problem. Recently, the PLLA–PEG block copolymers were successfully synthesised and electrospun into fibres for sustained release of hydrophilic antibiotics [69], DNA delivery [70], fibroblast cell attachment and proliferation [71]. Kim et al. [72] reported that the electrospun PLA–PEG block copolymer fibres present appropriate characteristics to be considered as a new kind of biodegradable scaffolds. Also, P(LA-*b*-CL) block copolymers are electrospun to non-woven fibrous mats as scaffolds for the culture of somatic cells, such as smooth muscle cells (SMCs) and endothelial cells (ECs) [73–75]. The results showed that these cells could adhere and proliferate well on P(LA-*b*-CL) fibrous scaffolds. Know et al. [76] synthesised the biodegradable high-molecular-mass poly(L-lactide-co- ϵ -caprolactone) (PLCL) by ring-opening copolymerisation and electrospinning the nano- and microstructured PLCL fibres, and they found that human umbilical vein endothelial cells (HUVECs) were well adhered and proliferated on these fibrous scaffolds.

PLGA is the copolymer of glycolide (G) and lactide (L) and has been electrospun as fibrous scaffolds. Katti et al. [26] studied the potential use of PLGA fibrous scaffolds as an antibiotic delivery vehicle for the treatment of wounds. Zong et al. [77] found that the PLGA fibrous scaffolds degrade faster than the casting film with the same composition due to the high surface area-to-volume ratio and the high water adsorption ability.

Poly(3-hydroxybutyrate-co-3-hydroxyvalerate) (PHBV) is another biodegradable and biocompatible copolymer derived from microbial polyesters. Lee et al. [78] found that the electrospun PHBV nanofibrous scaffolds provided a much more suitable environment for the attachment and growth of chondrocytes derived from rabbit ears, compared to the PHBV cast films. Choi et al. [79] studied the diameter and degradation rate of PHBV fibre and found that addition of a small amount of benzyl trialkyl ammonium chlorides in the electrospinning solution decreased the fibre diameter and accelerated the degradation rate of PHBV fibre.

8.2.2 Polymer Blends

Copolymerisation and polymer blending are two effective means to combine different polymers for yielding new materials properties. In comparison with the copolymerisation, polymer blending is a simpler and more effective method for tissue engineering applications. Thus, properties of electrospun scaffolds can be tailored with desired new functions by selecting a combination of proper components and adjusting the component ratio. For example, PLA is most promising and widely used as the candidate scaffolds for tissue engineering. However, its brittleness has limited its wider biomedical applications. PCL is a biodegradable, semi-crystalline and rubbery polymer owing to its low glass transition ($\sim -50^{\circ}\text{C}$) and melting temperatures ($\sim 60^{\circ}\text{C}$) [80]. It has been often utilised to improve the elasticity of PLA via blending with PCL, and PLA/PCL blend cast films were previously prepared as engineered tissue implants [81–83].

Our group studied the electrospinning of PLLA/PCL blends, especially focused on optimising the process conditions [84]. The PLLA/PCL blend fibres with defect-free morphology and uniform diameter could be electrospun by PLLA/PCL (1/1) blend with a solution concentration of 10 wt. %, applied voltage 20 kV and TCD 15 cm. For the first time, we explored the response of adipose-derived stem cells (ADSCs) on PLLA/PCL blend fibrous scaffold. The morphology and interactions between ADSCs and PLLA/PCL blend fibrous scaffolds were examined by using inverted phase contrast microscopy (IPCM) and SEM.

Figure 8.2 shows ADSCs attachment and growth on the PLLA/PCL fibrous scaffolds. After being seeded on the PLLA/PCL fibrous scaffolds for 1 day, most ADSCs do not adhere to the fibres, but they grow to typical elongated morphology (Fig. 8.2a, b). At 3 days, the ADSCs expand on the fibrous scaffolds with a pattern of pseudopods as shown in Fig. 8.2c, d. After 7 days, an increasing number of cells grow along the fibre orientation direction, forming a three-dimensional network

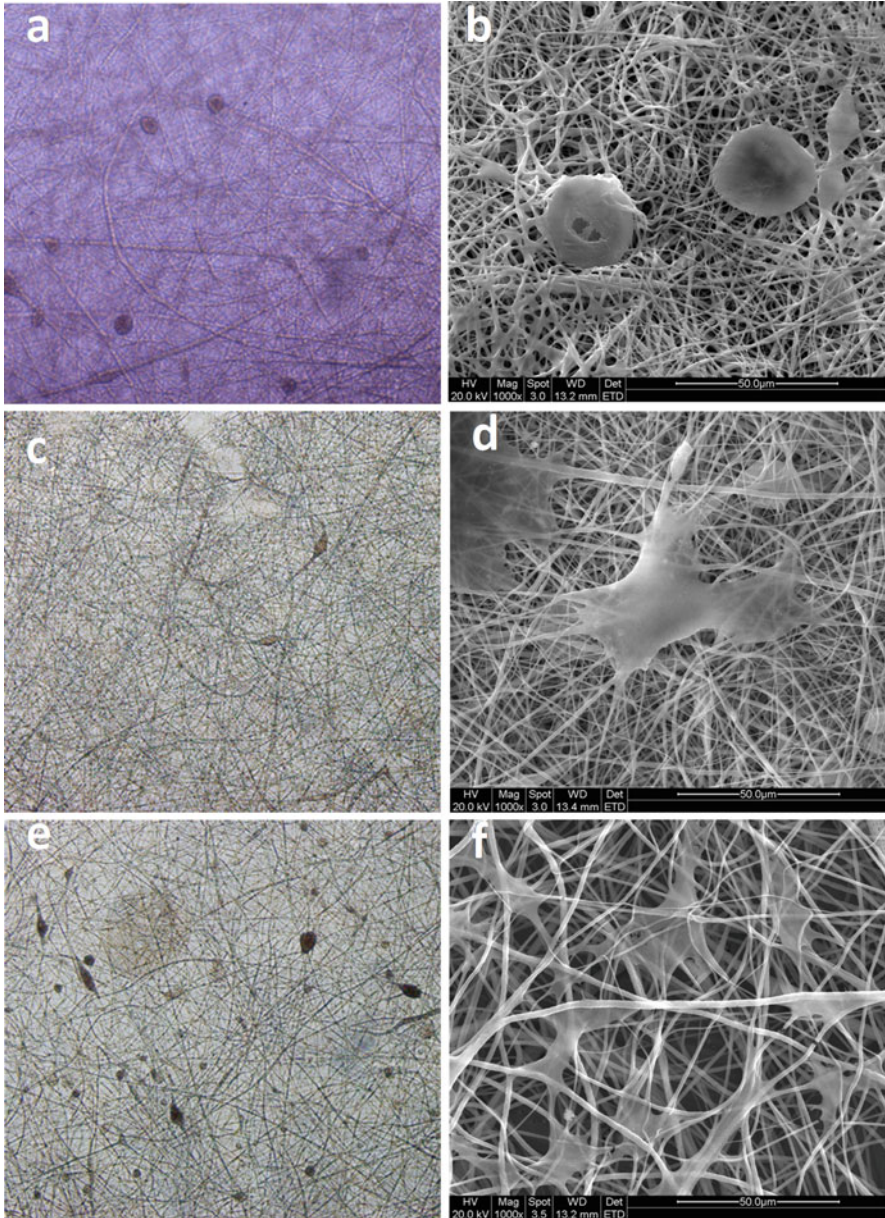


Fig. 8.2 Morphology ADSCs on scaffolds after seeding for 1 day [(a) by IPCM, (b) by SEM], 3 days [(c) by IPCM, (d) by SEM] and 7 days [(e) by IPCM, (f) by SEM] (Magnification: IPCM 100 \times ; SEM 1000 \times) (Reproduced from Ref. [84] by permission of John Wiley & Sons Ltd)

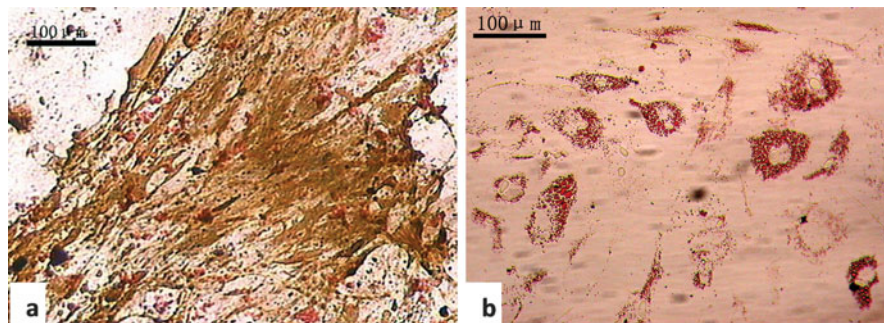


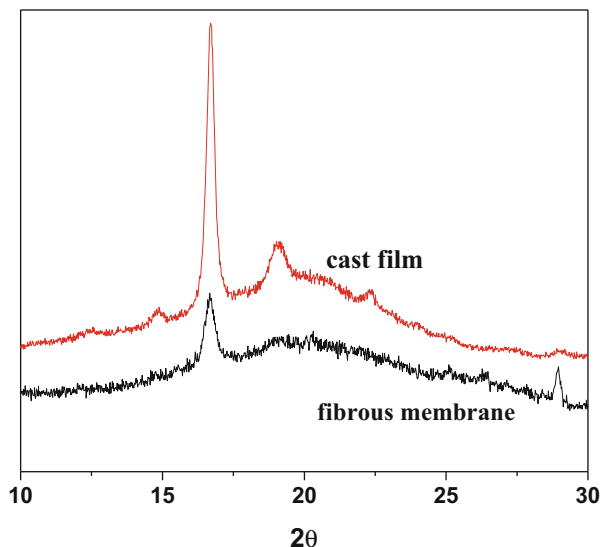
Fig. 8.3 Immunohistochemistry staining for characterisation of osteogenesis and adipogenesis: (a) von Kossa staining for osteogenic differentiation. The mineralised ECM was stained *brown*; (b) oil red O staining for adipogenic differentiation. The accumulated lipid was stained *red* (Magnification 200 \times) (Reproduced from Ref. [84] by permission of John Wiley & Sons Ltd)

with a fibrous pattern (Fig. 8.2e, f). These observations indicate that the PLLA/PCL blend fibres are biocompatible with ADSCs and are a good candidate for scaffold tissue engineering. The pluripotency of ADSCs on scaffolds was assessed by immunohistochemistry. The positive expression in Fig. 8.3 confirms the multilineage differentiation of ADSCs on scaffolds. In Fig. 8.3a, von Kossa staining shows calcium deposition in the ECM, which indicates osteogenesis. In Fig. 8.3b, oil red O staining shows the lipid accumulation in the ECM, which indicates adipogenesis.

In tissue engineering field, a biocompatible scaffold should meet various requirements to support the stem cell to differentiate into desired cell lineage. Similar to the pluripotency of ADSCs in conventional culture and expansion [85–88], the multilineage differentiation of ADSCs on such scaffold indicate the prospect to replace the native ECM for tissue engineering. Our group also compared the electrospun fibrous membrane with cast film of PLLA/PCL blend. The XRD patterns (Fig. 8.4) revealed that the crystallinity of electrospun PLLA/PCL blend fibres is significantly lower than that in the PLLA/PCL blend cast film, which is due to the rapid solidification of the polymer solution during electrospinning which hinders proper crystallisation.

Many other biocompatible polymers have been blended with PLA to electrospin the fibrous scaffolds. For example, PEG is often introduced into PLA because of its hydrophilicity and non-toxicity to modify the bulk properties of PLA. Spasova et al. [89] electrospun the nano- and microstructured PLLA/PEG blend fabrics with different compositions. They investigated the effect of the concentration of the mixed solutions and the ratio of PLLA/PEG on the fibre diameter and morphology. Wang et al. [90] also fabricated the PLA/PEG blend fibrous membranes. They found that the surface wettability of all membranes was influenced by PEG concentration, and the NIH3T3 cells could attach and spread on all samples. The blend of type I collagen and PEO could provide a convenient, non-toxic and non-denaturing way to generate fibrous scaffolds containing collagen [91].

Fig. 8.4 XRD patterns of electrospun fibrous membrane and cast film of PLLA/PCL (1/1) blend (Reproduced from Ref. [84] by permission of John Wiley & Sons Ltd)



Gelatin and PCL in 2,2,2-trifluoroethanol (TFE) at a ratio of 50:50 to produce a gelatin/PCL blend fibrous scaffold by electrospinning [43]. The scaffold showed enhanced mechanical properties and more favourable wettability than those obtained from either PCL or gelatin scaffolds alone. Bone marrow stromal cells (BMSCs) were found to attach and grow well on the surface of the blend fibrous scaffold, suggesting the potential use of gelatin/PCL blend fibrous scaffolds for preparation of the three-dimensional tissue construct.

8.2.3 Polymer Composites

The idea of incorporating nanoscale fillers into polymer matrix has been extended to prepare polymer composites for electrospun fibrous scaffolds. A number of research groups have tried to electrospin such polymer composites with silver particles [92, 93], calcium carbonate [94], calcium phosphate [95] and hydroxyapatite (HA)[96, 97]; the fabricated nanofibrous scaffolds were found to be useful in biomedical applications. Especially, carbon nanotubes (CNTs) have been compounded to impart more functions in polymeric materials, such as thermal, electrical, magnetic, optical and increased mechanical properties [98].

Till now, researchers have electrospun a number of polymer/CNT nanocomposites with different matrices, such as polyethylene oxide (PEO) [99–101], poly(methyl methacrylate) (PMMA) [102–104], poly(acrylonitrile) (PAN) [105, 106], epoxy [107], nylon [108], polycarbonate [109], polyurethane (PU) [110], polystyrene (PS) [110, 111] and polyimide (PI) [112]. Liu et al. [104] fabricated the high-strength and high-modulus PMMA/multiwalled carbon

nanotube (MWNT) composite nanofibres by electrospinning. Compared to the pure PMMA nanofibres, composite fibres with 5 wt. % MWNTs showed ~157% increase in tensile strength and 260% improvement in elastic modulus. Similarly, Chen et al. [112] electrospun PI/MWNT nanocomposite fibres with high strength and high toughness. Also, the 5% weight loss temperature of the electrospun PI fibrous membranes was significantly improved by ~20 °C with the incorporation of only 3.5 wt. % MWNTs. Baji et al. [113] aligned and dispersed MWCNTs in PA6,6 successfully to fabricate self-assembled CNT-based nanofibres by electrospinning PA6,6/MWCNT/formic acid/dichloromethane solution. The addition of MWCNTs increased significantly both modulus and strength of the electrospun fibres. Saeed et al. [114] attempted to electrospin PCL/MWNT nanocomposite fibres and found that the PCL/*p*-amino benzoic acid functionalised-MWNT nanocomposite fibres had better thermal stability than PCL and PCL/pristine-MWNT nanocomposite fibres. The functionalised nanocomposite nanofibres showed a relatively larger diameter than the pure PCL nanofibres and formed fewer beads than the PCL/pristine-MWNT nanocomposite fibres. As the content of functionalised-MWNTs exceeded 2 wt. %, the nanocomposites could not be electrospun. Mei et al. [115] successfully electrospun PLLA/MWNT/HA composite fibrous membrane. They found that the membrane promoted the adhesion and proliferation of human periodontal ligament cells but inhibited those of gingival epithelial cells.

There are some basic requirements for designing polymer scaffolds [116]. First, the materials are biocompatible, and the biodegradability is required. In some cases, the degradation rate should match the rate of neotissue formation. Second, the scaffold must possess the required structural integrity with the appropriate mechanical properties to prevent the pores of the scaffold from collapsing during neotissue formation. Third, the scaffold should be non-toxic to cells, positively interacting with the cells to promote cell adhesion, proliferation, migration and differentiated cell function. So, the polymeric material selection plays a key role in the fabrication of scaffolds. Additionally, new innovations in electrospinning, such as the scaffolds with oriented fibre alignment, and physical and chemical modifications of the scaffolds after electrospinning are able to render the scaffolds with enhanced properties and suitable functionality.

8.3 Scaffolds with Oriented Fibre Alignment for Tissue Engineering

The possibility of controlling fibre deposition pattern makes electrospinning a powerful approach for fabricating scaffolds with a defined architecture in terms of fibre orientation. The fibres could be aligned through collecting substrate and applying electric or magnetic fields [117–122]. One of the most alignment techniques is to use a rotating drum collector instead of grounded collecting plate, and the diameter of the fibres can be controlled and tailored through adjusting the

rotational speed of the drum [117, 121, 123, 124]. At rotational speeds slower than the fibre take-up speed, random fibres are obtained on the drum. At higher speeds, a centrifugal force is developed near the vicinity of the circumference of the rotating drum, which elongates the fibres before being collected on the drum [124]. However, at much higher speeds, the take-up velocity breaks the depositing fibre jet, and continuous fibres are not collected. Besides, in tissue engineering, the alignment is important for the applications of electrospun fibres in sensors, filters and electronic devices. Ghasemi-Mobarakeh et al. [125] fabricated both random and aligned electrospun PCL/gelatin composite nanofibrous scaffolds, and they found that the aligned nanofibres strongly supported the nerve stem cells and enhanced the neurite outgrowth and cell differentiation.

Also, previous studies demonstrated that aligned electrospun nanofibres could control the orientation of neurons caused by the contact guidance [9, 125–127]. For example, the cells cultured on the aligned nanofibres exhibited an alignment factor of 0.74, much higher than 0.19 on the randomly orientated scaffold [128]. Schnell et al. [127] examined the ability of aligned nanofibrous scaffolds to direct axonal outgrowth and glial cell migration in peripheral nerve regeneration. Both PCL and collagen/PCL nanofibrous scaffolds were found to support oriented outgrowth of axons and glial cell migration, the collagen/PCL blend was found to give superior guidance of axons. These experiments demonstrate the potential applications in which it is desirable to develop a nanofibrous scaffold containing aligned fibres.

Our group also fabricated aligned PLLA/PCL/F-MWNT composite membranes by electrospinning [129]. Firstly, MWNTs were functionalised with strong acid oxidation (denoted hereafter by F-MWNT) to improve their dispersion in PLLA/PCL (1/1) blends. Owing to the high rotation speed of the drum collector at 3000 rpm, the electrospun fibres are highly aligned. However, higher rotation speed also more possibly leads to breakage of the fibres. From Fig. 8.5, F-MWNTs are well dispersed in the electrospun composite fibres with 1.25 wt. % nano-filler and aligned along the fibre axis, leading to the smooth surface of electrospun fibres. However, when F-MWNTs are increased to 3.75 wt. %, MWNTs tend to aggregate in the spun fibres, and some protruded parts of F-MWNTs existed on the fibre surface, yielding the beaded structure and a wider fibre diameter distribution. Figure 8.6 shows the morphological changes of the PLLA/PCL blend and PLLA/PCL/F-MWNT composite fibrous membranes as they are degraded in PBS. At 1 week, all samples almost retain their smooth surface, swell and conglutinate with the adjacent fibres. And the increased porosity and lower crystallinity of the PLLA/PCL/F-MWNT composite fibrous membranes allow water molecules to diffuse into the fibre more easily, leading to further swelling and conglutination. At 5 weeks, the electrospun PLLA/PCL blend fibres become thinner due to biodegradation, and the electrospun composite fibres with 1.25 and 3.75 wt. % F-MWNTs become rougher and thinner. Furthermore, the fibrous membrane loses its original structure; and the disintegration of the fibres occurs in the composite membranes because of hydrolysis of PLLA and PCL.

As shown in Fig. 8.7, the cells attach and spread along the scaffolds. Typically, the ADSCs rearrange themselves in parallel to the aligned fibrous membranes with

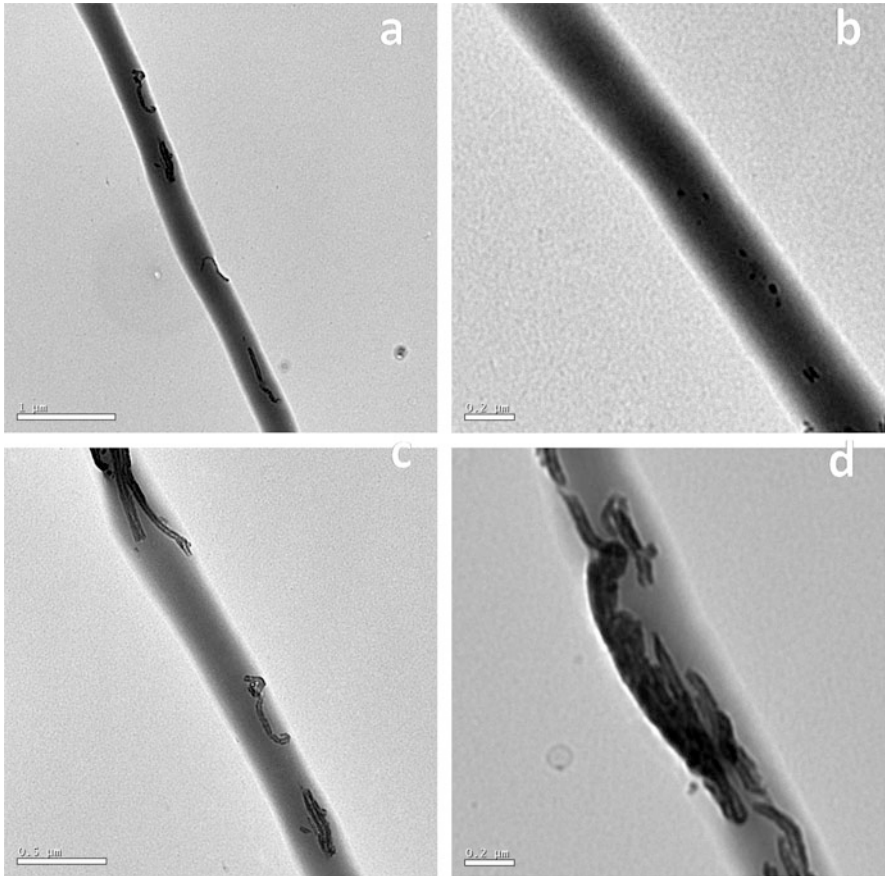


Fig. 8.5 TEM images of PLLA/PCL/F-MWNT composite fibres with 1.25 wt. % (a and b) and 3.75 wt. % (c and d) of F-MWNTs (Reprinted from Ref. [129], Copyright 2012, with permission from Elsevier)

0 wt. %, 1.25 wt. % and 3.75 wt. % of F-MWNTs. This phenomenon of reorientation, which is called contact guidance [9, 125–127], indicates the fibrous alignment induces the long axis of the cells to be in the same direction as the linear fibre by cytoskeletal remodelling. The results implied that controlled cellular orientation can be obtained by controlling the aligned fibres. This is important for the engineering of those tissues whose function comes from their oriented architecture, such as nerve, bone and smooth muscle.

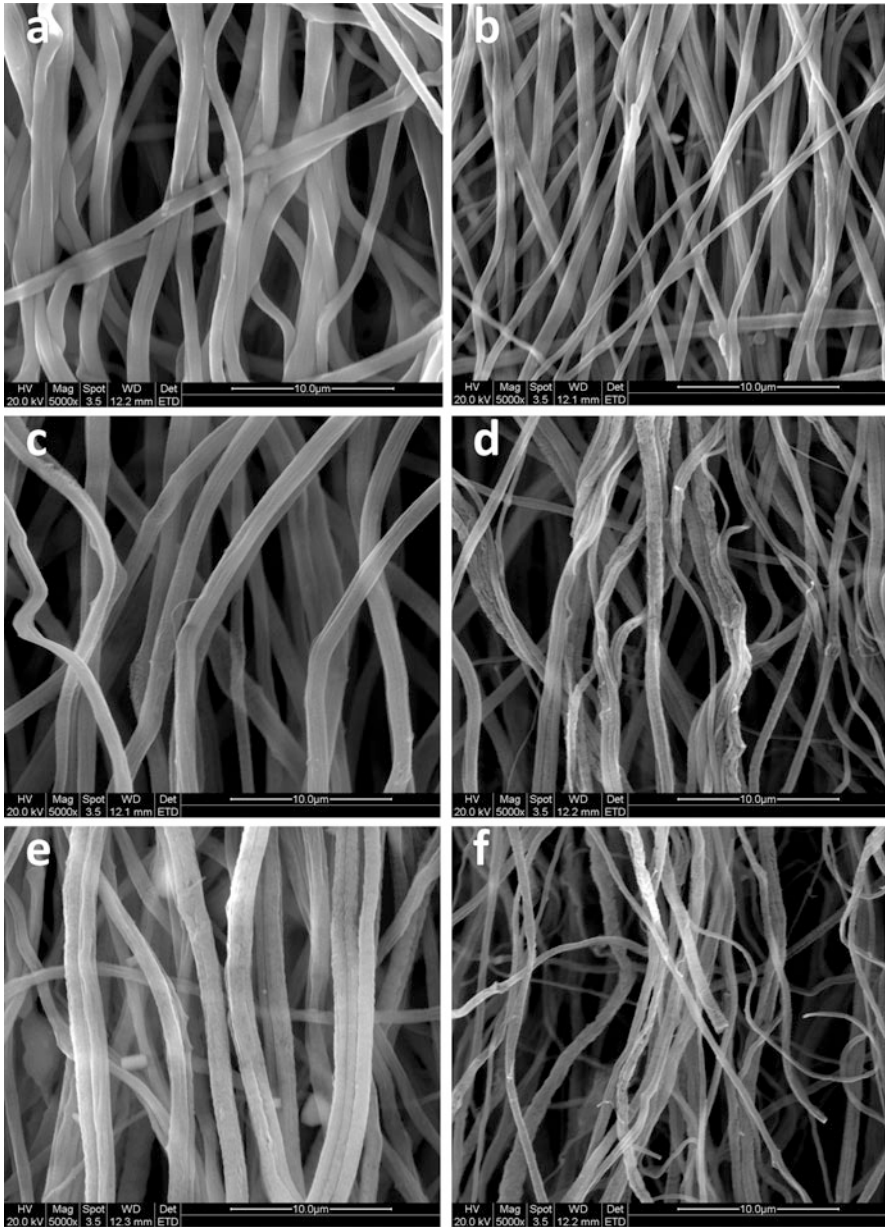


Fig. 8.6 SEM images of aligned electrospun PLLA/PCL/F-MWNT composite fibrous membranes at 1 and 5 weeks of degradation. (a) and (b), 0 wt. %; (c) and (d), 1.25 wt. %; (e) and (f), 3.75 wt. % (Reprinted from Ref. [129], Copyright 2012, with permission from Elsevier)

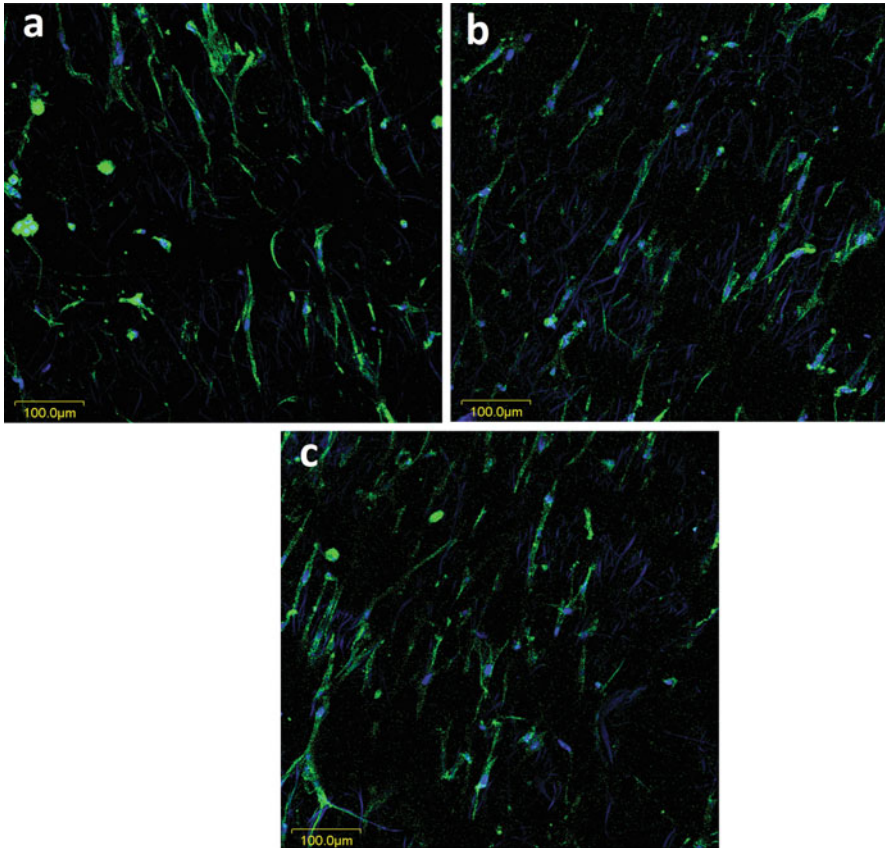
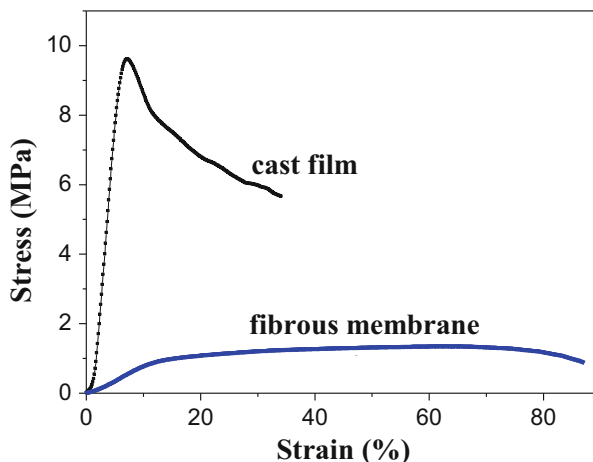


Fig. 8.7 Cell reorientation on the aligned PLLA/PCL/F-MWNT composite fibrous membranes with different content of F-MWNTs. (a) 0 wt. %, (b) 1.25 wt. % and (c) 3.75 wt. % (Reprinted from Ref. [129], Copyright 2012, with permission from Elsevier)

8.4 Mechanical Properties of Electrospun Polymer Scaffolds

The mechanical properties of the electrospun scaffolds must be matched to those of the native tissue. Thus the design of the scaffolds should mimic the architecture of natural tissues. Ideally, cells are contained in a ‘microenvironment’ that achieves a distribution of forces which encourages native tissue regeneration and maintenance while avoiding a cellular hypotrophic or hypertrophic response. Moreover, the flexibility of seeding stem cells and human cells on the electrospun fibrous scaffolds makes materials most suitable for tissue engineering applications [130, 131]. Besides, mimicking the structure of ECM, the fibrous scaffolds should be designed to possess its properties including high elasticity and stiffness [132–136]. This suggests a thorough understanding of the mechanical behaviours of

Fig. 8.8 Tensile stress–strain curves of the electrospun fibrous membrane and cast film of PLLA/PCL (1/1) blend (Reproduced from Ref. [84] by permission of John Wiley & Sons Ltd)



electrospun scaffolds is essential. For performance analysis, Young's modulus of elasticity, tensile strength and strain at break were investigated since these values are commonly reported for tissue engineering applications.

Electrospinning is different to other moulding processes and provides electrospun fibres with different mechanical properties. In our previous study [84], we evaluated mechanical properties of the PLLA/PCL blend fibrous membrane and cast film (Fig. 8.8). Since the electrospun PLLA/PCL (1/1) blend fibrous membrane has a higher porosity and lower crystallinity, its Young's modulus and tensile strength are expected to decrease to 6.46 MPa and 1.21 MPa from 89.0 MPa and 9.4 MPa of the PLLA/PCL (1/1) blend cast film, but its elongation at break increases to 85.6% from 32.4% of the cast film. The high porosity and ductility provide the electrospun PLLA/PCL (1/1) blend fibrous membrane with a potential as tissue scaffold. Chen et al. [112] also reported that the tensile strength and elongation at break (or toughness) of electrospun membrane are much higher than those of the cast film, due to the high orientation of the electrospun nanofibres in the membranes.

Shields et al. [31] reported that electrospun collagen fibres with a diameter of about 100 nm intended for articular cartilage repair have Young's modulus of 170 MPa and maximum stress of 3.3 MPa. These values closely match the cartilage mechanical properties of Young's modulus of 130 MPa and maximum stress of 20 MPa [137]. Soffer et al. [138] successfully electrospun silk into tubular structures with an inner diameter of ~3 mm and an average wall thickness of 0.15 mm. An average tensile strength of 2.42 ± 0.48 MPa and a linear modulus of 2.45 ± 0.47 MPa were obtained. Recently, inorganic particles, such as HA and CNTs, have been widely co-electrospun into polymer nanofibres for enhanced mechanical properties.

8.4.1 CNT-Reinforced Electrospun Fibrous Scaffolds

Many studies showed that the incorporation of CNTs reinforces the mechanical properties of electrospun fibres [139–142]. In our previous study [129], we evaluated mechanical properties of the aligned PLLA/PCL/F-MWNT fibrous scaffold. Figure 8.9 shows the stress–strain curves of PLLA/PCL blend and PLLA/PCL/F-MWNT composite fibrous membranes. Both tensile strength and Young’s modulus became substantially higher with increase of the F-MWNTs. At 1.25 wt. % F-MWNTs, the composite fibrous membrane shows improvements of 39.9 % in modulus and 76.2 % in tensile strength. And at 3.75 wt. % F-MWNTs, the Young’s modulus and tensile strength of the composite fibrous membrane further increase by 101.8 % and 134.6 %, respectively. Thus, the aligned F-MWNTs reinforce the electrospun PLLA/PCL blend fibrous membrane. The results have been observed in the electrospun PA6/MWNT, silk/MWNT and PAN/MWNT composite fibrous membranes [140–142]. As expected, the interfacial adhesion ensures the efficient load transfer from polymer matrix to F-MWNTs, which leads to high mechanical properties. Moreover, the ductility, as revealed by the elongation at break, shows to increase by 58.6 % and 34 % at 1.25 and 3.75 wt. % F-MWNTs, respectively, for the composite fibrous membrane in comparison with the PLLA/PCL blend membrane [129]. The poorer ductility of the composite membrane at the higher content of F-MWNT is largely due to the aggregation of the nano-fillers [140, 142].

Sen et al. [110] fabricated SWCNT-reinforced polystyrene (PS) and PU fibrous membranes using electrospinning method. They found that the SWCNT bundles are oriented parallel to the PS/SWCNT nanofibre axis. The tensile strength and the Young’s modulus of PU/ester-functionalised SWCNT composite membranes are enhanced by 104 and 250 % as compared to the electrospun pure PU membranes. They have also developed a flexible approach to the alignment of SWNT that allows their hierarchical assembly, and orientation of SWNT is directionally controllable [143]. Aligned nanofibrous nanocomposites of nylon 6 and surface-

Fig. 8.9 Tensile stress–strain curves of aligned electrospun PLLA/PCL/F-MWNT composite fibrous membranes with different contents of F-MWNTs. (a) 0 wt. %, (b) 1.25 wt. % and (c) 3.75 wt. % (Reprinted from Ref. [129], Copyright 2012, with permission from Elsevier)

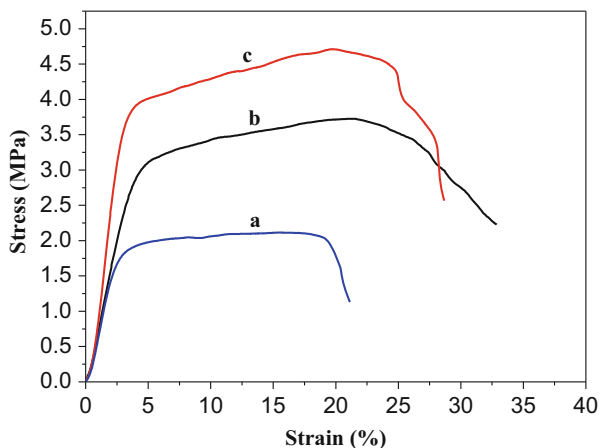
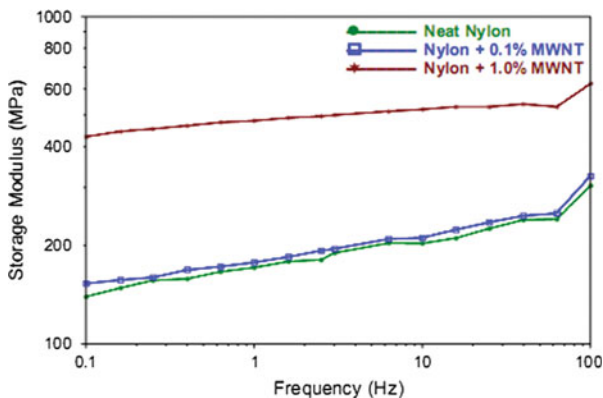


Fig. 8.10 Effect of MWNT on storage modulus of the non-woven aligned fibre mat at 6000 rpm (Reprinted from Ref. [108], Copyright 2007, with permission from Elsevier)



modified MWNTs were successfully prepared via electrospinning, using a rotating mandrel [108], which showed that the effects of nylon fibre alignment and MWNT orientation on the mechanical properties were manifested, which increased with high take-up speed and MWNT concentration. A twofold modulus increase is also observed for the neat nylon 6 as the speed increases from 3000 to 4500 rpm, but with little increase at 6000 rpm. The aligned fibres exhibited a much higher stiffness than the randomly aligned mat. At a given collector speed (6000 rpm), Fig. 8.10 shows an increase in modulus with MWNT loading. The largest increase in the modulus is the 1 wt. % MWNTs loading. Such factors as MWNTs and high take-up speed resulted in formation of aligned nanofibrous scaffolds with MWNTs alignment and mechanical stiffness. Ge et al. [105] reported highly oriented, large area continuous composite nanofibre sheets made from surface-oxidised MWNTs and poly(acrylonitrile) (PAN). They found that the tensile modulus values of the compressed composite nanofibre sheets were improved significantly to 10.9 and 14.5 GPa along the fibre winding direction at the MWNT loading of 10 and 20 wt. %, respectively.

It has been known that polyimide (PI) is among the ultrastrong polymers but usually possesses low toughness or elongation at break. High performance PI nanocomposites fibrous membranes were successfully fabricated with high toughness and enhanced overall mechanical properties by incorporation of CNTs [112]. Adding 1 wt. % CNTs can dramatically improve the overall tensile properties of PI membranes. With increasing the CNT content, the modulus of the membranes increases evidently. For example, the PI/CNT composite membrane with 10 wt. % CNTs possesses the highest tensile modulus, and the optimised tensile or yield strength is observed for the membrane containing 3.5 wt. % F-MWNTs, whose elongation at break can reach nearly 100 %. When the CNT content is further increased from 3.5 to 10 wt. %, all the values of the tensile or yield strength and elongation at break gradually decrease. For the membrane containing 10 wt. % MWNTs, its tensile strength is even lower than that of the neat PI membrane. Therefore, the tensile results may indicate that CNT agglomerations are probably formed to certain extent when the CNT content is above 3.5 wt. %.

8.4.2 HA-Reinforced Electrospun Fibrous Scaffolds

The development of scaffolds mimicking the composition, structure and mechanical properties of human bone matrix has become one of the major goals in the bone regeneration and tissue engineering fields. Human bone is a ceramic/biopolymer hybrid with a three-dimensional woven structure made up of 65–70 wt. % HA ($\text{Ca}_{10}(\text{PO}_4)_6(\text{OH})_2$) crystals and 30–35 wt. % type I collagen fibres. In bone, the HA crystals mainly contribute to its compressive strength and stiffness, while collagen fibres provide the corresponding tensile properties.

To mimic the human bone matrix, Kim et al. [96] fabricated a HA/gelatin fibrous scaffold by electrospinning. The HA/gelatin mixture was lyophilised and dissolved in the organic solvent HFP and then electrospun under controlled conditions. With this method, the HA nanocrystals are well distributed within the gelatin fibres. Compared with pure gelatin, the nanocomposite fibres significantly improve the bone-derived cellular activity, thus signifying good potential in the application of guided tissue (bone) regeneration. Stanishevsky et al. [144] also electrospun the HA/collagen composites for hard tissue scaffold applications and demonstrated that the strength of the fibres can be controlled by loading HA fillers. The properties of the electrospun material can be easily controlled by the HA content in the fibres.

Collagen fibres are self-assembled in an orderly fashion and generate channels or grooves. Mineral particles originate and develop at the grooves that can grow in length and width as the sheets of mineral platelets. The mineral platelets are placed parallel to each other and provide strength to the composite. Thus, the arrangement of collagen and bone crystals at the structural level can critically affect the mechanical integrity of the whole system [145, 146]. The strength of the tissue scaffolds processed by the conventional methods lacks the architecture of the natural composites, and hence their mechanical properties are drastically different from natural bone composites. However, the electrospinning technique is capable of mimicking the protein-guided mechanism and aligns the HA particles along the fibre axis direction.

Fibrous PCL/HA nanohybrids were fabricated by Bianco et al. [147], in which the HA content ranged from 2 to 55 wt. %. Electrospun mats showed a non-woven architecture; their average fibre size was $1.5 \pm 0.5 \mu\text{m}$ and porosity 80–90 %. Up to 6.4 wt. % HA, the nanohybrids displayed enhanced mechanical and dynamomechanical properties. However, for nanohybrids with 25–55 wt. % HA, the yielding stress, ultimate tensile strength and strain at failure decreased due to the increased micrometric HA clusters.

HA and PLA were fabricated into composite fibrous scaffolds by electrospinning [97]. A surfactant, hydroxyesteric acid (HSA), was used to effectively disperse hydrophilic HA particles in chloroform solutions of PLA. Cellular assay experiments indicated that the electrospun scaffolds have excellent cell attachment and proliferation properties as well as an enhanced expression of alkaline phosphatase at 7 days of culturing. Peng et al. [148] also attempted to improve the mechanical strength, modulus and toughness of the PLLA/HA electrospun scaffolds by aligning the needle-shaped HA particles within PLLA nanofibres.

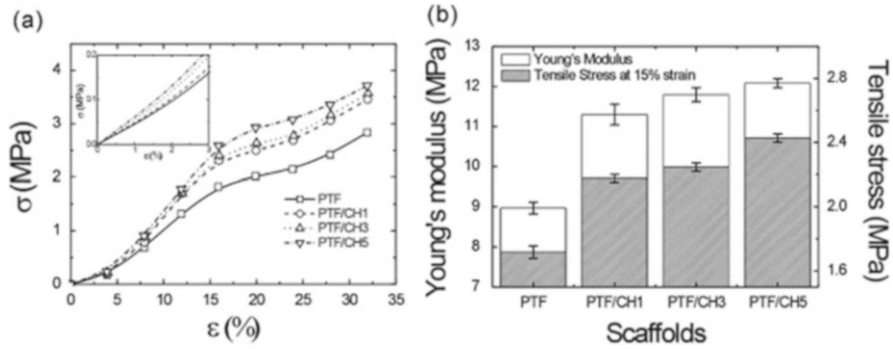


Fig. 8.11 (a) Stress–strain curves for the scaffolds and (b) comparisons of Young’s modulus and tensile stress at 15 % strain between PTF and PTF/CH scaffolds ($n = 5$). PTF refers the PCL nanofibres-embedded PCL/ β -TCP as a scaffold, where the symbols ‘P’, ‘T’ and ‘F’ denote PCL strut, β -tricalcium phosphate and PCL fibres, respectively. CH1, CH3 and CH5 refer to the collagen/HA with 1, 3 and 5wt. % of HA, respectively (Reprinted with the permission from Ref. [149], Copyright 2012 American Chemical Society)

For bone tissue regeneration, a porous scaffold must provide sufficient temporary mechanical support to withstand *in vivo* stresses and avoid excessive new tissue deformation. Bioceramics have been applied widely for bone tissue regeneration, attributable to their excellent biochemical cues for the cells. However, the major shortcoming of these materials is their brittleness compared to native bone. Recently, a simple coating technique with bioceramic has been developed to reinforce the scaffolds. For example, Yeo and Kim [149] fabricated the PCL nanofibres-embedded PCL/ β -tricalcium phosphate (β -TCP) composite scaffolds and used a simple coating process to reinforce the scaffolds with collagen/HA mixture. The stress–strain curves of the composite scaffolds as a function of the HA concentration in the coating solution (Fig. 8.11a) reveal a typical curve for porous materials. As shown in Fig. 8.11b, the Young’s modulus of the composite scaffolds increases with the HA concentration in the collagen coating solution. As coated by 5 wt. % collagen/HA mixture, the Young’s modulus and tensile stress at 15 % strain of surface-reinforced scaffolds increase from 8.9 MPa and 1.8 MPa of the untreated scaffolds to 12.1 MPa and 2.6 MPa, respectively. The reason may be the reinforcing effect of the coated nanosized HA particles and the slightly reduced porosity of the scaffolds [150]. From these results, we can infer that the simple coating process with bioceramics is beneficial to reinforcement of the electrospun fibrous scaffolds.

8.5 Surface Modification of Electrospun Scaffold for Biomedical Applications

As discussed above, the modifications of copolymerisation, blending, composition and alignment significantly improve physical and biological properties of electrospun fibrous scaffolds. Further, surface chemical or physical modifications

with bioactive molecules or cell-recognisable ligands are often essential to render the electrospun fibrous scaffolds with bio-modulating or biomimetic microenvironments for cells and tissues.

8.5.1 Chemical Immobilisation and Surface Graft Polymerisation

Chemical immobilisation and surface graft polymerisation have been introduced not only to confer surface hydrophilicity but also to introduce multifunctional groups on the surface of electrospun fibrous scaffolds for enhancing the adhesion, proliferation and differentiation of cells [25, 151–155]. Primary amine and carboxylate groups are most extensively employed to immobilise bioactive molecules. As reported by Kim and Yoo [156], biomolecules are covalently immobilised via peptide bond through amino groups, and then a matrix metalloproteinase (MMP)-cleavable linker is introduced between gene–vector complex and the electrospun scaffolds, so that gene release can be controlled by external MMP cleavage. Also, carboxylic groups on the surface of polymeric fibres with different amounts of polyacrylic acid are employed for conjugation with collagen [157]. Similarly, acrylic acid-immobilised fibres were conjugated to amine groups to prepare aminated fibres [158]. These fibres are further employed for in vitro cultivation of umbilical cord blood cells. For example, poly(acrylonitrile-co-maleic acid) (PANMA) is electrospun, and then lipase is immobilised onto the fibrous surface through the reaction between carboxylic groups of PANMA and the amine groups of lipase [159, 160]. Hydroxyl groups were also employed for the chemical immobilisation of bioactive molecules. For example, Jia et al. [161] synthesised hydroxyl-terminated PS (PS-OH) with initiator containing hydroxyl, and then alpha-chymotrypsin is covalently attached on the surface of the electrospun PS-OH fibres.

Ma et al. [25] reported a chemical approach for modification of the electrospun polyethylene terephthalate (PET) nanofibre surface by grafting gelatin to overcome the chemical and biological inertness of the PET surface. The electrospun PET scaffolds were treated with formaldehyde to generate hydroxyl groups. After methacrylic acids were polymerised on the modified electrospun fibre surface with Ce (IV) as the initiator, gelatins were conjugated to immobilise on the nanofibrous scaffolds. They also tested the bioactivity of the gelation-modified electrospun PET scaffold by using endothelial cells (ECs). The gelatin-modified PET scaffold showed an obvious improvement in cell adhesion, spreading and proliferation compared with the unmodified PET scaffold. The electrospun cellulose acetate fibrous scaffold was hydrolysed and followed by grafting of PEG diacylchloride, and lipase enzyme was then attached to the scaffold surface through the coupling with PEG spacers [153]. The results showed that the bound lipase exhibited much better retention ability of catalytic activity after exposure to cyclohexane (81 %), toluene (62 %) and hexane (34 %) than the activity of the

free lipase (25 %). Similarly, Aznar-Cervantes et al. [162] successfully modified the silk fibroin nano- and micromeshes through surface graft polymerisation of pyrrole. Both of silk fibroin and polypyrrole-coated silk fibroin meshes show quite similar bioactivity for human fibroblast's (hFb) attachment and growth. Similar results are obtained by seeding adult human mesenchymal stem cells (ahMSCs) on the above two meshes. But, mechanical properties of the meshes are greatly improved. After surface graft polymerisation of pyrrole, the Young's modulus of the modified meshes increases to 310.5 MPa from 266.7 MPa of the uncoated meshes. Furthermore, the modified meshes have higher electroactivity allowing anion storage and delivery during oxidation/reduction reactions in aqueous solutions. For hepatocyte culture, Chua et al. [163] grafted a hepatocyte-specified galactose ligand onto electrospun poly(ϵ -caprolactone-co-ethyl ethane phosphate) (PCLEEP) nanofibres. As shown in Fig. 8.12, the electrospun PCLEEP nanofibres are first cleaned by ethanol and grafted with poly(acrylic acid) (PAA) by photo-induced polymerisation. Then, 1-*O*-(6'-aminohexyl)-D-galacto-pyranoside (AHG) is conjugated to the PAA chains in a sodium phosphate buffer containing N-hydroxysulfosuccinimide (NHS) and 1-ethyl-3-(3-dimethylaminopropyl) carbodiimide hydrochloride (EDC). During cell culture, hepatocytes adhere to the surface through the galactose-asialoglycoprotein receptor (ASGPR). The results showed that hepatocytes are cultured on electrospun galactosylated scaffolds with superior biological properties such as cell attachment, albumin synthesis and 3-methylcholanthrene-induced cytochrome P450 function.

Except for the electrospun nanofibrous scaffolds, the spin-coating films are fabricated with the same materials and modified with the same procedure for comparison. After 8 days, hepatocytes cultured on modified electrospun scaffolds form spheroids that engulfed the galactosylated nanofibres (Fig. 8.13d–f). Compared with the modified cast films (Fig. 8.13a–c), the spheroids are immobilised on the scaffold and would not detach from the scaffold upon agitation. The results showed that hepatocyte spheroid immobilisation and stabilisation strategy through the use of galactosylated nanofibrous scaffolds would be advantageous in the design of a bioartificial liver assist device.

8.5.2 Surface Physical Adsorption and Assembly

For the above surface chemical modification, the immobilised molecules are not easily leached out from the surface-modified fibres when incubated over an extended period due to covalent immobilisation. But surface physical modifications, such as surface physical adsorption and assembly, are much simpler to load biomolecules onto electrospun scaffolds, which is to dip the scaffolds into an aqueous phase containing biomolecules.

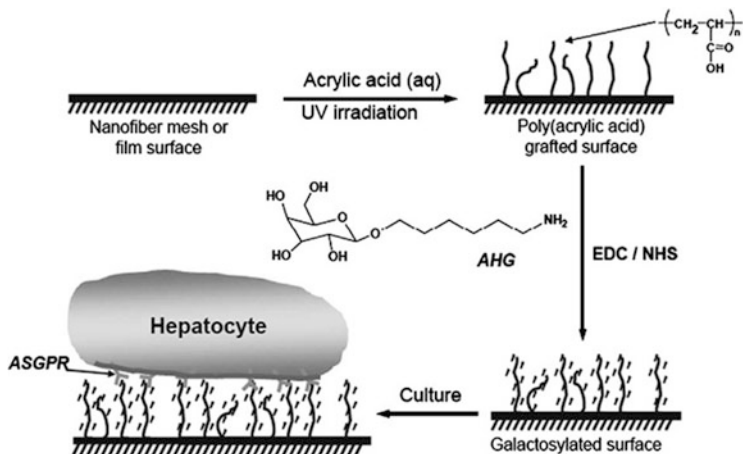


Fig. 8.12 Surface modification scheme for galactose conjugation to PCLEEP nanofiber mesh and spin-cast film (Reprinted from Ref. [163], Copyright 2005, with permission from Elsevier)

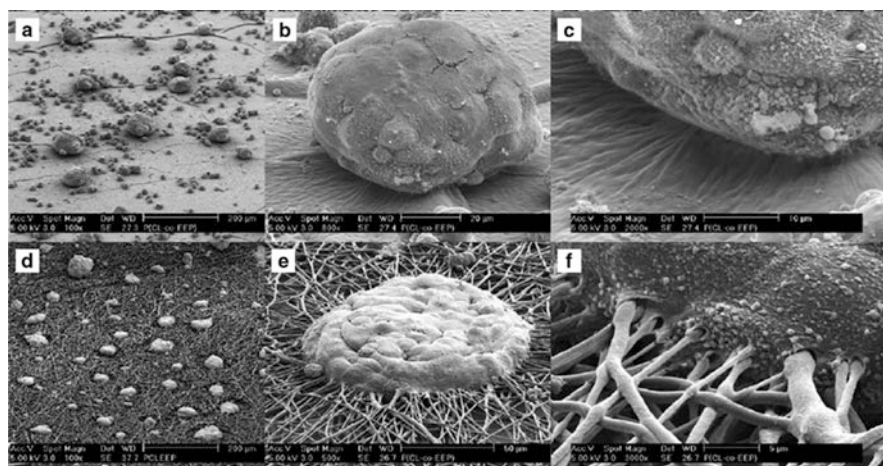


Fig. 8.13 SEM images of hepatocytes after 8 days of culture: (a–c) hepatocytes cultured on galactosylated spin-cast film formed around spheroids; (d–f) in contrast, hepatocytes cultured on galactosylated electrospun scaffold showed aggregates that engulfed the functional nanofibres (Reprinted from Ref. [163], Copyright 2005, with permission from Elsevier)

On the principle of physical interaction, biomolecules in the form of solutions or emulsions attach to the surface of scaffolds via electrostatic forces, hydrogen bonding, hydrophobic interaction and van der Waals interaction [164–167]. Heparin, a highly sulphated glycosaminoglycan, has strong binding affinity with various growth factors such as fibroblast growth factor (FGF), vascular endothelial growth

factor (VEGF), heparin-binding epidermal growth factor (HBEGF) and transforming growth factor- β (TGF- β). Firstly, heparin is immobilised on the surface of electrospun fibrous scaffolds, and growth factors are attached for local delivery of growth factors and consequent mitogenic induction [168]. Loading drug is a very straightforward and effective method due to the unique morphological feature of electrospun fibres. For example, to load a commercial antibiotic drug, Biteral®, the drug solution is simply dropped on PCL non-woven sheets for adsorption [169]. From the *in vitro* release data, nearly 80 % of the initial burst is observed within 3 h and the release ends after almost 18 h. A rapid drug release profile is highly desirable for preventing infections at an early stage.

The assembly of target molecules or functional nanoparticles such as silver or HA on the surface of electrospun fibres has been attempted for biomedical applications [170–173]. Seyedjafari et al. [174] reported that nano-HA (n-HA) was coated on the plasma-treated surface of electrospun PLLA nanofibres. They used human cord blood-derived unrestricted somatic stem cells (USSC) under osteogenic induction to investigate the capacity of the scaffolds for bone formation. During osteogenic differentiation, significantly higher values of ALP activity, biomineralisation and bone-related gene expression were observed on n-HA/PLLA compared to PLLA scaffolds. The results showed that surface-coated n-HA stimulates the effect of fibres on the orientation of USSC towards osteolineage.

A versatile surface modification method is layer-by-layer (LbL) multilayer assembly that allows surface of fibres to be precisely coated, and synthetic polyions, biopolymers such as DNA and enzymes, viruses, dendrimers, colloids, inorganic particles and dyes are easily incorporated into the multilayers [175]. Many groups have realised the potential of multilayers for biomedical applications [176–183]. Ge et al. [184] used electrospinning and LbL assembly to fabricate the hollow multilayered PE nanofibres by selectively removing the fibre templates. The PS/MWCNT nanofibres were employed as templates to self-assemble multilayered polyelectrolytes by LbL assembly; thus, hollow PE/MWCNT composite nanofibres were obtained by selectively removing part of the template [185]. Müller et al. [186] reported that the polyelectrolyte multilayer was deposited on the surface of electrospun fibres. The PS fibre surface was endowed with negative charges by sulphonation of phenyl groups, and then poly(allylamine hydrochloride) (PAH) and poly(styrene sulphonate) (PSS) was conducted on the PS fibre surface via LbL assembly, followed by the dissolution of PS core fibres, resulting in hollow polyelectrolyte complex tubes. Di-block oligonucleotides (polyA15G15 and polyT15C15) multilayers were also built-up based on the DNA hybridisation mechanism by LbL assembly. Upon build-up cycles, the DNA multilayer grew in a linear manner, showing a smoother surface compared to the PAH/PSS multilayer surface. It indicates that this facile surface modification of electrospun fibres with synthetic polymers and biopolymers could provide an opportunity for creating a variety of drug-releasing surfaces.

Our group also fabricated chondroitin sulphate (CS)/chitosan (CHS) multilayer-modified PLLA/PCL blend fibres with the goal of combining the good

biocompatibility of the natural extracellular matrix-like molecules. Firstly, 1,6-hexanediamine is dissolved in isopropyl alcohol; and hydrochloric acid solution is used to activate the PLLA/PCL blend substrate in order to obtain a stable positively charged surface that can be further used to deposit biomacromolecule polyelectrolytes by LbL assembly. The CS/CHS multilayer modified PLLA/PCL fibrous scaffolds were investigated by X-ray photoelectron spectroscopy (XPS) and contact angle. From Fig. 8.14, the unmodified PLLA/PCL blend fibrous surface generates the three expected peaks, indicating that this surface contains three carbon regions, i.e. the binding energies of 284.5 eV for C_{C-H} , 286.7 eV for C_{C-O} and 289.0 eV for $C_{C=O}$, respectively. After amination treated by 1,6-hexanediamine, the intensity of C_{C-H} peak increases notably, and there appears a new carbon peak at 287.2 eV, indicating the existence of an amide bond on the surface of PLLA/PCL fibres. For the CS/CHS multilayer assembled PLLA/PCL blend fibrous surface, the carbon peak of amide indicates that the CS/CHS multilayers cover the fibrous surface. Besides, there are obvious nitrogen peaks (400.1 eV) on both aminated and CS/CHS multilayer assembled PLLA/PCL fibres (Fig. 8.14c, e), while there is no detectable nitrogen on the electrospun PLLA/PCL blend fibres (Fig. 8.14a). Furthermore, Fig. 8.15 shows that the hydrophilicity of PLLA/PCL blend fibrous surface is evidently enhanced after the amination treatment and LbL assembly of CS and CHS layers. Compared with conventional coatings, polyelectrolyte LbL multilayers are stable and easy to process, indicating that the LbL assembly may be a good choice for modifying 3D scaffolds for drug delivery and tissue engineering.

8.6 Conclusion

Electrospun polymer fibrous scaffolds have held great promise and been of considerable potential for biomedical applications in the recent years. A successful fabrication of fibrous scaffolds must start with the proper polymeric materials, a judicious fabrication pathway and possible postmodification with functional reagent. Tremendous efforts have been made to search for suitable scaffold materials. An ideal scaffold should have similar biochemical and biomechanical properties to the ECM. The desirable properties of the electrospun fibrous scaffolds can be achieved by copolymerisation, blending and composition. Especially, inorganic particles, such as HA and CNTs, have been widely co-electrospun into polymer nanofibres for reinforcing the fibres. Besides, the oriented fibre alignment also significantly improves the physical and biological properties of fibrous scaffolds, which can be used to control the mechanical properties as well as the biological response. Furthermore, the surface physical and chemical modifications of electrospun fibres are often conducted to obtain the desired scaffold properties and enhance the interaction between cells and scaffolds in tissue engineering applications. Notably, LbL assembly is widely used attributable to the precise control on coating thickness and composition. As an advanced polymer processing

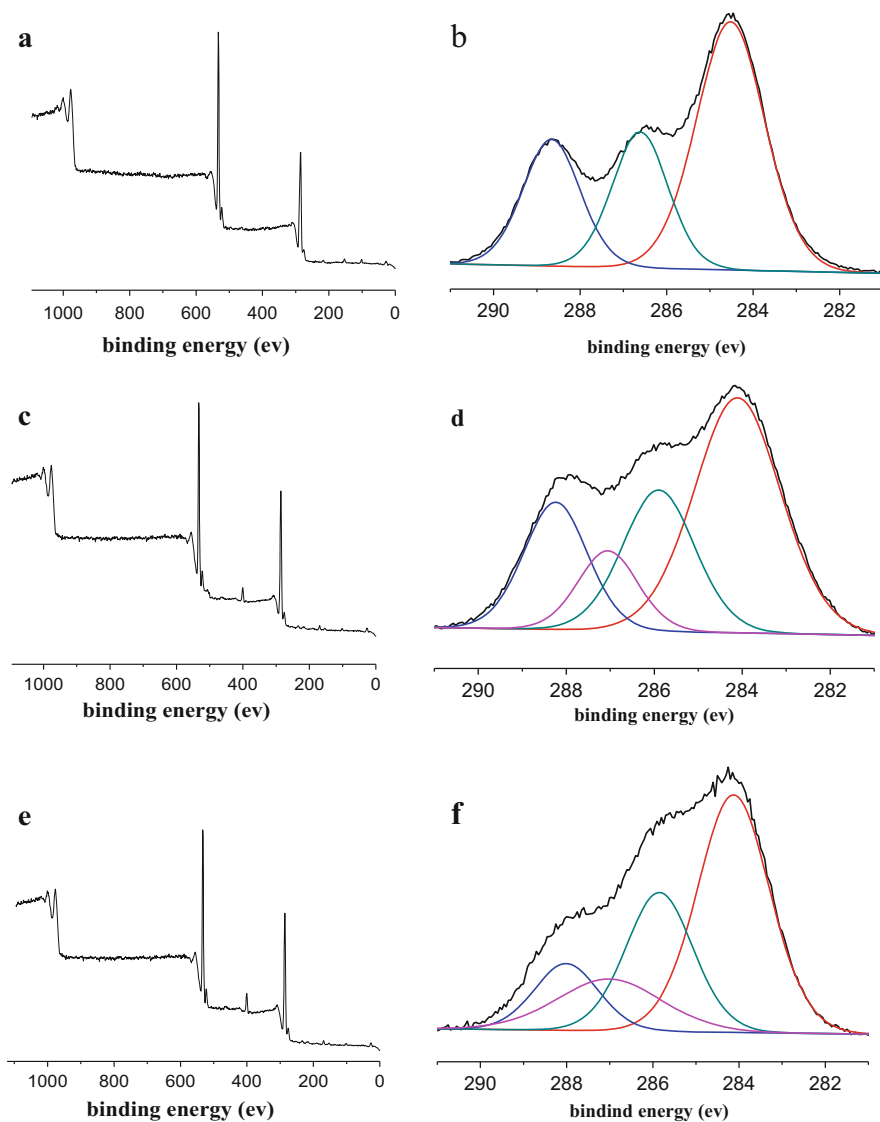
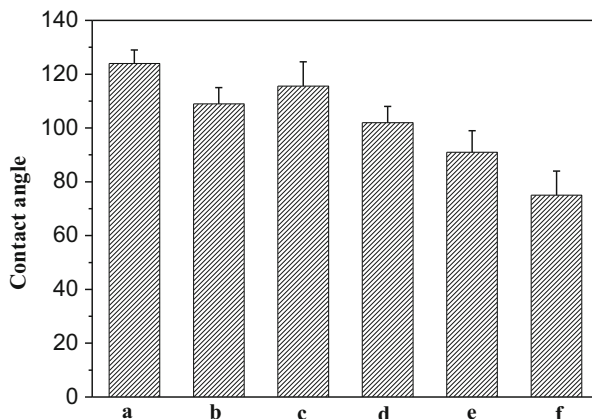


Fig. 8.14 XPS spectra of different PLLA/PCL fibrous membranes: (a) and (b) the unmodified PLLA/PCL, (c) and (d) aminated PLLA/PCL, and (e) and (f) CS/CHS assembled PLLA/PCL

technique, electrospinning has emerged for extensive applications in biomedical engineering, whereas its true potential has yet to be fully realised. It is expected to gain a better fundamental understanding of the electrospinning, develop the innovative electrospinning techniques and expand more applications in biomedical engineering in the future.

Fig. 8.15 Contact angle data of PLLA/PCL fibrous membranes with amination and different assembled layers. (a) The unmodified PLLA/PCL virgin, (b) amination, (c) one layer (d) two layers, (e) three layers and (f) five layers



Acknowledgement The authors sincerely thank the National Natural Science Foundation of China (21477118) and National Basic Research Program of China (973 Program) (2011CB606002) for support of this work.

References

1. Doshi J, Reneker DH (1995) Electrospinning process and applications of electrospun fibers. *J Electrostat* 35:151–160
2. Reneker DH, Chun I (1996) Nanometer diameter fibers of polymers, produced by electrospinning. *Nanotechnology* 7:216–223
3. Schreuder-Gibson H, Gibson P, Wadsworth L, Hemphil SL, Vontorcik J (2002) Effect of filter deformation on the filtration and air flow for elastomeric nonwoven media. *Adv Filtr Sep Technol* 15:525–537
4. Wang B, Luo L, Ding Y, Zhao D, Zhang Q (2012) Synthesis of hollow copper oxide by electrospinning and its application as a nonenzymatic hydrogen peroxide sensor. *Colloid Surf B Biointerfaces* 97:51–56
5. Wang XY, Kim YG, Drew C, Ku BC, Kumar J, Samuelson LA (2004) Electrostatic assembly of conjugated polymer thin layers on electrospun nanofibrous membranes for biosensors. *Nano Lett* 4:331–334
6. Gorji M, Jeddi AAA, Gharehaghaji AA (2012) Fabrication and characterization of polyurethane electrospun nanofiber membranes for protective clothing applications. *J Appl Polym Sci* 125(5):4135–4141
7. Liu HQ, Kameoka J, Czaplewski DA, Craighead HG (2004) Polymeric nanowire chemical sensor. *Nano Lett* 4:671–675
8. Riboldi SA, Sampaolesi M, Neuenschwander P, Cossu G, Mantero S (2005) Electrospun degradable polyesterurethane membranes: potential scaffolds for skeletal muscle tissue engineering. *Biomaterials* 26:4606–4615
9. Yang F, Murugan R, Wang S, Ramakrishna S (2005) Electrospinning of nano/micro scale poly(L-lactic acid) aligned fibers and their potential in neural tissue engineering. *Biomaterials* 26:2603–2610
10. Formhals A (1934) Apparatus for producing artificial filaments from material such as cellulose acetate. US patent no. 1975504

11. Zachariades AE, Porter RS, Doshi J, Srinivasan G, Reneker D (1995) High modulus polymers. A novel electrospinning process. *Polym News* 20:206–207
12. Fang X, Reneker DH (1997) DNA fibers by electrospinning. *J Macromol Sci B* 36:169–173
13. Srinivasan G, Reneker DH (1995) Structure and morphology of small diameter electrospun aramid fibers. *Polym Int* 36:195–201
14. Fong H, Reneker DH (1999) Elastomeric nanofibers of styrene-butadiene-styrene triblock copolymer. *J Polym Sci B Polym Phys* 37:3488–3493
15. Yarin AL, Koombhongse S, Reneker DH (2001) Taylor cone and jetting from liquid droplets in electrospinning of nanofibers. *J Appl Phys* 90:4836–4846
16. Yarin AL, Koombhongse S, Reneker DH (2001) Bending instability in electrospinning of nanofibers. *J Appl Phys* 89:3018–3026
17. Desai K, Kit K, Li JJ, Zivanovic S (2008) Morphological and surface properties of electrospun chitosan nanofibers. *Biomacromolecules* 9:1000–1006
18. Aluigi A, Vineis C, Varesano A, Mazzuchetti G, Ferrero F, Tonin C (2008) Structure and properties of keratin/PEO blend nanofibres. *Eur Polym J* 44:2465–2475
19. Sanders EH, Kloefkorn R, Bowlin GL, Simpson DG, Wnek GE (2003) Two-phase electrospinning from a single electrified jet: microencapsulation of aqueous reservoirs in poly(ethylene-co-vinyl acetate) fibers. *Macromolecules* 36:3803–3805
20. Pham QP, Sharma U, Mikos AG (2006) Electrospinning of polymeric nanofibers for tissue engineering applications: a review. *Tissue Eng* 12:1197–1211
21. Ferreira AM, Gentile P, Chiono V, Ciardelli G (2012) Collagen for bone tissue regeneration. *Acta Biomater* 8:3191–3200
22. Ma Z, Kotaki M, Inai R, Ramakrishna S (2005) Potential of nanofiber matrix as tissue engineering scaffolds. *Tissue Eng* 11:101–109
23. Khil MS, Cha DI, Kim HY, Kim IS, Bhattarai N (2003) Electrospun nanofibrous polyurethane membrane as wound dressing. *J Biomed Mater Res B Appl Biomater* 67B:675–679
24. Buttafoco L, Kolkman NG, Poot AA, Dijkstra PJ, Vermes I, Feijen J (2005) Electrospinning collagen and elastin for tissue engineering small diameter blood vessels. *J Control Release* 101:322–324
25. Ma Z, Kotaki M, Yong T, He W, Ramakrishna S (2005) Surface engineering of electrospun polyethylene terephthalate (PET) nanofibers towards development of a new material for blood vessel engineering. *Biomaterials* 26:2527–2536
26. Katti DS, Robinson KW, Ko FK, Laurencin CT (2004) Bio-resorbable nanofiber-based systems for wound healing and drug delivery: optimization of fabrication parameters. *J Biomed Mater Res B Appl Biomater* 70B:286–296
27. Pawlowski KJ, Barnes CP, Boland ED, Wnek GE, Bowlin GL (2004) Biomedical nanoscience: electrospinning basic concepts, applications, and classroom demonstration. *Mater Res Soc Symp Proc* 827:17–28
28. How TV, Guidoin R, Young SK, Part H (1992) Engineering design of vascular prostheses, proceedings of the institution of mechanical engineers. *J Eng Med* 206:61–72
29. Matthews JA, Wnek GE, Simpson DG, Bowlin GL (2002) Electrospinning of collagen nanofibers. *Biomacromolecules* 3:232–238
30. Matthews JA, Boland ED, Wnek GE, Simpson DG, Bowlin GL (2003) Electrospinning of collagen type II: a feasibility study. *J Bioact Compat Polym* 18:125–134
31. Shields KJ, Beckman MJ, Bowlin GL, Wayne JS (2004) Mechanical properties and cellular proliferation of electrospun collagen type II. *Tissue Eng* 10:1510–1517
32. Boland ED, Matthews JA, Pawlowski KJ, Simpson DG, Wnek GE, Bowlin GL (2004) Electrospinning collagen and elastin: preliminary vascular tissue engineering. *Front Biosci* 9:1422–1432
33. Telemeco TA, Ayres C, Bowlin GL, Wnek GE, Boland ED, Cohen N (2005) Regulation of cellular infiltration into tissue engineering scaffolds composed of submicron diameter fibrils produced by electrospinning. *Acta Biomater* 1:377–385

34. Rho KS, Jeong L, Lee G, Seo BM, Park YJ, Hong SD (2006) Electrospinning of collagen nanofibers: effects on the behavior of normal human keratinocytes and early-stage wound healing. *Biomaterials* 27:1452–1461
35. Ikada Y, Tabata Y (1998) Protein release from gelatin matrices. *Adv Drug Deliv Rev* 31:287–301
36. Kuijpers AJ, Engbers GH, Krijgsveld J, Zaat SA, Dankert J, Feijen J (2000) Cross-linking and characterisation of gelatin matrices for biomedical applications. *J Biomater Sci Polym Ed* 11:225–243
37. Kuijpers AJ, van Wachem PB, van Luyn MJ, Plantinga JA, Engbers GH, Krijgsveld J, Zaat SA, Dankert J, Feijen J (2000) In vivo compatibility and degradation of crosslinked gelatin gels incorporated in knitted Dacron. *J Biomed Mater Res* 51:136–145
38. Yamamoto M, Ikada Y, Tabata Y (2001) Controlled release of growth factors based on biodegradation of gelatin hydrogel. *J Biomater Sci Polym Ed* 12:77–88
39. Yao CH, Liu BS, Hsu SH, Chen YS, Tsai CC (2004) Biocompatibility and biodegradation of a bone composite containing tricalcium phosphate and genipin crosslinked gelatin. *J Biomed Mater Res* 69A:709–717
40. Balakrishnan B, Jayakrishnan A (2005) Self-cross-linking biopolymers as injectable in situ forming biodegradable scaffolds. *Biomaterials* 26:3941–3951
41. Nagura M, Yokota H, Ikeura M, Gotoh Y, Ohkoshi Y (2002) Structures and physical properties of cross-linked gelatin fibers. *Polym J* 34:761–766
42. Kidoaki S, Kwon IK, Matsuda T (2005) Mesoscopic spatial designs of nano and microfiber meshes for tissue-engineering matrix and scaffold based on newly devised multilayering and mixing electrospinning techniques. *Biomaterials* 26:37–46
43. Zhang Y, Ouyang H, Lim CT, Ramakrishna S, Huang ZM (2005) Electrospinning of gelatin fibers and gelatin/PCL composite fibrous scaffolds. *J Biomed Mater Res B Appl Biomater* 72:156–165
44. Ma Z, He W, Yong T, Ramakrishna S (2005) Grafting of gelatin on electrospun poly (caprolactone) nanofibers to improve endothelial cell spreading and proliferation and to control cell orientation. *Tissue Eng* 11:1149–1158
45. Gosline JM, Demont ME, Denny MW (1986) The structure and properties of spider silk. *Endeavour* 10:37–43
46. Altman GH, Diaz F, Jakuba C, Calabro T, Horan RL, Chen J (2003) Silk-based biomaterials. *Biomaterials* 24:401–416
47. Park WH, Jeong L, Yoo DI, Hudson S (2004) Effect of chitosan on morphology and conformation of electrospun silk fibroin nanofibers. *Polymer* 45:7151–7157
48. Meinel L, Hofmann S, Karageorgiou V, Kirker-Head C, McCool J, Gronowicz G (2005) The inflammatory responses to silk films in vitro and in vivo. *Biomaterials* 26:147–155
49. Dal Pra I, Freddi G, Minic J, Chiarini A, Armato U (2005) De novo engineering of reticular connective tissue in vivo by silk fibroin nonwoven materials. *Biomaterials* 26:1987–1999
50. Horan RL, Antle K, Collette AL, Wang Y, Huang J, Moreau JE, Volloch V, Kaplan DL, Altman GH (2005) In vitro degradation of silk fibroin. *Biomaterials* 26:3385–3393
51. Min BM, Lee G, Kim SH, Nam YS, Lee TS, Park WH (2004) Electrospinning of silk fibroin nanofibers and its effect on the adhesion and spreading of normal by human keratinocytes and fibroblasts in vitro. *Biomaterials* 25:1289–1297
52. Min BM, Jeong L, Nam YS, Kim JM, Kim JY, Park WH (2004) Formation of silk fibroin matrices with different texture and its cellular response to normal human keratinocytes. *Int J Biol Macromol* 34:223–230
53. Jin HJ, Chen J, Karageorgiou V, Altman GH, Kaplan DL (2004) Human bone marrow stromal cell responses to electrospun silk fibroin mats. *Biomaterials* 25:1039–1047
54. Sukigara S, Gandhi M, Ayutsede J, Micklus M, Ko F (2003) Regeneration of Bombyx mori silk by electrospinning—part 1: processing parameters and geometric properties. *Polymer* 44:5721–5727

55. Sukigara S, Gandhi M, Ayutsede J, Micklus M, Ko F (2004) Regeneration of *Bombyx mori* silk by electrospinning. Part 2. Process optimization and empirical modeling using response surface methodology. *Polymer* 45:3701–3708
56. Wang H, Zhang Y, Shao H, Hu X (2005) Electrospun ultra-fine silk fibroin fiber from aqueous solutions. *J Mater Sci* 40:5359–5363
57. Wang H, Shao H, Hu X (2006) Structure of silk fibroin fibers made by an electrospun process from a silk fibroin aqueous solution. *J Appl Polym Sci* 101:961–968
58. Zhu J, Shao H, Hu X (2007) Morphology and structure of electrospun mats from regenerated silk fibroin aqueous solutions with adjusting pH. *Int J Biol Macromol* 41:469–474
59. Zhu J, Zhang Y, Shao H, Hu X (2008) Electorspinning and rheology of regenerated *Bombyx mori* silk fibroin aqueous solutions: the effects of pH and concentration. *Polymer* 49:2880–2885
60. Yang F, Xu CY, Kotaki M, Wang S, Ramakrishna S (2004) Characterization of neural stem cells on electrospun poly(L-lactic acid) nanofibrous scaffold. *J Biomater Sci Polym Ed* 15:1483–1497
61. Jing Z, Xu XY, Chen XS, Liang QZ, Bian XC, Yang LX, Jing XB (2003) Biodegradable electrospun fibers for drug delivery. *J Control Release* 92:227–231
62. Boland ED, Wnek GE, Simpson DG, Pawlowski KJ, Bowlin GL (2001) Tailoring tissue engineering scaffolds using electrostatic processing techniques: a study of poly(glycolic acid) electrospinning. *J Macromol Sci A* 38:1231–1243
63. Boland ED, Telemeco TA, Simpson DG, Wnek GE, Bowlin GL (2004) Utilizing acid pretreatment and electrospinning to improve biocompatibility of poly(glycolic acid) for tissue engineering. *J Biomed Mater Res B Appl Biomater* 71B:144–152
64. Verreck G, Chun I, Rosenblatt J, Peeters J, Van Dijk A, Mensch J, Noppe M, Brewster ME (2003) Incorporation of drugs in an amorphous state into electrospun nanofibers composed of a water-insoluble, nonbiodegradable polymer. *J Control Release* 92:349–360
65. Son WK, Youk JH, Lee TS, Park WH (2004) The effects of solution properties and polyelectrolyte on electrospinning of ultrafine poly (ethylene oxide) fibers. *Polymer* 45:2959–2966
66. Ding B, Kim HY, Lee SC, Shao CL, Lee DR, Park SJ, Kwag GB, Choi KJ (2002) Preparation and characterization of a nanoscale poly(vinyl alcohol) fiber aggregate produced by an electrospinning method. *J Polym Sci B Polym Phys* 40:1261–1268
67. Yao L, Haas TW, Guiseppe-Elie A, Bowlin GL, Simpson DG, Wnek GE (2003) Electrospinning and stabilization of fully hydrolyzed poly(vinyl alcohol) fibers. *Chem Mater* 15:1860–1864
68. Boland ED, Coleman BD, Barnes CP, Simpson DG, Wnek GE, Bowlin GL (2005) Electrospinning polydioxanone for biomedical applications. *Acta Biomater* 1:115–123
69. Xu XL, Zhong W, Zhou SF, Trajtman A, Alfa M (2010) Electrospun PEG-PLA nanofibrous membrane for sustained release of hydrophilic antibiotics. *J Appl Polym Sci* 118:588–595
70. Luu YK, Kim K, Hsiao BS, Chu B, Hadjiargyrou M (2003) Development of a nanostructured DNA delivery scaffold via electrospinning of PLGA and PLA-PEG block copolymers. *J Control Release* 89:341–353
71. Bhattarai SR, Bhattarai N, Yi HK, Hwang PH, Cha DI, Kim HY (2004) Novel biodegradable electrospun membrane: scaffold for tissue engineering. *Biomaterials* 25:2595–2602
72. Kim K, Yu M, Zong X, Chiu J, Fang D, Seo YS, Hsiao BS, Chu B (2003) Control of degradation rate and hydrophilicity in electrospun non-woven poly(D, L-lactide) nanofiber scaffolds for biomedical applications. *Biomaterials* 24:4977–4985
73. Mo XM, Xu CY, Kotaki M, Ramakrishna S (2004) Electrospun P(LLA-CL) nanofiber: a biomimetic extracellular matrix for smooth muscle cell and endothelial cell proliferation. *Biomaterials* 25:1883–1890
74. Xu CY, Inai R, Kotaki M, Ramakrishna S (2004) Aligned biodegradable nanofibrous structure: a potential scaffold for blood vessel engineering. *Biomaterials* 25:877–886

75. Xu CY, Inai R, Kotaki M, Ramakrishna S (2004) Electrospun nanofiber fabrication as synthetic extracellular matrix and its potential for vascular tissue engineering. *Tissue Eng* 10:1160–1168
76. Kwon IK, Kidoaki S, Matsuda T (2005) Electrospun nano- to microfiber fabrics made of biodegradable copolyesters: structural characteristics, mechanical properties and cell adhesion potential. *Biomaterials* 26:3929–3939
77. Zong X, Fang D, Kim K, Ran S, Hsiao BS, Chu B, Brathwaite C, Li S, Chen E (2002) Nonwoven nanofiber membranes of poly(lactide) and poly (glycolide-co-lactide) via electrospinning and application for antiadhesions. *Polym Prepr (Am Chem Soc Div Polym Chem)* 43:659–660
78. Lee IS, Kwon OH, Meng W, Kang IK (2004) Nanofabrication of microbial polyester by electrospinning promotes cell attachment. *Macromol Res* 12:374–378
79. Choi JS, Lee SW, Jeong L, Bae SH, Min BC, Youk JH, Park WH (2004) Effect of organosoluble salts on the nanofibrous structure of electrospun poly(3-hydroxybutyrate-co-3-hydroxyvalerate). *Int J Biol Macromol* 34:249–256
80. Lee KH, Kim HY, Khil MS, Ra YM, Lee DR (2003) Characterization of nano-structured poly (ϵ -caprolactone) nonwoven mats via electrospinning. *Polymer* 44:1287–1294
81. Na YH, He Y, Shuai X, Kikkawa Y, Doi Y, Inoue Y (2002) Compatibilization effect of poly (ϵ -caprolactone)-b-poly(ethylene glycol) block copolymers and phase morphology analysis in immiscible poly(lactide)/poly(ϵ -caprolactone) blends. *Biomacromolecules* 3:1179–1186
82. Ajami-Henriquez D, Rodríguez M, Sabino M, Castillo RV, Müller AJ, Boschetti-de-Fierro A, Abetz C, Abetz V, Dubois P (2008) Evaluation of cell affinity on poly(L-lactide) and poly(ϵ -caprolactone) blends and on PLLA-b-PCL diblock copolymer surfaces. *J Biomed Mater Res A* 87:405–417
83. Calandrelli L, Calarco A, Laurienzo P, Malinconico M, Petillo O, Peluso G (2008) Compatibilized polymer blends based on PDLLA and PCL for application in bioartificial liver. *Biomacromolecules* 9:1527–1534
84. Liao GY, Chen L, Zeng XY, Zhou XP, Xie XL, Peng EJ, Ye ZQ, Mai YW (2011) Electrospun PLLA/PCL blend fibers and their cellular response to adipose-derived stem cells. *J Appl Polym Sci* 120:2154–2165
85. Gimble JM, Katz AJ, Bunnell BA (2007) Adipose-derived stem cells for regenerative medicine. *Circ Res* 100:1249–1260
86. Zuk PA, Zhu M, Mizuno H, Huang J, Futrell JW, Katz AJ, Benhaim P, Lorenz HP, Hedrick MH (2001) Multilineage cells from human adipose tissue: implications for cell-based therapies. *Tissue Eng* 7:211–228
87. Zuk PA, Zhu M, Ashjian P, De Ugarte DA, Huang JI, Mizuno H, Alfonso ZC, Fraser JK, Benhaim P, Hedrick MH (2002) Human adipose tissue is a source of multipotent stem cells. *Mol Biol Cell* 13:4279–4295
88. Rodríguez LV, Alfonso Z, Zhang R, Leung J, Wu B, Ignarro LJ (2006) Clonogenic multipotent stem cells in human adipose tissue differentiate into functional smooth muscle cells. *Proc Natl Acad Sci* 103:12167–12172
89. Spasova M, Stoilova O, Manolova N, Altankov G, Rashkov I (2007) Preparation of PLLA/PEG nanofibers by electrospinning and potential applications. *J Bioact Compat Polym* 22:62–76
90. Wang BY, Fu SZ, Ni PY, Peng JR, Zheng L, Luo F, Liu H, Qian ZY (2012) Electrospun polylactide/poly(ethylene glycol) hybrid fibrous scaffolds for tissue engineering. *J Biomed Mater Res Part A* 100A:441–449
91. Huang L, Nagapudi K, Apkarian RP, Chaikof EL (2001) Engineered collagen-PEO nanofibers and fabrics. *J Biomater Sci Polym Ed* 12:979–993
92. Son WK, Youk JH, Lee TS, Park WH (2004) Preparation of antimicrobial ultrafine cellulose acetate fibers with silver nanoparticles. *Macromol Rapid Commun* 25:1632–1637
93. Melaiye A, Sun ZH, Hindi K, Milsted A, Ely D, Reneker DH, Tessier CA, Youngs WJ (2005) Silver(I)-imidazole cyclophane gem-diol complexes encapsulated by electrospun tectophilic

- nanofibers: formation of nanosilver particles and antimicrobial activity. *J Am Chem Soc* 127:2285–2291
94. Fujihara K, Kotaki M, Ramakrishna S (2005) Guided bone regeneration membrane made of polycaprolactone/calcium carbonate composite nanofibers. *Biomaterials* 26:4139–4147
 95. Fan HS, Wen XT, Tan YF, Wang R, Cao HD, Zhang XD (2005) Compare of electrospinning PLA and PLA/b-TCP scaffold in vitro. *Mater Sci Forum* 475–479:2379–2382
 96. Kim HW, Song JH, Kim HE (2005) Nanofiber generation of gelatin-hydroxyapatite biomimetics for guided tissue regeneration. *Adv Funct Mater* 15:1988–1994
 97. Kim HW, Lee HH, Knowles JC (2006) Electrospinning biomedical nanocomposite fibers of hydroxyapatite/poly(lactic acid) for bone regeneration. *J Biomed Mater Res A* 79A:643–649
 98. Xie XL, Mai YW, Zhou XP (2005) Dispersion and alignment of carbon nanotubes in polymer matrix: a review. *Mater Sci Eng R* 49:89–112
 99. Zhou W, Wu Y, Wei F, Luo G, Qian W (2005) Elastic deformation of multiwalled carbon nanotubes in electrospun MWCNTs-PEO and MWCNTs-PVA nanofibers. *Polymer* 46:12689–12695
 100. Salalha W, Dror Y, Khalfin RL, Cohen Y, Yarin AL, Zussman E (2004) Single-walled carbon nanotubes embedded in oriented polymeric nanofibers by electrospinning. *Langmuir* 20:9852–9855
 101. Dror Y, Salalha W, Khalfin RL, Cohen Y, Yarin AL, Zussman E (2003) Carbon nanotubes embedded in oriented polymer nanofibers by electrospinning. *Langmuir* 19:7012–7020
 102. Sung JH, Kim HS, Jin HJ, Choi HJ, Chin IJ (2004) Nanofibrous membranes prepared by multiwalled carbon nanotube/poly(methyl methacrylate) composites. *Macromolecules* 37:9899–9902
 103. Sundaray B, Subramanian V, Natarajan TS, Krishnamurthy K (2006) Electrical conductivity of a single electrospun fiber of poly(methyl methacrylate) and multiwalled carbon nanotube nanocomposite. *Appl Phys Lett* 88:143114–143116
 104. Liu LQ, Tasis D, Prato M, Wagner HD (2007) Tensile mechanics of electrospun multiwalled nanotube/poly(methyl methacrylate) nanofibers. *Adv Mater* 19:1228–1233
 105. Ge JJ, Hou HQ, Li Q, Graham MJ, Greiner A, Reneker DH, Harris FW, Cheng SZD (2004) Assembly of well-aligned, multiwalled carbon nanotubes in confined polyacrylonitrile environments: electrospun composite nanofiber sheets. *J Am Chem Soc* 126:15754–15761
 106. Ra EJ, An KH, Kim KK, Jeong SY, Lee YH (2005) Anisotropic electrical conductivity of MWCNT/PAN nanofiber paper. *Chem Phys Lett* 413:188–193
 107. Allaoui A, Bai S, Cheng HM, Bai JB (2002) Mechanical and electrical properties of a MWNT/epoxy composite. *Compos Sci Technol* 62:1993–1998
 108. Jose MV, Steinert BW, Thomas V, Dean DR, Abdalla MA, Price G, Janowski GM (2007) Morphology and mechanical properties of nylon 6/MWNT nanofibers. *Polymer* 48:1096–1104
 109. Kim GM, Michler GH, Potschk P (2005) Deformation processes of ultrahigh porous multiwalled carbon nanotubes/polycarbonate composite fibers prepared by electrospinning. *Polymer* 46:7346–7351
 110. Sen R, Zhao B, Perea D, Itkis ME, Hu H, Love J, Bekyarova E, Haddo RC (2004) Preparation of single-walled carbon nanotube reinforced polystyrene and polyurethane nanofibers and membranes by electrospinning. *Nano Lett* 4:459–464
 111. Mazinani S, Aji A, Dubois C (2009) Polystyrene-carbon nanotubes electrospun fibers: process. *Struct Prop Polym* 50:3329–3342
 112. Chen D, Liu TX, Zhou XP, Tjiu WC, Hou HQ (2009) Electrospinning fabrication of high strength and toughness polyimide nanofiber membranes containing multiwalled carbon nanotubes. *J Phys Chem B* 113:9741–9748
 113. Baji A, Mai YW, Wong SC, Abtahi M, Du X (2010) Mechanical behavior of self-assembled carbon nanotube reinforced nylon6, 6 fibers. *Compos Sci Technol* 70:1401–1409
 114. Saeed K, Park SY, Lee HJ, Baek JB, Huh WS (2006) Preparation of electrospun nanofibers of carbon nanotube/polycaprolactone nanocomposite. *Polymer* 47:8019–8025

115. Mei F, Zhong JS, Yang XP, Ouyang XY, Zhang S, Hu XY, Ma Q, Lu JG, Ryu SK, Deng XL (2007) Improved biological characteristics of poly (1-Lactic Acid) electrospun membrane by incorporation of multiwalled carbon nanotubes/hydroxyapatite nanoparticles. *Biomacromolecules* 8:3729–3735
116. Fang J, Niu HT, Lin T, Wang XG (2008) Applications of electrospun nanofibers. *Chin Sci Bull* 53:2265–2286
117. Sundaray B, Subramanian V, Natarajan TS, Xiang RZ, Chang CC, Fann WS (2004) Electrospinning of continuous aligned polymer fibers. *Appl Phys Lett* 84:1222–1224
118. Pan H, Li L, Hu L, Cui X (2006) Continuous aligned polymer fibers produced by a modified electrospinning method. *Polymer* 47:4901–4904
119. Li D, Wang Y, Xia Y (2003) Electrospinning of polymeric and ceramic nanofibers as uniaxially aligned arrays. *Nano Lett* 3:1167–1171
120. Li D, Wang Y, Xia Y (2004) Electrospinning nanofibers as uniaxially aligned arrays and layer-by-layer stacked films. *Adv Mater* 16:361–366
121. Theron A, Zussman E, Yarin AL (2001) Electrostatic field-assisted alignment of electrospun nanofibres. *Nanotechnology* 12:384–390
122. Yang D, Lu B, Zhao Y, Jiang X (2007) Fabrication of aligned fibrous arrays by magnetic electrospinning. *Adv Mater* 19:3702–3706
123. Katta P, Alessandro M, Ramsier RD, Chase GG (2004) Continuous electrospinning of aligned polymer nanofibers onto a wire drum collector. *Nano Lett* 4:2215–2218
124. Fennessey SF, Farris RJ (2008) Fabrication of aligned and molecularly oriented electrospun polyacrylonitrile nanofibers and the mechanical behavior of their twisted yarns. *Polymer* 45:4217–4225
125. Ghasemi-Mobarakeh L, Prabhakaran MP, Morshed M, Nasr-Esfahani MH, Ramakrishna S (2008) Electrospun poly(ϵ -caprolactone)/gelatin nanofibrous scaffolds for nerve tissue engineering. *Biomaterials* 29:4532–4539
126. Bini TB, Gao S, Wang S, Ramakrishna S (2006) Poly(l-lactide-co-glycolide) biodegradable microfibers and electrospun nanofibers for nerve tissue engineering: an in vitro study. *J Mater Sci* 41:6453–6459
127. Schnell E, Klinkhammer K, Balzer S, Brook G, Kleeb D, Dalton P (2007) Guidance of glial cell migration and axonal growth on electrospun nanofibers of poly- ϵ -caprolactone and a collagen/poly- ϵ -caprolactone blend. *Biomaterials* 28:3012–3025
128. Baker SC, Atkin N, Gunning PA (2006) Characterisation of electrospun polystyrene scaffolds for three-dimensional in vitro biological studies. *Biomaterials* 27(16):3136
129. Liao GY, Zhou XP, Chen L, Zeng XY, Xie XL, Mai YW (2012) Electrospun aligned PLLA/PCL/functionalised multiwalled carbon nanotube composite fibrous membranes and their bio/mechanical properties. *Compos Sci Technol* 72:248–255
130. Wang YZ, Blasioli DJ, Kim HJ, Kim HS, Kaplan DL (2006) Cartilage tissue engineering with silk scaffolds and human articular chondrocytes. *Biomaterials* 27:4434–4442
131. Moroni L, Licht R, de Boer J, de Wijn JR, van Blitterswijk CA (2006) Fiber diameter and texture of electrospun PEOT/PBT scaffolds influence human mesenchymal stem cell proliferation and morphology, and the release of incorporated compounds. *Biomaterials* 27:4911–4922
132. Li WJ, Laurencin CT, Cateson EJ, Tuan RS, Ko FK (2002) Electrospun nanofibrous structure: a novel scaffold for tissue engineering. *J Biomed Mater Res* 60:613–621
133. Yoshimoto H, Shin YM, Terai H, Vacanti JP (2003) A biodegradable nanofiber scaffold by electrospinning and its potential for bone tissue engineering. *Biomaterials* 24:2077–2082
134. Powell HM, Supp DM, Boyce ST (2008) Influence of electrospun collagen on wound contraction of engineered skin substitutes. *Biomaterials* 29:834–843
135. Kenawy ER, Bowlin GL, Mansfield K, Layman J, Simpson DG, Sanders EH (2002) Release of tetracycline hydrochloride from electrospun poly(ethylene-co-vinylacetate), poly(lactic acid), and a blend. *J Control Release* 81:57–64

136. Goldberg M, Langer R, Jia XQ (2007) Nanostructured materials for applications in drug delivery and tissue engineering. *J Biomat Sci Polym Ed* 18:241–268
137. Zhang XH, Reagan MR, Kaplan DL (2009) Electrospun silk biomaterial scaffolds for regenerative medicine. *Adv Drug Deliv Rev* 61:988–1006
138. Soffer L, Wang X, Zhang X, Kluge J, Dorfmann L, Kaplan DL, Leisk G (2008) Silk-based electrospun tubular scaffolds for tissue-engineered vascular grafts. *J Biomater Sci Polym Ed* 19:653–664
139. Mathew G, Hong JP, Rhee JM, Lee HS, Nah C (2005) Preparation and characterization of properties of electrospun poly(butylene terephthalate) nanofibers filled with carbon nanotubes. *Polym Test* 24:712–717
140. Lee BS, Yu WR (2010) PA6/MWNT nanocomposites fabricated using electrospun nanofibers containing MWNT. *Macromol Res* 18:162–169
141. Wei K, Xia JH, Kim BS, Kim IS (2011) Multiwalled carbon nanotubes incorporated bombyx mori silk nanofibers by electrospinning. *J Polym Res* 18:579–585
142. Saeed K, Park SY (2010) Preparation and characterization of multiwalled carbon nanotubes/polyacrylonitrile nanofibers. *J Polym Res* 17:535–540
143. Gao JB, Yu AP, Itkis ME, Bekyarova E, Zhao B, Niyogi S, Haddon RC (2004) Large-scale fabrication of aligned single-walled carbon nanotube array and hierarchical single-walled carbon nanotube assembly. *J Am Chem Soc* 126:16698–16699
144. Stanishevsky A, Chowdhury S, Chinoda P, Thomas V (2008) Hydroxyapatite nanoparticle loaded collagen fiber composites: microarchitecture and nanoindentation study. *J Biomed Mater Res* 86:873–882
145. Stupp SI, Brawn PV (1997) Molecular manipulation of microstructures: biomaterials, ceramics, and semiconductors. *Science* 277:1242–1248
146. Stupp SI, LeBonheur V, Walker K, Li LS, Huggins KE, Keser M (1997) Supramolecular materials: self-organized nanostructures. *Science* 276:384–389
147. Bianco A, Federico ED, Moscatelli I, Camaioni A, Armentano I, Campagnolo L, Dottori M, Kenny JM, Siracusa G, Gusmano G (2009) Electrospun poly(ϵ -caprolactone)/Ca-deficient hydroxyapatite nanohybrids: microstructure, mechanical properties and cell response by murine embryonic stem cells. *Mater Sci Eng C* 29:2063–2071
148. Peng F, Shaw MT, Olson JR, Wei M (2011) Hydroxyapatite needle-shaped particles/poly(L-lactic acid) electrospun scaffolds with perfect particle-along-nanofiber orientation and significantly enhanced mechanical properties. *J Phys Chem C* 115:15743–15751
149. Yeo MG, Kim GH (2012) Preparation and characterization of 3D composite scaffolds based on rapid-prototyped PCL/ β -TCP struts and electrospun PCL coated with collagen and HA for bone regeneration. *Chem Mater* 24:903–913
150. Shor L, Gucer S, Wen X, Gandhi M, Sun W (2007) Fabrication of three-dimensional polycaprolactone/hydroxyapatite tissue scaffolds and osteoblast-scaffold interactions in vitro. *Biomaterials* 28:5291–5297
151. Turmanova S, Minchev M, Vassilev K, Danev G (2008) Surface grafting polymerization of vinyl monomers on poly(tetrafluoroethylene) films by plasma treatment. *J Polym Res* 15:309–318
152. Mori M, Uyama Y, Ikada Y (1994) Surface modification of polyethylene fiber by graft-polymerization. *J Polym Sci Polym Chem* 32:1683–1690
153. Kou RQ, Xu ZK, Deng HT, Liu ZM, Seta P, Xu YY (2003) Surface modification of microporous polypropylene membranes by plasma-induced graft polymerization of alpha-allyl glucoside. *Langmuir* 19:6869–6875
154. Liu ZM, Xu ZK, Wang JQ, Wu J, Fu JJ (2004) Surface modification of polypropylene microfiltration membranes by graft polymerization of N-vinyl-2-pyrrolidone. *Eur Polym J* 40:2077–2087
155. Yao C, Li XS, Neoh KG, Shi ZL, Kang ET (2008) Surface modification and antibacterial activity of electrospun polyurethane fibrous membranes with quaternary ammonium moieties. *J Membr Sci* 320:259–267

156. Kim HS, Yoo HS (2010) MMPs-responsive release of DNA from electrospun nanofibrous matrix for local gene therapy: in vitro and in vivo evaluation. *J Control Release* 145 (3):264–271
157. Park K, Ju YM, Son JS, Ahn KD, Han DK (2007) Surface modification of biodegradable electrospun nanofiber scaffolds and their interaction with fibroblasts. *J Biomater Sci Polym Ed* 18:369–382
158. Chua KN, Chai C, Lee PC, Tang YN, Ramakrishna S, Leong KW, Mao HQ (2006) Surface-aminated electrospun nanofibers enhance adhesion and expansion of human umbilical cord blood hematopoietic stem/progenitor cells. *Biomaterials* 27:6043–6051
159. Ye P, Xu ZK, Wu J, Innocent C, Seta P (2006) Nanofibrous membranes containing reactive groups: electrospinning from poly(acrylonitrile-co-maleic acid) for lipase immobilization. *Macromolecules* 39:1041–1045
160. Li SF, Chen JP, Wu WT (2007) Electrospun polyacrylonitrile nanofibrous membranes for lipase immobilization. *J Mol Catal B Enzym* 47:117–124
161. Jia HF, Zhu GY, Vugrinovich B, Kataphinan W, Reneker DH, Wang P (2002) Enzyme carrying polymeric nanofibers prepared via electrospinning for use as unique biocatalysts. *Biotechnol Prog* 18:1027–1032
162. Aznar-Cervantes S, Roca MI, Martinez JG, Meseguer-Olmo L, Cenis JL, Moraleda JM, Otero TF (2012) Fabrication of conductive electrospun silk fibroin scaffolds by coating with polypyrrole for biomedical applications. *Bioelectrochemistry* 85:36–43
163. Chua KN, Lim WS, Zhang P, Lu H, Wen J, Ramakrishna S, Leong KW, Mao HQ (2005) Stable immobilization of rat hepatocyte spheroids on galactosylated nanofiber scaffold. *Biomaterials* 26:2537–2547
164. Yoon JJ, Chung HJ, Park TG (2007) Photo-crosslinkable and biodegradable pluronic/heparin hydrogels for local and sustained delivery of angiogenic growth factor. *J Biomed Mater Res A* 83A:597–605
165. Lode A, Reinstorf A, Bernhardt A, Wolf-Brandstetter C, Konig U, Gelinsky M (2008) Heparin modification of calcium phosphate bone cements for VEGF functionalization. *J Biomed Mater Res A* 86A:749–759
166. McGonigle JS, Tae G, Stayton PS, Hoffman AS, Scatena M (2008) Heparin-regulated delivery of osteoprotegerin promotes vascularization of implanted hydrogels. *J Biomater Sci Polym Ed* 19:1021–1034
167. Stendahl JC, Wang LJ, Chow LW, Kaufman DB, Stupp SI (2008) Growth factor delivery from self-assembling nanofibers to facilitate islet transplantation. *Transplantation* 86:478–481
168. Joung YK, Bae JW, Park KD (2008) Controlled release of heparin-binding growth factors using heparin-containing particulate systems for tissue regeneration. *Expert Opin Drug Deliv* 5:1173–1184
169. Bolgen N, Vargel I, Korkusuz P, Menciloglu YZ, Piskin E (2007) In vivo performance of antibiotic embedded electrospun PCL membranes for prevention of abdominal adhesions. *J Biomed Mater Res B Appl Biomater* 81B:530–543
170. Li LS, Stupp SI (2005) One-dimensional assembly of lipophilic inorganic nanoparticles templated by peptide-based nanofibers with binding functionalities. *Angew Chem Int Ed* 44:1833–1836
171. Kalra V, Lee J, Lee JH, Lee SG, Marquez M, Wiesner U, Joo YL (2008) Controlling nanoparticle location via confined assembly in electrospun block copolymer nanofibers. *Small* 4:2067–2073
172. Dong H, Wang D, Sun G, Hinestroza JP (2008) Assembly of metal nanoparticles on electrospun nylon 6 nanofibers by control of interfacial hydrogen-bonding interactions. *Chem Mater* 20:6627–6632
173. Rujitanaroj PO, Pimpha N, Supaphol P (2008) Wound-dressing materials with antibacterial activity from electrospun gelatin fiber mats containing silver nanoparticles. *Polymer* 49:4723–4732

174. Seyedjafari E, Soleimani M, Ghaemi N, Shabani I (2010) Nanohydroxyapatite-coated electrospun poly(L-lactide) nanofibers enhance osteogenic differentiation of stem cells and induce ectopic bone formation. *Biomacromolecules* 11:3118–3125
175. Decher G (1997) Fuzzy nanoassemblies: toward layered polymeric multicomposites. *Science* 277:1232–1237
176. Delcorte A, Bertrand P, Wischerhoff E, Laschewsky A (1997) Adsorption of polyelectrolyte multilayers on polymer surfaces. *Langmuir* 13:5125–5136
177. Picart C, Mutterer J, Richert L, Luo Y, Prestwich GD, Schaaf P, Voegel JC, Lavalle P (2002) Molecular basis for the explanation of the exponential growth of polyelectrolyte multilayers. *Proc Natl Acad Sci U S A* 99:12531–12535
178. Thierry B, Winnik FM, Merhi Y, Silver J, Tabrizian M (2003) Bioactive coatings of endovascular stents based on polyelectrolyte multilayers. *Biomacromolecules* 4:1564–1571
179. Thierry B, Kujawa P, Tkaczyk C, Winnik FM, Bilodeau L, Tabrizian M (2005) Delivery platform for hydrophobic drugs: prodrug approach combined with self-assembled multilayers. *J Am Chem Soc* 127:1626–1627
180. Zhang J, Senger B, Vautier D, Picart C, Schaaf P, Voegel JC, Lavalle P (2005) Natural polyelectrolyte films based on layer-by-layer deposition of collagen and hyaluronic acid. *Biomaterials* 26:3353–3361
181. Tang ZY, Wang Y, Podsiadlo P, Kotov NA (2006) Biomedical applications of layer-by-layer assembly: from biomimetics to tissue engineering. *Adv Mater* 18:3203–3224
182. Kim BS, Park SW, Hammond PT (2008) Hydrogen-bonding layer-by-layer assembled biodegradable polymeric micelles as drug delivery vehicles from surfaces. *ACS Nano* 2:386–392
183. Quinn A, Such GK, Quinn JF, Caruso F (2008) Polyelectrolyte blend multilayers: a versatile route to engineering interfaces and films. *Adv Funct Mater* 18:17–26
184. Ge LQ, Pan C, Chen HH, Wang X, Wang C, Gu ZZ (2007) The fabrication of hollow multilayered polyelectrolyte fibrous mats and its morphology study. *Colloids Surf A* 293:272–277
185. Pan C, Ge LQ, Gu ZZ (2007) Fabrication of multi-walled carbon nanotube reinforced polyelectrolyte hollow nanofibers by electrospinning. *Compos Sci Technol* 67:3271–3277
186. Müller K, Quinn JF, Johnston AP, Becker RM, Greiner A, Caruso F (2006) Polyelectrolyte functionalization of electrospun fibers. *Chem Mater* 18:2397–2403

Chapter 9

Electrospun Nanofibrous Scaffolds for Soft Tissue Regeneration

Dave Wei-Chih Chen and Shih-Jung Liu

Abstract This chapter aims to provide a general overview on the applications of electrospun biodegradable nanofibrous scaffolds for soft tissue regeneration. The soft tissue and extracellular matrix is first introduced. The tissue or cellular host responses to injury, including inflammation, wound healing and foreign-body reaction, is outlined. The fabrication of nanofibrous scaffold made of biodegradable polymers via electrospinning is then presented. The properties of the fabricated scaffolds, including morphology, mechanical strength and biodegradability, are discussed in detail. The development of electrospun scaffolds for soft tissue regeneration in various clinical applications is also reviewed. Finally, the future trend for electrospun nanofibrous scaffolds is addressed.

Keywords Soft tissue regeneration • Inflammation • Wound healing • Foreign-body reaction • Electrospun nanofibrous scaffolds • Tissue engineering

9.1 Introduction

Technological improvement in biology, medicine, chemistry, engineering and material science have allowed deeper insights into the microstructural and molecular levels of organisation in tissues and biomaterials, providing innovative approaches and tools for medical treatments. The replacement of damaged or failed tissues/organs by natural tissue instead of adopting artificial implants has become an emerging strategy in tissue engineering. Scaffold tissue engineering is generally defined as engineering a suitably structured and biocompatible scaffold that is seeded with cells and other growth factors, allowing the tissues to be regenerated

D.W.-C. Chen
Chang Gung Memorial Hospital, Keelung Branch, F7, No 222 Mai-King Road, Keelung,
Taiwan
e-mail: achih121@ms75.hinet.net

S.-J. Liu (✉)
Mechanical Engineering, Chang Gung University, 259, Wen-Hwa 1st Road, Kwei-Shan,
Tao-Yuan 333, Taiwan
e-mail: shihjung@mail.cgu.edu.tw

in vitro and to partially develop the host tissue extracorporeally before implantation. To achieve the goal of tissue reconstruction, the scaffold should be of a porous, interconnected and permeable structure to permit the infiltration of cells and nutrients. It should also exhibit the appropriate surface morphology and chemistry for cell adhesion and proliferation. In addition, the scaffold also needs to exhibit mechanical properties comparable with the native tissue being engineered and the right degree of biodegradability, such that it degrades to form soluble non-toxic products when the tissue is fully formed. An ideal scaffold should therefore (1) allow cell attachment and migration, (2) deliver and retain cells and biochemical factors, (3) enable diffusion of vital cell nutrients and expressed products and (4) exert certain mechanical and biological influences to modify the behaviour of the cell phase.

Nanofibres prepared via electrospinning offer several advantages such as an extremely high surface-to-volume ratio, tunable porosity, flexibility with respect to scaffold size and shape and the ability to control the composition to achieve the desired results from its properties and functionality. Furthermore, the nanofibrous network is capable of creating a dynamic, three-dimensional (3D) microenvironment mimicking the native extracellular matrix (ECM) in which cells are maintained [1].

This chapter provides some general overview regarding the applications of electrospun biodegradable nanofibrous scaffolds for soft tissue regeneration. The soft tissue and extracellular matrix is introduced first. The tissue or cellular host responses to injury, including inflammation, wound healing and foreign-body reaction, is addressed. The fabrication of nanofibrous scaffold made of biodegradable polymers via electrospinning is then presented. The properties of the fabricated scaffolds, including morphology, mechanical strength and biodegradability, etc., are discussed in detail. The development of electrospun scaffolds for soft tissue regeneration in various clinical applications is also reviewed. Finally the future trend for electrospun nanofibrous scaffolds is addressed.

9.2 Soft Tissue and Extracellular Matrix

9.2.1 *Soft Tissue*

Soft biological tissues exist in many forms, each with a unique microstructure specialised for a specific function. Nonetheless, soft tissues are composed of the same basic constituents: cells and extracellular matrix (ECM) as shown in Fig. 9.1. The main functions of the soft tissue include tissue production, regeneration and remodelling of the ECM. The composition, structure and functions of ECM vary greatly in different tissues. In general, cellular material occupies approximately 20% of the total tissue volume, whereas the ECM accounts for the remaining 80% [2].

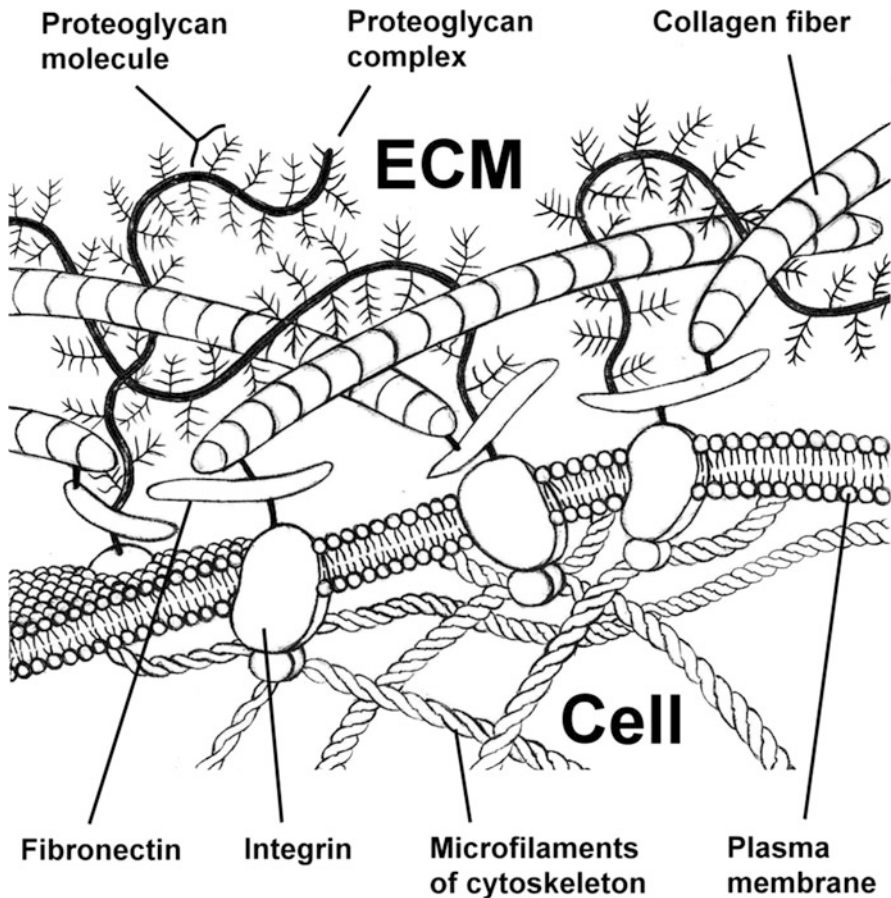


Fig. 9.1 Cell and extracellular matrix (ECM)

Cells are the fundamental structural and functional units of tissues and organs. In all tissues, cells are assembled during embryonic development into coherent groups through specific cell–cell and cell–matrix interactions. Each type of tissue has a distinctive pattern of structural organisation adapted to its particular function, which is strongly influenced by metabolic [3] or mechanical factors [4, 5].

Conversely, the ECM serves many functions such as [6]:

- It endows a tissue with strength and resilience and thereby maintains its shape.
- It serves as a biologically active scaffold on which cells can migrate or adhere.
- It helps regulate the phenotype of cells.
- It anchors many substances, including growth factors, proteases and their inhibitors.
- It provides an aqueous environment for the diffusion of nutrients, ions, hormones and metabolites between cells and the capillary network.

During normal development and as a component of tissue response to injury, adhesive interactions coordinate with cell surface receptors and, subsequently, with the cytoskeleton and the nucleus [7]. The resulting intracellular signaling affects a variety of events, including gene expression and cell proliferation, mobility and differentiation.

In many respects, therefore, the ECM regulates cell shape, orientation, movement and overall function; however, cells (e.g. fibroblasts) fashion and maintain the ECM. As such, a strong symbiotic relationship exists between these two components.

9.2.2 *Extracellular Matrix*

The ECM consists of two main components: protein fibres (collagen and elastin), which include elastic fibres that are extremely flexible and behave like rubber, and collagen fibres that are stiff and form the main tensile load-bearing components in tissues. The amorphous matrix or ground substance in which fibres are embedded is a viscous gel composed of water, proteoglycans (PGs) and other glycoproteins [8–10].

Matrix components and the mechanical forces that cells experience markedly influence the maintenance of cellular phenotype and affect cell shape, polarity and differentiated function through receptors for specific ECM molecules (such as integrins) on cell surfaces. The resulting changes in cytoskeletal organisation and the production of second messengers can modify gene expression. ECM plays a critical role in cytodifferentiation and organogenesis, and it is a scaffold that allows orderly repair after injury. The flow of information between cells and ECM is called dynamic reciprocity.

Therefore, from a mechanical point of view, soft connective tissue must be considered and analysed as a fibre-reinforced composite material [8, 11]. Fibrous proteins, particularly collagen, are the reinforcing fibres of the ground substance. The mechanical behaviour of the tissue is determined by the properties and quantity of the components and their interactions. Furthermore, the specific orientation of collagen fibres determines the anisotropic response of soft tissues. Because collagen elements are characterised by a stiffness that is significantly higher than that of the ground substance, they are largely responsible for the tensile behaviour of soft connective tissue. By contrast, because of the high length-thickness ratio of collagen elements, the compression behaviour of the tissue is mainly determined by the ground substance and its interaction with the fibrous network. The microstructural phenomena that develop within soft tissue during loading take time to develop completely in both compressive and tensile mechanical states. With regard to the latter, time dependence is less evident because microstructural rearrangements within collagen fibres take place more quickly.

9.2.2.1 Protein Fibres (Collagens and Elastin)

Collagen is characterised by a strongly hierarchical organisation. Small tropocollagen molecules link together to form fibrils, which in turn give rise to fibres and fibre bundles. Within soft tissue, collagen fibrils show a typical wavy configuration in the unstrained state, referred to as crimped, which is characterised by a helical nature with a periodicity between 10 and 100 μm , depending on tissue type [12]. Collagens are composed of a triple helix of three polypeptide α -chains; approximately 30 α -chains form nearly 20 distinct collagen types. Types I, II and III are interstitial or fibrillar collagens and are the most abundant. Types IV, V and VI are nonfibrillar (or amorphous) and are present in interstitial tissue and basement membranes.

PGs, most often decorin- [13, 14] and fibril-associated collagens with interrupted triple helix filaments [15], form interfibrillar bonds, which tie adjoining fibrils together to form fibres and seem to have a definite role in guaranteeing their mechanical coupling. Owing to their hierarchical organisation, collagen-reinforcing elements have a complex mechanical response that can be evaluated by analysing the mechanical behaviour of the components and the interactions that occur when a tensile load is applied.

Elastic fibres confer passive recoil to various tissues and are critical components of heart valves and the aorta, in which repeated pulsatile flow would cause unacceptable shear on noncompliant tissue, and of intervertebral discs, in which the repetitive forces of ambulation along the spine are dissipated. Elastin also forms the layers called laminae in the walls of arteries. Unlike collagen, elastin can be stretched. The stretching of an artery every time when the heart pumps blood is followed by the recoil of elastin, which restores the diameter of the artery between heartbeats.

9.2.2.2 Amorphous Matrix or Ground Substance

Amorphous matrix or ground substance is a viscous gel that is mainly composed of an electrolytic water solution containing positive sodium ions and highly negatively charged PGs. The PGs are long, molecular structures that develop along an axis of hyaluronic acid.

Hyaluronic acid consists of many repeats of a simple disaccharide which is stretched end to end. It binds a large amount of water, forming a viscous hydrate gel, which gives connective tissue turgor pressure and the capability to resist compression. This ECM component helps provide both resilience and a lubricating feature to many types of connective tissue, particularly those found in the cartilage of joints.

Other proteins are laterally attached to hyaluronan axis and structured around their own axis. Threads of amino acids called glycosaminoglycans (GAGs) are in turn attached along this last axis. All GAGs are covalently attached to a protein

backbone to form PGs, which has a structure that schematically resembles a bottlebrush.

The time-dependent mechanical properties of soft biological tissue are strongly influenced by the fluid fluxes that the amorphous matrix or ground substance undergoes when external loads are applied. Fluid flux phenomena depend on the rheological behaviour of the amorphous matrix or ground substance itself [16]. This behaviour is determined by the combined action of GAGs and hyaluronic acid [17]. Two main phenomena occur when compressive loads are applied to a tissue: the ground substance undergoes fluid fluxes within the solid skeleton, and the space between GAGs is reduced. Tissue compressive stiffness is, therefore, determined by ions. The movement of liquid phases within the porous solid structures of the tissue is a time-dependent phenomenon, which explains that the compressive stiffness of the tissue is correlated with the rate of the loading applied. In fact, high-strain rate conditions prevent ground substance flux from flowing, resulting in high compression stiffness owing to the incompressible nature of the gel. Reduction of the strain rate causes major fluid flux and in turn decreases the compression stiffness.

9.2.2.3 Cell–Matrix Interactions

Like cell–cell interactions, cell–matrix interactions have a high degree of specificity, requiring initial recognition, physical adhesion, electrical and chemical communication, cytoskeletal reorganisation and cell migration. Moreover, adhesion receptors may also act as transmembrane signaling molecules that transmit information about the environment to the inside of cells and mediate the effects of signals initiated by growth factors or compounds controlling tissue differentiation. Moreover, the ECM components (e.g. ligands) with which cells interact are immobilised and not in solution. However, soluble (secreted) factors also modulate cell–cell communication in the normal and pathologic regulation of tissue growth and maturation. Cell surface adhesion molecules that interact with ECM include the integrin adhesion receptors and the vascular selectins.

The integrins are cell receptors with diverse specificity that bind ECM proteins, other cell surface proteins and plasma proteins and control cell growth, differentiation, gene expression and motility [7]. Some integrins bind only a single component of the ECM, e.g. fibronectin, collagen or laminin. Other integrins interact with several of these polypeptides. In contrast to hormone receptors, which have high affinity and low abundance, integrins exhibit low affinity and high abundance and bind weakly to several different but related matrix molecules. This property allows integrins to promote cell–cell interactions as well as cell–matrix binding.

9.3 Inflammation, Wound Healing and Foreign-Body Reaction

Implant-induced tissue reactions are gaining increasing importance with the emergence of novel materials and devices. In-depth understanding of foreign-body and inflammatory responses is a prerequisite to solve biological problems that currently exist with some artificial implants.

Placement of a biomaterial in an *in vivo* environment requires injection, insertion or surgical implantation, all of which injure the tissues or organs involved. [18] Inflammation, wound healing and foreign-body reaction are generally considered components of the host tissue or cellular responses to an injury or implantation procedure.

The sequence of responses following an injury (Fig. 9.2) includes blood/material interactions, provisional matrix formation, acute inflammation, chronic inflammation, granulation tissue development, foreign-body reaction and fibrosis/fibrous capsule development. The overlap and simultaneous occurrence of these events should be considered; for example, the foreign-body reaction at the implant interface may be initiated with the onset of acute and chronic inflammation.

In the very early stage of the implantation process, blood/material interactions occur as proteins adsorb to the biomaterial surface, and a blood-based provisional matrix develops on and around the biomaterial. The provisional matrix forms the initial thrombus (blood clot) at the interface between the tissue and the biomaterial. Protein adsorption and formation of the fibrin-rich provisional matrix are closely linked in their mechanistic responses. Injury to the vascularised connective tissue

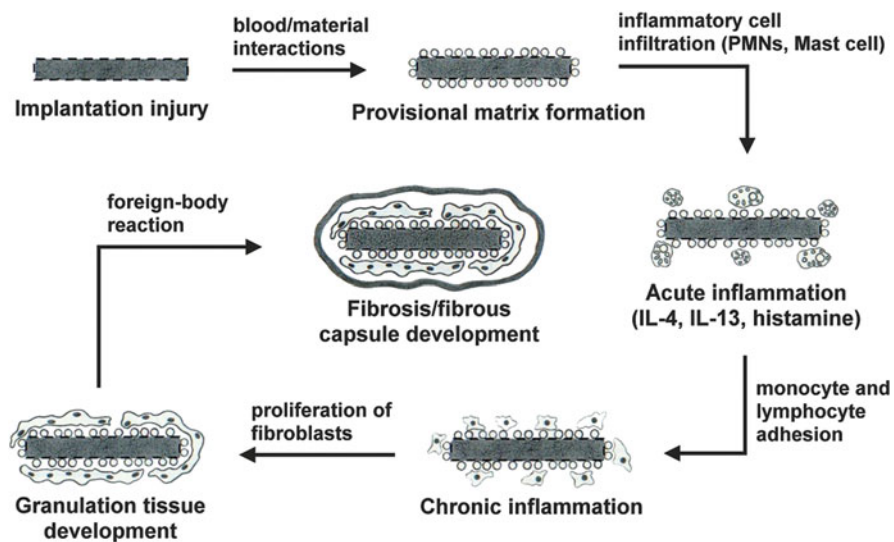


Fig. 9.2 The sequence of responses following an implant-induced tissue reaction

not only initiates the inflammatory responses (innate immunity) but also leads to thrombus formation, which involves activation of the extrinsic and intrinsic coagulation systems, the complement system, fibrinolytic system, kinin-generating system and platelets.

9.3.1 Inflammation

9.3.1.1 Acute Inflammation

Acute inflammation is an almost immediate response to injury and is non-specific; it may occur as a result of any injury short of one that is immediately fatal. The inflammatory response is usually of a short duration and typically occurs before the immune response is established. The primary purpose of inflammation is to remove the injurious agent and limit the extent of tissue damage.

Neutrophils (polymorphonuclear leukocytes [PMNs]) characterise the acute inflammatory response. In addition, mast cell degranulation with histamine release and fibrinogen adsorption is known to mediate acute inflammatory responses to implanted biomaterials [19, 20]. Interleukin-4 (IL-4) and interleukin-13 (IL-13) are also released from mast cells in the degranulation process and can play significant roles in determining the extent of the subsequent foreign-body reaction [21, 22].

Biomaterial-induced inflammatory responses may be modulated by histamine-mediated phagocyte recruitment and phagocyte adhesion to implant surfaces, which is facilitated by the adsorbed host fibrinogen. Both H1 and H2 histamine receptor antagonists greatly reduce the recruitment of monocytes/macrophages and neutrophils to implant surfaces. Protein adsorption and monocyte/macrophage adhesion are the significant elements of foreign-body reaction. The acute inflammatory response to biomaterials usually resolves quickly, often within 1 week, depending on the extent of injury at the implant site.

9.3.1.2 Chronic Inflammation

Acute infections are usually self-limiting and are rapidly controlled by the host defences. In contrast, chronic inflammation is self-perpetuating and may last for weeks, months or even years. The development of chronic inflammation may result from a recurrent or progressive acute inflammatory process or from low-grade responses that fail to generate an acute reaction.

Following acute inflammation, chronic inflammation is identified by the presence of mononuclear cells (e.g. monocytes and lymphocytes) at the implant site. Chronic inflammation is less uniform histologically than acute inflammation; thus, this term has been used diagnostically to identify a wide range of cellular responses. The presence of mononuclear cells, including lymphocytes and plasma cells, is

considered chronic inflammation. This chronic inflammatory response to biomaterials is usually of a short duration and is confined to the implant site.

Chronic inflammation also involves the proliferation of fibroblasts instead of formation and release of exudates. As a result, the risk of scarring and deformity is usually considered greater in chronic inflammation than in acute inflammation. Agents that induce chronic inflammation are typically low-grade, persistent irritants that are unable to penetrate deeply or spread rapidly.

Chronic inflammation has also been used to describe the foreign-body reaction, in which monocytes, macrophages and foreign-body giant cells are present at the biomaterial interface. With biocompatible materials, an early resolution of the acute and chronic inflammatory responses occurs; the chronic inflammatory response involving mononuclear cells usually lasts no longer than 2 weeks. The persistence of the acute and/or chronic inflammatory responses beyond a 3-week period usually indicates an infection.

9.3.2 Wound Healing

Following resolution of the acute and chronic inflammatory responses, granulation tissue develops and is identified by the presence of macrophages, infiltration of fibroblasts and neovascularisation of the healing tissue. Granulation tissue is the precursor to fibrous capsule formation and is separated from the implant or biomaterial by the cellular components of the foreign-body reaction, i.e. monocytes in a single or double layer, macrophages and foreign-body giant cells.

After fibrous encapsulation occurs, the lesion is generally referred to as a granuloma. A foreign-body granuloma is thus composed of the foreign body surrounded by giant cells within a zone of macrophages, lymphocytes and granulocytes and, finally, an encapsulating membrane of fibrous tissue.

The result of the inflammatory process is wound healing. Tissue injury, no matter how minute, disrupts tissue continuity (both structure and composition) and often causes a loss of function in the injured area. Ideally, restoration of the injured tissue would generate a new tissue that was identical to the pre-injury tissue. However, complete regeneration and restoration of continuity and function is an exception rather than the rule. Generally, as cells become more specialised, they lose their ability to proliferate and show poor regenerative potential. The healing of specialised tissue involves repair by fibrous tissue substitution (i.e. scar tissue); thus, tissue continuity is restored, but the original function of the injured tissue may be partially or completely lost.

In addition to the degree of specialisation, many factors may influence wound healing, and all of these variables should be considered when designing an implantation protocol. Florey [23] describes these factors in more detail than can be covered in this chapter. Briefly, some of the more important factors that directly affect wound healing are as follows: (1) the position of the wound in the body, (2) the interference of blood supply to the surrounding tissue, (3) the apposition and

immobilisation of cut surfaces and (4) the general health and nutritional status of the experimental subjects.

9.3.3 Foreign-Body Reaction

The foreign-body reaction (Fig. 9.3), comprising mainly macrophages and/or foreign-body giant cells, may persist at the tissue-implant interface for the lifetime of the implant. Generally, fibrosis (i.e. fibrous encapsulation) surrounds the biomaterial or implant with its interfacial foreign-body reaction, thereby isolating the implant and foreign-body reaction from the local tissue environment. Early in the inflammatory and wound healing responses, macrophages are activated upon adherence to the material surface.

The form and topography of the biomaterial surface determine the composition of the foreign-body reaction. With biocompatible materials, the composition of the foreign-body reaction in the implant site may be controlled by the surface properties of the biomaterial, the form of the implant and the ratio of the biomaterial surface area to the implant volume. For example, high surface-to-volume implants such as fabrics, porous materials, particulates or microspheres will have higher proportions of macrophages and foreign-body giant cells at the implant site than smooth-surface implants, in which fibrosis will play a more significant role.

Davila [24, 25] suggests that large implants impair the nutrient supply to the surrounding tissue. Studies on tumour production by implanted polymers suggest a similar situation [26, 27]. Thin fibres (30–50 microns in diameter) of most materials are well tolerated in tissue and have a thin fibrous capsule, a good blood supply and good cellularity. Davila has shown [25] that for a variety of inert materials, the diameter of the fibre has a greater influence on the foreign-body reaction than the type of material does. Davila's work establishes an explanation for the success of velours, felts, weaves, knits and other textile structures in implant applications.

The development of novel biomaterials, biomedical devices and tissue-engineered constructs necessitates thorough understanding of the biological responses to implanted materials. Once a biomaterial is introduced into the body, a sequence of events occurs in the surrounding tissue, ultimately ending in the formation of foreign-body giant cells at the tissue–material interface. The consequences of the reaction to the material surface can be devastating.

IMPLANTATION

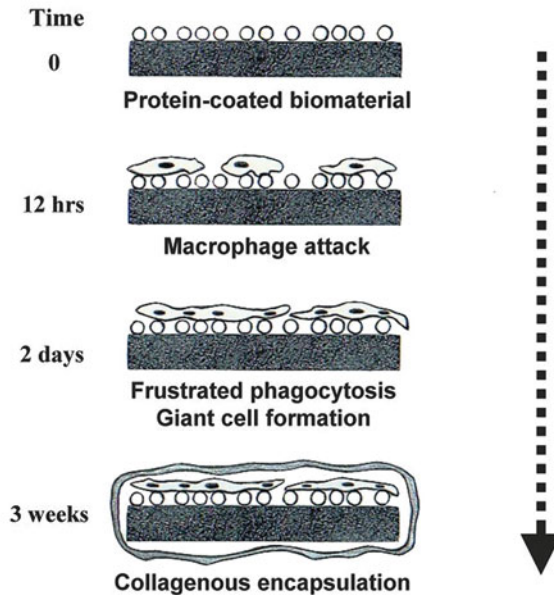


Fig. 9.3 Foreign-body reaction

9.4 Electrospinning of Nanofibrous Scaffold

9.4.1 Biomaterials for Scaffolds

The first issue with regard to tissue engineering is the choice of suitable material. Many different materials (natural and synthetic, biodegradable and permanent) have been investigated for use of scaffolds. Most of these materials have been known in the medical field before the advent of tissue engineering as a research topic. When choosing a material for a tissue engineering application, it needs to meet a number of requirements. Most importantly, the material must be biocompatible and induce minimum toxicity as well as inflammatory and possibly immune responses. An ideal material for the scaffolds should therefore have the following properties: (1) does not induce an inflammatory/toxic response, disproportionate to its beneficial effect, (2) is metabolised in the body after fulfilling its purpose leaving no trace, (3) can be easily processed into the final product form, (4) has acceptable shelf life and (5) can be easily sterilised. For scaffolds in tissue engineering, a high porosity and an adequate pore size are required to facilitate cell seeding and diffusion throughout the whole structure of both cells and nutrients.

Biodegradability is often an essential factor since scaffolds should preferably be absorbed by the surrounding tissues without the necessity of a surgical removal. The rate at which degradation occurs has to coincide as much as possible with the

rate of tissue formation: this means that while cells are fabricating their own natural matrix structure around themselves, the scaffold is able to provide structural integrity within the body and eventually it will break down leaving the neotissue, newly formed tissue which will take over the mechanical load.

A range of novel materials has been developed to enhance the bioactive or therapeutic properties of these nanofibrous scaffold via surface modifications, including the immobilisation of functional cell-adhesive ligands and bioactive molecules such as drugs, enzymes and cytokines [28]. In addition, scaffolds that are intended for tissue regeneration need to have the mechanical strength needed for the creation of a macroporous scaffold that will retain its structure after implantation, particularly in the reconstruction of hard, load-bearing tissues, such as bones and cartilages. Table 9.1 lists the mechanical properties of human tissue [29]. The biostability of many implants depends on such factors as strength, elasticity, absorption at the material interface and chemical degradation.

Potential materials with these characteristics include natural polymers, synthetic polymers, ceramics, metals and combinations of these materials. Despite biocompatible materials such as metals and ceramics have been used extensively for surgical implantations, they have two major disadvantages for tissue engineering applications. First, they are mostly not biodegradable, and, second, their processability is limited. For these reasons, polymeric materials have received increasing attentions from the scientific and medical communities.

Natural polymers, such as collagens, glycosaminoglycan, starch, chitin and chitosan, have been used to repair nerves, skin, cartilage and bone [29]. While naturally occurring biomaterials may most closely simulate the native cellular milieu, large batch-to-batch variations upon isolation from biological tissues is the main limitation for their wide applications. Poor mechanical performance is also a drawback for transplantation scaffolds made from natural polymers.

Within the subdivision of synthetic materials, one can further delineate between biodegradable and non-degradable materials. Biodegradable materials have been the more popular choice due to the elimination of a second surgery to remove the implanted scaffold [30]. Additionally, the rate of degradation can be controlled to some extent to coincide with the rate of new tissue formation, by altering parameters such as polymer blends, and ratio of amorphous to crystalline segments. Among the synthetic polymers, the aliphatic polyesters including polylactide (PLA), poly(glycolide), poly(lactic-co-glycolic acid) (PLGA) and poly(ϵ -caprolactone) (PCL) have been extensively investigated and have been approved by the Food and Drug

Table 9.1 Mechanical properties of human tissues [29]

Tissue	Tensile strength (Mpa)	Compressive strength (Mpa)	Modulus (MPa)
Cancellous bone	N/A	4–12	20–500
Cortical bond	60–160	130–180	3000–30,000
Cartilage	3.7–10.5	N/A	0.7–15.3
Ligament	13–46	N/A	65–541
Tendon	24–112	N/A	143–2310

Table 9.2 Characteristics of typical biodegradable polymers [30]

Polymer ^a	Melting point (°C)	Glass transition temperature (°C)	Modulus ^b (GPa)	Elongation (%)	Degradation time ^c (months)
PGA	225–230	35–40	7.0	15–20	6–12
PLLA	173–178	60–65	2.7	5–10	>24
PDLLA	Amorphous	55–60	1.9	3–10	12–16
PCL	58–63	–65–60	0.4	300–500	>24
PDS	N/A	–10–0	1.5	N/A	6–12
PGA–TMC	N/A	N/A	2.4	N/A	6–12
PLGA 85/15	Amorphous	50–55	2.0	3–10	5–6
75/25	Amorphous	50–55	2.0	3–10	4–5
65/35	Amorphous	45–50	2.0	3–10	3–4
50/50	Amorphous	45–50	2.0	3–10	1–2
Bone			10–20		
Steel			210		

^aPGA poly(glycolide), PLLA poly(L-lactide), PDLLA poly(DL-lactide), PCL poly(ϵ -caprolactone), PDS polydioxanone, PGA–TMC poly(glycolide)–trimethylene carbonate, PLGA poly(lactide-co-glycolide)

^bTensile or flexural modulus

^cTime to complete resorption

Administration (FDA) for the manufacture of various medical devices [31]. These polymers have been approved for, and have a history of safe use in, humans. After being introduced into the body, the polymeric materials induce only a minimal inflammatory response and biodegrade through the hydrolysis of its ester linkages. Table 9.2 summarises the characteristics of these biodegradable polymers.

There are, however, some limitations associated with these biodegradable polymers. All polyesters release acidic degradation products that can adversely affect biocompatibility. These polyesters tend to be relatively stiff materials. While this may be an advantage in load-bearing applications, it becomes a disadvantage when mechanical compliance with soft tissue or blood vessels is required. Furthermore, none of these polyesters provide a chemically reactive pendent chain for the easy attachment of drugs, crosslinkers or biologically active moieties. Thus, simple poly(α -hydroxy ester)s have performed well in establishing the foundation and feasibility of tissue engineering; it may not be optimally suited for the construction of polymeric cell scaffolds serving a variety of applications.

Despite the popularity and apparent benefits of using biodegradable materials, the use of toxic organic solvents for the fabrication of micro- and nanofibres is a major limitation of fibres obtained from synthetic polymers, which would require thorough washing or solvent evaporation treatment prior to use with cells. Natural polymers act as alternatives to synthetic polymers and offer a few advantages such as solubility in aqueous media due to their hydrophilic nature in addition to limited or nonexistent immunogenicity and cytotoxicity.

In order to more accurately mimic the natural ECM, research has also examined the electrospinning of natural materials such as collagen, chitosan, gelatin, fibrinogen, chitin and hyaluronic acid [29, 32]. However, these materials often lack the desired physical properties or are difficult to electrospin on their own, which has led to the development of hybrid materials, which consist of a blend of synthetic and natural materials.

9.4.2 *Electrospinning Process*

Currently, there are three techniques available for the synthesis of nanofibres, namely, electrospinning, self-assembly and phase separation. Among these techniques, electrospinning is the most widely studied technique and has also demonstrated the most promising results in terms of tissue engineering applications [32]. Despite its long history, the electrospinning technique has not gained too much attention as a potential polymer processing method for applications in tissue engineering and drug delivery until the recent 10 years.

Electrospinning is a simple and effective nanofabrication method and affords an opportunity to engineer the scaffolds with micro-to-nanoscale topography and high porosity similar to the natural extracellular matrix (ECM) [1]. It can be used to prepare nanofibrous membranes with diameters ranging from 5 to 500 nm, which are 10^2 to 10^4 times smaller than those prepared by the traditional method of solution or melt spinning. The high surface-to-volume ratio of electrospun scaffolds can enhance cell, drug loading and mass transfer properties. Electrospun fibres can be randomly distributed and highly oriented, allowing the control of the bulk mechanical properties as well as the biological response to the scaffolds. Furthermore, various pharmaceuticals and biomolecules including antibiotics and anticancer agents, proteins, living cells, DNA, RNA, etc., can be incorporated into electrospun scaffolds.

In an electrospinning process, a polymer solution placed inside a syringe is driven out from a melt capillary that is connected to high-voltage power supply (Fig. 9.4a). As the electrostatic attraction between the oppositely charged solution and collecting plate and the electrostatic repulsions between alike charges in the solution become stronger, the leading edge of the solution changes from a rounded meniscus to a cone (so-called Taylor cone, which was first proposed by G. Taylor in 1969 [33]). A fibre jet is thus ejected from the Taylor cone as the electric field strength exceeds the surface tension of the polymer solution. The fibre jet travels through the air allowing the solvent to evaporate. Nanofibres are collected in the form of non-woven membranes on a grounded collector after solvent evaporation. Electrospinning also provides the advantages of fabricating nanofibres from a huge range of materials. Of the major classes of materials, electrospinning is able to produce nanofibres of polymers, composites, semiconductors and ceramics [34].

Typically, the use of stationary collector will result in the formation of a randomly oriented fibre mat. By changing the collector geometry, nanofibres with

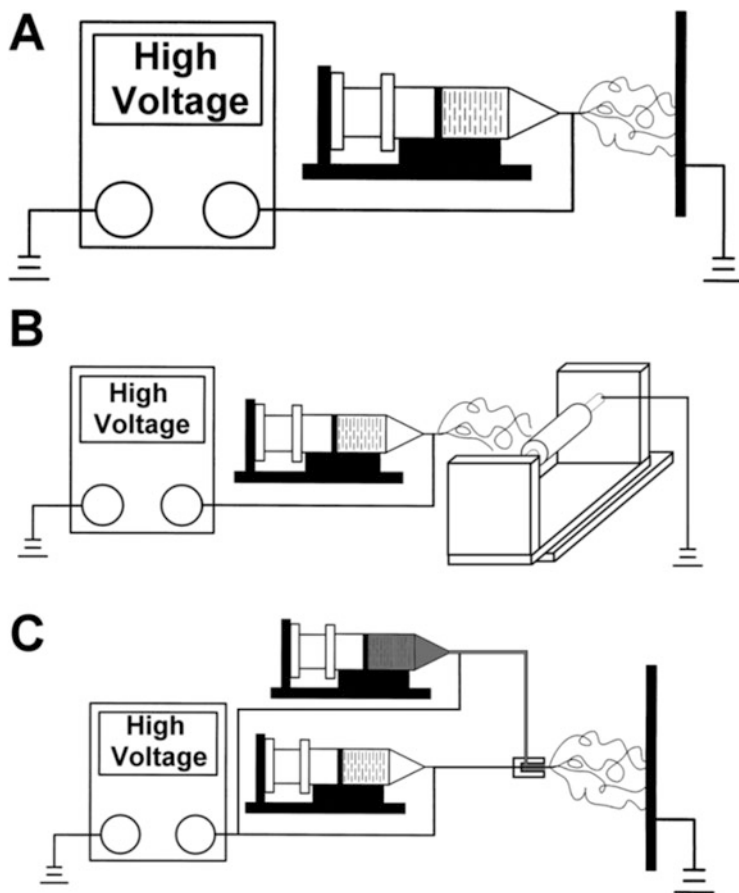


Fig. 9.4 Schematic for (a) the regular electrospinning setup, (b) employment of a rotating collector, (c) assembly for electrospinning of core–sheath nanofibres

various morphologies can be obtained. As an example, the assembly in Fig. 9.4b allows one to prepare nanofibrous membranes with high fibre orientations by employing a rotating collector, while a rotating mandrel can be used to form a tubular scaffold. In addition, the use of multi-nozzles for simultaneous spinning to form multiscale (mixed micro and nanoscale) or multi-materials fibrous scaffolds is also feasible (Fig. 9.4c). Other collector assemblies for preparing nanofibres of various morphologies can be found in the review paper by Teo and Ramakrishna in 2006 [35].

The fibre diameters and morphologies of electrospun nanofibrous membrane are strongly influenced by the processing parameters used in the electrospinning process. Among various parameters such as solvent, polymer concentration, applied voltage, flow rate, etc., the polymer concentration is most important which determines the spinnability of a solution. The solution must have a sufficiently high

polymer concentration for chain entanglements to occur. The polymer concentration influences both the viscosity and the surface tension of the solution, both of which are very important parameters in the electrospinning process. If the solution is too dilute, the polymer fibre will break up into droplets before reaching the collector (Fig. 9.5a) due to the effects of surface tension. Fibres gradually form with the increase in the concentration (Fig. 9.5b), and fibrous mat can be obtained with the increase in the polymer concentration (Fig. 9.5c). The nanofibrous membranes, prepared from polymer solution using the electrospinning technique, possess unique microporous structures which are formed by a stack of fibrous layers and interstices between the fibres. Nevertheless, if the solution is too concentrated, the fibres cannot be formed due to the high viscosity, which makes it difficult to control the solution flow rate through the capillary. Thus, an optimum range of polymer concentrations exists in which nanofibres can be electrospun when all other parameters are held constant.

Depending on electrospinning assemblies and materials/solvents used, the exact influence of the processing parameters on the morphologies of electrospun fibres may be varied. By adjusting the processing parameters such as solvent, applied voltage, flow rate, etc., nanofibrous membranes with various fibre diameters and morphologies can be obtained. A number of general relationships between processing parameters and fibre morphology reviewed and summarised by Sill and von Recum [1] are listed in Table 9.3.

9.4.3 *Electrospun Nanofibrous Scaffolds*

There are several requirements in the design of scaffolds for tissue engineering. Many of these requirements are complex and not yet fully understood. In addition to being biocompatible both in bulk and degraded form, these scaffolds should possess appropriate material properties to provide an ideal biomechanical environment for the neotissues. The scaffolds should also be porous and permeable to permit the ingress of cells and nutrients and should exhibit the appropriate surface structure and chemistry for cell attachment.

The use of electrospun fibres and fibre meshes in tissue engineering applications often involves several considerations, including choice of material, fibre orientation, porosity, surface modification and tissue application. Choices in materials include both natural and synthetic (biodegradable and non-degradable) materials, as well as hybrid blends of these two, which can provide an optimal combination of mechanical and biomimetic properties. By varying the processing and solution parameters, the fibre orientation (aligned vs. random) and porosity/pore size (cell infiltration) of the electrospun scaffold can be controlled and optimised for each individual application. Srinivasan et al. [36] showed that multiscale architectures (Fig. 9.6) have been found favourable not only in bone regeneration but also in the regeneration of soft tissues including cardiovascular tissue, neural tissue, cartilage, and skin. The unique properties of multiscale scaffolds have been pivotal in better

Fig. 9.5 SEM images of electrospun nanofibres (a) if the solution is too dilute, the polymer fibre will break up into droplets, (b) fibres gradually form with the increase in the concentration, (c) fibrous mat can be obtained with the increase in the polymer concentration

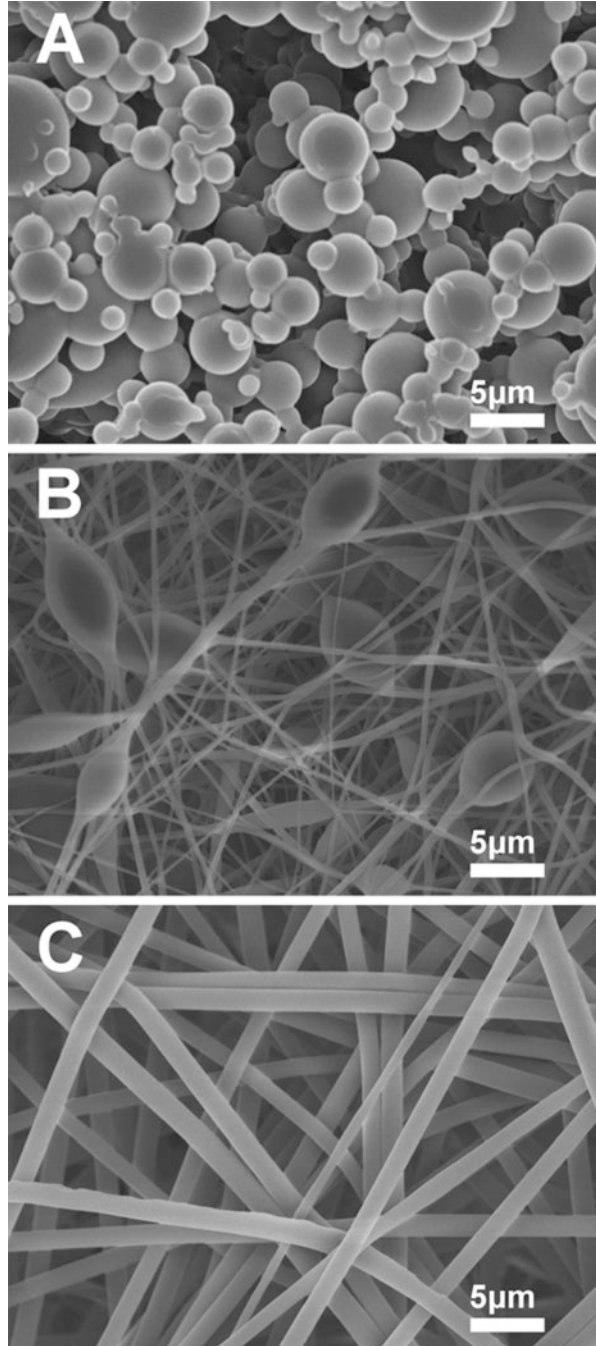


Table 9.3 Effects of processing parameters on fibre morphology [1]

Parameter	Fibre morphology
Applied voltage ↑	Fibre diameter initially ↓, then ↑ (not monotonic)
Flow rate ↑	Fibre diameter ↑ (beaded morphologies occur if the flow rate is too high)
Distance between capillary and collector ↑	Fibre diameter ↓ (beaded morphologies occur if the distance between the capillary and collector is too short)
Polymer concentration (viscosity) ↑	Fibre diameter ↑ (within optimal range)
Solution conductivity ↑	Fibre diameter ↓
Solvent volatility ↑	Fibres exhibit microtexture (pores on their surface, which increase surface area)

mimicking the ECM and promoting vascularisation. After fabrication, the surface of the scaffold can be modified with a high density of bioactive molecules due to the relatively high scaffold surface area. Due to the flexibility in material selection as well as the ability to control the scaffold properties, electrospun scaffolds have been employed in a number of different tissue applications including vascular, bone, neural and tendon/ligament.

Depending on the envisioned applications, pore size must be carefully controlled. The effect of implant pore size on tissue regeneration has been emphasised by experiments demonstrating optimum pore size of 5 μm for neovascularisation, 5–15 μm for fibroblast ingrowth, close to 20 μm for the ingrowth of hepatocytes, 20–125 μm for regeneration of adult mammalian skin, 40–100 μm for osteoid ingrowth and 100–350 μm for regeneration of bone. Fibrovascular tissues appear to require pores sizes greater than 500 μm for rapid vascularisation and for the survival of transplanted cells [29]. In addition to pore size and porosity, the shape and tortuosity can affect tissue ingrowth. Strong cell adhesion and spreading often favour proliferation, while rounded cell morphology is required for cell-specific function. Thus, a polymer scaffold must act as a suitable substrate to maintain differentiated functions without hindering proliferation.

Despite it has been reported that the electrospinning process may denaturalise the biological and structure properties of a natural protein such as collagen [37], the experimental result by Liu et al. [38] suggested that the PLGA/collagen nanofibrous matrix remains intact during the processing procedure and can act as an excellent scaffold for cell adhesion and growth. Presently, nanofibrous materials that mimic the native extracellular matrix and promote the adhesion of various cells are being developed as tissue-engineered scaffolds for the skin, cartilage, liver, kidney, heart, tendon/ligament, nerve, cornea, etc., which will be reviewed as follows.

Skin

Skin is a barrier which protects injured tissues, and the regeneration of skin is one of many important medical issues. When the skin is seriously damaged through disease or trauma, artificial skin using synthetic or natural polymer is essential due to limitation of self-repair and donor-site morbidity. Up to the present, skin is one of

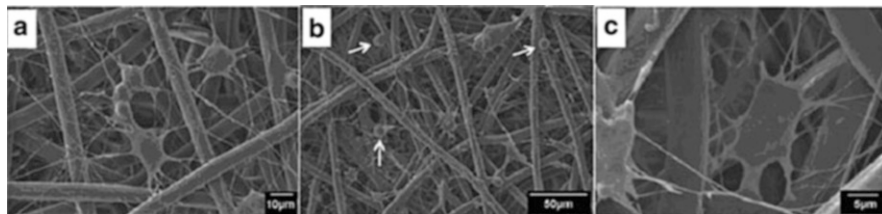


Fig. 9.6 SEM images of cell attachment after 12 h of incubation. (a) Cell attachment on multiscale scaffold. (b) Cell growth into the multiscale scaffold; *arrows* indicate spherical morphology of cells attached to microfibrils. (c) Cell access to the interior of the multiscale scaffold through the pores in the microfibrils (Reprinted from Ref. [36], with kind permission from Springer Science + Business Media)

the most investigated organs for tissue engineering. Electrospun scaffolds made of various materials, including collagen followed by crosslinking [39]; PCL [40]; PCL/collagen [41, 42] and PCL/gelatin [43]; PLA [44]; chitosan-grafted PCL [45]; poly(glycerol sebacate) [46]; hydrogel comprising poly(ethylene glycol) (PEG), poly(propylene glycol) (PPG) and PCL [47]; silk fibroin treated with plasma [48]; chitosan, gelatin and their blends [49]; polyvinyl alcohol (PVA), polyhydroxybutyrate (PHB) and their blends [50]; chitosan–PLGA–poly(ethylene oxide) (PEO) [51]; poly(vinyl alcohol) (PVA)/gelatin [52]; PLA/chitosan blends [53]; and PVA coated with chitosan, hyaluronic acid, collagen or silk fibroin [54], have been developed for the *in vitro* cultivation of fibroblasts. Good cell adhesion, growth and proliferation have been observed on these scaffolds *in vitro*. *In vivo*, several researchers applied the electrospun scaffolds as wound dressings [37, 38, 55–60] on animal models. It was found that nanofibrous membranes were functionally active in responses to fibroblasts and were very effective as wound healing accelerators in early-stage wound healing. These empirical results demonstrate that electrospun nanofibres may be a good candidate as a wound dressing for skin regeneration.

Cartilage

Articular cartilage has a limited capacity for self-repair. Untreated injuries of cartilage may lead to osteoarthritis. Articular cartilage repair remains a significant and growing clinical challenge with the ageing population. The ECM of articular cartilage is a 3D structure comprised of proteinaceous fibres and a hydrogel ground substance that together provides the physical and biological cues to instruct cell behaviour. Mass transport is one of the most significant challenges in tissue engineering. Large-scale cell transplantation in open structures is presently limited by inadequate nutrient delivery. Cells more than approximately 200 µm from a blood supply are either metabolically inactive or necrotic due to low oxygen tension [29]. It is for this reason that cartilage, with its very low metabolic activity, has been one of the few cell types successfully engineered into large tissue structures. *In vitro* studies of chondrocyte cultivation on electrospun nanofibrous scaffolds made of various materials, including PCL [61] and starch-compounded PCL [62], chitosan

[63], collagen-coated carboxymethyl chitosan [64] and double-layered nano-/microfibrous chitosan membranes [65], PLGA [66], alginate [67], PLLA [68] and PCL nanofibres/PLA microfibrils [69], have been successfully conducted. Other scaffolds have also been developed for growth and differentiation of mesenchymal stem cells (MSCs) for chondrogenesis [70–73]. All these fabricated scaffolds showed promising results for cell proliferation.

In the *in vivo* aspect, Casper et al. [74] implanted PCL nanofibre scaffolds, with or without chitosan coating, under the periosteum in 6-month-old rabbits. Transforming growth factor-beta 1 (TGF-beta 1) or vehicle was injected into each implant site. Cell infiltration was observed in these scaffolds. They observed that the cartilage yielded from the periosteum significantly increased by subperiosteal TGF-beta 1 injection. Abedi et al. [75] studied the autologous effects of transplantation of mesenchymal stem cells (MSCs) with a collagen-poly(vinyl alcohol) (PVA) scaffold. The histological observations showed that the MSCs/collagen-PVA repair group exhibited better chondrocyte morphology, continuous subchondral bone and much thicker newly formed cartilage compared with the control group at 12 weeks post operation. Cobrun et al. [76] developed fibrous scaffolds composed of poly(vinyl alcohol) and the biological cue chondroitin sulphate with fibre dimension on the nanoscale for application to articular cartilage repair. Their result showed that the nanofibrous scaffolds enhance chondrogenic differentiation of mesenchymal stem cells as indicated by increased ECM production and cartilage-specific gene expression while also permitting cell proliferation. When implanted it into rat osteochondral defects, acellular nanofibrous scaffolds supported enhanced chondrogenesis marked by proteoglycan production minimally apparent in defects left empty.

Liver

The emerging fields of tissue engineering and biomaterials might have begun to provide potential treatment options for liver failure. Freshly isolated porcine hepatocytes are a very attractive cell source in the cell-based therapies to treat liver failure because of unlimited availability. However, due to the loss of hepatocyte functions *in vitro*, there is a need to develop a functional culture system to keep the cells metabolically active. Several research groups developed nanofibrous scaffolds using self-assembling peptides for culturing hepatocyte [77–81]. Other than the peptide-based scaffolds, Hashemi et al. [82] tested the ability of electrospun PCL nanofibre scaffold to support and maintain hepatic differentiation of human cord blood-derived unrestricted somatic stem cells *in vitro*. They showed that hepatocyte-like cells differentiation on the PCL scaffold can be a candidate for tissue engineering and cell therapy of hepatic tissues. Furthermore, electrospun scaffolds of other materials including cellulose hydrogels [83], PLLA and collagen [84] have also been developed for hepatic differentiation studies. The research group of Chu et al. [85–87] has also developed bioartificial liver support system using electrospun chitosan nanofibres. They demonstrated that no infective porcine endogenous retroviruses were detected in canine models and the developed support system has a reliable microbiological safety profile.

Kidney

Relatively less work has been done on the tissue engineering of the kidney. Schindler et al. [88] proposed a nanofibrillar matrices prepared by electrospinning a polymer solution of polyamide onto glass coverslips. When the normal rat kidney cells were grown on nanofibres in the presence of serum, they displayed the morphology and characteristics of their counterparts *in vivo*. Zhang et al. [89] explored the substrate-mediated gene delivery by employing a DNA immobilised electrospun nanofibres. Their nanofibre-based gene delivery system exhibited high transfection efficiency, in which >65 % of human embryonic kidney 293 cells and >40 % of mesenchymal stem cells were transfected with green fluorescent protein gene. Bakota et al. [90] proposed an injectable multidomain peptide nanofibre hydrogel as a delivery agent for stem cell secretome. *In vitro* experiments demonstrated that release of stem cell secretome from the hydrogels in the presence of glomerular epithelial cells treated with high glucose significantly reduced protein permeability in a model of diabetes-induced kidney injury.

Tendon/Ligament

Interfacial tissues such as tendon and ligament are specialised and ubiquitous tissues in human body, which integrate soft and hard tissue, and are characterised by their complex and heterogeneous biochemical and structural properties. The repair of interfacial tissues after injuries remains challenging; current clinical methods of fixation and tissue regeneration have not resulted in full recovery of damaged tissues. An ideal graft such as tendon graft requires it to not only exhibit physiologically relevant mechanical properties but also be able to facilitate functional graft integration by promoting the regeneration of the native tendon-to-bone interface. Various efforts have been made in preparing different nanofibrous scaffolds for tissue engineering of tendon/ligament; some of them used the self-assembling peptide-based scaffolds [91], hybrid silk-based scaffolds covered with self-assembling nanofibres [92] and scaffolds prepared by the partial dissolution method [93]. As far as the electrospinning technique is used, Inanc et al. [94] used an electrospun PLGA nanofibre membrane scaffolds for the engineering of human periodontal ligament cells. Their results demonstrated the feasibility of periodontal ligament cell-containing, tissue-like and osteogenic differentiation properties of cells. Moffat et al. [95] designed a PLGA nanofibre-based scaffold for engineering rotator cuff tendon. It was observed that rotator cuff fibroblasts cultured on the aligned scaffolds attached along the nanofibres long axis, whereas the cells on the unaligned scaffold were polygonal and randomly oriented. Furthermore, mechanical properties of the aligned nanofibre scaffolds were significantly higher than those of the unaligned. Li et al. [96] developed a continuously graded, bone-like calcium phosphate coating on a non-woven mat of electrospun nanofibres, and they found that the gradient in mineral content resulted in a gradient stiffness of the scaffold, which further influenced the activity of mouse pre-osteoblast MC3T3 cells. Since tendon is a specific connective tissue composed of parallel collagen fibres, Yin et al. [97] demonstrated that the aligned electrospun nanofibre structure

provides an instructive microenvironment for hTSPC differentiation and may lead to the development of desirable engineered tendons. In addition, to improve the mechanical properties of engineered scaffolds, Sahoo et al. [98] and Teh et al. [99] adopted kitted silk as the scaffold materials for ligament tissue engineering applications. Meanwhile, scaffolds of other materials, including PCL/collagen and PLA/collagen [100], collagen–glycosaminoglycan [101], hydroxyapatite-coated PLGA [102], cellulose [93], hydrogel [103], etc., have been developed aiming for tendon repair applications. All these scaffolds exhibited enhancing capability for cell proliferation and differentiation. Recently, Erisken et al. [104] found that controlling the scaffold fibre diameter is critical in the design of scaffolds for functional and guided connective tissue repair. This provides some new insights into the role of matrix parameters in guiding soft tissue healing.

Cornea

The cornea is the transparent front part of the eye that covers the iris, pupil and anterior chamber. Only limited works have been conducted on the engineering of corneal replacement and for promoting regenerative healing of the cornea after disease and/or injury. English et al. [105] developed anisotropically aligned collagen nanofibres via electrospinning and solvent casting and successfully evaluated the response of corneal fibroblasts to the nanofibrous scaffold. They observed that the corneal fibroblasts aligned parallel to the direction of the aligned oriented electrospun mats. Muthusubramaniam et al. [106] grew the corneal fibroblasts isolated from bovine corneas on collagen nanofibrous scaffolds and found that matrix nanotopography downregulates the fibrotic phenotype, promotes formation of the quiescent keratocyte phenotype and influences matrix synthesis. Gao et al. [107] investigated the contribution of fibre arrangement to guiding the aligned growth of corneal stroma cells. They found that corneal stroma cells grew highly orderly on the aligned scaffold, while the cells grow disordered on the randomly oriented scaffold. In addition, the cells exhibited higher viability in aligned scaffold than that in randomly oriented scaffold.

Heart

The *in vitro* generation of a three-dimensional myocardial tissue-like construct that employs cells, biomaterials and biomolecules can be a promising strategy in cardiac tissue regeneration. Compared to the *in vitro* [108–110] and *in vivo* [111–113] progress made in the engineering of cardiovascular tissue using self-assembling peptides, the development of electrospun scaffolds is relatively limited. Heydarkhan-Hagvall et al. [114] developed three-dimensional electrospun ECM-based hybrid scaffolds, namely, gelatin/PCL and collagen/elastin/PCL scaffolds, for cardiovascular tissue engineering. Scanning electron microscopy and nuclei staining of cell-seeded scaffolds demonstrated the complete cell attachment to the surfaces of both hybrid scaffolds, while cell migration into the scaffold was predominantly seen in the gelatin/PCL hybrid. Balguid et al. [115] seeded human venous myofibroblasts in electrospun PCL scaffolds and found that cell penetration increased proportionally with increasing fibre diameter. They concluded that fibre

diameter is a crucial parameter to allow for homogeneous cell delivery in electrospun scaffolds. Chung et al. [116] developed small diameter tubes fabricated from poly(L-lactide-co- ϵ -caprolactone) copolymers via melt spinning and electrospinning for vascular tissue engineering scaffolds. They demonstrated that the mechanical properties of the prototype tubes exceeded the transverse tensile value of natural arteries of similar calibre. Stout et al. [117] investigated cardiac tissue cell functions on PLGA filled with carbon nanofibres that have a higher conductivity. Their results showed that cardiomyocyte density increases with greater amounts of carbon nanofibres in PLGA for up to 5 days. This indicates the conductive materials promoted the adhesion and proliferation of the cells. Courtney et al. [118] fabricated poly(ester urethane) urea scaffold via electrospinning and demonstrated that the high-velocity spun scaffolds exhibited highly native anisotropic mechanical properties closely resembling the native pulmonary heat valve leaflet. Li et al. [119] co-electrospun fibrous scaffolds from the blend of PLGA and two natural proteins, gelatin and elastin. They cultured H9c2 rat cardiac myoblasts on the scaffolds and found that myoblasts grew equally as well or slightly better on the scaffolds than on tissue-culture plastic. Recently, Hussain et al. [120] developed fibronectin-coated chitosan nanofibre scaffolds for cardiovascular tissue engineering. The experimental results demonstrated that the chitosan nanofibres retained their cylindrical morphology in long-term culture of ventricular cardiomyocytes and exhibited good cellular attachment and spreading in the presence of fibronectin.

Nerve

Despite many nerve prostheses have been proposed in recent years, in the case of consistent loss of nervous tissue, peripheral nerve injury is still a traumatic pathology that impairs patient's movements by interrupting his/her motor-sensory pathways. During the past few decades, tissue engineering has opened the door to new approaches. Bridging larger nerve gaps between proximal and distal ends requires exogenous tubular constructs with uniaxially aligned topographical cues to promote the axonal regrowth due to the lack of fibrin cable formation. An ideal scaffold for neural regeneration would be both fibrous and electrically conductive. It has been generally accepted that aligned nanofibre scaffolds enhance growth and proliferation of neural cells such as Schwann cells, dorsal root ganglion neurons, etc. Electrospinning technique may thus provide a potential alternative to engineering of nervous tissues. To date, various successes have been achieved to partially construct neural system function in rat models by employing the self-assembling peptide-based hydrogels [121–126]. Relatively, the progress in the engineering of neural prostheses using electrospun scaffolds of different materials mainly remains in the *in vitro* stage [127]. Only few *in vivo* studies have been reported. Panseri et al. [128] used the electrospun tubes made of PLGA/PCL blends to regenerate a 10-mm nerve gap in a rat sciatic nerve. Their results showed that in most of the treated animals, the electrospun tubes induced nervous regeneration and functional reconnection of the two severed sciatic nerve tracts. This indicates that electrospun tubes, even with no additional biological coating or drug loading treatment, are

promising scaffolds for functional nervous regeneration. Clements et al. [129] developed nerve guidance channels containing stacked thin films of aligned poly (acrylonitrile-co-methylacrylate) fibres and implanted the channels into rats. Their results indicated that the channels supported the regeneration across the nerve gap, thereby resulting in functional muscular reinnervation. Wang et al. [130] constructed a chitosan non-woven nanofibre mesh tubes consisting of oriented fibres by the electrospinning method which were bridge-grafted into rat sciatic nerve defects. Functional recovery and electrophysiological recovery of rats were observed in time. Kim et al. [131] prepared muscle precursor cell-seeded PCL nanofibres and placed the fibres under the female rat's urethra after pudendal nerve denervation. Their experimental results indicated that the nanofibres have not only provided support to the deficient sphincter but also actively improved the sphincter's function.

9.5 Conclusion

The technological improvement in biology, medicine, chemistry, engineering and material science have allowed to gain deeper insights into the architectural and molecular organisation of tissues and materials, providing innovative approaches and tools for medical treatments. Developments in this multidisciplinary field of tissue engineering have yielded a novel set of tissue replacement parts and implementation strategies. Scientific advances in biomaterials, stem cells, growth and differentiation factors and biomimetic environments have created unique opportunities to fabricate tissues *in vitro* from combinations of engineered extracellular matrices, cells and biologically active molecules. The major challenge now facing tissue engineering is the need for more complex functionality, as well as both functional and biomechanical stability in *in vitro* grown tissues destined for transplantation. The continued success of tissue engineering will grow from the convergence of engineering and basic research advances in tissue, matrix, growth factor, stem cell and material science. Eventually, it is expected that the engineered tissues would be able to be used for the replacement of damaged or failed tissues/organs directly.

Acknowledgements The authors thank Ms. Yu-Chun Kao for her assistance in preparing the figures.

References

1. Sill TJ, von Recum HA (2008) Electrospinning: application in drug delivery and tissue engineering. *Biomaterials* 29:1989–2006

2. Frank CB, Shrive NG (1999) Biological materials. In: Biomechanics of the musculo-skeletal system. Wiley, Chichester/New York, pp 107–126
3. Carmeliet P (2000) Mechanisms of angiogenesis and arteriogenesis. *Nat Med* 6:389–395
4. Ingber DE (2002) Mechanical signaling and the cellular response to extracellular matrix in angiogenesis and cardiovascular physiology. *Circ Res* 91:877–887
5. Carter DR, van der Meulen MCH, Beaupré GS (1996) Mechanical factors in bone growth and development. *Bone* 18:5S–10S
6. Schoen FJ (1997) Aortic valve structure-function correlations: role of elastic fibers no longer a stretch of the imagination. *J Heart Valve Dis* 6:1–6
7. Bokel C, Brown NH (2002) Integrins in development: moving on, responding to, and sticking to the extracellular matrix. *Dev Cell* 3:311–321
8. Minns RJ, Soden PD, Jackson DS (1973) The role of the fibrous components and ground substance in the mechanical properties of biological tissues: a preliminary investigation. *J Biomech* 6:153–165
9. Fawcett DW (1986) Bloom and Fawcett: a textbook of histology, 11th edn. WB.Saunders Company, Philadelphia
10. Alberts B, Bray D, Lewis J, Raff M, Roberts K, Watson JD (1994) Molecular biology of the cell, 3rd edn. Garland Publishing, New York
11. Limbert G, Taylor M (2002) On the constitutive modelling of biological soft connective tissues. A general theoretical framework and explicit forms of the tensors of elasticity for strongly anisotropic continuum fiber-reinforced composites at finite strain. *Int J Solid Struct* 39(8):2343–2358
12. Freed AD, Doehring TC (2005) Elastic model for crimped collagen fibrils. *J Biomech Eng* 127(4):587–593
13. Redaelli A, Vesentini S, Soncini M, Vena P, Mantero S, Montevecchi FM (2003) Possible role of decorin glycosaminoglycans in fibril to fibril force transfer in relative mature tendons – a computational study from molecular to microstructural level. *J Biomech* 36(10):1555–1569
14. Raspanti M, Alessandrini A, Ottani V, Ruggeri A (1997) Direct visualization of collagen-bound proteoglycans by tapping-mode atomic force microscopy. *J Struct Biol* 119:118–122
15. Eyre DR, Pietka T, Weis MA, Wu JJ (2004) Covalent cross-linking of the NC1 domain of collagen type IX to collagen type II in cartilage. *J Biol Chem* 279(4):2568–2574
16. Szwajczak E (2004) Dependence of hyaluronan aqueous solution viscosity on external fields, part II. *Russ J Biomech* 8(1):89–94
17. Nishimura M, Yan W, Mukudai Y, Nakamura S, Nakamasu K, Kawata M, Kawamoto T, Noshiro M, Hamada T, Kato Y (1998) Role of chondroitin sulphate-hyaluronan interactions in the viscoelastic properties of extracellular matrices and fluids. *Biochim Biophys Acta* 1380(1):1–9
18. Homsy CA (1970) Bio-compatibility in selection of materials for implantation. *J Biomed Mater Res* 4:341–356
19. Zdolsek J, Eaton JW, Tang L (2007) Histamine release and fibrinogen adsorption mediate acute inflammatory responses to biomaterial implants in humans. *J Transl Med* 5:31
20. Tang L, Jennings TA, Eaton JW (1998) Mast cells mediate acute inflammatory responses to implanted biomaterials. *Proc Natl Acad Sci U S A* 95(15):8841–8846
21. Keegan AD (2001) IL-4. In: Oppenheim JJ, Feldman M (eds) Cytokine reference. Academic, San Diego
22. McKenzie ANJ, Matthews DJ (2001) IL-13. In: Oppenheim JJ, Feldman M (eds) Cytokine reference. Academic, San Diego
23. Florey HW (1970) General pathology. Saunders, New York, pp 510–516
24. Davila JC (1966) Prosthesis and living tissue: conflict compatibility (editorial). *Ann Thorac Surg* 2:126
25. Davila JC, Lautsch EV, Palmer TE (1968) Some physical factors affecting the acceptance of synthetic materials as tissue implants. *Ann N Y Acad Sci* 146:138–147

26. Oppenheimer BS, Oppenheimer ET, Stout AP, Danishefsky I (1953) Malignant tumors resulting from embedding plastics in rodents. *Science* 118:305–306
27. Stinson NE (1964) The tissue reaction induced in rats and guinea pigs by polymethyl methacrylate and stainless steel. *Br J Exp Pathol* 45:21–29
28. Kubinova S, Sykova E (2010) Nanotechnologies in regenerative medicine. *Minim Invasive Ther Allied Technol* 19:144–156
29. Yang S, Leong KF, Du Z, Chua CK (2001) The design of scaffolds for use in tissue engineering. Part I. Traditional factors. *Tissue Eng* 7(6):679–689
30. Middleton JC, Tipton AJ (2000) Synthetic biodegradable polymers as orthopedic devices. *Biomaterials* 21:2335–2346
31. Nair LS, Laurencin CT (2007) Biodegradable polymers as biomaterials. *Prog Polym Sci* 32:762–798
32. Vasita R, Katti DS (2006) Nanofibers and their applications in tissue engineering. *Int J Nanomed* 1(1):15–30
33. Taylor G (1969) Electrically driven jets. *Proc Natl Acad Sci Lond* A313(1515):53–475
34. Huang ZM, Zhang YZ, Kotaki M, Ramakrishna S (2003) A review on polymer nanofibers by electrospinning and their applications in nanocomposites. *Compos Sci Technol* 63:2223–2253
35. Teo WE, Ramakrishna S (2006) A review on electrospinning design and nanofibre assemblies. *Nanotechnology* 17:R89–R106
36. Srinivasan S, Jayakumar R, Chennazhi KP, Levorson EJ, Mikos AG, Nair SV (2011) Multiscale fibrous scaffolds in regenerative medicine. *Adv Polym Sci* 246:1–20
37. Rho KS, Jeong L, Lee G, Seo BM, Park YJ, Hong SD, Roh S, Cho JJ, Park WH, Min BM (2006) Electrospinning of collagen nanofibers: effects on the behaviour of normal human keratinocytes and early-stage wound healing. *Biomaterials* 27:1452–1461
38. Liu SJ, Kau YC, Chou CY, Chen JK, Wu RC, Yeh WL (2010) Electrospun PLGA/collagen nanofibrous membrane as early-stage wound dressing. *J Membr Sci* 355:53–59
39. Dong B, Arnoult O, Smith ME, Wnek GE (2009) Electrospinnign of collagen nanofibers scaffolds from benign solvents. *Macromol Rapid Commun* 30:539–542
40. Reed CR, Han L, Andrady A, Caballero M, Jack MC, Collins JB, Saba SC, Lobo EG, Cairns BA, van Aalst JA (2009) Composite tissue engineering on polycaprolactone nanofibers scaffolds. *Ann Plast Surg* 62:505–512
41. Venugopal J, Ramakrishna S (2005) Biocompatible nanofibers matrices for the engineering of a dermal substitute for skin regeneration. *Tissue Eng* 11:847–854
42. Yang XC, Shah JD, Wang HJ (2009) Nanofiber enabled layer-by-layer approach toward three-dimensional tissue formation. *Tissue Eng Part A* 15:945–956
43. Chong EJ, Phan TT, Lim IJ, Zhang YZ, Bay BH, Ramakrishna S (2007) Evaluation of electrospun PCL/gelatin nanofibrous scaffold for wound healing and layered dermal reconstitution. *Acta Biomater* 3:321–330
44. Leong MF, Rasheed MZ, Lim TC, Chian KS (2009) In vitro cell infiltration and in vivo cell infiltration and vascularization in a fibrous, highly porous poly(D, L-lactide) scaffold fabricated by cryogenic electrospinning technique. *J Biomed Mater Res Part A* 91A:231–240
45. Chen HL, Huang J, Yu JH, Liu SY, Gu P (2011) Electrospun chitosan-graft-poly(epsilon-caprolactone)/poly(epsilon-caprolactone) cationic nanofibrous mats as potential scaffolds for skin tissue engineering. *Int J Biol Macromol* 48:13–19
46. Yi F, Laven DA (2008) Poly(glycerol sebacate) nanofibers scaffolds by core/shell electrospinning. *Macromol Biosci* 8:803–806
47. Loh XJ, Peh P, Liao S, Sng C, Li J (2010) Controlled drug release from biodegradable thermoresponsive physical hydrogel nanofibers. *J Control Release* 143:175–182
48. Jeong L, Yeo IS, Kim HN, Yoon HI, Jang DH, Jung SY, Min BM, Park WH (2009) Plasma-treated silk fibroin nanofibers for skin regeneration. *Int J Biol Macromol* 44:222–228

49. Dhandayuthapani B, Krishnan UM, Sethuraman S (2010) Fabrication and characterization of chitosan-gelatin nanofibers for skin tissue engineering. *J Biomed Mater Res Part B* 94B:264–272
50. Asran AS, Razghandi K, Aggarwal N, Michler GH, Groth T (2010) Nanofibers from blends of polyvinyl alcohol and polyhydroxy butyrate as potential scaffold material for tissue engineering of skin. *Biomacromolecules* 11:3413–3421
51. Lim HJ, Kim CJ, Oh EJ, Kim TJ, Jung SY, Choi JH, Lee WJ, Kwon OH, Chung HY (2011) Hybrid scaffolds composed of chitosan-PLGA-PEO nanofibers and PLGA microfibers for artificial skin. *Tissue Eng Regen Med* 8:108–115
52. Yang C, Wu XM, Zhao YH, Xu L, Wei SC (2011) Nanofibrous scaffold prepared by electrospinning of poly(vinyl alcohol)/gelatin aqueous solutions. *J Appl Polym Sci* 121:3047–3055
53. Shalumon KT, Sathish D, Nair SV, Chennazhi KP, Tamura H, Jayakumar R (2012) Fabrication of aligned poly(lactic acid)-chitosan nanofibers by novel parallel blade collector method for skin tissue engineering. *J Biomed Nanotechnol* 8:405–416
54. Lee SY, Jang DH, Kang YO, Kim OB, Jeong L, Kang HK, Lee SJ, Lee CH, Park WH, Min BM (2012) Cellular response to poly(vinyl alcohol) nanofibers coated with biocompatible proteins and polysaccharides. *Appl Surf Sci* 258:6914–6922
55. Park SN, Lee HJ, Lee KH, Suh H (2003) Biological characterization of EDC-crosslinked collagen-hyaluronic acid matrix in dermal tissue restoration. *Biomaterials* 24:1631–1641
56. Chen JP, Chang GY, Chen JK (2008) Electrospun collagen/chitosan nanofibrous membrane as wound dressing. *Colloids Surf A PhysicoChem Eng Asp* 313–314:183–188
57. Kumbar SG, Nukavarapu SP, James R, Nair LS, Laurencin CT (2008) Electrospun poly(lactic acid-co-glycolic acid) scaffolds for skin tissue engineering. *Biomaterials* 29:4100–4107
58. Yang Y, Zhu X, Cui W, Li X, Jin Y (2009) Electrospun composites mats of Poly[(D, L-lactide)-co-glycolide] and collagen with high porosity as potential scaffolds for skin tissue engineering. *Macromol Mater Eng* 294:611–619
59. Kurpinski KT, Stephenson JT, Janairo RRR, Lee HM, Li S (2010) The effect of fiber alignment and heparin coating on cell infiltration into nanofibrous PLLA scaffolds. *Biomaterials* 31:3536–3542
60. Chen DWC, Liao JY, Liu SJ, Chan EC (2012) Novel biodegradable sandwich-structured nanofibrous drug-eluting membranes for repair of infected wounds: an in vitro and in vivo study. *Int J Nanomed* 7:763–771
61. Li WJ, Danielson KG, Alexander PG, Tuan RS (2003) Biological response of chondrocytes cultured in three-dimensional nanofibrous poly(epsilon-caprolactone) scaffolds. *J Biomed Mater Res Part A* 67A:1105–1114
62. de Silva MA, Crawford A, Mundy J, Martins A, Araujo JV, Hatton PV, Reis RL, Neves NM (2009) Evaluation of extracellular matrix formation in polycaprolactone and starch-compounded polycaprolactone nanofibers meshes when seeded with bovine articular chondrocytes. *Tissue Eng Part A* 15:377–385
63. Subramanian A, Vu D, Larsen GF, Lin HY (2005) Preparation and evaluation of the electrospun chitosan/PEO fibers for potential applications in cartilage tissue engineering. *J Biomater Sci Polym Ed* 16:861–873
64. Lu GY, Sheng BY, Wei YJ, Wang G, Zhang LH, Ao Q, Gong YD, Zhang XF (2008) Collagen nanofibers-covered porous biodegradable carboxymethyl chitosan microcarriers for tissue engineering cartilage. *Eur Polym J* 44:2820–2829
65. Shim IK, Suh WH, Lee SY, Lee SH, Heo SJ, Lee MC, Lee SJ (2009) Chitosan nano-/microfibrous double-layered membrane with rolled-up three-dimensional structures for chondrocyte cultivation. *J Biomed Mater Res Part A* 90A:595–602
66. Shin HJ, Lee CH, Cho IH, Kim YJ, Lee JY, Kim IA, Park KD, Yui N, Shin JW (2006) Electrospun PLGA nanofibers scaffolds for articular cartilage reconstruction: mechanical stability, degradation and cellular responses under mechanical stimulation in vitro. *J Biomater Sci Polym Ed* 17:103–119

67. Bhattarai N, Li ZS, Edmondson D, Zhang MQ (2006) Alginate-based nanofibrous scaffolds: structural, mechanical, and biological properties. *Adv Mater* 18:1463–1467
68. Li WJ, Jiang YJ, Tuan RS (2006) Chondrocyte phenotype in engineered fibrous matrix is regulated by fiber size. *Tissue Eng* 12:1775–1785
69. Thorvaldsson A, Stenhamre H, Gatenholm P, Walkenstrom P (2008) Electrospinning of highly porous scaffolds for cartilage regeneration. *Biomacromolecules* 9:1044–1049
70. Xin XJ, Husaain M, Mao JJ (2007) Continuing differentiation of human mesenchymal stem cells and induced chondrogenic and osteogenic lineages in electrospun PLGA nanofibers scaffold. *Biomaterials* 28:316–325
71. Mohammadi Y, Soleimani M, Fallahi-Sichani M, Gazme A, Haddadi-Asl V, Arefian E, Kiani J, Moradi R, Atashi A, Ahmadbeigi N (2007) Nanofibrous poly(epsilon-caprolactone)/poly(vinyl alcohol)/chitosan hybrid scaffolds for bone tissue engineering using mesenchymal cells. *Int J Artif Organ* 30:204–211
72. Hu J, Feng K, Liu XH, Ma PX (2009) Chondrogenic and osteogenic differentiations of human bone marrow-derived mesenchymal stem cells on a nanofibrous scaffold with designed pore network. *Biomaterials* 30:5061–5067
73. Shafiee A, Soleimani M, Chamheidari GA, Shyedjafari E, Dodel M, Atashi A, Gheisari Y (2011) Electrospun nanofiber-based regeneration of cartilage enhanced by mesenchymal stem cells. *J Biomed Mater Res Part A* 99A:467–478
74. Casper ME, Fitzsimmons JS, Stone JJ, Meza AO, Huang Y, Ruesink TJ, O'Driscoll SW, Reinholz GG (2010) Tissue engineering of cartilage using poly-epsilon-caprolactone nanofibers scaffolds seeded in vivo with periosteal cells. *Osteoarthr Cartil* 18:981–991
75. Abedi G, Sotoudeh A, Soleymani M, Shafiee A, Mortazavi P, Afatoonian MR (2011) A collagen-poly(vinyl alcohol) nanofibers scaffold for cartilage repair. *J Biomater Sci Polym Ed* 22:2445–2455
76. Coburn JM, Gibson M, Monagles S, Patterson Z, Elisseff JH (2012) Bioinspired nanofibers support chondrogenesis for articular cartilage repair. *Proc Natl Acad Sci* 109:10012–10017
77. Navarro-Alvarez N, Soto-Gutierrez A, Rivas-Carrillo JD, Chen Y, Yamamoto T, Yuasa T, Misawa H, Takei J, Tanake N, Kobayashi N (2006) Self-assembling peptide nanofibers as a novel culture system for isolated porcine hepatocytes. *Cell Transplant* 15:921–927
78. Wang S, Nagrath D, Chen PC, Berthiaume F, Yarmush ML (2008) Three-dimensional primary hepatocyte culture in synthetic self-assembling peptide hydrogel. *Tissue Eng Part A* 14:227–236
79. Mehta G, Williams CM, Alvarez L, Lesniewski M, Kamm RD, Griffith LG (2010) Synergistic effects of tethered growth factors and adhesion ligands on DNA synthesis and function of primary hepatocytes cultured on soft synthetic hydrogel. *Biomaterials* 31:4657–4671
80. Sun LJ, Zhao XJ (2012) A self-assembling peptide RADA 16-I integrated with spider fibroin uncrystalline motifs. *Int J Nanomed* 7:571–580
81. Malinen MM, Palokangas H, Yliperttula M, Urtti A (2012) Peptide nanofibers hydrogel induces formation of bile canaliculi structures in three-dimensional hepatic cell culture. *Tissue Eng Part A* 18:2418–2425
82. Hashemi SM, Soleimani M, Zargarian SS, Haddadi-Asl V, Ahmadbeigi N, Soudi S, Gheisari Y, Hajarizadeh A, Mohammadi Y (2009) In vitro differentiation of human cord blood-derived unrestricted somatic stem cells into hepatocyte-like cells on poly(epsilon-caprolactone) nanofibers scaffolds. *Cell Tissue Organ* 190:135–149
83. Bhattacharya M, Malinen MM, Lauren P, Lou YR, Kuisma SW, Kanninen L, Lille M, Corlu A, GuGuen-Guillouze C, Ikkala O, Laukkanen A, Urtti A, Yliperttula M (2012) Nanofibrillar cellulose hydrogel promotes three-dimensional liver cell culture. *J Control Release* 164:291–298
84. Ghaedi M, Soleimani M, Shabani I, Duan YY, Lotfi AS (2012) Hepatic differentiation from human mesenchymal stem cells on a novel nanofibers scaffold. *Cell Mol Biol Lett* 17:89–106

85. Chu XH, Shi XL, Feng ZQ, Gu JY, Xu HY, Zhang Y, Gu ZZ, Ding YT (2009) In vitro evaluation of a multi-radial-flow bioreactor based on galactosylated chitosan nanofiber scaffolds. *Biomaterials* 30:4533–4538
86. Han B, Shi XL, Zhang Y, Chu XH, Gu JY, Xizo JQ, Ren HZ, Tan JJ, Gu ZZ, Ding YT (2012) Microbiological safety of a novel-artificial liver support system based on porcine hepatocytes: an experimental study. *Eur J Med Res* 17:13
87. Shi XL, Zhang Y, Chu XH, Han B, Gu JY, Xiao JQ, Tan JJ, Gu ZZ, Ren HZ, Yuan XW, Ding YT (2012) Evaluation of a novel hybrid bioartificial liver based on a multi-layer flat-plate bioreactor. *World J Gastroenterol* 18:3752–3760
88. Schindler M, Ahmed I, Kamal J, Nur-E-Kamal A, Grafe TH, Chung HY, Meiners S (2005) A synthetic nanofibrillar matrix promotes in vivo-like organization and morphogenesis for cells in culture. *Biomaterials* 26:5624–5631
89. Zhang J, Duan YJ, Wei D, Wang LY, Wang HJ, Gu ZW, Kong DL (2011) Co-electrospun fibrous scaffold-adsorbed DNA for substrate-mediated gene delivery. *J Biomed Mater Res A* 96A:212–220
90. Bakota EL, Wang Y, Danesh FR, Hartgerink JD (2011) Injectable multidomain peptide nanofibers hydrogel as a delivery agent for stem cell secretome. *Biomacromolecules* 12:1651–1657
91. Kumada Y, Zhang SG (2010) Significant type I and type III collagen production from human periodontal ligament fibroblasts in 3D peptide scaffolds without extra growth factors. *Plos One* 5:e10305
92. Chen KL, Sahoo S, He PF, Ng KS, Toh SL, Goh JCH (2012) A hybrid silk/RADA-based fibrous scaffold with triple hierarchy for ligament regeneration. *Tissue Eng Part A* 18:1399–1409
93. Mathew AP, Oksman K, Pierron D, Harmand MF (2012) Fibrous cellulose nanocomposites scaffolds prepared by partial dissolution for potential use as ligament or tendon substitutes. *Carbohydr Polym* 87:2291–2298
94. Inanc B, Arslan YE, Seker S, Elcin AE, Elcin YM (2009) Periodontal ligament cellular structures engineered with electrospun poly(DL-lactide-co-glycolide) nanofibrous membrane scaffold. *J Biomed Mater Res A* 90A:186–195
95. Moffat KL, Kwei ASP, Spalazzi JP, Doty SB, Levine WN, Lu HH (2009) Novel nanofibers-based scaffold for rotator cuff repair and augmentation. *Tissue Eng Part A* 15:115–126
96. Li XR, Xie JW, Lipner J, Yuan XY, Thomopoulos S, Xia YN (2009) Nanofiber scaffolds with gradations in mineral content for mimicking the tendon-to-bone insertion site. *Nano Lett* 9:2763–2768
97. Yin Z, Chen X, Chen JL, Shen WL, Gao L, Ouyang HW (2010) The regulation of tendon stem cell differentiation by the alignment of nanofibers. *Biomaterials* 31:2163–2175
98. Sahoo S, Toh SL, Goh JCH (2010) PLGA nanofibers-coated silk microfibrillar scaffold for connective tissue engineering. *J Biomed Mater Res B* 95B:19–28
99. Teh TKH, Toh SL, Goh JCH (2011) Aligned hybrid silk scaffold for enhanced differentiation of mesenchymal stem cells into ligament fibroblasts. *Tissue Eng Part C* 17:687–703
100. Ladd MR, Lee SJ, Stitzel JD, Atala A, Yoo JJ (2011) Co-electrospun dual scaffolding system with potential for muscle-tendon junction tissue engineering. *Biomaterials* 32:1549–1559
101. Caliarì SR, Harley BAC (2011) The effect of anisotropic collagen-GAG scaffolds and growth factor supplementation on tendon cell. *Biomaterials* 32:5330–5340
102. Liu WY, Yeh YC, Lipner J, Xie JW, Sung HW, Thomopoulos S, Xia YN (2011) Enhancing the stiffness of electrospun nanofibers scaffolds with a controlled surface coating and mineralization. *Langmuir* 27:9088–9093
103. Carr LR, Krause JE, Ella-Menye JR, Jiang SY (2011) Single nonfouling hydrogel with mechanical and chemical functionality gradients. *Biomaterials* 32:8456–8461
104. Erisken C, Zhang X, Moffat KL, Levine WN, Lu HH (2013) Scaffold fiber diameter regulates human tendon fibroblast growth and differentiation. *Tissue Eng Part A* 19:519–528

105. English A, Azeem A, Gaspar DA, Keane K, Kumar P, Keeney M, Rooney N, Pandit A, Zeugolis DI (2012) Preferential cell response to anisotropic electrospun fibrous scaffolds under tension-free conditions. *J Mater Sci Mater Med* 23:137–148
106. Muthusubramaniam L, Peng L, Zaitseva T, Paukshto M, Martin GR, Desai TA (2012) Collagen fibril diameter and alignment promote the quiescent keratocyte phenotype. *J Biomed Mater Res A* 100A:613–621
107. Gao Y, Yan J, Cut XJ, Wang HY, Wang Q (2012) Aligned fibrous scaffold induced aligned growth of corneal stroma cells in vitro culture. *Chem Res Chin Univ* 28:1022–1025
108. Davis ME, Motion JPM, Narmoneva DA, Takahashi T, Hakuno D, Kamm RD, Zhang SG, Lee RT (2005) Injectable self-assembling peptide nanofibers create intramyocardial microenvironments for endothelial cells. *Circulation* 111:442–450
109. Ceylan H, Tekinay AB, Guler MO (2011) Selective adhesion and growth of vascular endothelial cells on bioactive peptide nanofibers functionalized stainless steel surface. *Biomaterials* 32:8797–8805
110. Guo HD, Cui GH, Yang JJ, Wang C, Zhu J, Zhang LS, Jiang J, Shao SJ (2012) Sustained delivery of VEGF from designer self-assembling peptides improves cardiac function after myocardial infarction. *Biochem Biophys Res Commun* 424:105–111
111. Dubois G, Segers VFM, Bellamy V, Sabbah L, Peyrad S, Bruneval P, Hagege AA, Lee RT, Menasche P (2008) Self-assembling peptide nanofibers and skeletal myoblast transplantation in infarcted myocardium. *J Biomed Mater Res Part B* 87B:222–228
112. Webber MJ, Tongers J, Renault MA, Roncalli JG, Losordo DW, Stupp SI (2010) Development of bioactive peptide amphiphiles for therapeutic cell delivery. *Acta Biomater* 6:3–11
113. Lin YD, Luo CY, Hu YN, Yeh ML, Hsueh YC, Chang MY, Tsai DC, Wang JN, Tang MJ, Wei EI, Springer ML, Hsieh PCH (2012) Instructive nanofibers scaffolds with VEGF create a microenvironment for arteriogenesis and cardiac repair. *Sci Transl Med* 4:146ra109
114. Heydarkhan-Hagvall S, Schenke-Layland K, Dhanasopon AP, Rofail F, Smith H, Wu BM, Shemin R, Beygui RE, MacLellan WR (2008) Three-dimensional electrospun CCM-based hybrid scaffolds for cardiovascular tissue engineering. *Biomaterials* 29:2907–2914
115. Balguid A, Mol A, van Marion MH, Bank RA, Bouten CVC, Baaijens FPT (2009) Tailoring fiber diameter in electrospun poly(epsilon-caprolactone) scaffolds for optimal cellular infiltration in cardiovascular tissue engineering. *Tissue Eng Part A* 15:437–444
116. Chung SW, Ingle NP, Montero GA, Kim SH, King MW (2010) Bioresorbable elastomeric vascular tissue engineering scaffolds via melt spinning and electrospinning. *Acta Biomater* 6:1958–1967
117. Stout DA, Basu B, Webster TJ (2011) Poly(lactic-co-glycolic acid): carbon nanofibers composites for myocardial tissue engineering applications. *Acta Biomater* 7:3101–3112
118. Courtney T, Sacks MS, Stankus J, Guan J, Wagner WR (2006) Design and analysis of tissue engineering scaffolds that mimic soft tissue mechanical anisotropy. *Biomaterials* 27:3631–3638
119. Li M, Mondrinos MJ, Chen X, Gandhi MR, Ko FK, Lelkes PI (2006) Co-electrospun poly(lactide-co-glycolide), gelatin, and elastin blends for tissue engineering scaffolds. *J Biomed Mater Res Part A* 79A:963–973
120. Hussain A, Collins G, Yip D, Cho CH (2013) Functional 3-D co-culture model using bioactive chitosan nanofibers scaffolds. *Biotechnol Bioeng* 110:637–647
121. McGrath AM, Novikova LN, Novikova LN, Wiberg M (2010) BD PuraMatrix peptide hydrogel seeded with Schwann cells for peripheral nerve regeneration. *Brain Res Bull* 83:207–213
122. Gelain F, Panseri S, Antonini S, Cunha C, Donega M, Lowery J, Taraballi F, Cerri G, Montagna M, Baldissera F, Vescovi A (2011) Transplantation of nanostructured composite scaffolds results in the regeneration of chronically injured spinal cords. *ACS Nano* 5:227–236
123. Zhang WW, Zhan XD, Gao MY, Hamilton AD, Liu ZY, Jiang YW, Su HX, Dai X, He B, Kang XN, Zeng YX, Wu WT, Guo JS (2012) Self-assembling peptide nanofibers scaffold enhanced with RhoA inhibitor CT04 improves axonal. *J Nanomater* 724857.

124. Meng H, Chen RY, Xu LN, Li WC, Chen LY, Zhao XJ (2012) Peripheral nerve regeneration in response to synthesized nanofibers scaffold hydrogel. *Life Sci J Acta Zhengzhou Univ Oversea Ed* 9:42–46
125. Moradi F, Bahktiari M, Hoghataei MT, Nobakht M, Soleimani M, Hasanzadeh G, Fallah A, Zarbakhsh S, Hejazian LB, Shirmohammadi M, Maleki F (2012) BD PuraMatrix peptide hydrogel as a culture system for human fetal Schwann cells in spinal cord. *J Neurosci Res* 90:2335–2348
126. Nayagam BA, Back house SS, Cimenkaya C, Shepherd RK (2012) Hydrogel limits stem cell dispersal in the deaf cochlea: implications for cochlear implants. *J Neural Eng* 9:065001
127. Saracino GAA, Cigognini D, Silva D, Caprini A, Gelain F (2013) Nanomaterials design and tests for neural tissue engineering. *Chem Soc Rev* 42:225–262
128. Panseri S, Cunha C, Lowery J, Del Carro U, Taraballi F, Amadio S, Vescovi A, Gelain F (2008) Electrospun micro- and nanofibers tubes for functional nervous regeneration in sciatic nerve transactions. *BMC Biotechnol* 8:39
129. Clements IP, Kim YT, English AW, Lu X, Chung A, Bellamkonda RV (2009) Thin-film enhanced nerve guidance channels for peripheral nerve repair. *Biomaterials* 30:3834–3846
130. Wang W, Itoh S, Konno K, Kikkawa T, Ichinose S, Sakai K, Ohkuma T, Watabe K (2009) Effects of Schwann cell alignment along the oriented electrospun chitosan nanofibers on nerve regeneration. *J Biomed Mater Res Part A* 91A:994–1005
131. Kim IG, Piao S, Hong SH, Kim SW, Hwang TK, Oh SH, Lee JH, Lee JY (2012) The effect of a bioactive tissue-engineered sling in a rat of stress incontinence model. *J Biomed Mater Res Part A* 100A:286–292

Chapter 10

Biomimic Design of Periosteum: Construction Strategies, Scaffold Design and Cell Sources

Yin Xiao, Wei Fan, Ross Crawford, and Dietmar W. Hutmacher

Abstract In terms of bone physiology, the periosteum plays critical roles in both bone formation and defect healing. Periosteum is a dual-layered soft tissue membrane that contains osteogenic progenitor cells in the cambial layer, as well as blood supply and supportive cells in the fibrous layer. Transplantation of autogenous or allogeneous periosteum has been applied successfully in the repair of various-sized bone defects, especially in large bone defects. However, two major concerns exist in relation to the insufficient autologous donor tissues and donor site morbidity or immunological rejection related to allogeneic tissues. Periosteum tissue engineering is to mimic the natural structure of periosteum, which will guide bone formation in a physiological manner. This chapter provides current information about the construction strategies, scaffold design and cell sources for the periosteum tissue engineering based on the structure and functions of natural periosteum.

Keywords Scaffold • Periosteum • Tissue engineering • Stem cells • Bone • Biomaterials

10.1 Introduction

Restoring bone defects and its normal function has long since been the final ambition of orthopaedic surgeons regardless of the size of the defect. To realise this ambition, bone transplantation therapies, including autogenic, allogeneic and xenogeneic transplantations, have been attempted and studied [1]. However, these therapies are always faced difficulty with either insufficient supply of donor tissue

Y. Xiao (✉) • R. Crawford • D.W. Hutmacher
Institute of Health and Biomedical Innovation, Queensland University of Technology, Kelvin
Grove, QLD 4059, Australia
e-mail: yin.xiao@qut.edu.au

W. Fan
School of Stomatology, Wuhan University, Hubei, China

or possible immune rejections after transplantation, which prevents the bone transplantation from large-scale clinical applications.

Bone tissue engineering is to construct an artificial bone substitute to restore bone defects and normal function. Various biomaterials, such as collagen, polymers and bioceramics are used as scaffold materials for bone tissue engineering [2, 3]. These materials play dual roles in the bone defect area: as templates to restore the bone tissues and scaffolds to deliver therapeutic cells and/or various related growth factors [4–6]. However, the bone defect healing via engineered bone substitute is very much different from the natural healing process which is normally induced and guided by periosteum. Bone healing induced by periosteum have many advantages over other methods, such as healing with natural bone structure, optimal implant/host integration, appropriate vascularisation and minimal ectopic ossification.

Transplantation of autogenous or allogeneous periosteum has been applied successfully in the repair of various-sized bone defects, especially in large bone defects [7]. In spite of this, the supply of periosteum grafts always remains in shortage. To solve this problem, periosteum tissue engineering becomes one of the focused biomedical engineering areas. As recently pointed out in a review article by Zhang et al, periosteum tissue engineering could assist in structural de novo bone formation and is therefore a promising approach for bone defect restoration [8]. Since there have been many studies in this area, this chapter attempted to focus a brief review on the periosteum tissue engineering.

10.2 Structure and Functions of Periosteum

10.2.1 Structure of Periosteum

Periosteum is a dense connective tissue membrane covering the outer surface of most bones except the joint [9]. Histologically, the periosteum is thought to consist of two different layers (Fig. 10.1) [9–11]: the outer fibrous layer mainly contains fibroblast, blood vessel networks, collagen fibres and extracellular matrix [11, 12], and the inner layer, also referred to as the cambium layer, attaches directly to the bone surfaces and is highly cellular of mature osteoblasts and osteogenic progenitor cells [9, 11, 13–15]. Based upon these anatomical features, the periosteum can be described as a vascularised dual-layered ‘osteogenic device’ as it has both osteogenic cells and blood vessel networks [11, 16]. It supplies blood to bone, especially the cortical bone [17], and is regarded as the ‘umbilical cord’ of bone tissues [18].

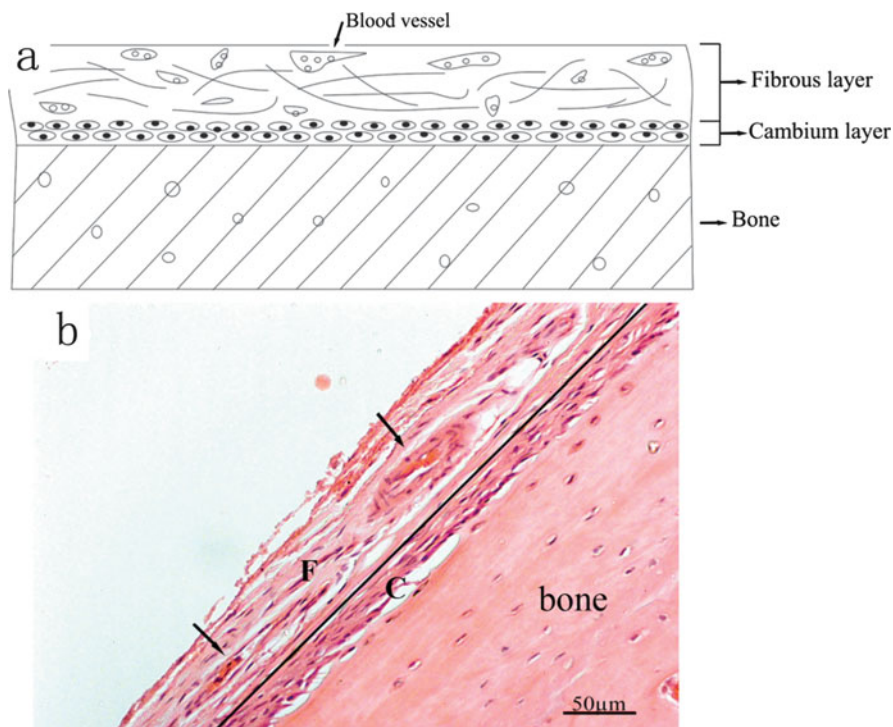


Fig. 10.1 Dual-layered structure of periosteum. (a) Schematic illustration of the two different layers of periosteum; (b) histological dual-layered structure of periosteum (*F* fibrous layer, *C* cambium layer, *arrows* blood vessels)

10.2.2 Function of Periosteum

Periosteum plays critical roles in both bone development and defect healing. There are two different patterns of *in vivo* bone development: intramembranous and endochondral ossifications, in both of which the periosteum plays critical roles [19]. For intramembranous ossification, the mesenchymal cells differentiate directly into osteogenic progenitor cells to form a primitive periosteum [20]. Then these progenitor cells in the periosteum differentiate into osteoblasts and bone formation process takes place. For the endochondral ossification, the perichondrium (cell layer surrounding cartilage) firstly develops from mesenchymal cells to form a cartilage template [11, 21]. Then the template develops into bone along with the perichondrium turning into the periosteum.

Periosteum also plays critical roles in bone fracture healing (Fig. 10.2). Without periosteum, many bone fractures would end up with non-union. The bone fracture healing process basically repeats the intramembranous and endochondral ossification processes as described above [22, 23]. Blood clots (haematoma) in the fracture area will trigger an acute inflammation, followed by blood vessel invasion and

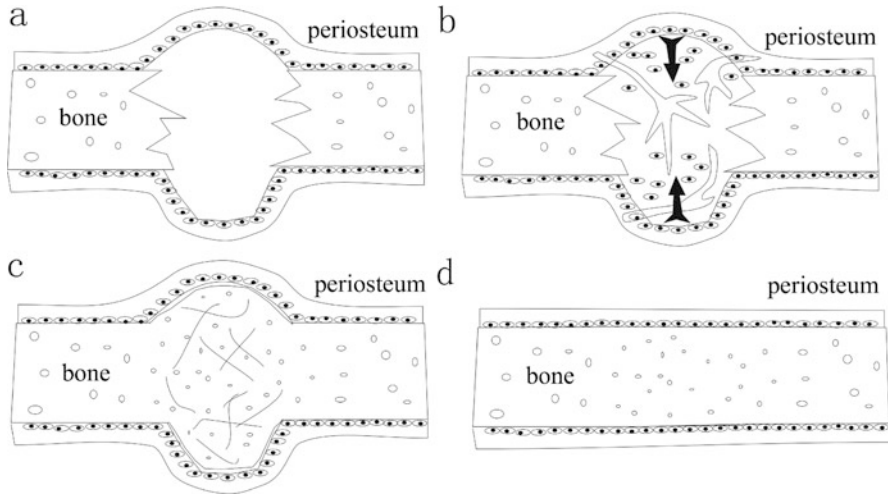


Fig. 10.2 Illustration of the role of periosteum in bone defect healing. (a) Bone fracture site and haematoma; (b) osteogenic progenitor cell migration and blood vessel infiltration into the fracture site from periosteum; (c) bone callus formation; (d) bone callus remodelling and healing

cartilage formation which will finally turn into bone callus (Fig. 10.2) [11, 23]. During this process, osteogenic progenitor cells could come from periosteum, endosteum, and bone marrow. Several studies had indicated that the progenitor cells from periosteum are most important to the healing response [9, 15, 24–28]. Uddstromer and colleagues had shown that periosteum plays the most important role in fracture healing [29, 30]. Oni and colleagues demonstrated that fracture healing was delayed when periosteum was removed [31, 32].

10.3 Construction Strategies for Periosteum Tissue Engineering

10.3.1 Bioartificial Periosteum

As mentioned above, periosteum could generally be described as a dual-functional organ: bone formation and blood supply. To engineer a functional periosteum, the following six strategies could be considered (Fig. 10.3): (1) acellular bioactive membrane [33, 34], (2) acellular bioactive membrane carrying growth factors [35, 36], (3) scaffold-free osteogenic cell sheet [37, 38], (4) membrane seeded with osteogenic cells [39, 40], (5) membrane seeded with osteogenic cells plus growth factors [41] and (6) membrane seeded with both osteogenic and angiogenic cells [42, 43].

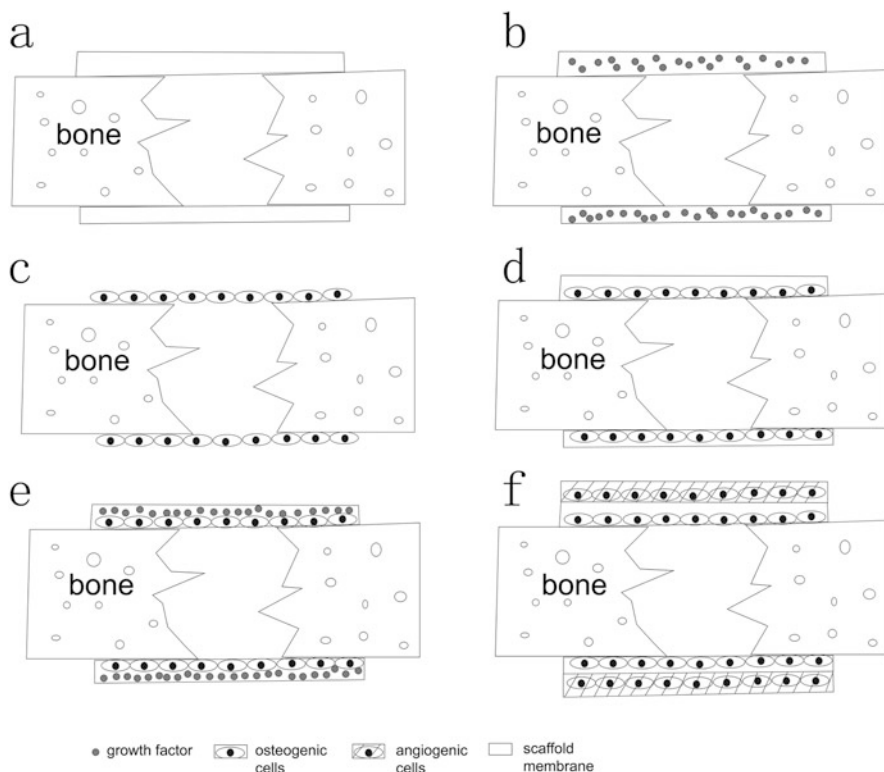


Fig. 10.3 Construction strategies for the periosteum tissue engineering. (a) Acellular membrane; (b) acellular membrane carrying growth factors; (c) osteogenic cell sheet; (d) membrane seeded with osteogenic cells; (e) membrane seeded with osteogenic cells and growth factors; (f) membrane seeded with osteogenic and angiogenic cells

The materials used to make the membrane scaffold could be fibrin, collagen, polymers or natural tissue membranes such as submucosa of intestines. Nevertheless, most studies published so far used acellular bioactive membranes, single osteogenic cell sheet or membranes carrying only osteogenic cells [33, 34, 37, 44]. For example, Neel et al. used an acellular periosteal replacement membrane for bone graft containment at the allograft-host junction [33]. Hattori [45] demonstrated the healing of a severe open fracture by applying a bioartificial periosteum made of collagen sponge carrying osteogenic cells. In another study, submucosa from the small intestine was used to mimic periosteum onto which bone marrow stromal cells (BMSCs) were seeded [46]. The obvious drawback of this approach is that scaffold materials have to be sourced from the small intestine, which means another surgical operation on the patient to harvest scaffold materials.

As these engineered periosteae are either acellular or single cell based, which is different from the dual-layered structure of periosteum, it would be difficult for these constructs to carry out both 'bone formation' and 'blood supply' functions

in vivo. Although much work has been done under the subject of periosteum tissue engineering [17, 47–49], very limited references could be found addressing dual-layered engineered periosteum that contains both osteogenic and angiogenic factors/cells, not to mention in vivo assessments of any such constructs. More importantly, a dual-layered membrane scaffold designed to accommodate osteogenic and angiogenic cells, respectively, should be developed to better mimic the real periosteum and achieve its full in vivo functions.

10.3.2 Dual-Layered Scaffold Design for Periosteum Tissue Engineering

In light of the limitations and obstacles of the current approaches towards engineering a periosteal replacement, significant improvements must be made in terms of design of scaffolds for such applications. Multifunctionalities of the periosteum as a tissue capable of initiating bone healing process, supplier of vascular networks to the underlying bone and a barrier membrane for soft tissue must be addressed. One approach to achieving this goal is to fabricate constructs using polymeric materials by mimicking the architecture and features of the periosteum. A potential design for a periosteum scaffold is shown in Fig. 10.4. Dual-layered scaffold mimicking both the fibrous and cambium layers of the native tissue would be appropriate (Fig. 10.4a).

Both layers of the envisioned scaffold could be fabricated using a modified electrospinning technique. Electrospinning is suitable due to its speed and versatility in generating polymeric fibres with diameters in the orders of tens to thousands of nanometres [50, 51]. Its enormous potential in the field of tissue engineering as a method of scaffold fabrication has been widely reported [52–54]. A modification of the electrospinning set-up allowed the fabrication of highly porous, cell-penetrable fibrous layer by simultaneous co-deposition of poly (β -caprolactone) (PCL)-based polymeric fibres with hyaluronic acid (HA) hydrogel

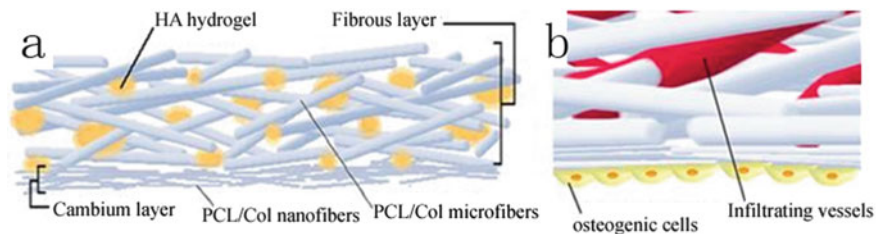


Fig. 10.4 Schematic representation of a dual-layered scaffold design for the application in periosteum tissue engineering

[55]. As the cambium layer, conventional electrospun submicron fibres (i.e. nanofibres) could be deposited on one side of the fibrous layer. The eventual goal is to allow infiltration of new capillaries and fibrous tissues into the constructs via the fibrous layer and delivery of osteogenic progenitor cells via the cambium layer's surface to aid in the repair of the underlying bone defect (Fig. 10.4b).

10.3.3 *Electrospinning Process for the Fabrication of Periosteum*

Prospective application of electrospun nanofibres shown in Fig. 10.5 as the cambium layer in the periosteum construct stems from widely reported studies pertaining to suitability of nanofibres as support structures for proliferation and differentiation of mesenchymal progenitor cells and scaffolds for new mesenchymal tissues. Li et al. reported a favourable response when mesenchymal stem cells were cultured on PCL nanofibres with specific expression of cartilage genes and deposition of cartilage-like matrix [56]. Yoshimoto et al. reported that a bone-like tissue rich in collagen type I and calcified minerals was obtained on the nanofibre scaffolds where mesenchymal stem cells of bone marrow origin were cultured in vitro [57]. Similar observations were made when a composite nanofibre formulation of PCL and collagen type I (PCL/Col) was used as scaffolds. The synthetic–natural polymeric composite fibres exhibited smooth morphology with a relatively uniform fibre diameter throughout the mesh. When the bone marrow mesenchymal cells were seeded and cultured on the surface of these nanofibre meshes, thick

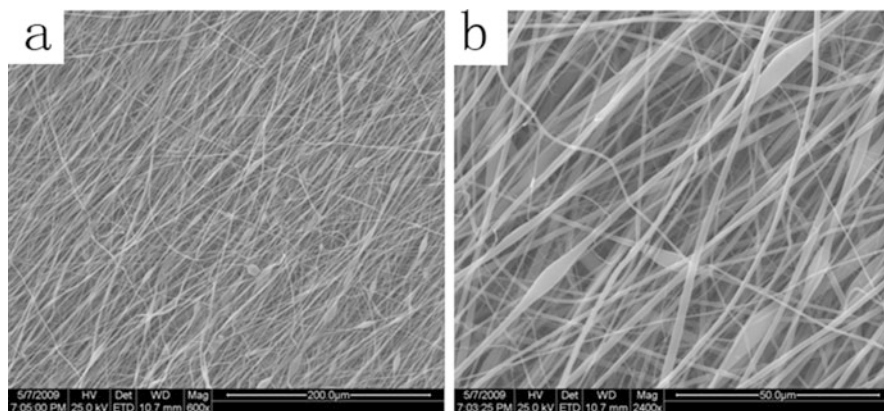


Fig. 10.5 Scanning electronic microscopy (SEM) images of electrospun nanofibres for the scaffold of periosteum cambium layer. Magnifications: (a) $\times 600$, (b) $\times 2400$

multilayering of cells and tissue was seen after 4 weeks of *in vitro* culture. This tissue demonstrated the deposition of collagen type I, osteocalcin proteins and heavy matrix mineralisation which suggested differentiation of the cells towards osteogenic lineage. The mesh's ability to support proliferation, differentiation and new bone-like tissue formation makes it a promising candidate as the cambium layer in the periosteum scaffold.

Engineering the fibrous layer required modifications to the electrospinning process to allow the fabrication of a phase which is porous enough to enable cellular infiltration. Furthermore, this layer must support endothelial cells and infiltrating capillaries. Conventional electrospinning often results in dense deposition of nanofibres not allowing cells to infiltrate into the structure [58–63]. Several approaches in attempts to tackle this problem have been reported with varying outcomes from direct blending of polymers with water-soluble gelatin [64], selective polymer leaching [65], salt leaching [66] and the use of micron-sized fibres [67]. Another plausible approach is the simultaneous deposition of electrospun micron-sized fibres with electrosprayed hydrogel (Fig. 10.6). In this approach, PCL/Col microfibres in the size range of 1–2 μm (Fig. 10.6a) were co-deposited with HA hydrogel via an electrospinning–electrospraying process [55]. Globules of the hydrogel were embedded throughout the fibrous structure of the resulting mesh (Fig. 10.6b – transverse view, 10.6c – planar view). A more open-pore structure was created by depositing slightly larger fibres using electrospinning [68], and the inclusion of the HA-based hydrogel would provide passages and compartments into which cells and tissues could migrate.

Rapid and extensive infiltration of osteoblasts was observed on these meshes after 10 days of *in vitro* culture (Fig. 10.7a). The cells could be seen in the interior of the fibrous matrix as pointed out by the arrow heads. Histological staining of the sections revealed cells populating the entire thickness of the mesh (Fig. 10.7b, arrow heads indicate cell nuclei). Monolayering of cells on the mesh's surface as traditionally seen on electrospun scaffolds was not observed. The suitability of this fibrous mesh as a periosteum scaffolding material was further investigated with a coculture system of endothelial cells and fibroblasts. It has been reported previously that coculturing endothelial cells with fibroblasts improved their viability, function and formation of tube-like structure *in vitro* [69–71]. Observations of the cocultured cells on the mesh revealed endothelial tube-like formations on the surface (Fig. 10.7c, arrow heads). These structures were similar to those previously reported when endothelial phenotype was preserved *in vitro* by coculturing with smooth muscle cells [72] or mesenchymal cells [73]. Furthermore, the assays performed on the section revealed that ingrowth of the endothelial networks occurred into the scaffolds' interior, i.e. subsurface migration (Fig. 10.7d). These results suggested that the fibrous meshes allowed the endothelial cell population to reorganise *in vitro* into tube-like structures often seen preceding the process of vasculogenesis. In addition, the architecture and pore geometry of the scaffold were sufficient in enabling migration of the endothelial capillary into the matrix.

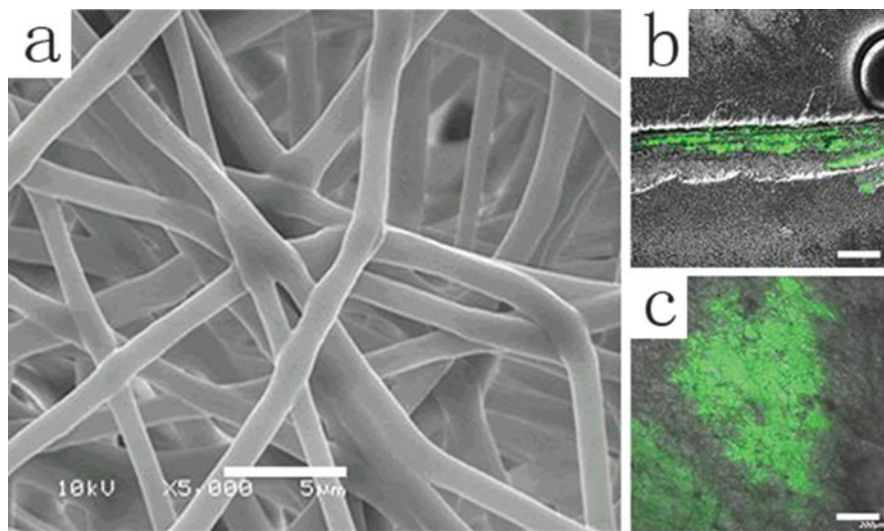


Fig. 10.6 Construction of fibrous layer for the periosteal tissue scaffolding. (a) PCL/Col scaffolds with microfibrils were fabricated. (b and c) The co-deposited HA-based hydrogels (labelled with *green* fluorescence) were distributed throughout the fibrous interior. *Bar* represents 5 µm in (a) and 200 µm in (b, c)

10.4 Cell Sources for Periosteum Tissue Engineering

To engineer a fully functional periosteum, i.e. bone formation and blood supply, two kinds of cells are required: osteogenic and angiogenic cells. For the osteogenic cells, there are many different choices. It can be mature osteoblasts or osteogenic progenitor cells (or stem cells).

10.4.1 Osteogenic Cells

Osteoblasts can be separated directly from bone tissues, while the progenitor or stem cells can come from different origins. Most often used stem cell source for osteogenesis is the bone marrow stromal cells (BMSC). Bone marrow contains two types of stem or progenitor cell systems: the haematopoietic cell system and non-haematopoietic BMSCs [74, 75]. When cultured *in vitro*, BMSCs rapidly attach to the culture surfaces and can be easily separated from the non-adherent haematopoietic cells by repeatedly washing. BMSCs, when cultured *in vitro*, are negative for CD45, CD14, CD31 and CD34, but positive for CD105, CD44, CD73 and CD90 cell surface markers [76]. They are a mixture of progenitor cells which can be differentiated into various mesodermal cells, especially osteoblasts, chondrocytes, fibroblasts or adipocytes [77]. The osteogenic abilities of BMSCs

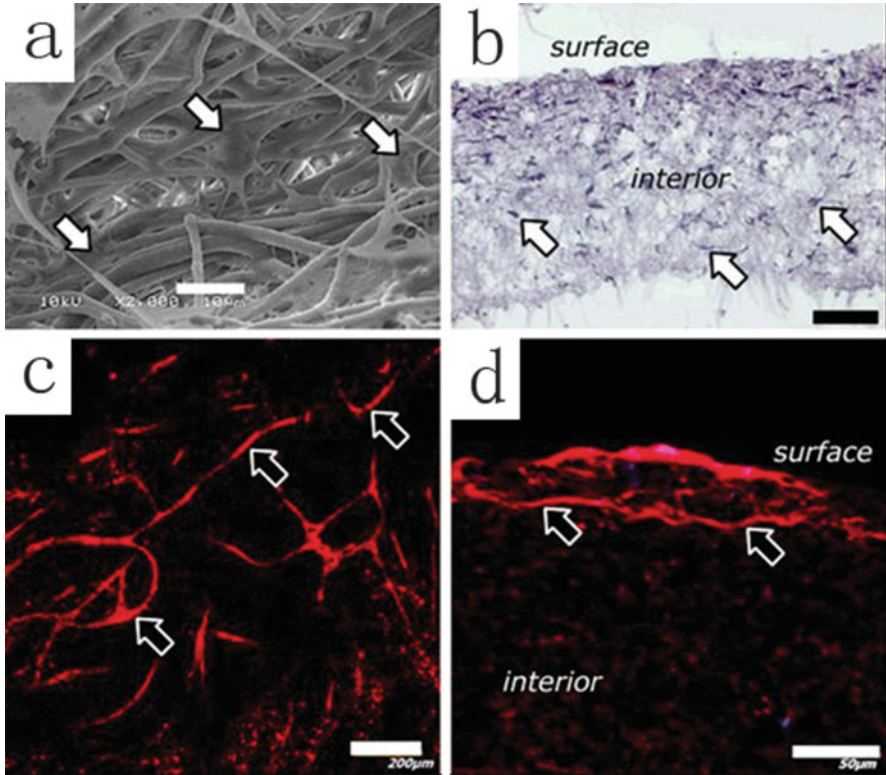


Fig. 10.7 Cellular infiltration into the fibrous matrix of the scaffolds. (a) SEM images showing the infiltration of human foetal osteoblasts (*arrows*) into the interior of the fibrous mesh. (b) Penetration of cells was uniform throughout the entire thickness of the scaffold (*arrows* indicating the cell nuclei). (c and d) Coculture of endothelial cells and fibroblasts on these meshes revealed self-assembly of ECs into capillary-like structures (*red* fluorescence) on the surface (c) as well as the interior of the mesh. (d) *Bar* represents 10 μm in (a), 50 μm in (b), 200 μm in (c), and 50 μm in (d)

have been well documented both *in vitro* and *in vivo* and have been applied to help bone defect restoration [78, 79]. Osteogenic progenitor cells can also be derived from fat tissues (adipocytes), dental tissue (such as dental pulp and periodontal ligament) or even the periosteum itself (from cambium layer), though the specific makers for these progenitor cells are still unclear [76, 80–82]. Osteogenic differentiation of these progenitor cells as well as their *in vivo* application for bone tissue engineering has been widely reported [80–82].

10.4.2 *Angiogenic Cells*

The other important cell type for functional periosteum tissue engineering is the angiogenic cells that can help in vivo vascularisation. For in vivo vasculogenesis and angiogenesis, there are several potential cell sources: mature endothelial cells (MECs or ECs) from vessels, such as cells from human umbilical vein (HUV), and endothelial progenitor cells (EPCs) from bone marrow or peripheral blood. MECs, especially those from the HUV, are often used as a cell source for in vitro and in vivo angiogenesis [83, 84]. A limiting factor with these cells is that allogeneic MECs may induce adverse immunological responses [85]. EPCs are actually a fraction of haematopoietic stem cells found in bone marrow and peripheral blood [86]; hence, bone marrow cells are a valuable source of autologous and immunologically neutral stem cells for vasculogenesis and angiogenesis [87]. Although the phenotype of EPC has not been completely clarified yet, they are now thought to be positive for CD133, CD34 and VEGFR2 but negative for CD45 and CD14 cell surface markers [88]. Based upon these markers, EPCs could be selected out from peripheral blood or bone marrow. Although the number of EPCs in bone marrow or peripheral blood is very low, when isolated and expanded in vitro, EPCs can proliferate and be expanded for at least twenty populations in comparison with MECs [86].

10.5 Conclusions

Periosteum tissue engineering is to mimic the natural structure of periosteum to guide bone formation in a physiological manner. This chapter tried to provide current information about the periosteum engineering with the emphasis on the construction strategies, scaffold design and cells sources based upon the structure and functions of periosteum in bone development and defect healing. An appropriate construction strategy that combines proper cell sources and scaffolds may help produce a fully functional engineered periosteum substitute.

References

1. Parikh SN (2002) Bone graft substitutes in modern orthopedics. *Orthopedics* 25 (11):1301–1309; quiz 10-1
2. Kim SS, Sun Park M, Jeon O, Yong Choi C, Kim BS (2006) Poly(lactide-co-glycolide)/hydroxyapatite composite scaffolds for bone tissue engineering. *Biomaterials* 27 (8):1399–1409
3. Niu X, Fan Y, Liu X, Li X, Li P, Wang J, Sha Z, Feng Q (2011) Repair of bone defect in femoral condyle using microencapsulated chitosan, nanohydroxyapatite/collagen and poly (l-lactide)-based microsphere-scaffold delivery system. *Artif Organs* 35(7):E119–E128

4. Nishikawa M, Myoui A, Ohgushi H, Ikeuchi M, Tamai N, Yoshikawa H (2004) Bone tissue engineering using novel interconnected porous hydroxyapatite ceramics combined with marrow mesenchymal cells: quantitative and three-dimensional image analysis. *Cell Transplant* 13 (4):367–376
5. Yoshikawa H, Myoui A (2005) Bone tissue engineering with porous hydroxyapatite ceramics. *J Artif Organs* 8(3):131–136
6. Premaraj S, Mundy B, Parker-Barnes J, Winnard PL, Moursi AM (2005) Collagen gel delivery of Tgf-beta3 non-viral plasmid DNA in rat osteoblast and calvarial culture. *Orthod Craniofac Res* 8(4):320–322
7. Knothe Tate ML, Ritzman TF, Schneider E, Knothe UR (2007) Testing of a new one-stage bone-transport surgical procedure exploiting the periosteum for the repair of long-bone defects. *J Bone Joint Surg Am* 89(2):307–316
8. Zhang X, Awad HA, O’Keefe RJ, Guldberg RE, Schwarz EM (2008) A perspective: engineering periosteum for structural bone graft healing. *Clin Orthop Relat Res* 466(8):1777–1787
9. Allen MR, Hock JM, Burr DB (2004) Periosteum: biology, regulation, and response to osteoporosis therapies. *Bone* 35(5):1003–1012
10. Squier CA, Ghoneim S, Kremenak CR (1990) Ultrastructure of the periosteum from membrane bone. *J Anat* 171:233–239
11. Malizos KN, Papatheodorou LK (2005) The healing potential of the periosteum molecular aspects. *Injury* 36(Suppl 3):S13–S19
12. Asaumi K, Nakanishi T, Asahara H, Inoue H, Takigawa M (2000) Expression of neurotrophins and their receptors (TRK) during fracture healing. *Bone* 26(6):625–633
13. Ito Y, Fitzsimmons JS, Sanyal A, Mello MA, Mukherjee N, O’Driscoll SW (2001) Localization of chondrocyte precursors in periosteum. *Osteoarthr Cart* 9(3):215–223
14. Nakahara H, Bruder SP, Haynesworth SE, Holecck JJ, Baber MA, Goldberg VM, Caplan AI (1990) Bone and cartilage formation in diffusion chambers by subcultured cells derived from the periosteum. *Bone* 11(3):181–188
15. Fang J, Hall BK (1997) Chondrogenic cell differentiation from membrane bone periosteum. *Anat Embryol (Berl)* 196(5):349–362
16. Allen MR, Burr DB (2005) Human femoral neck has less cellular periosteum, and more mineralized periosteum, than femoral diaphyseal bone. *Bone* 36(2):311–316
17. Hutmacher DW, Sittinger M (2003) Periosteal cells in bone tissue engineering. *Tissue Eng* 9 (Suppl 1):S45–S64
18. Chanavaz M (1995) The periosteum: the “umbilical cord” of bone. Quantification of the blood supply of cortical bone of periosteal origin. *Rev Stomatol Chir Maxillofac* 96(4):262–267
19. Yang Y (2009) Skeletal morphogenesis during embryonic development. *Crit Rev Eukaryot Gene Expr* 19(3):197–218
20. Chung UL, Kawaguchi H, Takato T, Nakamura K (2004) Distinct osteogenic mechanisms of bones of distinct origins. *J Orthop Sci* 9(4):410–414
21. Shapiro F (2008) Bone development and its relation to fracture repair. The role of mesenchymal osteoblasts and surface osteoblasts. *Eur Cell Mater* 15:53–76
22. Peters A, Schell H, Bail HJ, Hannemann M, Schumann T, Duda GN, Lienau J (2010) Standard bone healing stages occur during delayed bone healing, albeit with a different temporal onset and spatial distribution of callus tissues. *Histol Histopathol* 25(9):1149–1162
23. Dimitriou R, Tsiridis E, Giannoudis PV (2005) Current concepts of molecular aspects of bone healing. *Injury* 36(12):1392–1404
24. Engdahl E, Ritsila V, Uddstromer L (1978) Growth potential of cranial suture bone autograft. II. An experimental microscopic investigation in young rabbits. *Scand J Plast Reconstr Surg* 12 (2):125–129
25. O’Driscoll SW, Fitzsimmons JS (2000) The importance of procedure specific training in harvesting periosteum for chondrogenesis. *Clin Orthop Relat Res* 380:269–278

26. O'Driscoll SW, Salter RB (1986) The repair of major osteochondral defects in joint surfaces by neochondrogenesis with autogenous osteoperiosteal grafts stimulated by continuous passive motion. An experimental investigation in the rabbit. *Clin Orthop Relat Res* 208:131–140
27. O'Driscoll SW, Marx RG, Fitzsimmons JS, Beaton DE (1999) Method for automated cartilage histomorphometry. *Tissue Eng* 5(1):13–23
28. Wakitani S, Yamamoto T (2002) Response of the donor and recipient cells in mesenchymal cell transplantation to cartilage defect. *Microsc Res Tech* 58(1):14–18
29. Uddstromer L (1978) The osteogenic capacity of tubular and membranous bone periosteum. A qualitative and quantitative experimental study in growing rabbits. *Scand J Plast Reconstr Surg* 12(3):195–205
30. Uddstromer L, Ritsila V (1979) Healing of membranous and long bone defects. An experimental study in growing rabbits. *Scand J Plast Reconstr Surg* 13(2):281–287
31. Oni OO, Gregg PJ (1991) An investigation of the contribution of the extraosseous tissues to the diaphyseal fracture callus using a rabbit tibial fracture model. *J Orthop Trauma* 5(4):480–484
32. Oni OO, Stafford H, Gregg PJ (1992) A study of diaphyseal fracture repair using tissue isolation techniques. *Injury* 23(7):467–470
33. Neel M (2003) The use of a periosteal replacement membrane for bone graft containment at allograft-host junctions after tumor resection and reconstruction with bulk allograft. *Orthopedics* 26(5 Suppl):s587–s589
34. Jegoux F, Goyenvalle E, Cognet R, Malard O, Moreau F, Daculsi G, Aguado E (2010) Mandibular segmental defect regenerated with macroporous biphasic calcium phosphate, collagen membrane, and bone marrow graft in dogs. *Arch Otolaryngol Head Neck Surg* 136(10):971–978
35. Yonamine Y, Matsuyama T, Sonomura T, Takeuchi H, Furuichi Y, Uemura M, Izumi Y, Noguchi K (2010) Effectable application of vascular endothelial growth factor to critical sized rat calvaria defects. *Oral Surg Oral Med Oral Pathol Oral Radiol Endod* 109(2):225–231
36. Okafuji N, Shimizu T, Watanabe T, Kimura A, Kurihara S, Furusawa K, Hasegawa H, Kawakami T (2006) Tissue reaction to poly (lactic-co-glycolic acid) copolymer membrane in rhBMP used rabbit experimental mandibular reconstruction. *Eur J Med Res* 11(9):394–396
37. Ma D, Yao H, Tian W, Chen F, Liu Y, Mao T, Ren L (2011) Enhancing bone formation by transplantation of a scaffold-free tissue-engineered periosteum in a rabbit model. *Clin Oral Implants Res* 22:1193–1199
38. Ouyang HW, Cao T, Zou XH, Heng BC, Wang LL, Song XH, Huang HF (2006) Mesenchymal stem cell sheets revitalize nonviable dense grafts: implications for repair of large-bone and tendon defects. *Transplantation* 82(2):170–174
39. Warnke PH, Douglas T, Sivathanan S, Wiltfang J, Springer I, Becker ST (2009) Tissue engineering of periosteal cell membranes in vitro. *Clin Oral Implants Res* 20(8):761–766
40. Schonmeyer B, Clavin N, Avraham T, Longo V, Mehrara BJ (2009) Synthesis of a tissue-engineered periosteum with acellular dermal matrix and cultured mesenchymal stem cells. *Tissue Eng Part A* 15(7):1833–1841
41. Guo HG, Yao FL, Ma XL, Yao KD (2008) An experimental study on rabbit's radial bone defect healed by application of mimetic periosteum with tissue-engineered bone. *Zhonghua Zheng Xing Wai Ke Za Zhi* 24(1):63–67
42. Fan W, Crawford R, Xiao Y (2010) Enhancing in vivo vascularized bone formation by cobalt chloride-treated bone marrow stromal cells in a tissue engineered periosteum model. *Biomaterials* 31(13):3580–3589
43. Koob S, Torio-Padron N, Stark GB, Hannig C, Stankovic Z, Finkenzeller G (2011) Bone formation and neovascularization mediated by mesenchymal stem cells and endothelial cells in critical-sized calvarial defects. *Tissue Eng Part A* 17(3-4):311–321
44. Zhao L, Zhao J, Wang S, Xia Y, Liu J, He J, Wang X (2011) Evaluation of immunocompatibility of tissue-engineered periosteum. *Biomed Mater* 6(1):015005

45. Hattori K, Yoshikawa T, Takakura Y, Aoki H, Sonobe M, Tomita N (2005) Bio-artificial periosteum for severe open fracture—an experimental study of osteogenic cell/collagen sponge composite as a bio-artificial periosteum. *Biomed Mater Eng* 15(3):127–136
46. Zhang KG, Zeng BF, Zhang CQ (2005) Periosteum construction in vitro by small intestinal submucosa combined with bone marrow mesenchymal stem cell. *Zhonghua Wai Ke Za Zhi* 43(24):1594–1597
47. Fan W, Crawford R, Xiao Y (2008) Structural and cellular differences between metaphyseal and diaphyseal periosteum in different aged rats. *Bone* 42(1):81–89
48. Seeman E (2003) Periosteal bone formation—a neglected determinant of bone strength. *N Engl J Med* 349(4):320–323
49. Augustin G, Antabak A, Davila S (2007) The periosteum. Part 1: anatomy, histology and molecular biology. *Injury* 38(10):1115–1130
50. Li D, Xia YN (2004) Electrospinning of nanofibers: reinventing the wheel? *Adv Mater* 16(14):1151–1170
51. Reneker DH, Yarin AL, Fong H, Koombhongse S (2000) Bending instability of electrically charged liquid jets of polymer solutions in electrospinning. *J Appl Phys* 87(9):4531–4547
52. Pham QP, Sharma U, Mikos AG (2006) Electrospinning of polymeric nanofibers for tissue engineering applications: a review. *Tissue Eng* 12(5):1197–1211
53. Han D, Gouma PI (2006) Electrospun bioscaffolds that mimic the topology of extracellular matrix. *Nanomedicine* 2(1):37–41
54. Schindler M, Ahmed I, Kamal J, Nur-E-Kamal A, Grafe TH, Chung HY, Meiners S (2005) A synthetic nanofibrillar matrix promotes in vivo-like organization and morphogenesis for cells in culture. *Biomaterials* 26(28):5624–5631
55. Ekaputra AK, Prestwich GD, Cool SM, Huttmacher DW (2008) Combining electrospun scaffolds with electrosprayed hydrogels leads to three-dimensional cellularization of hybrid constructs. *Biomacromolecules* 9(8):2097–2103
56. Li WJ, Tuli R, Okafor C, Derfoul A, Danielson KG, Hall DJ, Tuan RS (2005) A three-dimensional nanofibrous scaffold for cartilage tissue engineering using human mesenchymal stem cells. *Biomaterials* 26(6):599–609
57. Yoshimoto H, Shin YM, Terai H, Vacanti JP (2003) A biodegradable nanofiber scaffold by electrospinning and its potential for bone tissue engineering. *Biomaterials* 24(12):2077–2082
58. He W, Ma Z, Yong T, Teo WE, Ramakrishna S (2005) Fabrication of collagen-coated biodegradable polymer nanofiber mesh and its potential for endothelial cells growth. *Biomaterials* 26(36):7606–7615
59. Jin HJ, Chen JS, Karageorgiou V, Altman GH, Kaplan DL (2004) Human bone marrow stromal cell responses on electrospun silk fibroin mats. *Biomaterials* 25(6):1039–1047
60. Min BM, Lee G, Kim SH, Nam YS, Lee TS, Park WH (2004) Electrospinning of silk fibroin nanofibers and its effect on the adhesion and spreading of normal human keratinocytes and fibroblasts in vitro. *Biomaterials* 25(7-8):1289–1297
61. Mo XM, Xu CY, Kotaki M, Ramakrishna S (2004) Electrospun P(LLA-CL) nanofiber: a biomimetic extracellular matrix for smooth muscle cell and endothelial cell proliferation. *Biomaterials* 25(10):1883–1890
62. Shin HJ, Lee CH, Cho IH, Kim YJ, Lee YJ, Kim IA, Park KD, Yui N, Shin JW (2006) Electrospun PLGA nanofiber scaffolds for articular cartilage reconstruction: mechanical stability, degradation and cellular responses under mechanical stimulation in vitro. *J Biomater Sci Polym Ed* 17(1-2):103–119
63. Venugopal JR, Zhang YZ, Ramakrishna S (2006) In vitro culture of human dermal fibroblasts on electrospun polycaprolactone collagen nanofibrous membrane. *Artif Organs* 30(6):440–446
64. Zhang Y, Ouyang H, Lim CT, Ramakrishna S, Huang ZM (2005) Electrospinning of gelatin fibers and gelatin/PCL composite fibrous scaffolds. *J Biomed Mater Res B Appl Biomater* 72(1):156–165

65. Kidoaki S, Kwon IK, Matsuda T (2005) Mesoscopic spatial designs of nano- and microfiber meshes for tissue-engineering matrix and scaffold based on newly devised multilayering and mixing electrospinning techniques. *Biomaterials* 26(1):37–46
66. Nam J, Huang Y, Agarwal S, Lannutti J (2007) Improved cellular infiltration in electrospun fiber via engineered porosity. *Tissue Eng* 13(9):2249–2257
67. Pham QP, Sharma U, Mikos AG (2006) Electrospun poly(epsilon-caprolactone) microfiber and multilayer nanofiber/microfiber scaffolds: characterization of scaffolds and measurement of cellular infiltration. *Biomacromolecules* 7(10):2796–2805
68. Eichhorn SJ, Sampson WW (2005) Statistical geometry of pores and statistics of porous nanofibrous assemblies. *J R Soc Interface* 2(4):309–318
69. Sorrell JM, Baber MA, Caplan AI (2007) A self-assembled fibroblast-endothelial cell co-culture system that supports in vitro vasculogenesis by both human umbilical vein endothelial cells and human dermal microvascular endothelial cells. *Cells Tissues Organs* 186(3):157–168
70. Oberringer M, Meins C, Bubel M, Pohlemann T (2007) A new in vitro wound model based on the co-culture of human dermal microvascular endothelial cells and human dermal fibroblasts. *Biol Cell* 99(4):197–207
71. Black AF, Berthod F, L'Heureux N, Germain L, Auger FA (1998) In vitro reconstruction of a human capillary-like network in a tissue-engineered skin equivalent. *FASEB J* 12(13):1331–1340
72. Elbjearami WM, West JL (2006) Angiogenesis-like activity of endothelial cells co-cultured with VEGF-producing smooth muscle cells. *Tissue Eng* 12(2):381–390
73. Rouwkema J, De Boer J, Van Blitterswijk CA (2006) Endothelial cells assemble into a 3-dimensional prevascular network in a bone tissue engineering construct. *Tissue Eng* 12(9):2685–2693
74. Bianco P, Riminucci M, Gronthos S, Robey PG (2001) Bone marrow stromal stem cells: nature, biology, and potential applications. *Stem Cells* 19(3):180–192
75. Bianco P, Kuznetsov SA, Riminucci M, Gehron Robey P (2006) Postnatal skeletal stem cells. *Methods Enzymol* 419:117–148
76. Mosna F, Sensebe L, Krampfer M (2010) Human bone marrow and adipose tissue mesenchymal stem cells: a user's guide. *Stem Cells Dev* 19(10):1449–1470
77. Reyes M, Lund T, Lenvik T, Aguiar D, Koodie L, Verfaillie CM (2001) Purification and ex vivo expansion of postnatal human marrow mesodermal progenitor cells. *Blood* 98(9):2615–2625
78. Lucarelli E, Donati D, Cenacchi A, Fornasari PM (2004) Bone reconstruction of large defects using bone marrow derived autologous stem cells. *Transfus Apher Sci* 30(2):169–174
79. Mastrogiacomo M, Papadimitropoulos A, Cedola A, Peyrin F, Giannoni P, Pearce SG, Alini M, Giannini C, Guagliardi A, Cancedda R (2007) Engineering of bone using bone marrow stromal cells and a silicon-stabilized tricalcium phosphate bioceramic: evidence for a coupling between bone formation and scaffold resorption. *Biomaterials* 28(7):1376–1384
80. Estrela C, Alencar AH, Kitten GT, Vencio EF, Gava E (2011) Mesenchymal stem cells in the dental tissues: perspectives for tissue regeneration. *Braz Dent J* 22(2):91–98
81. Lin CS, Xin ZC, Deng CH, Ning H, Lin G, Lue TF (2010) Defining adipose tissue-derived stem cells in tissue and in culture. *Histol Histopathol* 25(6):807–815
82. Gassling V, Douglas T, Warnke PH, Acil Y, Wiltfang J, Becker ST (2010) Platelet-rich fibrin membranes as scaffolds for periosteal tissue engineering. *Clin Oral Implants Res* 21(5):543–549
83. Koch S, Yao C, Grieb G, Prevel P, Noah EM, Steffens GC (2006) Enhancing angiogenesis in collagen matrices by covalent incorporation of VEGF. *J Mater Sci Mater Med* 17(8):735–741
84. Sarkar S, Lee GY, Wong JY, Desai TA (2006) Development and characterization of a porous micro-patterned scaffold for vascular tissue engineering applications. *Biomaterials* 27(27):4775–4782

85. Shepherd BR, Enis DR, Wang F, Suarez Y, Pober JS, Schechner JS (2006) Vascularization and engraftment of a human skin substitute using circulating progenitor cell-derived endothelial cells. *FASEB J* 20(10):1739–1741
86. Reyes M, Dudek A, Jahagirdar B, Koodie L, Marker PH, Verfaillie CM (2002) Origin of endothelial progenitors in human postnatal bone marrow. *J Clin Invest* 109(3):337–346
87. Zisch AH (2004) Tissue engineering of angiogenesis with autologous endothelial progenitor cells. *Curr Opin Biotechnol* 15(5):424–429
88. Ahrens I, Domeij H, Topcic D, Haviv I, Merivirta RM, Agrotis A, Leitner E, Jowett JB, Bode C, Lappas M, Peter K (2011) Successful in vitro expansion and differentiation of cord blood derived CD34+ cells into early endothelial progenitor cells reveals highly differential gene expression. *PLoS One* 6(8):e23210

Chapter 11

Characterisation of Hydrogel Scaffolds Under Compression

J. Tong, Y.-H. Hsu, K. Madi, A. Cossey, and A. Au

Abstract Although a variety of scaffolds have been developed in recent years for a range of applications, the repair of load-bearing tissues, such as articular cartilage in the knee, is still in its infancy due to the exceptional demands on mechanical strength and stiffness. Unfortunately, rigorous *in vitro* mechanical characterisation has often been superseded by *in vivo* testing in animals, where the loading scenarios often bear little resemblance to those in human, which has significantly restricted the potential range of clinical applications. A comprehensive mechanical characterisation is essential if scaffolds are to be used for load-bearing applications. In this chapter, we report the characterisation of viscoelastic behaviour of hydrogel scaffolds. The key factors, including the effects of constraint, strain rate and sample microstructure, on the mechanical properties of a hydrogel scaffold will be investigated. Some of the latest techniques such as micro-CT imaging, *in situ* image-guided failure assessment and digital volume correlation (DVC) will be explored in the characterisation of the hydrogel scaffold under uniaxial compression.

Keywords Cartilage • Bone • Scaffold • Compression • Mechanical properties • μ CT • DVC

11.1 Introduction

As surgical techniques and medical knowledge continue to advance, there is an increasing demand for engineered scaffolds that act as permanent or temporary support structures for the ingrowth of new tissues. Load-bearing applications, such

J. Tong (✉) • Y.-H. Hsu • K. Madi
School of Engineering, University of Portsmouth, Anglesea Building, Anglesea Road,
Portsmouth PO1 3DJ, UK
e-mail: jie.tong@port.ac.uk

A. Cossey
Spire Portsmouth Hospital, Portsmouth PO9 5NP, UK

A. Au
Smith & Nephew, 150 Minuteman Rd, Andover, MA 01810, USA

as repair of articular cartilage in the knee, require that the scaffolds have the necessary mechanical strength and stiffness close to those of native tissues.

Articular cartilage is a smooth, shock-absorbent material on the surface of articular joints [1]. It is responsible for providing lubrication and compressive stiffness to the joint during articulation while responding viscoelastically to mechanical loading [2]. Articular cartilage is difficult to treat following injuries, as it neither expresses the typical wound-healing phenotype observed in many other tissues nor spontaneously regenerates [3, 4]. Unlike highly vascular tissues such as the skin and bone, articular cartilage has a low cell density, leading to a poor capacity for self repair [5].

The use of biodegradable scaffolds to repair articular cartilage has been studied by many [6, 7]. Poly(lactide-co-glycolide)s have frequently been used for tissue engineering applications attributable to their good biodegradability, reasonable biocompatibility, mechanical strength and easy producibility [8]. Repair of osteochondral defects involves two types of distinct tissues, articular cartilage and subchondral bone. One possible solution may be the development of engineered osteochondral constructs [9–13]. A synthetic scaffold is resorbable hydrophilic made of a patented composite material with poly(lactide-co-glycolide), calcium sulphate and poly(glycolide) fibres [14] and designed to replace worn-out cartilage surfaces in order to restore mobility and relieve joint pain. It is formulated to be porous and resorbable to allow ingrowth of new healing tissues and to be suitable for filling osteochondral defects in the form of cylindrical plugs. These scaffolds have two layers; the bottom layer is designed to imitate the morphology of trabecular bone and the top layer to simulate articular cartilage. Although some clinical applications have been reported [15–18], there is a lack of information on the mechanical performance of the implant under physiological loading conditions. Preclinical assessments based on *in vitro* experiments under simulated physiological loading conditions are the necessary first steps towards a successful clinical implementation of the implant for knee repair purposes.

In this chapter, the monotonic and fatigue behaviour of the scaffold is examined under compression. Novel experimental techniques such as micro-CT imaging, *in situ* loading and digital volume correlation (DVC) have been utilised in the characterisation of strain distribution of the samples under uniaxial compression [19]. The results will hopefully provide a basic framework on the *in vitro* characterisation of synthetic scaffolds for load-bearing applications.

11.2 Background

A variety of biological and synthetic scaffolds have been developed for repair of articular cartilage and the underlying subchondral bone [10, 12–14, 20–27]. Bone and cartilage tissues exhibit viscoelastic behaviour, and the replacement scaffolds should have similar properties in order to maintain mechanical integrity with the surrounding tissues during physiological loading conditions. Synthetic scaffolds

often lack the physical and mechanical properties necessary to sustain long-term applications [2]. Although biocompatibility and bio-related issues have been studied widely, evaluation of mechanical properties has been an area of underdevelopment. Mechanical properties of scaffolds are often unreported; and for those reported, testing parameters and conditions vary greatly. Mechanical behaviour of cartilage/bone is known to vary with test conditions, such as strain rate, strain amplitudes and testing environment [28, 29]. This is a main challenge in the design of testing protocols of artificial scaffolds. Although a number of protocols have been used in the literature [12–14, 25, 30–40], a comparison between the results generated from different experimental procedures and protocols is difficult.

A range of strain rates has been used in the literature representative of the loading conditions experienced in the knee and hip. In compression tests, high strain rates have been shown to increase the measured elastic modulus [14, 30–37]. Lai et al. [34] reported an increase in compressive stiffness with strain rates from $3.3 \times 10^{-5}/s$ to $3.3 \times 10^{-4}/s$. Radin et al. [35] demonstrated that articular cartilage stiffness increased with strain rate over the range from $2.7 \times 10^{-3}/s$ to $0.124/s$. Carter et al. [33] analysed the influence of strain rate from $0.001/s$ to $10/s$ on the strength and the stiffness of trabecular bone specimens and found that both strength and modulus were approximately proportional to strain rate raised to the power of 0.06. Silyn-Roberts and Broom [36] conducted impact testing on cartilage-on-bone samples at a strain rate of $2.4 \times 10^3/s$ and showed that, at high strain rates, bone failures could occur without structural damage to the articular cartilage and that when failure did occur in the articular cartilage, the failure mode was more characteristic of a ‘brittle’ material.

A number of scaffolds and bones were tested in tension [26, 38, 39], which bears little resemblance to in vivo loading conditions experienced in the knee or hip. Most of compressive tests were carried out under unconfined loading conditions [12–14, 40], while confined configuration is more relevant to most in vivo loading conditions. In the confined tests reported, various clearances between the size of the specimen and the size of the confined chamber have been used, with some of them used smaller specimens [41], some used equal size [42, 43] and some used slightly larger specimens [44, 45]. Furthermore, the evaluation of the mechanical properties of scaffolds is rarely done under physiological conditions, i.e. in aqueous solution at $37^\circ C$. Mechanical properties of hydrated scaffold samples are known to be much lower than those of dry samples [13, 14, 21, 40].

Compression testing of hydrogel scaffolds was performed by Slivka et al. [14] to investigate the influence of physiological testing conditions, manufacturing methods, anisotropic properties caused by predominant fibre orientation, amounts of fibre reinforcement and viscoelasticity at a range of strain rates. Using the same testing modality, the mechanical properties of the scaffolds in physiological conditions were compared with those of articular cartilage from pig and goat. Most of these compressive tests were carried out under unconfined conditions. Moreover, stress relaxation (or creep) properties were often overlooked, despite that these are responsible for the time-dependent behaviour of scaffolds, which are most relevant to clinical applications.

Furthermore, human bone is subject to a variety of loading patterns during daily routine activities. A typical loading condition is repeated or cyclic loading as experienced in walking or running in daily life. Bone response under such loading conditions may be referred to as fatigue behaviour [46, 47]. Fatigue damage is a process of gradual mechanical degradation caused by repeated loading at stress or strain much lower than those required to fracture in a single application of force. As a result, damage due to cyclic loading is of significant interest for design and application of synthetic scaffolds. In a conventional fatigue test, specimens are subjected to a constant amplitude load till failure to determine the number of cycle to failure at a given load range. A number of studies based on this method have been published on the fatigue behaviour of bones [39, 48–60]. Some studies have also been carried out on synthetic biopolymers [61, 62]. A great number of samples may be needed to obtain the fatigue behaviour under variable stress amplitudes. Step-wise testing has since been introduced which would allow the generation of fatigue data with only a small number of samples [63, 64]. In stepwise tests, the samples are subject to loads with a range of amplitudes; in each, a number of cycles are allowed to elapse, thus providing an accelerated testing regime with increased volume of data at reduced test duration. One important parameter obtained from such tests is the evolution of secant modulus [51, 63, 65], which has been used as an indication to damage accumulation [60, 66].

Standard mechanical testing does not take into account the real morphology of the scaffold structure and complex physical phenomena such as strain localisation, which are important factors in dictating the mechanical response and damage evolution of the scaffold [67–70]. With the recent and rapid progress of microfocus computed tomography (μ CT), combined with the development of in situ experiments [67, 71, 72], digital volume correlation (DVC) has become a powerful tool to quantify deformation and failure modes of cellular materials [73–77]. Analysis of continuum level strain maps allows critical local strains to be identified thereby providing valuable information on design of scaffold microstructures. Few studies, however, have used this technique to investigate the mechanical behaviour of multiphase osteochondral scaffolds. Micro-CT images of a dual-layer osteochondral scaffold were obtained under compressive loading by Harley et al. [21]. Although the internal microstructure of the cartilaginous, interfacial and osseous regions of the scaffold was characterised, deformation of each layer was only estimated qualitatively from visual observation. In a recent study, Malekipour and co-workers [78] calculated the deformation of subchondral bone and articular cartilage in native osteochondral plugs from the observation of real-time micro-CT images, prior to and post compression. They showed evidence that the subchondral trabecular bone can absorb deformation energy during failure, thus protecting the articular cartilage from damage. Strain localisation often occurs in the trabecular bone [68, 70] and is likely to be the mechanism by which the energy is dissipated in the subchondral bone. If the bone phase of dual-layer osteochondral scaffolds has a similar morphology to that of trabecular bone, similar behaviour may be expected.

In what follows, the viscoelastic behaviour of a hydrogel scaffold is presented. Monotonic stress–strain curves were obtained under compression under simulated

typical physiological conditions to investigate the contribution of the bone layer on the overall viscoelastic behaviour, the effects of strain rate (walking/impact) and the effects of constraint (confined/unconfined). Preliminary multistep cyclic tests have been carried out on the bone samples to study the fatigue behaviour of the osteochondral scaffold under increasing compressive cyclic loading conditions. Damage development and failure modes of the scaffold were evaluated using image-guided failure analysis, together with the DVC method.

11.3 Mechanical Evaluation

11.3.1 Monotonic Testing

A hydrogel scaffold plug (Smith & Nephew), as shown in Fig. 11.1, was used for this study. The scaffold is made of a patented composite material with polylactide-co-glycolide, calcium sulphate and poly(glycolide) fibres [14]. The dual-layer design of the scaffold contains both cartilage (Scaffold C) and bone (Scaffold B) phases. The pores in the scaffold are interconnected to allow cell migration and

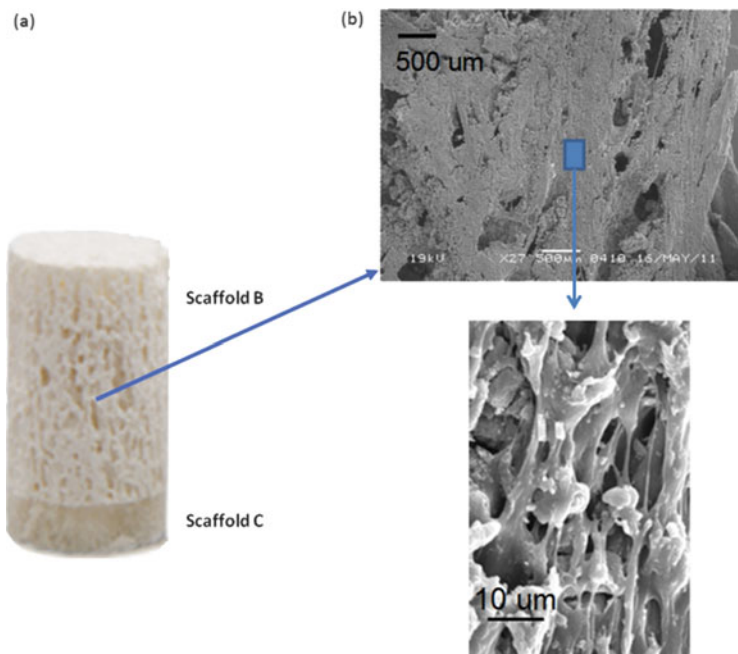


Fig. 11.1 (a) A hydrogel scaffold with a dual-layer structure: *top* layer, Scaffold B; *bottom* layer, Scaffold C. (b) Details of the scaffold structure containing fibres and calcium sulphate particles from SEM micrograph

extracellular matrix continuity. The diameter of the implant is about 11 mm, and the lengths of the cartilage and bone layers are $1.97 \text{ mm} \pm 0.22 \text{ mm}$ and $16.7 \text{ mm} \pm 0.34 \text{ mm}$, respectively, the latter taken at a ratio of 0.86 length over diameter [28, 33].

Monotonic tests were carried out on a servohydraulic testing machine (MTS Landmark® Servohydraulic Test System) equipped with an environmental chamber to which phosphate-buffered saline (PBS) solution was filled and controlled at a temperature of $37 \text{ }^\circ\text{C}$. The samples were soaked overnight prior to testing, and a cyclic preconditioning (ten cycles of compression at 0.008 strain, at a strain rate of 0.005/s, followed by unloading) was applied to eliminate residual stresses due to sample preparation and to achieve a steady-state mechanical response. The samples were loaded between two stainless steel loading platens. Smooth, impermeable platens were used in unconfined conditions, while a porous platen with a pore size of 300–600 μm (larger than the average pore size of the scaffolds $\sim 300 \mu\text{m}$ [79]) was selected under confined condition, as shown in Fig. 11.2. The diameter of the scaffolds was about $10.75 \pm 0.15 \text{ mm}$. The confining chamber was chosen slightly larger (10.98 mm). This small gap has the advantage to eliminate a potential friction between the top platen and the confining chamber [80, 81].

Monotonic tests were performed on the scaffold (dual layer) and Scaffold B (bone phase) specimens in unconfined and confined compression at two representative strain rates: walking (0.002/s) and impact (0.1/s) [33]. Engineering stress values were computed by dividing the reaction force by the initial area of each specimen. The compressive modulus of each specimen was taken to be the slope of the stress–strain curve in the most linear part of the pre-yield loading region. With the modulus defined in this manner, the initial small nonlinear behaviour due to surface irregularities of the specimen during contact with the platens is disregarded [33]. The compressive strength is defined as the peak stress to failure.

Stress–strain curves of the scaffold and Scaffold B specimens are presented in Figs. 11.3 and 11.4 for the selected conditions. All the curves exhibit typical foam-type behaviour, with a linear elastic region followed by a nonlinear yield plateau. The compressive moduli, calculated in the linear portion, are depicted in Fig. 11.5. The contribution of the bone layer on the overall viscoelastic behaviour, the effects

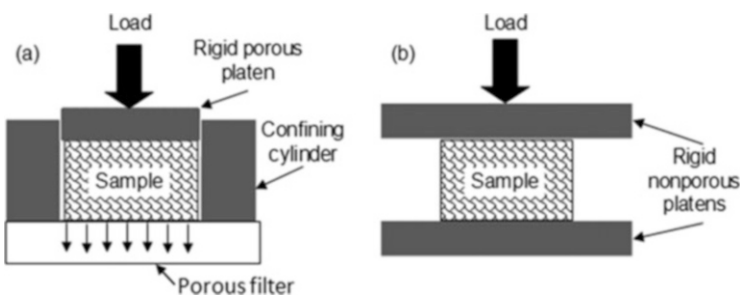
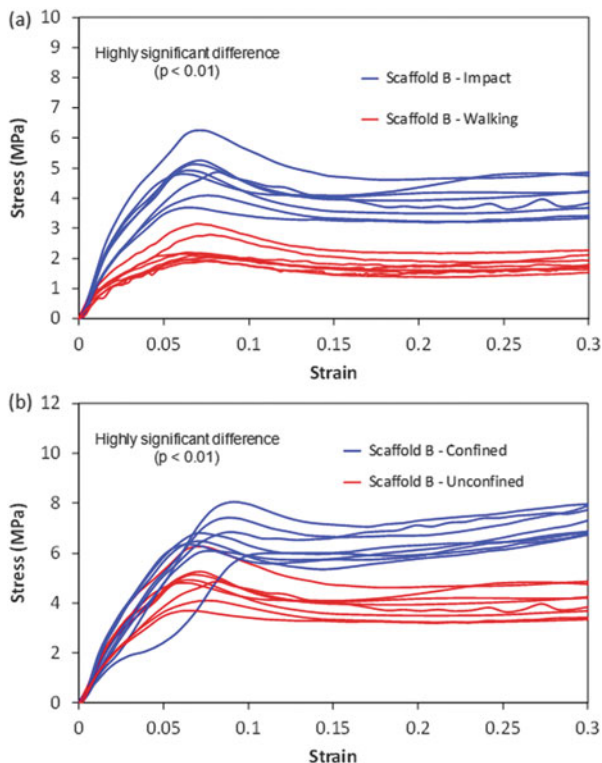


Fig. 11.2 Schematic of the experimental arrangements: (a) confined and (b) unconfined compression

Fig. 11.3 Stress–strain curves of Scaffold B obtained in PBS at 37 °C: (a) unconfined compression (walking vs. impact), (b) impact (confined vs. unconfined)



of strain rate (walking/impact) and confinement have been statistically investigated through the Student's T-test of the compressive modulus, as shown in Table 11.1.

The effects of confinement and strain rate on compressive modulus are highlighted. Higher yield strength and compressive modulus are obtained for Scaffold B and scaffold specimens when the strain rate is increased from walking to impact or when testing in a confined condition (vs. unconfined condition, except in walking for Scaffold B). For example, the average yield strength and modulus of Scaffold B specimens tested in the confined conditions during impact are 6.74 ± 0.69 MPa and 94.11 ± 6.45 MPa, respectively, while those tested during walking are 3.10 ± 0.82 MPa and 38.66 ± 9.84 MPa, respectively. Whatever the condition, a highly significant difference is observed for the effect of strain rate, while the effect of confinement varies from possible to significant difference (except for impact). The gap between the specimens and the confining chamber can reach up to 0.38 mm, which might explain why less 'highly significant difference' is observed for the effect of confinement. As illustrated in Fig. 11.3b, the difference between the confined and the unconfined stress–strain responses becomes more visible after 5 % strain. The effect of confinement on the compressive modulus is likely to be less significant for smaller diameter specimens. Except for the impact confined condition, no significant difference is observed between the

Fig. 11.4 Stress–strain curves of the scaffold obtained in PBS at 37 °C: (a) unconfined compression (impact vs. walking), (b) confined compression (impact vs. walking)

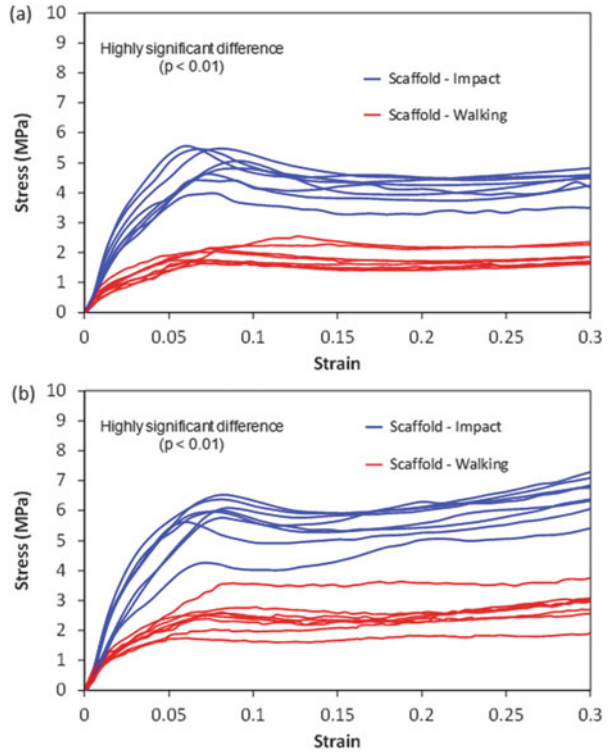
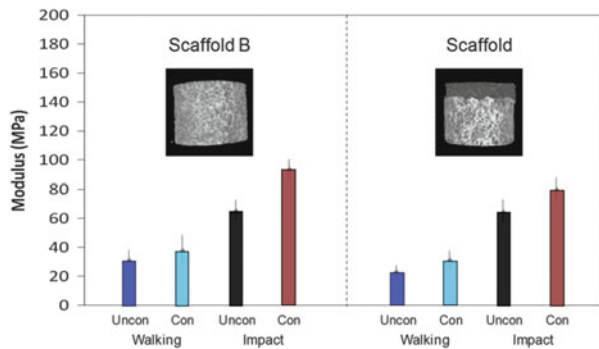


Fig. 11.5 Compressive moduli of Scaffold B and scaffold measured in PBS at 37 °C



stiffness of the bone layer (Scaffold B) and that of the dual layer (scaffold). Generally, the compressive moduli of Scaffold B are slightly higher (~20 %) than that of the scaffold.

Table 11.1 Student T-test results for compressive modulus of Scaffold B and scaffold measured under selected loading conditions

Confinement (uncon/con)	Scaffold B		Scaffold	
	Walking	Impact	Walking	Impact
	X	XXX	XX	XX
Strain rate (walking/impact)	TruFitB		TruFitB	
	Uncon	Con	Uncon	Con
	XXX	XXX	XXX	XXX
Scaffold B vs. scaffold	Walking		Impact	
	Uncon	Con	Uncon	Con
	X	X	O	XX

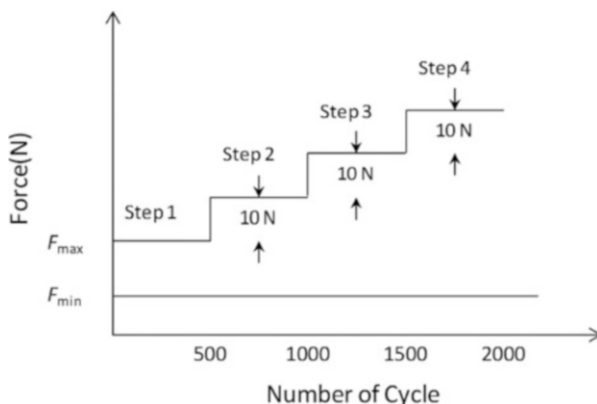
XXX highly significant difference ($P < 0.01$)

XX significant difference ($0.01 < P < 0.05$)

X highly significant difference ($0.05 < P < 0.1$)

O difference not established ($P > 0.1$)

Fig. 11.6 The loading scheme of a stepwise fatigue test ($F_{max} = 10$ N; $F_{min} = F_{preload} = 5$ N), following the protocol of Topolinski et al., 2011 [63]

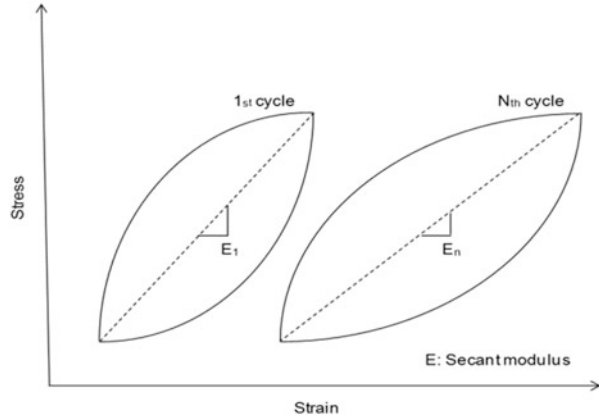


11.3.2 Fatigue Testing

Fatigue testing was carried out on a Bose ElectroForce 3200 Testing system equipped with an environmental chamber to which PBS solution was filled and controlled at a temperature of 37 °C. Each specimen was placed carefully at the centre of the platens inside the environmental chamber. During the testing, the specimens were unconstrained [63] between the platens of the testing machine as fixation of the specimen to the test platens may increase its stiffness [82]. Five specimens of Scaffold B (bone layer) were tested under load control [28, 48–50, 52, 53, 56, 57, 59, 63, 83–85] with a stepwise increase of maximum stress while keeping the minimum stress constant, following a testing protocol of Topolinski et al. [63].

A preload of 5 N was applied first to ensure good end contact, and this preload was subsequently kept constant as the minimum load throughout the test. The maximum load started from 10 N with a gain of 10 N at the successive steps, as shown in Fig. 11.6. The maximum load was kept constant during a period of

Fig. 11.7 Secant modulus (E_i) is defined as the stress range divided by the strain range at a given cycle i , which is determined by the slope of the line connecting the minimum and the maximum stress values of the cycle

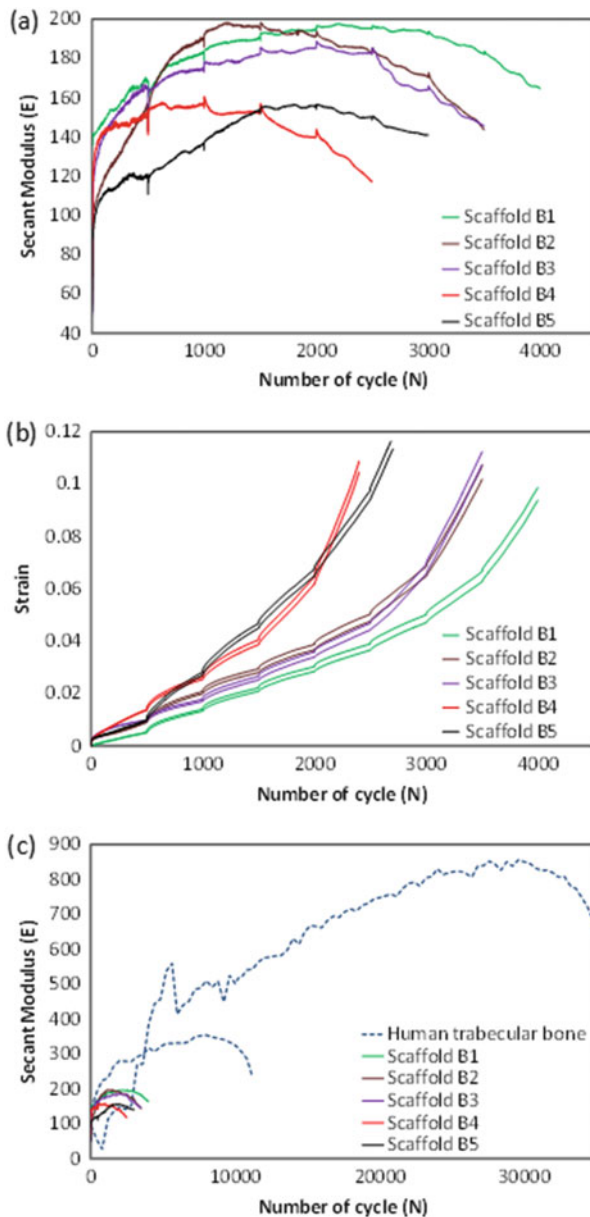


500 cycles and increased to the next level thereafter. The loading scheme was adopted from Topolinski et al. [63] to allow easy comparison with the results from the human trabecular bone [63]. The loading waveform was sinusoidal at a frequency of 1 Hz.

Engineering stress and strain were calculated by using the applied load, displacement and the original dimension of the specimens, where lateral deformation under compression was not considered. The changes in the secant modulus and the maximum and minimum strains with fatigue loading were recorded. The change in the secant modulus is taken as indicative of damage accumulation in the specimen [60, 66] in the fatigue studies of bones from the literature [39, 48, 51, 53–59, 63–65, 84]. The secant modulus at a given cycle was defined as $\Delta\sigma/\Delta\varepsilon = (\sigma_{\max} - \sigma_{\min}) / (\varepsilon_{\max} - \varepsilon_{\min})$, determined from the stress–strain curve. Figure 11.7 illustrates this as the slope of the line connecting the lowest and the highest point of a stress–strain loop. The secant modulus and strains were measured throughout the tests. The cyclic stress–strain curves were also compared with those obtained under the monotonic loading conditions.

The evolution of the secant modulus with cycles is shown in Fig. 11.8a for the five Scaffold B samples tested. In all the cases, it appears that an increase in secant modulus with cycle persisted for most of the loading steps, particularly the early ones. Only towards later at higher load levels, reductions in secant modulus become evident. The initial hardening seems to be somewhat unexpected, certainly in contrast to the continuing increase in the residual strain with cycle, as shown in Fig. 11.8b, where the maximum and the minimum compressive strains of the five samples are recorded. Interestingly, the samples with lower residual strains (B1, B2, B3) tend to have a higher secant modulus (Fig. 11.8a). Both maximum and minimum strains increased with the number of cycles during the entire test, and the gap between the maximum and the minimum strains is roughly constant for each sample, indicating that the strain range stays constant. In addition, the strain rate increases with the increase in the number of cycles. It is known that residual strain or cyclic creep plays an important role in material failure due to the

Fig. 11.8 (a) The evolution of secant modulus as a function of cycles for Scaffold B, (b) the development of the maximum and minimum strains with cycle and (c) the comparison of secant modulus of Scaffold B and human trabecular bone [63]



accumulated plastic deformation [60, 65]. Increase in strains with the number of cycles has been generally observed when testing bones under cyclic loading [57, 64], although increasing strain rate during the entire test was found in bovine trabecular bone [64]. Three stages of deformation during compressive fatigue tests have been reported for human trabecular bone [57], including a transient behaviour

characterised by a rapid increase of strain within the initial load cycles, a saturation of strain and an acceleration towards final catastrophic failure.

When the secant modulus of the Scaffold B specimens is compared with those of human trabecular bones [63], as shown in Fig. 11.8c, much lower secant modulus and total number of cycles to failure were obtained for the scaffold, although the patterns of evolution with cycle appear to be similar between the two. An initial increase in modulus has been observed for Scaffold B at most of the loading levels except the highest, which appears to be consistent with the observation in some of the reports [65, 86].

The stress–strain loops of the first cycles at the beginning of each fatigue loading step are presented in Fig. 11.9a. Each centre of the loops was moved to the origin (0,0), and then the points at the top of each loop were linked to form the initial cyclic stress–strain curve. Figure 11.9b shows the final cyclic stress–strain curve which was obtained similarly using the loops of the final cycles at the end of each loading step. These cyclic stress–strain loops at the first and the final cycles do not appear to differ significantly (c.f. Fig. 11.10, CSS_1 and CSS_f), suggesting that the stress softening may not be significant. Figure 11.10 shows a comparison of cyclic and monotonic stress–strain curves for a typical specimen of Scaffold B. Here LS1_0 to LS5_0 are monotonic stress–strain curves, while CSS_1 and CSS_f are the first and the final cyclic stress–strain curves. The monotonic curves are the

Fig. 11.9 Cyclic stress–strain responses: (a) loops of first cycles at the beginning of each loading step; (b) loops of the final cycles at the end of each loading step

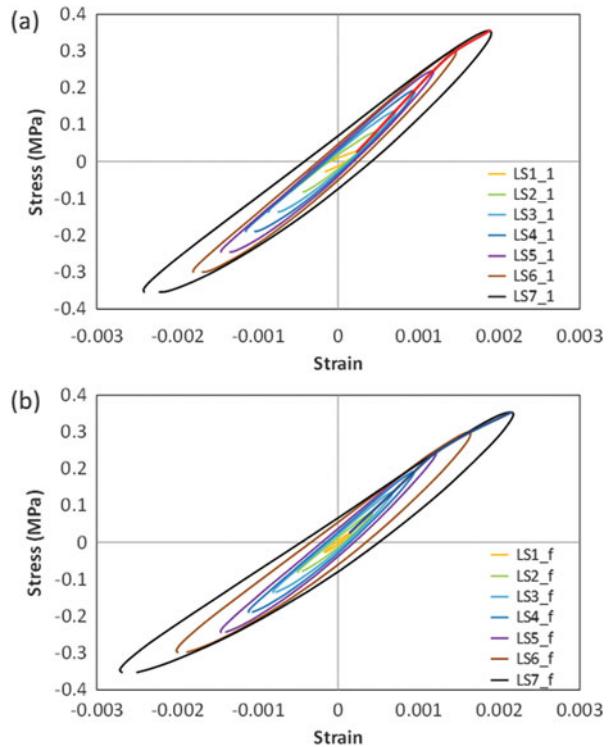


Fig. 11.10 Comparison of the cyclic and the monotonic stress–strain curves of a typical sample

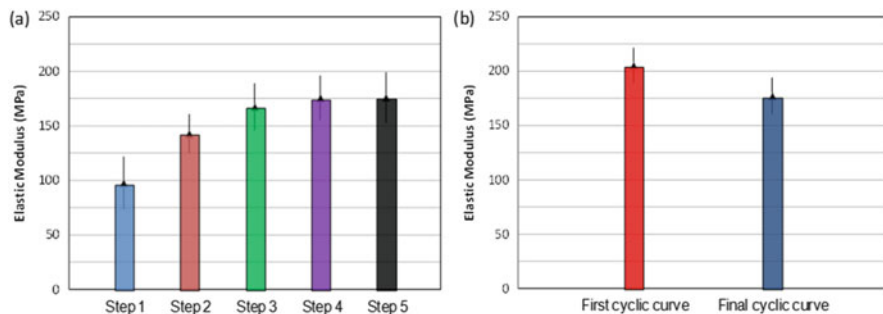
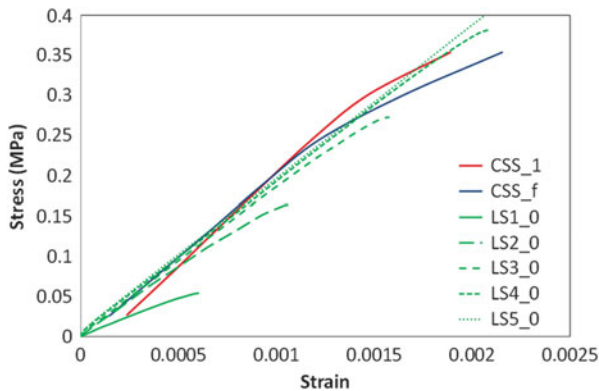


Fig. 11.11 The elastic modulus of (a) monotonic curves and (b) cyclic stress–strain curves

loading parts of a stress–strain curve at the beginning of each loading step. The slopes of these curves signify the modulus of elasticity.

A comparison of the mean elastic modulus of the stress–strain curves is shown in Fig. 11.11. The elastic modulus of monotonic stress–strain curves increases with the number of loading steps, and the moduli of the cyclic curves are generally higher than those of monotonic counterparts, suggesting stress hardening, consistent with the trend shown in Fig. 11.8a. However, the elastic modulus of first cyclic stress–strain curve is higher than that of final cyclic stress–strain curve, suggesting damage accumulation due to fatigue.

11.4 Damage Assessment

Studies on strain localisation and damage evolution of biological tissues and bio-materials are important to biomedical engineering applications of joint repair and replacement materials. With the recent and rapid progress of microfocus computed tomography (μ CT, Fig. 11.12), combined with in situ experiments and digital volume correlation (DVC), powerful tools are available to investigate the

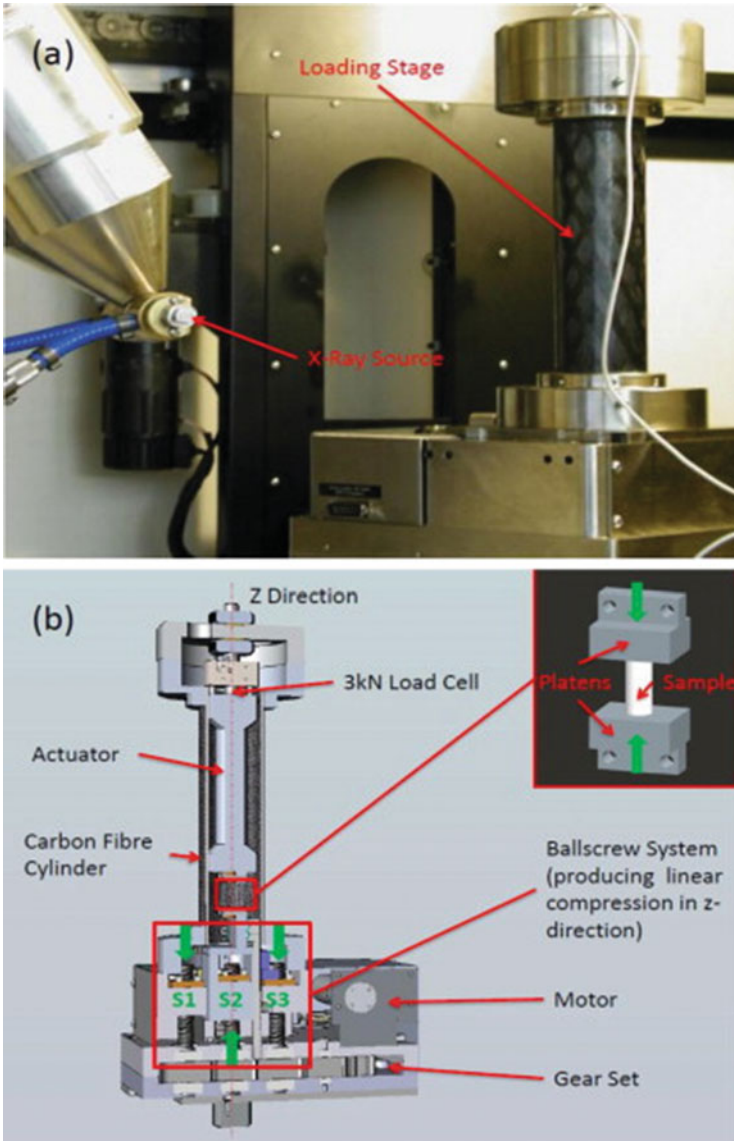


Fig. 11.12 (a) The micromechanical testing device is positioned in the micro-CT chamber, and (b) the linear compression applied to the sample is generated through a ball screw system that drives the jaws symmetrically in opposite directions (Reprinted with permission from Ref. [19]. Copyright © 2013 Elsevier)

deformation and failure modes of cellular materials. In this section, a 3D full-field study of strains and failure mechanisms are presented in the dual-layer scaffold (Fig. 11.1) under uniaxial compression.

11.4.1 Characterisation of 3D Morphology

The 3D morphology of the scaffold was characterised using micro-computed tomography (CT XRay101 Inspection System, Metris XTek Systems Ltd, Fig. 11.12a). The scanner was set to a voltage of 60 kV, a current of 51 μ A and an isotropic voxel size of 23 μ m. The volume images of the bone and the cartilage phases were cleaned by applying a 3D median filter and binarised to separate the pores from the struts. 3D morphometric indices were computed using the bone image analysis plug-in, BoneJ [87], as implemented in ImageJ. Morphological parameters of the scaffold (Fig. 11.1) were obtained and shown in Table 11.2. The mean strut thickness and mean strut spacing of the bone phase are about twice higher than those of the cartilage phase. A predominant plate-like structure is found for the bone phase (SMI~0.74–0.88), while a mixture of plate-like and rod-like structures is obtained for the cartilage phase (SMI~1.41–1.83). The morphometric indices of the bone phase compare well with those obtained from human bones extracted from proximal tibia [88] and distal femur [89].

11.4.2 In Situ Testing and Time-Lapsed Imaging

A novel customised micromechanical loading device (Deben Ltd., UK), equipped with a 3 kN miniature load cell, was used to load the sample in the micro-CT

Table 11.2 Morphometric values obtained from μ CT images of the specimens. The results obtained on the bone phase are compared with the values obtained on human bones extracted from the proximal tibia [88] and distal femur [89]

	BV/TV	Tb.th (mm)	Tb.sp (mm)	SMI
Bone phase alone (sample 1)	0.33	0.2 \pm 0.07	0.68 \pm 0.53	0.82
Bone phase alone (sample 2)	0.33	0.17 \pm 0.05	0.59 \pm 43	0.88
Dual layer (model 1)				
Bone phase with the dual layer	0.34	0.17 \pm 0.05	0.45 \pm 0.24	0.86
Cartilage phase with the dual layer	0.42	0.13 \pm 0.06	0.25 \pm 0.13	1.83
Dual layer (model 2)				
Bone phase with the dual layer	0.41	0.19 \pm 0.06	0.40 \pm 0.22	0.74
Cartilage phase with the dual layer	0.40	0.12 \pm 0.03	0.24 \pm 0.12	1.41
Proximal tibia [88]	0.28 \pm 0.03	0.22 \pm 0.01	0.55 \pm 0.05	0.70 \pm 0.45
Distal femur [89]	0.33 \pm 0.04	0.24 \pm 0.02	0.48 \pm 0.04	/

chamber (Nikon XTH-225 X-ray & CT Inspection System). The loading device is shown in Fig. 11.12b and it has been used in the previous studies [19, 90]. The loading stage uses an analogue resistive extensometer with a 16-bit AD converter for accurate elongation measurement, achieving a nominal strain resolution of $15 \mu\epsilon$.

The effect of bone thickness on the local strain fields was studied using material models with two thicknesses: 16.7 mm for model 1 and 8 mm for model 2. The lengths of the cartilage phase are similar in both models and measured as 1.97 mm and 2.19 mm, respectively. The local strain fields were also studied in the bone phase. The specimens were prepared by separating them manually from the cartilage phase using a circular saw. The lengths of the bone samples are 16.01 mm (sample 1) and 16.33 mm (sample 2). The diameter of all samples is 11 mm.

Before testing, the ends of the bone specimens were embedded about 1.5 mm into custom-made stainless steel end-caps using acrylic resin to minimise the end artefacts [67, 68]. The gauge length after the fixation was approximately 13 mm, thus achieving an aspect ratio of 1.18:1. For the dual-layer specimens, the end-caps were only glued to the edge of the bone phase due to the limited thickness of the cartilage phase. The lengths of the bone phase were about 15.2 mm and 6.5 mm, achieving an aspect ratio of 1.38:1 and 0.59:1, respectively.

In situ testing was carried out with a preload of 5 N applied, and a complete scan was performed using the scanner settings cited above. The specimens were then stepwise compressed along the longitudinal direction (OZ) to about 0.4 mm (yield) and about 1.1 mm (post-yield softening), at a constant displacement rate of 0.01 mm/s (see Figs. 11.13 and 11.14), representative of slow to normal walking loading conditions (0.001–0.002/s).

11.4.3 Digital Volume Correlation (DVC)

The DVC method was used to compute the 3D displacement and strain fields from a pair of images, namely, a reference reconstructed image obtained in the preloaded stage and a deformed image obtained after compressing the specimens to 0.4-mm displacement. The correlation algorithm, implemented into the LaVision DVC software (Davis, 8.0.1, LaVision GmbH, Goettingen, Germany), uses the fast Fourier transform (FFT) for computing cross-correlation of subvolumes.

Strain maps of the axial strain, ϵ_{zz} , and shear strain in the xz plane, ϵ_{xz} , in the bone phase along the specimen are illustrated in Fig. 11.15a. Evident axial strain localisation occurred in the bands oriented horizontally and more preferentially along the 45 direction. Locally, the axial strains may reach up to 10%, which are about 4–6 times the mean strains (Table 11.3). Elsewhere, the strains seem to be lower and more homogeneously distributed. Clockwise rotation (shear) is found precisely in these bands versus counterclockwise rotation elsewhere. These strain distributions are consistent with the failure mechanisms in the microstructure (Fig. 11.13a). At the specimen level, compression and rotation of the cells are

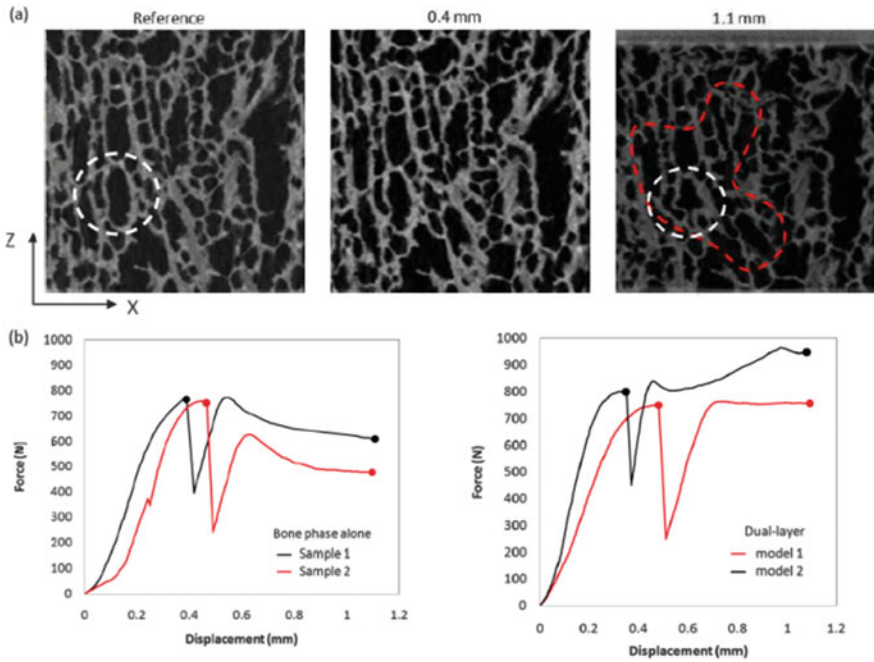


Fig. 11.13 (a) 2D sections extracted at the core of the bone phase representing the reference and the deformed morphologies (0.4- and 1.1-mm displacements) of the specimen. Bending of plate-like struts is evident after 1.1-mm displacement (marked in *white*); (b) force versus displacement curves for the bone and the dual-layer specimens

observed in the zones of high strains after compressing the sample to 1.1 mm (marked in red in Fig. 11.13a), while bending of plate-like struts occurred at the microstructural level (marked in white in Fig. 11.13a).

Strain fields in the dual layer are described as follows. The mean axial strain values are given in Table 11.3. It seems that the macroscopic bone strains are closer to the responses of the bone phase and the interface than that of the cartilage phase. The bone phase deforms about twice more than the cartilage phase (2.48 and 1.9 for models 1 and 2, respectively) and about 1.5 times more than the interface (1.46 and 1.24 for models 1 and 2, respectively). The strain of the bone phase within the dual layer is also very close to that of the bone phase. The analysis of the axial and the shear strain maps reveals the localised strain bands in the bone, similar to those obtained in the bone phase (see Figs. 11.15, 11.16 and 11.17). The histograms of the axial strain component look also similar (Fig. 11.15b). All the curves are bell-shaped and asymmetric with respect to the mean value, a consequence of strain localisation.

For model 1, the bands of high strain extend up to the upper interface without crossing the cartilage phase (Figs. 11.16 and 11.18a). The strains are heterogeneously distributed in the interface (Fig. 11.18a) with the maximal compressive strains of about 6–10%. On the other hand, the strains in the cartilage phase are

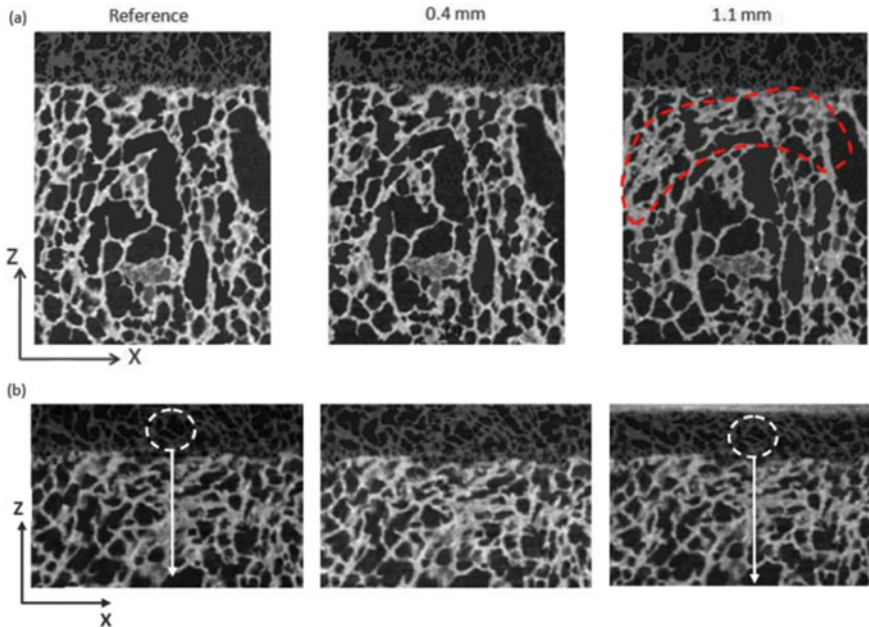


Fig. 11.14 2D sections extracted at the core of the dual-layer representing the reference and deformed morphologies (0.4- and 1.1-mm displacements) of the specimens: (a) model 1; (b) model 2. Buckling of rod-like struts is evident after 1.1-mm displacement (marked in white)

relatively homogeneously distributed (Fig. 11.16), with the maximal compressive strains of about 2%. Reducing by half the bone phase thickness (model 2) leads to more localised strains in both the interface and the cartilage phase (Figs. 11.17 and 11.18b). Locally, the maximal compressive strains of about 7% are reached inside the cartilage phase and more than 10% at the interface. At the microstructural level, buckling of rod-like struts was found in the cartilage phase (marked in white in Fig. 11.14b). In the interface, no apparent interfacial debonding was observed from the CT images, although the development of interfacial shear is evident from the shear strain maps (Fig. 11.18c and d).

11.5 Discussion

The mechanical behaviour of a polymer-based scaffold was characterised under uniaxial compression. Confining the scaffold or increasing the strain rate has been found to lead to higher compressive stresses, similar to the responses found in the human bone and articular cartilage [91, 92]. The compressive moduli of the dual-layer scaffold and Scaffold B (bone phase alone) are similar, as opposed to the wide range of compressive modulus of human trabecular bones (20–673 MPa) [33, 93–

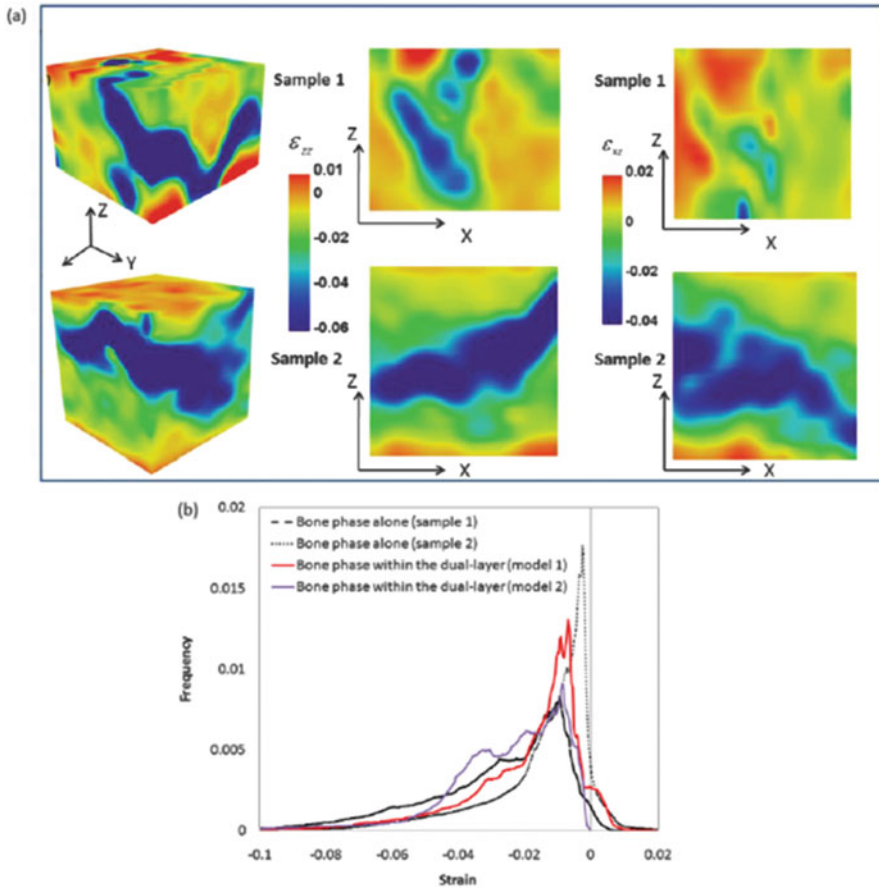


Fig. 11.15 (a) Visualisation of the axial strain, ϵ_{zz} , and shear strain, ϵ_{xz} , of the bone sample obtained with a subvolume size of 32 voxels (0.736 mm), overlapped by 50 %; (b) histograms of the axial strain, ϵ_{zz} , of the bone phase alone and the bone phase within the dual layer. The histograms were obtained with a class interval size of $\Delta\epsilon = 0.0001$. Dimensions of the volumes are $313 \times 313 \times 227$ voxels³ (i.e. $7.2 \times 7.2 \times 5.2$ mm³)

99] and bovine trabecular bones (117–2990 MPa) [95, 99–101] reported in the literature.

The compressive modulus of Scaffold B in unconfined compression was compared with that of human femoral and tibial bones tested under the similar loading conditions [33, 102, 103]. Carter et al. [33] reported that the average compressive modulus of human trabecular tibial bones extracted from the plateau was 56.6 ± 9.7 MPa during walking and 81.5 ± 8 MPa during impact. The mechanical properties of human tibial metaphysis trabecular bone was determined by Goldstein et al. [102] at a strain rate similar to that of walking, and the results are found to be site dependent. The compressive modulus was between 112 and 336 MPa in the medial side and between 52 and 251 MPa in the lateral side. There is a central

Table 11.3 Average axial strains values obtained by the DVC after compressing the bone phase and dual-layer specimens to 0.4-mm displacement

	Subvolume size (mm)	Average axial strain (%)	Standard deviation (%)
Bone phase alone (sample 1)	0.736	2.9	2.3
Bone phase alone (sample 2)	0.736	1.66	2.2
Dual layer (model 1)	0.736	1.78	1.71
Bone phase with the dual layer (77 %)	0.736	2.01	1.85
Cartilage phase with the dual layer (18 %)	0.736	0.81	0.35
Interface (5 %)	0.736	1.37	1.1
	0.253	1.24	1.56
Dual layer (model 2)	0.736	2.2	1.61
Bone phase with the dual layer (61 %)	0.736	2.54	1.81
Cartilage phase with the dual layer (30 %)	0.736	1.33	0.74
Interface (9 %)	0.736	2.04	1.1
	0.253	1.81	1.9

column of trabecular bone with extremely low modulus (between 21 and 105 MPa), which extends upwards from the intramedullary space towards the subchondral plate, possibly due to microstructural defects. Kuhn et al. [103] reported that the average compressive modulus of distal femoral metaphyseal trabecular bone was about 203 ± 196 MPa in the medial–lateral width and 298 ± 224 MPa in the anterior–posterior length. The large standard deviations in the femoral modulus data seem to reflect the dependence of properties on metaphyseal location. The average compressive modulus of Scaffold B was found to be 32 ± 6 MPa (walking) and 68 ± 8 MPa (impact), which is close to the data reported by Carter et al. [33] (56.6 ± 9.7 MPa, walking; 81.5 ± 8 MPa, impact). In addition, Harley et al. [13] suggested that target mechanical properties for a dry scaffold are defined by the Young's modulus of developing osteoid tissue (25–100 kPa) [104–106], rather than that of mature cortical or trabecular bone, as the scaffold is a site for induced regeneration of bone in an empty defect site rather than maintenance of an already mature bone.

Multistep fatigue tests have been carried out on Scaffold B under increasing compressive cyclic loading conditions. The modulus and the number of cycles to failure of the Scaffold B are, however, significantly lower than those of human trabecular bone [63] under the same testing protocol. The results of Scaffold B show an increase in the secant modulus and stress hardening during the initial steps of fatigue loading, consistent with that observed in human trabecular bone [63] under multistep fatigue testing. The initial hardening is also consistent with the results obtained under conventional constant amplitude fatigue testing. Linde and Hvid [86] reported that in human trabecular bones the stiffness increases until a

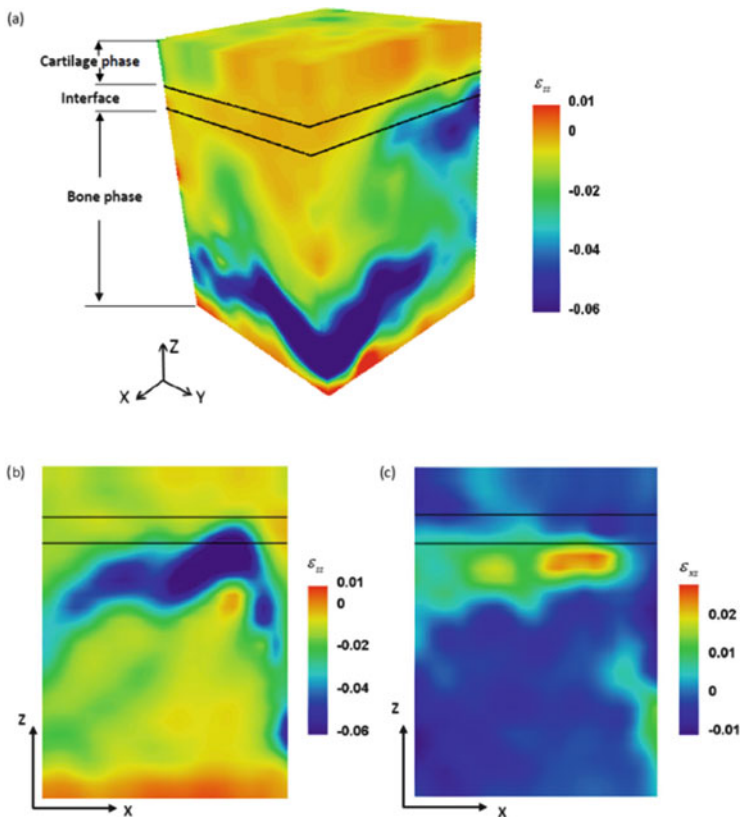


Fig. 11.16 (a) 3D visualisation of the axial strain, ϵ_{zz} , of the dual layer (model 1) obtained with a subvolume size of 32 voxels (0.736 mm), overlapped by 50%. Visualisation of the axial and shear strains, ϵ_{zz} and ϵ_{xz} , in a 2D section extracted from the core of the volume, (b) and (c), respectively. Dimensions of the volume are $313 \times 313 \times 416$ voxels³ (i.e. $7.2 \times 7.2 \times 9.6$ mm³). The interface thickness is about 1 mm

stress level about 50% of ultimate stress is reached followed by decreasing stiffness, although others reported decreasing in modulus from the beginning to the end [48, 52, 54–57, 107, 108]. Michel et al. [65] studied the fatigue behaviour of bovine trabecular bones under load control using a sinusoidal compressive load profile at a frequency of 2 Hz. The results show that the pattern of modulus change with the number of cycles was associated with the loading level. At low cyclic load levels, the modulus increased initially followed by a rapid drop in the final stage. At high cyclic loads, a continuous decrease in modulus from the beginning was found. The authors [65] suggested that both creep and damage accumulation may be responsible for fatigue failure of trabecular bone, i.e. bone fails by creep under high cyclic loads while by microcrack damage accumulation at low cyclic loads. A more recent study suggested, however, that creep effects are negligible in fatigue loading cases for trabecular bone [109]. Further work may be required to confirm the role of creep

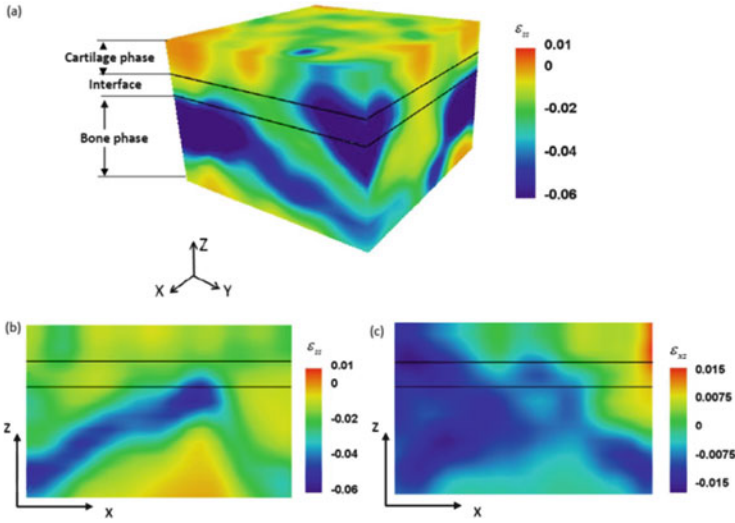


Fig. 11.17 (a) 3D visualisation of the axial strain, ϵ_{zz} , of the dual layer (model 2) obtained with a subvolume size of 32 voxels (0.736 mm), overlapped by 50%. Visualisation of the axial and shear strains, ϵ_{zz} and ϵ_{xz} , in a 2D section extracted from the core of the volume, (b) and (c), respectively. Dimensions of the volume are $313 \times 313 \times 224$ voxels³ (i.e. $7.2 \times 7.2 \times 5.2$ mm³). The interface thickness is about 1 mm

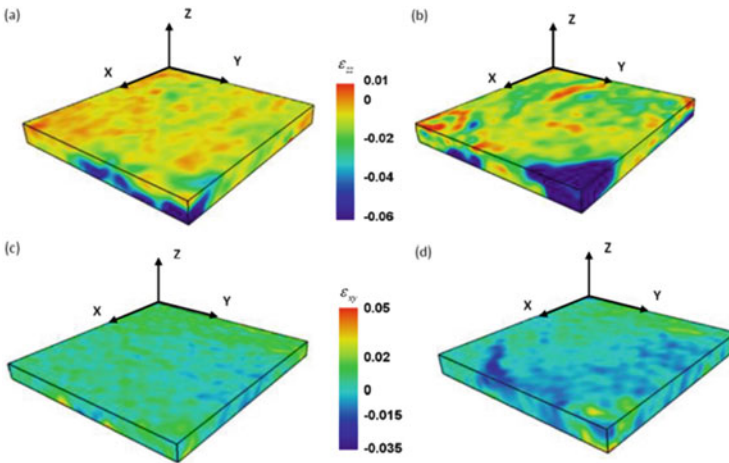


Fig. 11.18 3D visualisations of the axial and interfacial shear strain, ϵ_{zz} and ϵ_{xy} , of the interface, (a), (c) model 1; (b), (d) model 2. The results were obtained with a subvolume size of 11 voxels (0.253 mm), overlapped by 50%. Dimensions of the volumes are $313 \times 313 \times 40$ voxels³ (i.e. $7.2 \times 7.2 \times 0.92$ mm³)

under cyclic loading conditions. Multistep tests seem to be useful in assessing the fatigue behaviour of scaffolds. These tests allow the reduced number of samples/test duration for analysis of fatigue properties of biomaterials.

3D full-field strains in the dual-layer scaffold material were measured using the latest techniques, including micro-CT imaging, in situ loading and digital volume correlation, to gain new insights into the failure mechanisms in the bone, the cartilage and the transitional interface regions under compression. The analysis of the strain maps revealed large areas undergoing minimal deformation, whereas failure occurred preferentially in well-defined strain concentration bands. Compressive and shear failure modes were observed at the specimen level at a macroscopic strain of about 2%. Similar failure modes were reported by Nazarian and co-workers on human trabecular bones compressed at an apparent strain of 1.8% [68]. Turner and co-workers [70] have also reported oblique failure bands in trabecular bone specimens compressed at around 2% strain. At microstructural level, bending of plate-like individual struts was observed in the regions of high strain, which seems to be the main mode of failure. Indeed, the bone phase of the scaffolds has a predominant plate-like structure, and bending is often observed to be the failure mode of choice for plate-like structures [68].

In the dual-layer specimens, the bone phase and the interface seem to play an important role in protecting the cartilage phase from excessive deformation. Designing a dual-layer scaffold with a reduced bone phase thickness would promote damage within the cartilage phase and increase the damage in the bone phase and at the interface. In the cartilage phase, buckling of rod-like struts was observed locally. So far, we have yet to be able to perform a detailed analysis of the distribution of failed plate versus rod-like struts, while it is likely that both bending of the plates and buckling of the rods are responsible for failure of cartilage [68]. In the interface, high compressive strains combined with increased interfacial shear have been found, although no microcracking or interfacial debonding was observed from the CT images.

Some researchers [78, 110] have investigated the failure of osteochondral plugs in racehorse and bovine bone in simulated impact-induced trauma. In Malekipour et al. (2012) [78], plugs consisted of full cartilage and subchondral bones, thus achieving a lower aspect ratio for the bone phase (0.11 vs. 0.59 used herein for model 2). Microcracks extending from the calcified region down to the trabecular bone were observed as well as surface fissures in the cartilage. In Burgin and Aspden (2008) [110], however, the thickness of the bone phase was varied up to 12 mm to a maximum aspect ratio of 1.33, close to that of model 1 (~1.38). The modulus of the bone-on-cartilage samples reached a constant value when the bone thickness exceeded about 10 times the cartilage thickness. Under these conditions, impacts produced damage in the bone rather than in the cartilage. These results are consistent with our findings. No damage was found in the cartilage phase when the bone phase thickness was about 8 times or higher than the cartilage phase thickness. When the bone thickness was reduced by half, damage develops in the cartilage phase, and even more damage is found in the bone phase and in the interface. In addition, Malekipour et al. [78] found high strains in bone and concluded that bone

absorbs a relatively high level of energy, which may be protective to cartilage, consistent with our findings.

Some limitations in the study of strain distribution should be acknowledged. These include first-order shape functions that were used in the correlation algorithm to depict the shape change of the deformed subset. Future work will involve higher-order displacement gradients during the multipass approach, which will allow the localised effects to be measured more accurately [73]. The experiments should also be performed in an environment closer to *in vivo* conditions. Water acts as a plasticiser and tends to increase polymer flexibility and fluidity [111, 112], which might affect the results.

To summarise, the results from the characterisation of a hydrogel scaffold demonstrate that mechanical testing, image-guided failure analysis and digital volume correlation are valuable tools that may be applied to porous materials in general. The results and the methodologies used might be also of interest in the characterisation of other types of scaffolds for a range of applications in biomedical engineering.

Acknowledgements The authors would like to acknowledge Smith & Nephew for providing the samples and the University of Portsmouth for financial support.

References

1. Freeman MAR (1979) Adult articular cartilage. 2, Revised edn. Pitman Medical, Tunbridge Wells/GB
2. Suh J-K, Arøen A, Muzzonigro TS, Disilvestro M, Fu FH (1997) Injury and repair of articular cartilage: related scientific issues. *Oper Tech Orthop* 7(4):270–278
3. Yannas IV (2001) Tissue and organ regeneration in adults. Springer, New York
4. Spector M (2006) Biomaterials-based tissue engineering and regenerative medicine solutions to musculoskeletal problems. *Swiss Med Wkly* 136:293–301
5. Luyten FP, Dell'Accio F, De Bari C (2001) Skeletal tissue engineering: opportunities and challenges. *Best Pract Res Clin Rheumatol* 15(5):759–769
6. Freed LE, Vunjak-Novakovic G, Biron RJ, Eagles DB, Lesnoy DC, Barlow SK, Langer R (1994) Biodegradable polymer scaffolds for tissue engineering. *Nat Biotechnol* 12:689–693
7. Langer R, Vacanti JP, Vacanti CA, Atala A, Freed LE, Vunjak-Novakovic G (1995) Tissue engineering. *Biomed Appl Tissue Eng* 1(2):151–161
8. Seal BL, Otero TC, Panitch A (2001) Polymeric biomaterials for tissue and organ regeneration. *Mater Sci Eng R Rep* 34(4–5):147–230
9. Angele P, Kujat R, Nerlich M, Yoo J, Goldberg V, Johnstone B (1999) Engineering of osteochondral tissue with bone marrow mesenchymal progenitor cells in a derivatized hyaluronan-gelatin composite sponge. *Tissue Eng* 5(6):545–554
10. Hung CT, Lima EG, Mauck RL, Taki E, LeRoux MA, Lu HH, Stark RG, Guo XE, Ateshian GA (2003) Anatomically shaped osteochondral constructs for articular cartilage repair. *J Biomech* 36(12):1853–1864
11. Schaefer D, Martin I, Jundt G, Seidel J, Heberer M, Grodzinsky A, Bergin I, Vunjak-Novakovic G, Freed LE (2002) Tissue-engineered composites for the repair of large osteochondral defects. *Arthritis Rheum* 46(9):2524–2534

12. Sherwood JK, Riley SL, Palazzolo R, Brown SC, Monkhouse DC, Coates M, Griffith LG, Landeen LK, Ratcliffe A (2002) A three-dimensional osteochondral composite scaffold for articular cartilage repair. *Biomaterials* 23(24):4739–4751
13. Harley BA, Lynn AK, Wissner-Gross Z, Bonfield W, Yannas IV, Gibson LJ (2010) Design of a multiphase osteochondral scaffold. II Fabrication of a mineralized collagen–glycosaminoglycan scaffold. *J Biomed Mater Res Part A* 92(3):1066–1077
14. Slivka MA, Leatherbury NC, Kieswetter K, Niederauer GG (2001) Porous, resorbable, fiber-reinforced scaffolds tailored for articular cartilage repair. *Tissue Eng* 7(6):767–780
15. Carmont MR, Carey-Smith R, Saithna A, Dhillon M, Thompson P, Spalding T (2009) Delayed incorporation of a Trufit Plug: perseverance is recommended. *Arthroscopy* 25(7):810–814
16. Melton JT, Wilson AJ, Chapman-Sheath P, Cossey AJ (2010) TruFit CB® bone plug: chondral repair, scaffold design, surgical technique and early experiences. *Expert Rev Med Dev* 7(3):333–341
17. Dhollander AAM, Liekens K, Almqvist KF, Verdonk R, Lambrecht S, Elewaut D, Verbruggen G, Verdonk PCM (2012) A pilot study of the use of an osteochondral scaffold plug for cartilage repair in the knee and how to deal with early clinical failures. *Arthroscopy* 28(2):225–233
18. Pearce CJ, Gartner LE, Mitchell A, Calder JD (2012) Synthetic osteochondral grafting of ankle osteochondral lesions. *Foot Ankle Surg* 18:114–118
19. Madi K, Tozzi G, Zhang QH, Tong J, Cossey A, Au A, Hollis D, Hild F (2013) Computation of full-field displacements in a scaffold implant using digital volume correlation and finite element analysis. *Med Eng Phys* 35(9):1298–1312
20. Hsu YH, Lupton C, Tong J, Cossey A, Au A (2014) Mechanical characterisation of a scaffold under monotonic and cyclic loading conditions. *Int J Exp Comput Biomech* 2(4):359–375
21. Harley BA, Lynn AK, Wissner-Gross Z, Bonfield W, Yannas IV, Gibson LJ (2010) Design of a multiphase osteochondral scaffold III: fabrication of layered scaffolds with continuous interfaces. *J Biomed Mater Res A* 92(3):1078–1093
22. Toolan BC, Frenkel SR, Pachence JM, Yalowitz L, Alexander H (1996) Effects of growth-factor-enhanced culture on a chondrocyte-collagen implant for cartilage repair. *J Biomed Mater Res* 31:273–280
23. Athanasiou K, Schmitz JP, Agrawal CM (1998) The effects of porosity on in vitro degradation of polylactic-acid-polyglycolic acid implants used in repair of articular cartilage. *Tissue Eng* 4(1):53–63
24. Lu L, Zhu X, Valenzuela RG, Currier BL, Yaszemski MJ (2001) Biodegradable polymer scaffolds for cartilage tissue engineering. *Clin Orthop Relat Res* 391:S251–S270
25. Oka M, Ushio K, Kumar P, Ikeuchi K, Hyon SH, Nakamura T, Fujita H (2000) Development of artificial articular cartilage. *Proc Inst Mech Eng H J Eng Med* 214:59–68
26. Bera B (2009) Development of artificial articular cartilage. *Sadhana* 34(5):823–831
27. Oka M, Noguchi T, Kumar P, Ikeuchi K, Yamamuro T, Hyon SH, Ikada Y (1990) Development of an artificial articular cartilage. *Clin Mater* 6:361–381
28. Park S, Hung CT, Ateshian GA (2004) Mechanical response of bovine articular cartilage under dynamic unconfined compression loading at physiological stress levels. *OsteoArthritis Cartilage* 12:65–73
29. Korhonen RK, Jurvelin JS (2010) Compressive and tensile properties of articular cartilage in axial loading are modulated differently by osmotic environment. *Med Eng Phys* 32:155–160
30. Wright TM, Hayes WC (1976) Tensile testing of bone over a wide range of strain rates: effects of strain rate, microstructure and density. *Med Biol Eng Comput* 14(6):671–680
31. Currey JD (1988) Strain rate and mineral content in fracture models of bone. *J Orthop Res* 6:32–38
32. Schaffler MB, Burr DB (1988) Stiffness of compact bone: effects of porosity and density. *J Biomech* 21(1):13–16

33. Carter DR, Hayes WC (1977) The compressive behavior of bone as a two-phase porous structure. *J Bone Joint Surg (Am)* 59(7):954–962
34. Lai WM, Mow VC, Roth V (1981) Effects of nonlinear strain-dependent permeability and rate of compression on the stress behavior of articular cartilage. *J Biomech Eng* 103(2):61–66
35. Radin EL, Paul IL, Lowy M (1970) A comparison of the dynamic force transmitting properties of subchondral bone and articular cartilage. *J Bone Joint Surg (Am)* 52:444–456
36. Silyn-Roberts H, Broom ND (1990) Fracture behaviour of cartilage-on-bone in response to repeated impact loading. *Connect Tissue Res* 24(143–156)
37. Race A, Broom ND, Robertson P (2000) Effect of loading rate and hydration on the mechanical properties of the disc. *Spine* 25(6):662–669
38. Messner K (1993) Hydroxylapatite supported Dacron plugs for repair of isolated full-thickness osteochondral defects of the rabbit femoral condyle: mechanical and histological evaluations from 6–48 weeks. *J Biomed Mater Res* 12:1527–1532
39. Zioupos P, Casinos A (1998) Cumulative damage and the response of human bone in two-step loading fatigue. *J Biomech* 31:825–833
40. Slivka MA, Leatherbury NC, Kieswetter K, Niederauer GG (2000) In vitro compression testing of fiber-reinforced, bioabsorbable, porous implants. In: Mauli Agrawal C, Parr JE, Lin ST (eds) *Synthetic bioabsorbable polymers for implants*. American Society for Testing and Materials, West Conshohocken, pp 124–135
41. Buschmann MD, Soulhat J, Shirazi-Adl A, Jurvelin JS, Hunziker EB (1998) Confined compression of articular cartilage: linearity in ramp and sinusoidal tests and the importance of interdigitation and incomplete confinement. *J Biomech* 31:171–178
42. Williamson AK, Chen AC, Sah RL (2001) Compressive properties and function-composition relationships of developing bovine articular cartilage. *J Orthop Res* 19:1113–1121
43. Korhonen RK, Laasanena MS, Toyras J, Rieppob J, Hirvonen J, Helminen HJ, Jurvelin JS (2002) Comparison of the equilibrium response of articular cartilage in unconfined compression, confined compression and indentation. *J Biomech* 35:903–909
44. Perie D, Korda D, Iatridis JC (2005) Confined compression experiments on bovine nucleus pulposus and annulus fibrosus: sensitivity of the experiment in the determination of compressive modulus and hydraulic permeability. *J Biomech* 38:2164–2171
45. Soltz MA, Ateshian GA (1998) Experimental verification and theoretical prediction of cartilage interstitial fluid pressurization at an impermeable contact interface in confined compression. *J Biomech* 31:927–934
46. Martin RB (2003) Fatigue microdamage as an essential element of bone mechanics and biology. *Calcif Tissue Int* 73:101–107
47. Taylor M, Tanner KE (1997) Fatigue failure of cancellous bone: a possible cause of implant migration and loosening. *J Bone Joint Surg* 79-B:181–182
48. Pattin CA, Calert WE, Carter DR (1996) Cyclic mechanical property degradation during fatigue loading of cortical bone. *J Biomech* 29(1):69–79
49. O'Brien FJ, Taylor D, Lee TC (2003) Microcrack accumulation at different intervals during fatigue testing of compact bone. *J Biomech* 36:973–980
50. Yeni YN, Fyhrie DP (2002) Fatigue damage-fracture mechanics interaction in cortical bone. *Bone* 30(3):509–514
51. Cotton JR, Winwood K, Zioupos P, Taylor M (2005) Damage rate is a predictor of fatigue life and creep strain rate in tensile fatigue of human cortical bone samples. *J Biomech Eng* 127:213–219
52. Fleck C, Eifler D (2003) Deformation behaviour and damage accumulation of cortical bone specimens from the equine tibia under cyclic loading. *J Biomech* 36:179–189
53. Yamamoto E, Crawford RP, Chan DD, Keaveny TM (2006) Development of residual strains in human vertebral trabecular bone after prolonged static and cyclic loading at low load levels. *J Biomech* 39:1812–1818
54. Zioupos P, Wang XT, Currey JD (1996) The accumulation of fatigue microdamage in human cortical bone of two different ages in vitro. *Clin Biomech* 11:365–375

55. Moore TLA, Gibson LJ (2003) Fatigue microdamage in bovine trabecular bone. *J Biomech Eng* 125:769–776
56. Moore TLA, Gibson LJ (2003) Fatigue of bovine trabecular bone. *J Biomech Eng* 125:761–768
57. Dendorfer S, Maier HJ, Taylor D, Hammer J (2008) Anisotropy of the fatigue behaviour of cancellous bone. *J Biomech* 41:636–641
58. Carter DR, Hayes WC (1977) Compact bone fatigue damage – I. Residual strength and stiffness. *J Biomech* 10:325–337
59. Rapillard L, Charlebois M, Zysset P (2006) Compressive fatigue behavior of human vertebral trabecular bone. *J Biomech* 39:2133–2139
60. Dendorfer S, Maier HJ, Hammer J (2009) Fatigue damage in cancellous bone: an experimental approach from continuum to micro scale. *J Mech Behav Biomed Mater* 2(1):113–119
61. Palissery V, Taylor M, Browne M (2004) Fatigue characterization of a polymer foam to use as a cancellous bone analog material in the assessment of orthopaedic devices. *J Mater Sci Mater Med* 15(1):61–67
62. Meyer RW, Pruitt LA (2001) The effect of cyclic true strain on the morphology, structure, and relaxation behavior of ultra high molecular weight polyethylene. *Polymer* 42:5293–5306
63. Topolinski T, Cichanski A, Mazurkiewicz A, Nowicki K (2011) Study of the behavior of the trabecular bone under cyclic compression with stepwise increasing amplitude. *J Mech Behav Biomed Mater* 4(8):1755–1763
64. Guillén T, Ohrndorf A, Tozzi G, Tong J, Christ H-J (2012) Compressive fatigue behavior of bovine cancellous bone and bone analog materials under multi-step loading conditions. *Adv Eng Mater* 14(5):B199–B207
65. Michel MC, Guo X-DE, Gibson LJ, McMahon TA, Hayes WC (1993) Compressive fatigue behavior of bovine trabecular bone. *J Biomech* 26(4–5):453–463
66. Zioupos P, Gresle M, Winwood K (2008) Fatigue strength of human cortical bone: age, physical, and material heterogeneity effects. *J Biomed Mater Res A* 86A(3):627–636
67. Nazarian A, Muller R (2004) Time-lapsed microstructural imaging of bone failure behavior. *J Biomech* 37(1):55–65
68. Nazarian A, Stauber M, Zurakowski D, Snyder BD, Muller R (2006) The interaction of microstructure and volume fraction in predicting failure in cancellous bone. *Bone* 39(6):1196–1202. doi:10.1016/j.bone.2006.06.013
69. Stops AJF, Harrison NM, Haugh MG, O'Brien FJ, McHugh PE (2010) Local and regional mechanical characterisation of a collagen-glycosaminoglycan scaffold using high-resolution finite element analysis. *J Mech Behav Biomed Mater* 3(4):292–302
70. Thurner PJ, Wyss P, Voide R, Stauber M, Stampanoni M, Sennhauser U, Müller R (2006) Time-lapsed investigation of three-dimensional failure and damage accumulation in trabecular bone using synchrotron light. *Bone* 39(2):289–299
71. Buffiere JY, Maire E, Adrien J, Masse JP, Boller E (2010) In situ experiments with X ray tomography: an attractive tool for experimental mechanics. *Exp Mech* 50(3):289–305
72. Youssef S, Maire E, Gaertner R (2005) Finite element modelling of the actual structure of cellular materials determined by X-ray tomography. *Acta Mater* 53(3):719–730
73. Bay BK, Smith TS, Fyrhie DP, Saad M (1999) Digital volume correlation: three-dimensional strain mapping using X-ray tomography. *Exp Mech* 39:217–226
74. Germaneau A, Doumalin P, Dupre JC (2007) 3D strain field measurement by correlation of volume images using scattered light: recording of images and choice of marks. *Strain* 43(3):207–218
75. Liu L, Morgan EF (2007) Accuracy and precision of digital volume correlation in quantifying displacements and strains in trabecular bone. *J Biomech* 40(15):3516–3520
76. Roux S, Hild F, Viot P, Bernard D (2008) Three-dimensional image correlation from X-ray computed tomography of solid foam. *Compos A: Appl Sci Manuf* 39(8):1253–1265
77. Verhulp E, van Rietbergen B, Huiskes R (2004) A three-dimensional digital image correlation technique for strain measurements in microstructures. *J Biomech* 37(9):1313–1320

78. Malekipour F, Oetomo D, Vee Sin Lee P (2012) Osteochondral injury during simulated drop landing compression: pre and post impact micro-computed tomography. Paper presented at the 30th annual conference of biomechanics in sports, University of Melbourne, Australia
79. Madi K, Booker A, Tozzi G, Zhang Z-Y, Hsu Y-H, Lupton C, Tong J, Cossey A, Au A, N'Guyen F (2011) Viscoelastic modelling and full-field strain computation of biphasic scaffold for osteochondral defect repair. Paper presented at the ECCOMAS – international conference on tissue engineering, Lisbon, Portugal, June 2–4
80. Kalyanam S, Yapp RD, Insana MF (2009) Poro-viscoelastic behavior of gelatin hydrogels under compression-Implications for bioelasticity imaging. *J Biomech Eng* 131(8):1–13
81. DiSilvestro MR, Suh J-KF (2001) A cross-validation of the biphasic poroviscoelastic model of articular cartilage in unconfined compression, indentation, and confined compression. *J Biomech* 34:519–525
82. Linde F, Hvid I (1989) The effect of constraint on the mechanical behaviour of trabecular bone specimens. *J Biomech* 22(5):485–490
83. Caler WE, Carter DR (1989) Bone creep-fatigue damage accumulation. *J Biomech* 22:625–635
84. Haddock SM, Yeh OC, Mummaneni PV, Rosenberg WS, Keaveny TM (2004) Similarity in the fatigue behavior of trabecular bone across site and species. *J Biomech* 37:181–187
85. Fray ME, Altstadt V (2003) Fatigue behaviour of multiblock thermoplastic elastomers. 1. Stepwise increasing load testing of poly(aliphatic/aromatic-ester) copolymers. *Polymer* 44:4635–4642
86. Linde F, Hvid I (1987) Stiffness behaviour of trabecular bone specimens. *J Biomech* 20(1):83–89
87. Doubea M, Klosowska MM, Arganda-Carrerasb I, Cordelièresc FP, Doughertyd RP, Jacksone JS, Schmidf B, Hutchinsong JR, Shefelbinea SJ (2010) BoneJ: free and extensible bone image analysis in ImageJ. *Bone* 47(6):1076–1079
88. Beuf O, Ghosh S, Newitt DC, Link TM, Steinbach L, Ries M, Lane N, Majumdar S (2002) Magnetic resonance imaging of normal and osteoarthritic trabecular bone structure in the human knee. *Arthritis Rheum* 46(2):385–393
89. Ding M, Hvid I (2000) Quantification of age-related changes in the structure model type and trabecular thickness of human tibial cancellous bone. *Bone* 26(3):291–295
90. Tozzi G, Zhang Q-H, Tong J (2012) 3D real-time micromechanical compressive behaviour of bone–cement interface: experimental and finite element studies. *J Biomech* 45(2):356–363
91. Bursac PM, Obitz TW, Eisenberg SR, Stamenovic D (1999) Confined and unconfined stress relaxation of cartilage: appropriateness of a transversely isotropic analysis. *J Biomech* 32:1125–1130
92. Kelly N, McGarry JP (2012) Experimental and numerical characterisation of the elasto-plastic properties of bovine trabecular bone and a trabecular bone analogue. *J Mech Behav Biomed Mater* 9:184–197
93. Yang S, Leong K-F, Du Z, Chua C-K (2001) Review: the design of scaffolds for use in tissue engineering. Part I Traditional factors. *Tissue Eng* 7(6):679–689
94. Augat P, Link T, Lang TF, Lin JC, Majumdar S, Genant HK (1998) Anisotropy of the elastic modulus of trabecular bone specimens from different anatomical locations. *Med Eng Phys* 20:124–131
95. Keaveny TM, Pinilla TP, Crawford RP, Kopperdahl DL, Lou A (1997) Systematic and random errors in compression testing of trabecular bone. *J Orthop Res* 15(1):101–110
96. Kopperdahl DL, Keaveny TM (1998) Yield strain behavior of trabecular bone. *J Biomech* 31(7):601–608
97. Goulet RW, Goldstein SA, Ciarelli MJ, Kuhn JL, Brown MB, Feldkamp LA (1994) The relationship between the structural and orthogonal compressive properties of trabecular bone. *J Biomech* 27(4):375–389
98. Linde F, Hvid I, Madsen F (1992) The effect of specimen geometry on the mechanical behaviour of trabecular bone specimens. *J Biomech* 25(4):359–368

99. Poumarat G, Squire P (1993) Comparison of mechanical properties of human, bovine bone and a new processed bone xenograft. *Biomaterials* 14(5):337–340
100. Swartz DE, Wittenberg RH, Shea M, White AA III, Hayes WC (1991) Physical and mechanical properties of calf lumbosacral trabecular bone. *J Biomech* 24(11):1059–1068
101. Keaveny TM, Wachtel EF, Ford CM, Hayes WC (1994) Differences between the tensile and compressive strengths of bovine tibial trabecular bone depend on modulus. *J Biomech* 27(9):1137–1146
102. Goldstein SA, Wilson DL, Sonstegard DA, Matthews LS (1983) The mechanical properties of human tibial trabecular bone as a function of metaphyseal location. *J Biomech* 16(12):965–969
103. Kuhn JL, Goldstein SA, Ciarelli MJ, Matthews LS (1989) The limitations of canine trabecular bone as a model for human: a biomechanical study. *J Biomech* 22(2):95–107
104. Garcia AJ, Reyes CD (2005) Bio-adhesive surfaces to promote osteoblast differentiation and bone formation. *J Dent Res* 84(5):407–413
105. Kong HJ, Polte TR, Alsberg E, Mooney DJ (2005) FRET measurements of cell-traction forces and nano-scale clustering of adhesion ligands varied by substrate stiffness. *Proc Natl Acad Sci U S A* 102(12):4300–4305
106. Engler AJ, Sen S, Sweeney HL, Discher DE (2006) Matrix elasticity directs stem cell lineage specification. *Cell* 126:677–689
107. Schaffler MB, Radin EL, Burr DB (1989) Mechanical and morphological effects of strain rate on fatigue of compact bone. *Bone* 10:207–214
108. Zioupos P, Wang XT, Currey JD (1996) Experimental and theoretical quantification of the development of damage in fatigue tests of bone and antler. *J Biomech* 29:989–1002
109. Moore TLA, O'Brien FJ, Gibson LJ (2004) Creep does not contribute to fatigue in bovine trabecular bone. *J Biomech Eng* 126(3):321–329
110. Burgin LV, Aspden RM (2008) Impact testing to determine the mechanical properties of articular cartilage in isolation and on bone. *J Mater Sci* 19:703–711
111. Houchin ML, Neuenswander SA, Topp EM (2007) Effect of excipients on PLGA film degradation and the stability of an incorporated peptide. *J Control Release* 117(3):413–420
112. Kranz H, Ubrich N, Maincent P, Bodmeier R (2000) Physicomechanical properties of biodegradable poly(D, L-lactide) and poly(D, L-lactide-co-glycolide) films in the dry and wet states. *J Pharm Sci* 89(12):1558–1566

Chapter 12

Computational Design for Scaffold Tissue Engineering

Che-Cheng Chang, Yuhang Chen, Shiwei Zhou, Yiu-Wing Mai, and Qing Li

Abstract Structure of tissue scaffold plays a critical role in guiding and supporting cell proliferation and differentiation. One widely accepted way to create a desirable biomechanical environment is to have it match the mechanical and biological properties of native host tissue. However, conventional design process typically involves laborious trial and error, and it is sometimes very difficult to achieve the desired biomimeticity when multiple criteria are involved. This chapter aims to present a systematic methodology for the design of tissue scaffold structures, in which the stiffness and diffusivity criteria are taken into account to address various biomechanical requirements in tissue engineering. The scaffolds with periodic microstructures are considered herein, which can be fabricated using 3D printing or additive manufacturing technologies. In this design process, the finite element (FE)-based homogenisation technique is employed to characterise effective material properties, and topology optimisation is carried out using the inverse homogenisation technique, in which (1) bulk modulus, (2) diffusivity and (3) their combination are formulated as the design objectives. To assess the optimised design, we simulate and examine the bone tissue regeneration inside the scaffolds under certain biomechanical conditions in two different models, specifically Wolff's remodelling and the mechanobiology rules. The tissue regeneration results demonstrate how different design criteria lead to different outcomes, signifying the importance of scaffold design and the proposed methodology.

Keywords Scaffold • Tissue engineering • Topology optimisation • Homogenisation • Additive manufacturing • Diffusivity

C.-C. Chang • Y.-W. Mai • Q. Li (✉)

School of Aerospace, Mechanical & Mechatronic Engineering, The University of Sydney, Sydney, NSW 2006, Australia

e-mail: Qing.Li@Sydney.edu.au

Y. Chen

School of Engineering & Physical Sciences, Mechanical, Process & Energy Engineering, Heriot-Watt University, Edinburgh EH14 4AS, UK

S. Zhou

Centre for Innovative Structures and Materials (CISM), RMIT University, Melbourne, Australia

12.1 Introduction

A key to success in tissue engineering has been to develop sophisticated 3D porous scaffolds that provide appropriate biological and mechanical conditions for cells to generate desirable and functional tissues [1]. The complex roles of the microstructures of tissue scaffolds in the regulation of biomechanical environment are gradually recognised recently. However, the structural requirements can vary significantly from site to site and from tissue type to tissue type, making the design and fabrication highly case dependent and often involving laborious trial-and-error experimental processes. Furthermore, it can be difficult to assure a smooth biomechanical transition from empty scaffold to scaffold–tissue construct in the design stage given the random nature of traditional porous scaffold structure and neotissue ingrowth. To tackle this problem and better control the biomechanical outcomes of scaffolding, an inverse design procedure based on the periodic base cell has exhibited notable advantages [2–6]. Further, mathematical modelling is believed to be of significant potential in prediction of tissue growth, thereby helping design of more predictive scaffolds [7–9].

The development of various additive manufacturing and solid free-form fabrication (SFF) technologies is making the controllable base cell designs particularly attractive [10–14]. Exploitation of homogenisation [15] and its inverse form [2] offer a promising alternative to costly experimental characterisation and design of scaffolds. Biomimetic mechanical properties have become a possible design criterion since Hollister and his colleagues [2–4] introduced topology optimisation technique by matching the stiffness of designed scaffolds to that of trabecular bones. It would be interesting to study how different design criteria determine the performance of scaffolds. As such, a more suitable optimisation formulation can be established.

It is however unclear how tissue ingrowth gradually affects the biomechanical conditions that are obtained in an initial stage. It would be necessary to assess the fundamental hypothesis of whether a matching stiffness to host bone could best stimulate tissue generation in a timely fashion [16]. To investigate how scaffold interacts with tissue growth, Adachi et al. presented a computational model that transforms the remodelling algorithms of long bone to a base cell model [7–9]. Later, Byrne et al. [17] adopted the mechanobiological algorithm for remodelling simulation. Sanz-Herrera et al. [9] further explored the effect of tissue ingrowth on mechanical properties of constructs within a multiscale framework by accounting for host bone (macro) and scaffold pore (micro). Chen et al. incorporated degradation model of polymeric scaffolds [18] and tissue ingrowth model through mechanobiological simulation in the design analysis and optimisation; and they found that degradation and tissue regeneration may not necessarily take place in a harmonic way if no design optimisation is carried out [6]. These studies provided evidences how numerical remodelling could help better design scaffolds for more efficient *in vivo* and *in vitro* tests. To date, there is a growing need to

consolidate different scaffold design processes for better correlating biomechanical criteria with the resultant tissue growth.

This chapter aims to first explore how different design criteria affect scaffold structures and then determine how the different designs of scaffold structures could affect tissue regeneration on a microscopic level. Specifically, the inverse homogenisation method is adopted to optimise base cell topologies for either matching host bone behaviours or maximising the overall properties. The optimised scaffolds are then assessed and compared in terms of the effectiveness of tissue generation through Wolff's remodelling [19] and mechanobiology [17] rules.

12.2 Materials and Methods

The rapid development of additive manufacturing (3D printing) and the solid free-form fabrication (SFF) technologies [20] has enabled various direct and indirect fabrication of a full range of biomaterials, with sophisticated configurations, adequate geometric accuracy and structural stability [13]. For this reason, periodic scaffold architectures comprising of identical base cells (also known as representative volume element, RVE) have drawn increasing attention recently, largely attributable to their more controllable and tailorable effective material properties [21]. In this chapter, we will present a systematic methodology suitable for the analysis and design of such periodic structures to attain desirable biomechanical properties for tissue engineering applications.

12.2.1 *Characterisation of Effective Material Properties by Homogenisation*

The first step of tissue scaffold design is the determination of biomechanical properties of scaffold, which is often required to assess its potential performance prior to tissue engineering experiments. In a periodically structured scaffold, the size of base cell (100~500 μm) is considered much smaller than the bulk scaffold dimension (typically in cm scale). In this context, the asymptotic homogenisation technique [22–24] can be applied to unit cell models to characterise the effective (bulk) physical properties of a scaffold when compositional and microstructural configuration is given. In this chapter, the homogenised elasticity and diffusivity properties are derived as follows.

12.2.1.1 Elasticity Tensor

The homogenisation of the effective elasticity tensor \mathbf{C}^H can be conducted within the finite element (FE) framework, as [24]

$$C_{ij}^H(\rho^e) = \frac{1}{|\Omega|} \sum_{e=1}^{NE} \left(\mathbf{I} - \frac{\partial \mathbf{u}_i}{\partial \mathbf{x}} \right) [\mathbf{K}^e(\rho^e)] \left(\mathbf{I} - \frac{\partial \mathbf{u}_j}{\partial \mathbf{x}} \right) |\Omega^e| \quad (12.1)$$

where C_{ij}^H denotes the homogenised parameters of elasticity tensor; ρ^e denotes the density of element e , whose normalised form will be used as the design variable in the topology optimisation for inverse homogenisation; NE is the number of elements in the base cell model; $\mathbf{K}^e(\rho^e)$ is the elemental stiffness matrix; and $|\Omega|$ and $|\Omega^e|$ are the volumes of base cell (which is the volume of the entire base cell design domain) and e -th element, respectively. The homogenised stiffness tensor \mathbf{C}^H is thus expressed in the following form:

$$\mathbf{C}^H = \begin{bmatrix} C_{11}^H & C_{12}^H & C_{13}^H & & & \\ C_{21}^H & C_{22}^H & C_{23}^H & & & \\ C_{31}^H & C_{32}^H & C_{33}^H & & & \\ & & & C_{44}^H & & \\ & & & & C_{55}^H & \\ & & & & & C_{66}^H \end{bmatrix} \quad (12.2)$$

For the finite element analysis, the displacement field \mathbf{u} is obtained through solving the following equilibrium equation in the base cell model

$$\int_{\Omega} \frac{\partial}{\partial x} \mathbf{K}^e(\rho^e) \frac{\partial}{\partial \mathbf{x}} \mathbf{u} d\Omega = \int_{\Omega} \frac{\partial}{\partial \mathbf{x}} \mathbf{K}^e(\rho^e) d\Omega \quad (12.3)$$

where $\frac{\partial}{\partial \mathbf{x}} \mathbf{u}$ is also known as the characteristic strain of the base cell model. In a 3D case, there exist six unique characteristic strain fields, including three normal components and three shear components [25].

The elemental stiffness matrix \mathbf{K}^e is a function of the material density, ρ^e . This is often defined as $\mathbf{K}^e = f(\rho^e) \mathbf{K}$, where $f(\rho^e)$ is a real function, usually formulated based on the power law and the solid isotropic material with penalisation (SIMP) principle widely adopted in topology optimisation [26]. \mathbf{K} is the original stiffness matrix of the base material. Each element has a density between 0 (completely void) and 1 (completely solid) and a unique \mathbf{K}^e value.

The right-hand side of Eq. (12.3) is the ideological unit test strain. From an FEA perspective ($\mathbf{K}\mathbf{u} = \mathbf{f}$), the right-hand side of the equilibrium equation represents the nodal force (\mathbf{f} , where $\mathbf{f} = \int_{\Omega} \frac{\partial}{\partial \mathbf{x}} \mathbf{K}^e(\rho^e) d\Omega$) that induces the characteristic strain response. The global stiffness matrix on the left-hand side of the equation is the standard stiffness matrix assembly ($\mathbf{K} = \int_{\Omega} \frac{\partial}{\partial \mathbf{f}} \mathbf{f}^e(\rho^e) \frac{\partial}{\partial \mathbf{f}} d\Omega$). Assembling the

right-hand side of the equation over the discretised FE domain of base cell produces a force vector that can be applied on nodal level.

The periodic boundary condition is applied to all the nodal pairs on the opposite boundaries of the RVE model by means of coupling, i.e. the displacement of a node and its paired partner on the other side of RVE is made equal. For example, all nodes on the RVE boundary facing the negative- x direction are coupled to the nodes on the boundary facing the positive- x direction on the opposite face [16]. Thus the displacement field is continuous from one base cell to another. In normal strain scenarios, if symmetry is assumed, symmetry boundary condition can be applied: the nodal displacement on the boundaries facing the $x/y/z$ direction has zero $x/y/z$ displacement, respectively (otherwise it will penetrate the base cell right next to it). In the shear strain scenarios, on the other hand, the boundary nodes are not allowed to move in the non-shear directions. In the x - y shear strain case, for example, the nodes on all RVE boundaries are not allowed to move in the z direction, the nodes on the x boundary can only move in the x direction and the nodes on the y boundary can only move in the y direction. A summary of the prescribed boundary conditions is provided in Table 12.1 for clarification.

To reduce the computational cost of 3D FEA, geometric and kinematic symmetry conditions are applied whenever possible [27]. Specifically, the base cell centre is taken as the origin of a Cartesian coordinate system, and one-eighth of the cubic base cell is considered, whose six outer boundaries are located at $x, y, z = 0, 1$, respectively. The cubic RVE domain is meshed with structured cubic hexahedral elements for simplicity of modelling.

12.2.1.2 Diffusivity Tensor

The homogenisation of the effective diffusivity is implemented in a similar fashion to that of the stiffness tensor. The effective diffusivity tensor D_{ij}^H is calculated as

$$\mathbf{D}_{ij}^H(\rho^e) = \frac{1}{|\Omega|} \sum_{e=1}^{NE} \mathbf{D}^e(\rho^e) \left(\mathbf{I} - \frac{\partial \varphi}{\partial \mathbf{x}} \right) |\Omega^e| \quad (12.4)$$

where \mathbf{D}^e is the elemental diffusivity matrix of some chemical species across a given fluid. The homogenised diffusivity tensor can be expressed in the following form:

Table 12.1 Symmetry conditions for the different test strains [16]

Test strains	$x = 0, 1$	$y = 0, 1$	$z = 0, 1$
$\hat{\epsilon}_{ij}, i = j$	$u_x^e = 0$	$u_y^e = 0$	$u_z^e = 0$
$\hat{\epsilon}_{12}$	$u_y^e = u_z^e = 0$	$u_x^e = u_z^e = 0$	$u_z^e = 0$
$\hat{\epsilon}_{23}$	$u_x^e = 0$	$u_x^e = u_z^e = 0$	$u_x^e = u_y^e = 0$
$\hat{\epsilon}_{13}$	$u_y^e = u_z^e = 0$	$u_y^e = 0$	$u_x^e = u_y^e = 0$

$$\mathbf{D}^H = \begin{bmatrix} D_{11}^H & & \\ & D_{22}^H & \\ & & D_{33}^H \end{bmatrix} \quad (12.5)$$

The characteristic concentration field, φ , is obtained by solving the following equation:

$$\int_{\Omega} \frac{\partial}{\partial \mathbf{x}} \mathbf{D}^e(\rho^e) \frac{\partial}{\partial \mathbf{x}} \varphi d\Omega = \int_{\Omega} \frac{\partial}{\partial \mathbf{x}} \mathbf{D}^e(\rho^e) d\Omega \quad (12.6)$$

which is very similar to the equilibrium equation in the stiffness case. In 3D space, there exist three unique $\frac{\partial \varphi}{\partial \mathbf{x}}$ terms, corresponding to x , y and z directions. This equation can be solved as a standard thermal equation by first assembling the right-hand side of the equation to create the nodal force vector ($\mathbf{f} = \int_{\Omega} \frac{\partial}{\partial \mathbf{x}} \mathbf{D}^e(\rho^e) d\Omega$) and then the global diffusivity matrix ($\mathbf{K} = \int_{\Omega} \frac{\partial}{\partial \mathbf{x}} \mathbf{D}^e(\rho^e) \frac{\partial}{\partial \mathbf{x}} d\Omega$). The elemental diffusivity matrix, \mathbf{D}^e , is also a function of the density of individual element (ρ^e), i.e. $\mathbf{D}^e = f(\rho^e) \mathbf{D}$, where \mathbf{D} is the nominal diffusivity in the pure fluid phase.

The periodic boundary conditions can be applied by pairing all concentration degree of freedom (DoF) on the opposite boundary surfaces of the RVE. If symmetry can be assumed, symmetric boundary conditions and degree of freedom (DoF) constraints can be applied instead. For example, in the x strain case, every node on the positive and negative x RVE boundaries is given a concentration of zero (DoF constraint), whereas all other boundaries are left unconstrained (symmetry). The characteristic concentration is allowed to have a negative value since it is only a relative term.

12.2.2 Inverse Homogenisation and Topology Optimisation

Following the characterisation directly using the homogenisation, topology optimisation is carried out to determine the optimal material distribution in a base cell form that yields either the maximum or desired material properties [28, 29]. Such a design process is known as the ‘inverse homogenisation’, in which the desired homogenised properties determine the porous microstructure of a scaffold inversely.

12.2.2.1 Targeted Stiffness Tensor

The stiffness properties of bone scaffolds should match those of host bone for functional reasons [3, 30]. In topology optimisation context, we can translate such

requirement to a cost function in terms of the differences between the targeted stiffness \mathbf{C}^* and actual effective (i.e. homogenised) stiffness \mathbf{C}^H , as follows:

$$\left\{ \begin{array}{l} \min_{\rho^e} J_S(\rho^e) = \sum_{i,j=1}^6 \left(C_{ij}^* - C_{ij}^H(\rho^e) \right)^2 \\ \text{subject to : } 0 < \rho_{\min} \leq \rho^e \leq 1 \\ \frac{1}{NE} \sum_{e=1}^{NE} (1 - \rho^e) = V_0 \end{array} \right. \quad (12.7)$$

where ρ_{\min} is the minimum density that a finite element can have and the superscript e denotes elemental property. A non-zero value for elemental density ρ_{\min} is required to avoid singularity in the finite element calculation.

To prevent the formation of numerical artefacts such as checkerboard pattern, a nonlinear diffusion technique is adopted here [31, 32]. The method of moving asymptotes (MMA) algorithm [33] is employed to determine the topological evolution. The sensitivity function with respect to the design variable ρ^e can be determined by using the adjoint variable method and written as

$$\begin{aligned} \frac{\partial J_S}{\partial \rho^e} = & -2 \sum_{i,j=1}^6 r_{ij} \left(C_{ij}^* - C_{ij}^H(\rho^e) \right) \frac{\partial C_{ij}^H(\rho^e)}{\partial \rho^e} \\ & - \tau^2 \operatorname{div} \left[\frac{\partial \varphi}{\partial (\|\nabla \rho^e\|)} \frac{1}{\|\nabla \rho^e\|} \nabla \rho^e \right] \end{aligned} \quad (12.8)$$

where div stands for the divergence operator and

$$\frac{\partial C_{ij}^H(\rho^e)}{\partial \rho^e} = \sum_{e=1}^{NE} (\hat{\mathbf{u}}_i^* - \mathbf{u}_i^e)^T \frac{\partial \mathbf{K}^e(\rho^e)}{\partial \rho^e} (\hat{\mathbf{u}}_j^* - \mathbf{u}_j^e) |\Omega^e| \quad (12.9)$$

12.2.2.2 Targeted Diffusivity

The porous phase of a bone scaffold must allow unhindered nutrient transport and mass movement. In cartilage tissue engineering, for example, the effective diffusivity is expected to match that of the native tissue to mimic the local diffusion environment [34]. To design a base cell with a diffusivity target, we formulate a cost function (J_D) based on the difference between the desired diffusivity \mathbf{D}^* and the actual effective (homogenised) diffusivity \mathbf{D}^H of the model in a fashion similar to the stiffness topology optimisation formulation:

$$\begin{cases} \min_{\rho^e} J_D(\rho^e) = \sum_{i=1}^3 (D_{ii}^* - D_{ii}^H(\rho^e))^2 \\ \text{subject to : } 0 < \rho_{\min} \leq \rho^e \leq 1 \\ \frac{1}{NE} \sum_{e=1}^{NE} (1 - \rho^e) = V_0 \end{cases} \quad (12.10)$$

The sensitivity of the effective diffusivity is also a function of the elemental density as follows:

$$\frac{\partial J_D}{\partial \rho^e} = 2 \sum_{i=1}^3 (D_{ii}^* - D_{ii}^H(\rho^e)) \frac{\partial D_{ii}^H(\rho^e)}{\partial \rho^e} \quad (12.11)$$

Note that the sensitivity function in this case has a positive sign since a change in elemental density has the opposite effect on the diffusivity. For the mathematical similarity between diffusion and conduction problems [35], the readers are recommended to refer to the detailed derivation and a MATLAB program for the inverse conductive homogenisation calculation provided by us [36].

12.2.2.3 Combined Stiffness and Diffusivity

Both stiffness and diffusivity of a tissue scaffold can be maximised or be matched to the host tissue properties simultaneously to achieve biomimeticity [37]. Such a design task can be accomplished using multiobjective topology optimisation techniques [38–42]. In the case of maximisation, the objective function is formulated as follows:

$$\begin{cases} \min_{\rho^e} J(\rho^e) = \sum_{e=1}^{NE} \left[w_C \frac{C^*}{\sum_{i,j}^6 \delta_{ij} C_{ij}^H} + w_D \frac{D^*}{\sum_{i,j}^3 \delta_{ij} D_{ij}^H} \right] \\ \text{subject to : } 0 < \rho_{\min} \leq \rho^e \leq 1 \\ \frac{1}{NE} \sum_{e=1}^{NE} (1 - \rho^e) = V_0 \\ w_C + w_D = 1 \end{cases} \quad (12.12)$$

where w_C and w_D are the weight factors for the effective stiffness and effective diffusivity cost functions, respectively, C^* is the maximum stiffness, D^* is the maximum diffusivity and δ_{ij} is the Kronecker delta ($\delta_{ij} = 1$ when $i = j$, and $\delta_{ij} = 0$ when $i \neq j$). The cost functions $\frac{C^*}{\sum_{i,j}^6 \delta_{ij} C_{ij}^H}$ and $\frac{D^*}{\sum_{i,j}^3 \delta_{ij} D_{ij}^H}$ are the inverse of individual effective material properties and are normalised [39]. The weight factors indicate the relative importance of these two material properties in an individual design scenario ($w_C + w_D = 1$).

12.2.3 Computational Remodelling Simulation

In this chapter, we consider two different remodelling rules, namely, Wolff's rule [19] and mechanoregulatory [17] rules, as follows.

12.2.3.1 Modelling for Wolff's Rule

The tissue remodelling is a process of balancing bone apposition (osteoblastic process) and bone resorption (osteoclastic process) [43], which is driven by local mechanical stimuli. Mathematical models capable of simulating the remodelling process have been widely available on a macroscopic level [44–46], whereas relatively speaking, limited studies have been conducted on the microscopic level involving implanted scaffolds [7, 9, 17].

To describe how the load-bearing tissue grows within the scaffold pores, the remodelling rules established in long bone are considered phenomenologically applicable [7]. Following the typical remodelling rules in literature [45], tissue is regarded as 3D continuum media whose deformation is quasi-static and which is typically governed by linear elasticity theory. The apposition and resorption of tissue can be determined in terms of strain energy density (SED) as [19]

$$\psi^e = \frac{1}{2} \bar{\epsilon}^e \bar{\sigma}^e \quad (12.13)$$

where $\bar{\epsilon}^e$ and $\bar{\sigma}^e$ denote the elemental strain and stress, respectively. The change in elemental bone density ϑ^e is triggered when the elemental SED is higher or lower than the remodelling thresholds [44, 45], defined as

$$\gamma^e = \frac{\partial \vartheta^e}{\partial t} = \begin{cases} \alpha[\psi - (1+s)\psi_n], & \psi > (1+s)\psi_n \\ 0, & (1-s)\psi_n \leq \psi \leq (1-s)\psi_n \\ \alpha[\psi - (1+s)\psi_n], & \psi < (1-s)\psi_n \end{cases} \quad (12.14)$$

where ψ_n is a site-specific homeostatic equilibrium parameter and s the half-width of the 'lazy zone' [45]. As a constant, α reflects the bone remodelling rates for different tissues and sites. Thus $\vartheta^{e(n)}$ can be updated per time step Δt via a forward Euler algorithm, from time step n to time step $(n+1)$, as

$$\vartheta^{e(n+1)} = \vartheta^{e(n)} + \gamma^e \Delta t \quad (12.15)$$

The choice of time step Δt should be sufficiently small to ensure the stability of remodelling simulations.

It is noted that the scaffold and host tissue are more often than not subject to dynamic loading *in vivo*, in which the apposition and resorption of the bone are determined by the difference between the actual stimulus and local tissue

mechanical stimulation as reported by [47]. However, a precise determination of such loading spectrum and many other relevant biological factors is by no means easy. For this reason, a static loading has been assumed in the remodelling studies in bone and scaffold [7–9]. We will explore the relative effects of different scaffold stiffness on tissue regeneration. As long as the same load (direction, magnitude and pattern) is applied, the remodelling results can be well differentiated from different scaffold stiffnesses; thus, their relative performance can be properly determined.

As described by Sanz-Herrera et al. [9] and Byrne et al. [17], mesenchymal stem cells (MSC) could be seeded or could migrate along scaffold pore surfaces to form a continuous cellular layer after implanted into host. Under certain biomechanical conditions, such cells differentiate and generate osteoblasts, forming immature bone substance in the cellular layer with extremely low modulus. The immature tissue will further remodel into mineralised mature bone inside the scaffold. In this study, it is assumed that the remodelling starts from such an immature tissue layer that is evenly distributed on the scaffold surfaces [7, 9, 17].

12.2.3.2 Modelling for Mechanoregulatory Rule

Scaffold strain can produce certain level of biophysical stimulus and promote mesenchymal stem cells (MSCs) differentiation and proliferation. To model how the biophysical stimuli determine tissue regeneration, the mechanoregulatory rule is employed herein. The mechanoregulatory model adopts mechanical strain and fluid flow to modulate cell differentiation. This algorithm has shown considerable implication to model the growth details of various cell phenotypes under different levels of biophysical stimuli [48].

In this model, the pore region of the scaffold is considered to be initially occupied by granulation tissue after a certain period of culturing in a bioreactor, in which the lattices are constructed within each granulation element as a cellular media, allowing various cell phenotypes to potentially occupy. The number of lattice points is determined by the size of element and average diameter of tissue cells [6]. In this model, we randomly seeded 5% MSCs initially into each lattice which are allowed to further proliferate and differentiate. To account for the cell proliferation and migration, the random walk algorithm [17] is also implemented here.

Having defined the cell proliferation and migration in the *lattice scale*, the MSC differentiation stimulus S is defined in relation to local physical fields as [48]

$$S = \frac{\tau}{a} + \frac{v}{b} \begin{cases} S < 0.01 & \text{absorption} \\ 0.01 < S < 0.53 & \text{osteoblast} \rightarrow \text{mature bone} \\ 0.53 < S < 1 & \text{osteoblast} \rightarrow \text{immature bone} \\ 1 < S < 3 & \text{chondrocyte} \rightarrow \text{cartilage} \\ S > 3 & \text{fibroblast} \rightarrow \text{fibros tissue} \end{cases} \quad (12.16)$$

where τ and v are the octahedral shear strain and fluidic velocity within the base cell of tissue–scaffold construct, respectively. Following the literature, constants $a=0.0375$ and $b=3 \mu\text{ms}^{-1}$ that were measured from experiments are adopted to generate biophysical stimulus S for differentiation [17].

It is assumed that each MSC stays for 7 days [17], after which it becomes mature to be able to proliferate or differentiate. Thus, different cell phenotypes would be differentiated from MSCs according to the calculated biophysical stimulus S in Eq. (12.16), where only a certain percentage of mature MSCs in each lattice, defined by a differentiation probability p_d , differentiates every day. To calculate material properties in each lattice, we adopted the material parameters of different cell phenotypes and the algorithm reported by Byrne et al. [17].

12.3 Results and Discussion

12.3.1 Example with the Targeted Stiffness Tensor

Although trabecular bone is generally orthotropic and has three symmetric planes and nine independent elasticity constants, the studies on scaffold design with the inverse homogenisation were usually simplified into six orthotropic elastic properties (i.e. three Young’s moduli and three shear moduli) [2–4], making the objective function (Eq. (12.7)) more achievable.

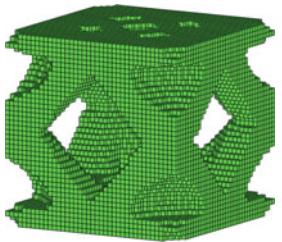
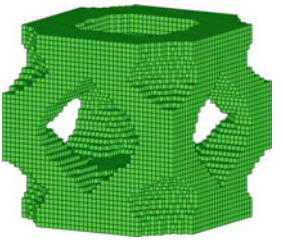
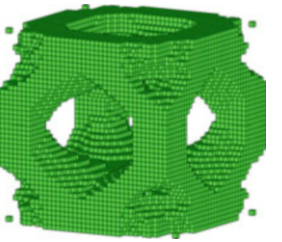
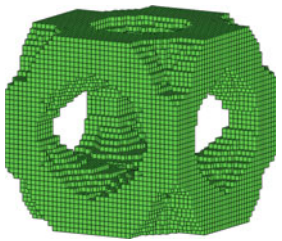
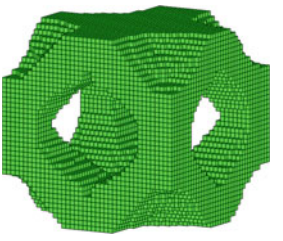
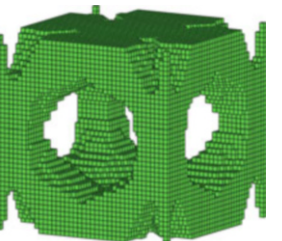
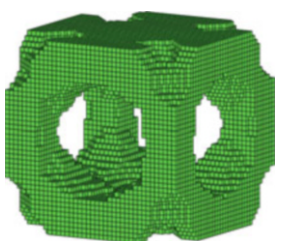
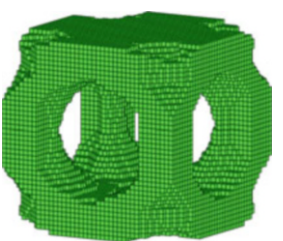
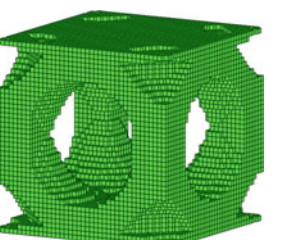
Within the base cell model ($40 \times 40 \times 40$ 8-node hex elements), the red, green and white colours are used to represent the neo-bony tissue, scaffold and connected voids in the results below, respectively (from dark to light in the greyscale copy of this chapter).

The elasticity tensor of mini-pig mandibular condyle trabecular bone with 50% porosity [2, 4] is used as the target stiffness here. The base material used for the scaffold design is isotropic with a Poisson’s ratio of $\nu=0.3$ and a Young’s modulus of 6 GPa, which is higher than that of mini-pig mandibular condyle trabecular bone (around 2.5 GPa), but matches common biomaterials used for fabricating tissue scaffolds [2, 4].

The elasticity tensor of such a trabecular bone \mathbf{C}^0 is weighted by a multiplier β , as $\mathbf{C}^* = \beta\mathbf{C}^0$, in order to study the effect of different levels of targets \mathbf{C}^* on bone remodelling. The porosity of 50% and original target elastic tensor \mathbf{C}^0 ($\beta = 1$) are based on in vitro tests and have been used in the previous studies [2, 4].

The figures in Table 12.2 display the optimised base cells of scaffold with prescribed (target) stiffness values. These designs exhibit a spatially bi-continuous architecture, whose formation is attributed to the anisotropy of the stiffness targets. A base cell with optimised stiffness [39] and optimised diffusivity or permeability [42, 49] would otherwise resemble the well-known tri-continuous Schwarz P architecture, which may be a more ideal structure for cell ingrowth.

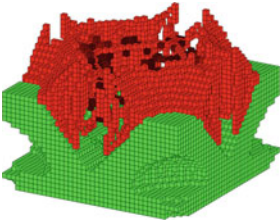
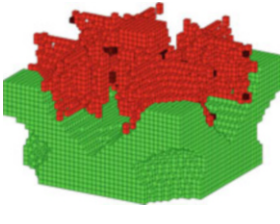
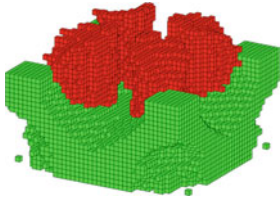
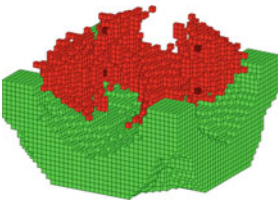

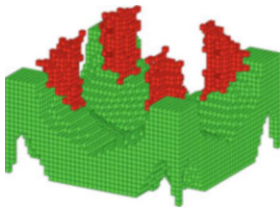
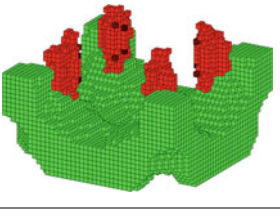
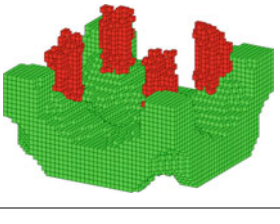
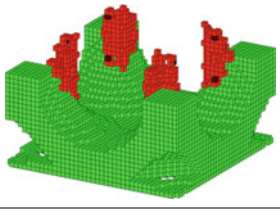
Table 12.2 Results of scaffold designs (porosity = 50 %)

$C^* = 0.80C^0$	$C^* = 0.85C^0$	$C^* = 0.90C^0$
		
		
		

Following the design optimisation, the scaffolds are examined for their remodelling performance in terms of neotissue volume. Here, a remodelling rate constant $\alpha = 0.75$ is used; we keep the lazy zone ($2s = 4/3$) and site-specific homeostatic equilibrium ($\psi_n = 0.03$) unchanged in all the remodelling simulations for comparison. The remodelling results in scaffolds with different stiffness values are shown in Table 12.3. These neotissue elements indicate different distribution patterns in the different base cells. Note that the generation of neotissue affects the stiffness of the scaffold, which in turn affects the remodelling in the subsequent steps.

Figure 12.1 compares the remodelling results for different base cells of scaffold over a time frame of 20 steps. Obviously, the stiffness design with $\beta = 1.00$ generates the highest bone volume, indicating its clear merit in stimulating

Table 12.3 Results of remodelling in scaffolds with different stiffnesses ($\alpha = 0.75$)

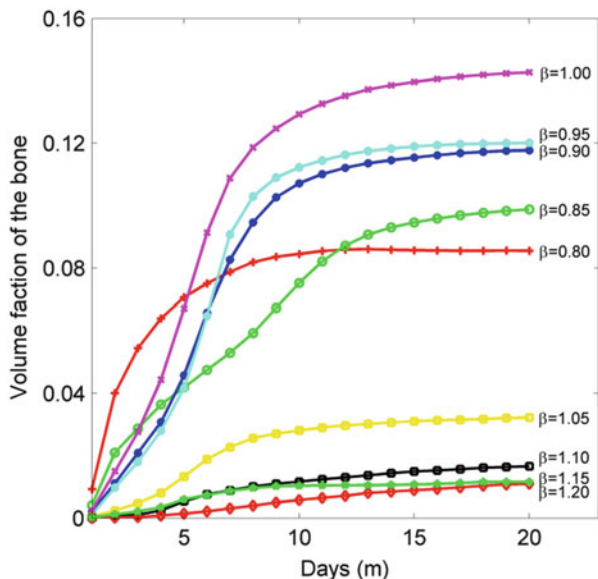
$C^* = 0.80C^0$	$C^* = 0.85C^0$	$C^* = 0.90C^0$
		
$C^* = 0.95C^0$	$C^* = 1.00C^0$	$C^* = 1.05C^0$
		
$C^* = 1.10C^0$	$C^* = 1.15C^0$	$C^* = 1.20C^0$
		

neotissue regeneration. Interestingly, although the tissue growth is not the fastest for $\beta = 1.00$ in the beginning, it exceeds all others after five time steps and maintains its leading position until reaching the state of equilibrium.

The reason why the scaffolds with lower β (e.g. $\beta = 0.80$) exhibits higher neotissue growth in the beginning is that their higher flexibility makes the high SED distribution spread out more evenly inside the scaffold structure. Nevertheless, this advantage quickly diminishes when neotissue stiffens the inner walls of the scaffolds.

In the bone remodelling simulations, the load is not applied directly onto the scaffolds but via a rigid plate on the top of the base cell. The remodelling parameters, ψ_n , s and the uniaxial loading are prescribed with the reasonable values to make tissue remodelling visible from an early stage and comparable in the final stage. It should be noted, however, that selection of the remodelling parameters does not influence the scaffold's relative performance in remodelling.

Fig. 12.1 Bone remodelling processes in scaffolds with different stiffness values over time ($\alpha = 0.75$) (Reprinted from Ref. [16], Copyright 2010, with permission from Elsevier)

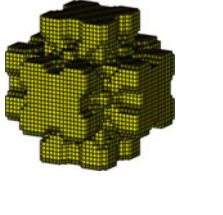
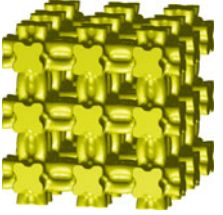
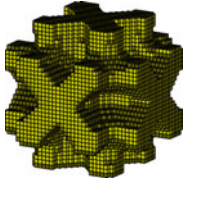
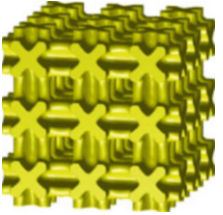
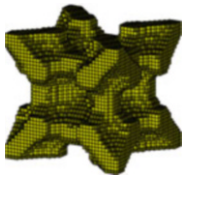
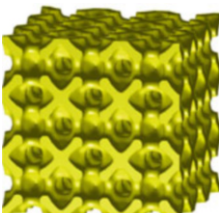
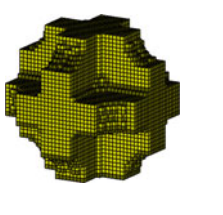



12.3.2 Example for Target Diffusivity

As shown in Table 12.4, different designs of base cells have been obtained using the topology optimisation technique where each model has attained its prescribed effective diffusivity value. The porosity of the base cells were 50 % in all design scenarios. Here we have considered two diffusivity targets: one is 0.75 times the theoretical maximum value (i.e. $D^H = 0.75D^{max}$) and the other is 0.5 times the theoretical maximum value (i.e. $D^H = 0.5D^{max}$), where D^{max} is 0.4 at a porosity of 50 %. Distinct structural features can be observed in these models with different diffusivity targets and among the models with the same diffusivity target but different initialisation settings (Table 12.4b–d).

The results show that for given a diffusivity target lower than the theoretical maximum ($D^{max} = 0.4$), topology optimisation process does not produce a unique solution. In fact, the resultant architecture of base cell is influenced by the choice of its initial model as well as optimisation parameters, as demonstrated by simulation results (b), (c) and (d) in Table 12.4. It is noted that although models (a) and (b) have different diffusivity targets, their structures are somehow similar, which is likely a result of using the same initial model. This reflects the nature of the inverse homogenisation where multiple design solutions may be found to be of a similar goal [50].

Table 12.4 Base cells of tissue scaffold with different diffusivity targets and different initialisation settings

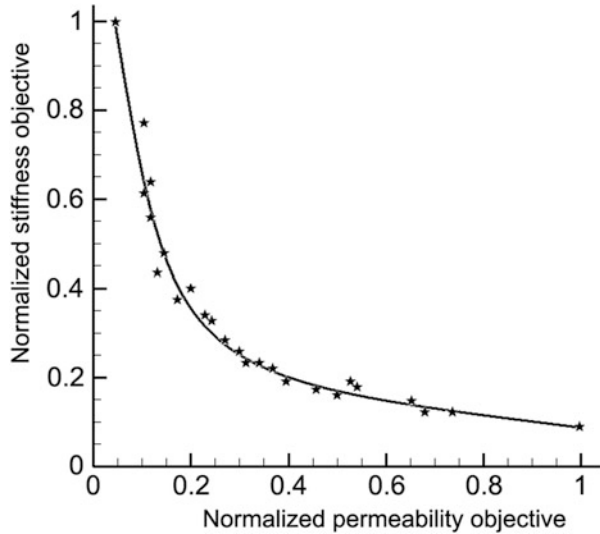
Design target	Optimised base cell	Periodic structure $3 \times 3 \times 3$
(a) Initial design 1: $\mathbf{D}^* = 0.75\mathbf{D}_{50\%}^{\max}$ $\mathbf{D}^H = \begin{bmatrix} 0.2995 & 0 & 0 \\ 0 & 0.2995 & 0 \\ 0 & 0 & 0.2995 \end{bmatrix}$		
(b) Initial design 1: $\mathbf{D}^* = 0.50\mathbf{D}_{50\%}^{\max}$ $\mathbf{D}^H = \begin{bmatrix} 0.2020 & 0 & 0 \\ 0 & 0.2020 & 0 \\ 0 & 0 & 0.2020 \end{bmatrix}$		
(c) Initial design 2: $\mathbf{D}^* = 0.50\mathbf{D}_{50\%}^{\max}$ $\mathbf{D}^H = \begin{bmatrix} 0.2000 & 0 & 0 \\ 0 & 0.2000 & 0 \\ 0 & 0 & 0.2000 \end{bmatrix}$		
(d) Initial design 3: $\mathbf{D}^* = 0.50\mathbf{D}_{50\%}^{\max}$ $\mathbf{D}^H = \begin{bmatrix} 0.2006 & 0 & 0 \\ 0 & 0.2006 & 0 \\ 0 & 0 & 0.2006 \end{bmatrix}$		

12.3.3 Example for Combined Stiffness and Diffusivity

We can also combine the stiffness and diffusivity criteria to create a multiobjective optimisation problem. In this chapter, we have formulated it as a maximisation problem of these two material properties as shown in Eq. (12.12). A full spectrum of base cell designs, each with a special weight factor from Eq. (12.12), has been obtained thereafter to construct the Pareto front (Fig. 12.2). The porosity of base cell remains to be 50% in all these optimal designs.

Some resultant base cells are shown in Table 12.5, where yellow blocks represent solid and the rest of the domain is void. At $w_C = 0$ (indicating the diffusivity

Fig. 12.2 Pareto front of the 3D multiobjective topology optimisation



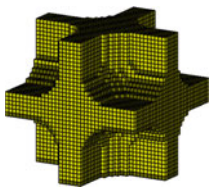
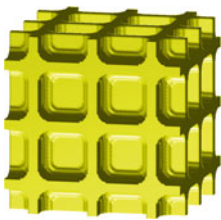
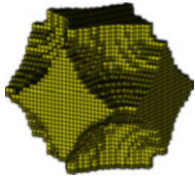
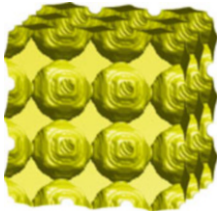
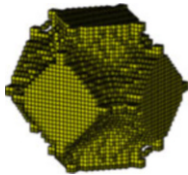
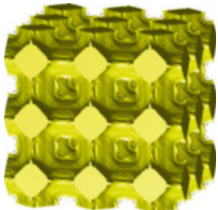
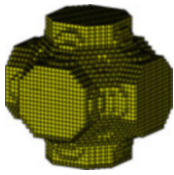
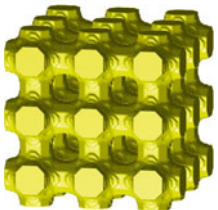
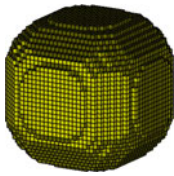

maximisation only [49]), solid phase becomes discontinuous, and the design cannot be fabricated and utilised in reality. As w_C increases, the solid interconnection strengthens. The solid phase has a rounder shape at a low w_C value and acquires a more rigid shape as w_C approaches to 1. When w_C reaches 1, the porous phase becomes discontinuous, which prevents all biotransport in the scaffold.

Following the multiobjective topology optimisation, three representative base cell designs shown in Table 12.5b–d are further examined for polymeric degradation and mechanoregulatory tissue regeneration. Figure 12.3 shows the percentages of cell phenotypes in different design cases in the course of regeneration. It can be seen that, as the emphasis on the diffusivity increases (i.e. from Case (b) to Case (d)), the corresponding design has more osteoblasts (approximately 15%) differentiated from MSCs.

Note that although Case (d) ($w_C = 0.48$) has a relatively lower stiffness in the initial design due to more emphasis on the diffusivity design ($w_D = 0.52$), it exhibits good connectivity of regenerated bony tissue structures, thereby presenting higher effective properties in both stiffness and permeability in the final tissue–scaffold construct. It also promotes effective tissue regeneration and results in more bone formation than the other two cases which have higher w_C . This may suggest that, as long as the scaffold stiffness meets the requirements for mechanical support, increasing the diffusivity of scaffold design can be more beneficial. In other words, the diffusivity criterion appears to play a more critical role than the stiffness criterion in the design of scaffold microarchitecture if enhancing tissue regeneration is the primary goal.

It must be pointed out that while the remodelling results shown in Table 12.3 and Fig. 12.3 provide important insights into the time-dependent outcomes of these several optimised scaffolds, the challenge remains how to optimise the scaffold for

Table 12.5 Optimised base cells with combined stiffness and diffusivity objective

Design with combined stiffness and diffusivity	Optimised base cell	Periodic structure 3 × 3 × 3
<p>(a) $w_C = 1.0, w_D = 0.0$</p> <p>$C_{11}^H = C_{22}^H = C_{33}^H = 0.4412$</p> <p>$C_{44}^H = C_{55}^H = C_{66}^H = 0.1006$</p> <p>$D_{11}^H = D_{22}^H = D_{33}^H = 0$</p>		
<p>(b) $w_C = 0.92, w_D = 0.08$</p> <p>$C_{11}^H = C_{22}^H = C_{33}^H = 0.3861$</p> <p>$C_{44}^H = C_{55}^H = C_{66}^H = 0.0880$</p> <p>$D_{11}^H = D_{22}^H = D_{33}^H = 0.0269$</p>		
<p>(c) $w_C = 0.64, w_D = 0.36$</p> <p>$C_{11}^H = C_{22}^H = C_{33}^H = 0.3443$</p> <p>$C_{44}^H = C_{55}^H = C_{66}^H = 0.0744$</p> <p>$D_{11}^H = D_{22}^H = D_{33}^H = 0.1538$</p>		
<p>(d) $w_C = 0.48, w_D = 0.52$</p> <p>$C_{11}^H = C_{22}^H = C_{33}^H = 0.3336$</p> <p>$C_{44}^H = C_{55}^H = C_{66}^H = 0.0714$</p> <p>$D_{11}^H = D_{22}^H = D_{33}^H = 0.3237$</p>		
<p>(e) $w_C = 0.0, w_D = 0.1$</p> <p>$C_{11}^H = C_{22}^H = C_{33}^H = 0$</p> <p>$C_{44}^H = C_{55}^H = C_{66}^H = 0$</p> <p>$D_{11}^H = D_{22}^H = D_{33}^H = 0.3975$</p>		

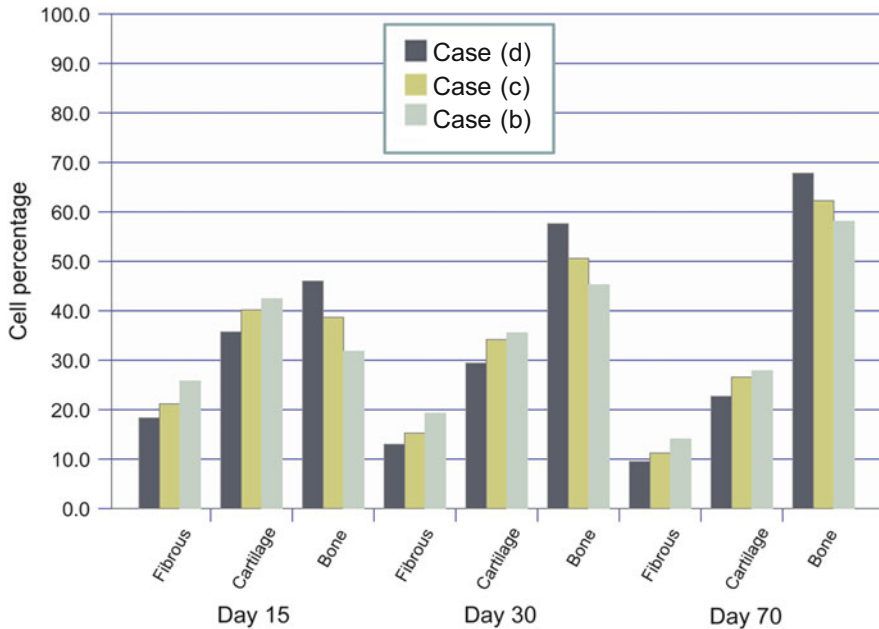


Fig. 12.3 Percentages of cell phenotypes during tissue regeneration within different scaffold architectures in the three representative cases (Reprinted from Ref. [6], Copyright 2011, with permission from Elsevier)

assuring an ongoing, rather than initial, performance. This implies that the remodelling-based design optimisation should be a topic for the futuristic studies.

12.4 Conclusion

This chapter developed a systematic methodology for structural design of periodic tissue scaffolds, in which the mechanical and biological requirements of scaffold were formulated as the stiffness and diffusivity criteria. In the periodic structures, base cell finite element (FE) models were created under periodic boundary conditions. To characterise the effective stiffness and effective diffusivity, the finite element-based homogenisation technique was employed. For any given base cell materials and configuration, the effective or homogenised properties can be obtained from the finite element analysis.

In order to attain desired effective material properties, an inverse homogenisation was formulated to seek possible base cell configuration. In this chapter, we considered three different design scenarios: (1) desired stiffness, (2) desired diffusivity and (3) combination of maximum stiffness and diffusivity. It was shown that these different criteria led to different base cell topologies.

To assess the performance of optimised scaffolds under different criteria, we also modelled the tissue regeneration in these scaffolds and examined their relative performances in terms of volume of functional tissues (e.g. bone). The remodelling calculation on these different scaffold structures provided some important insights into how to impose these design criteria for achieving certain tissue generation outcome.

It must be pointed out that the design optimisation presented in this chapter has restricted to two relatively simple criteria (elasticity and diffusivity) from a biomechanical perspective and topological variables from a structural perspective. As a matter of fact, tissue engineering is a highly complex process and involves a full range of multidisciplinary challenges and requirements. The future optimisation of scaffolds should therefore consider as many relevant factors as possible with other design variables, such as chemical composition and growth factor concentration, rather than structural topology.

Acknowledgement The financial supports from the Australian Research Council through the Future Fellowship and Discovery Scheme are greatly appreciated.

References

1. Langer R, Vacanti JP (1993) Tissue engineering. *Science* 260(5110):920–926
2. Lin CY, Kikuchi N, Hollister SJ (2004) A novel method for biomaterial scaffold internal architecture design to match bone elastic properties with desired porosity. *J Biomech* 37(5):623–636
3. Hollister SJ (2005) Porous scaffold design for tissue engineering. *Nat Mater* 4(7):518–524
4. Lin CY et al (2005) Functional bone engineering using ex vivo gene therapy and topology-optimized, biodegradable polymer composite scaffolds. *Tissue Eng* 11(9–10):1589–1598
5. Hollister SJ, Maddox RD, Taboas JM (2002) Optimal design and fabrication of scaffolds. *Biomaterials* 23:4095–4103
6. Chen Y, Zhou S, Li Q (2011) Microstructure design of biodegradable scaffold and its effect on tissue regeneration. *Biomaterials* 32(22):5003–5014
7. Adachi T et al (2006) Framework for optimal design of porous scaffold microstructure by computational simulation of bone regeneration. *Biomaterials* 27(21):3964–3972
8. MacArthur BD, Oreffo ROC (2005) Bridging the gap. *Nature* 433(7021):19
9. Sanz-Herrera JA, Garcia-Aznar JM, Doblare M (2009) On scaffold designing for bone regeneration: a computational multiscale approach. *ACTA Biomater* 5:219–229
10. Sun W et al (2004) Computer-aided tissue engineering: application to biomimetic modelling and design of tissue scaffolds. *Biotechnol Appl Biochem* 39(1):49–58
11. Sun W et al (2005) Bio-CAD modeling and its applications in computer-aided tissue engineering. *Comput Aided Des* 37:1097–1114
12. Marga F et al (2012) Toward engineering functional organ modules by additive manufacturing. *Biofabrication* 4(2):12
13. Williams JM et al (2005) Bone tissue engineering using polycaprolactone scaffolds fabricated via selective laser sintering. *Biomaterials* 26(23):4817–4827
14. Hollister SJ (2009) Scaffold design and manufacturing: from concept to clinic. *Adv Mater* 21(32–33):3330–3342

15. Fang Z, Starly B, Sun W (2005) Computer-aided characterization for effective mechanical properties of porous tissue scaffolds. *CAD Comput Aid Des* 31:65–72
16. Sturm S et al (2010) On stiffness of scaffolds for bone tissue engineering—a numerical study. *J Biomech* 43(9):1738–1744
17. Byrne DP et al (2007) Simulation of tissue differentiation in a scaffold as a function of porosity, Young's modulus and dissolution rate: application of mechanobiological models in tissue engineering. *Biomaterials* 28:5544–5554
18. Chen Y, Zhou S, Li Q (2011) Mathematical modeling of degradation for bulk-erosive polymers: applications in tissue engineering scaffolds and drug delivery systems. *Acta Biomater* 7(3):1140–1149
19. Huijkes R et al (2000) Effects of mechanical forces on maintenance and adaptation of form in trabecular bone. *Nature* 405(6787):704–706
20. Sun W et al (2004) Computer-aided tissue engineering: overview, scope and challenges. *Biotechnol Appl Biochem* 39:29–47
21. Cadman JE et al (2013) On design of multi-functional microstructural materials. *J Mater Sci* 48(1):51–66
22. Bensoussan A, Papanicolaou G, Lions JL (1978) Asymptotic analysis for periodic structures, vol 5, *Studies in mathematics and its applications*. North Holland Publishing Co., Amsterdam. xxiv, 700 23 cm
23. Sanchez-Palencia E (1980) Non-homogeneous media and vibration theory. *Lecture Notes in Physics*. Vol 127. Springer, Berlin
24. Guedes JM, Kikuchi N (1990) Preprocessing and postprocessing for materials based on the homogenization method with adaptive finite element methods. *Comput Methods Appl Mech Eng* 83:143–198
25. Hassani B, Hinton E (1998) A review of homogenization and topology optimization I – homogenization theory for media with periodic structure. *Comput Struct* 69(6):707–717
26. Bendsoe MP, Sigmund O (2013) *Topology optimization: theory, methods, and applications*. Springer Science & Business Media, Berlin
27. Silva ECN, Fonseca JSO, Kikuchi N (1998) Optimal design of periodic piezocomposites. *Comput Methods Appl Mech Eng* 159(1-2):49–77
28. Sigmund O (1994) Design of material structures using topology optimisation. Technical University of Denmark, Lyngby
29. Sigmund O (1994) Tailoring materials for specific needs. *J Intell Mater Syst Struct* 5(6):736–742
30. Catledge SA et al (2007) An electrospun triphasic nanofibrous scaffold for bone tissue engineering. *Biomed Mater* 2:142–150
31. Aubert G, Kornprobst P (2006) *Mathematical problems in image processing: partial differential equations and the calculus of variations*. 2nd edn. Springer, New York, xxxi:377
32. Wang MY, Zhou S, Ding H (2004) Nonlinear diffusions in topology optimization. *Struct Multidiscip Optim* 28(4):262–276
33. Svanberg K (1987) The method of moving asymptotes – a new method for structural optimization. *Int J Numer Methods Eng* 24(2):359–373
34. Malda J et al (2004) Oxygen gradients in tissue – engineered Pegt/Pbt cartilaginous constructs: measurement and modeling. *Biotechnol Bioeng* 86(1):9–18
35. Steven G, Li Q, Xie Y (2000) Evolutionary topology and shape design for general physical field problems. *Comput Mech* 26(2):129–139
36. Zhou S et al (2012) Design and fabrication of biphasic cellular materials with transport properties—a modified bidirectional evolutionary structural optimization procedure and MATLAB program. *Int J Heat Mass Transf* 55(25):8149–8162
37. Kang H, Lin C-Y, Hollister SJ (2010) Topology optimization of three dimensional tissue engineering scaffold architectures for prescribed bulk modulus and diffusivity. *Struct Multidiscip Optim* 42(4):633–644

38. Guest JK, Prevost JH (2006) Optimizing multifunctional materials: design of microstructures for maximized stiffness and fluid permeability. *Int J Solids Struct* 43(22-23):7028–7047
39. de Kruijf N et al (2007) Topological design of structures and composite materials with multiobjectives. *Int J Solids Struct* 44(22):7092–7109
40. Chen Y, Zhou S, Li Q (2009) Computational design for multifunctional microstructural composites. *Int J Mod Phys B* 23(06n07):1345–1351
41. Chen Y, Zhou S, Li Q (2010) Multiobjective topology optimization for finite periodic structures. *Comput Struct* 88(11):806–811
42. Hollister SJ, Lin CY (2007) Computational design of tissue engineering scaffolds. *Comput Methods Appl Mech Eng* 196(31–32):2991–2998
43. Parfitt AM (1994) Osteonal and hemi-osteonal remodeling – the spatial and temporal framework for signal traffic in adult human bone. *J Cell Biochem* 55(3):273–286
44. Carter DR (1984) Mechanical loading histories and cortical bone remodeling. *Calcif Tissue Int* 36:S19–S24
45. Huiskes R et al (1987) Adaptive bone-remodeling theory applied to prosthetic-design analysis. *J Biomech* 20(11–12):1135–1150
46. Rice JC, Cowin SC, Bowman JA (1988) On the dependence of the elasticity and strength of cancellous bone on apparent density. *J Biomech* 21(2):155–168
47. Beaupré GS, Orr TE, Carter DR (1990) An approach for time-dependent bone modeling and remodeling – theoretical development. *J Orthop Res* 8:651–661
48. Prendergast PJ, Huiskes R, Soballe K (1997) Biophysical stimuli on cells during tissue differentiation at implant interfaces. *J Biomech* 30(6):539–548
49. Guest JK, Prevost JH (2007) Design of maximum permeability material structures. *Comput Methods Appl Mech Eng* 196(4–6):1006–1017
50. Zhou S, Li Q (2008) Computational design of multi-phase microstructural materials for extremal conductivity. *Comput Mater Sci* 43(3):549–564

Chapter 13

Bioactive Scaffolds with Multifunctional Properties for Hard Tissue Regenerations

Chengtie Wu, Jiang Chang, and Yin Xiao

Abstract The impact of bone/dental diseases and trauma in the whole world has increased significantly in the past decades. It is of great importance to develop bioactive scaffolds with multifunctional properties, such as osteogenesis, angiogenesis, cementogenesis, drug delivery and antibacterial property for hard tissue regeneration. Conventional bioactive scaffolds cannot efficiently combine these functions. A new class of bioactive glass, referred to as mesoporous bioactive glass (MBG), was developed several years ago, which possesses highly ordered mesoporous channel structure and high-specific surface area. Due to their special nanostructure, MBG scaffolds show multifunctional potential for hard tissue regeneration application. In this chapter, we review the recent research advances of multifunctional MBG scaffolds, including the preparation of different forms of MBG scaffolds, osteogenesis, angiogenesis, cementogenesis, drug delivery and antibacterial property. The future perspective of MBG scaffolds was further discussed for hard tissue regeneration application by harnessing their special multifunction.

Keywords Bioactive scaffolds • Mesoporous bioactive glass • Multifunction • Osteogenesis • Angiogenesis

13.1 Introduction

The treatment of hard tissue defects, especially large bone and periodontal defects resulting from trauma, infection, tumour or genetic malformation, represents a major challenge for clinicians [1]. To solve these problems, bioactive porous

C. Wu (✉) • J. Chang

State Key Laboratory of High Performance Ceramics and Superfine Microstructure, Shanghai Institute of Ceramics, Chinese Academy of Sciences, 200050 Shanghai, People's Republic of China

e-mail: chentiewu@mail.sic.ac.cn

Y. Xiao

Institute of Health & Biomedical Innovation, Queensland University of Technology, 4059 Brisbane, QLD, Australia

scaffolds have been widely studied to regenerate the lost/damaged hard tissues [2]. For better regeneration of large hard tissue defects, bioactive scaffolds should possess not only osteoconductivity (for guidance of new bone growth) but also the ability to stimulate both osteogenesis (for promoting new bone formation) and angiogenesis (for inducing vascularisation) [1, 3–5]. In addition, in bone reconstruction surgery, osteomyelitis caused by bacterial infection is an ever-present and serious complication. Conventional treatments include systemic antibiotic administration, surgical debridement, wound drainage and implant removal [6]. These approaches, however, are rather inefficient and may result in additional surgical interventions for the patients.

A new approach for solving this problem is to introduce local drug release system into the implant site. The advantages of this treatment include high delivery efficiency, continuous action, reduced toxicity and convenience to the patients [6, 7]. For this reason, bioactive scaffolds with an in-built drug delivery and antibacterial property would be very useful for bone and periodontal tissue regeneration and could solve the risk of osteomyelitis incidences caused by infection of the bone. Therefore, ideal bioactive porous scaffolds for the treatment of large bone and periodontal defects should possess multiple functions by combining angiogenesis, osteostimulation and drug delivery with antibacterial properties. However, to our best knowledge, few bioactive porous scaffolds possess such ‘real’ multifunctional properties [8].

Conventional bioactive calcium phosphate (Ca-P)-based bioceramic scaffolds, such as hydroxyapatite (HAp) and β -tricalcium phosphate (β -TCP), possess osteoconductivity, but lack osteostimulation and drug delivery function due to few nanopores in the sintered scaffolds treated by high temperature. Recent study has shown that the sintered Ca-P-based bioceramics, especially HAp, lack full biodegradability after implantation [9, 10]. Although β -TCP ceramics have been regarded as biodegradable materials, their degradation kinetics tends to be slow [11].

Bioactive glasses have played an increasingly important role in bone tissue regeneration applications by virtue of their generally excellent osteoconductivity, osteostimulation and degradation rate [1, 12–16]. Typically, the melt bioactive glass, called 45S5 Bioglass[®], was pioneered by Hench [17, 18] and was first developed using traditional melt method at high temperature (1300–1500 °C). The 45S5 Bioglass[®] has been regarded as bioactive bone regeneration materials which are able to bond closely with the host bone tissue [17]. Further studies have also showed that the Ca and Si containing ionic products released from the 45S5 contribute to its bioactivity, as both Ca and Si are found to stimulate osteoblast proliferation and differentiation [19–24]. Xynos et al. further found that 45S5 Bioglass[®] is able to enhance the expression of a potent osteoblast mitogenic growth factor, insulin-like growth factor-2 (IGF-2) [23, 25]. However, the 45S5 Bioglass[®] has a number of limitations [25]. One of them is the fact that it needs to be melted at a very high temperature (>1300 °C), and the other is its lack of microporous structure inside the materials with low specific surface area; therefore, the bioactivity of melt bioactive glasses will mainly depend on the contents of SiO₂

[25]. Generally, the bioactivity of melt bioactive glasses will decrease with the increase in the SiO_2 contents [1, 18, 26]. In the early 1990s, in an effort to overcome the limitation of melt bioactive glasses, Li et al. prepared sol-gel bioactive glasses [27]. Although sol-gel bioactive glasses have better compositional range and bioactivity than melt bioactive glasses, the micropore distribution is not uniform and inadequate for efficient drug loading and release [25, 28, 29].

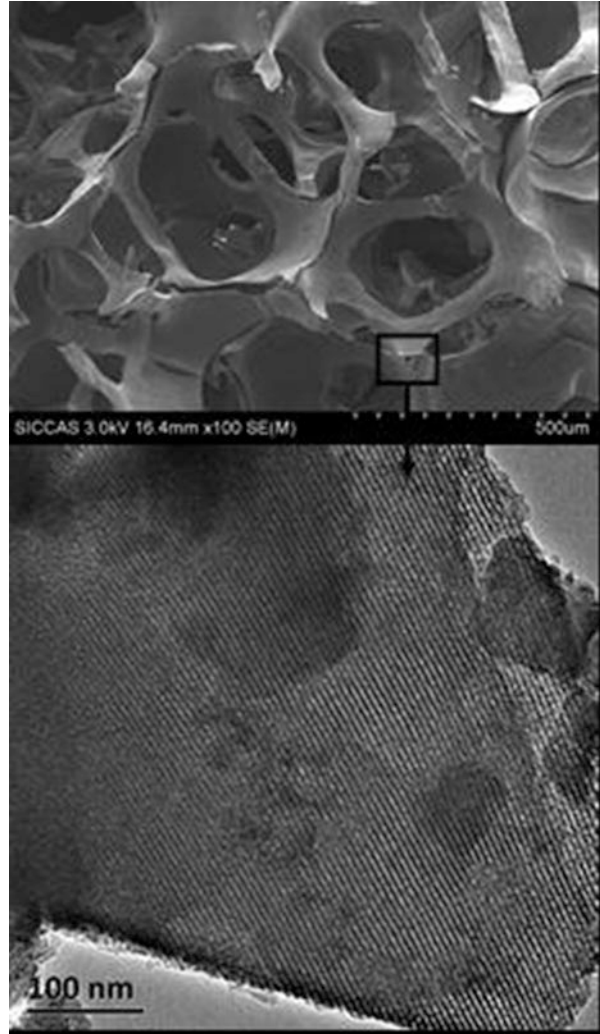
To overcome the limitations of conventional bioactive glasses (without well-ordered mesopore structures for drug delivery), it is of great importance to design and develop a new class of biomaterials which combine multifunctional properties, such as osteogenesis, angiogenesis, drug delivery and antibacterial characteristics. Yu et al., for the first time, prepared the mesoporous bioactive glass (MBG) particles in 2004 by the combination of sol-gel method and supramolecular chemistry of surfactants [30, 31]. Their study has paved a new avenue for applying nanotechnology to regenerative medicine by coupling drug delivery with bioactive materials. Their materials are based on a $\text{CaO-SiO}_2\text{-P}_2\text{O}_5$ composition and have a highly ordered mesopore channel structure with a nanoscale pore size ranging from 5 to 20 nm. Compared to conventional non-mesopore bioactive glasses (NBG), the MBG possesses a more optimal surface area, pore volume, ability to induce *in vitro* apatite mineralisation in SBF and excellent cytocompatibility [31–35]. However, for bone and periodontal tissue regeneration, MBG particles are not always ideal. It is of great interest and importance to develop MBG scaffolds with multifunctional properties. Therefore, in this chapter, we review the recent advances of MBG scaffolds, as multifunctional materials for hard tissue regeneration.

13.2 Preparation and Characterisation of Multifunctional MBG Scaffolds

MBG scaffolds could be prepared by three approaches [35]. The first is the porogen method, in which Yun et al. applied methyl cellulose as the porogen to prepare porous MBG scaffolds with large pore size of 100 μm and mesopore size of around 5 nm; however, the prepared large pores are not fairly uniform and interconnective though the mesoporous channels are well ordered [36].

The second is the polymer template method, which has been widely used. We, for the first time, prepared the MBG scaffolds with a large pore size of 400 μm by using polyurethane sponge as a porous template [37]. At the same time, Li et al. also prepared the MBG scaffolds using the same technique [38]. After that, we have developed a series of MBG scaffolds with varying compositions for drug delivery and bone tissue engineering applications as shown in Fig. 13.1 [7, 39–41]. The advantages of the MBG scaffolds prepared by the polyurethane sponge template method are their highly interconnective pore structure and controllable pore size (porosity), while the disadvantage is the low mechanical strength of the material

Fig. 13.1 SEM and TEM analysis for the MBG scaffolds prepared by spongy template method. SEM (*upper image*) showed highly interconnective porous scaffolds with large pore size of 300–500 μm ; TEM (*lower image*) showed that the large pore walls of scaffolds had well-ordered mesoporous channel structure (around 5 nm)



[42]. The compressive strength of the MBG scaffolds prepared by the polymer template method is lower than 200 kPa.

To better control the pore morphology, pore size, porosity and mechanical strength, 3D plotting technique (also called additive fabrication, direct writing or printing) has been developed to prepare porous MBG scaffolds. The significant advantage of this technique is that the architectures of the scaffolds can be concisely controlled by layer-by-layer plotting under mild conditions [43–45]. Yun and Garcia, et al. prepared the hierarchical 3D porous MBG scaffolds using a combination of double polymer template and rapid prototyping techniques [46, 47]. In their study, they mixed the MBG gel with methylcellulose and then printed, sintered

at 500–700 °C to remove polymer templates for obtaining the MBG scaffolds. The main limitation of their method for preparing MBG scaffolds is the need of methylcellulose and the additional sintering procedure. Although the obtained MBG scaffolds have uniform pore structure, their mechanical strength is compromised because of the incorporation of methylcellulose which results in some micropores. Recently, we reported a new facile method to prepare hierarchical and multifunctional MBG scaffolds with controllable pore architecture, excellent mechanical strength and mineralisation ability for bone regeneration application by a modified 3D printing technique using polyvinyl alcohol (PVA) as a binder as shown in Fig. 13.2. The 3D-printed MBG scaffolds obtained possess a high mechanical strength which is about 200 times of that of the MBG scaffolds prepared using traditional polyurethane foam as templates. The compressive strength could reach 16 MPa. Such scaffolds have highly controllable pore

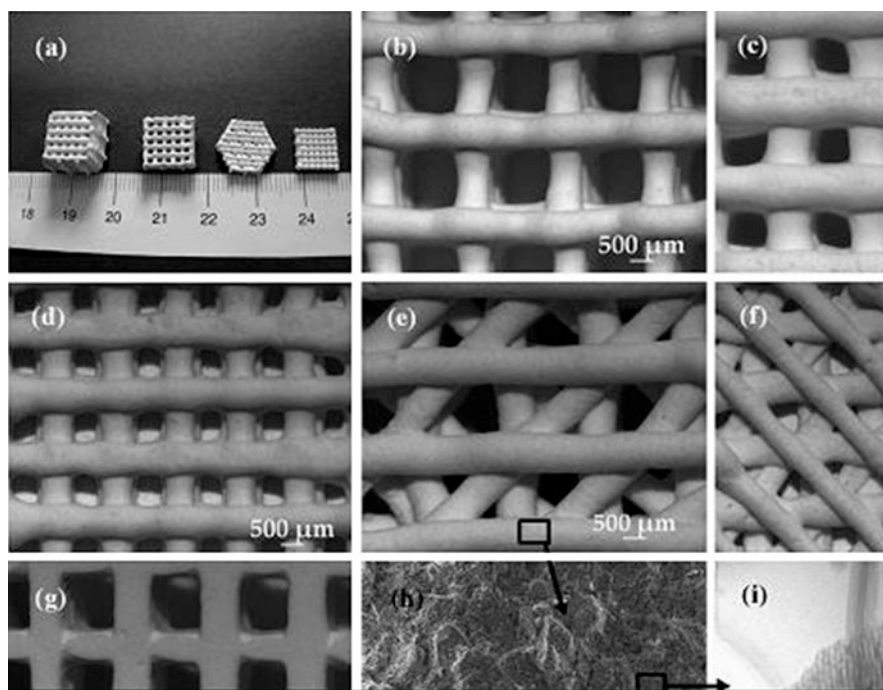


Fig. 13.2 MBG scaffolds, pore morphology and microstructure. (a) MBG scaffolds, obtained by the 3D printing method with different sizes, shapes and morphologies. (b, c and d) MBG scaffolds with different pore sizes (varying from $1307 \pm 40 \mu\text{m}$ (b) and $1001 \pm 48 \mu\text{m}$ (c) to $624 \pm 40 \mu\text{m}$ (d)). (d, e and f) MBG scaffolds with different pore morphologies. (g) Pore morphology of the bottom side for MBG scaffolds. The pores on the bottom side keep open. (h) SEM image of the microstructure of pore walls. (i) TEM micrographs demonstrating the well-ordered mesopore channel structure of the pore walls in scaffolds; the size of mesopore channel is about 5 nm (Reprinted with permission from Ref. [48] copyright 2011 by Elsevier)

Table 13.1 The mesoporous structure characteristics of MBG scaffolds

Scaffold compositions	Surface area (m ² /g)	Pore volume (cm ³ /g)	Pore size (nm)	References
CaO-P ₂ O ₅ -SiO ₂	350	0.33	4.8	[37]
CuO-CaO-P ₂ O ₅ -SiO ₂	310–330	0.36–0.44	3.8–4.7	[8]
CoO-CaO-P ₂ O ₅ -SiO ₂	127–180	0.15–0.19	4.1–4.5	[49]
SrO-CaO-P ₂ O ₅ -SiO ₂	88–200	0.11–0.27	5.0	[50]
MgO-CaO-P ₂ O ₅ -SiO ₂	269	0.34	3.6	[51]
B ₂ O ₃ -CaO-P ₂ O ₅ -SiO ₂	194–234	0.21–0.24	5.1–5.3	[41]
Fe ₂ O ₃ -CaO-P ₂ O ₅ -SiO ₂	268	–	4.5	[40]
ZrO ₂ -CaO-P ₂ O ₅ -SiO ₂	227–287	0.27–0.32	3.4–4.1	[7]

architecture, excellent apatite mineralisation ability and sustained drug delivery property [35, 48].

Currently, the prepared MBG scaffolds are mainly based on the compositions of CaO-P₂O₅-SiO₂-MxOy (M: Cu, Co, Zr, Zn, Sr and B) system. The incorporation of functional elements of Cu, Co, Zr, Zn, Sr or B decreased the surface area and mesopore volume of MBG scaffolds. However, they still maintain high mesoporous level, and their surface area and mesopore volume are generally in the range of 200–400 m²/g and 0.2–0.4 cm³/g, respectively. The well-ordered mesopore size of the prepared MBG scaffolds is in the range of 4–5.5 nm. The typical structural characteristics of the prepared MBG scaffolds with varied compositions are shown in Table 13.1.

13.3 The In Vitro and In Vivo Osteogenesis, Angiogenesis and Cementogenesis of Multifunctional MBG Scaffolds

In the past 5 years, we have systematically investigated the in vitro and in vivo osteogenesis, angiogenesis and cementogenesis of the MBG scaffolds incorporated with varied functional elements. It was found that these functional elements in the MBG scaffolds play an important role in improving their multifunctional properties. The functional effects of different elements in MBG scaffolds are summarised in Table 13.2.

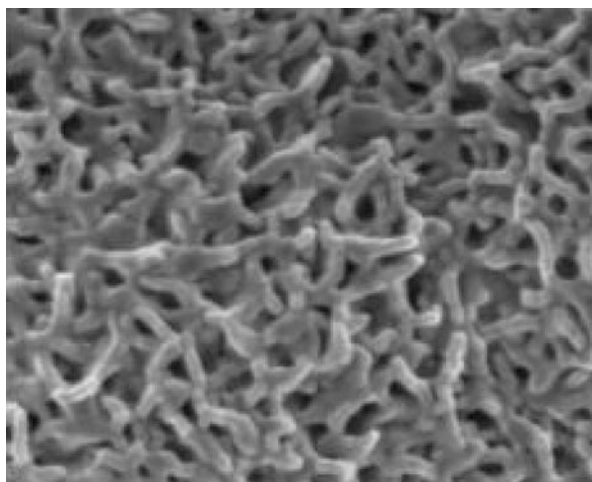
13.3.1 The Osteogenesis of MBG Scaffolds

It was found that the MBG scaffolds possess excellent apatite mineralisation ability as shown in Fig. 13.3, which was regarded one of the critical factors to contribute to

Table 13.2 The multifunctional properties the MBG scaffolds with varied compositions

Scaffold compositions	Multifunctional properties
CaO-P ₂ O ₅ -SiO ₂	Osteogenesis, drug delivery
MgO-CaO-P ₂ O ₅ -SiO ₂	
B ₂ O ₃ -CaO-P ₂ O ₅ -SiO ₂	
ZrO ₂ -CaO-P ₂ O ₅ -SiO ₂	
CoO-CaO-P ₂ O ₅ -SiO ₂	Osteogenesis, angiogenesis, drug delivery
CuO-CaO-P ₂ O ₅ -SiO ₂	
Fe ₂ O ₃ -CaO-P ₂ O ₅ -SiO ₂	Osteogenesis, hypothermia, drug delivery
SrO-CaO-P ₂ O ₅ -SiO ₂	Osteogenesis, cementogenesis, drug delivery
Li ₂ O-CaO-P ₂ O ₅ -SiO ₂	

Fig. 13.3 The MBG scaffolds possess excellent apatite mineralisation ability in the simulated body fluids



the *in vivo* bioactivity of bone regeneration materials. Compared with non-mesoporous bioactive glass (NBG) scaffolds, the MBG scaffolds have significantly improved apatite mineralisation ability in simulated body fluids attributable to their high surface area and mesoporous volume [35]. In this regard, Garcia et al. studied the mechanism of apatite mineralisation of MBG by using nuclear magnetic resonance spectroscopy [52]. The significant difference of the apatite formation mechanism between MBG and conventional NBG is that MBG does not require the typical ‘first three stages’ [52], but conventional NBG does [26]. In the first three stages, conventional NBG releases M⁺ ions and form Si-OH groups, and then Si-OH groups form networks by repolymerisation. However, the surface of MBG is already inherently ‘prepared’ to accelerate the first three stages of the conventional NBG [52].

In addition to the excellent apatite mineralisation ability in the simulated body fluids, the MBG scaffolds possess excellent *in vitro* osteogenesis, which is evidenced by the attachment, proliferation and differentiation of bone-forming cells in the scaffolds as shown in Fig. 13.4. The incorporation of Mg, Sr, B, Fe

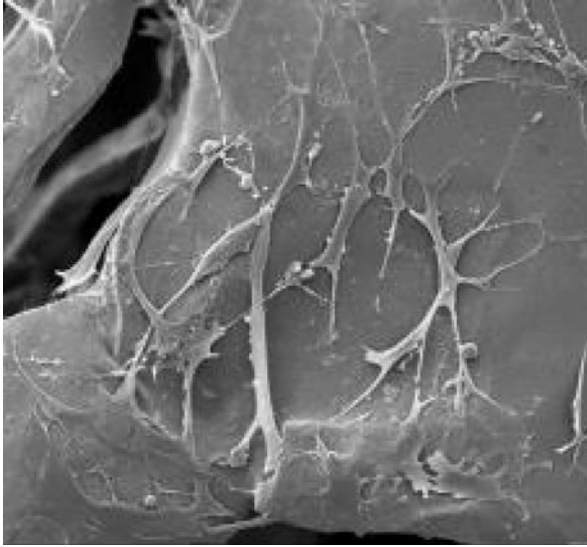


Fig. 13.4 BMSCs growing in MBG scaffolds

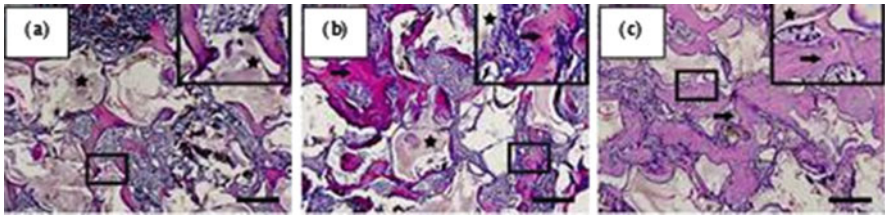


Fig. 13.5 The in vivo osteogenesis of the Sr-containing MBG scaffolds after implanted for 8 weeks. (a) MBG, (b) 2.5 % Sr-MBG and (c) 5 % Sr-MBG

and Zr significantly enhanced the cell proliferation and bone-related gene expression of osteoblasts or bone marrow stromal cells (BMSCs) [41, 42, 51].

Critical-sized femur defects in ovariectomised rats were created to simulate an osteoporotic phenotype. After implanted for 8 weeks, the results showed that the MBG scaffolds induced new bone formation in the osteoporotic bone defects, and the incorporation of Sr into the MBG scaffolds significantly stimulated new bone formation in the osteoporotic bone defects, indicating that the MBG scaffolds possess excellent in vivo osteogenesis (see Fig. 13.5).

13.3.2 The Angiogenesis of MBG Scaffolds

It is known that angiogenesis of porous scaffolds is of great importance to stimulate the tissue formation. Some studies have suggested that insufficient level of oxygen,

a condition known as hypoxia, plays a critical role in cell recruitment, cell differentiation and vessel formation, linking osteogenesis closely to angiogenesis [53–56]. Hypoxia-inducible factor-1 (HIF-1), a transcriptional factor consisting of α - and β -subunits (HIF-1 α and HIF-1 β), has already been identified as one of the critical proteins directly reacting to hypoxia [57]. Under a hypoxic condition, HIF-1 α binds to HIF-1 β and initiates the transcription of hypoxia-sensitive genes that include vascular endothelial growth factor (VEGF) among others [58, 59]. Hypoxia can be artificially mimicked by stabilising HIF-1 α expression and has been suggested as a potential strategy to promote neovascularisation [60–62].

To prepare the hypoxia-mimicking MBG scaffolds, we have incorporated Cu or Co into the MBG scaffolds to induce the pro-angiogenesis of BMSCs. The results showed that incorporation of chemical Cu (Fig. 13.6) and Co (Fig. 13.7) ions into MBG scaffolds is a viable way to inducing hypoxia effect on the BMSCs. Both Cu-MBG scaffolds and their ionic extracts could stimulate hypoxia-inducible factor (HIF)-1 α and vascular endothelial growth factor (VEGF) expression in human bone marrow stromal cells (hBMSCs). In addition, both Cu-MBG scaffolds and their ionic extracts significantly promoted the osteogenic differentiation of hBMSCs by improving their bone-related gene expression (alkaline phosphatase (ALP), osteopontin (OPN) and osteocalcin (OCN)) [8]. Similarly, low amounts of Co (<5%) incorporated into the MBG scaffolds had no significant cytotoxicity, and their incorporation significantly enhanced VEGF protein secretion, HIF-1 α expression and bone-related gene expression in BMSCs, and also the Co-MBG scaffolds support BMSC attachment and proliferation [49]. The study suggested that parts of Cu or Co in MBG scaffolds significantly improved both the angiogenesis and osteogenesis of BMSCs with a multifunctional effect for bone tissue engineering.

13.3.3 The Cementogenesis of MBG Scaffolds

In addition to the osteogenesis and angiogenesis of MBG scaffolds in vitro and in vivo, Sr- or Li-containing MBG scaffolds significantly stimulated the proliferation and bone-/cementum-related gene expression of periodontal ligament cells. Sr plays an important role in influencing the mesoporous structure of MBG scaffolds in which high contents of Sr decreased the well-ordered mesopores as well as their surface area/pore volume. Sr²⁺ ions could be released from Sr-MBG scaffolds in a controlled way. The incorporation of Sr into MBG scaffolds has significantly stimulated alkaline phosphatase (ALP) activity and osteogenesis-/cementogenesis-related gene expression (ALP, Runx2, Col I, OPN and CEMP1) of PDLCs. Furthermore, the Sr-MBG scaffolds in simulated body fluid environment still maintain their excellent apatite mineralisation ability. The study suggested that the incorporation of Sr into MBG scaffolds is a viable way to stimulate the biological response of PDLCs [50].

The Li-MBG scaffolds with hierarchically large pores (300–500 μ m) and well-ordered mesopores (5 nm) were also successfully prepared by incorporating Li⁺ ions into the scaffolds. We further investigated the cell proliferation and

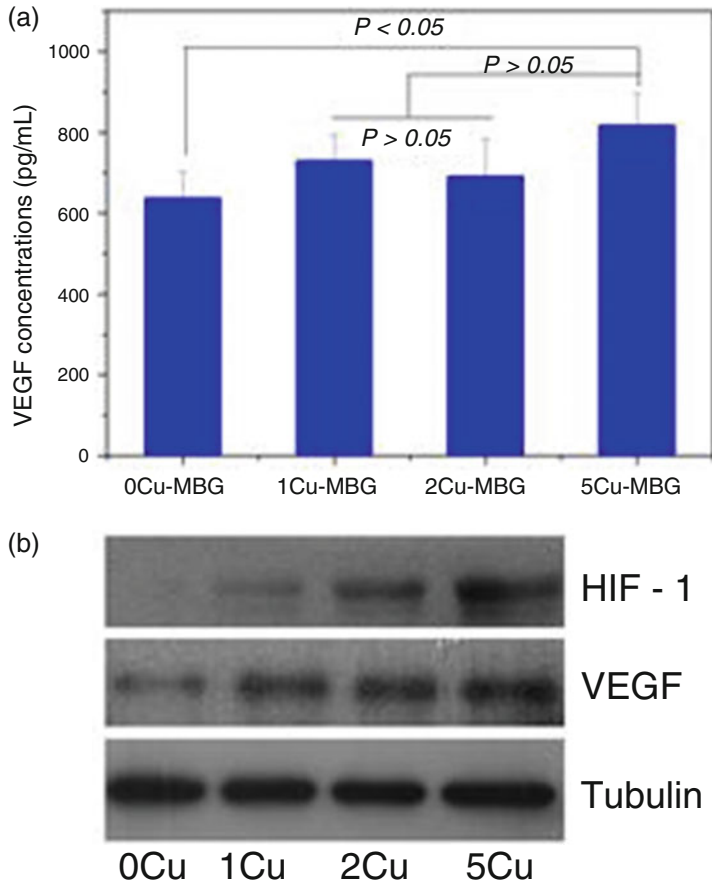


Fig. 13.6 VEGF secretion by ELISA (a) and HIF-1 α and VEGF expression by western blotting (b) for hBMSCs on Cu-MBG scaffolds (Reprinted with permission from Ref. [8] copyright 2013 by Elsevier)

cementogenic differentiation, including Wnt- and Shh-related gene expression of hPDLCs cultured with the Li-MBG scaffolds and Li⁺ ion-containing medium. It was found that the incorporation of 5% Li⁺ into MBG scaffolds significantly enhanced cell proliferation and cementogenic differentiation, as well as activation of Wnt and Shh signaling pathways in hPDLCs (see Fig. 13.8). Li⁺ by itself was sufficient to promote the cell proliferation, differentiation and cementogenic-related gene expression in hPDLCs. These results suggested that the Li⁺ ions released from such bioactive MBG scaffolds play an important role in enhancing cementogenesis of PDLCs on bioactive scaffolds and this biological reaction may be via activation of Wnt and Shh signaling pathways [63].

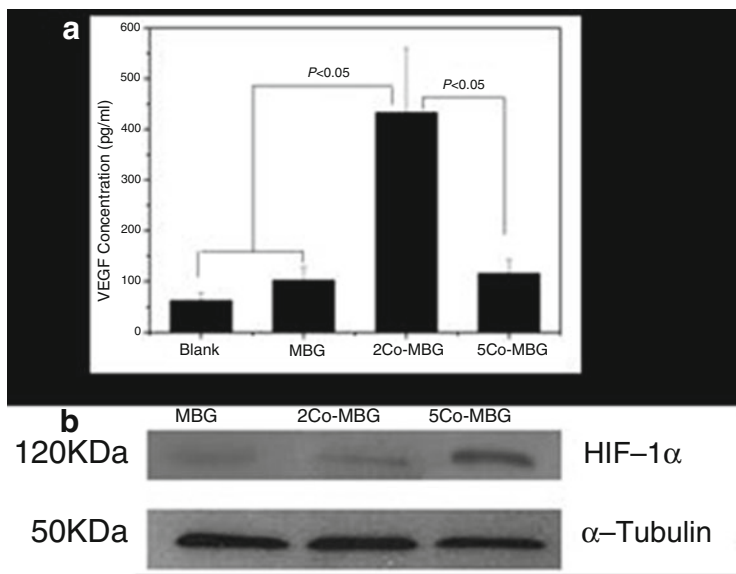


Fig. 13.7 VEGF secretion by ELISA (a) and HIF-1 α expression by western blotting (b) for hBMSCs on Co-MBG scaffolds (Reprinted with permission from Ref. [49] copyright 2012 by Elsevier)

13.4 The Drug Delivery, Antibacterial Property and Tissue Stimulation of Multifunctional MBG Scaffolds

One of the significant advantages for MBG scaffolds is that they possess higher specific surface area and pore volume than conventional bioactive glasses. The loading efficiency of drug and growth factors in MBG is significantly higher than that in conventional bioactive glasses [64, 65]. The drug release kinetics in MBG is lower than that in conventional bioactive glasses. These characteristics make MBG useful for drug delivery. In the past 5 years, the MBG scaffolds with varied compositions have been used for the study of drug delivery [25, 35]. Up to now, the MBG scaffolds have been used for delivery of gentamicin [7, 51, 65], ampicillin [49], dexamethasone [41], dimethylallyl glycine (DMOG) and vascular endothelial growth factor (VEGF) [66]. The studies have indicated that the controllable delivery of ampicillin in the MBG scaffolds significantly inhibited the viability of bacteria (see Fig. 13.9).

Dexamethasone was loaded into MBG scaffolds, and it was found that the MBG scaffolds could efficiently load dexamethasone and release it in a controllable way. The sustained release of dexamethasone from the MBG scaffolds significantly enhanced alkaline phosphatase activity and gene expressions (Col I, Runx2, ALP and BSP) of osteoblasts in the scaffolds (see Fig. 13.10), suggesting that dexamethasone-loaded MBG scaffolds show great potential as a release system to

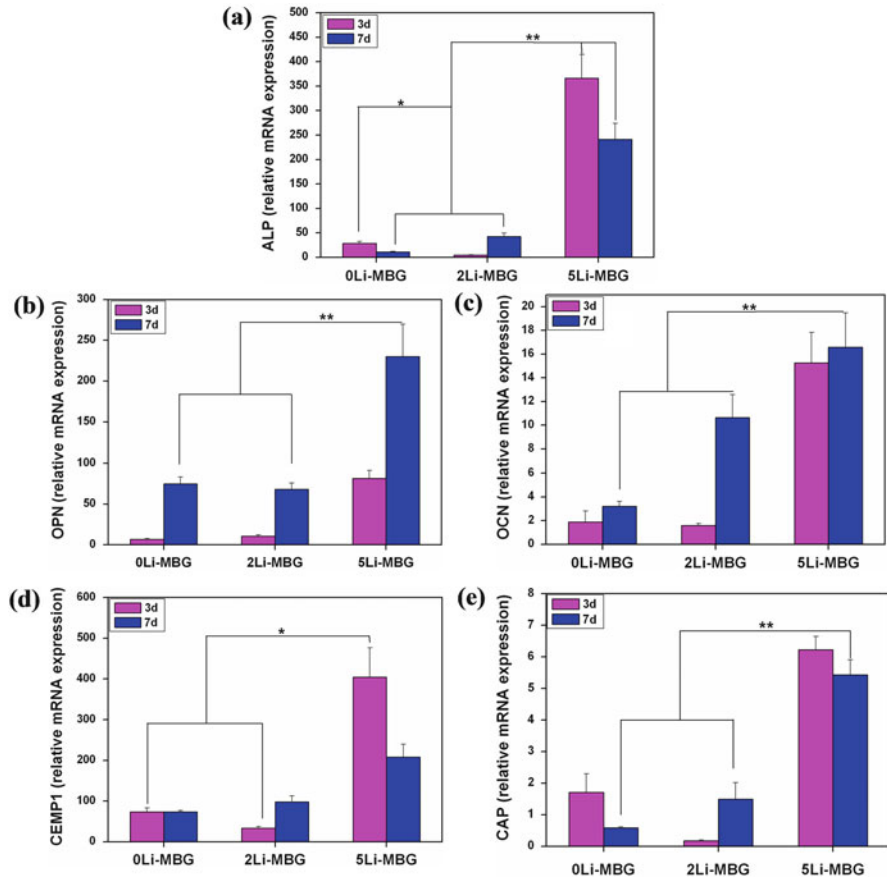


Fig. 13.8 The effect of Li contents in MBG scaffolds on bone-related gene expression of ALP (a), OPN (b), OCN (c) and cementum-specific markers of CEMP1 (d) and CAP (e) for hPDLs (Reprinted with permission from Ref. [63] copyright 2012 by Elsevier)

enhance osteogenesis and may be used for bone tissue engineering applications in the future [35, 41].

Recently, we have loaded DMOG in MBG scaffolds. The results showed that the loading and release of DMOG in the MBG scaffolds can be efficiently controlled by regulating their mesoporous properties via the addition of different contents of mesopore-template agent. DMOG delivery in the MBG scaffolds had no cytotoxic effect on the viability of hBMSCs. DMOG delivery significantly induced HIF-1 α stabilisation, VEGF secretion and bone-related gene expression of hBMSCs in the MBG scaffolds. Furthermore, it was found that the MBG scaffolds with slow DMOG release significantly enhanced the expression of bone-related genes than those with instant DMOG release. The results suggested that the controllable delivery of DMOG in the MBG scaffolds can mimic a hypoxic microenvironment,

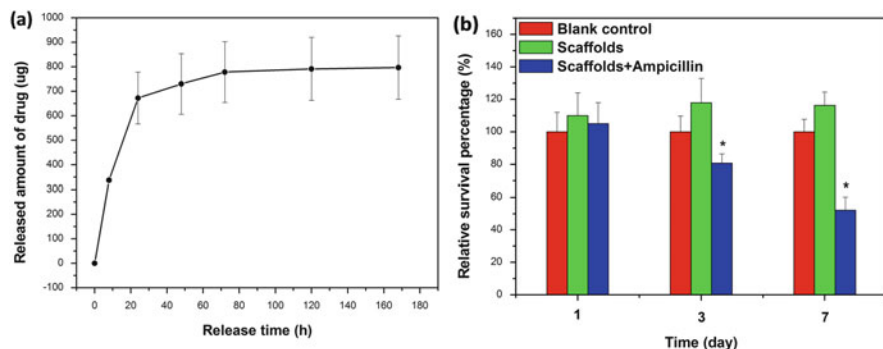


Fig. 13.9 Sustained release of ampicillin from the MBG scaffolds (a) and its antibacterial effect (b). *significant difference for the group of scaffolds loaded with ampicillin, compared to blank control and scaffolds groups not loaded with ampicillin ($P < 0.05$) (Reprinted with permission from Ref. [49] copyright 2012 by Elsevier)

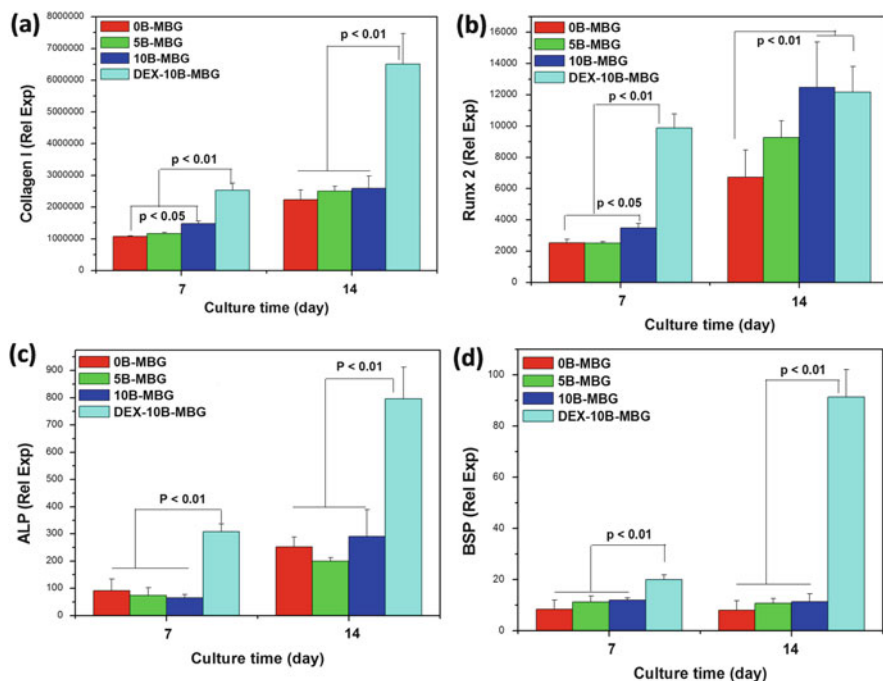


Fig. 13.10 The bone-relative gene expression of Collagen I (a), Runx 2 (b), ALP (c) and BSP (d) for osteoblasts by RT-qPCR. The incorporation of 10% of B into MBG scaffolds enhanced the expression of Collagen I (at day 7) and Runx 2 (at day 7 and 14). DEX-loaded B-MBG scaffolds significantly enhanced the expression of Collagen I, Runx2, ALP and BSP of osteoblasts, compared to non-DEX-loaded B-MBG scaffolds (Reprinted with permission from Ref. [41] copyright 2011 by Elsevier)

which not only improves the angiogenic capacity of hBMSCs but also enhances their osteogenic differentiation.

In addition to the drug delivery, MBG scaffolds could be used for the delivery of vascular endothelial growth factor (VEGF). It was found that tMBG scaffolds have significantly higher loading efficiency and more sustained release of VEGF than non-mesoporous bioactive glass (NBG) scaffolds; and VEGF delivery from the MBG scaffolds improved the viability of endothelial cells. The study suggested that the mesopore structures in the MBG scaffolds play an important role in improving the loading efficiency, decrease the burst effect and maintain the bioactivity of VEGF, indicating that MBG scaffolds are an excellent carrier of VEGF for potential bone tissue engineering application [35, 66].

13.5 Conclusions and Perspective

In this chapter, we reviewed the recent research advances of multifunctional MBG scaffolds for hard tissue regeneration. Three preparation methods, characterisation, *in vitro/in vivo* osteogenesis, angiogenesis, cementogenesis, drug delivery and the corresponding functional effect on antibacterial, tissue stimulation have been reviewed. The MBG scaffolds allow combining the multifunctional properties as outlined above by varying their chemical compositions and delivering different drug and growth factors. The multifunctional properties were regarded to be of great importance to the improvement of the bone/periodontal regeneration and anti-infection ability. Therefore, multifunctional MBG scaffolds showed great potential for hard tissue regeneration. However, up to now, most of the studies have been focused on the *in vitro* experiments, and only few *in vivo* studies have been conducted to confirm their osteogenesis. Other functions of MBG scaffolds, such as angiogenesis, cementogenesis and antibacterial properties, should be further confirmed *in vivo* by using large animal models.

Acknowledgements Funding for related study was provided by the Recruitment Program of Global Young Talent, China (Dr Wu), the National High-Technology Research and Development Program of China (863 Program, SS2015AA020302), the National Natural Science Foundation of China (Grant 31370963), the Program of Shanghai Outstanding Academic Leaders (15XD1503900) and the Key Research Program of Chinese Academy of Sciences (Grant KGZD-EW-T06) and ARC Discovery (DP120103697).

References

1. Hench LL, Thompson I (2010) Twenty-first century challenges for biomaterials. *J R Soc Interface* 7(Suppl 4):S379–S391. doi:rsif.2010.0151.focus [pii] [10.1098/rsif.2010.0151.focus](https://doi.org/10.1098/rsif.2010.0151.focus)
2. Park JK, Shim JH, Kang KS, Yeom J, Jung HS, Kim JY, Lee KH, Kim TH, Kim SY, Cho DW, Hahn SK (2011) Solid free-form fabrication of tissue-engineering scaffolds with a poly(lactic-

- co-glycolic acid) grafted hyaluronic acid conjugate encapsulating an intact bone morphogenetic protein-2/poly(ethylene glycol) complex. *Adv Funct Mater* 21(15):2906–2912
3. Kim TG, Shin H, Lim DW (2012) Biomimetic scaffolds for tissue engineering. *Adv Funct Mater* 22(12):2446–2468
 4. Wang C, Xue Y, Lin K, Lu J, Chang J, Sun J (2012) The enhancement of bone regeneration by a combination of osteoconductivity and osteostimulation using beta-CaSiO₃/beta-Ca₃(PO₄)₂ composite bioceramics. *Acta Biomater* 8(1):350–360
 5. Hu YC, Zhong JP (2009) Osteostimulation of bioglass. *Chin Med J (Engl)* 122(19):2386–2389
 6. Zhao LZ, Yan XX, Zhou XF, Zhou L, Wang HN, Tang HW, Yu CZ (2008) Mesoporous bioactive glasses for controlled drug release. *Microporous Mesoporous Mater* 109(1–3):210–215
 7. Zhu Y, Zhang Y, Wu C, Fang Y, Wang J, Wang S (2011) The effect of zirconium incorporation on the physiochemical and biological properties of mesoporous bioactive glasses scaffolds. *Microporous Mesoporous Mater* 143:311–319
 8. Wu C, Zhou Y, Xu M, Han P, Chen L, Chang J, Xiao Y (2013) Copper-containing mesoporous bioactive glass scaffolds with multifunctional properties of angiogenesis capacity, osteostimulation and antibacterial activity. *Biomaterials* 34(2):422–433
 9. Lu JX, Descamps M, Dejou J, Koubi G, Hardouin P, Lemaître J, Proust JP (2002) The biodegradation mechanism of calcium phosphate biomaterials in bone. *J Biomed Mater Res* 63(4):408–412
 10. Ducheyne P, Radin S, King L (1993) The effect of calcium phosphate ceramic composition and structure on in vitro behavior. I Dissolution. *J Biomed Mater Res* 27(1):25–34
 11. Xu S, Lin K, Wang Z, Chang J, Wang L, Lu J, Ning C (2008) Reconstruction of calvarial defect of rabbits using porous calcium silicate bioactive ceramics. *Biomaterials* 29(17):2588–2596
 12. Misra SK, Ansari T, Mohn D, Valappil SP, Brunner TJ, Stark WJ, Roy I, Knowles JC, Sibbons PD, Jones EV, Boccaccini AR, Salih V (2010) Effect of nanoparticulate bioactive glass particles on bioactivity and cytocompatibility of poly(3-hydroxybutyrate) composites. *J R Soc Interface* 7(44):453–465
 13. Chen QZ, Thompson ID, Boccaccini AR (2006) 45S5 Bioglass-derived glass-ceramic scaffolds for bone tissue engineering. *Biomaterials* 27(11):2414–2425
 14. Jones JR, Tsigkou O, Coates EE, Stevens MM, Polak JM, Hench LL (2007) Extracellular matrix formation and mineralization on a phosphate-free porous bioactive glass scaffold using primary human osteoblast (HOB) cells. *Biomaterials* 28(9):1653–1663
 15. Jones JR, Ehrenfried LM, Hench LL (2006) Optimising bioactive glass scaffolds for bone tissue engineering. *Biomaterials* 27(7):964–973
 16. Wu ZY, Hill RG, Yue S, Nightingale D, Lee PD, Jones JR (2011) Melt-derived bioactive glass scaffolds produced by a gel-cast foaming technique. *Acta Biomater* 7(4):1807–1816
 17. Hench LL (1991) Bioceramics: from concept to clinic. *J Am Ceram Soc* 74:1487–1510
 18. Hench LL (1998) Biomaterials: a forecast for the future. *Biomaterials* 19(16):1419–1423
 19. Gough JE, Jones JR, Hench LL (2004) Nodule formation and mineralisation of human primary osteoblasts cultured on a porous bioactive glass scaffold. *Biomaterials* 25(11):2039–2046
 20. Gough JE, Notingher I, Hench LL (2004) Osteoblast attachment and mineralized nodule formation on rough and smooth 45S5 bioactive glass monoliths. *J Biomed Mater Res A* 68(4):640–650
 21. Valerio P, Pereira MM, Goes AM, Leite MF (2004) The effect of ionic products from bioactive glass dissolution on osteoblast proliferation and collagen production. *Biomaterials* 25(15):2941–2948
 22. Xynos ID, Edgar AJ, Buttery LD, Hench LL, Polak JM (2001) Gene-expression profiling of human osteoblasts following treatment with the ionic products of Bioglass 45S5 dissolution. *J Biomed Mater Res* 55(2):151–157

23. Xynos ID, Edgar AJ, Buttery LD, Hench LL, Polak JM (2000) Ionic products of bioactive glass dissolution increase proliferation of human osteoblasts and induce insulin-like growth factor II mRNA expression and protein synthesis. *Biochem Biophys Res Commun* 276(2):461–465
24. Hoppe A, Guldal NS, Boccaccini AR (2011) A review of the biological response to ionic dissolution products from bioactive glasses and glass-ceramics. *Biomaterials* 32(11):2757–2774
25. Wu C, Chang J, Xiao Y (2011) Mesoporous bioactive glasses as drug delivery and bone tissue engineering platforms. *Ther Deliv* 2(9):1189–1198
26. Hench LL, Polak JM (2002) Third-generation biomedical materials. *Science* 295(5557):1014–1017
27. Li R, Clark AE, Hench LL (1991) An investigation of bioactive glass powders by sol-gel processing. *J Appl Biomater* 2(4):231–239
28. Arcos D, Lopez-Noriega A, Ruiz-Hernandez E, Terasaki O, Vallet-Regi M (2009) Ordered mesoporous microspheres for bone grafting and drug delivery. *Chem Mater* 21(6):1000–1009. doi:[10.1021/Cm801649z](https://doi.org/10.1021/Cm801649z)
29. Wu C, Chang J (2013) Silicate bioceramics for bone tissue regeneration. *J Inorg Mater* 28(1):29–39
30. Yan X, Yu C, Zhou X, Tang J, Zhao D (2004) Highly ordered mesoporous bioactive glasses with superior in vitro bone-forming bioactivities. *Angew Chem Int Ed Engl* 43(44):5980–5984
31. Yan X, Huang X, Yu C, Deng H, Wang Y, Zhang Z, Qiao S, Lu G, Zhao D (2006) The in-vitro bioactivity of mesoporous bioactive glasses. *Biomaterials* 27(18):3396–3403
32. Leonova E, Izquierdo-Barba I, Arcos D, Lopez-Noriega A, Hedin N, Vallet-Regi M, Eden M (2008) Multinuclear solid-state NMR studies of ordered mesoporous bioactive glasses. *J Phys Chem C* 112(14):5552–5562
33. Garcia A, Cicuendez M, Izquierdo-Barba I, Arcos D, Vallet-Regi M (2009) Essential role of calcium phosphate heterogeneities in 2D-hexagonal and 3D-cubic SiO₂-CaO-P₂O₅ mesoporous bioactive glasses. *Chem Mater* 21(22):5474–5484
34. Alcaide M, Portoles P, Lopez-Noriega A, Arcos D, Vallet-Regi M, Portoles MT (2010) Interaction of an ordered mesoporous bioactive glass with osteoblasts, fibroblasts and lymphocytes, demonstrating its biocompatibility as a potential bone graft material. *Acta Biomater* 6(3):892–899. doi:S1742-7061(09)00401-2 [pii] [10.1016/j.actbio.2009.09.008](https://doi.org/10.1016/j.actbio.2009.09.008)
35. Wu C, Chang J (2012) Mesoporous bioactive glasses: structure characteristics, drug/growth factor delivery and bone regeneration application. *Interface Focus* 2:292–306
36. Yun H, Kim SE, Hyun YT, Heo S, Shin J (2008) Hierarchically mesoporous-macroporous bioactive glasses scaffolds for bone tissue regeneration. *J Biomed Mater Res B Appl Biomater* 87:374–380
37. Zhu Y, Wu C, Ramaswamy Y, Kockrick E, Simon P, Kaskel S, Zreiqat H (2008) Preparation, characterization and in vitro bioactivity of mesoporous bioactive glasses (MBGs) scaffolds for bone tissue engineering. *Microporous Mesoporous Mater* 112(1–3):494–503
38. Li X, Wang XP, Chen HR, Jiang P, Dong XP, Shi JL (2007) Hierarchically porous bioactive glass scaffolds synthesized with a PUF and P123 cotelated approach. *Chem Mater* 19(17):4322–4326. doi:[10.1021/Cm0708564](https://doi.org/10.1021/Cm0708564)
39. Wu C, Fan W, Gelinsky M, Xiao Y, Simon P, Schulze R, Doert T, Luo Y, Cuniberti G (2011) Bioactive SrO-SiO₂ glass with well-ordered mesopores: characterization, physiochemistry and biological properties. *Acta Biomater* 7(4):1797–1806
40. Wu C, Fan W, Zhu Y, Gelinsky M, Chang J, Cuniberti G, Albrecht V, Friis T, Xiao Y (2011) Multifunctional magnetic mesoporous bioactive glass scaffolds with a hierarchical pore structure. *Acta Biomater* 7(10):3563–3572
41. Wu C, Miron R, Sculeaan A, Kaskel S, Doert T, Schulze R, Zhang Y (2011) Proliferation, differentiation and gene expression of osteoblasts in boron-containing associated with dexamethasone deliver from mesoporous bioactive glass scaffolds. *Biomaterials* 32(29):7068–7078
42. Wu C, Zhang Y, Zhu Y, Friis T, Xiao Y (2010) Structure-property relationships of silk-modified mesoporous bioglass scaffolds. *Biomaterials* 31(13):3429–3438

43. Franco J, Hunger P, Launey ME, Tomsia AP, Saiz E (2010) Direct write assembly of calcium phosphate scaffolds using a water-based hydrogel. *Acta Biomater* 6(1):218–228. doi:S1742-7061(09)00283-9 [pii] [10.1016/j.actbio.2009.06.031](https://doi.org/10.1016/j.actbio.2009.06.031)
44. Miranda P, Pajares A, Saiz E, Tomsia AP, Guiberteau F (2008) Mechanical properties of calcium phosphate scaffolds fabricated by robocasting. *J Biomed Mater Res A* 85(1):218–227. doi:[10.1002/jbm.a.31587](https://doi.org/10.1002/jbm.a.31587)
45. Miranda P, Saiz E, Gryn K, Tomsia AP (2006) Sintering and robocasting of beta-tricalcium phosphate scaffolds for orthopaedic applications. *Acta Biomater* 2(4):457–466. doi:S1742-7061(06)00022-5 [pii] [10.1016/j.actbio.2006.02.004](https://doi.org/10.1016/j.actbio.2006.02.004)
46. Yun HS, Kim SE, Hyeon YT (2007) Design and preparation of bioactive glasses with hierarchical pore networks. *Chem Commun* 21:2139–2141. doi:[10.1039/B702103h](https://doi.org/10.1039/B702103h)
47. Garcia A, Izquierdo-Barba I, Colilla M, de Laorden CL, Vallet-Regi M (2011) Preparation of 3-D scaffolds in the SiO₂-P₂O₅ system with tailored hierarchical meso-macroporosity. *Acta Biomater* 7(3):1265–1273
48. Wu C, Luo Y, Cuniberti G, Xiao Y, Gelinsky M (2011) Three-dimensional printing of hierarchical and tough mesoporous bioactive glass scaffolds with a controllable pore architecture, excellent mechanical strength and mineralization ability. *Acta Biomater* 7(6):2644–2650
49. Wu C, Zhou Y, Fan W, Han P, Chang J, Yuen J, Zhang M, Xiao Y (2012) Hypoxia-mimicking mesoporous bioactive glass scaffolds with controllable cobalt ion release for bone tissue engineering. *Biomaterials* 33(7):2076–2085
50. Wu C, Zhou Y, Lin C, Chang J, Xiao Y (2012) Strontium-containing mesoporous bioactive glass scaffolds with improved osteogenic/cementogenic differentiation of periodontal ligament cells for periodontal tissue engineering. *Acta Biomater* 8:3805–3815
51. Zhu Y, Li X, Yang J, Wang S, Gao H, Hanagata N (2011) Composition-structure-property relationship of the CaO-MxOy-SiO₂-P₂O₅ (M = Zr, Mg, Sr) mesoporous bioactive glass (MBG) scaffolds. *J Mater Chem* 21:9208–9218
52. Eden M, Gunawidjaja PN, Lo AYH, Izquierdo-Barba I, Garcia A, Arcos D, Stevansson B, Grins J, Vallet-Regi M (2010) Biomimetic apatite mineralization mechanisms of mesoporous bioactive glasses as probed by multinuclear (31)P, (29)Si, (23)Na and (13)C solid-state NMR. *J Phys Chem C* 114(45):19345–19356
53. Fan W, Crawford R, Xiao Y (2010) Enhancing in vivo vascularized bone formation by cobalt chloride-treated bone marrow stromal cells in a tissue engineered periosteum model. *Biomaterials* 31(13):3580–3589
54. Fu OY, Hou MF, Yang SF, Huang SC, Lee WY (2009) Cobalt chloride-induced hypoxia modulates the invasive potential and matrix metalloproteinases of primary and metastatic breast cancer cells. *Anticancer Res* 29(8):3131–3138
55. Basini G, Grasselli F, Bussolati S, Baioni L, Bianchi F, Musci M, Careri M, Mangia A (2011) Hypoxia stimulates the production of the angiogenesis inhibitor 2-methoxyestradiol by swine granulosa cells. *Steroids* 76:1433–1436
56. Oladipupo S, Hu S, Kovalski J, Yao J, Santeford A, Sohn RE, Shohet R, Maslov K, Wang LV, Arbeit JM (2011) VEGF is essential for hypoxia-inducible factor-mediated neovascularization but dispensable for endothelial sprouting. *Proc Natl Acad Sci U S A* 108(32):13264–13269
57. Semenza GL (2009) Regulation of oxygen homeostasis by hypoxia-inducible factor 1. *Physiology (Bethesda)* 24:97–106
58. Liu W, Shen SM, Zhao XY, Chen GQ (2012) Targeted genes and interacting proteins of hypoxia inducible factor-1. *Int J Biochem Mol Biol* 3(2):165–178
59. Ahluwalia A, Tarnawski AS (2012) Critical role of hypoxia sensor—HIF-1alpha in VEGF gene activation. Implications for angiogenesis and tissue injury healing. *Curr Med Chem* 19(1):90–97
60. Finney L, Vogt S, Fukai T, Glesne D (2009) Copper and angiogenesis: unravelling a relationship key to cancer progression. *Clin Exp Pharmacol Physiol* 36(1):88–94

61. Gerard C, Bordeleau LJ, Barralet J, Doillon CJ (2010) The stimulation of angiogenesis and collagen deposition by copper. *Biomaterials* 31(5):824–831
62. Hu GF (1998) Copper stimulates proliferation of human endothelial cells under culture. *J Cell Biochem* 69(3):326–335
63. Han P, Wu C, Chang J, Xiao Y (2012) The cementogenic differentiation of periodontal ligament cells via the activation of Wnt/beta-catenin signalling pathway by Li(+) ions released from bioactive scaffolds. *Biomaterials* 33(27):6370–6379
64. Xia W, Chang J (2006) Well-ordered mesoporous bioactive glasses (MBG): a promising bioactive drug delivery system. *J Control Release* 110(3):522–530
65. Zhu YF, Kaskel S (2009) Comparison of the in vitro bioactivity and drug release property of mesoporous bioactive glasses (MBGs) and bioactive glasses (BGs) scaffolds. *Microporous Mesoporous Mater* 118(1–3):176–182. doi:[10.1016/j.micromeso.2008.08.046](https://doi.org/10.1016/j.micromeso.2008.08.046)
66. Wu C, Fan W, Chang J, Xiao Y (2013) Mesoporous bioactive glass scaffolds for efficient delivery of vascular endothelial growth factor. *J Biomater Appl* 28(3):367–374

Chapter 14

Challenges for Cartilage Regeneration

Fariba Dehghani and Ali Fathi

Abstract Articular cartilage is a resilient connective tissue, which covers the surface of bones to facilitate their movements against each other. Due to unique mechanical properties, cartilage has a prominent role in locomotion and mobility of the human body. This tissue however has limited capability of regeneration and repair due to its low metabolism and avascular structure. Trauma, degenerative conditions and inflammatory arthritis lead to lifetime disability states and pain. The scope of this chapter is to first provide an overview of mechanical, biological and micro-architectural properties of articular cartilage and the effect of aging on these characteristics. Then the cartilage treatment techniques that have been proposed for different types of cartilage defects are discussed. Cell-based therapies, such as autologous chondrocyte implantation (ACI) technique, have been developed to achieve reproducible results regardless of patients' age, gender and physical conditions. The second generation of ACI is a tissue engineering-based technique, which includes the use of appropriate cell type, bioactive molecules such as growth factors and proper scaffold to regenerate cartilage. The favourable types of cells, biological compounds and properties of biomaterials for cartilage regeneration have also been discussed in this chapter. Finally, the biomaterial products that have been examined in clinical trial for cartilage repair are outlined, and their properties and clinical results are discussed.

Keywords Articular cartilage • Tissue engineering • Scaffold • Tissue regeneration • Biopolymer

14.1 Articular Cartilage Properties and Aging

Hyaline articular cartilage covers the ends of articulating bones [1]. It is a resilient connective tissue with low friction and high load-bearing capacity. Cartilage serves a critical role in mobility of one bone against another. Chondrocyte is the main cell

F. Dehghani (✉) • A. Fathi

School of Chemical and Biomolecular Engineering, The University of Sydney, Sydney, NSW 2006, Australia

e-mail: Fariba.Dehghani@Sydney.edu.au

type scattered within an extracellular matrix (ECM) of cartilage [2]. Breakdown or any degree of damage in this tissue leads to substantial reduction in mobility of the human body and pain and subsequently has negative impact on patients' lifestyle. Cartilage has limited capability of regeneration and repair due to its low metabolism and the absence of vascularisation in its structure [3, 4]. To design and engineer a cartilage, it is essential to have better understanding over the mechanical and biological properties of this tissue. Mechanical, physiochemical and biological properties of articular cartilage are mainly affected by its biochemical composition as well as its structural properties that are reviewed in this section.

14.1.1 Biochemical Composition

The composition of articular cartilage varies during the tissue development. In a mature cartilage, 70–80 % of its content is water. The solid fraction of articular cartilage is mainly collagen (50–75 %), proteoglycan (15–30 %) and other protein molecules [5, 6]. The collagen network provides shear and tensile stiffness, whereas proteoglycan molecules bring about compressive stiffness to cartilage ECM. The collagen network also suppresses the high swelling tendency of the proteoglycan molecule and preserves the functional integrity of cartilage [7]. The mixture of collagen and proteoglycan, therefore, forms an integrated mesh-like network with superior mechanical properties. Concentration of collagenous proteins and proteoglycan along with non-collagenous proteins in the structure of articular cartilage substantially affects the mechanical properties and functionality of articular cartilage.

Collagen has a primary role in the function and structure of all connective tissues throughout the human body. Collagen is composed of repeating amino acid sequences (mainly glycine, proline and hydroxyproline) and possesses a triple helix structure. In articular cartilage, collagen type II is predominant [8], which provides shear and tensile stiffness to cartilage ECM. In addition to collagen type II, cartilage ECM is composed of other types of collagen.

Other fibrillar and globular collagen types, such as types V, VI and IX, also exist in cartilage ECM [9]. The roles of these types of collagen are still unknown, but it is believed that they support the integration of cartilage structure by affecting the intermolecular interaction in collagen type II [5, 6].

Proteoglycans are large macromolecules consisted of a protein segment in core, covered with polysaccharide chain, known as glycosaminoglycan. The molecular weight of proteoglycans varies in the range of 50,000 kDa to 100 kDa [10, 11]. Proteoglycan networks function as a mesh, which covers the organised collagen network. Majority of this biopolymer is one of the factors that provide structural integrity to cartilage. The primary proteoglycan in articular cartilage network is aggrecan. This proteoglycan consists of a hyaluronan core with chondroitin and keratin sulphate in side chains. The presence of these two carboxyl and sulphate groups gives articular cartilage network a negative charge (known as a fixed charge

density) [12]. This overall negative charge leads to hydrophilic and high swelling properties to cartilage network [7, 13]. The mechanical functionality of cartilage on the other hand is highly dependent on the fluid pressurisation within the tissue. Loss of proteoglycan can, therefore, decrease water intake capacity and thus fluid pressure within the cartilage network. Lack of fluid pressure in cartilage substantially decreases the mechanical strength of this tissue [13].

Cartilage ECM also contains a small fraction of non-collagenous proteins and other matrix constituents. Non-collagenous proteins include cartilage oligomeric proteins, fibronectin, thrombospondin, matrix glycine–leucine–alanine, chondrocalcin, superficial proteins and elastin [14]. Other matrix constituents of cartilage ECM are lipids, phospholipids and inorganic crystal compounds [15, 16]. The role of each of these molecules in the function of articular cartilage is still not clear. Collagen and proteoglycan are the two predominant compounds that affect the cartilage functionality. In this chapter, therefore, the main focus is on collagen type II and proteoglycan rather than other minor compounds [7]. In addition to biochemical composition, the microstructures and micro-layouts of articular cartilage affect the biomechanical and biological properties of cartilage.

14.1.2 Cartilage Microstructure

The structure of articular cartilage substantially varies from the surface of articular cartilage to bone [17, 18]. The biochemistry, cell morphology and cell arrangement vary in different regions within articular cartilage. The schematic overview of articular cartilage is shown in Fig. 14.1. The tissue can be divided into superficial, middle, deep and calcified regions.

The top surface of articular cartilage is covered with very thin proteinaceous layer, termed as lamina splendens [18]. The zonal region right beside the lamina splendens is a superficial zone, which has a thickness within the range of 4 to 8 mm for the healthy cartilage of a man [17]. The cells in this region are densely packed with discoidal shapes that are oriented along with the collagen fibres [19]. The middle or transitional layer zone occupies 40–60% of the total articular cartilage thickness (equivalent to 16–22 mm in healthy male cartilage) [17]. The deep zone is the last region of purely hyaline tissue. The thin layer, which separates the deep zone from calcified region of articular cartilage, is called tidemark. The calcified region is the transitional zone between elastic cartilage and rigid bone tissues [20].

14.1.3 Cartilage Mechanical Function

The main role of articular cartilage is to act as low-friction, load-bearing, wear-resistant surface for mobility of bones over decades of continuous use. The force applied on cartilage depends on the location of the joint. The forces exerted on the

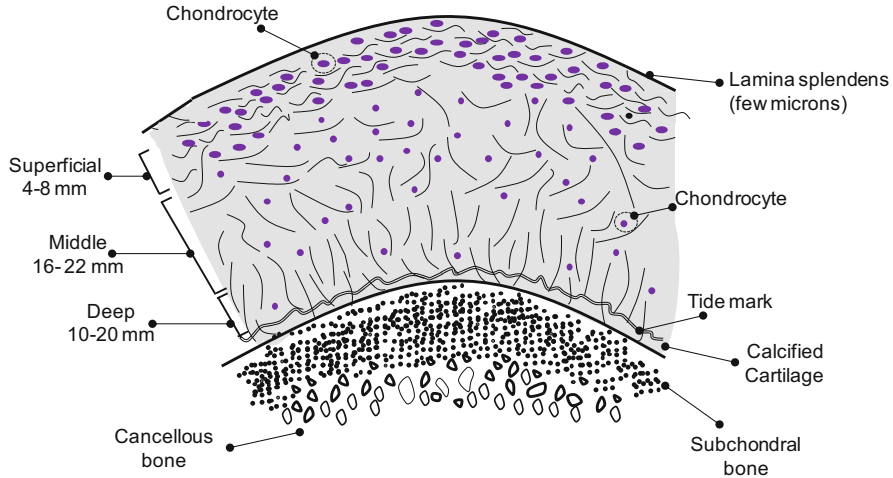


Fig. 14.1 Schematic layout of articular cartilage and thickness of different zones of articular cartilage in a healthy knee joint (The image is generated by accumulating data from different sources [18, 21–23])

shoulder, ankle, heap and knee are 1.5, 2.5, 3.3 and 3.5 times of the human body weight, respectively [24]. The biochemical characteristics of articular cartilage directly affect the performance of the tissue in the joint and its mechanical functionality. Any change in mechanical and biochemical properties of articular cartilage might dramatically alter the loading profile exerted on the joint, which may degrade tissue and eventually lead to loss of articular cartilage [3, 4].

The deformation of cartilage plays an important role in its mechanical functionality, which is governed by the rate of absorbance or release of fluid, mainly water, through its solid structure [25, 26]. For example, sudden loading on cartilage releases water from its structure; this subsequently absorbs the impact of stress and covers the tissue. In addition, release of water leads to expansion of cartilage which in turn increases the surface area of contact (between cartilage and the bone) and thus decreases the impact of stress on skeleton [25, 26].

Loading and deformation of articular cartilage generate a combination of compressive, tensile and shear stresses along with friction throughout the tissue [27]. Some of the important mechanical behaviour of articular cartilage is summarised in Table 14.1 and are discussed in this section. It is important to note that all mechanical properties of cartilage are continuously changed during human growth and affected due to health condition [28–32].

14.1.3.1 Compression Behaviour

Compressive loading is one of the primary types of mechanical stress exerted on articular cartilage. The confined compressive modulus experienced by articular

Table 14.1 Important mechanical properties of native cartilage

Mechanical properties		Refs
Compression modulus (MPa)	0.08–2.1	[31, 33, 34]
Tensile modulus (MPa)	4.8–25	[25]
Strain at failure (mm/mm)	30 %	[35]
Practical strain rate	0–1 mm/s	[33]
Shear modulus (MPa)	0.07–0.65	[36, 37]
Coefficient of friction	0.001	[38]

cartilage varies in the range of 0.08 to 2.1 MPa from superficial to deep layers of adult bovine cartilage, respectively [31, 32, 39]. The mechanism of cartilage to cope with high compressive stresses is predominantly described by permeability of cartilage structure.

Cartilage structure has a low liquid permeability, leading to high resistance of tissue against fluid flow within its structure. Under compression, therefore interstitial fluid is subjected to very high pressure. After unloading, the fluid is redistributed (from high pressure to low pressure spots) within the tissue and imparts viscoelastic properties to the cartilage [26, 40, 41]. Volumetric changes and viscoelastic properties of articular cartilage are, therefore, the two predominant factors affecting the compressive behaviours of articular cartilage.

Volumetric changes occur as fluid moves out from the structure of articular cartilage under compression. Upon the unloading of the tissue from compression stress, cartilage recovers its initial dimension and absorbs the lost fluid. In this cycle hence, the solid structure exhibits both high viscoelasticity and water uptake properties to be able to cope with compression stresses and also keep its original shape [38]. Over a course of a day, however, the bulk of cartilage is compressed in the range of 15–20 % of its initial volume, which can be fully recovered within a period of inactivity (e.g. sleeping period) [42].

14.1.3.2 Tensile Properties

Tension in cartilage occurs either when two cartilages slide against each other and pull towards a single direction or when a cartilage is compressed, pulling the surrounding tissue towards the loading region. As cartilage is subjected to tension, collagen fibres within the tissue structure align and stretch along the loading axis. As the strain is in the range of 0–15 %, the crosslinked collagen network starts stretching, and thus the cartilage exhibits linear response [43]. As the strain increases, the crosslinked collagen fibres themselves start stretching. In higher range of strain (above 15 %) therefore, cartilage exhibits higher stiffness [44, 45]. The structural and physical properties of articular cartilage therefore affect the behaviour of this tissue under tension condition. These include collagen fibre density, their length and degree of crosslinking and strength of ionic bonds between collagen and proteoglycan networks [46, 47].

The tensile modulus of mature articular cartilage is significantly higher than its compression modulus, and it varies in the range of 4.8–25 MPa from deep to the superficial layers, respectively [25]. The tensile modulus of articular cartilage increases by maturation [29, 48].

14.1.3.3 Shear Stress

Articular cartilage is subjected to shear stress in its deep tissue when the joint undergoes rotational or translational movement. In theory, pure shear just causes stretching of tissue (it causes no compressive stress on the tissue). The shear stress on cartilage is independent on the fluid pressure within its structure, and thus it can be used to characterise the solid fraction of cartilage regardless of fluid dynamics in it [49]. The equilibrium shear stress in cartilage varies in the range of 0.05–0.7 MPa [36, 37].

14.1.3.4 Friction Behaviour

Friction quantifies the resistive force between two subjects as they are in contact with each other and move laterally relative to each other. Native cartilage gives mobility to the bone by its lubrication properties. Under high dynamic and static load conditions, the coefficient of friction for human cartilage is very low, and it is in the order of 0.001 [38]. Several theories have been proposed to explain low friction force between cartilage surfaces. These include but not necessarily limited to elasto-hydrodynamic lubrication [50, 51] and fluid pressurisation theories [52, 53]. It shows that the synovial fluid becomes thicker due to the deformation of applied compression on cartilage, which gives superior lubrication properties to articular cartilage. Compression and lubrication properties of cartilage therefore are closely correlated.

14.1.4 Articular Cartilage Aging and Pathology

Articular cartilage is a highly resilient connective tissue with very important biomechanical role in the human body. Cartilage has an essential function in the movement of the human body and mobility of bones against each other. Any breakdown in this tissue results in substantial reduction in standards of living and substantial level of pain. Cartilage from skeletally immature, mature and older patients exhibits very different biomechanical and biological properties. As cartilage ages, it becomes more prone to injuries [54, 55]. The damage to this tissue might result from torsional loading, joint misalignment, foreign bodies in the joint and osteoarthritis. It is critical to first understand the aging process of cartilage and

then the factors that lead to cartilage damage to be able to develop an effective treatment strategy for articular cartilage defects.

Similar to many organs, aging has significant impact on the characteristics of cartilage. Skeletally mature, immature and old cartilages are different in respect to their thickness [54, 55], vascularisation, chondrocyte population [56] and chondrocyte regeneration quality [57, 58]. Immature cartilage contains blood vessels as it is still undergoing tissue formation (endochondral ossification). It is also thicker than mature cartilage and its thickness decreases by aging [54, 55]. The population of chondrocyte cells also decreases overtime by aging [56]. In addition to chondrocytes' cell reduction in mature cartilage, aging also brings lower metabolic activity, increases apoptosis (a process of programmed cell death) and elevates passive responses of cells to growth factors [57, 58].

Biomechanical properties of cartilage change by aging. For example, the degree of crosslinking in collagen increases [59] as protein and lipids are covalently bonded with sugars (i.e. glycation). The length and molecular weight of proteoglycan also decrease as its protein content decreases [60]. These variations reduce the stiffness/strength of cartilage and induce the risk of tissue failure [61]. Studies showed that generally a cartilage approaches its peak in elasticity in 40 years of age, while the viscoelastic energy reaches its maximum value earlier within 16–29 years old. Both elasticity and viscoelasticity decline at a steady rate [62]. Collagen alignment also decreases in the middle and deep zone of cartilage by age which in turn decreases the tensile properties of cartilage [63].

Both biological and biomechanical properties of articular cartilage decrease by time. The problematic issues are, therefore, the lack of healing responses and also the decrease in the initial mechanical properties of cartilage. The overall changes in the biochemical properties of articular cartilage are schematically shown in Fig. 14.2.

Repeated non-physiological loading on tissue over the years and biological, biomechanical and other systematic changes on articular cartilage are the factors that make the tissue vulnerable to damage. Cartilage damages are either due to injuries or osteoarthritis. In addition to the impact of aging on the nature of articular cartilage, other factors such as hormonal therapy and diseases play a role in properties of cartilage. For instance, oestrogen replacement in ovariectomised sheep leads to substantial changes in the structure and mechanical properties of articular cartilage, which is relevant to menopausal women [64]. In addition, anti-inflammatory treatments such as intra-articular administration of methylprednisolone diversely affect the properties of articular cartilage [65]. Some diseases such as diabetes also have negative impact on cartilage properties [66].

14.1.4.1 Cartilage Injuries

Sudden impact, repeating loads, damage in other connective tissue and also foreign bodies affect the loading profile on cartilage and, therefore, result in cartilage damage as shown schematically in Fig. 14.3. The effect of load and stress on

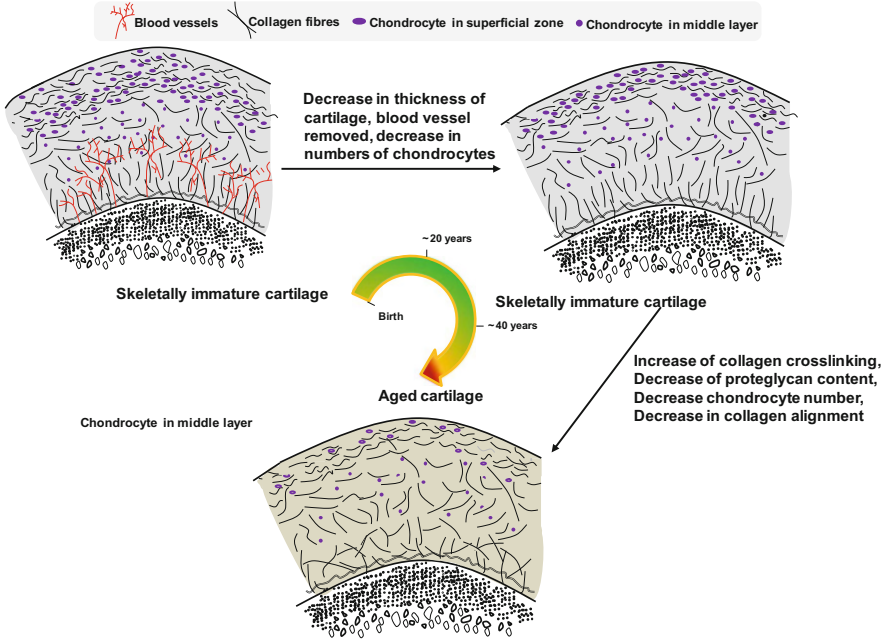


Fig. 14.2 Biochemical changes in the structure of cartilage from skeletally immature cartilage to mature and aged cartilage (The image is regenerated by accumulating data from different references [54, 55, 60–63])

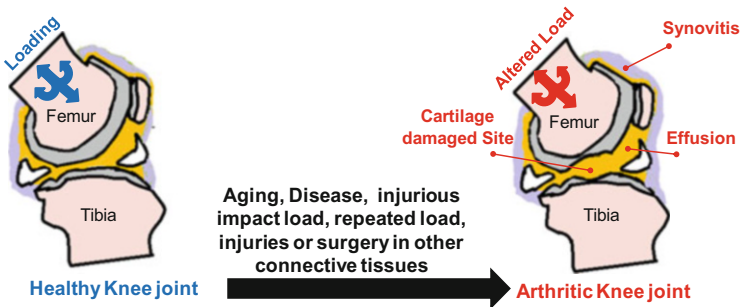


Fig. 14.3 Cartilage injuries, causes and their effect on loading profile in connective tissue

cartilage is a function of frequency of loading and their period of exposure. Due to the viscoelastic nature of articular cartilage and based on the theory of confined compression moduli, both load and strain rates significantly affect cartilage stiffness which should be taken into account for determining the load of injury. For instance, during the normal physical activity, the knee cartilage is subjected to 3.5 times the body weight [24]. Therefore, for a male with an average weight of 70 Kg, the force on his joint is subject to around 1.5 MPa stress by assuming the surface

area of tibial plateau of 1670 mm^2 [67]. During running, this load approaches to $50 \text{ MPa}\cdot\text{s}^{-1}$ and $100 \text{ MPa}\cdot\text{s}^{-1}$ that depends on the stress rate. However, the impact of loading from injury on cartilage is any load with time between two peak loads in the order of milliseconds (e.g. $<30 \text{ ms}$) along with at least one of the following criteria: (i) stress rate greater than $1000 \text{ MPa}\cdot\text{s}^{-1}$, (ii) loading rate above $100 \text{ kN}\cdot\text{s}^{-1}$ or (iii) strain rate in excess of $500 \text{ mm}\cdot\text{mm}^{-1}\cdot\text{s}^{-1}$ [68]. It is important to note that these criteria are only applied to healthy cartilage; aging and other systematic changes in cartilage make cartilage more vulnerable to damage.

14.1.4.2 Osteoarthritis

Osteoarthritis (OA) is one of the major health issues worldwide and it is a burden for elderly population. Symptomatic OA manifests itself with severe pain in the joint and lack or even loss of mobility in the defected joint [69, 70]. The cost of treatment and healthcare for promoting the lifestyle of patients who suffered from OA is enormous. The Australian Institute of Health and Welfare reported that OA affects more than 1.3 million Australians in 2007 [71]. The existing trend suggests that in 2050, more than seven million Australians will be affected by OA [72].

The OA mostly caused by biochemical and biomechanical changes that systematically occur in articular cartilage. It might also be attributed to traumatic joint injuries such as accident and sport. It is estimated that approximately 11 % of Australian working force (young and middle-aged population) suffers from arthritis (mainly OA) [72].

14.1.5 *Natural Articular Cartilage Repairing Process*

There are two types of cartilage damages: partial- and full-thickness defects [73]. Partial-thickness damage is limited to the cartilage, and the subchondral bone is not violated in this type of damages. The site of defect has, therefore, no access to bone marrow-derived stem cells [3]; the cartilage thus lacks in intrinsic capability to heal the defected site [3, 74]. The defected site in this case might significantly expand by time since there is no healing process naturally commenced by the tissue [74]. This damage eventually leads to OA by aging. On the other hand, in full-thickness cartilage defect, the lesion has access to bone marrow-derived stem cells which allows the cartilage to undergo some spontaneous healing process [75].

In the full-thickness damage, also called osteochondral defect, the healing process extends greatly after 2 weeks. The subchondral blood vessels bring progenitor cells (mainly mesenchymal stem cells) into the defected site. These cells are more bioactive in generating cartilage ECM compared to natural chondrocytes. The migration, differentiation and proliferation of mesenchymal stem cells (MSC) at the defected site take place 2 weeks post injury. The blood from subchondral bone forms a fibrin clot, which contains platelets. These can secrete biofactors to recruit

mesenchymal stem cells to form cartilage. MSCs produce collagen type II and collagen type I to fill the defected site. After approximately 6–8 weeks, the defected site is filled with collagen type I and type II [76–78]. From this point onwards, the production of collagen type II is completely switched to collagen type I. After 1 year the repaired cartilage consists of hyaline and fibrocartilage tissue [75, 79]. Fibrocartilage tissue suffers from lack of mechanical strength and physical stability [80]. These lead to cartilage matrix degeneration through fibrillation [81], chondrocyte loss and dedifferentiation and GAG loss [82]. Subsequently, deep cracks appear within the structure of cartilage after the first year, and subsequently complete failure of cartilage occurs [76–78].

Lack of chondrogenesis cell in partial- and also formation of fibrocartilage in full-thickness articular cartilage damages might lead to the OA occurrence in a patient. Therefore, articular cartilage damage must be treated with therapeutic strategies at very early stages.

14.2 Therapies for Articular Cartilage Damages

Several cartilage repair techniques have been proposed to treat different types of cartilage defects. Conventional therapeutic strategies are classified in two groups, therapeutic intervention without biological compounds or with active biologics. In this section an overview of these two groups of therapies is provided.

14.2.1 Therapeutic Intervention without Active Compounds

No biological compound is used in this group of therapeutic interventions. The efficiency of these treatment techniques relies on their stimulation impact on chondral or subchondral tissue for cartilage regeneration. The main techniques in this category are lavage, chondral shaving, debridement, Pridie drilling and microfracture that are described briefly in this section.

14.2.1.1 Lavage and Arthroscopy

Lavage or irrigation of the defected site with solution of sodium chloride, Ringer or Ringer and lactate has been practised for treatment of OA of the knee. The defected site in this technique is rinsed, using closed-needle hole or arthroscopic techniques [83]. It is claimed that thorough rinsing of tissue removes intra-articularly active pain signaling molecules from the defected site, thus leading to the relief of pain in patients. The irrigation of cartilage surface might also lead to extraction of proteoglycan and aggrecans from the superficial surface of articular cartilage, which might temporarily improve the adhesion of repaired cells at the defected site

[84, 85]. In clinical studies, however, lavage (irrespective of whether it is performed with closed-needle hole or arthroscopic techniques) appears to resolve the issue for a short period of time [86, 87]. This approach is more effective for the patients with history of trauma (such as sports injury, tearing of the ligament or meniscus or traumatic structural lesions) compared to the cases with other types of OA [84, 88].

14.2.1.2 Chondral Shaving

Chondral shaving is conducted with arthroscopic techniques to mechanically remove the defected site, using appropriate surgical instrument. In recent years, it is only performed for treatment of chondromalacia patellae pain. The results of in vivo studies suggest that this procedure does not have any impact on cartilage regeneration in mature rabbits after 12 weeks. The remaining cartilage also underwent degeneration due to apoptotic cell loss [89–91].

14.2.1.3 Debridement

This approach involves meniscectomy process in which the chondral defected site is mechanically isolated, the lesion site underwent lavage process and all free bodies are removed from the joint [92]. The removal of chondral defect tissues leads to cell apoptosis and thus cartilage degeneration at the surrounding tissue. In addition, the meniscectomy process leads to skeletal malalignment and significant changes in the loading profile at the joint. The results of in vitro, in vivo and clinical studies demonstrated that debridement alone exacerbates the osteoarthritic conditions [93, 94].

14.2.1.4 Pridie Drilling

In this technique, therapeutic holes at the defected site are drilled from the articular cartilage surface into the subchondral bone marrow. The drilling is performed close to the defected articular cartilage sites. This stimulates the spontaneous repair reaction at the defected site [95–97]. The intervention to drill the holes (2 mm–2.5 mm in diameter) includes such methods as osteochondritis dissecans, which is a painful process. It is claimed that this technique is beneficial for OA patients by promoting the migration of chondrogenesis cells to the surface of the defected site [95, 98, 99]. In vitro and in vivo studies showed that Pridie drilling on rabbit resulted in formation of fibrocartilage tissue. This method may be accompanied with inflammation at the defected joint [100]. Clinical studies, however, showed that Pridie drilling is a safe treatment for cartilage repair for a short period only [101].

14.2.1.5 Microfracture

The biological basis of this technique is the same as Pridie drilling. The only differences between Pridie drilling and microfracture techniques are the size and numbers of holes [102]. In microfracture technique, micro-sized pores (from 500 μm to 1 mm in diameter) are generated within the entire articular cartilage lesion site. This technique is efficient for lesions with average size of less than 2.3 cm^2 . The depth of holes is approximately 4 mm and 3–4 holes are generated per cm^2 of the cartilage defected site. The smaller diameter of holes in this technique, compared to Pridie technique, leads to less adverse impact on biomechanical properties of the subchondral bone [103]. Animal studies confirmed the regeneration of tissue by using this method. In clinic, the microfracture technique is mainly applied for articular cartilage damages in young athletes [102]. Positive results are reported for cartilage treatments by microfracture; in 75 % of cases, pain relief and improvement in joint functionality are reported. However, application of this method for the patients with OA with lack of adequate number of bone marrow-derived mesenchymal stem cells is not promising [88, 104].

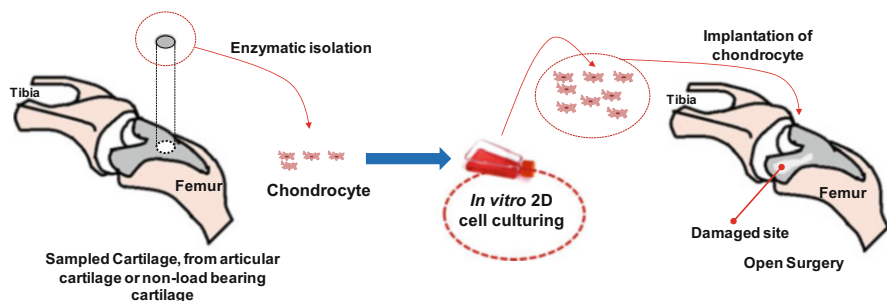
14.2.2 *Allogeneic Osteochondral and Chondral Grafting (Full Osteochondral Allograft)*

In this technique, allogeneic osteochondral or chondral graft is used to fill the articular cartilage defected site, which has no intention to stimulate cartilage repair responses. It relies on replacing the defected tissue with healthy cartilage that is usually derived from cadavers [105, 106]. Patients with substantial osteochondral defects such as tumour reaction, osteonecrosis, broad OA, osteochondritis dissecans and extensive trauma have benefited from this treatment technique. However, there are immunological problems associated with this technique which might lead to complete rejection of the grafted tissue. Animal studies showed that allogeneic grafts survived under immunosuppressive conditions. In addition, matching the histocompatibility between the grafted and native tissue is required to reduce cell-mediated cytotoxicity and antibody titre [107, 108]. Clinical studies with this treatment technique revealed that the immunoresponses in the human body are less than those in animals [109–111]. In addition, the osteochondral transplant grafts survive for a longer period of time even after freezing and lyophilisation [109–111]. The success rates of 65–85 % are reported for this treatment technique even after follow-up period of 10 years [112, 113]. The application of this method, however, is limited due to scarcity of fresh donor and problems associated with the handling and storage of frozen allograft tissues. It is also critical to contemplate the risk of disease transmission for allogeneic osteochondral and chondral grafting [88].

Table 14.2 Results from clinical studies of MF and FOA techniques for articular cartilage defect treatment

Treatment technique	No. of joint	Average age (yrs.)	Lesion size (cm ²)	Results, year (successful cases %) ¹	Refs.
MF	11	38.5	2	1 (100), 1.5 (0)	[114]
FOA	20	42	NR	2(90), 5 (35), 10 (15)	[115]
	14	37	NR	2(57), 5(43), 10 (29)	[116]

¹For example 2 (90) represented: after 2 years of follow-up time, there are 90 % of successful cases

**Fig. 14.4** Schematic overview of classical ACI technique for articular cartilage treatment

Among all the previously mentioned techniques for cartilage repair, microfracture (MF) and fresh osteochondral allograft (FOA) are the only methods with acceptable biological basis. Different human studies investigated the efficacy of these techniques for treatment of articular cartilage defect. The results from the clinical studies on efficacy of MF and FOA techniques are summarised in Table 14.2.

14.2.3 Autologous Implantation Technique

Different cell-based therapies have been proposed such as autologous chondrocyte implementation (ACI) technique for treatment of cartilage defects [117]. ACI is established in 1994 [117] and thereafter fully approved by the US Food and Drug Administration (FDA) in 1997 [118]. This treatment technique is schematically shown in Fig. 14.4. The first generation of ACI technique provided significant and long-term benefits for patients as per providing tissue functionality and pain relief with better lifestyle. The major problematic issues in this method are the serious damage that imposed at the donor collection site [88]; monolayer in vitro culture of chondrocyte, which leads to the formation of fibrocartilage [119]; and also hypertrophy or ossification of the patched periosteum [120].

14.2.4 Motivation for Tissue Engineering

A demand for tissue engineering of cartilage arises from two perspectives, the high risk of failure in using traditional treatment techniques and the large numbers of patients suffering from articular cartilage defects. Articular cartilage damages can occur during childhood, in young adults and also in elderly people. Osteochondrosis and osteochondritis are joint defects that occur mainly in children due to the lower capacity of skeletally immature cartilage to high range of stresses. The rate of knee cartilage injuries is more than 25 % of participants in any sport activity. In addition, articular cartilage damage in elbow and shoulder joints commonly occurs in athletes who play baseball and cricket, for example [121–123]. It is estimated that one out of three children suffers from severe cartilage damage requiring medical treatment. The cost of treatment for articular cartilage damage is estimated to be \$ 1.8 billion per annum considering that more than 30 million school-aged children just in the USA participate in sport activities [124].

During the last decade, the first generation of ACI technique has been the major approach for the treatment of cartilage defects [118]. Cartilage tissue engineering is considered as a second generation of ACI and has been proposed to address the issues with current cartilage treatments to improve autologous chondrocyte implementation techniques [125–129]. Tissue engineering involves using suitable type of cells, scaffolds and bioactive molecules such as growth factors [130]. Tissue engineering approaches will be discussed comprehensively in the next section.

14.3 Tissue Engineering of Cartilage

Tissue engineering is the modern approach in treatment of articular cartilage defects using suitable types of cells, biomaterials and bioactive molecules such as growth factors [130]. The schematic overview of tissue engineering approaches for treatment of damaged cartilage is shown in Fig. 14.5. Briefly, suitable cell types such as chondrocyte and stem cell (e.g. from autologous sources) are harvested from patients, and then the cells are cultured *in vitro*. Chondrogenesis biofactors may be used to promote the capacity of cells for cartilage regeneration. A biomaterial matrix is required for 3D cell growth, which is comprised of scaffolds for *in vitro* cell growth or a cell carrier system for *in vivo* applications. For cartilage tissue engineering, there are two approaches, namely, *in vitro* and *in vivo* cartilage regeneration. In the former, cells are seeded on the scaffolds and the construct is cultured for a specific period of time. The resulted autologous tissue is then transplanted into the patient via arthrotomy (open surgery) or arthroscopy. In the latter, the suspension of cells in bioengineered matrix is injected into the articular cartilage damaged site. Selection of proper cells and incorporation of chondrogenesis biofactors and the bioengineered matrix have pivotal role in

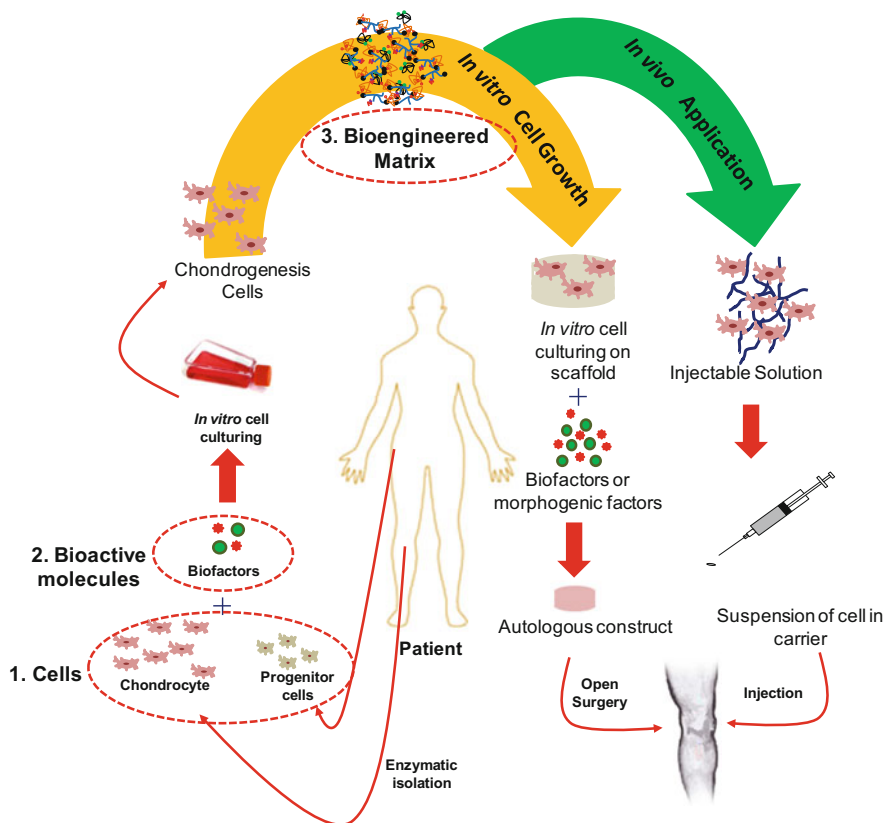


Fig. 14.5 Modern ACI treatment technique for articular cartilage repair

modern ACI technique [131]. Suitable cell types, bioactive compounds and characteristics of biomaterials for cartilage tissue engineering are discussed below.

14.3.1 Cells

Several different cell sources are proposed for cartilage tissue engineering. Autologous chondrocyte, isolated from hyaline or articular cartilage, however is regarded as the most common cell type. By extracting cells from patient's own body, the issue of any immune response can be avoided. In addition, chondrocyte is already differentiated into target cartilage phenotype and can secrete cartilage ECM, such as collagen and proteoglycan [132]. For the cases with extensive cartilage damage or disease, procurement of autologous chondrocyte is not possible. An alternative method is to use allogeneic chondrocyte from a donor tissue. This approach, however, is limited by disease transmission and also host body immune response.

In general, the major issue in the application of both allogeneic and autologous chondrocytes is the limited numbers of available cells, the instability of chondrocyte in monolayer culture and the lack of intrinsic repair capacity [131]. A promising alternative cell source for cartilage tissue engineering is autologous progenitor cells or stem cells [133].

Adult stem cells reside throughout the different parts of the body and can be differentiated along different pathways such as chondrogenesis and osteogenesis lineages. Stem cells from fat tissue (adipose) and bone marrow mesenchymal stem cells (BM-MSC) have been extensively used for different tissue engineering applications [133]. Stem cells exhibit multipotent differentiation capacity which can be used to improve clinical treatment techniques in various locomotion tissues [134], including the bone [135], fat [136], ligament [137, 138] and articular cartilage [136, 139].

Stem cells exhibit high proliferation and growth rate, and thus for cell procurement, little sampling from donor site is required. The sampling process for adipose stem cells is also straightforward and less invasive compared to chondrocyte procurement. The process therefore is advantaged by minimal donor site morbidity and pain level. For a direct comparison between the efficacy of chondrocyte and stem cells for cartilage repair, two populations of patients are treated with either chondrocyte or stem cells [140]. The results from this study showed that articular cartilage defect treatment with autologous stem cells is as successful as the one using chondrocyte. By considering the limited number and low quality of chondrocyte in the defected tissues, treatment with stem cells has more potential for ACI applications.

The use of BM-MSC also enables simultaneous repair of the bone and cartilage, which ultimately results in promoting remodelling and integration of the regenerated cartilage with the host tissue [141, 142]. However, the monolayer culture of both stem cells and chondrocytes possesses the issue of telomere shortening,¹ loss of proliferative rate and multipotency [143–145]. An alternative source for stem cell is embryonic stem cell that has unlimited capacity for proliferation in monolayer culturing and is promising for a broad range of tissue engineering applications [133]; however, commercialisation of embryonic stem cell-based discoveries is banned in many countries, such as European countries.

14.3.2 Bioactive Factors

Regeneration and growth of cartilage and its integration with the surrounding tissues rely on the biochemical signaling of cells within the regenerating tissue. Bioactive factors include small drug-like molecules, growth factors or any other

¹Human (and other) somatic cells without telomerase gradually lose telomeric sequences as a result of incomplete replication.

molecule that has cell motif sites and can bond with cells to create biological responses. The intensity, duration and sequence of stimulation factors affect the metabolic activity of cells and their ECM exertion.

14.3.2.1 Chondrogenesis Small Drug-Like Molecules

Small drug-like molecules have developed to selectively regulate transcriptional factors of subcellular localisations and activities [146, 147]. For cartilage tissue engineering, kartogenin is identified as a small molecule which can promote chondrogenesis and chondrocyte differentiation of MSC by disrupting interaction of filamin-A with transcription factor CBF β . This regulates the CBF β -RUNX1 transcriptional program, which ultimately induces chondrogenesis. The positive effect of this molecule on chondrogenesis has been studied and proved by in vitro and two animal model studies that were subjected to osteoarthritis disease. Application of drug-like selective regulator molecules for transcriptional subcellular factors is limited for their intrinsic complexity. Chondrogenesis of BM-MSC is, therefore, mostly promoted by using exogenous anabolic factors, loaded within the network of scaffold.

14.3.2.2 Growth Factors

Chondrogenesis can be promoted by using exogenous anabolic factors [148]. The growth factors include but not limited to TGF- β [148, 149] and BMP family [150–152] that have been used to promote chondrogenesis. Most commonly used growth factors for articular cartilage applications and their in vitro and in vivo effects are summarised in Table 14.3.

TGF- β superfamily is involved in tissue repair and inflammation responses following a cartilage injury [153, 154]. Controversy results are obtained for the effect of TGF- β superfamily for cartilage tissue engineering. For therapeutic application, TGF- β superfamily can prolong cartilage life by minimising or even eliciting the biological and biomechanical changes in cartilage over the years. For tissue engineering applications, some studies confirmed the positive effect of TGF- β 1 in chondrogenesis proliferation and growth. The positive effect of TGF- β 1 in cartilage tissue engineering, however, depends on the differentiation state of cells; for freshly isolated chondrocytes, addition of TGF- β 1 had no significant effect on cell growth. The incorporation of growth factor, however, significantly affects the proliferation and proteoglycan synthesis of chondrocyte, cultured in vitro after 1 week of isolation [155]. TGF- β 1 had negative impact for cartilage repair. For instance, it is observed that the synthesis of proteoglycan by arthritic chondrocytes is decreased when adding TGF- β 1 to the media [156]. This reduction may result in formation of articular cartilage with unfavourable properties.

Bone morphogenetic protein (BMP) superfamily also plays an important role in endochondral bone and cartilage formations. More than 20 types of BMP have been

Table 14.3 Different growth factors, used for articular cartilage tissue engineering, and results achieved in vitro and in vivo

Growth factor	Results	Refs.
TGF- β 1	No significant effect on freshly isolated cells	[153–158]
	Improve proteoglycan synthesis on chondrocytes after 1 week of post-isolation	
	Proteoglycan synthesis decreased by arthritic chondrocytes	
BMP-1	Promotes the expression of proteoglycan and collagen more than TGF- β 1	[154, 159, 160]
BMP-2	Regulates proteoglycan and collagen production and helps to adjust the biomechanical and biochemical properties of regenerated tissue	[159, 160]
BMP-4	Increases cell proliferation, proteoglycan formation as well as bone formation	[160, 161]
BMP-7	Decreases collagen type I expression, increases proteoglycan and ECM production and cellular proliferation	[162, 163]
BMP-12 and BMP-13	Promotes synthesis of GAG, less significant effect compared to BMP-2	[164]

identified. In tissue engineering applications, BMPs are commonly used for bone repair and regeneration. For cartilage tissue engineering, BMPs also enhance the osteochondral integration of the defected cartilage by promoting osteogenesis and chondrogenesis at the defected site. It is shown that BMP-1 has more stimulation effect on cells to express proteoglycan and collagen compared to TGF- β 1 [165]. BMP-2 also regulates the formation of collagen and proteoglycan from chondrocytes [159, 160]. In addition it promotes the healing process of cartilage defects in vivo [154]. BMP-4 stimulates proteoglycan expression and osteochondral tissue formation and also enhances cellular proliferation for articular cartilage regeneration [160, 161]. Addition of such BMP growth factors as BMP-7, BMP-12 and BMP-13, particularly BMP-2, enhances ECM formation [160] and cell proliferation [162]. In addition, BMP-7 suppresses expression of collagen type I and differentiation of fibroblast in vivo [163], which inhibits the formation of fibrocartilage at the defected site [164].

14.3.3 Biomaterials for Cartilage Regeneration

In a tissue engineering approach, biomaterials are used either for fabrication of 3D scaffolds for in vitro tissue regeneration or synthesis of an injectable vehicle to deliver cells/drugs to the defected site of cartilage for in vivo cartilage regeneration. In both techniques, biomaterials play a critical role in cellular growth and tissue regeneration. The physicochemical and biological properties of biomaterials substantially affect the functionality of repaired cartilage [166].

14.3.4 Properties for Biomaterials

Biomaterials are used as physical supports for cell growth and to avoid spillover and asymmetric distribution of cells. This is important to promote synthesis of cartilage ECM and to regenerate functional tissues. In case of cartilage tissue engineering, the biomaterials support the newly formed tissues to promote the integration of repaired cartilage with host tissue. The physical and biological properties of biomaterial used for scaffold fabrication play important roles in cell responses, adhesion and infiltration to form functional 3D structure cartilage [166]. Biomaterials must be biocompatible and exhibit cell adhesive surface properties with suitable microstructure for 3D cell proliferation. They also must be mechanically strong to support the newly regenerated tissue *in vivo*.

14.3.4.1 Biocompatibility and Surface Properties

Particular attention has been paid on the biocompatibility of biomaterials. Biocompatibility is predominantly affected by the chemical and biological properties of biomaterials used for cartilage repair. A biomaterial is biocompatible when it elicits neither cytotoxic effects nor inflammatory responses within the surrounding tissue [167].

Surface properties of biomaterials affect *in vitro* cellular adhesion, phenotype maintenance, intracellular signaling and *in vivo* cell recruitment, healing and osteochondral integrations [168–170]. Cell responses to the ECM matrix and the new regenerated tissues are mediated through an interfacial layer formed on the surface of scaffold or biomaterial. This layer is formed by non-specific absorption (not chemical conjugation) of ECM proteins with a biomaterial when it is in a proper physiological environment. As an example, hydrophilic properties of a polymer such as gelatine and poly(vinyl alcohol) promote the formation of interfacial layer and thus enhance the adhesion of cells [171]. The incorporation of peptides in the form of long chain of ECM proteins (such as fibronectin, laminin, elastin and collagen) or short peptide sequences, derived from ECM proteins (such as arginine–glycine–aspartic acid), provides cell binding sites on scaffold to mediate cell responses, thereby enhancing tissue regeneration [172, 173].

14.3.4.2 Microstructural and Mechanical Properties

The microstructure, porosity and pore interconnectivity are critical factors for biomaterials that are used for tissue engineering. Porosity allows the cell migration into the 3D structure of scaffold, and pore interconnectivity is a key factor for nutrient, oxygen and waste transfer into and from the cells in scaffolds [174–178]. For each cell type a range of pore sizes is required to mimic the innate tissue and allow the cells' adhesion and regeneration [179]. For *in vitro* cartilage tissue

engineering, the average pore size in the range of 250–500 μm is recommended [180]. Small pore size resulted in occlusion and obstruction of pores, which then prevents cellular penetration within the 3D structure of scaffolds. Pores in the range of 75–100 μm can result in growth of un-mineralised osteoid tissues [181]. Additionally, only fibrous tissues penetrate within a scaffold with an average pores size of 10 μm or less. Low average pore size, therefore, leads to the formation of fibrocartilage rather than cartilage. Meanwhile, the mechanical strength of physical supports decreases by increasing the average pore size. Therefore, it is important to tune the void volume (or average pore size) in scaffolds for cartilage tissue engineering to both enable the migration of chondrogenic cells and maintain the required structural strength [178].

For *in vivo* cartilage tissue engineering, chondrogenic cells are suspended within the polymeric matrix, and the suspension is gelled *in situ*. There is no need for cells to immigrate through pores, and thus large pores from 250 to 500 μm are not necessary anymore. It is shown that small pores that are less than 100 μm in biomaterials induce osteochondral formation *in vivo*, while a larger pore size leads to osteogenesis before cartilage formation [182]. As an example, chondrocyte maintains its phenotype, and cartilage ECM is produced by encapsulating cells within an injectable chitosan/starch/ β -glycerol hydrogel with average pore size in the range of 19.8–26.4 μm [183].

The biomaterials provide a temporary mechanical support to bearing *in vivo* loadings and stresses during the tissue regeneration. One of the key factors in successful tissue engineering is to develop a mechanically strong scaffold that its degradation rate corresponds to the rate of regeneration of ECM. External loads and stresses stimulate cell proliferation, remodelling and tissue regeneration [184–186]. It is essential that loads gradually transfer from the biomaterials (supporting cell growth and tissue regeneration) to the regenerated cartilage to promote tissue remodelling. It is therefore, critical to control the degradation rate and mechanical strength of scaffold to ensure sufficient structural integrity of matrix is retained during the regeneration of cartilage [187]. The rapid degradation of biomaterials is not desirable as it provokes excessive stresses and impact loads to the developed tissues prior to sufficient growth and remodelling cartilage. This effect might result in complete failure of regenerated tissue construct. On the other hand, the slow degradation of biomaterials may shield the cells against external stimulating stresses, which can decrease the proliferation and growth rate of chondrogenesis cells. It is important to design scaffolds with the mechanical properties that mimic cartilage tissues for *in vitro* and *in vivo* applications. The compressive modulus of native cartilage varies from 0.08 to 2.1 MPa [31, 32, 39] and its tensile modulus in between 4.8 and 25 MPa [25]. It might be possible to use biomaterials that may not fully meet these mechanical properties, as the newly formed cartilage might provide extra structural integrity after implantation.

14.3.5 Scaffold for In Vitro Tissue Engineering

Tissue engineering techniques have been proposed for the treatment of articular cartilage defects. In modern ACI, 3D scaffolds are used to address the issues associated with monolayer culture of chondrogenesis cells in vitro such as dedifferentiation and ossification of chondrogenesis cells [126]. In vitro cell studies showed that chondrocyte phenotype can be maintained up to 8 months of post seeding in 3D scaffold [188]. In the clinical approach for the treatment of cartilage defect, chondrogenesis cells (chondrocytes or stem cells) are seeded on a biodegradable scaffold and cultured in vitro. The construct is harvested in vitro, and cell viability and chondrogenesis of cultured cells are continually tested for a period of 6 weeks. Subsequently, the regenerated tissue, formed within the scaffold, is transplanted at the defected site (most commonly with open surgery). The efficacy of this technique for the treatment of articular cartilage defect is substantially affected by the characteristics of scaffolds used for in vitro cell growth [188]. Different biomaterials are attempted for the fabrication of scaffolds for cartilage regenerations. These include biodegradable synthetic and natural polymers that are either hydrophobic or hydrophilic.

14.3.5.1 Synthetic Polymers

Synthetic polymers exhibit reproducible and predictable physicochemical, mechanical and degradation properties, all of which can be closely tuned to fulfil the requirements. In addition, the risk of toxicity, immunogenicity and infections is low in the application of synthetic polymers for different biomedical applications since they constituted of well-known molecular structure. Poly(α -hydroxy esters) are widely used for cartilage tissue engineering, and they are often processed to form 3D porous structures with hydrophobic properties. Meanwhile, poly(vinyl alcohol) (PVA), poly(ethylene glycol) and polyacrylates (PEs) formed hydrophilic structures with high water content, called hydrogel. Hydrogels are a class of biomaterials, composed of natural or synthetic polymer chains with very high water content (above 30 wt%) [189]. Hydrogels become the material of choice as scaffold for cartilage tissue engineering applications attributable to their hydrophilic properties, high water content, superior permeability of nutrients, long chain molecules, proteins and oxygen [174, 179, 190–193]. Some of the in vitro and in vivo outcomes, from the applications of main synthetic polymers as scaffold for tissue growth, are summarised in Table 14.4 and comprehensively discussed in the following sections.

Table 14.4 The pros and cons observed from in vivo and in vitro applications of synthetic polymers for cartilage repair

Biomaterial	Positive outcomes	Negative outcomes	Refs.
PGA	Maintenance of chondrocyte phenotype in vitro and in vivo	Initial in vitro cell culturing is necessary to initiate ECM formation in vitro	[194–197]
PLGA	Can maintain the chondrocyte phenotype in 2 weeks of in vitro	Initial in vitro culturing is necessary prior to in vivo implantation	[194–197]
PLA	Minimising release of acid as the result of degradation	Biochemical properties inferior to native tissue	[198, 199]
	Maintaining structural mechanical support for a long time	Low cell adhesive surface properties	
	Cartilaginous appearance		
PCL	High structural integrity in in vitro culturing	Very low chondrocyte adhesion and proliferation	[200–202]
PVA	Similar water content as natural cartilage	Dedifferentiate chondrocyte due to very low mechanical properties	[203–207]
	Has high growth factor loading capacity		
	Osteochondral		
PEG-ma	Photo-crosslinkable, suitable for cell encapsulation	Lack of mechanical strength for load-bearing cartilage	[208–210]
	Chondrogenesis cells induced cartilage ECM formation by the addition of required growth factors		
PEG-da	Photo-crosslinkable and suitable for cartilage regeneration	Lack of cell motif sites	[211–215]
	Tuneable mechanical and physical properties to match the requisites for cartilage repair		
	Can act as a crosslinking agent for different PEG-based polymers		
OPF	Formation of cartilage-like tissue by using OPF hydrogel for cartilage regeneration both in vitro and in vivo	The lack of cell motif sites might lead to low chondrogenesis cell proliferation and growth	[216–218]
		Non-biodegradable properties of this hydrogel might lead to unpredictable problems and unreproducible results	

Poly(α -Hydroxy Esters)

Poly(α -hydroxy esters) (PHEs) is a class of synthetic biodegradable polymers that have been used for the preparation of scaffolds for cartilage tissue engineering.

They include poly(lactic acid) (PLA), poly(glycolic acid) (PGA), poly(lactic-co-glycolic acid) (PLGA) and poly(ϵ -caprolactone) (PCL). Based on the position of methyl group in the lactic acid monomer, there are three stereoisomers of PLA (D (-), L(+) and D,L). The degree of crystallinity in PLLA is higher than those of PDLA and PDLLA. All PHE polymers have had the FDA approval for different biomedical applications [219].

PHEs can be easily processed, and their degradation and mechanical and physical properties are tuneable over a wide range by changing their molecular weight, crystallinity and copolymer composition. Their degradation process via a random, bulk hydrolysis of ester bonds in the polymer chain, however, might induce premature bulk failure of scaffolds. In addition, the release of acidic degradation products can cause strong inflammatory responses [220, 221]. These synthetic polymers degrade to monomeric acids and thereafter to carbon dioxide and water through de-esterification phase. PGA molecules are degraded to glycine and PLA to lactic acid. In vivo, polymeric degradation products are excreted by natural pathways via respiratory routes and renal filtration [222].

The kinetics of degradation in PHEs are affected by different factors, including (i) copolymer composition, (ii) molecular weight, (iii) degree of crystallinity, (iv) polydispersity index, (v) structural morphology (pore size and porosity) and (vi) distribution of chemically active compounds such as proteins in their structures [223, 224]. In PLGA scaffolds, for example, the degradation rate strongly depends on lactic/glycolic monomer ratio and crystallinity of lactic monomer [223]. PHE scaffolds exhibit two profiles of degradation, surface and bulk degradation. Surface degradation presents easier diffusion of soluble oligomer and neutralisation of the carboxylic end groups by surrounding buffer solution in vitro or in vivo. Conversely, the degradation rate in bulk is promoted by autocatalysis [225]. Therefore, PLA with a methyl pending group degrades slower compared to PGA without any pending group. In addition, the hydrolysis of amorphous polymers such as PDLLA is faster due to lack of crystalline regions [225].

The mechanical properties of PHEs depend on the molecular weight, microstructure and crystallinity of polymers. In general, PGA is more hydrophilic and rigid, whereas PLA is more flexible (higher elastic modulus) with low degradation rate. Copolymerisation of these two polymers in different ratios can be used to form PLGA polymer with optimised mechanical, degradation and water uptake properties. PLGA has amorphous structure because PLA and PGA are not tightly coupled and, therefore, it exhibits higher degradation rate compared to both PGA and PLA [226].

PLA, PLGA and PGA are used for cartilage tissue engineering in the forms of fibres (electrospun as discussed in Chap. 8) or foamed scaffolds. In vitro and in vivo studies showed the maintenance of chondrocyte phenotype on PLGA and PGA scaffolds [194, 197]. But functional cartilage could only be achieved by short-term in vitro chondrocyte culturing on the scaffolds and then in vivo implantation of constructs [195, 196]. Electrospun PLA scaffolds have been used for in vitro cartilage tissue engineering. Chondrocyte maintains its chondrogenic phenotype after 7 days of culturing on PLA [199]. One-year animal studies using allogeneic

perichondrial cells [227] and autogenous perichondrial cells [198] on PLA scaffold showed inconsistent subchondral bone regeneration.

In addition, regenerated tissues have been disadvantaged by inferior biochemical properties compared to natural cartilage [198]. The limited application of these types of polymers for cartilage tissue regeneration is due to the poor cell adhesion to their surface. PLA has been conjugated with monomethoxy poly(ethylene glycol) (mPEG) to increase its hydrophilicity and cellular adhesive properties [228]. The compressive modulus of PLA/mPEG polymer, however, decreased significantly compared to PLA [228].

Poly(ϵ -caprolactone) or PCL is aliphatic linear polyester, which undergoes autocatalysed bulk hydrolysis. The degradation process of this biomaterial is slow due to its semi-crystalline nature and hydrophobicity [229, 230]. The packed macromolecular arrays retard fluid diffusion into the bulk of hydrophobic PCL. This polymer is, therefore, used as a long-term implant (e.g. for years) in different biomedical applications. To increase the degradation rate of this polymer and also its processability, PCL is copolymerised with different PHEs [229, 230]. The copolymerisation, however, substantially decreases the mechanical strength of PCL copolymer and thus limited their applications for cartilage tissue engineering. In addition, the hydrophobic surface of this synthetic polymer might adversely affect the cell adhesion and proliferation. To achieve PCL-based scaffolds with more favourable biological properties, composite scaffolds of PCL and naturally derived polymers such as PCL with chitosan [231], hyaluronan, fibrin [232] and elastin [200, 201] have been prepared. In one study PCL porous scaffold has been fabricated using gas foaming by high pressure CO₂ and salt leaching techniques. Then elastin is impregnated into these pore structures. The *in vitro* study demonstrated that chondrocyte cell adhesion and proliferation within the 3D structure of this PCL/elastin composite scaffold are substantially enhanced compared to neat PCL [201].

Acidic degradation products of PHEs can cause adverse tissue reactions and might induce immunoresponsive reactions. To counteract the acidic degradation process for some of PHEs and also to stabilise the pH of the surrounding environment, these polymers are combined with basic compounds [223, 224]. Calcium phosphate compounds and bioactive glasses are the two main additives used for this purpose. The addition of bioactive glass might also modify the mechanical properties of scaffolds and promote osteoconductivity of biomaterial. Bioactive glasses are thus used for bone tissue engineering rather than cartilage regeneration.

One of the major drawbacks of PHEs is their hydrophobicity, which can adversely affect the cell phenotype, cellular growth and proliferation. Different techniques, such as surface modification [200, 201], NaOH surface treatment [233] and ammonia plasma treatment [234], have been attempted to promote chondrogenesis cell adhesion on the surface of PHE. For instance, coating the surface of PLLA with chitosan and collagen enhances the cellular adhesion. However, cell proliferation and differentiation in PLA/collagen scaffold is inhibited due to blockage of pores.

Poly(vinyl Alcohol) (PVA)

PVA is hydrophilic biocompatible polymer that can be crosslinked to form hydrogel. It is historically used for cartilage regeneration applications [235] and can be engineered to have similar water uptake properties as native cartilage [203]. PVA hydrogel can be cut into the required shapes and then transplant into the patient's body through an open surgery process. In vitro cell studies on pure PVA hydrogel showed that low mechanical strength of the construct might lead to dedifferentiation of seeded chondrocyte, and hence further processing is required to increase its mechanical strength. Poly(lactic-co-glycolic acid) microparticles have been embedded within PVA hydrogel network, and insulin-like growth factor-1 (IGF-1) has been loaded in the hydrogel, which showed that the sustained release of IGF-1 can enhance cartilage formation which might lead to effective integration of the construct with the surrounding tissue [207].

Poly(ethylene Glycol)-Based Polymers

Poly(ethylene glycol) (PEG), also known as poly(oxyethylene) or poly(ethylene oxide), is one of the most extensively investigated non-biodegradable, synthetic, hydrophilic polymers for different cartilage tissue engineering applications [236]. This is due to its hydrophilicity, acceptable cell compatibility and non-cytotoxicity. PEG can also be easily functionalised with different reactive end groups. Copolymer of hydrophilic poly(ethylene glycol) (PEG) and different biodegradable and biocompatible polyesters, such as polylactide (PLA), poly(ϵ -caprolactone) and poly(glycolide) (PGA), have drawn great attention for their tuneable characteristic parameters [237].

PEG macromer is functionalised with methacrylate (ma) groups to form a photocrosslinkable hydrogel, suitable for cartilage tissue engineering [208]. Different chondrogenesis cell types, including chondrocytes, embryonic stem cells and MSCs, are encapsulated with PEG-ma hydrogels and induced to form cartilage tissue in the presence of growth factor [208–210]. Diacrylate (da)-functionalised macromers of PEG have also been developed for different cartilage tissue engineering applications [211–215]. The lack of cell motif sites within its structure is the main drawback of this polymer. Due to high activity of PEG-da macromer, it can be used as a chemical crosslinking agent for different PEG-based macromers [212].

More biomimetic derivative macromers of PEG have been synthesised by conjugating collagen-mimetic peptide $-(\text{Pro-Hyp-Gly})_x-$ with PEG macromers. In vitro cell study showed that MSC proliferates and both collagen and proteoglycan are produced within this hydrogel [238]. In addition, the incorporation of PEG to chondroitin sulphate-based hydrogels increases the production of cartilage ECM proteins from MSCs seeded within this hydrogel [239]. PEG can also be functionalised by the addition of fumarate groups to the macromer using fumaric acid. Oligo(poly(ethylene glycol) fumarate) (OPF) is the fumarate-functionalised,

photo-crosslinkable PEG macromer. In a rabbit model with osteochondral defects, acellular OPF hydrogel has been used, and it is observed that native MSCs migrate within the 3D structure of these hydrogels to form fibrocartilage at the lesion site. Encapsulation of external MSCs within the OPF hydrogel structure results in regeneration of cartilage [218]. Different *in vitro* and *in vivo* studies have been conducted to investigate the capability of OPF hydrogels to deliver different growth factors to the defected site to promote natural process of cartilage tissue regeneration. These studies showed the potential of OPF hydrogels for encapsulation of different growth factors for cartilage tissue engineering [216, 217]. Tuneable properties, easy to process and functionalised, hydrophilic and biocompatible properties of PEG-based hydrogels are the main advantages of this group of biomaterials for cartilage tissue engineering.

Polyacrylates (PEs)

Poly(2-hydroxyethyl methacrylate) (PHEMA), poly(methyl methacrylate), poly(ethyl methacrylate) and poly(tetrahydrofurfuryl methacrylate) are the main polyacrylate-based hydrogels used for cartilage tissue engineering. It has been attempted to use PHEMA/MMA hydrogel for articular cartilage repair. However, the regenerated tissue exhibited lower mechanical strength compared to the surrounding native cartilage. Compliance of the fabricated PHEMA/poly(methyl methacrylate) hydrogel might lead to the formation of fibrocartilage as a result of implantation of construct *in vivo* [240]. Sawtell et al. also reported the cartilage inductive properties of PEMA/poly(tetrahydrofurfuryl methacrylate) hydrogel. *In vitro* studies showed the expression of GAG from seeded chondrocytes on this hydrogel. This results indicated the potential of PEMA/poly(tetrahydrofurfuryl methacrylate) hydrogel for cartilage repair [241]. Animal studies on this hydrogel showed the regeneration of hyaline cartilage at the subchondral defected site in rabbits [242]. The non-biodegradation properties of this group of biomaterials might lead to some uncontrollable biological behaviour by the cartilaginous construct after *in vivo* implantation. This is the main drawback in the application of these polyacrylate biomaterials for cartilage repair.

14.3.5.2 Naturally Derived Hydrogels

The feasibility of using biopolymers such as protein and polysaccharides for cartilage tissue engineering has been examined [5, 6]. The presence of cell motif sites in naturally derived polymer promotes their cellular adhesive properties. Protein-based hydrogels that have been attempted for cartilage tissue engineering include collagen, fibrin, silk and elastin-like polypeptides (ELPs). Commonly used polysaccharides are hyaluronic acid, agarose, alginate and chitosan. The common methods used for crosslinking these polymers and a summary of their properties are listed in Table 14.5, while more details are provided in the following discussion.

Table 14.5 Natural hydrogels for in vitro cartilage tissue engineering

Biomaterial	Crosslinking method	Comments	Refs.
Collagen types I and II	Physical/chemical (mixed with alginate) glutaraldehyde)	Bioactive, but poor mechanical properties	[243–249]
		Chondrogenesis after 3 days when mixed with alginate	
		No cell degeneration after 24 weeks	
		For physical crosslinking, possible to incorporate cells and chondrogenesis biofactors	
		Chemical crosslinking slightly increases the mechanical properties, but there is a risk of cytotoxicity	
		In vivo cell study with chemically crosslinked collagen in rabbit model	
		Might be immunogenic	
Fibrin	Physical	Poor mechanical properties	[88, 250–252]
		Immuno-responsive effect	
		Promote natural healing process at the defected site	
		Chondrocyte and biofactors can be incorporated	
Silk	Physical	High mechanical strength, risk of immunoresponses	[253–256]
		Tedious purification required to minimise this risk	
		Stem cells and chondrocyte maintained chondrogenic phenotype	
		Might initiate adverse immunoresponses	
		Required complicated purification process	
Alginate	Chemical (ion induced)	Easy to produce, cost-effective	[176, 243, 257–259]
		Chondrocytes and biofactors can be incorporated within its structure	
		Low bioactivity, slow and inconsistent degradation rate	
		Low cell adhesive properties	
Chitosan	Physical/chemical (genipin and glutaraldehyde)	Easy to process and functionalised	[260–263]
		Chondrocyte maintains its phenotype in this hydrogel	
		Good cell adhesion and proliferation	
		Possess low mechanical properties	
Chondroitin sulphate	Physical	Inhibit GAG production	[259, 264–268]
		High cost	

(continued)

Table 14.5 (continued)

Biomaterial	Crosslinking method	Comments	Refs.
Elastin-like polypeptides	Physical/chemical (glutaraldehyde)	Maintain chondrocyte phenotype	[201, 269–272]
		Functionalised to form covalent bonding and crosslinking	
		Tuneable chemical structure to promote chondrogenesis	
		Lack of mechanical strength	
		High cost	

Collagen

Collagen type II and type I are used for cartilage repair as these are the key types of collagens that exist in this organ [243, 273]. Chondrogenesis cells bind to collagen hydrogel via integrins, which induces chondrogenesis signaling that promotes cartilage formation. Collagen type II initiates and maintains chondrogenesis phenotype of mesenchymal stem cells enhancing the effect of TGF- β 1 on cartilage formation [243]. The main advantage associated with collagen type I is its potential to spontaneously form hydrogel at physiological temperature and pH. Despite the fact that collagen type I is only found in the structure of diseased or damaged cartilage, the studies showed that the articular chondrocyte maintains its phenotype in collagen type I. Chondrocytes synthesised cartilage ECM component (e.g. collagen type II and proteoglycan) when using hydrogels fabricated from collagen type I [248]. Chondrocytes embedded within a collagen type I hydrogel are used for the treatment of full-thickness articular cartilage defect in small animals. Moderate regeneration of articular cartilage surface is reported [248]. In another study, however, it is shown that after 2 weeks of in vitro culture, only 30 % of chondrocytes on collagen type I hydrogel maintained their chondrocytic phenotype (spherical shape) [249]. Nevertheless, when using hydrogels from collagen type II, more than 60 % of chondrocytes maintained their spherical shape [249]. Buma et al. developed a composite hydrogel of collagen types I and II to further mimic the biochemical properties of natural cartilage. In this approach deep layer of hydrogel is formed from collagen type I for subchondral recruitment of stem cells. The more superficial layers of hydrogel, however, are composed of collagen type II that maintains chondrogenesis phenotype of cells [274]. Results from the application of collagen type II hydrogels for treatment of osteochondral defect in rabbit model showed the formation of both hyaline cartilage and the bone at the defected site. However, the mechanical properties of regenerated tissues are significantly lower than native tissues [244].

Several strategies have been undertaken to enhance the mechanical strength of collagen-based hydrogels such as crosslinking [243], mixing collagen with a synthetic polymer such as PLGA [275], bioactive glass [275] and hydroxyapatite [276]. For chemical crosslinking of collagen, the amine side group of lysine and hydroxylysine is chemically bonded with a crosslinking agent. Glutaraldehyde

[245], hexamethylene diisocyanate [277] and 1-ethyl-3-(3-dimethylaminopropyl) carbodiimide [246] are the examples of crosslinkers [247]. However, the effect of chemical crosslinking on mechanical properties and degradation of collagen hydrogel is trivial [243, 278].

Elastin and Elastin-Like Polypeptides (ELPs)

Elastin is 68 kDa protein comprised of approximately 800 amino acid residues [279]. It has elasticity and mechanical strength that mimic native cartilage and ligament tissues [280]. Elastin contains hydrophobic and hydrophilic domains, which provides crosslinking sites with neighbouring molecules [281]. Application of elastin in tissue engineering, however, is limited for many years by its extreme water insolubility [282]. This has been improved by increasing availability of animal-derived soluble elastin through acidic (α -elastin) [283, 284], alkaline (k-elastin) [284] and enzymatic hydrolysis of elastin [285, 286]. In addition, a recently developed recombinant full-length elastin precursor, known as recombinant tropoelastin (rhTE), has been developed suitable for biomedical applications [285]. It is viable to synthesise elastin-like polypeptides (ELPs) by polymerisation of pentapeptide motif VPGVG and control physical and functional properties at the generic or chemical level [279].

Early studies showed the positive effect of elastin in promoting production of chondrocyte ECM such as collagen type II and proteoglycan in long-term monolayer culture of chondrocyte without dedifferentiation [269]. After 10 days of culturing chondrocyte in thermosensitive ELP solution, its phenotype is maintained and both collagen type II and GAG are produced [269]. Primary chondrocyte [287] and adult stem cell [288] have been cultured using coacervated ELP structure for cartilage tissue engineering. It has been demonstrated that ELP promotes the differentiation of stem cell that has undergone chondrocytic pathway even in the absence of any specific chondrocyte growth factor [288]. Elimination of growth factor significantly reduces the cost of differentiation and cartilage regeneration [285]. However, the shear moduli of ELP are fourfold lower than that of articular cartilage. The addition of crosslinking agent is one option to enhance the mechanical strength of ELP [37, 287]. For instance ELP is functionalised with glutamine to fabricate an enzymatic crosslinking site and create hydrogel [270]. This ELP-based hydrogel exhibits chondrogenesis behaviour and produces cartilage ECM proteins [270].

ELP-based biomaterials are chemically crosslinked from their active lysine group to increase their mechanical properties [289–291]. Lim et al. fabricated ELP hydrogel by reacting lysine containing ELPs with an organophosphorus crosslinker, β -[tris(hydroxymethyl)phosphino]propionic acid (THPP) in less than 5 min [289]. Both in vitro and in vivo cell studies confirmed the formation of cartilage ECM with these hydrogels [289, 290]. The mechanical strength of elastin-based hydrogel can be enhanced by synthesising this class of molecules with more

crosslinking sites. It is also feasible to use naturally derived elastin and mix it with mechanically stronger tropoelastin to enhance their mechanical properties [292].

Level of crosslinking, formulation, molecular weight and concentration of ELPs are the important factors that may affect the properties of ELP hydrogel and its performance for cartilage repair [271]. It is found that the molecular weight of ELPs has negligible effect on the physiochemical and biological properties of regenerated cartilage [293]. However, the crosslinking and also mechanical properties of ELP have significant impact on cartilage regeneration. The human tropoelastin has been crosslinked with genipin and created a hydrogel with compressive modulus in the range reported for articular cartilage [272]. This sample is then press-fitted into osteochondral defect site in a knee joint of rabbit for *in vivo* studies. Preliminary results showed no significant inflammation and high level of hyaline articular cartilage formation.

The high cost of producing elastin by recombinant technology or protein synthesis, immunogenicity of naturally derived elastin and low mechanical properties are the hurdles for application of elastin for cartilage repair despite its excellent biological properties.

Fibrin

Fibrin, which is produced by enzymatic cleavage of fibrinogen, is used for cartilage tissue engineering due to its role in natural wound healing [88, 250]. It promotes healing process within the extravascular space. Similar to other natural polymers, products of fibrin degradation are not toxic [250]. Fibrin has been used as a scaffold to deliver chondrocyte [294], mesenchymal stem cell [295] or growth factors [296] for cartilage tissue engineering applications. The natural healing process is optimised by implanting fibrin clot at the defected site [297, 298]. It can, therefore, promote spreading of endogenous blood over the large volume of the lesion site, which otherwise would be occupied with a developing haematoma. Chondrogenesis cells have been incorporated within the network of fibrin hydrogel to further enhance the healing process [251]. Both *in vitro* and *in vivo* results confirmed the positive impact of incorporated chondrogenesis cells with fibrin clot for cartilage regeneration [299, 300]. Despite these positive results, due to the low mechanical strengths and immunoresponsive effect of fibrin, this protein has minimal potential to be used directly for cartilage tissue engineering [252, 301, 302].

Silk

Silk fibroin is a typical protein that forms the filament of native silkworm. It has a broad range of applications due to its unique physicochemical properties. Silk mimics many characteristic properties of cartilage extracellular matrix and has potential for cartilage repair. These properties include high mechanical strength, flexibility, low degradation rate and water permeability [254, 303–305]. The

physically crosslinked silk hydrogel is used for chondrogenesis of bone marrow-derived mesenchymal stem cells, in which chondrogenic growth factors are used in culture media [306]. The chondrogenesis of MSCs is further increased by the incorporation of IGF-1 growth factor to silk hydrogel [307]. In vitro cell study on silk hydrogel showed great promise for the application of this type of hydrogel for full-thickness cartilage repair using both chondrocytes and stem cells [308, 309]. A structural protein blend system based on silkworm, silk fibroin and recombinant human tropoelastin has also been developed to form a scaffold with high mechanical strength, controllable degradation behaviour and elasticity [310, 311]. These studies showed human mesenchymal stem cell adhered and proliferated on this scaffold, exhibiting high potential of this protein blend for cartilage repair.

Care must be taken in purification of silk to remove sericin from fibroin silk to inhibit adverse immune response at the host tissue. In vivo studies demonstrated that pure fibroin silk has low immunogenicity and elicits foreign body response. Limited studies claimed that granuloma might form due to abandoned phagocytic response to silk by giant body cells and macrophages [256]. Compared with other biopolymer, however, silk is a desirable natural polymer for cartilage repair.

Chitosan

Chitosan, a positively charged polymer, is a linear polysaccharide that consists of randomly distributed N-acetyl-D-glucosamine and β -(1,4)-linked-D-glucosamine units [312]. It has been broadly used for biomedical applications for the low cost, low toxicity and immunostimulatory effects [260]. Molecular structure of chitosan resembles glycosaminoglycan, which also presents in the molecular structure of GAG. It thus interacts with different articular cartilage growth factors, adhesion proteins and receptors; hence chitosan can stimulate chondrogenesis of cells. In addition, physicochemical and biological properties of chitosan rely on the activity of glucosamine residues from acetylation [313], alkylation [314], carboxymethylation [315] and conjugation of chitosan with methacrylic acid and lactic acid [316, 317]. These techniques have been used to fulfil the characteristics of chitosan-based hydrogels for cartilage repair. The mechanical properties of these chitosan-based hydrogels are increased. Chitosan has been crosslinked with different reagents such as glutaraldehyde [318, 319], 1-ethyl-3-(3-dimethylaminopropyl) carbodiimide hydrochloride [320] and genipin [321–323] to increase its mechanical properties.

Porous chitosan hydrogel has been produced by gas foaming and lyophilisation techniques to create porosity in 3D structure and enhance cell proliferation [261, 321, 324]. For example, Ji et al. simultaneously used gas-foamed and crosslinked chitosan (using either genipin or glutaraldehyde) under higher pressure CO₂ [321, 326]. These pores allowed the nutrient and oxygen transfer, hence the proliferation of fibroblast cells in 3D structure of chitosan hydrogel. In another study, it is demonstrated that chitosan enhances the natural regeneration process of articular cartilage in the rat joint [325]. Polyelectrolytic complex of chondroitin

sulphate and chitosan also provides a good mechanical structure for the adhesion and attachment of chondrocytes and MSC [162, 262]. Chondrocyte cells maintained their round or polygonal morphology and had undergone modest degree of mitosis [326]. Chitosan is used to promote cartilage wound healing as an injectable formulation. As an example, BST-CarGel, a chitosan-based biomaterial, is commercially available for cartilage regeneration [327, 328]. However, due to low mechanical strength, neat chitosan cannot be used for the fabrication of 3D hydrogels for regeneration of full cartilage.

Chondroitin Sulphate

Chondroitin sulphate (CS) is a GAG-based biomaterial composed of a chain of *N*-acetylgalactosamine and glucuronic acid [329]. It has been initially used in articular cartilage repair as a preventive and healing compound [330]. The *in vitro* [264, 265] and *in vivo* [266] studies demonstrated that CS promotes the metabolic activity of cartilage, preventing cartilage from degeneration in osteoarthritis.

Controversy results nevertheless reported in the literature for the application of CS hydrogel for cartilage repair. Many studies provided evidence that CS hydrogel inhibits the secretion of cartilage ECM such as collagen precursors [331]. *In vitro* studies showed that the addition of CS (with concentration of 100 mg/ml) also reduced GAG content in cartilage ECM in long-term culture despite chondrocyte viability [332]. In addition, photo-crosslinkable methacrylate derivative of CS inhibits the synthesis of cartilage ECM compounds [239]. This effect might be due to the presence of negative charge on the CS hydrogel, which attracts free cations within the culture medium. This effect increases the osmolarity within the hydrogel, which has an adverse impact on cell growth within the hydrogel [259].

This issue associated with CS is resolved by using a combination of CS with other hydrogels. For instance, it is found that chondrocyte maintained its phenotype and GAG production was not interfered in the mixture of chitosan with CS [267]. In addition, proteoglycan (related to GAG) production increased in CS-based hydrogel that covalently bonded with collagen type I [268]. Chondrocyte proliferated within this hydrogel and produced proteoglycan. Addition of CS in PEG hydrogel also improved the expression of chondrogenic gene from chondrocytes, enhancing the production of cartilage ECM compared to pure PEG hydrogel [333]. Compared with other biopolymers, CS production cost is high. In addition, its applications may have negative impact on ECM generation for cartilage repair. These data illuminate the limited applications of CS and low potential of using this compound for cartilage repair to date [259].

Hyaluronan (Hyaluronic Acid)

Hyaluronan (hyaluronic acid, HA) is the primary physiological component of the articular cartilage matrix [334]. The physical interaction between the molecule networks of hyaluronan can form extensively long, biodegradable and biocompatible molecules [335]. Theoretically, HA is superior for cartilage repair if it can be implanted in an unmodified form [336]. However, high degradation rate and poor mechanical strength are the major hurdles for its direct application in cartilage repair. The degradation of hyaluronan might lead to chondrolysis under certain conditions [337]. Different approaches, such as esterification [338] and crosslinking [335, 339], have been undertaken to improve its properties. However, these methods showed adverse effect on HA biocompatibility [340].

HA has been used for chondrocyte and stem cell encapsulations to regenerate cartilage. The *in vitro* and *in vivo* studies underlined the feasibility of cell proliferation and synthesis of cartilage ECM in a modified form of HA [341, 342] and as a cell carrier for chondrocytes [343, 344] or bone marrow-derived stem cells [345, 346]. Despite all biological and physiochemical issues associated with hyaluronan, Hyalograft C, a hyaluronic acid-based biomaterial, has been commercialised for cartilage repair, and it is in clinical trial phase.

Alginate

Alginate is a binary copolymer of (1 → 4)-linked β-D-mannuronic acid-*co*-α-L-guluronic acid. It can readily form bonds with different divalent metal ions, including calcium, magnesium and barium. This chemical bonding can be used to form alginate hydrogels for different biomedical applications, such as cartilage repair. Superior biological properties, high cell response and low cost are the main advantages of alginate hydrogels. Alginate is used for different cartilage tissue engineering applications such as preserving chondrocyte phenotype, organisation and turnover and differentiation of adipose-derived adult stem cells and bone marrow-derived stem cells for 3D cell growth [176, 243, 257, 258]. *In vitro* studies showed that chondrocytes, seeded within an alginate hydrogel, synthesised high level of cartilage ECM protein (i.e. collagen type II). The chondrogenesis of cells can be further promoted by the addition of BMP-2 in the structure of alginate hydrogel [347].

The effect of alginate hydrogel on chondrogenesis of chondrocytes has also been studied by comparing the *in vitro* results from 3D growth in alginate with conventional 2D culture in flask [347], which showed higher expression of collagen type II from chondrocytes seeded within alginate hydrogel compared to control normal 2D growth in the presence of IGF-1 and BMP-1 growth factors. Cai et al. showed that bone marrow-derived mesenchymal stem cells can be well distributed within an alginate hydrogel [348]. After 2 weeks of *in vitro* culturing that hydrogel is implanted into nude mice, the encapsulated bone marrow-derived mesenchymal stem cells exhibited continued process of induced chondrogenesis *in vivo*. High

expression of cartilage extracellular matrix proteins (such as collagen type II and aggrecan) confirmed that the alginate-based cartilaginous implants are actively chondrogenic during bone marrow-derived mesenchymal stem cell terminal differentiation.

The main drawbacks in application of alginate for cartilage repair are lack of cell motif sites within its structure and also low and unpredictable degradation behaviour [259]. The former might lead to a low level of chondrogenesis cell adhesion that prevents cell proliferation within the 3D structure. In addition, alginate is negatively charged that inhibits the absorption of proteins to its structure and interferes with the diffusion of biofactors and proteins. Low cell adhesion and protein absorption both might lead to decreasing chondrogenesis cell proliferation within the alginate hydrogels. Previous studies showed that functionalisation of alginate with arginine–glycine–aspartic acid (RGD) sequence enhances the chondrocyte adhesion [349] and thus can address low cell adhesive properties of this biomaterial.

The slow degradation rate of alginate and its unpredictable profile might have adverse effect on the application of this polymer for cartilage repair. Bouhadir et al. addressed this issue by preparing a biodegradable alginate hydrogel using periodate-oxidised alginate. This polymer is crosslinked with calcium ions and the hydrogel degraded within 9 days in PBS solution [350]. In vivo application of this alginate-based hydrogel showed that chondrocyte encapsulated initiated native cartilage formation at the defected site after 7 days of implantation [350]. The most challenging issue in application of alginate for cartilage repair is the extraction of this material from different sources that might have different physicochemical properties, mechanical strengths and degradation rates [259].

14.3.6 Injectable Hydrogels for In Vivo Cartilage Formation

Injectable hydrogels have been used to deliver chondrogenesis cells or drugs to the defected site in a minimally invasive manner to decrease patient morbidity upon the treatment procedure. As shown schematically in Fig. 14.6, a solution that contains a polymer, cells, drug or any combination of these three is injected to the lesion site. The polymeric solution is then crosslinked in situ to form a solid structure at the site. The cells along with the polymeric matrix are surrounded with chondrogenic biological and mechanical signaling that enhances cartilage regeneration. The polymeric matrices are usually degraded gradually, while cartilage ECM is synthesised by chondrogenic cells that are either externally provided or migrated from subchondral regions. Cartilaginous physicochemical environment and delivery of chondrogenic cell/drugs in minimally invasive manner are the main advantages of this technique.

The favourable polymers for injection are those that possess the following characteristics:

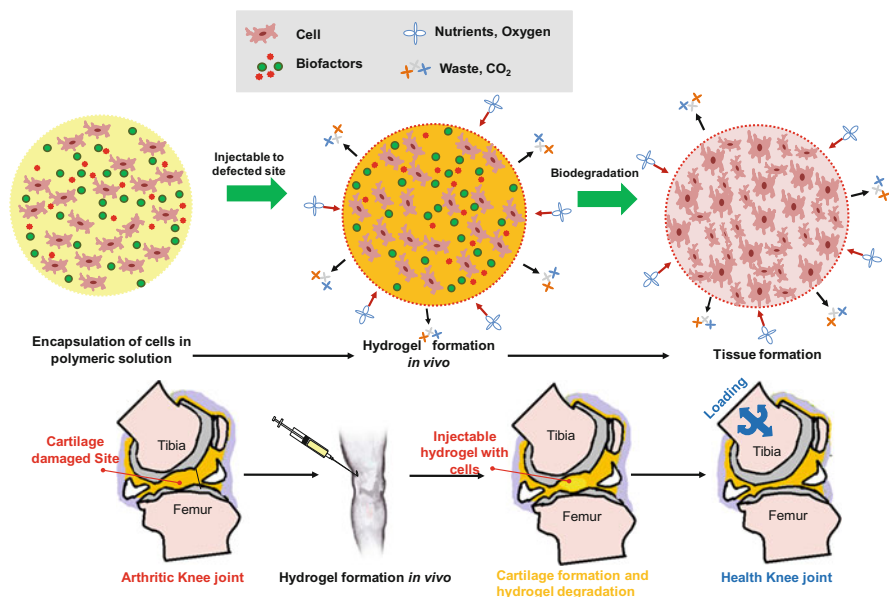


Fig. 14.6 Schematic overview of cartilage tissue engineering, using injectable hydrogels as cell carrier

- Cell adhesive property, biofactor loading capacity and sufficient mechanical strength
- Adjustable gelation properties to facilitate injectability during surgical operation and rapid hydrogel formation in the body to inhibit transfer of formulation to surrounding tissues
- Biocompatibility without toxic chemicals and severe conditions for gelation to promote cell viability

Different strategies have been attempted for in situ gelation such as redox polymerisation, photo-polymerisation, Michael addition, Schiff and enzymatic reactions and physical approaches such as pH induction and thermogelation. The following sections provide an insight into each of these methods.

14.3.6.1 Chemical Reaction

Chemical stimulus induces in situ gelation of polymeric solution by forming chemical changes in the molecular structure of precursors or by formation of covalent bond in polymeric system. The chemical reactions include redox and photo-polymerisation of acrylate-functionalised macromers, Michael addition, Schiff reaction scheme and enzymatic reactions. It is critical to select the conditions that precursors, initiators and catalysts are soluble in aqueous media to develop a biocompatible formulation [351]. A brief summary of injectable chemical stimuli

Table 14.6 Different gelation techniques to crosslink injectable hydrogels for cartilage tissue engineering

Polymer	Gelling strategy	Gelling time	Mechanical/degradation behaviour	Refs.
KGM/collagen-PLA ^a	Redox APS/TEMED	15 min	G' = 0.87–2.15 MPa	[352]
OPF/gelatin ^b	Redox APS/TEMED	8 min	NR	[353]
Chitosan (acrylated) ^a	Redox APS/TEMED	NR	Degrade in 18 days in PBS	[354]
PEG-da/HA ^b	UV photo-crosslink	NR	NR	[355]
PEG-dimethacrylate ^a	UV photo-crosslink	NR	60–590 kPa	[356, 357]
PEG-dimethacrylate/ PDS ^a	UV photo-crosslink	NR	40–70 kPa	[358]
PLA-PEG-PLA/AES ^a	UV photo-crosslink	NR	7 kPa–97 kPa by 6 weeks of culture	[359]
Methacrylated hyaluronic acid ^{ab}	Laser photo-crosslink	NR	5kPa–120 kPa by 6 weeks of culture	[360, 361]
Methacrylated alginate ^a	UV photo-crosslink	NR	NR	[362]
Gelatin-methacrylate ^a	UV photo-crosslink	30 s	0.5 kPa–10 kPa	[363, 364]
Col-PEG with thiolated PEG ^b	Michael addition	30 min	15 kPa–18 kPa	[238]
Chitosan-hyaluronic acid ^c	Schiff reaction	1–4 min	10 kPa–30 kPa	[365]
Hyaluronic acid//H ₂ O ₂ ^a	Enzymatic reaction	10–20 s	0.1 kPa–2 kPa	[366]
Tyramine chitosan/ HRP/H ₂ O ₂ ^a	Enzymatic reaction	NR	1 kPa–5 kPa, 40 % mass loss in 3 weeks	[367]

NR not reported in the reference

^achondrocyte

^bMSC cell growth

^cacellular

systems, used for cartilage tissue engineering, is presented in Table 14.6. This section is focused on the properties, type of cell, gelation and degradation behaviour and mechanical properties of this class of hydrogels for cartilage repair.

Redox Polymerisation and Photo-Crosslinking

Acrylate- or methacrylate-functionalised macromers are crosslinked by free radicals, produced from redox reaction in an aqueous solution. Two systems have been used to initiate these reactions that include ammonium persulphate/N,N,

N,N'-tetramethylethylenediamine (APS/TEMED) or APS/L-ascorbic acid (AA) [352, 368]. APS/TEMED redox initiation system is used to crosslink collagen-coated PLA micro-carriers in hydrogel precursor of konjac glucomannan (KGM) for cartilage repair. The composite collagen-PLA/KGM precursor formed hydrogel at 37 °C in 15 min [352]. In vitro studies showed proliferation of chondrocyte cells on this in situ formed hydrogel, demonstrating the potential of this hydrogel for cartilage repair.

In addition, OPF macromer is crosslinked with redox initiation system to form injectable hydrogels for cartilage regeneration [217, 353]. Park et al. loaded TGF- β 1 growth factor into the structure of OPF hydrogel crosslinked with PEG-da using redox initiation system of APS/TEMED [353]. In their study the biological properties of injectable hydrogel were enhanced by addition of gelatin microspheres that were crosslinked with GA. It is observed that MSCs that are encapsulated within OPF/gelatin maintained viable and synthesised cartilaginous ECM proteins [353]. In another study, injectable OPF/gelatin hydrogel is used for coculture of osteogenic and chondrogenic cells to adjacent subchondral bone condition [217]. In vitro studies showed the synthesis of GAG, collagen type II and aggrecan by encapsulated MSC in OPF/gelatin hydrogel. These data suggested that OPF/gelatin and the developed crosslinking strategy may have potential for cartilage tissue engineering [217, 353].

In addition to synthetic polymers, such as OPF, naturally derived polymers such as chitosan are also crosslinked with redox initiation system. Acrylate-functionalised chitosan hydrogel is crosslinked with redox initiation system of APS/TEMED and used for cartilage repair [354]. Encapsulated chondrocytes within this hydrogel maintained their spherical phenotype. The hydrogel is completely degraded in 8 days, using lysozyme to mimic physiological environment [354].

Redox polymerisation is considered as a biologically benign process. The generation of free radical ions, however, might have negative impact on cells, biofactors and surrounding tissues. The biological consequences of releasing free radicals are a major concern of using this strategy. Further research is required to be conducted to fully understand their effects prior to broad applications in cartilage and other tissue engineering [369].

Different biomaterials are photo-crosslinked under ultraviolet (UV), visible and laser light sources. Photo-initiators are used to release free radicals to initiate the crosslinking. Irgacure 2959 and eosin/triethanolamine are the most widely used photo-initiator in biomedical applications which are FDA approved and commercially available. Both synthetic and naturally derived polymers can be photo-crosslinked to form hydrogel. Synthetic macromers, such as PEG-da, PEG-dimethacrylate/star-shaped poly(dimethylsiloxane) methacrylate, methacrylate end-capped PLA-PEG-PLA, mono-2-(acryloyloxy)-ethyl succinate grafter poly(vinyl alcohol) and OPF/PEG diacrylate, are photo-crosslinked for biomedical applications. In addition, naturally derived copolymers, including methacrylated chondroitin sulphate, methacrylated HA, PLA methacrylated HA, methacrylated

glycol chitosan, heparin methacrylamide, methacrylated alginate and methacrylated alginate, are photo-crosslinked to form in situ injectable hydrogels.

PEG is functionalised with methacrylate groups to form photo-crosslinkable hydrogel, suitable for cartilage tissue engineering. Chondrocyte embedded within the 3D structure of this hydrogel induces chondrogenic ECM production. Mesenchymal stem cell [355] and also embryonic cell [210] are encapsulated in this photo-crosslinkable hydrogel. By using growth factor (β -TGF), cartilage is formed in both of these two studies [210, 355, 370]. A solution of PEG-da and HA with TGF- β 3 and Irgacure 2959 is used to deliver MSC in vivo [355]. After subcutaneous injection, the skin of mice is exposed to UV light. PEG-da macromers are photo-crosslinked, leading to formation of in situ hydrogel. The encapsulated MSC synthesised collagen type II and proteoglycan. This result showed the chondrogenesis properties of PEG-da/HA injectable hydrogel that can be used for cartilage regeneration [355]. PEG-dimethacrylate is also photo-crosslinked by UV radiation [356, 357]. Chondrocyte is encapsulated within this injectable hydrogel, and upon in situ gelation, GAG and collagen type II are produced.

The compressive modulus of this hydrogel is varied in the range of 60–590 kPa by changing the concentration of macromer in injectable precursor [356, 357]. The modulus of hydrogels affects both anabolic and catabolic activity of encapsulated cells [356, 357]. For instance, GAG is synthesised in softer hydrogel fabricated from PEG-dimethacrylate, while in hydrogels with a higher mechanical strength, collagen type II is mainly produced by encapsulated chondrocyte cells. RGD is incorporated into the 3D structures of PEG-dimethacrylate-based hydrogels to enhance cell proliferation. PEG-dimethacrylate and star-shaped poly (dimethylsiloxane) (PDS) methacrylate are crosslinked with acryloyl-PEG-RGD by photo-polymerisation. The compressive modulus of this hydrogel varies in a range of 40–70 kPa, depending on the composition of injectable precursor. Despite favourable biological performance of PEG-based hydrogels, application in cartilage repair is limited due to the lack of biodegradability [358].

Methacrylated end-capped PLA-PEG-PLA can be photo-crosslinked by forming IPN hydrogel with mono-2-(acryloyloxy)-ethyl succinate (AES)-grafted PVA. This IPN hydrogel is fabricated to achieve desirable mechanical, biological and gelation properties for cartilage tissue engineering [359]. This study showed that when chondrocytes are encapsulated in this hydrogel, cartilage ECM is formed within 6-week culture. The entanglement of cartilage ECM within the structure of hydrogel dramatically enhanced the compressive modulus of construct from 7 to 97 kPa [359].

Naturally derived macromer of chondroitin sulphate, functionalised with methacrylate groups, is synthesised to form hydrogel with UV, using Irgacure 2959 as photo-initiator [371]. High cell viability is detected for encapsulated chondrocytes during the in situ gelation. In the presence of suitable enzyme (chondroitinase with concentration of 0.8 mg/ml), the hydrogel is degraded within 24 h, whereas in the absence of this enzyme, the hydrogel retains its structure up to 7 days [371]. IPN hydrogel of methacrylated chondroitin sulphate and PEG-dimethacrylate is also

formed for cartilage regeneration [239]. The compressive modulus of this hydrogel is controlled by changing the concentration of polymers [239].

Methacrylated hyaluronic acid is crosslinked using eosin/triethanolamine as photo-initiator [360]. The crosslinking process is activated using argon laser at 514 nm. Eosin is excited by laser to the triplet state, and then triethanolamine releases an electron to produce the free radical anion of eosin and radical cation of ethanolamine. This free radical cation can polymerise methacrylated HA. Laser beam can reach deep tissue; therefore, it could have more applications for cartilage tissue engineering compared to visible light and UV [360]. In vitro and in vivo study confirmed that chondrocyte maintains its spherical phenotype when encapsulated within this system [360], and chondrogenic proteins, such as collagen type II, are synthesised [361]. In vitro studies showed that in 6 weeks, chondrogenesis is induced in the presence of TGF- β 3 using this hydrogel with encapsulated MSC cells. The formation of cartilage ECM and synthesis of GAG and collagen type II by MSCs resulted in an increased compressive modulus from 5 kPa to 120 kPa [361].

Alginate is functionalised with methacrylate groups to form photo-crosslinkable biopolymer. The effect of concentration of Irgacure 2595, the photo-crosslinker reagent, on the physical properties of this hydrogel is examined, which included swelling behaviour, compressive modulus and degradation behaviour. After 3 weeks, chondrocyte maintained its spherical phenotype [362]. In addition to alginate and hyaluronic acid, gelatin-methacrylate (Gel-ma) that creates hydrogel under UV within 30 s has been attempted for cartilage repair [363]. The compressive modulus of this hydrogel varied from 0.5 to 10 kPa based on the concentration of polymer [364]. Although adverse biological effect has not been observed in using the hydrogel formation strategy, the impact of UV radiation for in situ delivery for non-invasive operation and surrounding tissues is still questionable due to free radical formation [369].

Michael Addition

Michael addition is the 1,4-addition of nucleophiles to α,β -unsaturated ketones or esters (electrophiles) [369]. Amine- and thiol-functionalised macromers are the main nucleophiles, whereas acrylate-, methacrylate- and methacrylamide-functionalised macromers are the main electrophiles in Michael addition. The combination of these two in polymer solution is required for in situ gelation [369]. This reaction scheme is favourable for biomedical applications such as cartilage repair due to its high gelation efficiency in physiological condition without any side products. Different combinations of synthetic and naturally derived polymers are used to form in situ gelled systems for cartilage repair, using Michael addition.

Thiolated hyaluronic acid and PEG vinylsulfone (PEG-VS) macromers are in situ crosslinked within 14 min, using Michael addition scheme. Encapsulated chondrocyte maintained their phenotype after 21 days, while this hydrogel is

degraded within this period. GAG and collagen type II are produced when using these cell-laden hydrogel underlining their high potential for cartilage repair [372]. To accelerate the in situ gelation of hyaluronic acid-based hydrogels, poly(ethylene glycol)-bis-maleimide (PEG-BM) is used. This system exhibited in situ gelation within approximately 1 min through Michael addition scheme.

Heparin-based hydrogels are formed, using thiolated heparin and Michael addition scheme [373]. Thiolated heparin and PEG-da are in situ gelled at physiological condition using Michael addition. This hydrogel promotes the in vitro re-differentiation of encapsulated dedifferentiated rabbit chondrocytes. In vivo studies are conducted by transplanting the hydrogel in the subcutaneous dorsum of mice, which showed the proliferation of chondrocyte in vivo and formation of cartilage without using any biofactors [373].

Semi-interpenetrated network (SIPN) scaffold is also fabricated by incorporating in situ gelled heparin-based precursors (thiolated heparin-PEG-da system) and poly(L-lactide-*co*- ϵ -caprolactone) (PLCSL) scaffold. BMP-2 and chondrocytes are encapsulated within this system and is locally delivered to the defected cartilage site to promote the formation of calcified fibrocartilaginous transition region. This hydrogel enhanced the integrity of regenerated cartilage and secured its attachment to the surrounding tissue [374]. In addition, thiolated gelatin is crosslinked using PEG-da through Michael addition scheme. The gelation time is in between 3 and 5 min depending on the concentration of macromers in the precursor system. Bone marrow-derived MSCs are encapsulated within this hydrogel and exhibited a high level of viability. This system has been used for different cartilage regeneration applications [375]. More complicated systems are designed by conjugation of synthetic and naturally derived copolymers to closely tune the gelation, degradation and mechanical properties of this group of hydrogels.

Collagen-mimetic peptide (Col-P), which contains a GFOGER sequence (responsible to maintain chondrocyte phenotype), is conjugated with poly(ethylene glycol) tetraacrylate to form Col-P-*co*-PEG macromer. This macromer could form gel in 30 min upon mixing with thiolated PEG in physiological environment (37 °C and 7.4 pH) [238]. The encapsulated MSCs showed a higher degree of chondrogenesis compared with the thiolated PEG hydrogel without the addition of peptide sequence (no conjugation of Col-P). The compressive modulus of hydrogels is tuned from 15 to 18 kPa by changing the concentration of macromers within the precursor solution. The softer gel induced a higher degree of chondrogenesis differentiation of MSCs compared to the stiffer gel [238], due to a lower mass transfer rate in the latter system.

Schiff Reaction

Schiff-based reaction schemes are based on the chemical reactions between an amine and aldehyde groups. It is one of the promising schemes in the formation of in situ gelled hydrogels due to high yield in physiological condition [365]. *N*-Succinyl-chitosan and aldehyde hyaluronic acid macromers are synthesised and

chemically conjugated to form an injectable precursor. The in situ gelation time of this system in physiological environment varied from 1 to 4 min [365]. The crosslinking density within the macromers affects the mechanical properties within 10 kPa to 30 kPa, and the degradation time varies between 1 and 30 days. In vitro studies showed that the encapsulated chondrocytes retained their phenotype, when encapsulated in this hydrogel [365]. Most of the injectable hydrogels, formed with this reaction scheme, suffered from low mechanical properties. This class of hydrogels, therefore, is not widely used for cartilage tissue engineering.

Enzymatic Reaction

Enzymes can form new bonds or can cleave specific bonds in a polymer to induce gelation. Due to the specificity of enzymatic reactions, the other chemical moieties in polymers are not interfered. Therefore, enzymatic gelation is a rational platform with low risk of side products. Enzymes such as horseradish peroxidase (HRP) [376], phosphatase [377], tyrosinase [378], thermolysin [379], α -galactosidase [380] and esterase [381] have been used to prepare hydrogels through enzymatic reactions. The gelation occurred by crosslinking polymer networks or by decreasing the solubility of polymer in aqueous solution².

HRP is the most widely used enzyme for the preparation of hydrogel for cartilage tissue regeneration. Tyramine-*co*-hyaluronic acid (THA) macromer is synthesised which undergoes instant gelation in the presence of HRP. For in vivo studies, THA is dissolved in H₂O₂ and subcutaneously injected into rats, followed by separate injection of HRP [366]. This polymer instantly formed hydrogel after the addition of HRP. The gelation time and the mechanical strength of the resulted hydrogel are controlled by changing the concentration of HRP. The gelation time is less than 10 s when HRP concentration is from 1.3 to 2.2 unit/ml. This hydrogel exhibited compressive modulus of 0.1–2 kPa [366].

Chitosan is also functionalised with tyramine groups [367], which are crosslinked with HRP/H₂O₂ system to form hydrogel. The compressive modulus of this hydrogel varies in the range of 1–5 kPa by changing the concentration of functionalised chitosan from 1 to 2 wt%. In the presence of lysozyme, chitosan hydrogel is rapidly degraded and loses 60% of its weight after 3 weeks. The chondrocyte viability in this hydrogel is high and their phenotype is maintained after 2 weeks of encapsulation [367].

Enzymes are involved in the gelation process. After the formation of gels, the enzymes act as impurities that might have biological impact on encapsulated cells and also the host tissue. Additionally, the denaturation of an enzyme in the body may induce immunogenicity. Due to these reasons, the application of this group of in situ gelled precursors for cartilage tissue engineering is limited [369].

²Hydrogel is formed through condensation process upon decrease of solubility of polymer in aqueous solution.

14.3.6.2 Physically Induced Gelation

Hydrogel can be formed via physical stimulation of polymers to create interaction between molecules. Thermo- and pH-responsive stimulators are the most common approach for the fabrication of hydrogels. In physical stimuli, intermolecular interactions such as van der Waals, hydrogen and covalent bonding result in phase transition behaviour. Physically induced gelation scheme, therefore, provides a mild condition for delivery of chondrogenesis cells to the defected site, which might exhibit low cytotoxicity and enhance cell viability and regenerate cartilage at the defected site. This section provides an overview for different types of physically induced gelation systems (pH and thermoresponsive) that have been attempted for cartilage repair.

pH-Induced Gelation

Changes in pH can induce in situ gelation of polymers. Different synthetic and naturally derived polymers can be functionalised with carboxylic acid-derived monomers, such as methacrylic acid (MAA [382, 383] and AA [384–386]), to synthesise copolymers that can undergo gelation by variation of pH [387]. The functionalised polymer with MAA and AA exhibited pKa value of approximately 5 and 4.8, respectively [387]. It is, therefore, feasible to incorporate the cells into the solution, when the pH is below the pKa. The hydrogel is formed by increasing the pH above this value. However, cells and growth factors tolerate physiological pH (6–7.5) and cannot maintain viable out of this range for a long period. Care must be taken in using pH-sensitive hydrogels to ensure having less impact on cell viability. For this reason, pH-sensitive hydrogels have not been used broadly for tissue engineering of cartilage.

Thermogelation

Temperature variation has an impact on the molecular conformation of thermoresponsive polymers. Two types of these polymers are identified, (i) lower critical solution temperature (LCST) and (ii) upper critical solution temperature (UCST), shown schematically in Fig. 14.7. In the former, the polymer maintains miscible only at any temperature below the LCST. In the latter, however, the opposite phenomenon occurs, in which the polymer is only miscible above the UCST. Thermogelation is a promising and clean approach for hydrogel formation and development of an injectable formulation due to the absence of any chemical, reagent and enzyme that might exhibit an adverse effect on cell viability and performance. Table 14.7 summarises different thermoresponsive injectable hydrogels that are synthesised for cartilage regeneration. These injectable systems are discussed more in depth in this section.

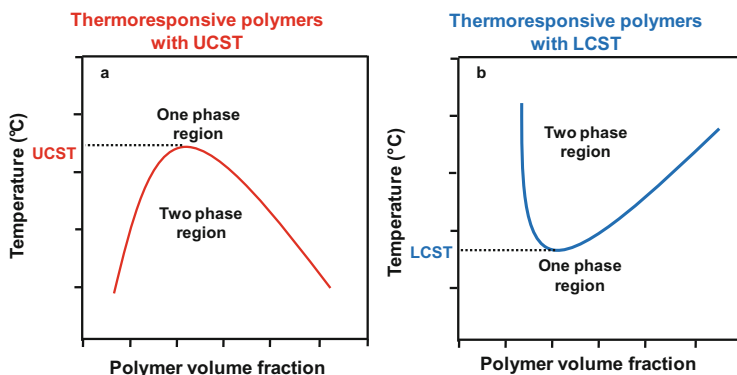


Fig. 14.7 Schematic illustration of phase transition behaviour for thermosensitive polymers with upper critical solution temperature (UCST) (a) and lower critical solution temperature (LCST) (b)

The polymers that possess LCST below the body fluid are favourable for tissue engineering. In this case, the biofactors and cells are incorporated into the solution at low temperature with low risk of denaturation and minimal impact on cell viability. Poly(*N*-isopropylacrylamide) (PNIPAAm), Pluronic®, elastin-like polypeptides (ELPs), chitosan-derived polymers, functionalised hyaluronic acid and heparin are the main synthetic and naturally derived polymers used to form thermoresponsive precursor for cartilage tissue engineering.

The LCST of PNIPAAm (32 °C) is close to physiological temperature (37 °C), and it can be readily tuned by adding hydrophilic and hydrophobic side chains to its molecular structure. PNIPAAm is a biocompatible polymer with very high rate of phase transition behaviour. Therefore, PNIPAAm is the most commonly used thermoresponsive polymer for tissue engineering applications. PNIPAAm-based copolymers form gel through coil-to-globe phase transition process [403]. Hydrogel formations are initiated by increasing the temperature above the LCST of copolymer [404]. For fabrication of biodegradable PNIPAAm-based hydrogels, it is critical to conjugate hydrophilic moieties, such as acrylic acid or PEG, and a hydrophobic segment to PNIPAAm-based macromers [387, 388]. The mechanical properties of PNIPAAm-based copolymers are increased by conjugating hydrophobic moieties such as *n*-alkyl acrylate and poly(lactide) macromers [387]. The incorporation of hydrophobic macromer resulted in increasing compressive modulus [387].

Yun et al. synthesised more biocompatible PNIPAAm-based copolymer by the incorporation of acrylic acid (AAc) segments to PNIPAAm molecule to form P(NIPAAm-*co*-AAc). TGF- β 3 growth factor is encapsulated within this hydrogel to promote cartilage formation. In vitro cell study showed that chondrocytes retained their phenotype after 8 weeks. A solution of precursor, chondrocyte and TGF- β 3 growth factor is injected subcutaneously into nude mice and formed gel at the injected location. After 8 weeks, the regenerated cartilage acquired normal histological and physiochemical properties [389].

Table 14.7 Different thermoresponsive hydrogels for cartilage regeneration

Polymer precursor	Gelling temperature	Degradation behaviour	Mechanical properties	Refs.
P(NIPAAm- <i>co</i> -propylacrylic acid) ^a	37 °C	NR	1 kPa (Comp Mod)	[387, 388]
P(NIPAAm-propylacrylic acid-butyl acrylate) ^a	>37 °C	NR	2 kPa (Comp Mod)	[387, 388]
P(NIPAAm- <i>co</i> -acrylic acid) ⁺	~37 °C	Retain for 8 weeks	NR	[389]
P(NIPAAm-PLDLA-dextran) ⁺	32 °C	Retain for 4 weeks	NR	[390]
PNIPAAm-g-methylcellulose ⁺	~32 °C	Retain for 4 weeks	NR	[391, 392]
DNA-modified ELP ⁺	~35 °C	NR	G ^d = 80 pa	[287, 393]
P(NIPAAm-AAc-NAS-HEMAPLA) ^b	18 °C–26 °C	85 wt% in 21 days	~0.5 MPa (Tensile Mod)	[394]
Chitosan/GP ⁺	37 °C	Retain in 3 weeks	NR	[395, 396]
Chitosan/GP/starch ⁺	37 ± 2 °C	67 % loss in 56 days	NR	[183]
Chitosan/PPO-PEO ⁺	25 °C	Retained in 28 days	NR	[397]
Chitosan/PNIPAAm ^d	<37 °C	NR	NR	[398]
Chitosan/PNIPAAm/HA ⁺	30 °C	NR	NR	[399]
PEO-PPO-PEO ⁺	37 °C	Fast dissolution rate	Very weak	[400–402]

NR not reported in the study

^aAcellular matrix

^bchondrocyte

^csmooth muscle cells

^dMSCs

A porous structure of poly(NIPAAm)-based hydrogel is formed by the incorporation of PLDLA and dextran (conjugation via chemical bonding) to form a copolymer with LCST at 32 °C. The chondrogenic ECM protein, such as collagen type II, is formed after 4 weeks of encapsulation of chondrocyte within this hydrogel. To assess the phenotype of chondrocyte after culturing within this hydrogel, they are detached from the surface by decreasing the temperature from 37 °C to below 32 °C (LCST of hydrogel). The detached chondrocyte exhibited a round shape which confirmed that its phenotype is maintained during this period.

Poly(NIPAAm)-g-methylcellulose copolymer is also synthesised to form hydrogel at 32 °C [391, 392]. ATDC5, a chondrogenic cell line, is encapsulated in this hydrogel to assess its chondrogenesis properties. The in vitro studies confirmed the high potential of this injectable hydrogel for cartilage tissue engineering due to the low degree of cytotoxicity and high cell proliferation within this hydrogel [391, 392].

Another thermoresponsive hydrogel is produced by the conjugation of chitosan with PNIPAAm. This copolymer is water soluble with the LCST less than 37 °C [398]. MSCs are mixed with this copolymer solution and injected for assessing the application of hydrogel for cartilage tissue engineering. The hydrogel is formed in the body temperature and promising results were acquired; chondrocytic markers were produced including GAGs and collagen type II at the injected site [398].

HA is also conjugated with PNIPAAm to form thermoresponsive poly (NIPAAm-co-HA) hydrogel. Preliminary studies on this hydrogel showed continuous and sustained release of fluorescein isothiocyanate (FITC)-labelled bovine serum albumin up to 60 h by *in vivo* subcutaneous injection on the dorsal surface of rabbit. These data demonstrated the potential of thermosensitive hydrogel for cartilage tissue engineering [405].

Chitosan/PNIPAAm copolymer is grafted with hyaluronic acid (HA) to further mimic the properties of natural cartilage ECM. Chitosan/PNIPAAm/HA hydrogel formed injectable hydrogel above 5 wt% at 30 °C. *In vitro* cell study with this hydrogel showed that chondrocyte maintains its morphology and posed a high degree of proliferation and differentiation [399].

These studies underlined that most of PNIPAAm copolymers conjugated with natural or synthetic polymers are suitable for chondrogenesis cells to produce cartilage ECM. They might be favourable systems for developing an injectable formulation; however, it is still in its infancy, and further research is required to select a polymer with desirable injection properties, stability, degradation rate and mechanical strength for regenerating cartilage.

Synthetic and naturally derived polymers, such as block copolymers of ethylene oxide (PEO) and propylene oxide (PPO), elastin-like polypeptides (ELPs) and chitosan with thermoresponsive properties, were used to form injectable hydrogels for cartilage tissue engineering. Block copolymer of silk and elastin peptide sequence (SELP) were used as acellular therapy for cartilage tissue repair in a rabbit model of an osteochondral defect [406, 407]. In this study SELP was injected into the osteochondral defect site on the femoral condyles of rabbit knee and crosslinked *in vivo* [407]. SELP hydrogels were also used for cartilage tissue engineering, using mesenchymal stem cell (MSC). Molecular structure of SELP copolymer is changed to achieve a thermosensitive copolymer, named SELP-47 K. This copolymer undergoes gelation at 37 °C. MSCs are encapsulated within SELP-47 K hydrogel in the presence and absence of chondrogenic TGF- β 3 growth factor. After 28 days, cartilaginous matrix components (sGAG and collagen type II) are formed by MSC encapsulated in SEL-47 K hydrogel in both cases (in the presence and absence of TGF- β 3) [393]. This result showed that ELP can act as an engineered bioactive molecule to stimulate chondrogenesis pathway in MSC.

A thermosensitive chitosan-based hydrogel was fabricated, using β -glycerol phosphate disodium salt (GP) as sol-gel initiator at physiological pH and temperature [395]. GP showed an osteogenic effect when added to bone marrow stromal cells. *In vitro* study of chitosan/GP hydrogel showed its capability to deliver an osteogenic mixture of β -transforming growth factor (β -TGF) and encapsulated chondrocyte over 3 weeks [396]. The use of chitosan as a cationic polysaccharide

in this mixture led to the adhesion of hydrogel to tissue surface which normally bear net anionic characteristic. In addition, chitosan/GP mixed with chondrocyte is used as cytocompatible space filler [408]. BioSyntech Inc. (Laval, Quebec, Canada) developed the thermoresponsive (chitosan/GP) solution, which is in clinical trial for cartilage tissue engineering [409].

The properties of chitosan/GP hydrogel were further improved by the incorporation of starch to the thermoresponsive mixture [183]. The injectable chitosan/GP/starch mixture had a gelation temperature of 37 ± 2 °C. The hydrogel also exhibited microporous structure with 67 % of degradation within 56 days in PBS solution containing 0.02 mg/ml of lysozyme. Chondrocyte remained its phenotype after 14 days of culturing within this hydrogel [183].

In addition, injectable chitosan-based hydrogel was developed by fabricating interpenetrating polymeric network of chitosan with other natural polymers such as alginate and hyaluronate, hyaluronic acid and heparin, which enhanced the production of collagen type II and increased the rate of cellular proliferation after 2 weeks of cell growth [410, 411]. Combining chitosan with other biomaterials, however, does not necessarily result in favourable effects. For example, the combination of chitosan with chondroitin sulphate and dermatan sulphates showed adverse effect on production of collagen type II and morphology of chondrocyte cells [412].

Alternatively, chitosan-based thermosensitive hydrogel is prepared by graft copolymerisation with Pluronic® (block copolymer based on ethylene oxide and propylene oxide) (PPO–PEO). This thermosensitive hydrogel (chitosan/PPO–PEO) is used for cartilage tissue engineering and had sol–gel transition temperature of 25 °C. Chondrocyte proliferation and GAG production are significantly increased after 28 days by using chitosan/PPO–PEO in situ gelled precursor [397].

Copolymer of hyaluronic acid conjugated with heparin and Pluronic® (block copolymer based on ethylene oxide and propylene oxide) (PPO–PEO) is synthesised to form in situ gelled at 37 °C in less than 10 min. TGF- β 3 is successfully loaded within the structure of hydrogel and continuously released from hydrogel for 20 days. This resulted in formation of cartilage ECM at full-thickness cartilage defect of rabbit knee [413].

HA is also conjugated with PNIPAAm to form thermosensitive hydrogel p (NIPAAm-co-HA). Preliminary studies on this hydrogel showed continuous and sustained release of FITC-labelled bovine serum albumin up to 60 h by in vivo subcutaneous injection on the dorsal surface of rabbit. This demonstrated the potential of this thermosensitive hydrogel for cartilage tissue engineering [405].

Therapeutic agents such cartilaginous bioactive compounds as BMP-2 were also delivered to the cartilage lesion site with a HA-based injectable hydrogels to control the release of bioactive compounds [414]. These HA-based hydrogels are conjugated with a heparin sulphate proteoglycan and are used to deliver BMP-2. The controlled and slow release of BMP-2 and the presence of proteoglycan within the structure of this hydrogel had an anabolic influence on articular cartilage in an osteoarthritis model. The synthesis of proteoglycans and other cartilaginous ECMs is stimulated upon the injection of this hydrogel at the lesion site [414].

14.3.7 Products Approached Clinical Trial for Cartilage Repair

Current cell-based therapies for cartilage repair fall into three categories: (1) cell or tissue implementation [415–418], (2) cartilage or bone grafts [419, 420] and (3) bone marrow stimulation through either abrasion, arthroplasty, Pridie drilling or microfracture [96, 421, 422]. Promising clinical results have been reported for most of these treatments [327]. Based on the preferred treatment by the surgeon, different classes of biomaterials can be selected. The major available products for cartilage repair are BST-CarGel (e.g. filler in bone marrow stimulation) and Hyalograft C, CaReS, TruFit, NeoCart, Pluronic and PEG-da-based injectable hydrogel. A brief summary of these treatments is provided in Table 14.8. This section aims to provide insight about the properties, type of cell and results of animal and clinical studies.

14.3.7.1 BST-CarGel

BST-CarGel is developed to stabilise blood clot at the defected site by dispersing biological adhesive solution at the wound site. This technique involves the use of an aqueous solution of chitosan in glycerol phosphate buffer at pH 7 [396]. Intrinsic biocompatible and biodegradable properties of components and neutral pH of this solution make it biocompatible, biodegradable and adhesive to native tissue. In surgical applications, BST-CarGel is mixed with blood with a ratio of 1:3 to generate normal clot with reinforced properties and impede clot retraction. BST-CarGel is injected (normally with 18-G needle) at the lesion site in liquid form and solidifies in 10 min [423, 424]. The cationic nature of chitosan increases the adhesive property of the mixture to cartilage lesion and thus ensures longer clot residency at the cartilage defected site. This method provides critical blood components, red cells and nutrients above the bone marrow wound site (holes or microfracture) to ensure initiation and activation of tissue regeneration and repair [327].

Animal studies have been conducted using BST-CarGel [424, 440, 441]. Skeletally mature rabbit (8–15 months old) are used to assess the characteristics of regenerated cartilage after implementation of BST-CarGel. It is observed that BST-CarGel stimulates the proliferation of stromal cells through the gel towards the lesion site. Vascularisation within the subchondral bone is also significantly increased which indicates positive impact for cartilage regeneration. The BST-CarGel, which is mainly chitosan, is degraded via neutrophil phagocytosis after approximately 1 month [440].

In another animal study, 3–6-year-old sheep models are used, in which BST-CarGel is injected in a surgically prepared 1-cm² condylar and trochlear defects. The cartilage regeneration in this defected side is compared with a negative control (microfracture only without any filler) after 6 months of implantation. It is

Table 14.8 General information of commercial scaffolds/hydrogels for cartilage tissue engineering applications

Commercial product	Application/method of delivery	Mechanical/gelling properties	Rehabilitation program	Opinion	Ref.
Chitosan (BST-CarGel)	Blood clot formation, 10 s of mixing and then injection with 18-G needle	Solidifies in 10 min	The knee is immobilised for 24 h with soft braces. Soft braces are recommended for the first 2 weeks. The joint is non-load bearing for at least 6 weeks post surgery by using crutches. It is possible to have a full load bearing in 9–11 weeks after the surgery. The patients are not allowed to participate in any intense sport activity within the first year after the surgery	Safe, no unpredicted effect based on blood analysis and physical examination and better level of pain, stiffness and function based on WOMAC questionnaires	[327, 328, 396, 423, 424]
Benzoic acid of hyaluronic acid (Hyalograft C)	Full articular cartilage replacement, arthroscopic and mini-arthrotomy implantation	Degrades in 4 months, insoluble in water	Immobilised for 24 h after surgery with braces and non-load bearing for 4 weeks. Gradually proceed to full load bearing within 10–12 weeks. No intense sport activity at least in the first year of surgery	It can provide excellent outcome for the active and young only	[342, 425–430]
Collagen type I (CaReS)	Full articular cartilage replacement, open surgical process to fill the cartilage defect site	Not reported	Knee joint immobilises for 48 h (<10° of flexion). From the third day after surgery, knee flexion is limited to 30° for 21 days and thereafter to 60° for another 21 days Bicycle training after 6 weeks from surgery and muscle enhancement training after	IKDC score in all patients significantly increased; pain significantly is decreased. Surgeons rated 61% of the outcomes as very good	[1165], [431, 432]]

<p>PLGA/calcium sulphate (TruFit)</p>	<p>The defected site is drilled, and the plugs are inserted at the defected site to promote cancellous bone and cartilage formation</p>	<p>Degradation in 9 months</p>	<p>12 weeks. No intense sport or physical activity for 1 year No braces are used as support, 0–60 ° of passive flexion, for the first 4 weeks after operation, partial load bearing, between 4 and 6 complete range of movement and cycling and swimming to strengthen the joint</p>	<p>80 % improvement in KOOS score after 12 months; after this time, the patients' conditions are worsening because of pain and joint functionality. Repeated operation is required in 70 % of cases after 18 months</p>	<p>[73, 389, 433–437]</p>
<p>Collagen type I (NeoCart)</p>	<p>Full articular cartilage replacement, open surgical process to fill the cartilage defected site</p>	<p>Not very robust, might damage before implantation</p>	<p>For approximately 10 days, the joint is immobilised; for 6 weeks after surgery, non-load bearing on the surgical knee; for 12 weeks muscle enhancement training. Within the first year after surgery, no intense sport physical activity</p>	<p>Improvement based on VAS scale and level of pain, approximately 85 % success rate in increasing knee function</p>	<p>[438, 439]</p>

Therapeutic strategies include (1) cell or tissue implementation, (2) cartilage or bone grafts and (3) bone marrow stimulation

observed that there is a high level of adhesion between the BST-CarGel/blood clot, bone and cartilage. The volume and quality of hyaline cartilage regenerated at the defected site are also increased. In addition, relatively mature articular cartilage is observed in the sheep model [424, 441].

Depending on the size and the location of the lesion, there are two approaches that surgeons can use to implant BST-CarGel: (1) mini-open and (2) arthroscopic approaches [327] in clinical applications. In the former a mini-arthrotomy is used to facilitate visualisation of the lesion and delivery of BST-CarGel. Arthroscopic method is feasible only when the entire lesion site is within arthroscopic field of view. It is critical to deliver the mixture of BST-CarGel and blood over individual bone marrow stimulation channels (holes or microfractures) and then over the remaining lesion. In most of the cases, therefore, incision is required to implant BST-CarGel at the exact lesion site.

In 2003–2004 Health Canada's Special Access Program for medical device assessed the BST-CarGel for cartilage repair in human cases. In this study, 33 patients (22 males and 11 females) are treated with BST-CarGel. The treatment is carried out on a case-by-case basis, and it is not legally contemplated as a clinical trial due to the absence of negative control. The outcomes of this study are not reliable as there is no control on the examination of patients and lesion [327]. For example, the size of the lesion ranged from 0.5 cm² to 12 cm²; BST-CarGel is delivered for 22 patients by arthroscopy and for 11 patients by mini-arthrotomy. Nevertheless, the treated patients suffered from both traumatic and degenerative lesions.

It is concluded that BST-CarGel treatment is safe as no complication is observed from physical examination of 33 patients and their blood tests. The Western Ontario and McMaster (WOMAC) Universities Osteoarthritis Index [328] questionnaires are administrated preoperatively and postoperatively after 3, 6 and 12 months. After 12 months postoperatively, pain, stiffness and function index value (based on WOMAC questionnaires) are significantly decreased underlining clinical benefit of using BST-CarGel [327].

The lesion grade (depth), location, size and status of the opposing chondral surface are factors that play a critical role in selecting BST-CarGel for cartilage repair. BST-CarGel has not yet been approved for sale in any country, and further investigations and clinical trials are still required.

14.3.7.2 Hyalograft C

Hyaluronic acid (HA)-based scaffolds such as Hyaff 11 have been used for cartilage tissue engineering applications. Hyaff 11 is made of linear derivative of HA modified by complete esterification of the carboxyl functions of glucuronic acid with benzyl group [338]. HA-containing scaffolds are biocompatible and support cell–cell interaction, cluster formation and extracellular matrix production for cartilage tissue engineering [442]. Hyaff 11 is a 3D fibrous scaffold that is

fabricated from 20- μm thick fibres that are insoluble in water [338, 443]. This scaffold undergoes a hydrolysis process, releasing benzyl alcohol and hyaluronan [427].

Hyalograft C is a tissue engineering graft, comprised of autologous chondrocyte, grown on Hyaff 11 scaffolds. This product was attempted for treatment of knee cartilage defects caused by either trauma or osteochondritis diseases in 1999 [429, 444]. In most cases arthroscopic techniques have been used for implantation of Hyalograft C due to the easy handling properties of Hyaff 11 [445]. Hyalograft C has been approved by the Food and Drug Administration (FDA) and is successfully used for the treatment of different articular cartilage defects in more than 3600 patients [428–430].

Several clinical studies are conducted to assess the therapeutic effect of Hyalograft C for articular cartilage treatment [425, 429, 444]. In one clinical study, 53 patients (31 males and 22 females) with mean age of 32 ± 12 years are contemplated for the treatment with Hyalograft C. The average size of cartilage defect is $4.4 \pm 1.9 \text{ cm}^2$ in these patients who are examined for 7 years. Based on the cartilage lesion site, either arthroscopic or mini-arthrotomy (medial or lateral parapatellar arthrotomy) techniques have been used to access the lesion site of patients. The procedure for the preparation of implant involves several steps. For enzymatic isolation of autologous chondrocytes, articular cartilage is harvested from non-weight-bearing area of the knee joint. The chondrocytes are expanded on conventional monolayer cell culture flasks for 2 weeks and then seeded on Hyaff 11 and cultured for another 2 weeks *in vitro*. Before the implantation of construct, the lesion site is debrided, and cartilage defect site is prepared by complete excision of all nonviable tissues [446]. The defected cartilage site is cleaned to the depth of 2 mm to avoid disrupting the subchondral plate. Subsequently, the knee joint is drained of fluid to assist graft delivery and visualisation. Afterwards, the implant with the required size and shape is delivered either with arthroscopic or mini-arthrotomy implantation. In most of the cases, except for patellar and selected trochlear lesions, there is no need for open surgery, and the Hyalograft C implant can be delivered with arthroscopy [425, 428]. Due to the intrinsic adhesive properties of Hyaff 11, there is no need to use additional fixation devices such as tissue glues. This approach eradicates the use of inorganic chemicals in implantation, which promotes the biocompatibility of implants [425]. Hyalograft C provides required support for *in vivo* cartilage growth during the rehabilitation procedure, and it is completely dissolved and degraded after 4 months post implantation [426].

Based on different clinical tests, Hyalograft C autograft can provide excellent outcome for the repair of deep articular cartilage defects for young and active patients who suffered from singular defects, with good knee alignment and stable joint [444, 447–449]. The effect for other patients is questionable, and it appears that the patients with secondary indications may require further surgeries due to the continuation of pain and swelling after 6-month to 5-year implantation of Hyalograft C [444]. Therefore, further follow-up studies are required to determine the long-term effect of cartilage defect treatment with Hyalograft C.

14.3.7.3 CaReS

Cartilage Regeneration System (CaReS) is a collagen type I hydrogel, prepared from rat tail tendon [432]. In this process, chondrocytes are isolated from the autologous cartilage biopsy specimen. Subsequently, the isolated cells are suspended in a double-buffered 4-(2-hydroxyethyl)-1-piperazineethanesulfonic acid (HEPES)³ solution and gently mixed with type I collagen with the volume ratio of 1:1 (HEPES to collagen). The final mixture (chondrocyte and collagen type I) is then allowed to form hydrogel when they are incubated at 37 °C. Generally, the cell-seeded implants are cultured in autologous serum for a period of 10–13 days [431]. Quality control analysis is conducted to determine cell viability of higher than 80 % and expression of collagen type II for ensuring chondrogenesis from the seeded cells [431, 432].

The therapeutic effect of clinical treatment with CaReS is studied from 2003 to 2008 on 116 patients (67 males and 49 females) with average age of 32.5 ± 8.9 years. The patients suffered from cartilage defects as the result of either trauma degeneration (84 patients) or osteochondritis dissecans (32 patients) with an average defected size of 5.37 ± 2.7 cm² (35 patients with lesion size less than 4 cm² and 81 above this value) [431]. Chondral defect site is at femoral condyle, patella/trochlea or tibial plateau sites.

Depending on the cartilage defected site, medial or lateral parapatellar arthrotomy has been used to access the lesion site [431]. The defected cartilage site is debrided down to the subchondral bone. The base of the cartilage defect site is then coated with fibrin glue. After which the CaReS implants (with 1-mm wider diameter than the defected site) are push-fitted into the trimmed chondral defected site. Generally, a hydrogel is fabricated with twice the height of the defected cartilage. It is then fitted into the defected site by squeezing the hydrogels and removing 50 % of its water content.

The functional outcomes of the treatment procedure with CaReS are evaluated using the International Cartilage Repair Society (ICRS) and the International Knee Documentation Committee (IKDC) scales. ICRS is a four-level scale, used to categorise functionality and status of cartilage and pain level, while IKDC is a subjective knee assessment questionnaire. At mean follow-up time (30.2 months), IKDC score is significantly ($p < 0.001$) improved compared to preoperative condition (from 42.2 ± 13.8 to 70.5 ± 18.7). The pain level is also significantly decreased ($p < 0.001$) from 6.7 ± 2.2 to 3.2 ± 3.1 from preoperative condition to latest follow-up time. The IKDC results and pain comprehensive reduction level in patients demonstrated the benefit of CaReS for the treatments of traumatic or degenerative articular cartilage defects. During the surgery and in particular the debridement of the subchondral bone, bone marrow space is opened, which provides access for chondroprogenitor cells to CaReS hydrogel (culture with autologous chondrocyte). Therefore, cells can migrate to the defected site and produce

³HEPES is a buffer solution, widely used in vitro cell culturing to maintain neutral pH in media.

cartilage extracellular matrix. It is suggested that autologous chondrocytes cultured on CaReS hydrogel are not the exclusive cell source for cartilage formation [431].

14.3.7.4 TruFit

TruFit bone (or cartilage) substitute plugs (Smith & Nephew, Andover, MA) are cylindrical-shaped scaffolds comprised of PLGA and calcium sulphate that are mechanically stable [433]. These scaffolds are commercially available with different diameters (7, 9 and 11 mm) [434] and are clinically used to promote cartilage and bone regeneration to restore osteochondral defects [435]. The scaffolds are designed to degrade within a year after implantation (approximately 9 months) [73]. They are used for back filling femoral donor site during mosaicplasty or for primary repair of full-thickness articular cartilage of the femoral condyle lesions [436]. During the operation, the defected sites are drilled and the plugs (TruFit scaffolds) inserted into the drilled site. TruFit scaffolds promote cancellous bone formation due to the presence of osteoinductive calcium sulphate components in its structure with regeneration of fibrocartilage on the surface [450]. It is claimed that this material promotes the regeneration of articular cartilage in full-thickness chondral defect by supporting chondrogenesis cell migration from the surrounding tissue to the defected site [433]. Different in vitro animal and human studies support the positive impact of using TruFit plugs for cartilage regeneration.

TruFit implants can be bioabsorbed in vivo within 1 year after implantation to create space for further regeneration of cartilage ECM [73]. A mini-open surgery at the defected site is performed to deliver the implant TruFit plugs to the osteochondral lesion site. The defected site is then shaved, and the edges of the damaged cartilage are trimmed back to stable healthy location. The scaffolds are then inserted into the defected site to promote osteochondral tissue regeneration [433]. Single or multiple holes (based on the decision made by the surgeon to use single plug or multiple plugs) are drilled with the depth from 8 to 12 mm [437]. It is critical that the diameter of drilled holes and plugs is matched with the size of the lesion site. The plug is then filled with implant and surface of implant is adjusted with healthy cartilage. It is reported that this tamping process might deform the implant; therefore, a bridge distance of 1–2 mm is contemplated while using multiple plugs [437]. It is important that the edges of implants are in direct contact with the surrounding chondral surface to induce normal cartilage regeneration. This strategy enables natural migration of chondrogenesis cells to the site and thereafter regeneration of articular cartilage [437].

The functional outcome of treatment with TruFit is assessed with clinical outcome score (KOOS). The study is conducted on 10 patients (15–50 years old) with 20 % grade III and 80 % grade IV cartilage defect and an average lesion size of 2.65 cm². After 1 year, 80 % of patients (8 out of 10) had improvement based on clinical outcome score (KOOS). The clinical outcomes of the operation for the other two patients are poor according to the implemented clinical outcome score. Subsequent monitoring (in 18 months and 24 months) revealed that the clinical

outcome score of patients is reduced significantly. Pain and inflammation are increased in patients and joint functionality is significantly decreased. The implants are removed from 7 patients (7 out of 8). Histological analysis showed the formation of hyaline cartilage on the implants, but a bony cyst is also formed within the regenerated cartilage rather than bony restoration [437].

In a recent clinical study, 15 patients with almost similar lesion grade and an average size of 2 cm² are treated with TruFit plugs. After 1 year, same as the previous clinical study, 80 % of patients are improved. Three patients out of 15 have undergone reoperation in less than 1 year. The study is undergoing to evaluate the efficacy of TruFit in the long term [450].

14.3.7.5 NeoCart

NeoCart implant (Histogenics Corporation, Waltham, Massachusetts) is a 3D biodegradable bovine collagen type I scaffold. For cartilage tissue engineering application, NeoCart is seeded with autologous chondrocytes followed by in vitro cultured in bioreactor to promote cartilage regeneration. The resulting product is a chondrogenic active implant, which is rich in proteoglycan and glycosaminoglycan compounds. Preclinical trials and in vitro studies demonstrated that NeoCart implantation at lesion site leads to hyaline cartilage repair at full-thickness defect sites. It is proposed that NeoCart can be used for the treatment of full-thickness (grade III) cartilage lesion of femoral condyle. The treatment process comprised of five main steps, namely, biopsy, cell isolation, cell expansion, 3D culture in bioreactor and implantation [438].

Different in vitro and animal studies are performed to investigate the efficacy of this method for articular cartilage treatment [438]. The development process of NeoCart commenced from the isolation of chondrocyte cells from biopsy specimen taken from the patient. For harvesting cells, approximately 200–400 mg of tissue is taken from non-weight-bearing portion of femoral condyle or from the femoral notch of the lateral knee. During this process, the subchondral bone is not interfered. The biopsy specimen is then processed in laboratory to isolate chondrocyte cells. The cells are then seeded on 3D collagen type I hydrogel and culture in bioreactor. The operation condition, such as hydrostatic pressure, inside the bioreactor is tuned to stimulate chondrocytes to synthesise cartilage glycoprotein [439, 451]. After the levels of produced glycosaminoglycan and proteoglycan approached to a defined value, the scaffolds are removed from the bioreactor and further cultured in static condition. The average culture time (i.e. dynamic and static) is 67 ± 18 days. The cartilage lesion site is then shaved and trimmed before the implantation of the NeoCart. After this step the implant is cut to fit in the defected site and implanted by an open surgery. The surgical knee is then immobilised for 10 ± 2 days after the surgery [438] followed by a passive range of motion to strengthen the joint and surrounding muscles. For 6 weeks after implantation, the surgical knee is non-load bearing with restriction only to rehabilitation similar to femoral condyle microstructure and ACI-type protocols.

The efficacy of NeoCart for the treatment of full-thickness articular cartilage defect is studied on ten patients with grade III cartilage lesion of femoral condyle with an average defect size of 2.2 cm². The patients are in the range of 18–55 years old. In two cases, the implants are damaged due to intraoperative motion testings and the procedure is not preceded. The other patients had an isolated grade III chondral injury to the weight-bearing region either in the medial or lateral condyle. Based on visual analogue scale and pain scores, there are significant improvements in all 8 patients. The results of average range of motion evaluation and also knee function assessment with IKDC scale, however, indicated that 7 out of 8 patients had improvement after operation using this implant [438].

14.3.7.6 Pluronic and PEG-da Systems

Pluronic®⁴ is a commercially available polymeric system that undergoes physical crosslinking at physiological temperature (37 °C). This biomaterial is used as an injectable system for cartilage regeneration. Chondrocyte suspended in pluronic solution is used for mandibular condylar reconstruction [452]. Pluronic® solution is advantaged by its mild gelation and favourable biocompatibility properties. However, the application of pluronic solution in cartilage tissue engineering is limited due to its very poor mechanical strength, quick dissolution and high permeability [400]. A combination of Pluronic® with other injectable polymers has been used. These formulations include Pluronic®/PEG/NIPAAm, Pluronic®/poly(lactic acid/glycolic acid) (PLGA)[401, 402], Pluronic®/chitosan and Pluronic®/HAPromising [397].

Pluronic®/HA known as a X-HA is used at articular defect model of full-thickness defect of rabbit [413]. Adipose-derived stem cells are stimulated to undergo chondrogenic differentiation, using X-HA hydrogel, loaded with TGF-β. Copolymer of hyaluronic acid conjugated with heparin and Pluronic ® is synthesised to form the hydrogel at 37 °C in less than 10 min. TGF-β3 is successfully loaded within the structure of this hydrogel and could be released continuously in 20 days, which promoted cartilage ECM formation at full-thickness cartilage defect of rabbit knee [413]. Due to superior biological properties of naturally derived polymers, different protein-based polymers such as elastin-like polypeptides are also used for fabrication of hydrogel.

A PEG-da-based injectable hydrogel achieved clinical trial for the treatment of cartilage defects [453]. This PEG-da-based hydrogel is designed to support cartilage matrix production with easy surgical applications. In this approach, to bond the PEG-da-based hydrogel with the cartilage, chondroitin sulphate adhesive is first applied to the lesion site, and the joint is filled with polymer solution. The polymer solution contains 100 mg/ml PEG-da, 5 mg/ml hyaluronic acid and 0.5 mg/ml of Irigacure as photo-initiator in PBS [453]. A specially designed cone is used to apply

⁴Pluronic® is triblock copolymer of PEO–PPO–PEO.

light to the polymer solution to induce the gelation at a constant rate. Fifteen patients with symptomatic cartilage defects are treated with this injectable hydrogel after microfracture, and three patients are treated just with microfracture as control. After 6 months of surgery, no adverse effect is reported and the use of adhesive photo-crosslinked polymer allowed for greater filling of the defected site [453]. In addition, the patients who are treated with the injectable hydrogels reported a decrease in overall pain severity overtime

14.4 Conclusion

Articular cartilage is highly resilient connective tissue with unique mechanical properties which facilitate the mobility of the human body. The avascular structure and low metabolic activity of this tissue resulted in limited capability of this tissue for self-regeneration and repair. Early treatment approaches lead to unpredictable outcomes which are substantially interrelated with age, gender and physical conditions of patients. Tissue engineering approaches are therefore deemed to be more efficient for in vitro or in vivo regeneration of cartilage. Clinical studies on the commercially available biomaterials for cartilage tissue engineering showed that in the most of cases, the long-term final outcomes are unpredictable. The success rate in the best cases based on current results is 80 % for TruFit and 85 % for NeoCart. Many available treatments involve open surgery for transplantation of implant. The massive invasion in the joint has adverse impacts on the healing process of surgical knees. As a result, complicated rehabilitation protocols are generally recommended to patients after surgeries. The side effects of open surgeries and also not fully satisfied rehabilitation process in patients result in the failure of many treatment cases. Additionally, the defected cartilage may include an irregular shape that cannot be repaired by standard-sized scaffolds. Therefore, less invasive approaches such as injectable systems for delivery of cartilaginous construct to the defected site are favoured to tackle the current problems in cartilage tissue engineering. Injectable hydrogels have been contemplated as a non-invasive means for cartilage tissue engineering applicable for regular and irregular shaped cartilage lesions.

References

1. Simon TM, Jackson DW (2006) Articular cartilage: injury pathways and treatment options. *Sports Med Arthrosc* 14:146–154
2. Mankin HJ (1982) The response of articular cartilage to mechanical injury. *J Bone Joint Surg Am* 64:460–466
3. LaPorta TF, Richter A, Sgaglione NA, Grande DA (2012) Clinical relevance of scaffolds for cartilage engineering. *Orthop Clin N Am* 43:245–254

4. Brittberg M (2010) Cell carriers as the next generation of cell therapy for cartilage repair: a review of the matrix-induced autologous chondrocyte implantation procedure. *Am J Sports Med* 38:1259–1271
5. Poole CA (1993) The structure and function of articular cartilage matrixes. *Inflamm Dis Ther* 12:1–35
6. Wu W, Billingham RC, Pidoux I, Antoniou J, Zukor D, Tanzer M et al (2002) Sites of collagenase cleavage and denaturation of type II collagen in aging and osteoarthritic articular cartilage and their relationship to the distribution of matrix metalloproteinase 1 and matrix metalloproteinase 13. *Arthritis Rheum* 46:2087–2094
7. McCarty WJ, Nguyen QT, Hui AY, Chen AC, Sah RL (2011) *Comprehensive biomaterials*. Elsevier, London
8. Deshmukh K, Nimni ME (1973) Isolation and characterization of cyanogen bromide peptides from the collagen of bovine articular cartilage. *Biochem J* 133:615–622
9. Eyre DR, Wu J-J (1995) Collagen structure and cartilage matrix integrity. *J Rheumatol Suppl* 43:82–85
10. Roughley PJ, Lee ER (1994) Cartilage proteoglycans: structure and potential functions. *Microsc Res Tech* 28:385–397
11. Watanabe H, Yamada Y, Kimata K (1998) Roles of aggrecan, a large chondroitin sulfate proteoglycan, in cartilage structure and function. *J Biochem* 124:687–693
12. Maroudas A, Muir H, Wingham J (1969) Correlation of fixed negative charge with glycosaminoglycan content of human articular cartilage. *Biochim Biophys Acta Gen Subj* 177:492–500
13. Ateshian GA, Lai WM, Zhu WB, Mow VC (1994) An asymptotic solution for the contact of two biphasic cartilage layers. *J Biomech* 27:1347–1360
14. Broom ND (1984) Further insights into the structural principles governing the function of articular cartilage. *J Anat* 139(Pt 2):275–294
15. Boskey AL (1981) Current concepts of the physiology and biochemistry of calcification. *Clin Orthop Relat Res* 157:225–257
16. Poole AR, Matsui Y, Hinek A, Lee ER (1989) Cartilage macromolecules and the calcification of cartilage matrix. *Anat Rec* 224:167–179
17. Hall FM, Wyshak G (1980) Thickness of articular cartilage in the normal knee. *J Bone Joint Surg Am* 62:408–413
18. MacConaill MA (1951) The movements of bones and joints; the mechanical structure of articulating cartilage. *J Bone Joint Surg (Br)* 33B:251–257
19. Stockwell RA (1971) The interrelationship of cell density and cartilage thickness in mammalian articular cartilage. *J Anat* 109:411–421
20. Radin EL, Rose RM (1986) Role of subchondral bone in the initiation and progression of cartilage damage. *Clin Orthop Relat Res* 213:34–40
21. Hunziker EB, Herrmann W, Schenk RK (1983) Ruthenium hexamine trichloride (RHT)-mediated interaction between plasmalemmal components and pericellular matrix proteoglycans is responsible for the preservation of chondrocytic plasma membranes in situ during cartilage fixation. *J Histochem Cytochem* 31:717–727
22. Kumar P, Oka M, Toguchida J, Kobayashi M, Uchida E, Nakamura T et al (2001) Role of uppermost superficial surface layer of articular cartilage in the lubrication mechanism of joints. *J Anat* 199:241–250
23. Wu JP, Kirk TB, Zheng MH (2008) Study of the collagen structure in the superficial zone and physiological state of articular cartilage using a 3D confocal imaging technique. *J Orthop Surg Res* 3:29
24. Mathew G, Hanson BP (2009) Global burden of trauma: need for effective fracture therapies. *Indian J Orthop* 43:111–116
25. Temple MM, Bae WC, Chen MQ, Lotz M, Amiel D, Coutts RD et al (2007) Age- and site-associated biomechanical weakening of human articular cartilage of the femoral condyle. *Osteoarthr Cartil* 15:1042–1052

26. Mansour JM, Mow VC (1976) The permeability of articular cartilage under compressive strain and at high pressures. *J Bone Joint Surg Am* 58:509–516
27. Freeman MAR (1979) Adult articular cartilage. Pitman Medical, Tunbridge Wells
28. Chen AC, Bae WC, Schinagl RM, Sah RL (2001) Depth- and strain-dependent mechanical and electromechanical properties of full-thickness bovine articular cartilage in confined compression. *J Biomech* 34:1–12
29. Williamson AK, Chen AC, Masuda K, Thonar EJMA, Sah RL (2003) Tensile mechanical properties of bovine articular cartilage: variations with growth and relationships to collagen network components. *J Orthop Res* 21:872–880
30. Johannessen W, Elliott DM (2005) Effects of degeneration on the biphasic material properties of human nucleus pulposus in confined compression. *Spine (Phila Pa 1976)* 30:E724–E729
31. Schinagl RM, Gurskis D, Chen AC, Sah RL (1997) Depth-dependent confined compression modulus of full-thickness bovine articular cartilage. *J Orthop Res* 15:499–506
32. Athanasiou KA, Agarwal A, Dzida FJ (1994) Comparative study of the intrinsic mechanical properties of the human acetabular and femoral head cartilage. *J Orthop Res* 12:340–349
33. Katakai D, Imura M, Ando W, Tateishi K, Yoshikawa H, Nakamura N et al (2009) Compressive properties of cartilage-like tissues repaired in vivo with scaffold-free, tissue engineered constructs. *Clin Biomech* 24:110–116
34. Changoor A, Fereydoonzad L, Yaroshinsky A, Buschmann MD (2010) Effects of refrigeration and freezing on the electromechanical and biomechanical properties of articular cartilage. *J Biomech Eng* 132:064502
35. Bray JC, Merrill EW (1973) Poly(vinyl alcohol) hydrogels for synthetic articular cartilage material. *J Biomed Mater Res* 7:431–443
36. Buckley MR, Gleghorn JP, Bonassar LJ, Cohen I (2008) Mapping the depth dependence of shear properties in articular cartilage. *J Biomech* 41:2430–2437
37. Setton LA, Mow VC, Howell DS (1995) Mechanical behavior of articular cartilage in shear is altered by transection of the anterior cruciate ligament. *J Orthop Res* 13:473–482
38. Linn FC (1967) Lubrication of animal joints. I. The arthrotripsometer. *J Bone Joint Surg Am* 49:1079–1098
39. Athanasiou KA, Rosenwasser MP, Buckwalter JA, Malinin TI, Mow VC (1991) Interspecies comparisons of in situ intrinsic mechanical properties of distal femoral cartilage. *J Orthop Res* 9:330–340
40. Maroudas A, Bullough P (1968) Permeability of articular cartilage. *Nature* 219:1260–1261
41. Basalo IM, Mauck RL, Kelly T-AN, Nicoll SB, Chen FH, Hung CT et al (2004) Cartilage interstitial fluid load support in unconfined compression following enzymatic digestion. *J Biomech Eng* 126:779–786
42. Armstrong CG, Bahrani AS, Gardner DL (1979) In vitro measurement of articular cartilage deformations in the intact human hip joint under load. *J Bone Joint Surg Am* 61:744–755
43. Akizuki S, Mow VC, Muller F, Pita JC, Howell DS, Manicourt DH (1986) Tensile properties of human knee joint cartilage: I. Influence of ionic conditions, weight bearing, and fibrillation on the tensile modulus. *J Orthop Res* 4:379–392
44. Freeman MA (1969) Tensile properties of articular cartilage. *Nature* 220:1127–1128
45. Roth V, Mow VC (1980) The intrinsic tensile behavior of the matrix of bovine articular cartilage and its variation with age. *J Bone Joint Surg Am* 62:1102–1117
46. Kempson GE, Muir H, Pollard C, Tuke M (1973) Tensile properties of the cartilage of human femoral condyles related to the content of collagen and glycosaminoglycans. *Biochim Biophys Acta Gen Subj* 297:456–472
47. Schmidt MB, Mow VC, Chun LE, Eyre DR (1990) Effects of proteoglycan extraction on the tensile behavior of articular cartilage. *J Orthop Res* 8:353–363
48. Williamson AK, Chen AC, Sah RL (2001) Compressive properties and function—composition relationships of developing bovine articular cartilage. *J Orthop Res* 19:1113–1121

49. Hayes WC, Mockros LF (1971) Viscoelastic properties of human articular cartilage. *J Appl Physiol* 31:562–568
50. Belyi VA, Kupchinov BI, Ermakov SF, Rodnenkov VG, Bobrysheva SN (1988) Lubricants to recover tribological properties of human joints. *Int SAMPE Symp Exhib* 33:645–651
51. Dowson D, Jin ZM (1986) Micro-elastohydrodynamic lubrication of synovial joints. *Eng Med* 15:63–65
52. Krishnan R, Kopacz M, Ateshian GA (2004) Experimental verification of the role of interstitial fluid pressurization in cartilage lubrication. *J Orthop Res* 22:565–570
53. Kupchinov BI (1989) Tribological aspects of the functioning of joints. *Trenie Iznos* 10:1013–1018
54. Armstrong CG, Gardner DL (1977) Thickness and distribution of human femoral head articular cartilage. Changes with age. *Ann Rheum Dis* 36:407–412
55. Meachim G (1971) Effect of age on the thickness of adult articular cartilage at the shoulder joint. *Ann Rheum Dis* 30:43–46
56. Vignon E, Arlot M, Vignon G (1977) The cellularity of fibrillated articular cartilage. A comparative study of age-related and osteoarthrotic cartilage lesions from the human femoral head. *Pathol Biol* 25:29–32
57. Adams CS, Horton WE Jr (1998) Chondrocyte apoptosis increases with age in the articular cartilage of adult animals. *Anat Rec* 250:418–425
58. Barbero A, Grogan S, Schafer D, Heberer M, Mainil-Varlet P, Martin I (2004) Age related changes in human articular chondrocyte yield, proliferation and post-expansion chondrogenic capacity. *Osteoarthr Cartil* 12:476–484
59. Eyre DR, Dickson IR, Van NK (1988) Collagen cross-linking in human bone and articular cartilage. Age-related changes in the content of mature hydroxyppyridinium residues. *Biochem J* 252:495–500
60. Axelsson I, Bjelle A (1979) Proteoglycan structure of bovine articular cartilage. Variation with age and in osteoarthritis. *Scand J Rheumatol* 8:217–221
61. Bank RA, Bayliss MT, Lafeber FPJG, Maroudas A, Tekoppele JM (1998) Osteochondral resurfacing of the knee joint with allograft. Clinical analysis of 33 cases. *Biochem J* 330:345–351
62. Ding M (2000) Age variations in the properties of human tibial trabecular bone and cartilage. *Acta Orthop Scand Suppl* 292:1–45
63. Hyttinen MM, Arokoski JP, Parkkinen JJ, Lammi MJ, Lapvetelainen T, Mauranen K et al (2001) Age matters: collagen birefringence of superficial articular cartilage is increased in young guinea-pigs but decreased in older animals after identical physiological type of joint loading. *Osteoarthr Cartil* 9:694–701
64. Turner AS, Athanasiou KA, Zhu CF, Alvis MR, Bryant HU (1997) Biochemical effects of estrogen on articular cartilage in ovariectomized sheep. *Osteoarthr Cartil* 5:63–69
65. Murray RC, DeBowes RM, Gaughan EM, Zhu CF, Athanasiou KA (1998) The effects of intra-articular methylprednisolone and exercise on the mechanical properties of articular cartilage in the horse. *Osteoarthr Cartil* 6:106–114
66. Athanasiou KA, Fleischli JG, Bosma J, Laughlin TJ, Zhu CF, Agrawal CM et al (1999) Effects of diabetes mellitus on the biomechanical properties of human ankle cartilage. *Clin Orthop Relat Res* 182–9
67. Wluka AE, Wang Y, Davis SR, Cicuttini FM (2005) Tibial plateau size is related to grade of joint space narrowing and osteophytes in healthy women and in women with osteoarthritis. *Ann Rheum Dis* 64:1033–1037
68. Aspden RM, Jeffrey JE, Burgin LV (2002) Impact loading of articular cartilage. *Osteoarthr Cartil* 10:588–589; author reply 90.
69. Lohmander LS, Ostender A, Englund M, Roos H (2004) High prevalence of knee osteoarthritis, pain, and functional limitations in female soccer players twelve years after anterior cruciate ligament injury. *Arthritis Rheum* 50:3145–3152

70. Roos H, Adalberth T, Dahlberg L, Lohmander LS (1995) Osteoarthritis of the knee after injury to the anterior cruciate ligament or meniscus: the influence of time and age. *Osteoarthr Cartil* 3:261–267
71. A picture of osteoarthritis in Australia. Australian Institute of Health and Welfare; 2007 series no. 5, Cat. no. PHE 93, Canberra: AIHW
72. Painful realities: The economic impact of arthritis in Australia. Canberra: Arthritis Australia 2012
73. Ahmed TAE, Hincke MT (2010) Strategies for articular cartilage lesion repair and functional restoration. *Tissue Eng Part B* 16:305–329
74. Goldberg VM, Caplan AI, Barry FP, Fink DJ, Marshak DR, Burns JS (2002) Osteoarthritis cartilage regeneration. Osiris Therapeutics, Inc., Columbia
75. McCormick F, Yanke A, Provencher MT, Cole BJ (2008) Minced articular cartilage – basic science, surgical technique, and clinical application. *Sports Med Arthrosc* 16:217–220
76. Furukawa T, Eyre DR, Koide S, Glimcher MJ (1980) Biochemical studies on repair cartilage resurfacing experimental defects in the rabbit knee. *J Bone Joint Surg Am* 62(A):79–89
77. Shapiro F, Koide S, Glimcher MJ (1993) Cell origin and differentiation in the repair of full-thickness defects of articular cartilage. *J Bone Joint Surg Am* 75:532–553
78. Hjertquist SO, Lemperg R (1971) Histological, autoradiographic, and microchemical studies of spontaneously healing osteochondral articular defects in adult rabbits. *Calcif Tissue Res* 8:54–72
79. Temenoff JS, Mikos AG (2000) Review: tissue engineering for regeneration of articular cartilage. *Biomaterials* 21:431–440
80. Adachi N, Ishikawa M, Sera S, Ochi M (2007) Articular cartilage regeneration (Knee joint). *Bone* 21:473–476
81. Ghadially JA, Ghadially R, Ghadially FN (1977) Long-term results of deep defects in articular cartilage. A scanning electron microscope study. *Virchows Arch B Cell Pathol* 25:125–136
82. Squires GR, Okouneff S, Ionescu M, Poole AR (2003) The pathobiology of focal lesion development in aging human articular cartilage and molecular matrix changes characteristic of osteoarthritis. *Arthritis Rheum* 48:1261–1270
83. Chang RW, Falconer J, Stulberg SD, Arnold WJ, Manheim LM, Dyer AR (1993) A randomized, controlled trial of arthroscopic surgery versus closed-needle joint lavage for patients with osteoarthritis of the knee. *Arthritis Rheum* 36:289–296
84. Ike RW, Arnold WJ (1992) Arthroscopic lavage of osteoarthritic knees. *J Bone Joint Surg – B* 74:788–789
85. Hunziker EB, Kapfinger E (1998) Removal of proteoglycans from the surface of defects in articular cartilage transiently enhances coverage by repair cells. *J Bone Joint Surg – B* 80:144–150
86. Felson DT (2010) Arthroscopy as a treatment for knee osteoarthritis. *Best Pract Res Clin Rheumatol* 24:47–50
87. Anderson MA, Payne JT, Kreeger JM, Wagner-Mann CC, Schmidt DA, Mann FA (1993) Effects of intra-articular chlorhexidine diacetate lavage on the stifle in healthy dogs. *Am J Vet Res* 54:1784–1789
88. Hunziker EB (2002) Articular cartilage repair: Basic science and clinical progress. A review of the current status and prospects. *Osteoarthr Cartil* 10:432–463
89. Tew SR, Kwan APL, Hann A, Thomson BM, Archer CW (2000) The reactions of articular cartilage to experimental wounding: Role of apoptosis. *Arthritis Rheum* 43:215–225
90. Mitchell N, Shepard N (1987) Effect of Patellar Shaving in the Rabbit. *J Orthop Res* 5:388–392
91. Hunziker EB, Quinn TM (2003) Surgical removal of articular cartilage leads to loss of chondrocytes from cartilage bordering the wound edge. *J Bone Joint Surg – A* 85:85–92
92. McLaren AC, Blokker CP, Fowler PJ, Roth JN, Rock MG (1991) Arthroscopic debridement of the knee for osteoarthrosis. *Can J Surg* 34:595–598

93. Messner K, Fahlgren A, Ross I, Andersson B (2000) Simultaneous changes in bone mineral density and articular cartilage in a rabbit meniscectomy model of knee osteoarthritis. *Osteoarthr Cartil* 8:197–206
94. Messner K, Fahlgren A, Persliden J, Andersson BM (2001) Radiographic joint space narrowing and histologic changes in a rabbit meniscectomy model of early knee osteoarthritis. *Am J Sports Med* 29:151–160
95. Müller B, Kohn D (1999) Indication for and performance of articular cartilage drilling using the Pridie method. *Orthopade* 28:4–10
96. Insall JN (1967) Intra-articular surgery for degenerative arthritis of the knee. A report of the work of the late K. H. Pridie. *J Bone Joint Surg (Br)* 49:211–228
97. Insall J (1974) The Pridie debridement operation for osteoarthritis of the knee. *Clin Orthop Relat Res* 101:61–67
98. Goldman RT, Scuderi GR, Kelly MA (1997) Arthroscopic treatment of the degenerative knee in older athletes. *Clin Sports Med* 16:51–68
99. Beiser IH, Kanat IO (1990) Subchondral bone drilling: a treatment for cartilage defect. *J Foot Surg* 29:595–601
100. Hice G, Freedman D, Lemont H, Khoury S (1990) Scanning and light microscopic study of irrigated and nonirrigated joints following burr surgery performed through a small incision. *J Foot Surg* 29:337–344
101. Schmidt H, Schulze KJ, Cyffka R (1988) Results of treatment of cartilage damage by Pridie drilling of the knee joint. *Ergebnisse der Behandlung von Knorpelschäden durch PRIDIE-Bohrung am Kniegelenk* 35:117–122
102. Breinan HA, Martin SD, Hsu HP, Spector M (2000) Healing of canine articular cartilage defects treated with microfracture, a type-II collagen matrix, or cultured autologous chondrocytes. *J Orthop Res* 18:781–789
103. Sledge SL (2001) Microfracture techniques in the treatment of osteochondral injuries. *Clin Sports Med* 20:365–378
104. Pittenger MF, Mosca JD, McIntosh KR (2000) Human mesenchymal stem cells: progenitor cells for cartilage, bone, fat and stroma. 3–11.
105. Paccola CAJ, Xavier CAM, Goncalves RP (1979) Fresh immature articular cartilage allografts. A study on the integration of chondral and osteochondral grafts both in normal and in papain-treated knee joints of rabbits. *Arch Orthop Trauma Surg* 93:253–259
106. Lee TQ, Shrader TA, Wang YP, Glaser FE, Kim WC, McMahan PJ (1999) The use of entire fresh patellar allograft for articular cartilage replacement in rabbits: a long-term interdisciplinary study. *J Musculoskelet Res* 3:305–316
107. Stevenson S (1987) The immune response to osteochondral allografts in dogs. *J Bone Joint Surg Am* 69:573–582
108. Hickey MJ, Ohta I, Shigetomi M, Hurley JV, Kuwata N, O'Brien BM (1994) Vascularized heterotopic osteochondral allografts in a rat model following long-term immunosuppression. *J Reconstr Microsurg* 10:255–260
109. Bakay A, Csonge L, Papp G, Fekete L (1998) Osteochondral resurfacing of the knee joint with allograft. Clinical analysis of 33 cases. *Int Orthop* 22:277–281
110. Bell RS, Davis A, Allan DG, Langer F, Czitrom AA, Gross AE (1994) Fresh osteochondral allografts for advanced giant cell tumors at the knee. *J Arthroplasty* 9:603–609
111. Marco F, Lopez-Oliva F, Fernandez F-AJM, de Pedro JA, Perez AJ, Leon C et al (1993) Osteochondral allografts for osteochondritis dissecans and osteonecrosis of the femoral condyles. *Int Orthop* 17:104–108
112. McDermott AG, Langer F, Pritzker KP, Gross AE (1985) Fresh small-fragment osteochondral allografts. Long-term follow-up study on first 100 cases. *Clin Orthop Relat Res* 197:96–102
113. Mahomed MN, Beaver RJ, Gross AE (1992) The long-term success of fresh, small fragment osteochondral allografts used for intraarticular post-traumatic defects in the knee joint. *Orthopedics* 15:1191–1199

114. Kreuz PC, Steinwachs MR, Erggelet C, Krause SJ, Konrad G, Uhl M et al (2006) Results after microfracture of full-thickness chondral defects in different compartments in the knee. *Osteoarthr Cartil* 14:1119–1125
115. Jamali AA, Emmerson BC, Chung C, Convery FR, Bugbee WD (2005) Fresh osteochondral allografts: results in the patellofemoral joint. *Clin Orthop Relat Res* 437:176–185
116. Torga SR, Teitge RA (2006) Fresh osteochondral allografts for patellofemoral arthritis: long-term follow up. *Clin Orthop Relat Res* 444:193–200
117. Brittberg M, Lindahl A, Nilsson A, Ohlsson C, Isaksson O, Peterson L (1994) Treatment of deep cartilage defects in the knee with autologous chondrocyte transplantation. *N Engl J Med* 331:889–895
118. Trattnig S, Millington SA, Marlovits S (2007) MR imaging of osteochondral grafts and autologous chondrocyte implantation. *Eur Radiol* 17:103–118
119. Schnabel M, Marlovits S, Eckhoff G, Fichtel I, Gotzen L, Vecsei V et al (2002) Dedifferentiation-associated changes in morphology and gene expression in primary human articular chondrocytes in cell culture. *Osteoarthr Cartil* 10:62–70
120. Kuroda T, Matsumoto T, Mifune Y, Fukui T, Kubo S, Matsushita T et al (2011) Therapeutic strategy of third-generation autologous chondrocyte implantation for osteoarthritis. *Ups J Med Sci* 116:107–114
121. Tandogan NR, Karaeminogullari O, Ozyurek A, Ersozlu S (2004) Periarticular fractures of the knee in child and adolescent athletes. *Acta Orthop Traumatol Turc* 38(Suppl 1):93–100
122. Parkkari J, Pasanen K, Mattila VM, Kannus P, Rimpela A (2008) The risk for a cruciate ligament injury of the knee in adolescents and young adults: a population-based cohort study of 46 500 people with a 9 year follow-up. *Br J Sports Med* 42:422–426
123. Hickey GJ, Fricker PA, McDonald WA (1997) Injuries of young elite female basketball players over a six-year period. *Clin J Sport Med* 7:252–256
124. Adirim TA, Cheng TL (2003) Overview of injuries in the young athlete. *Sports Med* 33:75–81
125. Tuli R, Li W-J, Tuan RS (2003) Current state of cartilage tissue engineering. *Arthritis Res Ther* 5:235–238
126. Iwasa J, Engebretsen L, Shima Y, Ochi M (2009) Clinical application of scaffolds for cartilage tissue engineering. *Knee Surg Sports Traumatol Arthrosc* 17:561–577
127. Le DC, Guery J, Laulan J (2004) Results of a five-year series of 44 trapeziectomies associated with ligamentoplasty and interposition arthroplasty. *Chir Main* 23:149–152
128. Bruns J, Kersten P, Lierse W, Silbermann M (1993) Autologous transplantation of rib perichondrium in treatment of deep cartilage defects of the knee joint of sheep. Morphologic comparison of two resorbable fixation methods. *Unfallchirurg* 96:462–467
129. Getgood A, Brooks R, Fortier L, Rushton N (2009) Articular cartilage tissue engineering: today's research, tomorrow's practice? *J Bone Joint Surg (Br)* 91:565–576
130. Langer RS, Vacanti JP (1993) Tissue engineering. *Science* 260:920–926
131. Park I-K, Cho C-S (2010) Stem cell-assisted approaches for cartilage tissue engineering. *Int J Stem Cells* 3:96–102
132. Kim IL, Mauck RL, Burdick JA (2011) Hydrogel design for cartilage tissue engineering: a case study with hyaluronic acid. *Biomaterials* 32:8771–8782
133. Hwang NS, Elisseff J (2009) Application of stem cells for articular cartilage regeneration. *J Knee Surg* 22:60–71
134. Pittenger MF, Mackay AM, Beck SC, Jaiswal RK, Douglas R, Mosca JD et al (1999) Multilineage potential of adult human mesenchymal stem cells. *Science* 284:143–147
135. Noël D, Djouad FCJ (2002) Regenerative medicine through mesenchymal stem cells for bone and cartilage repair. *Curr Opin Investig Drugs* 3:1000–1004
136. Barry FPMJ (2004) Mesenchymal stem cells: clinical applications and biological characterization. *Int J Biochem Cell Biol* 36:568–584

137. Trubiani ODP, Traini T, Pizzicannella J, Scarano A, Piattelli A, Caputi S (2005) Morphological and cytofluorimetric analysis of adult mesenchymal stem cells expanded ex vivo from periodontal ligament. *Int J Immunopathol Pharmacol* 18:213–221
138. Trubiani OOG, Caputi S, Piattelli A (2006) Adult mesenchymal stem cells in dental research: a new approach for tissue engineering. *Int J Immunopathol Pharmacol* 19:451–460
139. Caplan AI (2007) Adult mesenchymal stem cells for tissue engineering versus regenerative medicine. *J Cell Physiol* 213:341–347
140. Nejadnik H, Hui JH, Feng Choong EP, Tai BC, Lee EH (2010) Autologous bone marrow-derived mesenchymal stem cells versus autologous chondrocyte implantation: an observational cohort study. *Am J Sports Med* 6:1110–1116
141. Fan HHY, Zhang C, Li X, Lv R, Qin L, Zhu R (2006) Cartilage regeneration using mesenchymal stem cells and a PLGA-gelatin/chondroitin/hyaluronate hybrid scaffold. *Biomaterials* 27:4573–4580
142. Uematsu K, Hattori K, Ishimoto Y, Yamauchi J, Habata T, Takakura Y et al (2005) Cartilage regeneration using mesenchymal stem cells and a three-dimensional poly-lactic-glycolic acid (PLGA) scaffold. *Biomaterials* 26:4273–4279
143. Banfi A, Bianchi G, Notaro R, Luzzatto L, Cancedda R, Quarto R (2002) Replicative aging and gene expression in long-term cultures of human bone marrow stromal cells. *Tissue Eng* 8:901–910
144. Parsch D, Fellenberg J, Bruemendorf TH, Eschlbeck A-M, Richter W (2004) Telomere length and telomerase activity during expansion and differentiation of human mesenchymal stem cells and chondrocytes. *J Mol Med* 82:49–55
145. Vacanti V, Kong E, Suzuki G, Sato K, Canty JM, Lee T (2005) Phenotypic changes of adult porcine mesenchymal stem cells induced by prolonged passaging in culture. *J Cell Physiol* 205:194–201
146. Zhu S, Wurdak H, Wang J, Lyssiotis CA, Peters EC, Cho CY et al (2009) A small molecule primes embryonic stem cells for differentiation. *Cell Stem Cell* 4:416–426
147. Wurdaka H, Zhua S, Mina KH, Aimoneb L, Lairsona LL, Watsonb J et al (2010) A small molecule accelerates neuronal differentiation in the adult rat. *PNAS* 107:16542–16547
148. Richardson SM, Hoyland JA, Mobasher R, Csaki C, Shakibaei MAM (2010) Mesenchymal stem cells in regenerative medicine: opportunities and challenges for articular cartilage and intervertebral disc tissue engineering. *J Cell Physiol* 222:23–32
149. Johnstone B, Hering TM, Caplan AI, Goldberg VM, Yoo JU (1998) In vitro chondrogenesis of bone marrow-derived mesenchymal progenitor cells. *Exp Cell Res* 238:265–272
150. Chiou MXY, Longaker MT (2006) Mitogenic and chondrogenic effects of fibroblast growth factor-2 in adipose-derived mesenchymal cells. *Biochem Biophys Res Commun* 343:644–652
151. Longobardi LORL, Aakula S, Johnstone B, Shimer K, Chytil A, Horton WA, Moses HL, Spagnoli A (2006) Effect of IGF-I in the chondrogenesis of bone marrow mesenchymal stem cells in the presence or absence of TGF-beta signaling. *J Bone Miner Res* 21:626–636
152. LA Solchaga PK, Porter JD, Goldberg VM, Caplan AI, Welter JF (2005) FGF-2 enhances the mitotic and chondrogenic potentials of human adult bone marrow-derived mesenchymal stem cells. *J Cell Physiol* 203:398–409
153. Frenkel SR, Saadeh PB, Mehrara BJ, Steinbrech DS, Cocker RS, McCormick SA et al (1998) Transforming growth factor beta superfamily members: role in cartilage modeling. *Surg Forum* 49:516–518
154. Frenkel SR, Saadeh PB, Mehrara BJ, Chin GS, Steinbrech DS, Brent B et al (2000) Transforming growth factor beta superfamily members: role in cartilage modeling. *Plast Reconstr Surg* 105:980–990
155. Van der Kan P, Vitters E, van der Berg W (1992) Differential effect of transforming growth factor beta on freshly isolated and cultured articular chondrocytes. *J Rheumatol* 19:140–145

156. Verschure PJ, Joosten LAB, Van der Kraan PM, Van der Berg WB (1994) Responsiveness of articular cartilage from normal and inflamed mouse knee joints to various growth factors. *Ann Rheum Dis* 53:455–460
157. Blunk T, Sieminski AL, Gooch KJ, Courter DL, Hollander AP, Nahir M et al (2002) Differential effects of growth factors on tissue-engineered cartilage. *Tissue Eng* 8:73–84
158. Sporn MB, Roberts AB, Wakefield LM, Assoian RK (1986) Transforming growth factor- β : biological function and chemical structure. *Science (Washington, D C, 1883-)* 233:532–534
159. Valcourt U, Gouttenoire J, Moustakas A, Herbage D, Mallein-Gerin F (2002) Functions of transforming growth factor- β family type I receptors and smad proteins in the hypertrophic maturation and osteoblastic differentiation of chondrocytes. *J Biol Chem* 277:33545–33558
160. Pecina M, Jelic M, Martinovic S, Haspl M, Vukicevic S (2002) Articular cartilage repair: the role of bone morphogenetic proteins. *Int Orthop* 26:131–136
161. Luyten FP, Yu YM, Yanagishita M, Vukicevic S, Hammonds RG, Reddi AH (1992) Natural bovine osteogenin and recombinant human bone morphogenetic protein-2B are equipotent in the maintenance of proteoglycans in bovine articular cartilage explant cultures. *J Biol Chem* 267:3691–3695
162. Mattioli-Belmonte M, Gigante A, Muzzarelli RA, Politano R, De BA, Specchia N et al (1999) N, N-dicarboxymethyl chitosan as delivery agent for bone morphogenetic protein in the repair of articular cartilage. *Med Biol Eng Comput* 37:130–134
163. Kaps C, Bramlage C, Smolian H, Haisch A, Ungethum U, Burmester G-R et al (2002) Bone morphogenetic proteins promote cartilage differentiation and protect engineered artificial cartilage from fibroblast invasion and destruction. *Arthritis Rheum* 46:149–162
164. Gooch KJ, Blunk T, Courter DL, Sieminski AL, Vunjak-Novakovic G, Freed LE (2002) Bone morphogenetic proteins-2, -12, and -13 modulate in vitro development of engineered cartilage. *Tissue Eng* 8:591–601
165. O'Connor WJ, Botti T, Khan SN, Lane JM (2000) The use of growth factors in cartilage repair. *Orthop Clin North Am* 31:399–410
166. Hunziker EB (1999) Biologic repair of articular cartilage. Defect models in experimental animals and matrix requirements. *Clin Orthop Relat Res* 367:S135–S146
167. Risbud M, Endres M, Ringe J, Bhonde R, Sittering M (2001) Biocompatible hydrogel supports the growth of respiratory epithelial cells: possibilities in tracheal tissue engineering. *J Biomed Mater Res* 56:120–127
168. Boyan BD, Hummert TW, Dean DD, Schwartz Z (1996) Role of material surfaces in regulating bone and cartilage cell response. *Biomaterials* 17:137–146
169. McClary KB, Ugarova T, Grainger DW (2000) Modulating fibroblast adhesion, spreading, and proliferation using self-assembled monolayer films of alkythioliates on gold. *J Biomed Mater Res* 50:428–439
170. Quirk RA, Chan WC, Davies MC, Tendler SJB, Shakesheff KM (2001) Poly(L-lysine)-GRGDS as a biomimetic surface modifier for poly(lactic acid). *Biomaterials* 22:865–872
171. Chu PK, Chen JY, Wang LP, Huang N (2002) Plasma-surface modification of biomaterials. *Mater Sci Eng R* R36:143–206
172. Humphries MJ, Akiyama SK, Komoriya A, Olden K, Yamada KM (1986) Identification of an alternatively spliced site in human plasma fibronectin that mediates cell type-specific adhesion. *J Cell Biol* 103:2637–2647
173. Shin H, Jo S, Mikos AG (2003) Biomimetic materials for tissue engineering. *Biomaterials* 24:4353–4364
174. Peppas NA, Hilt JZ, Khademhosseini A, Langer R (2006) Hydrogels in biology and medicine: from molecular principles to bionanotechnology. *Adv Mater* 18:1345–1360
175. Khademhosseini A, Langer R (2007) Microengineered hydrogels for tissue engineering. *Biomaterials* 28:5087
176. Nichol JW, Khademhosseini A (2009) Modular tissue engineering: engineering biological tissue from the bottom up. *Soft Matter* 5:1312–1319

177. Vacanti JP, Morse MA, Saltzman WM, Domb AJ, Perez-Atayde A, Langer R (1988) Selective cell transplantation using bioabsorbable artificial polymers as matrices. *J Pediatr Surg* 23:3–9
178. Mikos AG, Sarakinos G, Lyman MD, Ingber DE, Vacanti JP, Langer R (1993) Prevascularization of porous biodegradable polymers. *Biotechnol Bioeng* 42:716–723
179. Annabi N, Nichol JW, Zhong X, Ji C, Koshy S, Khademhosseini A et al (2010) Controlling the porosity and microarchitecture of hydrogels for tissue engineering. *Tissue Eng Part B* 16:371–380
180. Di Maio E, Mensitieri G, Iannace S, Nicolais L, Li W, Flumerfelt RW (2005) Structure optimization of polycaprolactone foams by using mixtures of CO₂ and N₂ as blowing agents. *Polym Eng Sci* 45:432–441
181. Zhang Y, Fan W, Ma Z, Wu C, Fang W, Liu G et al (2010) The effects of pore architecture in silk fibroin scaffolds on the growth and differentiation of mesenchymal stem cells expressing BMP7. *Acta Biomater* 6:3021–3028
182. Karageorgiou V, Kaplan D (2005) Porosity of 3D biomaterial scaffolds and osteogenesis. *Biomaterials* 26:5474–5491
183. Ngoenkam J, Faikrua A, Yasothornsrikul S, Viyoch J (2010) Potential of an injectable chitosan/starch/ β -glycerol phosphate hydrogel for sustaining normal chondrocyte function. *Int J Pharm* 391:115–124
184. Duncan RL, Turner CH (1995) Mechanotransduction and the functional response of bone to mechanical strain. *Calcif Tissue Int* 57:344–358
185. Carter DR, Blenman PR, Beaupre GS (1988) Correlations between mechanical stress history and tissue differentiation in initial fracture healing. *J Orthop Res* 6:736–748
186. Jin M, Emkey GR, Siparsky P, Trippel SB, Grodzinsky AJ (2003) Combined effects of dynamic tissue shear deformation and insulin-like growth factor I on chondrocyte biosynthesis in cartilage explants. *Arch Biochem Biophys* 414:223–231
187. Hutmacher DW (2000) Scaffolds in tissue engineering bone and cartilage. *Biomaterials* 21:2529–2543
188. Gerard C, Catuogno C, Amargier-Huin C, Grossin L, Hubert P, Gillet P et al (2005) The effect of alginate, hyaluronate and hyaluronate derivatives biomaterials on synthesis of non-articular chondrocyte extracellular matrix. *J Mater Sci Mater Med* 16:541–551
189. Lee KY, Mooney DJ (2001) Hydrogels for tissue engineering. *Chem Rev* 101:1869–1879
190. Slaughter BV, Khurshid SS, Fisher OZ, Khademhosseini A, Peppas NA (2009) Hydrogels in regenerative medicine. *Adv Mater* 21:3307–3329
191. Peppas NA (1987) *Hydrogels in medicine and pharmacy*. CRC Press, Florida
192. Jabbari E (2006) Biomimetic hydrogel/apatite nanocomposite scaffolds for bone regeneration. *Mater Res Soc Symp Proc* 897E
193. Jabbari E, Nozari S (2000) Swelling behavior of acrylic acid hydrogels prepared by g-radiation crosslinking of polyacrylic acid in aqueous solution. *Eur Polym J* 36:2685–2692
194. Freed LE, Marquis JC, Nohria A, Emmanuel J, Mikos AG, Langer R (1993) Neocartilage formation in vitro and in vivo using cells cultured on synthetic biodegradable polymers. *J Biomed Mater Res* 27:11–23
195. Liu Y, Chen F, Liu W, Cui L, Shang Q, Xia W et al (2002) Repairing large porcine full-thickness defects of articular cartilage using autologous chondrocyte-engineered cartilage. *Tissue Eng* 8:709–721
196. Chu CR, Coutts RD, Yoshioka M, Harwood FL, Monosov AZ, Amiel D (1995) Articular cartilage repair using allogeneic perichondrocyte-seeded biodegradable porous polylactic acid (PLA): a tissue-engineering study. *J Biomed Mater Res* 29:1147–1154
197. Vacanti CA, Langer R, Schloo B, Vacanti JP (1991) Synthetic polymers seeded with chondrocytes provide a template for new cartilage formation. *Plast Reconstr Surg* 88:753–759
198. Douchis JS, Bae WC, Chen AC, Sah RL, Coutts RD, Amiel D (2000) Cartilage repair with autogenic perichondrium cell and polylactic acid grafts. *Clin Orthop Relat Res* 377:248–264

199. W-j L, Danielson KG, Alexander PG, Tuan RS (2003) Biological response of chondrocytes cultured in three-dimensional nanofibrous poly(*ε*-caprolactone) scaffolds. *J Biomed Mater Res A* 67A:1105–1114
200. Annabi N, Fathi A, Mithieux SM, Weiss AS, Dehghani F (2011) Fabrication of porous PCL/elastin composite scaffolds for tissue engineering applications. *J Supercrit Fluids* 59:157–167
201. Annabi N, Fathi A, Mithieux SM, Martens P, Weiss AS, Dehghani F (2011) The effect of elastin on chondrocyte adhesion and proliferation on poly(ϵ -caprolactone)/elastin composites. *Biomaterials* 32:1517–1525
202. W-j L, Danielson KG, Alexander PG, Tuan RS (2003) Biological response of chondrocytes cultured in three-dimensional nanofibrous poly(*ε*-caprolactone) scaffolds. *J Biomed Mater Res Part A* 67A:1105–1114
203. Ushio K, Oka M, Hyon S-H, Hayami T, Yura S, Matsumura K et al (2003) Attachment of artificial cartilage to underlying bone. *J Biomed Mater Res Part B* 68B:59–68
204. Gu Z, Xiao J, Zhang X (1999) Development of artificial articular cartilage-PVA-hydrogel. *Beijing Keji Daxue Xuebao* 21:40–43
205. Oka M (2001) Biomechanics and repair of articular cartilage. *J Orthop Sci* 6:448–456
206. Guo T, Yang T, Xiao J, Long H, Chen Y, Pei F et al (2009) Repair of articular cartilage defect in rabbits by novel biomimetic composite material of polyvinyl alcohol hydrogel/nano-hydroxyapatite + polyamide 66. *Zhonghua Chuangshang Zazhi* 25:748–750
207. Spiller KL, Liu Y, Holloway JL, Maher SA, Cao Y, Liu W et al (2012) A novel method for the direct fabrication of growth factor-loaded microspheres within porous nondegradable hydrogels: Controlled release for cartilage tissue engineering. *J Control Release* 157:39–45
208. Elisseeff J, Anseth K, Sims D, McIntosh W, Randolph M, Yaremchuk M et al (1999) Transdermal photopolymerization of poly(ethylene oxide)-based injectable hydrogels for tissue-engineered cartilage. *Plast Reconstr Surg* 104:1014–1022
209. Sharma B, Williams CG, Khan M, Manson P, Elisseeff JH (2006) In vivo chondrogenesis of mesenchymal stem cells in a photopolymerized hydrogel. *Plast Reconstr Surg* 119:112–120
210. Hwang NS, Varghese S, Theprungsirikul P, Canver A, Elisseeff J (2006) Enhanced chondrogenic differentiation of murine embryonic stem cells in hydrogels with glucosamine. *Biomaterials* 27:6015–6023
211. Nguyen QT, Hwang Y, Chen AC, Varghese S, Sah RL (2012) Cartilage-like mechanical properties of poly(ethylene glycol)-diacrylate hydrogels. *Biomaterials* 33:6682–6690
212. Shung AK, Behravesh E, Jo S, Mikos AG (2003) Crosslinking characteristics of and cell adhesion to an injectable poly(propylene fumarate-co-ethylene glycol) hydrogel using a water-soluble crosslinking system. *Tissue Eng* 9:243–254
213. Park H, Temenoff JS, Holland TA, Tabata Y, Mikos AG (2005) Delivery of TGF- β 1 and chondrocytes via injectable, biodegradable hydrogels for cartilage tissue engineering applications. *Biomaterials* 26:7095–7103
214. Sokmen N, Ayhan F, Ayhan H (2008) Gelatine containing photopolymerized poly(ethylene glycol) diacrylate hydrogels for drug delivery. *Polym Prepr (Am Chem Soc, Div Polym Chem)* 49:1054–1055
215. Drapala PW, Brey EM, Mieler WF, Venerus DC, Kang DJJ, Perez-Luna VH (2011) Role of thermo-responsiveness and poly(ethylene glycol) diacrylate cross-link density on protein release from poly(*N*-isopropylacrylamide) hydrogels. *J Biomater Sci Polym Ed* 22:59–75
216. Holland TA, Bodde EWH, Cuijpers VMJI, Baggett LS, Tabata Y, Mikos AG et al (2007) Degradable hydrogel scaffolds for in vivo delivery of single and dual growth factors in cartilage repair. *Osteoarthritis Cartilage* 15:187–197
217. Guo X, Park H, Liu G, Liu W, Cao Y, Tabata Y et al (2009) In vitro generation of an osteochondral construct using injectable hydrogel composites encapsulating rabbit marrow mesenchymal stem cells. *Biomaterials* 30:2741–2752

218. Guo X, Park H, Young S, Kretlow JD, Van den Beucken JJ, Baggett LS et al (2010) Repair of osteochondral defects with biodegradable hydrogel composites encapsulating marrow mesenchymal stem cells in a rabbit model. *Acta Biomater* 6:39–47
219. Stoltz JF, Magdalou J, Netter P, Pinzano A, Zille H, Paquet J et al (2010) Evaluation of intra-articular delivery of hyaluronic acid functionalized biopolymeric nanoparticles in healthy rat knees. *Biomed Mater Eng* 20:235–242
220. Bergsma EJ, Rozema FR, Bos RR, de Bruijn WC (1993) Foreign body reactions to resorbable poly(L-lactide) bone plates and screws used for the fixation of unstable zygomatic fractures. *J Oral Maxillofac Surg* 51:666–670
221. Martin C, Winet H, Bao JY (1996) Acidity near eroding polylactide-polyglycolide in vitro and in vivo in rabbit tibial bone chambers. *Biomaterials* 17:2373–2380
222. An YH, Woolf SK, Friedman RJ (2000) Pre-clinical in vivo evaluation of orthopaedic bioabsorbable devices. *Biomaterials* 21:2635–2652
223. Dunn AS, Campbell PG, Marra KG (2001) The influence of polymer blend composition on the degradation of polymer/hydroxyapatite biomaterials. *J Mater Sci Mater Med* 12:673–677
224. Heidemann W, Jeschkeit S, Ruffieux K, Fischer JH, Wagner M, Kruger G et al (2001) Degradation of poly(D, L)lactide implants with or without addition of calciumphosphates in vivo. *Biomaterials* 22:2371–2381
225. Rezwani K, Chen QZ, Blaker JJ, Boccaccini AR (2006) Biodegradable and bioactive porous polymer/inorganic composite scaffolds for bone tissue engineering. *Biomaterials* 27:3413–3431
226. Bazile DV, Ropert C, Huve P, Verrecchia T, Marland M, Frydman A et al (1992) Body distribution of fully biodegradable [¹⁴C]-poly(lactic acid) nanoparticles coated with albumin after parenteral administration to rats. *Biomaterials* 13:1093–1102
227. Chu CR, Douchis JS, Yoshioka M, Sah RL, Coutts RD, Amiel D (1997) Osteochondral repair using perichondrial cells. A 1-year study in rabbits. *Clin Orthop Relat Res* 340:220–229
228. Xiong L, He Z (2011) Synthesis and application for porous scaffold materials of monomethoxy polyethylene glycol/poly(lactide) diblock copolymer. *J Macromol Sci Part B Phys* 50:1226–1233
229. Pitt CG, Jeffcoat AR, Zweidinger RA, Schindler A (1979) Sustained drug delivery systems. I. The permeability of poly(ϵ -caprolactone), poly(DL-lactic acid), and their copolymers. *J Biomed Mater Res* 13:497–507
230. Ye WP, Du FS, Jin WH, Yang JY, Xu Y (1997) In vitro degradation of poly(caprolactone), poly(lactide) and their block copolymers: influence of composition, temperature and morphology. *React Funct Polym* 32:161–168
231. Coombes AGA, Verderio E, Shaw B, Li X, Griffin M, Downes S (2002) Biocomposites of non-crosslinked natural and synthetic polymers. *Biomaterials* 23:2113–2118
232. Schagemann JC, Kurz H, Casper ME, Stone JS, Dadsetan M, Sun Y-L et al (2010) The effect of scaffold composition on the early structural characteristics of chondrocytes and expression of adhesion molecules. *Biomaterials* 31:2798–2805
233. Park GE, Webster TJ (2005) Mechanisms of increased chondrocyte adhesion on nanometer surface featured NaOH-treated PLGA. *J Biomed Nanotechnol* 1:306–312
234. Thissen H, Chang KY, Tebb TA, Tsai WB, Glattauer V, Ramshaw JAM et al (2006) Synthetic biodegradable microparticles for articular cartilage tissue engineering. *J Biomed Mater Res Part A* 77A:590–598
235. Peppas NA, Merrill EW (1977) Crosslinked poly(vinyl alcohol) hydrogels as swollen elastic networks. *J Appl Polym Sci Symp* 21:1763–1770
236. Amini AA, Nair LS (2012) Injectable hydrogels for bone and cartilage. *Biomed Mater* 7: (13pp)
237. Nguyen MK, Lee DS (2010) Injectable biodegradable hydrogels. *Macromol Biosci* 10:563–579

238. Liu SQ, Tian Q, Hedrick JL, Hui JHP, Ee PLR, Yang YY (2010) Biomimetic hydrogels for chondrogenic differentiation of human mesenchymal stem cells to neocartilage. *Biomaterials* 31:7298–7307
239. Bryant SJ, Arthur JA, Anseth KS (2005) Incorporation of tissue-specific molecules alters chondrocyte metabolism and gene expression in photocrosslinked hydrogels. *Acta Biomater* 1:243–252
240. Malmonge SM, Zavaglia CA, Belangero WD (2000) Biomechanical and histological evaluation of hydrogel implants in articular cartilage. *Braz J Med Biol Res* 33:307–312
241. Sawtell RM, Downes S, Kayser MV (1995) An in vitro investigation of the PEMA/THFMA system using chondrocyte culture. *J Mater Sci Mater Med* 6:676–679
242. Reissis N, Kayser M, Bentley G, Downes S (1995) A hydrophilic polymer system enhanced articular cartilage regeneration in vivo. *J Mater Sci Mater Med* 6:768–772
243. Bosnakovski D, Mizuno M, Kim G, Takagi S, Okumura M, Fujinaga T (2006) Chondrogenic differentiation of bovine bone marrow mesenchymal stem cells (MSCs) in different hydrogels: influence of collagen type II extracellular matrix on MSC chondrogenesis. *Biotechnol Bioeng* 93:1152–1163
244. Wakitani S, Goto T, Pineda SJ, Young RG, Mansour JM, Caplan AI et al (1994) Mesenchymal cell-based repair of large, full-thickness defects of articular cartilage. *J Bone Joint Surg Am* 76:579–592
245. Harriger MD, Supp AP, Warden GD, Boyce ST (1997) Glutaraldehyde crosslinking of collagen substrates inhibits degradation in skin substitutes grafted to athymic mice. *J Biomed Mater Res* 35:137–145
246. Wissink MJB, Beermink R, Poot AA, Engbers GHM, Beugeling T, Van Aken WG et al (2001) Relation between cell density and the secretion of von Willebrand factor and prostacyclin by human umbilical vein endothelial cells. *Biomaterials* 22:2283–2290
247. Van LMJA, Van WPB, Olde DLHH, Dijkstra PJ, Feijen J, Nieuwenhuis P (1992) Secondary cytotoxicity of crosslinked dermal sheep collagens during repeated exposure to human fibroblasts. *Biomaterials* 13:1017–1024
248. Nehrer S, Breinan HA, Ramappa A, Hsu HP, Minas T, Shortkroff S et al (1998) Chondrocyte-seeded collagen matrices implanted in a chondral defect in a canine model. *Biomaterials* 19:2313–2328
249. Kon E, Delcogliano M, Filardo G, Altadonna G, Marcacci M (2009) Novel nano-composite multi-layered biomaterial for the treatment of multifocal degenerative cartilage lesions. *Knee Surg Sports Traumatol Arthrosc* 17:1312–1315
250. Haisch A, Loch A, David J, Pruss A, Hansen R, Sittinger M (2000) Preparation of a pure autologous biodegradable fibrin matrix for tissue engineering. *Med Biol Eng Comput* 38:686–689
251. Fortier LA, Nixon AJ, Mohammed HO, Lust G (1997) Altered biological activity of equine chondrocytes cultured in a three-dimensional fibrin matrix and supplemented with transforming growth factor β -1. *Am J Vet Res* 58:66–70
252. Li W-J, Tuan RS (2005) Polymeric scaffolds for cartilage tissue engineering. *Macromol Symp* 227:65–75
253. Horan RL, Antle K, Collette AL, Wang Y, Huang J, Moreau JE et al (2005) In vitro degradation of silk fibroin. *Biomaterials* 26:3385–3393
254. Qin G, Kaplan DL (2012) Silk-based biomaterials: biology, properties, and clinical applications. CRC Press, Boca Raton, pp 421–31.
255. Dal Pra I, Freddi G, Minic J, Chiarini A, Armato U (2005) De novo engineering of reticular connective tissue in vivo by silk fibroin nonwoven materials. *Biomaterials* 26:1987–1999
256. Altman GH, Diaz F, Jakuba C, Calabro T, Horan RL, Chen J et al (2002) Silk-based biomaterials. *Biomaterials* 26:401–416
257. Mehlhorn AT, Schmal H, Kaiser S, Lepski G, Finkenzeller G, Stark GB et al (2006) Mesenchymal stem cells maintain TGF- β -mediated chondrogenic phenotype in alginate bead culture. *Tissue Eng* 12:1393–1403

258. Cheng N-C, Estes BT, Awad HA, Guilak F (2009) Chondrogenic differentiation of adipose-derived adult stem cells by a porous scaffold derived from native articular cartilage extracellular matrix. *Tissue Eng Part A* 15:231–241
259. Balakrishnan B, Banerjee R (2011) Biopolymer-based hydrogels for cartilage tissue engineering. *Chem Rev* 111:4453–4474
260. De Souza R, Zahedi P, Allen CJ, Piquette-Miller M (2009) Biocompatibility of injectable chitosan–phospholipid implant systems. *Biomaterials* 30:3818–3824
261. Jancar J, Slovikova A, Amler E, Krupa P, Kecova H, Planka L, et al (2007) Mechanical response of porous scaffolds for cartilage engineering. *Physiol Res* 56:S17–S25
262. Medrado GCB, Machado CB, Valerio P, Sanches MD, Goes AM (2006) The effect of a chitosan-gelatin matrix and dexamethasone on the behavior of rabbit mesenchymal stem cells. *Biomed Mater* 1:155–161
263. Sa-Lima H, Caridade SG, Mano JF, Reis RL (2010) Stimuli-responsive chitosan-starch injectable hydrogels combined with encapsulated adipose-derived stromal cells for articular cartilage regeneration. *Soft Matter* 6:5184–5195
264. Lippiello L (2003) Glucosamine and chondroitin sulfate: biological response modifiers of chondrocytes under simulated conditions of joint stress. *Osteoarthr Cartil* 11:335–342
265. Chan PS, Caron JP, Rosa GJM, Orth MW (2005) Glucosamine and chondroitin sulfate regulate gene expression and synthesis of nitric oxide and prostaglandin E(2) in articular cartilage explants. *Osteoarthr Cartil* 13:387–394
266. Uebelhart D, Thonar EJ, Delmas PD, Chantraine A, Vignon E (1998) Effects of oral chondroitin sulfate on the progression of knee osteoarthritis: a pilot study. *Osteoarthr Cartil* 6(Suppl A):39–46
267. Sechriest VF, Miao YJ, Niyibizi C, Westerhausen-Larson A, Matthew HW, Evans CH et al (2000) GAG-augmented polysaccharide hydrogel: a novel biocompatible and biodegradable material to support chondrogenesis. *J Biomed Mater Res* 49:534–541
268. van Susante JLC, Pieper J, Buma P, van Kuppevelt TH, van Beuningen H, van der Kraan PM et al (2001) Linkage of chondroitin-sulfate to type I collagen scaffolds stimulates the bioactivity of seeded chondrocytes in vitro. *Biomaterials* 22:2359–2369
269. Betre H, Chilkoti A, Setton L. A (2002) A two step recovery system based on thermally sensitive elastin-like polypeptide scaffolds for cartilage tissue engineering. *Proceedings of the Second Joint EBMS/BMES Conference* pp 829–30
270. McHale MK, Setton LA, Chilkoti A (2006) Synthesis and in vitro evaluation of enzymatically cross-linked elastin-like polypeptide gels for cartilaginous tissue repair. *Tissue Eng* 11:1768–1779
271. Ong SR, Trabbic-Carlson KA, Nettles DL, Lim DW, Chilkoti A, Setton LA (2006) Epitope tagging for tracking elastin-like polypeptides. *Biomaterials* 27:1930–1935
272. Hrabchak C, Rouleau J, Moss I, Woodhouse K, Akens M, Bellingham C et al (2010) Assessment of biocompatibility and initial evaluation of genipin cross-linked elastin-like polypeptides in the treatment of an osteochondral knee defect in rabbits. *Acta Biomater* 6:2108–2115
273. Stark Y, Suck K, Kasper C, Wieland M, van Griensven M, Scheper T (2006) Application of collagen matrices for cartilage tissue engineering. *Exp Toxicol Pathol* 57:305–311
274. Pieper JS, van Tienen T, van Susante JLC, van der Kraan PM, Veerkamp JH et al (2003) Cross-linked type I and type II collagenous matrices for the repair of full-thickness articular cartilage defects – a study in rabbits. *Biomaterials* 24:3255–3263
275. Lu HH, El-Amin SF, Scott KD, Laurencin CT (2003) Three-dimensional, bioactive, biodegradable, polymer-bioactive glass composite scaffolds with improved mechanical properties support collagen synthesis and mineralization of human osteoblast-like cells in vitro. *J Biomed Mater Res A* 64:465–474
276. Nandakumar A, Fernandes H, de Boer J, Moroni L, Habibovic P, van Blitterswijk CA (2010) Fabrication of bioactive composite scaffolds by electrospinning for bone regeneration. *Macromol Biosci* 10:1365–1373

277. Nowatzki PJ, Tirrell DA (2003) Physical properties of artificial extracellular matrix protein films prepared by isocyanate crosslinking. *Biomaterials* 25:1261–1267
278. Nimni ME, Cheung D, Strates B, Kodama M, Sheikh K (1987) Chemically modified collagen: a natural biomaterial for tissue replacement. *J Biomed Mater Res* 21:741–771
279. Sandberg LB, Soskel NT, Leslie JG (1981) Elastin structure, biosynthesis, and relation to disease states. *N Engl J Med* 304:566–579
280. Nettles DL, Chilkoti A, Setton LA (2010) Applications of elastin-like polypeptides in tissue engineering. *Adv Drug Deliv Rev* 62:1479–1485
281. Alberts B, Johnson A, Lewis J, Raff M, Roberts K, Walter P (2002) Cell junctions, cell adhesion, and the extracellular matrix. Garland Science, New York
282. Daamen WF, Hafmans T, Veerkamp JH, van Kuppevelt TH (2001) Comparison of five procedures for the purification of insoluble elastin. *Biomaterials* 22
283. Partridge SM, Davis HF, Adair GS (1955) Connective tissue. II. Soluble proteins derived from partial hydrolysis of elastin. *Biochem J* 61:11–21
284. Mandli I, Kellers SML (1970) Chemistry and molecular biology of the intercellular matrix. In: Balzas EA (ed) New York. Academic Press, p 665
285. Rnjak-Kovacina J, Daamen WF, Pierna M, Rodríguez-Cabello JC, Weiss AS (2011) Elastin biopolymers. In: Ducheyne P (ed) *Comprehensive biomaterials*. Elsevier Science, Amsterdam, pp 329–346
286. Antonicelli F, Bellon G, Debelle L, Hornebeck W (2007) Elastin-elastases and inflammation. *Curr Top Dev Biol* 79:99–155
287. Betre H, Setton LA, Meyer DE, Chilkoti A (2002) Characterization of a genetically engineered elastin-like polypeptide for cartilaginous tissue repair. *Biomacromolecules* 3:910–916
288. Betre H, Ong SR, Guilak F, Chilkoti A, Fermor B, Setton LA (2006) Chondrocytic differentiation of human adipose-derived adult stem cells in elastin-like polypeptide. *Biomaterials* 27:91–99
289. Lim DW, Nettles DL, Setton LA, Chilkoti A (2007) Rapid cross-linking of elastin-like polypeptides with (Hydroxymethyl)phosphines in aqueous solution. *Biomacromolecules* 8:1463–1470
290. Trabbic-Carlson K, Setton LA, Chilkoti A (2003) Swelling and mechanical behaviors of chemically cross-linked hydrogels of elastin-like polypeptides. *Biomacromolecules* 4:572–580
291. Lim DW, Nettles DL, Setton LA, Chilkoti A (2008) In situ cross-linking of elastin-like polypeptide block copolymers for tissue repair. *Biomacromolecules* 9:222–230
292. Annabi N, Mithieux SM, Weiss AS, Deghani F (2010) Cross-linked open-pore elastic hydrogels based on tropoelastin, elastin and high pressure CO₂. *Biomaterials* 31:1655–1665
293. Nettles DL, Haider MA, Chilkoti A, Setton LA (2009) Neural network analysis identifies scaffold properties necessary for in vitro chondrogenesis in elastin-like polypeptide biopolymer scaffolds. *Tissue Eng Part A* 16:11–20
294. Silverman RP, Passaretti D, Huang W, Randolph MA, Yaremchuk MJ (1999) Injectable tissue-engineered cartilage using a fibrin glue polymer. *Plast Reconstr Surg* 103:1809–1818
295. Worster AA, Brower-Toland BD, Fortier LA, Bent SJ, Williams J, Nixon AJ (2001) Chondrocytic differentiation of mesenchymal stem cells sequentially exposed to transforming growth factor- β 1 in monolayer and insulin-like growth factor-I in a three-dimensional matrix. *J Orthop Res* 19:738–749
296. Nixon AJ, Fortier LA, Williams J, Mohammed H (1999) Enhanced repair of extensive articular defects by insulin-like growth factor-I-laden fibrin composites. *J Orthop Res* 17:475–487
297. Whatley JS, DeJardin LM, Arnoczky SP (2000) The effect of an exogenous fibrin clot on the regeneration of the triangular fibrocartilage complex: an in vivo experimental study in dogs. *Arthroscopy* 16:127–136

298. Paletta GA, Arnoczky SP, Warren RF (1992) The repair of osteochondral defects using an exogenous fibrin clot. An experimental study in dogs. *Am J Sports Med* 20:725–731
299. van Susante JL, Buma P, Schuman L, Homminga GN, van den Berg WB, Veth RPH (1999) Resurfacing potential of heterologous chondrocytes suspended in fibrin glue in large full-thickness defects of femoral articular cartilage: an experimental study in the goat. *Biomaterials* 20:1167–1175
300. Hendrickson DA, Nixon AJ, Grande DA, Todhunter RJ, Minor RM, Erb H et al (1994) Chondrocyte-fibrin matrix transplants for resurfacing extensive articular cartilage defects. *J Orthop Res* 12:485–497
301. Kawabe N, Yoshinai M (1991) The repair of full-thickness articular cartilage defects. Immune responses to reparative tissue formed by allogeneic growth plate chondrocyte implants. *Clin Orthop Relat Res* 268:279–293
302. Henning CE, Lynch MA, Yearout KM, Vequist SW, Stallbaumer RJ, Decker KA (1990) Arthroscopic meniscal repair using an exogenous fibrin clot. *Clin Orthop Relat Res* 252:64–72
303. Gobin AS, Froude VE, Mathur AB (2005) Structural and mechanical characteristics of silk fibroin and chitosan blend scaffolds for tissue regeneration. *J Biomed Mater Res Part A* 74A:465–473
304. Scheibel T (2006) Silk—a biomaterial with several facets. *Appl Phys A Mater Sci Process* 82:191–192
305. Vepari C, Kaplan DL (2007) Silk as a biomaterial. *Prog Polym Sci* 32:991–1007
306. Meinel L, Hofmann S, Karageorgiou V, Zichner L, Langer R, Kaplan D et al (2004) Engineering cartilage-like tissue using human mesenchymal stem cells and silk protein scaffolds. *Biotechnol Bioeng* 88:379–391
307. Uebersax L, Merkle HP, Meinel L (2008) Insulin-like growth factor I releasing silk fibroin scaffolds induce chondrogenic differentiation of human mesenchymal stem cells. *J Control Release* 127:12–21
308. Wang Y, Blasioli DJ, Kim H-J, Kim HS, Kaplan DL (2006) Cartilage tissue engineering with silk scaffolds and human articular chondrocytes. *Biomaterials* 27:4434–4442
309. Wang Y, Kim U-J, Blasioli DJ, Kim H-J, Kaplan DL (2005) In vitro cartilage tissue engineering with 3D porous aqueous-derived silk scaffolds and mesenchymal stem cells. *Biomaterials* 26:7082–7094
310. Hu X, Wang X, Rnjak J, Weiss AS, Kaplan DL (2010) Biomaterials derived from silk-tropoelastin protein systems. *Biomaterials* 31:8121–8131
311. Hu X, Park S-H, Gil ES, Xia X-X, Weiss AS, Kaplan DL (2011) The influence of elasticity and surface roughness on myogenic and osteogenic-differentiation of cells on silk-elastin biomaterials. *Biomaterials* 32:8979–8989
312. Dash M, Chiellini F, Ottenbrite RM, Chiellini E (2011) Chitosan—A versatile semi-synthetic polymer in biomedical applications. *Prog Polym Sci* 36:981–1014
313. Kubota N, Tatsumoto N, Sano T, Toya K (2000) A simple preparation of half N-acetylated chitosan highly soluble in water and aqueous organic solvents. *Carbohydr Res* 324:268–274
314. Lin H-Y, Chou C-C (2004) Antioxidative activities of water-soluble disaccharide chitosan derivatives. *Food Res Int* 37:883–889
315. Bedekar AN, Pise AC, Thatte CS, Rathnam MV (2010) Study on optimization of carboxymethylation of chitosan obtained from squilla chitin. *Asian J Chem* 22:7675–7682
316. Gong Y, Zhu Y, Liu Y, Ma Z, Gao C, Shen J (2007) Layer-by-layer assembly of chondroitin sulfate and collagen on aminolyzed poly(L-lactic acid) porous scaffolds to enhance their chondrogenesis. *Acta Biomater* 3:677–685
317. Milosavljevic NB, Milasinovic NZ, Popovic IG, Filipovic JM, Kalagasidis KMT (2011) Preparation and characterization of pH-sensitive hydrogels based on chitosan, itaconic acid and methacrylic acid. *Polym Int* 60:443–452
318. Ma L, Gao C, Mao Z, Zhou J, Shen J, Hu X et al (2003) Collagen/chitosan porous scaffolds with improved biostability for skin tissue engineering. *Biomaterials* 24:4833–4841

319. Shanmugasundaram N, Ravichandran P, Neelakanta RP, Ramamurty N, Pal S, Panduranga RK (2001) Collagen-chitosan polymeric scaffolds for the in vitro culture of human epidermoid carcinoma cells. *Biomaterials* 22:1943–1951
320. Lu G, Kong L, Sheng B, Wang G, Gong Y, Zhang X (2007) Degradation of covalently cross-linked carboxymethyl chitosan and its potential application for peripheral nerve regeneration. *Eur Polym J* 43:3807–3818
321. Ji C, Annabi N, Khademhosseini A, Dehghani F (2011) Fabrication of porous chitosan scaffolds for soft tissue engineering using dense gas CO₂. *Acta Biomater* 7:1653–1664
322. Ji C, Annabi N, Hosseinkhani M, Sivaloganathan S, Dehghani F (2012) Fabrication of poly-DL-lactide/polyethylene glycol scaffolds using the gas foaming technique. *Acta Biomater* 8:570–578
323. Mwale F, Iordanova M, Demers CN, Steffen T, Roughley P, Antoniou J (2005) Biological evaluation of chitosan salts cross-linked to genipin as a cell scaffold for disk tissue engineering. *Tissue Eng* 11:130–140
324. Ji C, Khademhosseini A, Dehghani F (2011) Enhancing cell penetration and proliferation in chitosan hydrogels for tissue engineering applications. *Biomaterials* 32:9719–9729
325. Lu JX, Prudhommeaux F, Meunier A, Sedel L, Guillemin G (1999) Effects of chitosan on rat knee cartilages. *Biomaterials* 20:1937–1944
326. Suh JK, Matthew HW (2000) Application of chitosan-based polysaccharide biomaterials in cartilage tissue engineering: a review. *Biomaterials* 21:2589–2598
327. Shive MS, Hoemann CD, Restrepo A, Hurtig M, Duval N, Ranger P et al (2006) BST-CarGel: in situ chondroinduction for cartilage repair. *Oper Tech Orthop* 16:271–278
328. Bellamy N, Buchanan WW, Goldsmith CH, Campbell J, Stitt LW (1988) Validation study of WOMAC: a health status instrument for measuring clinically important patient relevant outcomes to antirheumatic drug therapy in patients with osteoarthritis of the hip or knee. *J Rheumatol* 15:1833–1840
329. Seyrek E, Dubin P (2010) Glycosaminoglycans as polyelectrolytes. *Adv Colloid Interface Sci* 158:119–129
330. Uebelhart D, Thonar EJ, Zhang J, Williams JM (1998) Protective effect of exogenous chondroitin 4,6-sulfate in the acute degradation of articular cartilage in the rabbit. *Osteoarthritis Cartil* 6(Suppl A):6–13
331. Handley CJ, Brooks P, Lowther DA (1980) Suppression of collagen synthesis by chondrocytes by exogenous concentrations of proteoglycan subunit. *Biochem Int* 1:270–276
332. Bian L, Kaplun M, Williams DY, Xu D, Ateshian GA, Hung CT (2009) Influence of chondroitin sulfate on the biochemical, mechanical and frictional properties of cartilage explants in long-term culture. *J Biomech* 42:286–290
333. Varghese S, Hwang NS, Canver AC, Theprungsirikul P, Lin DW, Elisseeff J (2008) Chondroitin sulfate based niches for chondrogenic differentiation of mesenchymal stem cells. *Matrix Biol* 27:12–21
334. Akmal M, Singh A, Anand A, Kesani A, Aslam N, Goodship A et al (2005) The effects of hyaluronic acid on articular chondrocytes. *J Bone Joint Surg (Br)* 87:1143–1149
335. Goa KL, Benfield P (1994) Hyaluronic acid. A review of its pharmacology and use as a surgical aid in ophthalmology, and its therapeutic potential in joint disease and wound healing. *Drugs* 47:536–566
336. Responde DJ, Natoli RM, Athanasiou KA (2012) Identification of potential biophysical and molecular signalling mechanisms underlying hyaluronic acid enhancement of cartilage formation. *J R Soc Interface* 9:3564–3573
337. Bulpitt P, Aeschlimann D (1999) New strategy for chemical modification of hyaluronic acid: preparation of functionalized derivatives and their use in the formation of novel biocompatible hydrogels. *J Biomed Mater Res* 47:152–169
338. Campoccia D, Doherty P, Radice M, Brun P, Abatangelo G, Williams DF (1998) Semisynthetic resorbable materials from hyaluronan esterification. *Biomaterials* 19:2101–2127

339. Vercruyse KP, Marecak DM, Marecek JF, Prestwich GD (1997) Synthesis and in vitro degradation of new polyvalent hydrazide cross-linked hydrogels of hyaluronic acid. *Bioconjug Chem* 8:686–694
340. Barbucci R, Magnani A, Rappuoli R, Lamponi S, Consumi M (2000) Immobilisation of sulphated hyaluronan for improved biocompatibility. *J Inorg Biochem* 79:119–125
341. Aigner J, Tegeler J, Hutzler P, Campoccia D, Pavesio A, Hammer C et al (1998) Cartilage tissue engineering with novel nonwoven structured biomaterial based on hyaluronic acid benzyl ester. *J Biomed Mater Res* 42:172–181
342. Grigolo B, Lisignoli G, Piacentini A, Fiorini M, Gobbi P, Mazzotti G et al (2001) Evidence for redifferentiation of human chondrocytes grown on a hyaluronan-based biomaterial (HYAFF11): molecular, immunohistochemical and ultrastructural analysis. *Biomaterials* 23:1187–1195
343. Knudson CB (1993) Hyaluronan receptor-directed assembly of chondrocyte pericellular matrix. *J Cell Biol* 120:825–834
344. Brun P, Abatangelo G, Radice M, Zacchi V, Guidolin D, Gordini DD et al (1999) Chondrocyte aggregation and reorganization into three-dimensional scaffolds. *J Biomed Mater Res* 46:337–346
345. Radice M, Brun P, Cortivo R, Scapinelli R, Battaliard C, Abatangelo G (2000) Hyaluronan-based biopolymers as delivery vehicles for bone-marrow-derived mesenchymal progenitors. *J Biomed Mater Res* 50:101–109
346. Solchaga LA, Dennis JE, Goldberg VM, Caplan AI (1999) Hyaluronic acid-based polymers as cell carriers for tissue-engineered repair of bone and cartilage. *J Orthop Res* 17:205–213
347. Grunder T, Gaissmaier C, Fritz J, Stoop R, Hortschansky P, Mollenhauer J et al (2004) Bone morphogenetic protein (BMP)-2 enhances the expression of type II collagen and aggrecan in chondrocytes embedded in alginate beads. *Osteoarthr Cartil* 12:559–567
348. Cai X, Lin Y, Ou G, Luo E, Man Y, Yuan Q et al (2007) Ectopic osteogenesis and chondrogenesis of bone marrow stromal stem cells in alginate system. *Cell Biol Int* 31:776–783
349. Genes NG, Rowley JA, Mooney DJ, Bonassar LJ (2004) Effect of substrate mechanics on chondrocyte adhesion to modified alginate surfaces. *Arch Biochem Biophys* 422:161–167
350. Bouhadir KH, Lee KY, Alsberg E, Damm KL, Anderson KW, Mooney DJ (2001) Degradation of partially oxidized alginate and its potential application for tissue engineering. *Biotechnol Prog* 17:945–950
351. Li Y, Rodrigues J, Tomas H (2012) Injectable and biodegradable hydrogels: gelation, biodegradation and biomedical applications. *Chem Soc Rev* 41:2193–2221
352. Hong Y, Gong Y, Gao C, Shen J (2008) Collagen-coated polylactide microcarriers/chitosan hydrogel composite: injectable scaffold for cartilage regeneration. *J Biomed Mater Res Part A* 85A:628–637
353. Park H, Guo X, Temenoff JS, Tabata Y, Caplan AI, Kasper FK et al (2009) Effect of swelling ratio of injectable hydrogel composites on chondrogenic differentiation of encapsulated rabbit marrow mesenchymal stem cells in vitro. *Biomacromolecules* 10:541–546
354. Hong Y, Song H, Gong Y, Mao Z, Gao C, Shen J (2007) Covalently crosslinked chitosan hydrogel: Properties of in vitro degradation and chondrocyte encapsulation. *Acta Biomater* 3:23–31
355. Sharma B, Williams CG, Khan M, Manson P, Elisseeff JH (2007) In vivo chondrogenesis of mesenchymal stem cells in a photopolymerized hydrogel. *Plast Reconstr Surg* 119:112–120
356. Villanueva I, Hauschulz DS, Mejic D, Bryant SJ (2008) Static and dynamic compressive strains influence nitric oxide production and chondrocyte bioactivity when encapsulated in PEG hydrogels of different crosslinking densities. *Osteoarthr Cartil* 16:909–918
357. Nicodemus GD, Skaalure SC, Bryant SJ (2011) Gel structure has an impact on pericellular and extracellular matrix deposition, which subsequently alters metabolic activities in chondrocyte-laden PEG hydrogels. *Acta Biomater* 7:492–504

358. Hou Y, Schoener CA, Regan KR, Munoz Pinto D, Hahn MS, Grunlan MA (2010) Photocross-linked PDMSstar-PEG hydrogels: synthesis, characterization, and potential application for tissue engineering scaffolds. *Biomacromolecules* 1:648–656
359. Martens PJ, Bryant SJ, Anseth KS (2003) Tailoring the degradation of hydrogels formed from multivinyl poly(ethylene glycol) and poly(vinyl alcohol) macromers for cartilage tissue engineering. *Biomacromolecules* 4:283–292
360. Nettles DL, Vail TP, Morgan MT, Grinstaff MW, Setton LA (2004) Photocrosslinkable hyaluronan as a scaffold for articular cartilage repair. *Ann Biomed Eng* 32:391–397
361. Erickson IE, Huang AH, Sengupta S, Kestle S, Burdick JA, Mauck RL (2009) Macromer density influences mesenchymal stem cell chondrogenesis and maturation in photocrosslinked hyaluronic acid hydrogels. *Osteoarthr Cartil* 17:1639–1648
362. Jeon O, Bouhadir KH, Mansour JM, Alsberg E (2009) Photocrosslinked alginate hydrogels with tunable biodegradation rates and mechanical properties. *Biomaterials* 30:2724–2734
363. Nichol JW, Koshy ST, Bae H, Hwang CM, Yamanlar S, Khademhosseini A (2010) Cell-laden microengineered gelatin methacrylate hydrogels. *Biomaterials* 31:5536–5544
364. Hu X, Ma L, Wang C, Gao C (2009) Gelatin hydrogel prepared by photo-initiated polymerization and loaded with TGF- β 1 for cartilage tissue engineering. *Macromol Biosci* 9:1194–1201
365. Tan H, Rubin JP, Marra KG (2010) Injectable in situ forming biodegradable chitosan-hyaluronic acid based hydrogels for adipose tissue regeneration. *Organogenesis* 6:173–180
366. Jin R, Moreira TLS, Dijkstra PJ, van Blitterswijk CA, Karperien M, Feijen J (2010) Enzymatically-crosslinked injectable hydrogels based on biomimetic dextran-hyaluronic acid conjugates for cartilage tissue engineering. *Biomaterials* 31:3103–3113
367. Tran NQ, Joung YK, Lih E, Park KM, Park KD (2010) Supramolecular hydrogels exhibiting fast in situ gel forming and adjustable degradation properties. *Biomacromolecules* 11:617–625
368. Hu P, Xu B (2003) Injectable hydrogel scaffold for cartilage tissue engineering. Tsinghua University, People's Republic of China, p 6
369. Ko DY, Shinde UP, Yeon B, Jeong B (2010) Recent progress on in situ formed gels for biomedical applications. *Prog Polym Sci*
370. Sharma D, George P, Button PD, May BK, Kasapis S (2011) Thermomechanical study of the phase behaviour of agarose/gelatin mixtures in the presence of glucose syrup as co-solute. *Food Chem* 127:1784–1791
371. Li Q, Williams CG, Sun DDN, Wang J, Leong K, Elisseeff JH (2003) Photocrosslinkable polysaccharides based on chondroitin sulfate. *J Biomed Mater Res Part A* 68A:28–33
372. Habibovic P, Juhl MV, Clyens S, Martinetti R, Dolcini L, Theilgaard N et al (2010) Comparison of two carbonated apatite ceramics in vivo. *Acta Biomater* 6:2219–2226
373. Kim M, Kim SE, Kang SS, Kim YH, Tae G (2011) The use of de-differentiated chondrocytes delivered by a heparin-based hydrogel to regenerate cartilage in partial-thickness defects. *Biomaterials* 32:7883–7896
374. Lee J, Choi WI, Tae G, Kim YH, Kang SS, Kim SE et al (2011) Enhanced regeneration of the ligament–bone interface using a poly(l-lactide-co- ϵ -caprolactone) scaffold with local delivery of cells/BMP-2 using a heparin-based hydrogel. *Acta Biomater* 7:244–257
375. Zhang J, Skardal A, Prestwich GD (2008) Engineered extracellular matrices with cleavable crosslinkers for cell expansion and easy cell recovery. *Biomaterials* 29:4521–4531
376. Davis NE, Ding S, Forster RE, Pinkas DM, Barron AE (2010) Modular enzymatically crosslinked protein polymer hydrogels for in situ gelation. *Biomaterials* 31:7288–7297
377. Yang Z, Liang G, Xu B (2007) Enzymatic control of the self-assembly of small molecules: a new way to generate supramolecular hydrogels. *Soft Matter* 3:515–520
378. Chen T, Embree HD, Brown EM, Taylor MM, Payne GF (2003) Enzyme-catalyzed gel formation of gelatin and chitosan: potential for in situ applications. *Biomaterials* 24:2831–2841

379. Toledano S, Williams RJ, Jayawarna V, Ulijn RV (2006) Enzyme-triggered self-assembly of peptide hydrogels via reversed hydrolysis. *J Am Chem Soc* 128:1070–1071
380. Burke MD, Park JO, Srinivasarao M, Khan SA (2005) A novel enzymatic technique for limiting drug mobility in a hydrogel matrix. *J Control Release* 104:141–153
381. Hughes M, Xu H, Frederix PWJM, Smith AM, Hunt NT, Tuttle T et al (2011) Biocatalytic self-assembly of 2D peptide-based nanostructures. *Soft Matter* 7:10032–10038
382. Hoare T, Pelton R (2004) Functional group distributions in carboxylic acid containing poly (N-isopropylacrylamide) microgels. *Langmuir* 20:2123–2133
383. Jones JA, Novo N, Flagler K, Pagnucco CD, Carew S, Cheong C et al (2005) Thermoresponsive copolymers of methacrylic acid and poly(ethylene glycol) methyl ether methacrylate. *J Polym Sci A Polym Chem* 43:6095–6104
384. Han CK, Bae YH (1998) Inverse thermally-reversible gelation of aqueous N-isopropylacrylamide copolymer solutions. *Polymer* 39:2809–2814
385. Chen G, Hoffman AS (1995) Graft copolymers that exhibit temperature-induced phase transitions over a wide range of pH. *Nature* 373:49–52
386. Schilli CM, Zhang M, Rizzardo E, Thang SH, Chong YK, Edwards K et al (2004) A new double-responsive block copolymer synthesized via RAFT polymerization: poly (N-isopropylacrylamide)-block-poly(acrylic acid). *Macromolecules* 37:7861–7866
387. Garbern JC, Hoffman AS, Stayton PS (2010) Injectable pH- and temperature-responsive poly (N-isopropylacrylamide-co-propylacrylic acid) copolymers for delivery of angiogenic growth factors. *Biomacromolecules* 11:1833–1839
388. Pollock JF, Healy KE (2010) Mechanical and swelling characterization of poly(N-isopropyl acrylamide-comethoxy poly(ethylene glycol) methacrylate) sol-gels. *Acta Biomater* 6:1307–1318
389. Yun K, Moon HT (2008) Inducing chondrogenic differentiation in injectable hydrogels embedded with rabbit chondrocytes and growth factor for neocartilage formation. *J Biosci Bioeng* 105:122–126
390. Huang X, Zhang Y, Donahue HJ, Lowe TL (2007) Porous thermoresponsive-co-biodegradable hydrogels as tissue-engineering scaffolds for 3-dimensional in vitro culture of chondrocytes. *Tissue Eng* 13:2645–2652
391. Sa-Lima H, Tuzlakoglu K, Mano JF, Reis RL (2011) Thermoresponsive poly (N-isopropylacrylamide)-g-methylcellulose hydrogel as a three-dimensional extracellular matrix for cartilage-engineered applications. *J Biomed Mater Res Part A* 98A:596–603
392. Lue S, Liu M, Ni B (2011) Degradable, injectable poly(N-isopropylacrylamide)-based hydrogels with low gelation concentrations for protein delivery application. *Chem Eng J* 173:241–250
393. Haider M, Cappello J, Ghandehari H, Leong K (2008) In vitro chondrogenesis of mesenchymal stem cells in recombinant silk-elastinlike hydrogels. *Pharm Res* 25:692–699
394. Guan J, Hong Y, Ma Z, Wagner WR (2008) Protein-reactive, thermoresponsive copolymers with high flexibility and biodegradability. *Biomacromolecules* 9:1283–1292
395. Cho J, Heuzey MC, Bégin A, Carreau PJ (2005) Physical gelation of chitosan in the presence of beta-glycerophosphate: the effect of temperature. *Biomacromolecules* 6:3267–3275
396. Chenite A, Chaput C, Wang D, Combes C, Buschmann MD, Hoemann CD et al (2000) Novel injectable neutral solutions of chitosan form biodegradable gels in situ. *Biomaterials* 21:2155–2161
397. Park KM, Lee SY, Joung YK, Na JS, Lee MC, Park KD (2009) Thermosensitive chitosan-pluronic hydrogel as an injectable cell delivery carrier for cartilage regeneration. *Acta Biomater* 5:1956–1965
398. Abe M, Takahashi M, Tokura S, Tamura H, Nagano A (2004) Cartilage-scaffold composites produced by bioresorbable beta-chitin sponge with cultured rabbit chondrocytes. *Tissue Eng* 10:585–594

399. Iwasaki N, Kasahara Y, Yamane S, Igarashi T, Minami A, Nisimura S-i (2011) Chitosan-based hyaluronic acid hybrid polymer fibers as a scaffold biomaterial for cartilage tissue engineering. *Polymers* 3:100–113
400. Liu Y, Lu W-L, Wang J-C, Zhang X, Zhang H, Wang X-Q et al (2007) Controlled delivery of recombinant hirudin based on thermo-sensitive Pluronic F127 hydrogel for subcutaneous administration: in vitro and in vivo characterization. *J Control Release* 117:387–395
401. Cohn D, Lando G, Sosnik A, Garty S, Levi A (2006) PEO-PPO-PEO-based poly(ether ester urethane)s as degradable reverse thermo-responsive multiblock copolymers. *Biomaterials* 27:1718–1727
402. Jeong B, Bae YH, Kim SW (2000) In situ gelation of PEG-PLGA-PEG triblock copolymer aqueous solutions and degradation thereof. *J Biomed Mater Res* 50:171–177
403. de las Alarcon CH, Pennadam S, Alexander C (2005) Stimuli responsive polymers for biomedical applications. *Chem Soc Rev* 34:276–285
404. Heskins M, Guillet JE (1968) Solution properties of poly(*N*-isopropylacrylamide). *J Macromol Sci Chem A2*:1441
405. Ha DI, Lee SB, Chong MS, Lee YM (2006) Preparation of thermo-responsive and injectable hydrogels based on hyaluronic acid and poly(*N*-isopropylacrylamide) and their drug release behaviors. *Macromol Res* 14:87–93
406. Cappello JCJ, Dorman M, Mikolajczak M, Textor G, Marquet M, Ferrari F (1990) Genetic engineering of structural protein polymers. *Biotechnol Prog* 6:198–202
407. Nettles DL, Vali TP, Flahiff CM, Walkenhorst J, Carter AJ, Setton LA (2005) Injectable silk-elastin for articular cartilage defect repair. *Trans of the ORS Washington, DC*, p 1366
408. Hoemann CD, Sun J, Légaré A, McKee MD, Buschmann MD (2005) Tissue engineering of cartilage using an injectable and adhesive chitosan-based cell-delivery vehicle. *Osteoarthr Cartil* 13:318–329
409. Ruel-Gariépy E, Shive M, Bichara A, Berrada M, Le Garrec D, Chenite A et al (2004) A thermosensitive chitosan-based hydrogel for the local delivery of paclitaxel. *Eur J Pharm Biopharm* 57:53–63
410. Li Z, Zhang M (2005) Chitosan–alginate as scaffolding material for cartilage tissue engineering. *J Biomed Mater Res A* 75A:485–493
411. Yamane S, Iwasaki N, Majima T, Funakoshi T, Masuko T, Harada K et al (2005) Feasibility of chitosan-based hyaluronic acid hybrid biomaterial for a novel scaffold in cartilage tissue engineering. *Biomaterials* 26:611–619
412. Chen Y-L, Lee H-P, Chan H-Y, Sung L-Y, Chen H-C, Hu Y-C (2007) Composite chondroitin-6-sulfate/dermatan sulfate/chitosan scaffolds for cartilage tissue engineering. *Biomaterials* 28:2294–2305
413. Jung HH, Park K, Han DK (2010) Preparation of TGF- β 1-conjugated biodegradable pluronic F127 hydrogel and its application with adipose-derived stem cells. *J Control Release* 147:84–91
414. Safran CB, Farach-Carson MC, Jia X, Srinivasan PP, Jha A (2012) Injectable delivery system for heparan sulfate-binding growth factors. University of Delaware, USA, p 30
415. Dell’Accio F, Vanlauwe J, Bellemans J, Neys J, de Bari C, Luyten FP (2003) Expanded phenotypically stable chondrocytes persist in the repair tissue and contribute to cartilage matrix formation and structural integration in a goat model of autologous chondrocyte implantation. *J Orthop Res* 21:123–131
416. Grande DA, Pitman MI, Peterson L, Menche D, Klein M (1989) The repair of experimentally produced defects in rabbit articular cartilage by autologous chondrocyte transplantation. *J Orthop Res* 7:208–218
417. Miot S, de Freitas PS, Wirz D, Daniels AU, Sims TJ, Hollander AP, Mainil-Varlet P et al (2006) Cartilage tissue engineering by expanded goat articular chondrocytes. *J Orthop Res* 24(5):1078–1085
418. Martin I, Obradovic B, Treppo S, Grodzinsky AJ, Langer R, Freed LE et al (2000) Modulation of the mechanical properties of tissue engineered cartilage. *Biorheology* 31:1–2

419. Bugbee WD, Convery FR (1999) Osteochondral allograft transplantation. *Clin Sports Med* 18:67–75
420. Hangody L, Feczkó P, Bartha L, Bodó G, Kish G (2001) Mosaicplasty for the treatment of articular defects of the knee and ankle. *Clin Orthop Relat Res* 391:S328–S336
421. Steadman JR, Rodkey WG, Singleton SB, Briggs KK (1997) Microfracture technique for full-thickness chondral defects: technique and clinical results. *Oper Tech Orthop* 7:300–304
422. Johnson LL (2001) Arthroscopic abrasion arthroplasty: a review. *Clin Orthop Relat Res* 391: S306–S317
423. Hoemann C, Sun J, McKee M, Hurtig M, Rivard GE, Rossomacha E, et al (2005) Rabbit hyaline cartilage repair after marrow stimulation depends on the surgical approach together with an in situ stabilized chitosan-GP blood clot. *Transactions 11th Canadian connective tissue conference*, 1372
424. Hoemann CD, Hurtig M, Rossomacha E, Sun J, Chevrier A, Shive MS et al (2005) Chitosan-glycerol phosphate/blood implants improve hyaline cartilage repair in ovine microfracture defects. *J Bone Joint Surg Am* 87:2671–2686
425. Gobbi A, Kon E, Berruto M, Francisco R, Filardo G, Marcacci M (2006) Patellofemoral full-thickness chondral defects treated with Hyalograft-C: a clinical, arthroscopic, and histologic review. *Am J Sports Med* 34:1763–1773
426. Benedetti L, Cortivo R, Berti T, Berti A, Pea F, Mazzo M et al (1993) Biocompatibility and biodegradation of different hyaluronan derivatives (Hyafl) implanted in rats. *Biomaterials* 14:1154–1160
427. Giroto D, Urbani S, Brun P, Renier D, Barbucci R, Abatangelo G (2003) Tissue-specific gene expression in chondrocytes grown on three-dimensional hyaluronic acid scaffolds. *Biomaterials* 24:3265–3275
428. Marcacci M, Berruto M, Brocchetta D, Delcogliano A, Ghinelli D, Gobbi A et al (2005) Articular cartilage engineering with Hyalograft C: 3-year clinical results. *Clin Orthop Relat Res* 435:96–105
429. Nehrer S, Domayer S, Dorotka R, Schatz K, Bindreiter U, Kotz R (2006) Three-year clinical outcome after chondrocyte transplantation using a hyaluronan matrix for cartilage repair. *Eur J Radiol* 57:3–8
430. Weidenbecher M, Henderson JH, Tucker HM, Baskin JZ, Awadallah A, Dennis JE (2007) Hyaluronan-based scaffolds to tissue-engineer cartilage implants for laryngotracheal reconstruction. *Laryngoscope* 117:1745–1749
431. Schneider U, Rackwitz L, Andereya S, Siebenlist S, Fensky F, Reichert J et al (2011) A prospective multicenter study on the outcome of type I collagen hydrogel-based autologous chondrocyte implantation (CaReS) for the repair of articular cartilage defects in the knee. *Am J Sports Med* 39:2558–2565
432. Welsch GH, Mamisch TC, Zak L, Blanke M, Olk A, Marlovits S et al (2010) Evaluation of cartilage repair tissue after matrix-associated autologous chondrocyte transplantation using a hyaluronic-based or a collagen-based scaffold with morphological MOCART scoring and biochemical T2 mapping: preliminary results. *Am J Sports Med* 38:934–942
433. Carmont MR, Carey-Smith R, Saithna A, Dhillon M, Thompson P, Spalding T (2009) Delayed incorporation of a TruFit plug: perseverance is recommended. *Arthroscopy* 25:810–814
434. Melton JTK, Wilson AJ, Chapman-Sheath P, Cossey AJ (2010) TruFit CB bone plug: chondral repair, scaffold design, surgical technique and early experiences. *Expert Rev Med Devices* 7:333–341
435. Kerker JT, Leo AJ, Sgaglione NA (2008) Cartilage repair: synthetics and scaffolds: basic science, surgical techniques, and clinical outcomes. *Sports Med Arthrosc* 16:208–216
436. McNickle AG, Provencher MT, Cole BJ (2008) Overview of existing cartilage repair technology. *Sports Med Arthrosc* 16:196–201
437. Joshi N, Reverte-Vinaixa M, Diaz-Ferreiro EW, Dominguez-Oronoz R (2012) Synthetic resorbable scaffolds for the treatment of isolated patellofemoral cartilage defects in young

- patients: magnetic resonance imaging and clinical evaluation. *Am J Sports Med* 40:1289–1295
438. Crawford DC, Heveran CM, Cannon WD Jr, Foo LF, Potter HG (2009) An autologous cartilage tissue implant NeoCart for treatment of grade III chondral injury to the distal femur: prospective clinical safety trial at 2 years. *Am J Sports Med* 37:1334–1343
 439. Kim HT, Zaffagnini S, Mizuno S, Abelow S, Safran MR (2006) A peek into the possible future of management of articular cartilage injuries: gene therapy and scaffolds for cartilage repair. *J Orthop Sports Phys Ther* 36:765–773
 440. Hoemann CD, Sun J, McKee MD, Chevrier A, Rossomacha E, Rivard GE et al (2006) Chitosan-glycerol phosphate/blood implants elicit hyaline cartilage repair integrated with porous subchondral bone in microdrilled rabbit defects. *Osteoarthritis Cartil* 15:78–89 (Epub 2006 Aug 8)
 441. Buschmann MD, Hoemann CD, Hurligt MB (2006) Cartilage repair: analysis and strategies. In: William RJ (ed) *Cartilage repair with chitosan/glycerol-phosphate stabilised blood clots*. Totowa Human Press, Totowa, pp 83–106
 442. Grigolo B, Lisignoli G, Piacentini A, Fiorini M, Gobbi P, Mazzotti G et al (2002) Evidence for redifferentiation of human chondrocytes grown on a hyaluronan-based biomaterial (HYAff 11): molecular, immunohistochemical and ultrastructural analysis. *Biomaterials* 23:1187–1195
 443. Pavesio A, Abatangelo G, Borriero A, Brocchetta D, Hollander AP, Kon E et al (2003) Hyaluronan-based scaffolds (Hyalograft C) in the treatment of knee cartilage defects: preliminary clinical findings. *Novartis Found Symp* 249:203–17; discussion 29–33, 34–8, 39–41
 444. Nehrer S, Dorotka R, Domayer S, Stelzeneder D, Kotz R (2009) Treatment of full-thickness chondral defects with hyalograft C in the knee: a prospective clinical case series with 2 to 7 years' follow-up. *Am J Sports Med* 37(Suppl 1):81S–87S
 445. Kon E, Di MA, Filardo G, Tetta C, Busacca M, Iacono F et al (2011) Second-generation autologous chondrocyte transplantation: MRI findings and clinical correlations at a minimum 5-year follow-up. *Eur J Radiol* 79:382–388
 446. Marcacci M, Zaffagnini S, Kon E, Visani A, Iacono F, Loretto I (2002) Arthroscopic autologous chondrocyte transplantation: technical note. *Knee Surg Sports Traumatol Arthrosc* 10:154–159
 447. Henderson I, Lavigne P, Valenzuela H, Oakes B (2007) Autologous chondrocyte implantation: superior biologic properties of hyaline cartilage repairs. *Clin Orthop Relat Res* 455:253–261
 448. Knutsen G, Drogset JO, Engebretsen L, Grontvedt T, Isaksen V, Ludvigsen TC et al (2007) A randomized trial comparing autologous chondrocyte implantation with microfracture. Findings at five years. *J Bone Joint Surg Am* 89:2105–2112
 449. Cole BJ (2008) A randomized trial comparing autologous chondrocyte implantation with microfracture. *J Bone Joint Surg Am* 90:1165; author reply –6
 450. Dhollander AAM, Liekens K, Almqvist KF, Verdonk R, Lambrecht S, Elewaut D et al (2012) A pilot study of the use of an osteochondral scaffold plug for cartilage repair in the knee and how to deal with early clinical failures. *Arthroscopy* 28:225–233
 451. Safran MR, Kim H, Zaffagnini S (2008) The use of scaffolds in the management of articular cartilage injury. *J Am Acad Orthop Surg* 16:306–311
 452. Weng Y, Cao Y, Silva CA, Vacanti MP, Vacanti CA (2001) Tissue-engineered composites of bone and cartilage for mandible condylar reconstruction. *J Oral Maxillofac Surg* 59:185–190
 453. Sharma B, Fermanian S, Gibson M, Unterman S, Herzka DA, Cascio B et al (2013) Human cartilage repair with a photoreactive adhesive-hydrogel composite. *Sci Transl Med* 5:167ra6, 10 pp